Investigating the Corrosion Behaviour and Pressureless Sintering of FeMn-Alloys for Biodegradable Implant Applications

by

Christabelle Tonna

Department of Metallurgy and Materials Engineering
Faculty of Engineering

A dissertation submitted to the Faculty of Engineering in partial fulfilment of the requirements of the award of Doctor of Philosophy in Engineering.

August 2023

L-Università ta' Malta

FACULTY/INSTITUTE/CENTRE/SCHOOL__ENGINEERING_____

DECLARATION OF AUTHENTICITY FOR DOCTORAL STUDENTS

(a) Authenticity of Thesis/Dissertation

I hereby declare that I am the legitimate author of this Thesis/Dissertation and that it is my original work.

No portion of this work has been submitted in support of an application for another degree or qualification of this or any other university or institution of higher education.

I hold the University of Malta harmless against any third party claims with regard to copyright violation, breach of confidentiality, defamation and any other third party right infringement.

(b) Research Code of Practice and Ethics Review Procedure

I declare that I have abided by the University's Research Ethics Review Procedures. Research Ethics & Data Protection form code _____4939_16042020_Christabelle Tonna_____.

☒ As a Ph.D. student, as per Regulation 66 of the Doctor of Philosophy Regulations, I accept that my thesis be made publicly available on the University of Malta Institutional Repository.

□ As a Doctor of Sacred Theology student, as per Regulation 17 (3) of the Doctor of Sacred Theology Regulations, I accept that my thesis be made publicly available on the University of Malta Institutional Repository.

□ As a Doctor of Music student, as per Regulation 26 (2) of the Doctor of Music Regulations, I accept that my dissertation be made publicly available on the University of Malta Institutional Repository.

□ As a Professional Doctorate student, as per Regulation 55 of the Professional Doctorate Regulations, I accept that my dissertation be made publicly available on the University of Malta Institutional Repository.

Copyright Notice

Abstract

FeMn alloys (Mn wt.% 30-35), have emerged as a particularly attractive option as a solution for the limitations presented by pure Fe as a biodegradable metal for temporary implants. Such alloys are antiferromagnetic and have shown in early publications that they could offer adequate mechanical properties and biocompatibility for orthopaedic applications. Another favoured approach involves alloying FeMn with noble elements like Ag, in order to create micro-galvanic couples, which in turn enhance corrosion. Despite the promise shown by these alloys in several publications, the understanding of their degradation mechanism remains limited, with multiple publications sharing similar materials and methodologies, reaching contradictory conclusions. This generally results either from short-span testing providing an incomplete picture of material behaviour, or limited consideration of the impact of testing parameters on the test outcomes.

In this work, the first of two major sections were aimed at the study of powder-processed Fe35Mn, and in select tests also (Fe35Mn)5Ag, using a variety of techniques to determine their behaviour over the first 24 h of testing. Potentiodynamic testing (PDP), electrochemical impedance spectroscopy (EIS) and *in situ* pH and dissolved oxygen (DO) micro-probe measurements at the sample surface, were some of the techniques used to gather this information. Tests were carried out in HBSS, HBSS containing Ca^{2+} (HBSS+Ca) and the latter with added bovine serum albumin protein (HBSS+BSA). Static immersion tests of Fe35Mn in the same electrolytes were carried out to provide information regarding the alloy's long-term degradation behaviour whereas *in vivo* testing in GAERS rats for 6 months was aimed at demonstrating how considerable the gap between *in vitro* and *in vivo* findings, really is.

All results pointed towards increased corrosion for both FeMn and FeMnAg when compared to Fe. Outcomes across all testing phases highlighted the impact of Ca^{2+} ions in the HBSS on the degradation of Fe-based alloys as the same

ions interact with phosphates in the solution and metal ions originating from the sample to create Ca/P-rich precipitates that act as a partially-protective barrier to further degradation. Although the same precipitates were unstable on the microgalvanically corroding FeMnAg surface, the charge transfer resistance for this material after 24 h was similar to that of FeMn. This and other supporting results indicated that noble-phase additions, while effective in accelerating corrosion over the short term, might not hold much promise for long-term effectiveness in the body. The same applies to the impact of MnO-inclusions, typically present in powder-processed FeMn samples, on corrosion. Whereas EIS measurements indicated that MnO inclusions could be behaving as micro-cathodes within the austenitic matrix, the behaviour of samples with and without MnO was indistinguishable after the first 24 h. When investigating the influence of BSA over the degradation of FeMn, results indicated that protein reduces the corrosion resistance *in vitro*. This was likely due to the tendency of BSA to chelate Ca^{2+} ions, which prevented or delayed the precipitation of Ca/P-precipitates and encouraged localised corrosion as opposed to the uniform corrosion observed in HBSS+Ca. Despite these findings, analysis of FeMn and FeMnAg pin surfaces tested in rat vertebrae for 6 months showed only signs of very limited uniform corrosion, even though FeMnAg accumulated a slightly thicker layer of corrosion products. Moreover, whereas Ca/P-precipitates and metal hydroxides were present on sample surfaces tested *in vivo*, the major product detected via XRD was $CaCO_3$; a product absent in all *in vitro* analyses. This highlights the need for further efforts to bridge the gap between *in vitro* and *in vivo* testing, as is the aim of international testing standards in the pipeline.

Apart from corrosion studies, FeMn is also the centre of development of multiple novel processing methods that allow this material to be processed into implants with the desired shapes and sizes. With most of these methods including the use of powder metallurgy, issues related to the high vapour pressure and high temperature reactivity of Mn need to be addressed. In fact, in the second part of the thesis, blended elemental (B35; blended Fe and Mn elemental powders), milled (M35; Fe and Mn intricately mixed but still present in their elemental form) and alloyed (A35; fully alloyed Fe35Mn) powders, were prepared using high energy ball-milling. Analysis was carried out through microscopy of

powders and pressed-and-sintered coupons, carbon analysis and thermal analysis techniques including thermogravimetry with mass-spectroscopy (TG-MS) and differential thermal analysis (DTA). Results indicated that the alloyed powder exhibited a lower tendency to oxidise compared to M35 and B35 powder. Carbon analysis also showed that an increase in ball milling time resulted in an increase in C content in the pre-processed powders due to enhanced diffusion of the organic process control agent over time. This led to the alloyed powders additionally having better carbothermal reduction capacity, allowing for further reduction of oxides as observed both in thermal analyses of powders as well as cross-sectional analysis of pressed-and-sintered samples. However, the high percentage of carbon content also led to precipitation of a higher amount of interconnected M_3C carbides at grain boundaries.

The same materials were then used in the preparation of cubic scaffolds using a modified replication method wherein the polyurethane foam used as a template in the traditional replication method, was replaced with a 3D-printed customised acrylate-based template, allowing for more control on the structure of the implant. The process was conducted in either of two configurations; *exposed*, where the sample was exposed to the sintering N_2-$5H_2$ atmosphere, and *shielded*, wherein the sample was covered by a stainless steel shield creating a micro-atmosphere around the sample surface. Results showed that the microstructures of the resulting scaffolds were less affected by the material used, be it M35 or A35, and more impacted by the processing configuration used. In general, samples contained an austenitic matrix from which in excess of 7 wt.% Mn was lost to sublimation and formation of mixed metal oxides and interconnected carbides. All these phases led to rather brittle structures. *Shielded* structures had superior microstructural homogeneity as a result of the micro-atmosphere formed whereas *exposed* structures had cores rich in carbides and edge struts richer in oxides. Carbothermal reduction assisted oxide removal from the surface, but kinetic limitations persisted leading to strut cores littered with oxides. This work highlighted the challenges in achieving the right balance to preserve the antiferromagnetic characteristic of these FeMn alloys, reduce oxidation and have effective carbothermal reduction.

Acknowledgements

I would like to start by thanking Prof. Ing. Joseph Buhagiar, not only for his supervision but also for his constant encouragement and unwavering support. This thanks is extended to my co-supervisors, Prof. Pierre Schembri Wismayer MD, Prof. Ing. Maurice Grech and Dr Arif Rochman, who all provided valuable insight related to their respective expertise.

The indispensable contributions of the technical team at the Department of Metallurgy and Materials Engineering laboratories deserve special mention. My deepest thanks to Ing. Mary Grace Micallef, Ing. James Camilleri, Mr. Nicholas Gingell, Mr. Noel Tonna, Mr. Daniel Dimech, Mr. Andrew Agius, Ms. Sara Rocio Morales Ballesteros, and Ms. Antonella Sammut for their unwavering technical support and the countless cups of solace-inducing coffee that sustained me throughout this doctoral journey. Acknowledgements also go to the staff and students at the Department of Anatomy laboratories, whose gracious assistance facilitated my sterile static immersion testing.

I am also profoundly indebted to Dr. Sviatlana Lamaka and Dr. Cheng Wang from the Hereon Institute in Geesthacht. Their gracious invitation to collaborate in their labs for several months provided me with invaluable insights into localized pH and DO measurements. Similar thanks goes to Prof. Raquel de Oro Calderon who welcomed me for a two-month stay at the Institute of Chemical Technologies and Analytics within the Technical University of Vienna for extensive thermal analysis. Her extensive expertise in powder metallurgy proved indispensable.

No words can adequately express my appreciation for the support of my closest friends and fellow students who either walked the walk with me in the lab, or in spirit. Thanks to Eleanor, Deandra, Jeanelle, Dylan, Yanica, Graziella, Luana, and Clayton. Their companionship made this journey not only academically rewarding but also personally enriching.

Last but not least, I want to thank my family for their support during this journey. Thanks to my parents and my brother who provided encouragement, advice, and motivation when I needed it the most. Without their support I wouldn't have been able to complete my thesis, and for that, I am endlessly grateful.

This project would not have been possible without the funding provided by the Malta Council for Science and Technology through the FUSION: R&I Technical Development Project for Project BioSA (Biodegradable Iron for Orthopaedic Scaffold Applications) (R&I-2017-037-T).

Publications

1. **C. Tonna** and L. Saliba, "Iron and its alloys for Bone Regeneration Scaffolds - A Review", *Xjenza Online*, vol. 7, no. 1, pp. 49–64, 2019. doi: 10.7423/XJENZA.2019.1.05.

2. **C. Tonna**, C. Wang, D. Mei, S. Lamaka, M. Zheludkevich and J. Buhagiar,"Biodegradation behaviour of Fe-based alloys in Hanks' Balanced Salt Solutions: Part I. Material characterisation and corrosion testing", Bioactive Materials, vol. 7, pp. 426-440, 2022. doi: 10.1016/j.bioactmat.2021.05.048.

3. C. Wang, **C. Tonna**, D. Mei, J. Buhagiar, M. Zheludkevich and S. Lamaka, "Biodegradation behaviour of Fe-based alloys in Hanks' Balanced Salt Solutions: Part II. The evolution of local pH and dissolved oxygen concentration at metal interface", Bioactive Materials, vol. 7, pp. 412-425, 2022. doi: 10.1016/j.bioactmat.2021.05.014.

4. L. Saliba, K. Sammut, **C. Tonna**, F. Pavli, V. Valdramidis, R. Gatt, R. Giordimaina, L. Camilleri, W. Atanasio, J. Buhagiar, P. Schembri Wismayer, "FeMn and FeMnAg biodegradable alloys: A biological *in vitro* and *in vivo* investigation", Heliyon, *Online access*. doi: 10.1016/j.heliyon.2023.e15671.

5. J. Buhagiar, **C. Tonna**, A. Rochman, M. Grech, A. Curmi, P. Schembri Wismayer. Process for production of metal scaffolds and foams. International application published under the Patent Cooperation Treaty (PCT) with an International Publication Number WO 2021/255195 A1, World Intellectual Property Organization (WIPO), International Bureau (2021).

Conferences Attended

1. **C.Tonna**, J. Buhagiar, "Investigating the effect of bovine serum albumin additions in Hanks' solution on the corrosion mechanism of powder-processed FeMn alloys", Presentation given at the 14th Symposium on Biodegradable Metals: 2022 Aug 24-28; Alicante, Spain.
   Awarded for 3rd best Oral Presentation.

2. **C. Tonna**, C. Wang, D. Mei, S. Lamaka, M. Zheludkevich, J. Buhagiar, "Biodegradable Fe-based alloys: The effect of electrolyte constituents on corrosion progression *in vitro*". Poster presented at the BIONECA conference for Emerging Biomaterials for Regenerative Cardiology and Neurology: 2021 Jul 27-29; Prague, Czech Republic.

Contents

List of Figures

List of Tables

Glossary

AAS	Atomic Absorption Spectroscopy
BCC	Body-centred Cubic
BCP	Biphasic Calcium Phosphate
BSA	Bovine Serum Albumin
CNTs	Carbon Nanotubes
CPE	Constant Phase Element
CT	Computed Tomography
DMEM	Dulbecco's Modified Eagle Medium
DO	Dissolved Oxygen
DPBS	Dulbecco's Phosphate Buffered Saline
DTA	Differential Thermal Analysis
DTG	Differential Thermogravimetry
EBSS	Earle's Balanced Salt Solution
EDS	Electron Dispersive Spectroscopy
EIS	Electrochemical Impedance Spectroscopy
FCC	Face-centred Cubic
FTIR	Fourier Transform Infrared Spectroscopy
HA	Hydroxyapatite
HBSS	Hanks' Balanced Salt Solution
HCP	Hexagonal Close Packed
HMTA	Hexamethylenetetramine
ICP-OES	Inductively Coupled Plasma – Optical Emission Spectroscopy
IEP	Isoelectric Point
LBPF	Laser Bed Powder Fusion
LMD	Laser Metal Deposition
LYS	Lysine

MA	Masteralloy
MEM	Minimum Essential Medium
MIC	Microbially-induced Corrosion
MRI	Magnetic Resonance Imaging
OCP	Open Circuit Potential
PCL	Polycaprolactone
PDP	Potentiodynamic testing
PCL	Polycaprolactone
PDP	Potentiodynamic testing
PGA	Polyglycolic Acid
PLA	Polylactic Acid
PLGA	Polylactic-co-Glycolic Acid
PU	Polyurethane
PVA	Polyvinyl Alcohol
SBF	Simulated Body Fluid
SCE	Saturated Calomel Electrode
SECM	Scanning Electrochemical Microscopy
SEM	Scanning Electron Microscope
SIET	Scanning Ion-selective Electrode Technique
SKPFM	Scanning Kelvin Probe Force Microscopy
SLA	Stereolithography
SLM	Selective Laser Melting
SPS	Spark Plasma Sintering
SVET	Scanning Vibrating Electrode Technique
TCP	Tricalcium Phosphate
TG-MS	Thermogravimetry-Mass Spectroscopy
TOPIF	Topologically Ordered Porous Iron Foams
TRIP	Transformation Induced Plasticity
TWIP	Twinning Induced Plasticity
UV	Ultraviolet
XPS	X-Ray Photoelectron Spectroscopy
XRD	X-Ray Diffraction

1

Introduction

1.1 Application overview

A number of studies over the years have claimed that bone is the second most transplanted tissue in the world [1]. This rank might be somewhat unexpected for those aware of bone's ability to regenerate in response to applied stimuli. However, the size of some defects caused by trauma, infection, cancer-removal surgeries and other medical procedures could extend beyond the bone's healing capacity. Such defects require assistance from natural or synthetic implants to encourage bone regeneration. To this end, it is estimated that over four million surgeries are done annually using bone substitutes or grafts [2].

The structure of bone, schematically illustrated in Figure 1.1, consists of two major components [3]. The spongy internal "cancellous" structure has around 50-90% porosity whereas the outer "cortical" shell is more dense having around 10% porosity [4]. Implants used for bone regeneration, collectively referred to as "bone scaffolds" are generally designed to be highly porous to mimic cancellous bone. They serve as a support structure, taking on the typical loads applied whilst also providing a surface onto which new bone can form. Many have discussed the ideal features and behaviour that should characterise the ideal scaffold [5–7]. Bose *et al.* [5] mention four core requirements:

1. **Porous structure** - The scaffold structure must have an interconnected porous network that allows for vascularisation, mobility of cells and general

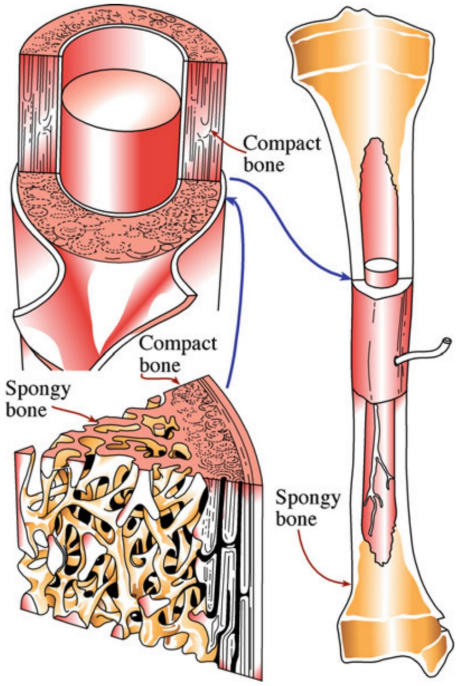

Figure 1.1: Schematic representation of the structure of bone [3].

mass transfer of physiological constituents that maintain regular bodily function [6]. There seems to be an agreement that the minimum pore size for this to be realised, should be 100 µm. The ideal porosity sizes reported in literature vary considerably with values within the range of 150 and 1200 µm all having been mentioned within the context of this subject. Microporosity has also deemed beneficial for tissue ingrowth due to resultant increase in surface area [7];

2. **Mechanical properties** - The vast range of pore volumes in cancellous bone implies an equally vast range of mechanical properties depending on the specific bone and patient. Yield strengths could vary between 0.5 and 200 MPa whereas Young's Moduli could span between 0.5 and 20 GPa [4]. The ideal mechanical properties should therefore be considered on a case-by-case basis with the ideal properties being as close as possible to the bone being replaced. Since bone tissue adapts itself to better cope with regularly applied loads according to Wolff's law [8], care must be taken not to design

scaffolds which are too stiff, due to risk of stress-shielding[1];

3. **Biodegradability** - Whereas permanent implants tend to result in need of a secondary intervention for implant removal, the use of degradable materials lends a significant advantage for patients in need of bone scaffolds. Not only would degradable scaffolds reduce the risks associated with permanent implants like loosening and long-term complications, but they could also be more effective in gradually transferring the applied loads onto the regenerated bone [5]. As with mechanical properties, it is impossible to cite an ideal *fixed* degradation rate since this is heavily influenced by the size of the defect, the features of the scaffold design as well the location of the implant. However, in a review by Zheng *et al.* [10], it was said that the implant should be able to provide sound mechanical support during the first 12 to 24 weeks and therefore, accelerated initial degradation as experienced by several materials of interest in the field, could be problematic at this stage;

4. **Biocompatibility** - The most obvious requirement, is biocompatibility. Both the material implanted as well as any degradation products should not elicit any local or systemic problematic effects in the host body. Osteoconductive and osteoinductive[2] characteristics are also desired in a bone scaffold [5]. In order to be compatible with MRI technologies, implants should also be non-magnetic [9].

1.1.1 Synthetic scaffold solutions and leading research

To this day, the gold standard implants used for bone regeneration surgeries, are autografts i.e. bone harvested from the patients themselves. Whilst this is

[1]Stress-shielding refers to the phenomenon where a significant difference between the Young's moduli of the implant and the bone results in misdistribution of applied loads with the bone bearing less than required for healthy regeneration. This could lead to an early onset of osteoporosis [9].

[2]Osteoconduction refers to the ability to allow bone forming cells to attach and proliferate on the materials for formation of new bone, whereas osteoinduction refers to the ability to *induce* new bone formation through interaction with the surrounding implantation environment [5].

considered to carry the least risk, use of autografts implies the necessity of a secondary surgery to extract the bone as well as the inevitable donor site morbidity. Naturally, the size of the autograft also carries a certain limit to avoid causing additional problems at the extraction site. The alternative is to use allografts. These are bones harvested from cadavers which carry higher risk of infection and disease transmission however as opposed to autografts, are not limited by size and availability [7].

Apart from harvested bone, bioceramics have also found their way into the market in the form of several calcium-phosphate compounds. Since the main component of bone is hydroxyapatite (HAp) ($Ca_{10}(PO_4)_6(OH)_2$), the similarity of Ca/P-based materials to this compound, results in bioactive characteristics which encourage new bone formation. Commonly studied compounds include α-tricalcium phosphate (α-TCP), β-tricalcium phosphate (β-TCP), β-tetracalcium phosphates and nano-HAp structures [1]. While these materials are widely available as pellets, wedges and blocks [11], recent research is making possible their availability as injectable cements which could lead to better defect filling and healing [12, 13]. For orthopaedic implantations, Ca/P-based materials generally exhibit good biocompatibility, resorption and osteoconductivity, however they are still considerably limited by their brittle nature and limited mechanical strength [1]. When it comes to ceramic materials, bioactive glasses composed of Na_2O, CaO, SiO_2 and P_2O_5 are also available on the market for a range of grafting purposes. With a devolopent history of over five decades, bioactive glasses and their degradation products today are both able to encourage ostegenesis, however, like most bioceramics they still lack the ability to be used in load-bearing scenarios due to their inherent brittleness [14].

Polymeric materials have been researched extensively over the past years. Natural polymers like chitosan, gelatin, alginate and collagen generally lack adequate mechanical strength and tend to degrade rapidly. Some synthetic polymers like polylactic acid (PLA), polyglycolic acid (PGA), polycaprolactone (PCL) and polylactic-co-glycolic acid (PLGA) have properties that can be widely adjusted, however, suitable initial mechanical properties, tend to be lost rapidly once put in the working environment [5]. Moreover, some synthetic polymers like PLA and PGA exhibit degradation reactions that are characterised by acidification of their

surroundings, which leads to a prominent autocatalyic effect that adversely effects cell proliferation and the healing process, despite the general biocomptability of the materials [1, 5].

1.1.2 Socioeconomic considerations and market trends

A recent study carried out by the University Medical Centre at Regensburg in Germany has analysed data provided by the German Federal Statistical Office related to bone substitute use in Germany between 2008 and 2018 [15]. The data revealed a clear increase in orthopaedic surgeries over the period but a decrease in the use of autologous grafts. The clinical shortcomings of autografts have led to an increase in use of allografts and an even higher increase of 23.8% in synthetic biomaterials. Of the latter, the plot shown in Figure 1.2 shows that while ceramics remain the most popular choice with orthopaedic surgeons, the use of newly developed biomaterials is on the increase. Despite this, one must not presume an increase in newly approved medical devices, as further regulatory burdens are being placed on manufacturers within the European Union, with regulations like the Medical Device Regulation (MDR) that came into force in May 2021 [16]. Strict recertification requirements have also led to multiple implant withdrawals

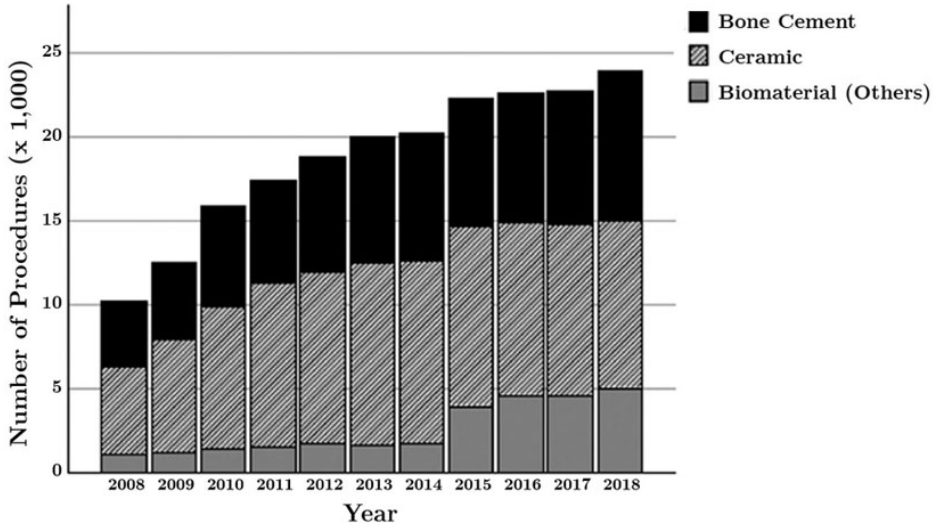

Figure 1.2: Statistics showing the total use of various biomaterials for bone reconstruction surgery, as used in Germany between 2008 and 2018 [15].

from the market [15]. In fact, most reviews on commercially available bone grafting materials, often list certified devices that are no longer obtainable.

When looking at products that *are* available for healthcare institutions, a significant portion consists of composite bone substitutes that synergise the osteoconductivity of bioceramics with the toughness offered by a polymeric matrix [1, 5, 19]. In fact, commercially available products like MasterGraft® by Medtronic, Vitoss® by Stryker, AlloMatrix® by Wright and CopiOs® by Zimvie are among bone substitutes consisting of Ca/P compounds coupled with natural polymers, often demineralised bone matrix (DBM) [20].

To the author's knowledge, synthetic polymer support structures have only been approved for periodontal applications, as in the case of Fishograft®, a PLGA copolymer by Ghimas. No biodegradable polymeric-based implant is available for use in load-bearing bone defects [21].

On the other hand, metallic scaffold structures have reached the market with Spineart's additively manufacture Ti-LIFE technology and Zimmer Biomet's Trabecular Tantalum™ [17, 18], both shown in Figure 1.3. Naturally, permanent scaffolds come with all the negative attributes of having permanent foreign body structures in the body, especially when their function is no longer required. This leads to the main topic of interest in this work; biodegradable metals.

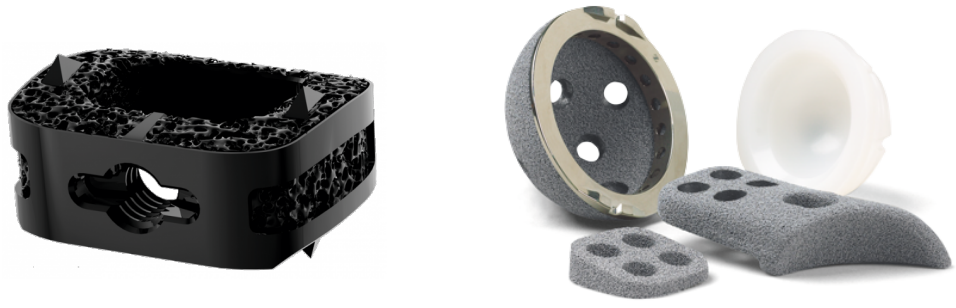

(a) **(b)**

Figure 1.3: Examples of (a) additively manufactured Ti scaffolds using TiLIFE technology [17] and (b) Trabecular Tantalum™ inserts [18].

1.2 Biodegradable Metals

Without a doubt, magnesium (Mg) has been the most studied metal in the field of biodegradable metals. Mg is non-toxic and its Mg^{2+} ions are present in abundance in the body with an active role in various metabolic activities. The main degradation product that forms upon contact with the physiological environment, is a non-toxic soluble oxide that can be safely excreted through the urinary tract [22]. The main persisting limitation of Mg, especially for applications in orthopaedics, is the exceedingly fast degradation rate which is accompanied by hydrogen evolution that could interfere with the natural healing process [23]. Additionally, while the mechanical property profile of most Mg-alloys lies within the range of properties exhibited by bone, they still remain rather inadequate for load-bearing implants.

The fruit of the worldwide effort put into the understanding and manipulation of Mg-based alloys for biodegradable implants, can be summarised by mentioning the successful award of the CE marking[1] to Biotronik's cardiovascular stent Magmaris, in 2016. Magmaris consists of a Mg-alloy containing rare Earth metals, zirconium and yttrium for improved radial strength. Its 150 μm^2 struts are coated with a 7 µm drug-eluting PLLA coating that retards its degradation such that complete resorption is completed only within the first 12 months, as the application requires. Clinical trials BIOSOLVE-I/IV [25–28] all led to encouraging results, and Biotronik went on to develop thinner strutted stents named DREAMS-3G, which are now also in clinical trial stage [29]. Despite huge leaps, Magmaris and DREAMS-3G are not yet available in clinics apart for use in human trials, however their advancement has in many ways motivated other groups in the field to push forward with their own developments [22, 23].

Zinc (Zn) and its alloys has also attracted significant attention in the field. With an electrode potential of -0.76 V vs SCE (Saturated calomel electrode), the driving force for degradation is slightly lower compared to that of Mg (-2.37 V vs SCE) which makes Zn and its alloys more attractive for orthopaedic applications where mechanical support by the implant is generally desired for a longer stretch

[1] CE markings indicate that the product meets the set safety, health and environment protection standards [24].

of time when compared to cardiovascular applications [30]. The main drawback of Zn and its alloys, is their comparatively poor mechanical properties. While these could be improved by strategic alloying, reviews on the subject still indicate that Zn-based implants are unlikely to be used for load-bearing orthopaedic applications [30]. Seperate *in vivo* studies with pure Zn stents implanted in rabbit [31] and rat [32] aortas have also brought to light that despite the lack of hydrogen evolution accompanying Zn degradation in the body, the exact corrosion mechanism is not yet properly understood, with both localised and uniform degradation modes observed in the different studies. Moreover, Zn-based degradation products including several oxides, hydroxides and phosphates, tend to be insoluble, which could impact the long-term biodegradability of the implants [30].

As recently as 2021, Redlich *et al.* [33] proposed molybdenum (Mo) as a new biodegradable metal candidate. In their initial studies, the authors showed that Mo corrodes uniformly over a period of 28 days, with thin non-passivating products forming on the surface. The degradation rate of around 10 µm/y is in line with the requirements set for temporary cardiovascular stents and the response to endothelial and smooth muscle cells was also promising when considering this application [33, 34].

1.3 Iron and its alloys

1.3.1 Background

While Fe is not as abundant as Mg and Zn in the body, it has a critical role in maintaining homeostasis. It is approximated that adults have 45-55 mg of Fe per kg of body weight, 70% of which is present in hemoglobin. A recommended daily intake of 1-2 mg of Fe is said to allow vital biochemical activities like oxygen transport to progress normally [35]. While Fe overload is associated with serious ailments, clinically approved therapies exist that allow for safe treatment should the level of serum ferritin or transferrin saturation exceed certain limits [36]. The vitality of Fe in the body, as well as its attractive mechanical properties led researches to explore its use for temporary load-bearing implants in 2001.

The first documented recommendation of Fe as a degradable material for cardiovascular stents, is the now famous study by Peuster *et al.* [37] wherein pure Fe stents were implanted in the descending aorta of sixteen New Zealand white rabbits. Although the study shows there was "no significant neointimal proliferation, no pronounced inflammatory response, and no systemic toxicity", a photo of an aorta cut-off in Figure 1.4, clearly shows that there was no significant degradation of the implanted stent despite signs of some corrosion product accumulation. Essentially, the stent behaved like a permanent implant.

Despite the insufficiently slow degradation rate shown in the first *in vivo* study, the mechanical advantages and early positive biocompatiblity results [38–40], fuelled interested research groups to address the corrosion limitation and study Fe alloys further. Compared to both Mg and Zn, the superior mechanical property profile of Fe [10] could allow stents and orthopaedic implants to be prepared from thinner sections without compromising functionality and without risking adverse effects to the patient [41]. Moreover, the degradation of Fe alloys does not generate harmful gas evolution as observed with Mg and its alloys.

The review presented in Section 2.1 of this work provides an in-depth evaluation of research on the degradation behaviour of Fe and prominent Fe alloys in the field. FeMn and FeMn alloyed with noble metals have attracted the interest of several different groups and are the focus of this research work. However, despite this interest, the understanding of Fe alloy corrosion in the body is far from un-

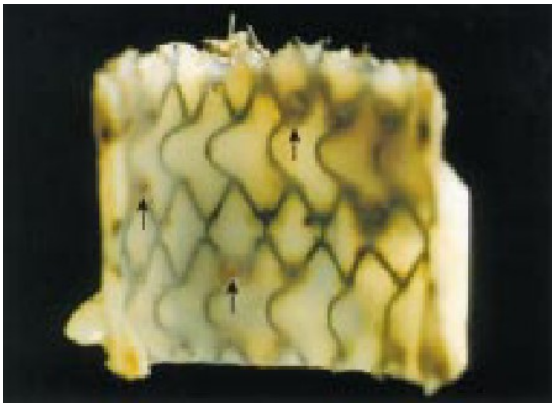

Figure 1.4: Cut-off of pure Fe stent in the aorta of rabbit 12 months after implantation. Arrows point at corroded material [37].

derstood. Many have explored different alloy preparation, elemental compositions and surface treatments in order to obtain more favourable degradation behaviour but few publications have dealt with the unavoidable and crucial influence of testing conditions, in particular electrolyte formulations, on the behaviour of the metal as well as its representativeness of the *in vivo* environment. This contrasts with the effort put into the understanding of Mg degradation wherein the influence of individual organic, inorganic and biological electrolyte constituents has been studied in detail [42], computational models have taken comprehension of degradation mechanisms to new heights [43] and countless *in vivo* studies have provided a sound basis for further implant development [44].

When it comes to processing of Fe-based alloys for biodegradable implant applications, powder metallurgy is by far the most popular route [19]. Over the years, some have conducted testing on dense coupons prepared using powder metallurgy while others have developed means to prepare macro-porous Fe-based scaffold structures that fit the requirements of the ideal scaffold outlined herein. More recently, other groups have taken such processes a step further in order to allow for fabrication of custom, ordered, porous geometries that could allow for improved properties as well as better bone healing by fitting unique patient defects. With such processes, a lot of the initial research is often done using Fe which serves well to test out concepts. However, as discussed in detail in the review presented in Section 2.2, processing using Mn in particular poses several challenges that have limited the successful implementation of these processes for more adequate alloy compositions for scaffold applications.

1.4 Scope of Research

The scope of this work is to enhance the understanding of the predominant degradation mechanisms for Fe-based alloys, with particular focus on powder-processed Fe35Mn for orthopaedic applications. This is to be done using a variety of techniques, including electrochemical testing, static immersion as well as specialised methods like *in situ* microprobe measurements that up till the time of testing, had never been used to provide detailed data in regards to these materials within the field. These *in vitro* methods as well as *in vivo* testing are to be used in tandem

to determine the impact of the sample composition and microstructure as well as the testing electrolyte formulation and testing environment on the degradation of the same materials over extended periods of time, and identify behavioural trends.

Considering current progress on processing of customised scaffolds for biodegradable applications, this work is also targeted at testing different powder pre-processing methods that could help reduce the well-known disadvantages of using Mn in powder processing, each described in detail in Chapter 2. Following this initial study, the scope is to also test out the feasibility of modifying the often-used traditional polyurethane replication method to prepare customisable porous scaffolds using Fe35Mn, presenting a new potential approach to prepare patient-specific solutions for bone regeneration.

A detailed list of aims and objectives for this dissertation is presented at the end of the literature review presented in Chapter 2, following which the scope of the dissertation with respect to gaps in literature, is easier to identify and highlight. For a detailed overview of research objectives, please refer to Section 2.5.

1.5 Thesis Structure

The following text is structured as follows. Chapter 2 presents a literature review that has been split in two major parts. The first part includes a review of relevant literature related to corrosion studies on Fe and FeMn-based alloys. The second part then highlights considerations that need to be taken when working with Mn powders as well as a review of current scaffold processing techniques. Detailed research questions and objectives are presented at the end of the chapter after the research gaps identified through the literature review are established.

Chapter 3 describes the materials, equipment and methodologies employed to achieve the results presented and discussed in Chapter 4. Both Chapters 3 and 4 are sectioned similarly. As with Chapter 2, these chapters are split in two major sections; *Corrosion testing* and *Powder-processing of FeMn for scaffold applications*. The corrosion testing section is further split up in five testing phases,

listed below, each contributing further knowledge on the corrosion behaviour of Fe-based alloys.

- **Phase One - Corrosion testing of porous alloys** - includes initial testing with microporous coupons prepared from Fe, FeMn and FeMnAg in commonly tested electrolytes;
- **Phase Two - Further corrosion analysis using EIS** - presents further analysis of microstructural influences on the corrosion behaviour of FeMn alloys;
- **Phase Three - Investigating the influence of BSA additions to Ca-containing HBSS using EIS** - includes corrosion analysis for tests carried out on FeMn alloys in protein-containing electrolyte;
- **Phase Four - Static Immersion testing** - includes results for static immersion tests with up to 28 days of immersion in various electrolytes of interest;
- **Phase Five - *In vivo* testing** - presents post *in vivo*-testing corrosion analysis.

The processing sections are similarly split up in three sub-sections. The first section presents detailed analysis of powders of interest prepared through various methods, to be used in subsequent sections. Following this, the same powders were pressed-and-sintered for microstructural analysis. The second section therefore shows the influence of the initial powders and varying sintering temperatures, on the resulting microstructures. Finally, promising powder materials analysed in the first two sections were used to prepare scaffolds using the modified replication technique, as described in detail in Chapter 3. Analysis of the resulting scaffold structures is presented in the final sub-section.

Main conclusions and suggestions for future work related to the two major investigations presented in this work, are listed and discussed in Chapter 5.

2

Literature Review

This review is split into two main sections. The first section is related to corrosion testing of Fe-based alloys including critical assessment of principal works in the field in relation to various aspects of material design and corrosion testing variables. The second part of the review is then focused on processing of Fe-based alloys using powder-metallurgy, moving from processing considerations, to a review of existent technologies and others in development.

2.1 Corrosion performance of Fe-based alloys

2.1.1 Degradation mechanism of pure Fe *in vitro*

In order to be able to address the issue of the slow degradation rate of pure Fe, one must first develop an understanding of the general degradation mechanism of pure Fe in physiological solutions. In a leading paper by Zheng *et al.* [10], the authors provide a general four-stage outline to describe the degradation of biodegradable metals in physiological solutions.

The process is initiated as the metal surface comes in contact with the electrolyte. Different regions with slightly distinct potential differences behave as local anodes and cathodes. At anodic sites, metal dissolution takes place following reaction 2.1. For pure Fe, the dominant reaction taking place at cathodic regions, is the reduction of dissolved oxygen in the electrolyte, as presented in reaction 2.2. Since both reactions need to be able to progress unhindered for

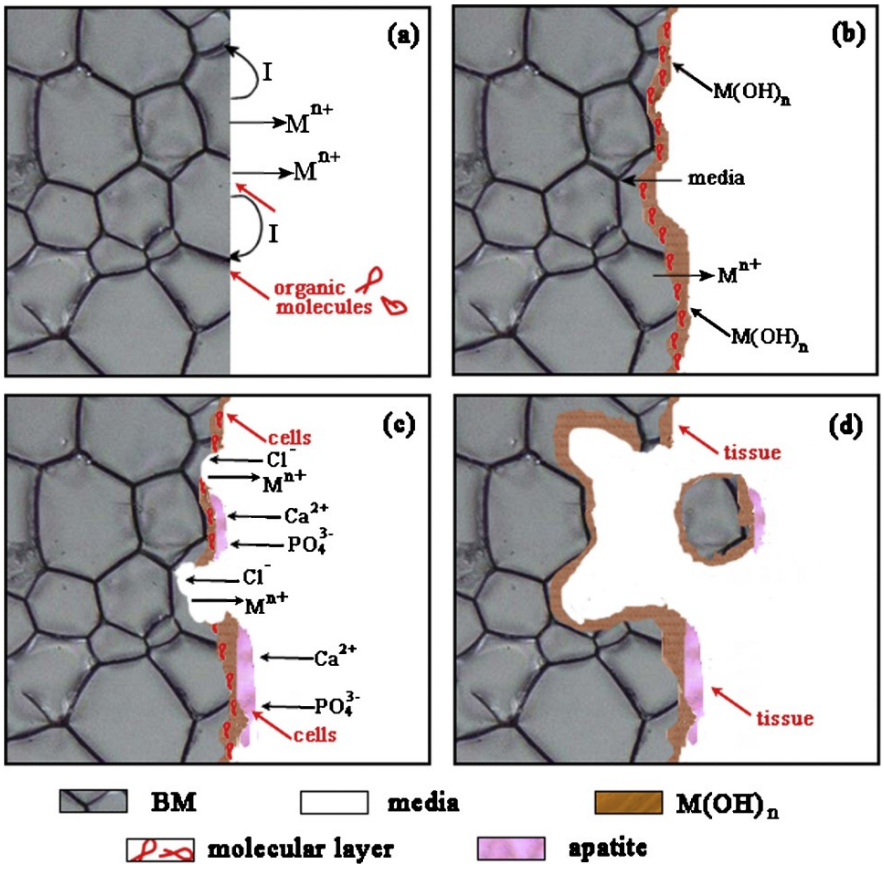

Figure 2.1: Schematic representation of the typical degradation process of pure Fe immersed in typical physiological media [10].

corrosion to take place, lack of availability of dissolved oxygen (DO) at the metal surface for the oxygen reduction reaction (ORR) to take place, could pose serious limitations in service as will be discussed [45]. For a pure Fe surface, grains and grain boundaries can serve as local cathodes and anodes respectively, as illustrated in Figure 2.1a [46].

$$Fe \rightarrow Fe^{2+} + 2e^- \tag{2.1}$$

$$O_2 + 2H_2O + 4e^- \rightarrow 4OH^- \tag{2.2}$$

The same figure illustrates the simultaneous adsorption of organic molecules, which could include protein and amino acids, for instance. Naturally, the adsorption of similar media *in vitro*, depends on the formulation of the testing

electrolyte and could significantly affect the corrosion progress, as discussed in Section 2.1.4.2 [10].

In the second stage, metal cations generated in reaction 2.1, react with OH^- ions in the electrolyte to form metal (II) hydroxide layers on the corroding surface according to reaction 2.3. Further oxidation in line with reaction 2.4, results in the formation of iron (III) hydroxides [46], as illustrated in Figure 2.1b.

$$Fe^{2+} + 2OH^- \rightarrow Fe(OH)_2 \tag{2.3}$$

$$4Fe(OH)_2 + O_2 + 2H_2O \rightarrow 4Fe(OH)_3 \tag{2.4}$$

Hermawan *et al.* [46] also describes the typical corrosion product formation as a layer of magnetite (Fe_3O_4) in contact with the metal surface, with a haematite (Fe_2O_3) layer on top.

As corrosion progresses, weak regions in the metal hydroxide layers are attacked by higher concentrations of H^+ generated in metal cation hydrolysis reactions, as shown in reaction 2.5 [47]. The presence of chloride ions in the medium results in the continued enlargement of generated pits as self-catalytic corrosion becomes dominant in pitted areas due to increasingly aggressive local environments [10, 46].

$$FeCl_2 + H_2O \rightarrow FeOH^+ + 2Cl^- + H^+ \tag{2.5}$$

The third stage illustrated in Figure 2.1c also depicts the formation of Ca^{2+}- and PO_4^{3-}-rich products on the corrosion products. Such hydroxyapatite-like products are often reported in corrosion product analysis in studies in the field when local conditions are favourable for their formation, and are considered to be a positive presence in biodegradable implant applications for the encouragement of bone attachment to the implant surface [48].

The final stage in Figure 2.1d illustrates the potential dislodging of eroded implant regions. Although this effect is commonly reported in the study of Mg-based alloys with rapidly progressing degradation leading to chunks of metal being removed from the main implant, Zheng *et al.* [10] indicate that this is less usually encountered with Fe-based alloys.

Published research articles including studies of pure Fe, have often reported that the unalloyed metal degrades 'uniformly'. Microstructural images of corrosion tested surfaces generally reveal uniformly corroded topographies with slight preferential attack of grain boundary regions as described in the model above [49–52]. Zhu *et al.* [52] speculated that degradation progressing with this corrosion mechanism could result in total degradation of a typical stent *in vivo*, within a month from implantation. However, as described in Section 2.1.4.4, this is rather unlikely when considering the additional influencing factors within the biological environment. Zhang *et al.* [51] also reported that the uniform degradation mechanism only progressed consistently up till 21 days of immersion, before the build-up of phosphates described in Figure 2.1c, limited the corrosion reactions. In two separate contradictory studies, preferential attack of grain boundary regions was not observed but the authors instead observed pits on the corroding Fe surfaces [53, 54].

As further discussed in Section 2.1.4.1, the processing method greatly impacts the corrosion progress and principal mechanisms. Obayi *et al.* [55] confirmed the theory originally published by Ralston *et al.* [56] that the corrosion rate decreases with decrease in grain size when testing in a passivating environment, due to a faster and denser formation of corrosion product layers that act as a barrier layer for further corrosion progress. Conflicting results were subsequently shared in a publication by Carluccio *et al.* [57] who concluded that Selective Laser Melted (SLM) Fe degraded faster when compared to cast Fe, due to the former's finer grain size. However, the authors also noted that higher dislocation and defect densities, as well as potential impurities in the SLM (selective laser melted) Fe microstructure, could also have contributed to a faster degradation rate. A similar conclusion was reached by Moravej *et al.* [39], who claimed that faster corrosion rates could be achieved with electroformed Fe when compared to cast microstructures due to the finer grain sizes achieved by the electroforming process, as well as the structural defects arising from the same processing technique.

2.1.2 Analytical techniques for corrosion analysis *in vitro*

This section aims to provide the foundations for understanding the corrosion testing results published in literature as well as those presented in this thesis. This overview of the most commonly used analytical methods for *in vitro* corrosion testing, will cover the basic principles governing the technique as well as the fundamental information needed for data interpretation.

2.1.2.1 Potentiodynamic testing and Tafel extrapolation

Potentiodynamic polarisation (PDP) testing is a popular technique used in the field as a means to obtain a relatively quick approximation of material corrosion rates. Electrochemical reactions taking place at the surface of a metal immersed in a solution, can be either anodic or cathodic, as mentioned when describing the general degradation mechanism of pure Fe. In the case of pure Fe, the anodic reaction corresponds to that of metal dissolution (reaction 2.1), whereas the cathodic reaction corresponds to the reduction of the electrolyte (oxygen reduction reaction, reaction 2.2). According to Faraday's Law, the rate at which electrons flow to and from the corroding surface as part of these reactions, can be described using the *corrosion current density* (also written as i_{corr} or i_o), which in turn is linearly proportional to the mass loss per unit area per unit time, or corrosion rate [58].

The value of i_{corr} could be measured and calculated using Tafel extrapolation. In order to generate a Tafel plot, the *open circuit potential*, OCP (also written as E_o or E_{corr}) is first established over a set period of time. The OCP corresponds to the potential, measured against a stable reference electrode, at which the rate of anodic and cathodic reactions is equal, resulting in a net current flow of zero. An applied potential sweep is then carried out at a set scan speed over a specific range of potentials, typically around ± 250 mV vs. OCP. The result is a semi-logarithmic plot of absolute current values against potential, as shown in Figure 2.2.

The plot shown in Figure 2.2 can be described using the Butler-Volmer equation which illustrates the dependency of the corrosion current on the applied potential. It also describes the non-linear behaviour of the current at relatively

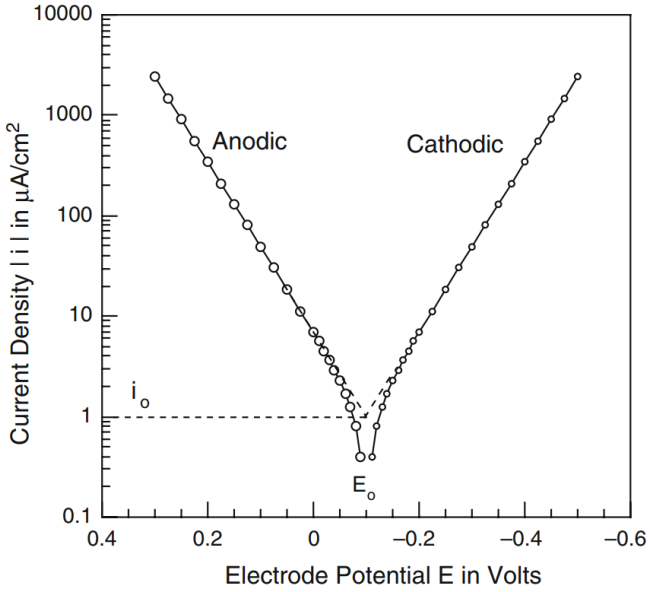

Figure 2.2: A sample plot of the Butler-Volmer equation with marked Tafel slopes [58].

small overpotentials ($E - E_o$, η), wherein the rate of the opposite reaction still has a significant influence over the measured current. When the applied overpotential, is significantly large, the influence of the opposite reaction becomes negligible so that the Butler-Volmer reaction could be given as

$$i = i_o e^{\alpha n F(E-E_o)/RT} \tag{2.6}$$

where i is the measured current, α is the charge-transfer coefficient, n is the number of electrons involved in the reaction, F is equal to Faraday's constant, E is the potential, R is the gas constant and T is the temperature in Kelvin [58]. Equation 2.6 could be rewritten as

$$\eta_a = b_a log \frac{i}{i_o} \tag{2.7}$$

where

$$b_a = \frac{2.303RT}{\alpha n F} \tag{2.8}$$

to describe the linear relationship between the anodic overpotential (η_a) and the

current generally observed at around 50-120 mV away from OCP [58]. Similarly

$$\eta_c = b_c log \frac{i}{i_o} \tag{2.9}$$

where

$$b_c = -\frac{2.303RT}{(1-\alpha)nF} \tag{2.10}$$

describes the linear relationship between the cathodic overpotential (η_c) and the current. Equations 2.7 and 2.9 are known as the Tafel equations whereas b_a and b_c describe the anodic and cathodic Tafel slopes respectively. Extrapolating the linear portion of the Tafel curves back towards E_o gives a value for i_o, as shown in Figure 2.2.

Although this method is widely used, one must keep in mind that this theory applies only under certain conditions.

1. Both reactions are under activation control i.e. the reaction is not dependant on a gradient concentration of certain ions or molecules around the η values mentioned above;

2. There is a clearly defined linear Tafel region within the overpotentials indicated;

3. The anodic and cathodic reactions do not vary over the potentials used in the test;

4. The corrosion that takes place is not localised i.e. "chunks" are not displaced from the surface [58].

2.1.2.2 Electrochemical Impedance Spectroscopy

2.1.2.2.1 Background

Electrochemical Impedance Spectroscopy (EIS) is a technique that uses small AC perturbations (generally up to 10 mV) across a range of frequencies, superimposed on an applied potential or the corrosion potential (OCP) of a system, to study its frequency-dependant response. EIS is widely used in the understanding of

corrosion reactions and mechanisms, batteries and photovoltaic systems and the characterisation of coatings, amongst others. For the study of electrochemical interfaces, a range of 10^{-2} to 10^{5} Hz is generally selected [58, 59].

EIS studies require systems to be at steady-state conditions for the duration of the measurement. The application of an AC signal allows the measurement equipment to characterise the behaviour as the system, or different aspects of a system, *relax* from one different steady-state to another, and back. As opposed to DC techniques where the instantaneous current response is frequency-independent and could be represented using the ideal resistor, AC systems use a combination of three main circuit elements, namely resistors, capacitors and inductors, to describe more complex behaviours using equivalent circuits. The test outcome is a measurement of impedance, which simply put, is the resistance to AC flow [58]. Dedicated software may be used to design equivalent circuit models to which the test data can then be 'fitted', providing values of interest related to corresponding physical system features.

2.1.2.2.2 Basics of equivalent circuits

A simple EIS experiment involves the application of a potential difference between two electrodes immersed in a typically highly conductive, ionic liquid. The flow of current through the latter could be represented electrically as a small solution resistance, R_s. At the electrode-electrolyte interface, current flow faces an additional resistance, known as the charge-transfer resistance, R_{ct}, as current flow transfers from electronic to ionic conduction. This parameter is highly dependant on the characteristics of the electrode, its ability to participate in electrochemical reactions as well as the adsorption of electrolyte molecules and ions to the electrode surface. Apart from this, electrical charges accumulated at the surface, attract oppositely charged solvated ions, creating what is known as the double-layer capacitance, C_{dl} [60]. The capacitive effect arises from the fact that hydrated ions are typically separated from electrode surfaces by a minimum distance d of 0.2 to 0.3 nm, creating a separation of charges [59]. There are multiple models that illustrate the electrical double layer. Figure 2.3a shows the Helmholtz representation of the electrode-electrolyte interface with negatively charged ions

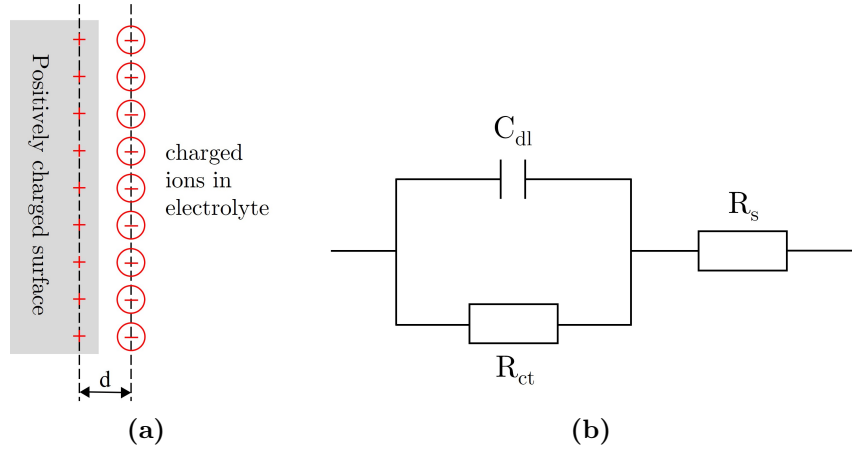

Figure 2.3: (a) Schematic representation of the Helmholtz model for electrical double-layer at the electrode-electrolyte interface [Adapted from [61]] and (b) Randles' equivalent circuit representing the electrode interface and adjacent solution resistance [Adapted from [58]].

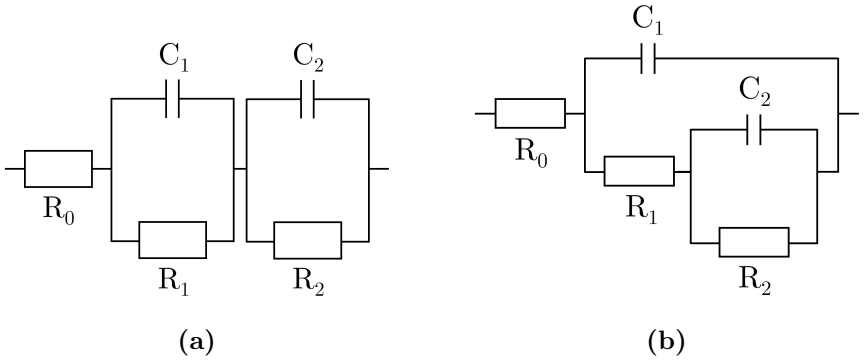

Figure 2.4: Two mathematically equivalent circuits with two time constants [Adapted from [62]].

adsorbed to a positively charged surface. One of the simplest and most referred to equivalent circuits, known as the Randles' circuit, electrically represents the simple scenario described above. A schematic representation of Randles' circuit is shown in Figure 2.3b, where the electrolyte resistance R_s is placed in a series connection to the electrode interface represented by a parallel connection of the charge transfer resistance R_{ct} and double-layer capacitance C_{dl} [58].

Randles' circuit is an example of a single-time constant equivalent circuit i.e. it represents a system in which there is a single charge-transfer controlled

process [60]. This time constant, τ, is a measure of the delayed response of a particular system to the alternating signal applied, and is the product of the resistance and the capacitance [58]. More complex systems typically consist of two or more time constants. Figure 2.4 shows two examples of equivalent circuits with two time constants. The circuit in Figure 2.4a is often used to represent the behaviour of a metal with a compact coating, whereas that in Figure 2.4b has been used to describe porous electrodes and electrodes with a porous coating, among other interpretations [60]. One must note that although some circuits like the ones shown in Figure 2.4, may be mathematically equivalent, choosing the incorrect one may not provide a good representation of the physical system under investigation, and can therefore still mislead the researcher [62].

2.1.2.2.3 Data representation and interpretation

When analysing equivalent circuits, the standard rules of electrical circuitry apply. The total impedance for n elements connected in series and the total impedance for n elements connected in parallel, are given in equations 2.11 and 2.12 respectively [59].

$$Z = \sum Z_n \tag{2.11}$$

$$\frac{1}{Z} = \sum \frac{1}{Z_n} \tag{2.12}$$

The impedance of a resistance, a capacitance and an inductance, can be expressed using equations 2.13, 2.14 and 2.15 respecitvely [58].

$$Z_R = R \tag{2.13}$$

$$Z_C = -\frac{1}{j\omega C} \tag{2.14}$$

$$Z_L = j\omega L \tag{2.15}$$

where R is the resistance in ohms (Ω), C is the capacitance in farads (F), L is the inductance in henries (H), ω is the radial frequency of the AC signal in rads^{-1} and j is the imaginary number $\sqrt{-1}$.

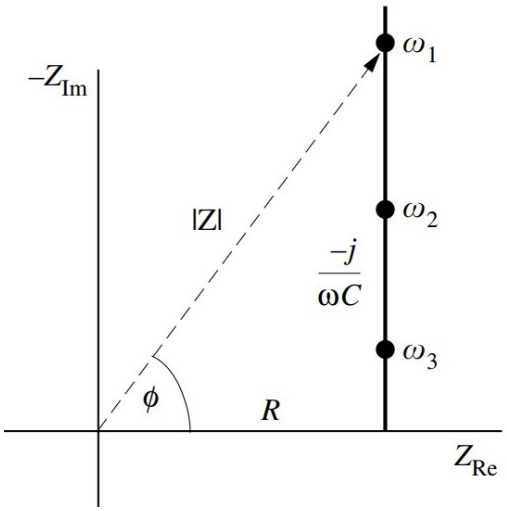

Figure 2.5: Impedance vector for a resistance and capacitance connected in series, represented on the complex plane [59].

As evidenced by the presence of the complex number j, the impedance has both real (Z_{Re} or Z') and imaginary (Z_{Im} or Z'') components. Z_{Re} represents the resistive part of the circuit, whereas Z_{Im} represents the ability of the system to store energy [60]. Therefore, impedance can be graphically represented as a vector with modulus impedance $|Z|$, at an angle ϕ representing the phase shift present between the applied potential and the current response. The phase shift for an ideal resistor is equal to 0° whereas for a capacitor and an inductor it is -90° and 90°, respectively. The schematic representation of the impedance of a resistor and capacitor connected in series on the complex plane, is shown in Figure 2.5.

The Nyquist diagram is commonly used to show both the real and imaginary components of impedance at different frequencies. Figure 2.6a shows a Nqyuist plot for a sample Randles' circuit illustrated in the same figure. Nyquist plots maintain their popularity as they allow for relatively quick estimation of key impedance parameters. The resistances R_t and R_Ω for instance, could be easily read off the Z_{Re} scale, while the presence of a perfect semi-circular loop indicates that there is only one time-constant [60].

Another commonly used plot for EIS data is the Bode plots which includes a log $|Z|$ against the log frequency plot, alongside a plot of phase shift against the same x-axis. This is represented for the same sample Randles' circuit, in

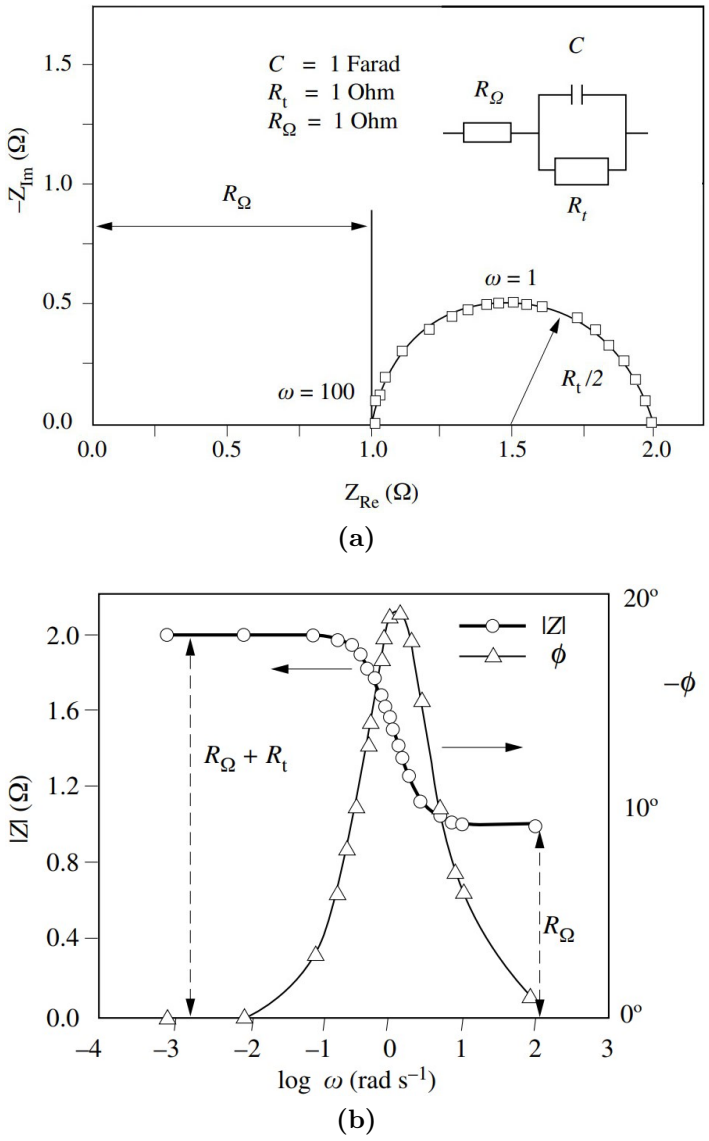

Figure 2.6: (a) Nyquist and (b) Bode impedance diagrams for a sample Randles' equivalent circuit [Adapted from [59]].

Figure 2.6b. Apart from giving a clearer picture of system behaviour at specific frequencies, Bode plots provide an easier way to determine the 'path-of-least-impedance' for a given frequency. In the example shown, low- and high-frequency ranges indicate that the circuit reached 'near DC' conditions as the 0° phase shifts indicate only resistive contributions. The lower phase shift in mid-frequency ranges on the other hand point towards the influence of the circuit's capacitance.

2.1.2.2.4 Physical interpretation of Constant Phase Elements

Real systems rarely behave in the ideal way represented by Randles' model or other circuits illustrated in Section 2.1.2.2.2. For the simple equivalent circuit of a double layer capacitance connected in parallel to the charge transfer resistance, the Nyquist plot often takes the shape of a *depressed* semi-circle, as opposed to the perfect semi-circle illustrated in Figure 2.6a. Contributions to this deviation can be both through geometric and energetic surface heterogeneity, although some have argued that the latter has a more prominent effect on Constant Phase Element (CPE) behaviour [63]. Although, there has not yet been a widely acknowledged correlation between surface roughness and CPE values, this surface feature along with defect dispersion, porosity, fractal geometry and surface reactivity dispersion, have all been listed in multiple works as contributors to CPE behaviour [59, 64]. It has therefore become common practice to replace capacitors with CPEs, in most scenarios.

The impedance of a CPE can be represented by

$$Z = \frac{1}{Q(j\omega)^{\alpha}} \tag{2.16}$$

where Q is the CPE coefficient in S.s^n and α is the CPE exponent. Both values are independent of frequency. When $\alpha = 1$, the CPE behaves like a perfect capacitor whereas when $\alpha = 0$, it behaves like a resistor.

Despite the usefulness of CPEs for improving the goodness-of-fit of modelled data, the values associated with the element offer little insight into the physical understanding of the system features or behaviours it represents. For instance, equation 2.17 can be used for instance to derive the thickness of a coating from the coating's true capacitance value.

$$C = \frac{\varepsilon_0 \varepsilon A}{l} \tag{2.17}$$

where ε_o is the dielectric constant of free space, ε is the dielectric constant of the electrolyte and A is equal to the exposed area in cm^2. The CPE coefficient cannot be used in a similar fashion. There has therefore been many studies investigating a reliable approach for the conversion of CPE values to true capacitance. One

of the more widely used equations was suggested by Hsu *et al.* [65], where for a parallel R-CPE branch, the capacitance may be calculated using equation 2.18.

$$C = R^{\frac{1-\alpha}{\alpha}}.Q^{\frac{1}{\alpha}} \tag{2.18}$$

It is reported that this equation only gives a reliable conversion for relatively high values of α [65].

2.1.2.2.5 Physical representation of diffusion phenomena

The model of the electrode-electrolyte interface described by Helmholtz in Figure 2.3a, is by far one of the simplest representations. The Stern model adds a diffuse layer adjacent to the double-layer, to depict a region containing a higher concentration of the counterions depicted in Figure 2.3a as they move towards the charged surface. This, and other diffusion-controlled systems, may require the addition of a diffusion impedance element to the equivalent circuit. Taking Randles' circuit as an example, Figure 2.7a shows the incorporation of the *Warburg* element; a commonly used diffusion element with a phase shift ϕ = -45°. As shown in Figure 2.7b, this element is represented using a 45° straight line at the low-frequency impedance region of a Nyquist plot [58].

The original Warburg model is based on a number of strict assumptions, described in detail by Huang *et al.* [66], that are considerably difficult to achieve in real-life scenarios with complex porous electrodes, as will be used in this work.

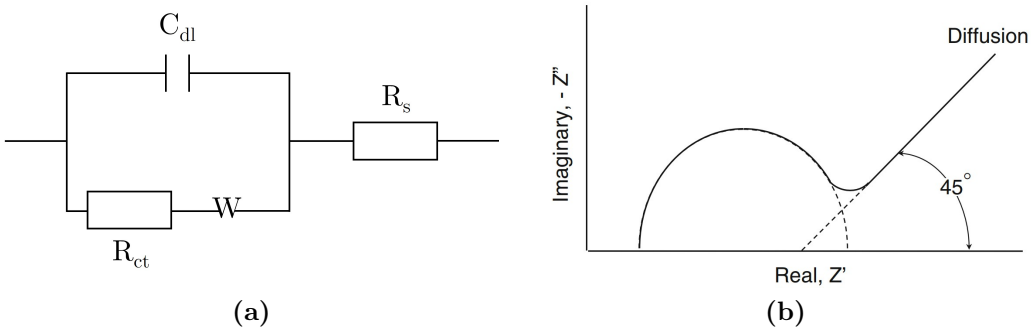

Figure 2.7: (a) Randles' equivalent circuit with additional Warburg diffusion impedance, W and (b) its Nyquist representation [Adapted from [58]].

Although a complete understanding of the effect of various pore features on diffusion phenomena is beyond the scope of this work, it is important to note that simple changes in the pore geometry, tortuosity factor[1], packing density, as well as whether the pores are open or closed, cause significant deviations from the standard Warburg behaviour, as shown in a study by Cooper *et al.* [67].

2.1.2.3 Weight loss measurements

The weight loss method is generally used to calculate the corrosion rate of the material after relatively long immersion times. The samples are removed from the immersion setup at set intervals and dried for analysis. The corrosion rate could be calculated following careful removal of the generated corrosion products, typically using chemical or electrochemical means, although mechanical methods could be opted for in some cases [58]. The ASTM-G1 standard (*Standard Practice for Preparing, Cleaning, and Evaluating Corrosion Test Specimens, 2012*) [68] offers a list of methods that could be used with specific groups of materials including iron and steels. The amount of weight lost could then be related to the corrosion rate in mm/y using equation 2.19 [68].

$$Corrosion\ rate = \frac{(8.76 \times 10^4)W}{ATD} \tag{2.19}$$

where W is the mass loss in grams, A is the exposed area in cm^2, T is the time of exposure in h and D is the density in g/cm^3. One of the drawbacks of this technique, especially when considering existing literature, is the difficulty in properly assessing whether the corrosion products were in fact removed with the chosen cleaning method and whether or not the underlying material was also subject to material removal. Moreover, there are numerous instances in publications in the field wherein the authors provide weight loss measurements but do not provide any information about the material removal procedure or clearly state that corrosion products were not removed at all. More on the limitations and considerations related to weight loss measurements will be discussed in Section 2.1.4.3.

[1]Tortuosity factor refers to the resistance to diffusive flow due to complexity of flow paths.

2.1.2.4 *In situ* measurements at corroding surface

The wide-ranging studies on Mg alloys in the field has led to the application of particularly specialised methods for better understanding of reactions happening within micrometers of the surface as a result of active corrosion and interactions with the local testing environment.

Scanning Vibrating Electrode Technique (SVET) has been used to measure current density distributions over active surfaces [69–72] as opposed to calculating one i_{corr} value for a system using potentiodynamic testing or weight loss measurements. Moreover, evaluation of calculated corrosion rates and analysis of corroded surfaces often lead to hypotheses regarding potential multi-stepped corrosion mechanisms including the effects of pH changes on localised reactions. Although such hypotheses are sometimes based off bulk pH measurements, research on Mg alloys has showed that corrosion is primarily affected by local environment changes that are not necessarily noticeable in bulk measurements [73–75]. For Mg alloys, where the principal cathodic reaction is the hydrogen evolution reaction, local measurement of incresed alkalinity using the Scanning Ion-selective Electrode Technique (SIET) or Scanning Electrochemical Microscopy (SECM) could help identify cathodic regions on the surface. Likewise, an increase in OH^- resulting from oxygen reduction (reaction 2.2) on corroding Fe-based alloys, could help improve the understanding of local phenomena, especially when either SVET or SIET is coupled with dissolved oxygen measurement techniques, as exemplified in [69].

So far, there has been no published work including localised measurements on biodegradable Zn and Zn-based alloys. Published *in situ* measurements on corroding Fe and Fe-based alloys only include the work presented in this thesis, all of which has been published in peer-reviewed journals [76, 77].

2.1.3 Material design for corrosion acceleration

2.1.3.1 Addition of secondary elements

Corrosion acceleration through the addition of alloying elements can be achieved in two principal ways as outlined by Schinhammer *et al.* [78]:

- by adding an alloying element that is soluble in Fe, resulting in a material with a lower corrosion potential, or
- by adding an element that results in a secondary phase that is more noble than Fe, thus creating a microgalvanic cell within the same material.

Both strategies have been extensively studied as presented in the following sections.

2.1.3.1.1 FeX

The addition of a single element or phase to the Fe matrix through alloying or surface manipulation, has rendered numerous interesting studies. A brief overview of the performance outcomes from key publications will be provided in this section. However, despite several positive results, these studies fail to address the limitation of ferromagnetism that the ferrous component of these materials retains.

Liu *et al.* [40] were first to test the suitability of a variety of alloying elements typically used to strengthen steel. In their work they prepared Fe-3wt.%X alloys were X varied from manganese, cobalt (Co), aluminium (Al), tungsten (W), tin (Sn), boron (B), carbon (C) and sulphur (S). Co, W, C and S were found to be effective in increasing the potentiodynamic corrosion rate in Hanks' solution, although the increase was rather low. Despite the fact that this study deemed certain alloying elements unsuitable for the biodegradable implants, the amounts added were rather low and using different ratios could yield more favourable results, as shown for FeMn in the following section.

Despite the common use of phosphorus (P) as a corrosion inhibitor in steel manufacture, the effect of adding P below and above the solubility limit in Fe, was studied by multiple groups [79–81] yielding conflicting results. Whereas Wegener *et al.* [80] measured slightly increased corrosion rates after 7 days immersion in Simulated Body Fluid (SBF) with the addition of 0.6 and 1.6 wt.% P, the other studies noted a slight reduction in corrosion rate with Fe containing approximately 0.5 wt.% P.

Čapek *et al.* [82] used palladium (Pd) as the alloying element in the preparation of single phase Fe2Pd by Spark Plasma Sintering (SPS). A three-fold increase

in corrosion rate was recorded for Fe2Pd following a 70-day immersion test in SBF when compared to Fe. In a series of studies by Huang *et al.*, 5 wt.% of Pd, platinum (Pt) [83], gold (Au) and Ag [84], were added to Fe and processed using the same method. With the addition of Pd, i_{corr} doubled when compared to Fe, whereas with the addition of Pt, the i_{corr} value was seven times that measured for Fe. Results from the 30-day immersion test followed a similar pattern. In the case of Pd and Pt, the used wt.% was always within the solubility limit, however a more commonly adopted strategy is the addition of a noble metal to create a strong galvanic couple between the Fe matrix and formed intermetallic phases or immiscible noble elements. This was the result achieved with the addition of Au and Ag where the noble metal inclusions resulted in accelerated microgalvanic corrosion all over the sample surfaces leading to macroscopically uniform corrosion in both immersion and electrochemical tests [84].

Conflicting results were published by Čapek *et al.* [85] and Wegener *et al.* [80] in relation to the performance of FeAg alloys. Čapek *et al.* prepared Fe2Pd, Fe2Ag and Fe2C using powder metallurgy. Both static immersion tests and potentiodynamic tests confirmed that whereas corrosion was increased with the addition of Pd and C, the formation of AgCl on the surface prevented further corrosion of the Fe2Ag alloys. Wegener *et al.* reported only a small improvement in corrosion following immersion testing, but mainly attributed the measured increase to the higher surface area exposed to the electrolyte rather than the Ag contribution. One must note that in both studies the tests were conducted in SBF whereas Huang *et al.* [84] carried out tests in an unspecified Hanks' solution. The effect of electrolyte composition on corrosion performance will be discussed in more detail in Section 2.1.4.2.

Other attempts at creating a microgalvanic effect using an FeX design has been made with 316L stainless steels [86–88], Zn [53, 89, 90], W [91, 92], carbon nano-tubes (CNTs) [91] and more recently, tantalum (Ta) [93]. All studies bar those involving alloying with 316L stainless steel, showed an increase in degradation under test conditions. Adding up to 5 wt.% Fe_2O_3 to Fe also resulted in accelerated corrosion behaviour as confirmed using both immersion, PDP and EIS testing [94]. A more bioactive design includes the incorporation of bioglasses or biodegradable ceramics that do not have the necessary property profile to be

used for load-bearing applications, like hydroxyapatite (HA) [95–97], tricalcium phosphate (TCP) [96–98], biphasic calcium phosphate (BCP) [96, 97] and calcium silicate [99]. All cited works generally observed an increase in degradation with the tested composites *in vitro*, in part because the ceramics themselves are designed to dissolve with time.

2.1.3.1.2 FeMn

Without a doubt, FeMn alloys have been the most studied Fe alloys in the field. Originally suggested by Hermawan *et al.* [100], FeMn alloys with a certain wt.% Mn could overcome the ferromagnetic limitation of pure Fe and most Fe alloys through the formation of FCC γ-austenite or HCP ε-martensite, while offering potential for improved corrosion rates. The material design in itself forms part of the first strategic approach suggested by Schinhammer *et al.* [78], as Mn with an electrode potential of -1.18 V, could effectively increase the corrosion susceptibility by shifting the electrode potential of Fe downwards from -0.44 V [78]. Moreover, the formation of ε or BCC α'-martensite could also result in significant strengthening apart from potential mechanical property improvements through solid-solution strengthening [101]. While the FeMn phase diagram illustrated in Figure 2.8a indicates that the incorporation of above approximately 28 wt.% Mn should lead to a fully austenitic structure, it does not explain the complexities of martensitic transitions for FeMn systems. Figure 2.8b shows the phase fractions measured on quenched cast FeMn alloys indicating that lower Mn concentrations favour the formation of α'-martensite whereas higher concentrations lead to ε-martensite formation upon rapid cooling or applied strain [101, 102].

In their first studies Hermawan *et al.* [100, 105] showed how as-pressed and sintered Fe35Mn with an austenitic microstructure exhibited promising magnetic, mechanical and degradation behaviour with almost eight times the corrosion rate of pure Fe as measured using PDP tests in Hanks' solution [100, 105]. Consequent studies by the group, explored the potential of varying Mn content in the range 20-35 wt.% [46, 106]. As-sintered Fe20Mn and Fe25Mn exhibited a biphasic austenitic and ε-martensite microstructure whereas Fe30Mn and Fe35Mn consisted only of austenite in the as-sintered condition. Clearly, biphasic microstruc-

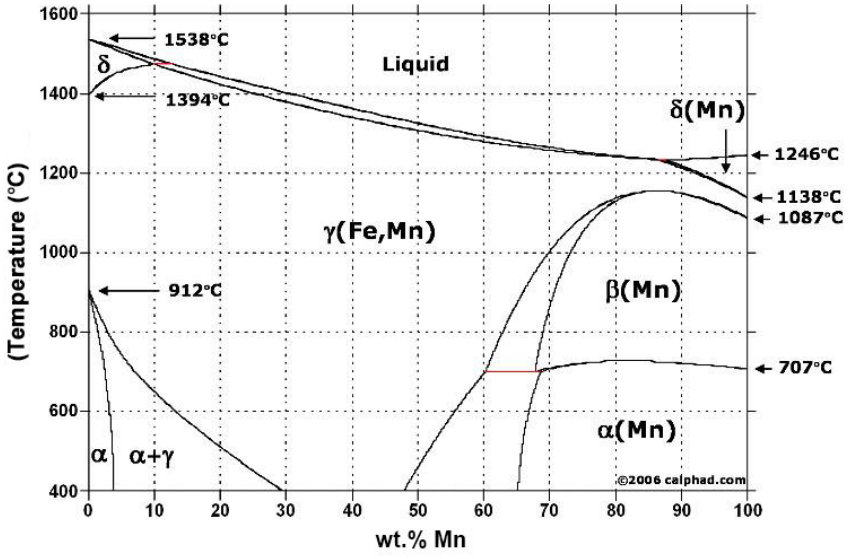

(a)

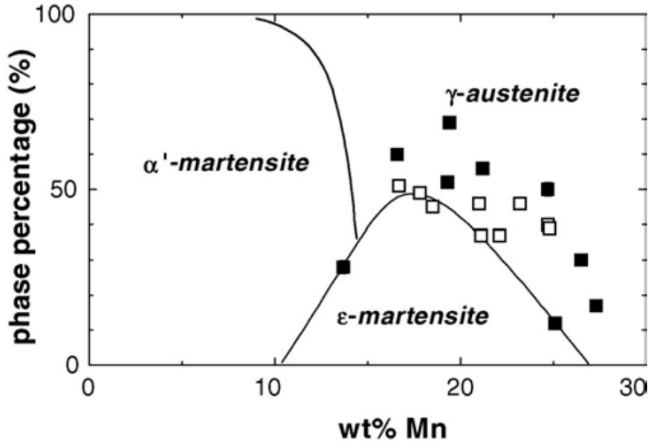

(b)

Figure 2.8: (a) FeMn equivalent phase diagram [Adapted from [103]] and (b) relative fraction of phases of quenched as-cast FeMn [101]. Filled and open boxes in (b) refer to experimental data obtained in [101] and [104], respectively.

tures led to a microgalvanic corrosion mechanism resulting in higher PDP corrosion rates. Static immersion tests of the same materials did not indicate a similar difference in corrosion rates in the initial study [46] while dynamic immersion tests confirmed the initial observations [106]. The influence of testing conditions on corrosion will be discussed further in Section 2.1.4.3.

Dargusch *et al.* [107] also observed biphasic austenitic and ε-martensite as-sintered microstructures with 20, 30 and 35 wt.% additions of Mn. However, as opposed to the previously mentioned studies, the corrosion rate increased with an increase in Mn content as confirmed with PDP and immersion tests in Hanks' solution. EIS results also indicated reduced resistances of both charge transfer resistance as well as corrosion product resistances with the addition of Mn, although the modelling of the EIS spectra in this study is not particularly convincing. Shuai *et al.* [108] reported similar austenitic/martensitic microstructures with selective laser melted (SLM) Fe25Mn and noted doubled corrosion rates with localised grain boundary attack following static immersion tests in SBF. Kupkova *et al.* [109] achieved two-phase sintered Fe25Mn, Fe30Mn and Fe35Mn structures however in this case grains had ferritic cores with austenitic shells due to insufficient homogenisation during heat treatment. The authors noted accelerated localised corrosion of such structures in PDP tests, with the ferritic cores corroding preferentially. Similar trends were observed in a study by Dehestani *et al.* [110] on powder-processed Fe30Mn. Sotoudeh Bagha *et al.* [111] noted increased PDP corrosion rates with pressed fully austenitic Fe30Mn whereas Chou *et al.* [112] reported eleven times the i_{corr} of Fe when PDP testing dense 3D-printed Fe30Mn. Contrastingly, Čapek *et al.* [113] measured much slower corrosion rates for hot-forged Fe30Mn compared to Fe following a 10-week immersion test in SBF, however this seems to be the only study where such a decrease was published.

In an effort to reduce any risks associated with Mn release *in vivo*, some have studied the effectiveness of additions of low concentrations of Mn on corrosion behaviour. Static immersion testing of Fe3Mn in Hanks' solution [40] and Fe(0.7-6.9)Mn in physiological saline [114] led to lower corrosion rates of the wrought FeMn alloys when compared to pure Fe prepared in the same way. These results stunted further research on similar alloys and focused research on alloys with over 20 wt.% Mn.

When it comes to corrosion product formation, the addition of Mn also implies that the oxidation of Mn in reaction 2.20, is another potential anodic reaction during corrosion.

$$Mn \rightarrow Mn^{2+} + 2e^{-} \tag{2.20}$$

In fact, various studies have detected products like MnOOH, $Mn(OH)_2$ and Mn_2O_3 among corrosion products often following immersion tests [46, 107]. Different studies provide different and often contradicting views on the influence of the corrosion products formed on the corrosion resistance of the corroding metal. Dargusch *et al.* [107] concluded that the intermixing of Fe and Mn-oxides result in lattice mismatch that facilitate ion transfer through the layer and enhance corrosion. On the other hand, in a study by Heiden et al [115], there was no observed corrosion for Fe20Mn tested in osteogenic medium in the first 50 days of immersion due to the protective effect of oxides. In most cases, the identification and influence of specific corrosion products, especially when it comes to oxides/hydroxides, tends to come down to the authors' hypotheses based on SEM/EDS analyses. Therefore, the exact influence of Mn oxides/hydroxides and other Mn-rich products, remains a question that needs further investigation.

2.1.3.1.3 FeMnX

The approach with FeMnX alloys is generally similar to that adopted with FeX alloys, with the added benefit of the antiferromagnetic characteristics if strategic amounts of Mn and/or other austenite stabilising elements are incorporated.

A number of studies have been published on FeMnC alloys, more often referred to as TRIP (Transformation Induced Plasticity) and TWIP (Twinning Induced Plasticity) steels. As the names imply, the addition of carbon is mainly aimed at improving the mechanical properties thus making it possible to have better strength to volume ratios for cardiovascular and orthopaedic applications alike. The alloys have been shown to have attractive degradation characteristics although it must be said that most articles do not study the specific influence of C addition on degradation. Hufenbach *et al.* [116] reported almost double the corrosion rate of vacuum-melted Fe30Mn1C when compared to Fe1C as measured using PDP testing. Gebert *et al.* [117] tested the same material in various NaCl concentrations and pH values and in each case, the Mn-enriched boundaries in the alloy served as sites for preferential attack such that signs of active dissolution were observed in each testing solution, as opposed to pure Fe. Interestingly, Gambaro *et al.* [118] showed that C has a stronger austenite-stabilising ability

than Mn when Fe12Mn1.2C had a fully austenitic microstructure as opposed to biphasic Fe20Mn0.6C. However, as opposed to the work by Hermawan *et al.* [46], the alloy containing 20 wt.% Mn had a slightly lower corrosion rate than that containing 12 wt.% after 14 days immersed in Hanks' solution despite its biphasic structure. On the other hand, this could be due to faster formation of $MnCO_3$ which protected the alloy from further dissolution. Having said this, in their review Venezuela *et al.* [45] also mention similar outcomes from another study wherein fully austenitic Fe30Mn1C exhibited faster corrosion rates than biphasic γ and ε Fe30Mn.

In famously referenced work, Schinhammer *et al.* [78] first suggested the addition of Pd to FeMn to enhance the corrosion microgalvanically through the formation of finely dispersed intermetallic (Fe,Mn)Pd inclusions. Following 48 h of static immersion in SBF, the authors recorded approximately 2, 0.5 and 0.15 mg/cm^2 weight loss for Fe10Mn1Pd, Fe10Mn and Fe respectively. A similar pattern was confirmed using EIS wherein the FeMnPd alloy exhibited the lowest |Z| values. In a subsequent study, the authors increased the Mn content to overcome the formation of martensitic phases. Similar results were obtained as Fe, Fe21Mn0.7C and Fe21Mn0.7C1Pd exhibited a corrosion rate of 0.2, 0.13 and 0.1 mm/year respectively based on weight loss measurements; results that were once again supported by EIS measurements [119].

Liu *et al.* [120] were the first to suggest the use of FeMnSi for biodegradable applications due to their unique shape-memory alloy characteristic. In their work they presented rather contradictory results on the alloys' degradation. Whereas PDP results indicated that vacuum-melted Fe30Mn6Si corroded fastest in Hanks' solution followed by Fe30Mn and Fe, surface analysis following a 6 month immersion period indicated that Fe was covered in a brownish corrosion product whereas the bright surface of the FeMn surface was clearly visible indicating lower corrosion rates. No clear explanation was provided for this contradiction, however other studies seem to support the results obtained through PDP testing. Drevet *et al.* [121] also studied vacuum melted Fe(23-30)Mn5Si alloys in Hanks' solution and confirmed through PDP and weight loss measurements that all FeMnSi alloys corroded faster than Fe30Mn. The authors also hypothesised that SiO_2 nonmetallic inclusions could have accelerated corrosion by behaving cathodically, although

no proof was published. In a number of research articles Xu *et al.* [122–125] studied the performance of sintered FeMnSi alloys. Notably, an increase from 0 to 4 wt.% Si in sintered and forged Fe28MnxSi led to an increase in corrosion rate from 15.8 to 21.1 μA/cm^2, as measured in SBF from PDP tests [122].

Various degrees of success in corrosion increase were achieved with the addition of 10 wt.% hydroxyapatite to Fe30Mn [126], additions of up to 2 wt.% Mg and Ca to Fe35Mn [127] as well as Fe30Mn1C0.8Cu [128] and Fe(35-x)Mn-xCu (x = 0-10wt.%) [129], among others.

2.1.3.1.4 FeMnAg

The study of FeMnAg deserves particular attention due to the widespread interest in the alloy within the field. Considering the relatively high standard electrode potential of silver at 0.7996 V [84], and the immiscibility of Ag with both Fe and Mn according to both the FeAg and AgMn phase diagrams, the microstructure of FeMnAg should give rise to strong microgalvanic corrosion. In fact, Niendorf *et al.* [130] used Scanning Kelvin Probe Force Microscopy (SKPFM) to confirm that the Ag-rich phase is cathodic with respect to a TWIP FeMn matrix. Apart from this, using Ag to add a noble phase, is a much more economic option than Pd for instance.

In a series of articles, Sotoudeh Bagha *et al.* [131] added 1-3 wt.% Ag to Fe30Mn and noted a decrease in corrosion rate from 2.61 to 2.31 mm/y based on PDP tests in Hanks' solution. However, they also noted an increase in density, and in turn a decrease in surface area, with increase in Ag concentration. In fact, with similarly dense coupons processed from nanostructured powders, the same test indicated an increase in corrosion rate from 0.25 to 0.58 mm/y for Fe30Mn and Fe30Mn3Ag respectively [111]. Dargusch *et al.* [132] also tested the addition of 1 wt.% Ag to powder-processed Fe30Mn in the same solution and continued to confirm that FeMnAg tends to corrode faster than FeMn. The authors emphasised that while weight loss measurements following a 30 day immersion period indicated a similar trend, the corrosion rates calculated were much lower than those derived from PDP tests. Caligari Conti *et al.* [133] had already made this observation in a previous study where they studied the effect of adding 2

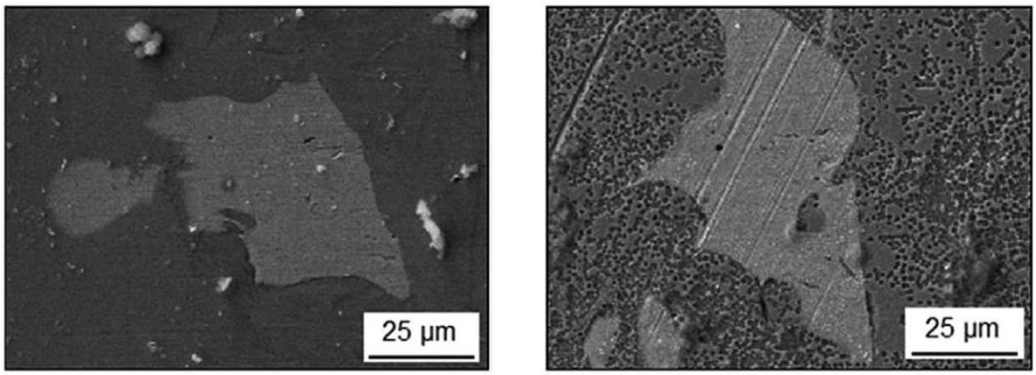

(a) (b)

Figure 2.9: SEM micrographs of FeMnC5Ag (a) before and (b) after 38 h of EIS testing [134].

to 5 wt.% Ag to Fe30Mn, also through powder metallurgy. Whereas when PDP testing in Phosphate Buffered Saline (PBS), the corrosion rates for FeMn(2-5)Ag were around 6 times those for FeMn, there was no statistically relevant difference between the corrosion rates calculated following a 14-day immersion test.

The addition of 5 wt.% Ag to Fe22Mn0.6C processed using SLM was studied mainly via EIS testing by Wiesener *et al.* [134]. Analysis of the surface clearly showed that the Ag-rich phase was cathodically protected while the FeMn matrix closest to the same phase showed distinctly more aggressive dissolution as the FeMn further away got progressively more decoupled from the cathode driving the anodic reaction. This was also observed by Dargusch *et al.* [132]. Micrographs of FeMnCAg before and after electrochemical testing are shown in Figure 2.9. Higher activity near the Ag-rich phase however, led to facilitated deposition of protective oxides and phosphates on the area resulting in early deactivation of its cathodic capacity. The higher total impedances measured for the FeMnAg alloy when compared to FeMn also confirmed this [134]. Similarly, when adding 0.6-1.2 wt.% Ag to Fe30Mn6Si, Babacan *et al.* [135] indicated that although the inclusion of Ag increased corrosion current densities with respect to Fe30Mn, higher concentrations led to a rapid decrease in current density due to precipitation of AgCl on the Ag-rich surface, which reduces its activity, as indicated by Čapek *et al.* [85] with Fe2Ag.

Liu *et al.* published work on the study of vacuum-melted FeMnAg alloys and proposed Fe30Mn5Ag for further study due their superior mechanical and degradation characteristics when compared to other tested formulations (0-10 wt.% Ag) [136]. They were the first and only group to label the cathodic Ag-rich phase as Ag_3Fe_2. ICP-OES testing of the Hanks' solutions used in a 14-day immersion test also interestingly revealed, that Mn ions were much more abundant in solution as opposed to Fe ions, which the authors indicated were used in the formation of insoluble Fe-based corrosion products.

The principal works that disputes the corrosion accelerating ability of Ag, are the recent studies by Loffredo *et al.* [137, 138] on cold-rolled Fe16Mn0.7C0.4Ag. Both electrochemical and long term (180 days) immersion tests indicated that there were no appreciable differences in the corrosion behaviour of FeMnCAg and FeMnC alloys. In their first study, contrary to general assumption, they observed pits on the surface of FeMnC following 14 days immersion, whereas the FeMnCAg alloy remained relatively smooth. They attributed this observation to a potentially accelerated corrosion reaction upon immersion, which rapidly passivated the surface to an extent [137]. However, further studies showed that both FeMnC and FeMnCAg alloys followed a similar pattern of relatively fast corrosion rate during the first 2 months, at which point predominant $MnCO_3$ corrosion products give way to a thin dense layer of phosphate-rich products which reduce the corrosion rate to a stable near-nil level during the consequent 4 months.

2.1.3.2 Surface modifications and coatings

Over the years, other techniques like ion implantation and micro-patterning emerged, allowing for a secondary phase to be present up to a few nanometers to micrometers from the surface of the Fe coupon. Huang *et al.* [139] achieved encouraging results when ion implanting Ag in Fe, whereas Cheng *et al.* [50] and Huang *et al.* [49] reported accelerated and macroscopically uniform degradation when surface patterning using Au and Pt respectively. The issue with this approach is that the microgalvanic effects only last as long as the integrity of the

surface layer allows [49, 139] apart from the fact that the processing technique is often limited to application on flat or relatively simple geometries.

When it comes to applying coatings to Fe-based metals especially for orthopaedic applications, the vast majority of studies involve bioceramic coatings aimed at creating improved bioactivity. However, hydroxyapatite-like materials as coatings has not had positive effects on corrosion accleration [140, 141]. Others suggested the use of a sputtered gold layer to enhace degradation [142]. The best results have been achieved by biodegradable polymer coatings. Iron coated with poly(lactic-co-glycolic) acid (PLGA) [143], polylactic acid (PLA) [144, 145] and polyethyleneimine (PEI) [146, 147] have all led to corrosion rate increases. In general, polymer hydrolysis tends to result in locally lowered pH that could accelerate Fe dissolution or dissolve formed corrosion products including iron hydroxides, leading to less hindered charge transfer [143, 144].

Naturally, this is not a comprehensive overview of the work done on surface modification and coatings. A more detailed overview could be found in published reviews including [41, 45, 48, 148].

2.1.4 Influencing factors on degradation behaviour

Having primarily seen the influence of alloying elements on the corrosion behaviour of Fe-based alloys, it is also worthwhile to analyse the effects of other influences that are less often reviewed in existing publications.

While cross-publication correlations can be made in the coming sections, the review is more focused on work wherein the impact of specific parameters were studied by a single group of investigators so as not to overlook other potential testing factors that may have a measurable sway over the results.

2.1.4.1 Effect of processing technique

The influence of grain boundary area on the corrosion behaviour of pure Fe has already been touched on in Section 2.1.1 wherein the conflicting conclusions of Obayi *et al.* [55] and Carluccio *et al.* [57] were presented. In general, it is agreed that grain boundaries tend to lead to accelerated degradation due to associated higher energy levels. However, whereas Carluccio *et al.* noted that corrosion

rates were higher for SLM and Laser Metal Deposited (LMD) samples which had higher grain boundary area compared to cast Fe, Obayi *et al.* showed that larger grain boundary areas led to slightly decreased corrosion rates in both PDP and static immersion tests. The latter attributed this to the faster initial degradation of fine grained samples leading to early onset of a "barrier" effect by accumulated metal oxides.

Elemental distribution is another aspect that is highly dependant on the processing parameters. Dehestani *et al.* [110] used coarse (30-200 µm) and fine (< 44 µm) Fe mixed with Mn to prepare pressed and sintered Fe30Mn coupons. Due to relatively large diffusion distances involved with the use of coarse Fe powder, the samples failed to form a complete FeMn solid solution leading to ferritic grain cores with austenitic shells which contrasted with the homogenous austenitic microstructures formed when using fine Fe powder. The biphasic microstructure in the former coupled with higher porosity due to less efficient sintering, resulted in corrosion rates of 1.36 ± 0.09 mm/y as opposed to 0.29 ± 0.05 mm/y. Kupková *et al.* [109] observed the exact same "onion-like" microstructure in Figure 2.10 when preparing sintered Fe(25, 30, 35)Mn samples which led to similar results with Fe-rich cores degrading preferentially. However, such elemental segregation is not solely possible in pressed and sintered metals. Shuai *et al.* [108] showed very similar microstructures with SLM-processed Fe25Mn. Despite ball-milling the FeMn powders for 2 h prior to SLM, which should in itself have homogenised the mixture, heavy segregation led to some areas in the microstructure having only 2.6 wt.% Mn. Although the authors did not provide a specific explanation for this segregation, it is likely that the fast laser scanning speeds of 3 $\mathrm{m\,s^{-1}}$

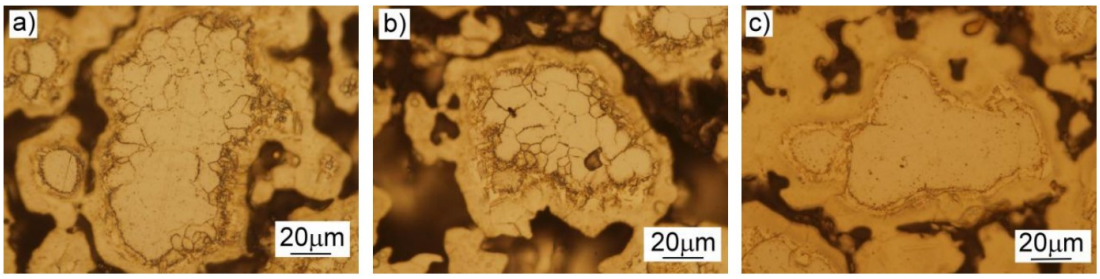

Figure 2.10: "Onion-like" microstructures of sintered Fe25Mn, Fe30Mn and Fe35Mn with Fe-rich cores and Mn-rich outer layers [109].

could have led to this effect as well as uncharacteristically large pores. In fact, Liu *et al.* [149], observed similar Fe-enriched areas when preparing SLM-Fe20Mn using various speeds between 700 and 900 $mm\,s^{-1}$, but not at the comparatively low 600 $mm\,s^{-1}$. Once again in this case, higher laser scanning speeds led to increased porosities as well as high stresses induced due to fast cooling, which also elicited the formation of a higher amount of a second non-equilibrium phase, α'-martensite. As is often the case, in this study, biphasic structures also exhibited higher i_{corr} values.

Internal stresses were also commented on by Moravej *et al.* [39] when testing electroformed Fe. Annealing of the electroformed coupons reduced some of the stresses induced from fast cooling of the part and resulted in lowered corrosion rates as measured in multiple immersion tests. One must mention that annealing also caused the average grain size to increase from 4 µm to 6 µm which might have also played a role in reducing the corrosion rate due to decreasing grain boundary area.

However, rapid cooling rates are not the only cause for induced stresses. Varying studies with contrasting outcomes were published related to the effects of internal stresses caused by cold work. The corrosion rate of Fe15Mn0.7C as measured from weight loss data by Loffredo *et al.* [137] increased with increase in cold work from 0 to 50%. Interestingly, the addition of just 0.4 wt.% Ag removed any influence of cold work on the corrosion rate. No statistically significant differences in PDP and weight loss data were reported in another study on Fe14Mn1C wherein the influence of up to 20% cold work was investigated [150]. In this case, no phase changes or drastic changes in grain size were recorded as a consequence of cold work, which might have had something to do with the lack of observed changes in corrosion behaviour. In another study 77% cold work of cast Fe20Mn led to a 43% *decrease* in PDP corrosion rate, however the authors did not provide a clear indicator of what could have caused this rather unexpected result [151]. On the other hand, the same study suggested that strains induced from simple machining operations such as turning during sample preparation, also has an influence on the corrosion rate. In fact, oxides generated due to degradation at the machined surface, were much finer grained compared to the core of the coupon,

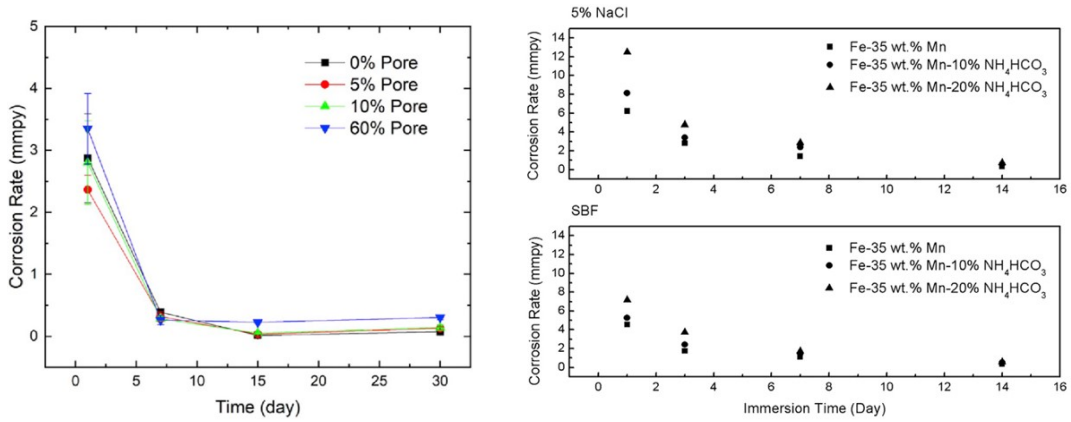

(a) **(b)**

Figure 2.11: Corrosion rate evolution of (a) Fe30Mn with varying porosity immersed in α-MEM [152] and (b) Fe35Mn with varying porosity immersed in 5% NaCl and SBF [153].

which eventually resulted in destabilisation of the corrosion product layer during immersion tests, followed by an increase in corrosion rate after 50 days.

With sintered samples, porosity has also been shown to increase internal stresses in the material. Huang *et al.* [152] prepared porous Fe30Mn with varying percentage porosity and detected higher concentrations of stress induced α'-martensite with increase in volume porosity. In this case, the higher corrosion rate exhibited by more porous samples could be partially attributed to microgalvanic corrosion, but also to the increased surface area resulting from the higher percentage porosity.

Irrespective of processing method and testing conditions, higher surface area in general leads to more metal exposed to the testing electrolyte [105, 152–156]. What is often observed when surface area is the primary cause for faster degradation, is that it is only effective in the first few days of *in vitro* testing, as shown in multiple immersion testing studies with different testing conditions [152, 153]. After a certain number of days, the corrosion rates decrease and converge irrespective of the original sample porosity, as illustrated in the plots in Figure 2.11. However, Zhang *et al.* [153] also commented on the stability of corrosion products on highly porous surfaces, mentioning that corrosion products on Fe35Mn samples with around 48.2% porosity tended to "lose intactness" as opposed to those

present on 27.3% porous samples - a characteristic that could lead to sudden increases in corrosion as the freshly corroded metal is once again exposed.

An aspect that is rarely discussed is the influence of contaminants or oxides in the samples, especially with powder processed materials when containing Mn or other oxygen-sensitive constituents. MnO for instance, is a very stable oxide that is often difficult to eliminate from sintered FeMn alloys, as described in more detail in Section 2.2.2.1. Hermawan *et al.* [105] studied how MnO inclusions evolve with cold work and theorised about the potential cathodic role of such inclusions in Fe-based microstructures. There is no current literature available that indicates the specific influence of MnO inclusions on the corrosion rate however many have overlooked its presence in their materials and its potential impact on their results, sometimes even mislabelling MnO peaks in XRD data [107, 108, 110].

2.1.4.2 Effect of testing electrolyte

The logistical difficulties of carrying *in vivo* testing has made *in vitro* corrosion testing indispensable in screening proposed materials and identifying potential modifications for further development. However, decades after the emergence of the biodegradable metals field, researchers are still faced with a complete lack of testing protocols. While this applies for all testing variables, this section emphasises the influence of the electrolyte on testing outcomes. As mentioned when discussing the influence of processing parameters, this lack of standardisation means that reliable comparisons could only be made within work carried out by individual groups. Values lose most of their meaning when they are a result of any number of variable parameters.

2.1.4.2.1 Typically used electrolytes and additional constituents

The list of commonly used electrolytes for *in vitro* testing can be split in three main categories.

Simple saline solutions are NaCl solutions, most often with a NaCl concentration of 0.9 wt.%, known as physiological saline. This formulation is widely known to be both highly aggressive and too simplistic to represent the *in vivo* environment. More complex saline solutions like Ringer's and Phosphate Buffered Saline

(PBS), contain other chlorides and in some recipes, HCO_3^-. In their simplicity, such electrolytes are generally most useful for comparing the behaviour of materials and excluding the influence of precipitates or complex interactions between ions originating from the metal and from the electrolyte [42].

More regularly encountered in literature is the use of Simulated Body Fluid (SBF), the recipe of which varies considerably from one study to the other, even when referred to with a more specific name like Hanks' Balanced Salt Solution (HBSS) or Earle's Balanced Salt Solution (EBSS). In contrast to saline solutions, SBFs may also contain HCO_3^-, the $HPO_4^{2-}/H_2PO_4^-$ pH buffer system, Ca^{2+} and SO_4^{2-}, synthetic pH buffers and glucose [42].

Even more complex solutions are cell culture media. While the inorganic constituents of these solutions are similar to those found in SBFs, cell culture media contain bio-relevant organic molecules that allow cells to grow in biological research. Due to these organic molecules, the susceptibility of these solutions to microbial infestation is very high, limiting their use in non-sterile conditions to a few hours. Using antibiotics could help prevent microbial growth however one must keep in mind that even antibiotics could effect ongoing reactions, as was found for Mg [157]. While the most complex media, may seem to be the most representative of the *in vivo* environment, Mei *et al.* [158] studied the individual influence of typical inorganic and organic ions found in these solutions and noticed little correlation between changes in corrosion rates of Mg and organic molecules in their usual concentrations. On the other hand the combined effect of Ca^{2+}, HPO_4^{2-} and HCO_3^- present in most SBFs, strongly decrease the corrosion rate of Mg, whereas the absence of either one of these three favours accelerated corrosion [75].

Another aspect of testing electrolytes that has been studied in detail for Mg and its alloys, relates to pH buffering systems. HEPES and Tris/HCl buffers have both been proven to accelerate the corrosion of Mg in multiple publications [157, 159]. Apart from interacting with OH^- and Mg^{2+} ions, delaying precipitation of protective phosphates, carbonates and oxides, localised pH measurements revealed that the pH is not actually buffered by HEPES and Tris/HCl, neither at the corroding surface, nor in the bulk [73]. When testing Zn, Wang *et al.* [160] and Liu *et al.* [161] both found that HEPES and Tris buffers successfully

control the pH close to the corroding surface but interfere similarly with the ions in solution, and therefore are still not ideally used.

In reality, the system that matches the pH buffering employed by the body, is the bicarbonate buffer system (HCO_3^-/CO_2) [42]. This operates according to Le Chatelier's principle wherein the bicarbonate in the electrolyte balances the carbonic acid (reaction 2.22) formed through the reaction of dissolved CO_2 with H_2O, as shown in reaction 2.21.

$$CO_2 + H_2O \leftrightarrow H_2CO_3 \tag{2.21}$$

$$H_2CO_3 \longleftrightarrow HCO_3^- + H^+ \tag{2.22}$$

The choice of electrolyte is generally a compromise between practicality and its relevance for a study on a particular application when combined to other testing parameters. Nevertheless, the influence of electrolyte components on the degradation of Fe and Fe alloys is much less explored compared to the hundreds of publications on the subject related to Mg [42].

2.1.4.2.2 Influence of electrolyte components

As shown multiple times with Mg, Zhang *et al.* [154] confirmed that Fe also corrodes faster in saline solutions compared to SBFs. However, while there was a clear difference between the two in the first few days from immersion, the corrosion rates in both electrolytes seemed to converge over the 7 day immersion test as corrosion products accumulated on both surfaces. Gebert *et al.* [117] did not carry out weight loss measurements to back this result however they also measured higher corrosion rates for Fe30Mn1C in physiological saline when compared to Ca-containing SBF, using PDP measurements. In any case, both deemed the saline solution to be too unrepresentative to be used in further testing.

Mouzou *et al.* [162] published one of the very few studies on the impact of specific changes within the formulation of SBF on degradation of Fe alloys. In their study, cast Fe20Mn1.2C was immersed for 14 days under cell-culture conditions (37°C, 5% CO_2) in a commercial Hanks' solution (commHBSS) and a modified Hanks' solution (modHBSS) wherein the latter contained Ca^{2+} ions

and the concentration of sodium bicarbonate ($NaHCO_3^-$) was an order of magnitude higher than in commHBSS. For an undisclosed reason, modHBSS was also supplemented with HEPES buffer, making the exact influence of Ca^{2+} and the additional bicarbonate, somewhat more difficult to ascertain. The combined effect of the changes in modHBSS led to a corrosion rate of 0.115 mm/year compared to 0.165 mm/year for commHBSS. FeOOH was detected on both corroded surfaces however the principal reason for the lowered corrosion rate in modHBSS was attributed the the higher precipitation of $MnCO_3$ on the metal surface in this electrolyte. Due to the much higher concentration of HCO_3^- in modHBSS, the solubility limit of carbonates in the solution was exceeded leading to easier precipitation of such products in modHBSS providing the famous "barrier" effect for further degradation. The influence of Ca^{2+} and HEPES presence in modHBSS was not specifically commented on.

In literature, the use of such a high concentration of bicarbonate, is not particularly common and that is reflected in the few times that authors list $MnCO_3$ as one the corrosion products. In fact, the only other times that evidence of a significant amount of $MnCO_3$ was detected on corroded surfaces was in studies by Loffredo *et al.* [137] and by Gambaro *et al.* [118] in which various FeMnC alloys were tested using the same exact immersion testing parameters used by Mouzou *et al.* [162] in the previous example. Gambaro *et al.* also mentioned the presence of Fe and Ca on the products labelled as $MnCO_3$ indicating that they could actually be $(Fe,Mn)CO_3$ with some Ca ions substituting the other metal ions. All three carbonates share very similar XRD patterns [118].

Mn carbonates were also detected by Dong *et al.* [163] when testing pure Fe, Mg and Zn in Dulbecco's Modified Eagle Medium (DMEM) which also typically contains a high concentration of carbonates (approx. 1.5 $g\,L^{-1}$). No carbonates were detected in Tris/HCl-buffered SBF in the same study. Somewhat unexpectedly, DMEM seemed to be a less aggressive medium compared to the SBF when testing the Mg and Zn coupons but not much difference in degradation was measured for pure Fe in both electrolytes over the 28-day testing period. In fact the degraded surfaces, shown in Figure 2.12 were very similar, as was their elemental constitution. The authors attributed this to the stronger electrostatic attraction that exists between typical Mg and Zn oxides/hydroxides and the amino acids

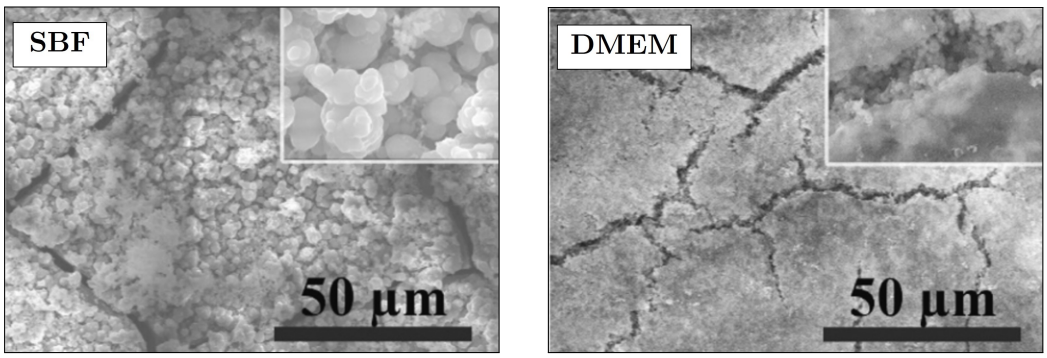

(a) (b)

Figure 2.12: SEM micrographs of pure Fe surface after a 14 day immersion test in (a) Ca-containing SBF and (b) DMEM [163].

present in DMEM which might have caused better "barrier" properties. However, in another study where DMEM was used as corrosive medium, barely any corrosion of Fe20Mn was observed in the first 50 days from immersion, suggesting otherwise [115]. One should note that this might have been affected by the rather small volume of testing solution used as the authors chose to immerse their samples in 0.5 mL and replace the medium every 2 days. Others have noted lowered corrosion rates in similar media, like Huang *et al.* [152] when testing Fe30Mn in Minimum Essential Medium (MEM) compared to typical SBFs, however did not really comment on what were the main affecting factors.

Despite the occasional use of synthetic buffers [162], no one has really studied their influence on corrosion reactions and kinetics with regards to Fe alloys. Schinhammer *et al.* [164] used a custom setup including a pH electrode coupled with a CO_2 controller to actively control the balance in equation 2.22. The setup worked very well in buffering the pH around the corroding Mg alloy, WZ21. The metal in Tris/HCl and HEPES-buffered Ca^{2+}-containing SBF, with rather poor control of pH, corroded significantly faster than in CO_2-buffered SBF. Interestingly, the metal in contact with Tris and HEPES-buffered SBF also corroded faster than that immersed in unbuffered PBS. Not only did the latter maintain its pH closer to the ideal 7.4 value but it did not contain components that tend to precipitate protective products, as explained in Section 2.1.4.2.1 and was therefore expected to corrode faster than any Ca^{2+}-containing SBF. Schinhammer *et*

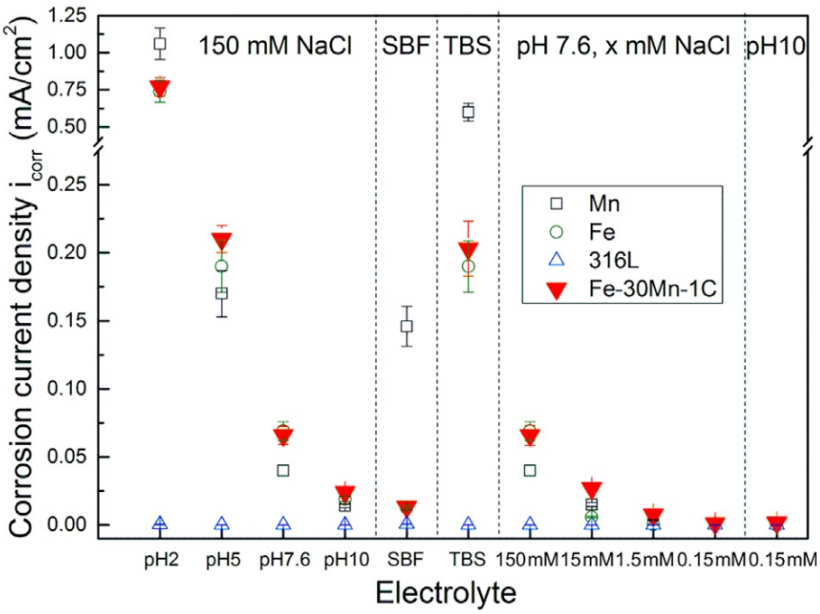

Figure 2.13: i_{corr} values for Fe30Mn1C immersed in SBF, TBS (Tris-buffered saline), varying NaCl concentrations and varying pH of 150 mM NaCl [117].

al. also tested pure Fe in CO_2-buffered pH but did not compare its performance compared to a sample in unbuffered electrolyte, rather comparing to values provided by Moravej *et al.* [165], limiting the relevance of the comparison. However, in another study, the authors showed that EIS measurements of Fe21Mn0.7C1Pd corroding in HEPES-buffered SBF exhibited only one time constant as opposed to the two-time constant scenario typically observed in SBF, indicating a clear influence of HEPES on the corroding system [166].

Gebert *et al.* [117] also compared the PDP corrosion rates of Fe30Mn1C in physiological saline with Tris-buffered physiological saline. As presented in Figure 2.13, the metal corroded faster in the buffered solution potentially indicating that buffers also interfere with formation of protective oxides/hydroxides by interacting with OH^-, as for Mg-alloys. Figure 2.13 also shows the somewhat obvious correlation with NaCl concentration and the relationship to pH. The latter highlights how the corrosion behaviour could shift in badly buffered solutions.

On a related note, Qi *et al.* [145] also performed an in-depth study on the influence of pH on the dominant corrosion reactions, especially as a function of the dissolved oxygen (DO) concentration in the electrolyte. As was presented in

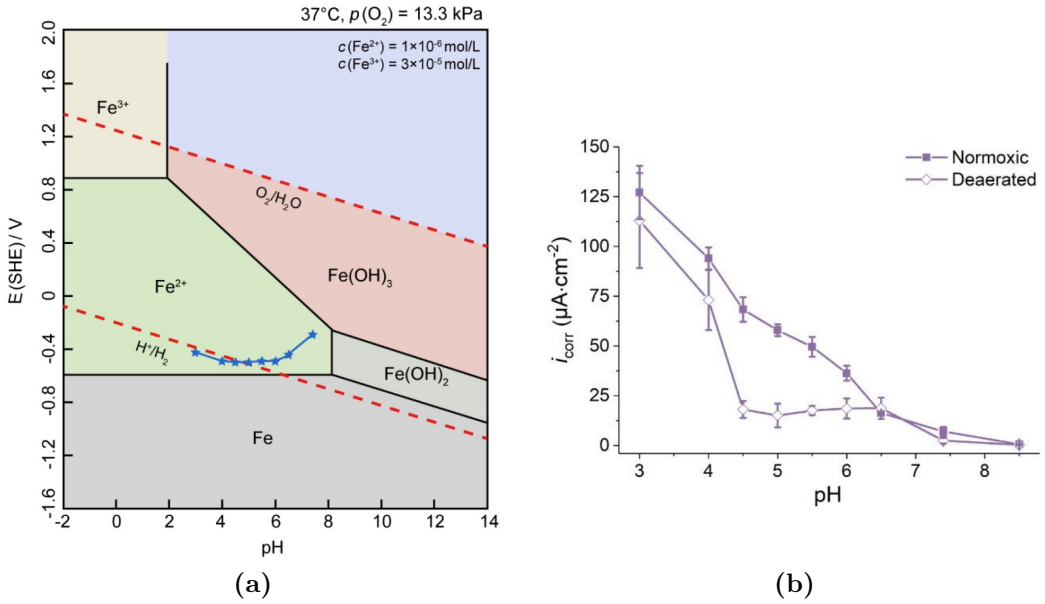

(a) **(b)**

Figure 2.14: (a) Modified Fe-H_2O Pourbaix diagram to represt the biomimetic environment at 37°C with blue plots showing experimental E_{corr} data for Fe in Hanks' solution at different pH values and (b) i_{corr} values for pure Fe tested in normoxic and deareated Hanks' solution at different pH [145].

initial chapters of this review, the DO concentration could easily be the limiting reaction for the dissolution of Fe. However, few have performed degradation analyses with DO in mind, as opposed to Mg alloys [42, 69, 167]. In their study, Qi *et al.* first modified the Fe-H_2O Pourbaix diagram to reflect the physiological environment at 37°C which resulted in lowering of the H^+/H_2 line as shown in Figure 2.14a. Experimentally measured electrode potentials of Fe in Hanks' solution are plotted in blue stars on the same figure and indicate that below an approximate pH value of 5, the likelihood of the redox reaction 2.23 increases significantly.

$$Fe + 2H^+ \rightarrow Fe^{2+} + H_2 \tag{2.23}$$

In fact, the corrosion current density of pure Fe in normoxic i.e. containing a typical O_2 concentration (measured 8 mg L^{-1} O_2) Hanks' solution exhibited an approximate linear increase with decrease in pH. On the other hand, in deareated (0.5 mg L^{-1} O_2) Hanks' solution, there was a sudden increase in current density below a pH of 4.8, as the limited corrosion due to lack of DO was overcome

by the evolution of H_2, as shown in Figure 2.14b. Not only is the dissolution of Fe encouraged at lower pH, but hydroxides like $Fe(OH)_3$ and $Fe(OH)_2$ and also several phosphates including Ca/P products are also unstable preventing the barrier effect from taking place.

2.1.4.2.3 Additions of protein

One way in which *in vitro* testing environments could differ significantly from *in vivo* environments, is the presence of proteins. While proteins are present in abundance in both cardiovascular and orthopaedic environments, the influence of proteins on the degradation of biodegradable metals is far from understood. Up till now, researchers have agreed that the main three ways in which protein influences degradation is through adsorption and electrostatic interactions, chelation (especially of metal cations) and pH buffering. However the mechanisms in which these take place in specific situations are still being investigated [75, 168].

Literature discussing the influence of protein on Fe-based alloys is rather limited. In an early study, Wagener *et al.* [169] noted no difference in PDP curves for Fe immersed in SBF (with Ca^{2+}) and the same SBF with 10 $g\,L^{-1}$ Bovine Serum Albumin (BSA). However, they noted that there seemed to be less Ca/P product precipitation on samples tested in BSA. Quite contrarily, Mardina *et al.* [170] noted a Ca-rich layer on the sample tested in solution containing 20 $g\,L^{-1}$ BSA and no products at all on the samples tested in protein-free electrolyte after 40 days of static immersion. Despite this observation, the corrosion rates calculated in this experiment yielded no statistically significant difference between corrosion rates of samples tested in the two solutions. Oriňaková *et al.* [147] used the same concentration of BSA to test pure Fe in protein-containing HBSS (with Ca^{2+}). As illustrated in Figure 2.15, testing in protein led to significant pitting as opposed to relatively uniform corrosion in protein-free HBSS. The authors attributed this effect to "complexation" (or chelation) of Fe with BSA leading to enhanced metal dissolution.

Published studies relating to testing of FeMn alloys in protein are even more scarce. Caligari Conti *et al.* [150] tested wrought Fe14Mn1.2C in Ca^{2+}-free SBF and 1 $g\,L^{-1}$ BSA, Mouzou *et al.* [162] tested Fe20Mn1.2C in DPBS (Dulbecco's

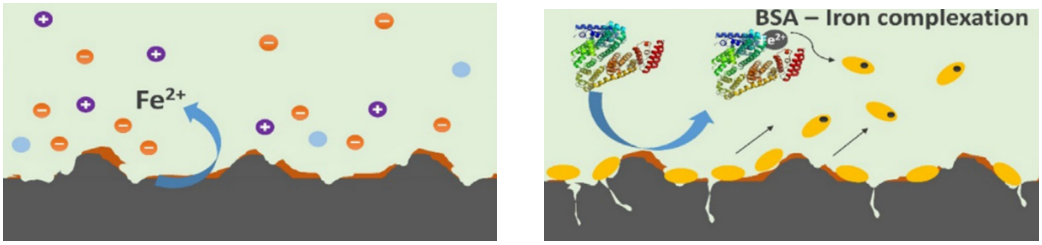

(a) (b)

Figure 2.15: Schematic representation of degradation process of Fe in (a) HBSS and (b) HBSS with 20 g L^{-1} BSA addition according to Oriňaková *et al.* [147].

Phosphate Buffered Saline) and 1 g L^{-1} albumin, whereas Huang *et al.* [171] tested wrought and SLM-processed Fe22Mn0.6C in HEPES-buffered SBF with 10 g L^{-1} BSA. The studies reported drastically different results. The first study, like Wagener *et al.* [169], reported no differences observed during PDP testing. Weight loss measurements after 14 days of immersion on the other hand indicated that samples tested in protein lost half the weight lost by those tested in simple HBSS, suggesting lower corrosion rates in the presence of BSA. One should note, that in this study the corrosion products were not chemically removed and therefore the weight measured included any adherent oxides, precipitates or protein. Mouzou *et al.* [162] claimed that the corrosion rate of Fe20Mn1.2C after 14 days immersion was essentially equal to zero, implying that the presence of albumin, protected the metal. Contrastingly, when testing in 10 g L^{-1} BSA, Huang *et al.* noted lower and more stable impedance values in SBF using EIS, indicating faster corrosion rates over the first 24 hours in the presence of protein. Like Wagener *et al.* [169], they also noted less Ca/P-product formation in BSA, which complements the fact that the mid-frequency time-constant (which is generally related to protective product formation), was completely suppressed in BSA-containing electrolyte. By observing changing impedances at 0.1 Hz (i.e. at low frequency), the authors suggested that protein seemed to encourage corrosion upon immersion, but as it starts to adsorb to the metal surface, it serves as a barrier for further dissolution.

Due to the well known fact that albumin could alter corrosion mechanisms via adsorption, this phenomenon is often used to justify lowered corrosion rates.

Table 2.1: IEP for typical Mg and Fe-oxides as well as albumin (BSA) and lysozyme (LYS) [169].

	$MgO/Mg(OH)_2$	$FeO/Fe(OH)_2$	BSA	LYS
IEP	10.8-14	6.6-8.6	4.8-5.2	10.5-11.8

However only Mardina *et al.* [170] following addition of 20 $g\,L^{-1}$ BSA, confirmed the presence of albumin adsorbed to the Fe surface using Fourier Transform Infrared Spectroscopy (FTIR). Oriňaková *et al.* [147] on the other hand did not detect protein using either XPS or Raman despite using the same protein concentration. Wagener *et al.* [169] aimed to provide an explanation for varying albumin adsorption after measuring much less nitrogen[1] on Fe tested in BSA-containing solution, compared to Mg. They refer to the isoelectric point (IEP)[2] of typical surface oxides for both metals as well as the IEP for albumin and lysozyme (LYS). A substance with an IEP lower than the pH of the surrounding solution, would typically have an overall negative charge, and vice versa. Therefore, when considering the information presented in Table 2.1, it follows that in a solution with a pH of around 7.4, BSA would be strongly negatively charged, whereas typical Mg-oxides would be strongly positively charged, encouraging rapid adsorption. The difference between IEPs is much less considerable when considering Fe-oxides, which could explain why little to no BSA is generally detected in post-test analyses. The opposite could be said for the interaction of Fe- and Mg-oxides tested in LYS, where the protein is likely to adsorb more easily to Fe-based surfaces, as also confirmed by Wagener *et al.* in their study. Moreover, adsorption could be hindered by active anodic dissolution, which is probably why PDP curves, especially anodic curves, rarely show any signs of protein influence [150, 170].

Studies related to the testing of Zn and Mg in protein-containing solutions could further indicate how protein could influence the corrosion of Fe alloys. Dong *et al.* [175] studied the effect of varying BSA concentration from 1 to 6 $g\,L^{-1}$ in

[1] Relative high atomic % of nitrogen and intensity of amide bands in XPS are techniques generally used to confirm presence of protein [172, 173]

[2] Also known as the isoelectric point (pI) and refers to the pH at which the molecule of interest has a net zero charge [174].

SBF when testing pure Zn. The authors measured higher polarisation resistances with time with increase in BSA content, using EIS. As mentioned with other studies, Ca/P-product precipitation seemed to be inhibited in protein-containing solutions leading to corrosion product layer thickness that were 10-20 times lower than in normal SBF. Dong *et al.* hypothesised that the negatively charged BSA adsorbed to the surface of the corroding Zn leading to occluded conditions that encouraged pit formation. Despite the use of similar concentrations of BSA, Liu *et al.* [176] reported very different results when testing Zn in PBS. In their study, an increase in BSA led to lowered charge transfer and corrosion layer resistance. Unlike Dong *et al.* they made no reference to pitting corrosion, and instead suggested that increasing the protein content affected the density of the adsorbed layer leading to less compact and hence less protective layers.

Similar to Liu *et al.* [176], Harandi *et al.* [172], used PDP and EIS to show that resistances could be 5 times lower in HBSS with 40 $\mathrm{g\,L^{-1}}$ BSA compared to HBSS when testing pure Mg. Based on EIS modelling over time, they showed that slow increases in resistances potentially indicate slow adsorption of BSA to the corroding surface in the first hours following immersion, while eventual decreases in resistance could be related to chelation of corrosion products by amino acid groups in the BSA molecule, which disrupt the corrosion product film and accelerate corrosion. Once again, other studies provide drastically different results. Mei *et al.* [75] studied the same materials in the same electrolyte and indicated that chelation of Ca^{2+} ions upon immersion results in relatively fast corrosion rates at the beginning, but as precipitation of phosphates commences, the degradation slows down.

To summarise, there seems to be two main factors that contribute to the effect of protein on metal corrosion. Adsorption and chelation, as noted in this section, are often part of the discussion when protein is concerned. However the primary influencing factor is the time-dependant effect, relating to which there seems to be a lot of conflicting theories; either protein inhibits corrosion at the start and eventually the corrosion products are destabilised by the chelating capability of the protein [169, 172, 175], or corrosion is accelerated at the start but slow adsorption leads to a strengthened barrier-effect with time [75, 171]. The second factor, is the concentration effect. Here, cited studies indicate that

increasing concentration leads to increased resistances [175] whereas other studies claim that low quantities leads to a stable dense barrier formation, but increasing the concentration leads to an unstable adsorbed layer which facilitates corrosion [173, 176]. The latter was confirmed when testing with 0.1 and 10 $g\,L^{-1}$ BSA in physiological saline [173].

Other testing parameters also leave a significant impact on the influence of protein. For instance, Mei *et al.* [75] noted that surface-to-volume ratio, flow of solution, refreshment of static immersion testing solution and albumin source all also have significant effects on measured corrosion metrics. What must also be recognised, is that sterile testing conditions are considered a must when conducting long-term testing with protein, due to the high probability of microbial growth in non-sterile conditions [75]. The latter could lead to microbially-influenced corrosion (MIC) due to altered electrochemical processes at the metal surface for instance leading to pitting corrosion [177]. Once again, the specific influence of bacteria and/or biofilms on the corrosion mechanism of Fe and Fe-based alloys, has not been investigated in detail thus far.

2.1.4.3 Other influences on testing outcomes and analysis

Many reviews have somewhat erroneously compared corrosion rates obtained from PDP and from weight loss measurements. However, many have consistently obtained considerably higher corrosion rates from PDP measurements [107–109, 137, 152] with comparable corrosion rates from both tests being the exception [107, 150] and often the result of some other testing influence. In truth, the testing method also affects the dominant corrosion mechanism. Whereas with PDP tests, the surrounding environment shifts according to the reactions being *forced* at the surface by applying an overpotential, in immersion tests the material generally has the time to affect the changes in its surroundings depending on its freely corroding condition. In fact, the influence of the "barrier" layer that typically accumulates with time at the surface during immersion testing is rarely discussed when PDP testing is concerned. Nor is localised corrosion like pitting or crevice corrosion ever induced due to the accumulated products, but rather

due to existing defects or features that make the material susceptible to such a mechanism [113].

To provide a specific example, Čapek *et al.* [113] carried out both PDP and weight loss measurements on hot-forged Fe30Mn. Whereas the i_{corr} of Fe30Mn from PDP tests was an order of magnitude higher compared to the i_{corr} for pure Fe, the corrosion rate for Fe30Mn as measured from weight loss measurements was about 75% lower. Based on immersion tests carried out in unbuffered physiological saline (0.9% NaCl), the authors noted that the corrosion of FeMn was giving rise to a significant increase in pH (from 5.7 to 7.1) compared to the increase due to Fe corrosion (from 5.7 to 5.8). A local increase in pH during immersion testing would result in a high concentration of OH^- that suppresses the cathodic reaction while stabilising $Fe(OH)_2$ and $Fe(OH)_3$, among other protective products. These events occur over a period of time that extends beyond typical PDP testing periods and are not likely to take place in a condition other than free corrosion i.e. at OCP.

Interestingly, when using PDP to test solutions containing protein, the influences of protein adsorption onto the metal surface that is often discussed with immersion testing in such electrolytes, is not evident [150, 170, 175]. Whereas some have claimed that adsorption takes place upon contact with the testing solution, the high rate of metal dissolution that takes place during anodic polarisation, is likely to interfere with that same phenomenon.

Another aspect of immersion testing that has a significant influence on the degradation, is the ratio of electrolyte volume to sample surface area. As a rule of thumb, many studies have adopted the guidelines of the ASTM-G31 standard [178] that indicates that a minimal volume per unit area of 0.2 $mL\,mm^{-2}$ should be used. In the instance of Čapek *et al.* [113] for example, while the points above still stand, the authors used just 0.011 $mL\,mm^{-2}$. Although the medium was refreshed once a week, this was likely not sufficient for there to be enough ions to prevent stalling of degradation. Nevertheless, this approach has been used by other groups [123] and some also chose not to refresh the solution at all [46, 162], certain studies not refreshing the solution over a period of 180 days [138]. Others use a very high volume-to-area ratio instead of refreshing the electrolyte periodically [119, 132].

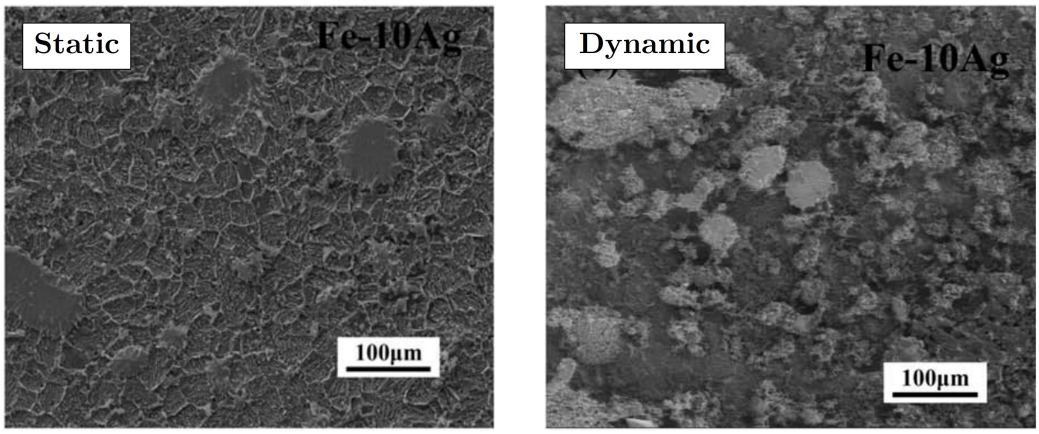

Figure 2.16: SEM image of Fe10Ag after a 30 day (a) static and (b) dynamic immersion test in Hanks' solution [84].

On a related note, immersion setups can be either static or dynamic, with the latter being used mainly to simulate the flow of blood through arteries for Fe-based alloys being tested for cardiovascular applications. In studies where the two types of immersion tests were carried out on the same materials, dynamic immersion consistently resulted in higher corrosion rates [39, 40, 83, 84]. When testing Fe-Ag and Fe-Au alloys, the measured corrosion rates were twice as high in dynamic immersion, resulting in surfaces that were visibly more attacked, as shown in Figure 2.16. The most likely reason for this increase is due to the "flushing" effect that takes place with the flow of fresh (or used) electrolyte exposing fresh material and preventing or delaying corrosion products from settling on the corroding surface. Moravej *et al.* [39] also mentioned that the pH of the solution adjacent to the corroding surface also takes longer to increase when using a dynamic setup. In the case of Huang *et al.* [83], the dynamic immersion setup also allowed the DO concentration to be controlled within the range 2.8-3.2 $\mathrm{mg\,L^{-1}}$, providing consistent fuel within the bulk electrolyte for the cathodic reaction to advance unhindered. This could not be said for certain in a static immersion setup where local DO concentration could easily become exhausted.

Furthermore, weight loss measurements are based on the premise that the corrosion products are fully removed from the metal sample - something that is

not always done, or at least not specified, in certain publications [52, 55, 106, 111, 115, 137, 138, 150, 179]. When weight loss measurements are attempted, it is not uncommon that there is a difficulty in removing the products chemically [78] or that the authors mention the need to use a brush to gently scrub the surfaces clean [78, 107, 107, 154, 180, 181]. In a review on corrosion studies with Mg, the authors explicitly mentioned the difficulty of achieving accurate and reliable results when cleaning the test samples in the commonly used chromic acid solutions. The truth is that there is always a good chance that either the corrosion products are not fully removed, or that the cleaning solution also partially attacks the metal matrix [42]. While the ASTM-G1 standard [68] provides various cleaning options for iron and iron alloys, one must keep in mind that the standard was not necessarily developed with all potential alloy compositions in mind. To this end, it is the author's opinion that one should always carry out tests on blank samples to acquire an indication of how the method employed affects the metal underneath. To the authors' knowledge, this measure has never been provided in literature. Moreover, there are at least eight different methods that have been used by various groups as summarised in Table 2.2, so one cannot assume that the

Table 2.2: Methods employed to clean corrosion products from iron-based alloys prior to weight loss measurements.

Cleaning method	Ref.
Ultrasonicating in 3.5 g hexamethylenetetramine dissolved in 500 mL HCl and adding water up to 1000 mL	[51], [110], [182]
Picric acid	[114]
Brushing in 15% H_2SO_4 solution	[153], [154]
Immersed for 30 min at 80-90°C in solution containing 5% NaOH, 20% granulated zinc and 75% reagent water	[127]
Clark solution (100 mL HCl, 5 g $SnCl_2$ and 2 g Sb_2O_3)	[113]
Gently brushing in solution of 15 gL^{-1} citric acid and 280 gL^{-1} H_3PO_4	[107]
10M NaOH solution	[39], [40]
Washed in ethanol or methanol and/or acetone	[162], [183]

impact on the substrates in different articles, was similar. Further approximations are carried out when testing porous samples. Since the equation used to calculate the corrosion rate is inversely proportional to the exposed surface area (2.19), having porous samples whose surface area is generally approximated to be equal to the apparent area, could lead to significant errors in the presented values. With porous samples, there is also an increased risk of incomplete cleaning, as methods like brushing become increasingly difficult to carry out effectively.

2.1.4.4 Degradation performance *in vivo*

Despite the importance of representative *in vitro* testing, *in vivo* tests remain the most useful tests at indicating the material or device's promise. The amount of *in vivo* tests carried out on Fe-based alloys have so far been rather limited, however there has been an encouraging increase in the past five years. One particular study by Zheng *et al.* [184] has actually led to ongoing clinical testing of a drug-eluting Zn and (poly-d-lactic acid)-coated Fe stent called IBS Titan™ by Lifetech Scientific [185, 186]. *In vivo* studies are crucial to take the understanding of Fe alloy biodegradation to the next level. A list of notable *in vivo* studies and corresponding observations are listed in Table 2.3.

.

It has already been well established in this review, that varying *in vitro* testing conditions can cause major changes to a materials' degradation behaviour. In a rigorous review related to studies on biodegradable Mg-based materials, Sanchez *et al.* [193], mentioned how many have started to see a valid correlation between *in vitro* and *in vivo* studies as "impossible" due to the myriad of affecting physiological factors that cannot be effectively replicated *in vitro*. In their study, the authors compared the corrosion rates derived from electrochemical, immersion and *in vivo* testing in order to attempt to derive a correlation factor between *in vitro* and *in vivo* tests, as shown in Figure 2.17. They concluded that for Mg-alloys, *in vivo* degradation rate could be anywhere between 1 and 5 times lower than *in vitro* corrosion rates.

Table 2.3: List of selected published *in vivo* studies and notable observations.

Composition	Implant type	Animal model	Implantation site	Interval	Observations	Ref.
Fe	16x(3-6)mm Stent	New Zealand white rabbits	Descending aorta	6, 12, 18 months	Observed no appreciable corrosion after 18 months; mild inflammatory response of stented vessel; no local or systemic toxicity.	[37]
Fe	Stent (Biotronik, Germany)	Juvenile swine	Aorta	28 days	Iron stents led to no differences in inflammatory scores compared to cobalt chromium stents; no recoil observed after 28 days.	[187]
Fe	Discs	Wistar rats	Subcutaneous (Dorsal area)	1, 12, 24 weeks	No corrosion detected after 6 month implantation period; observed fibrous connective tissue proliferation around the implant that usually forms around permanent implants.	[188]
Fe (Zn buffer coating with drug-eluting PDLA top coat)	Stent	Bama mini-pigs	Coronary artery	6 months	No systemic toxicity; no corrosion was observed in the first 90 days due to the Zn buffer layer which continued to provide mechanical support up to 180 days; localised strut attack observed after 180 days using μ-CT.	[184]
Ta-sputtered Fe	5x2 mm wire	New Zealand white rabbits	Femur	1, 4 months	Ta-sputtered Fe exhibited over twice the degradation as bare Fe as deduced from μ-CT volume loss measurement; implants degraded uniformly as opposed to severely pitted bare Fe; Ta-sputtering enhanced osteoblast adhesion; no signs of cellular or tissue toxicity observed.	[93]

Table 2.3 (Continued): List of selected published *in vivo* studies and notable observations.

Composition	Implant type	Animal model	Implantation site	Interval	Observations	Ref.
Fe-0.8P	15x10 foams	Merino sheep	Tibiae	6, 12 months	No inflammatory reactions after 12 months; non-mineralised bone observed after 12 months; despite promising *in vitro* results in previous work, cellular samples remained largely intact after 12 months although degradation products were observed.	[189]
Fe(0.5-6.9)Mn	3x1.4 mm disks	NMRI rats	Subcutaneous	3, 6, 9 months	No significant corrosion observed, although signs of corrosion visible; identified no differences in corrosion kinetics between alloy compositions.	[114]
Fe30Mn	20x0.5 mm wire	Sprague-Dawley rats	Femur	6 months	No appreciable bioresorption observed; randomly dispersed iron oxide crystals on surface of roughened implant; increased bone contact; no systemic toxicity observed.	[190]
Fe30Mn	10x6 mm foams	New Zealand white rabbits	Femur	12, 24, 48, weeks	New bone observed histologically as early as 12 weeks post-operatively; 10.1-20.9% decrease in volume in 48 weeks as measured using µ-CT.	[191]
Fe35Mn Fe35Mn1Ag	15x6 mm pins	Sprague-Dawley rats	Subcutaneous	4, 12 weeks	Gas pockets observed for close to FeMn and FeMnAg implantation sites but caused no complications; addition of Ag positively impacted degradation rates (by approx. a factor of 2), although these remained low; observed acute inflammatory response but an absence of chronic systemic toxicity.	[132]

Table 2.3 (Continued): List of selected published *in vivo* studies and notable observations.

Composition	Implant type	Animal model	Implantation site	Interval	Observations	Ref.
Fe35Mn	Scaffolds	Sprague-Dawley rates	Calvarial defect	4 Weeks	Newly formed bone was observed in contact with the implant after 4 weeks; Osteoblasts were also found in the area indicating an active bone forming process.	[182]
Fe28.5Mn28.5Si	2x4x0.5 mm pin	Wistar rats	Subcutaneous/ tibiae	14, 28 days	Absence of any sign of local reaction indicates good biocompatibility; uniform degradation observed at both implantation sites; considerably more Ca/P compounds observed at tibial implant surface indicating active bone remodelling.	[192]
Fe Fe10Mn1Pd Fe21Mn0.7C1Pd	1.6x8 mm pins	Sprague-Dawley rats	Femur	4, 12, 24, 52 weeks	No signs of local or systemic toxicity; signs of mild degradation observed; no significant weight loss after 52 weeks; no significant differences in corrosion rates between tested alloys although slightly different corrosion mechanisms identified between Fe and FeMn-based alloys.	[180]
Fe-5HA Fe-5TCP Fe-3HA-2TCP	5x2x0.5 mm	Indonesian thin-tailed sheep	Tibiae	3, 9, 14, 35, 50, 70 days	Observed improved bone healing effectiveness of Fe-composites compared to Fe through radiography	[96]

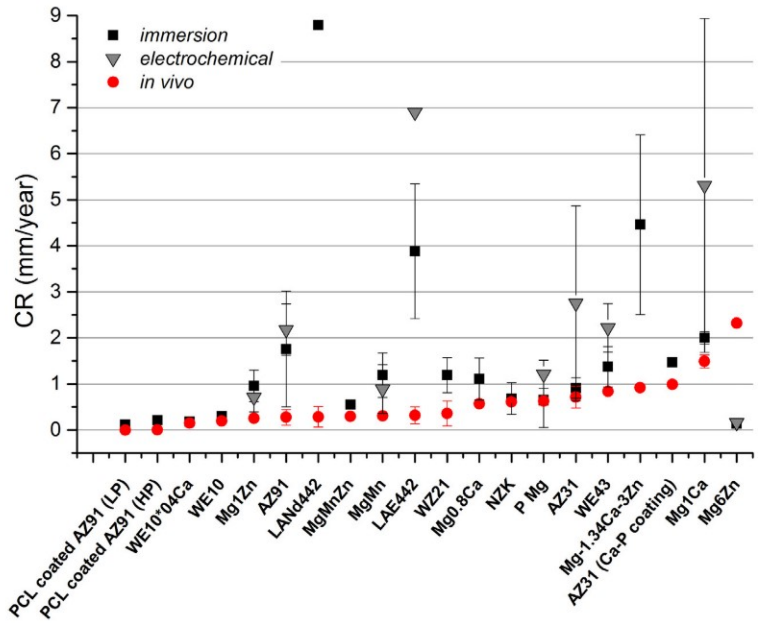

Figure 2.17: Comparison of average corrosion rates for various Mg alloys as measured using electrochemical and immersion tests *in vitro* and *in vivo* testing [193].

Although a similar analysis would be futile with the amount of existent *in vivo* studies on Fe-based alloys, the findings summarised in Table 2.3 indicate that a similar pattern is observed for Fe-based alloys. In general, the majority of studies where barely any *in vivo* degradation was observed, followed promising *in vitro* tests with accelerated degradation [96, 132, 180, 189]. In fact, positive outcomes and lack of adverse reactions in *in vivo* tests are likely due to the limited degradation observed, as initially postulated by Peuster *et al.* [37]. To the author's knowledge, at worst, the materials were deemed to be "mild local irritants" [190].

Although most of the analyses following *in vivo* studies have been qualitative in nature, some have attempted to discuss potential reasons for the seemingly excessively slow degradation rates observed. The barrier effect caused by oxides and phosphates, commonly described in *in vitro* tests, is a potential explanation [114, 180]. The same barrier effect could also take place due to formation of fibrous tissue which is actually commonly observed adjacent to permanent implants [96, 132].

In a popularly cited study, Kraus *et al.* [180] implanted the materials extensively studied by Schinhammer *et al.* [78, 119, 166, 194] in rat femurs. Barely any degradation was observed following a 1 year implantation period and no quantifiable difference was observed in the corrosion of Fe, Fe10Mn1Pd and Fe21Mn0.7C1Pd despite the strong microgalvanic effect induced by Pd-rich intermetallics *in vitro*. The authors noted how access to O_2 at bone implantation sites could be severely limited, thus starving the cathodic oxygen reduction reaction. It is interesting to note that the amount of O_2 in blood is significantly lower than the amount present in most solutions like Hanks' solution, and therefore the corrosion rate when testing in such solutions could even be an overestimation when developing materials for cardiac applications [132].

In contrast to the work by Kraus *et al.*, Dargusch *et al.* [132] actually noted a difference in degradation behaviour between Fe35Mn and Fe35Mn1Ag implanted subcutaneously in rats, by an approximate factor of two. The authors also reported the first observation of gas formation in the study of Fe-based alloys for biomedical applications. The amount generated was still significantly lower than that typically observed during the degradation of Mg and its alloys and caused no adverse effects. Dargusch *et al.* explained how acute inflammatory response following the implantation procedure could lead to drops in pH to around 4-5.2 units, moving away from the typical *in vitro* testing pH of 7.4. The drop could in turn shift the cathodic reaction to H_2 as explained in Section 2.1.4.2.2 with the help of the modified Fe-H_2O Pourbaix diagram [145].

Despite the limited degradation, a number of studies have noted successful bone integration within the implantation period [93, 96, 190–192] although Traverson *et al.* [190] noted that it was difficult to determine whether increased bone contact was due to new bone ingrowth or abutment of formed metal oxides with adjacent bone.

These studies continue to highlight the necessity of standardising procedures even for *in vivo* testing, keeping in mind different implant forms and sites of interest. This should also include methods of measuring corrosion rates as well as acceptable implantation intervals at which corrosion rates should be calculated [193] since degradation rates cannot really be linearised for the reasons discussed above.

2.2 Processing using Powder Metallurgy

2.2.1 Overview

Processing methods of both metals and ceramics through the powder route, know their beginning in the very first years of human civilisation. When it comes to processing of Fe-based alloys for biodegradable applications, powder processing was also one of the first techniques used in the preparation of test samples [100]. While techniques like casting and forging are still used within the field, many look towards powder processing particularly for the enhanced flexibility such techniques often offer, both in terms of material composition and achievable geometries [48].

This section briefly introduces the principal sintering methods and modes that are relevant to the field and which will be referred to throughout the review.

2.2.1.1 Solid-state sintering

Solid-state sintering is generally the term used when referring to the conventional sintering process wherein pressure and heat are applied (not necessarily at the same time) in order to create dense solids without reaching the materials' melting point. This is achieved fundamentally due to a drive for reduction in surface energy. This drive, allows for diffusional-flow of defects that result in various clearly distinguishable sintering stages, represented in Figure 2.18. Interparticle contacts are initially formed providing regions for consequent neck formation. As the temperature increases, resultant interconnected pores become increasingly

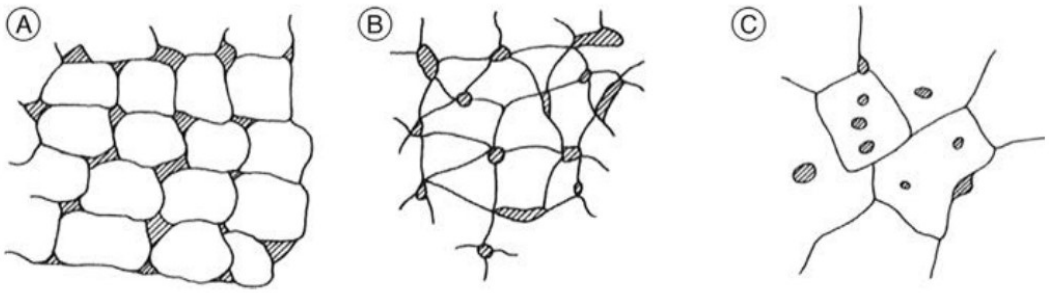

Figure 2.18: Schematic representation of stages in solid-state sintering with shaded gray areas representing pores [195].

more isolated allowing for further pore volume reduction and grain coarsening with time and temperature [195]. Depending on the specific material and processing parameters, material can move through viscous or plastic flow depending on crystallinity, vapour transport for materials with low vapour pressures, diffusion along the surface or grain boundaries as well as bulk diffusion through the grains [195, 196]. It is also important to note the impact of particle size on densification. Whereas finer particle sizes (< 40 µm) tends to lead to very dense parts with high level of shrinkage, sintering of larger particles tends to stop at an earlier stage such that further densification is realised through pore rearrangement, not closure.

2.2.1.2 Liquid-phase sintering

Liquid-phase sintering refers to a scenario where a phase within the alloy being sintered, has a melting point that is below the sintering temperature being used. In this case, the liquid flow will cause faster rearrangement of the alloy constituents should capillary forces allow. Depending on the solubility of the solid and liquid phases within each other as well as the equilibrium state of the system at the melting point of the secondary constituent, further densification will take place through formation of solid solutions or reprecipitation [196]. In a scenario where the two constituents are practically immiscible, as in the case of Fe or FeMn and Ag (melting point of 962°C [132]), the liquid phase will remain within the region where it flowed until solidification [197, 198].

2.2.1.3 Pressureless sintering

In a situation where the powders are loosely packed and there are no external forces encouraging contact between adjacent surfaces, the sole driver for densification, is the reduction of surface energy. This is referred to as pressureless sintering [196]. Although often classified under solid-state sintering, liquid and transient liquid phases can also assist with densification when employing pressureless sintering. This densification is predominantly active in Fe-based foam processing techniques like the replication method first suggested by Quadbeck *et al.* [81, 183, 189, 199–203] and the TOPIF (Topologically Ordered Porous

Iron Foams) technique developed by Sharma *et al.* [204]. Both methods will be discussed in more detail in Sections 2.3.1 and 2.3.2. Due to the relatively high surface areas involved in pressureless sintering, special considerations need to be taken due to limitations related to the reactivity of the powders, as will be discussed in Section 2.2.2.

2.2.2 Special considerations when using Mn powder

While powder-processing can be adventageous in a lot of ways, the use of Mn powder to prepare FeMn alloys, makes processing significantly more complex. A lot of what can be said about the use of Mn in powder-processed steels, has been published by Andrej Šalak, a pioneer in the field of ferrous powder metallurgy. After extensive studies on the potential use of Mn in steels as an alloying element to replace other problematic elements like Cu and Ni, Šalak published his final monograph entitled "Manganese in Powder Metallurgy Steels", in 2012 [205]. This volume served as a principal reference in the review that follows.

2.2.2.1 Oxidation

Without a doubt the main issue that has limited the use of Mn in powder metallurgy steels is its high affinity to oxygen and the incredibly stable oxides that it forms. The opposite characteristic is in fact what mainly drives metallurgists to use more expensive Cu, Ni and Si in its place in the production of steels. This section will outline the issues related to sintering of FeMn from a thermodynamic point-of-view and ways in which oxidation may be tackled. However, one must keep in mind, that most literature on the subject is not concerned with high Mn concentrations as is typical in biodegradable metal research, but is generally limited to approximately 13 wt.% as is used in Hadfield steels and much lower concentrations [205].

2.2.2.1.1 Ellingham-Richardson diagram

The Ellingham-Richardson diagram in Figure 2.19 presents data based on thermodynamic principles. The diagram is a plot of ΔG, that is, the change in Gibbs'

free energy measured in Joules (J), against temperature in which the plotted lines represent oxidation reactions for metals reacting with one mole of O_2 according to equation 2.24.

$$\Delta G = \Delta H - T\Delta S \tag{2.24}$$

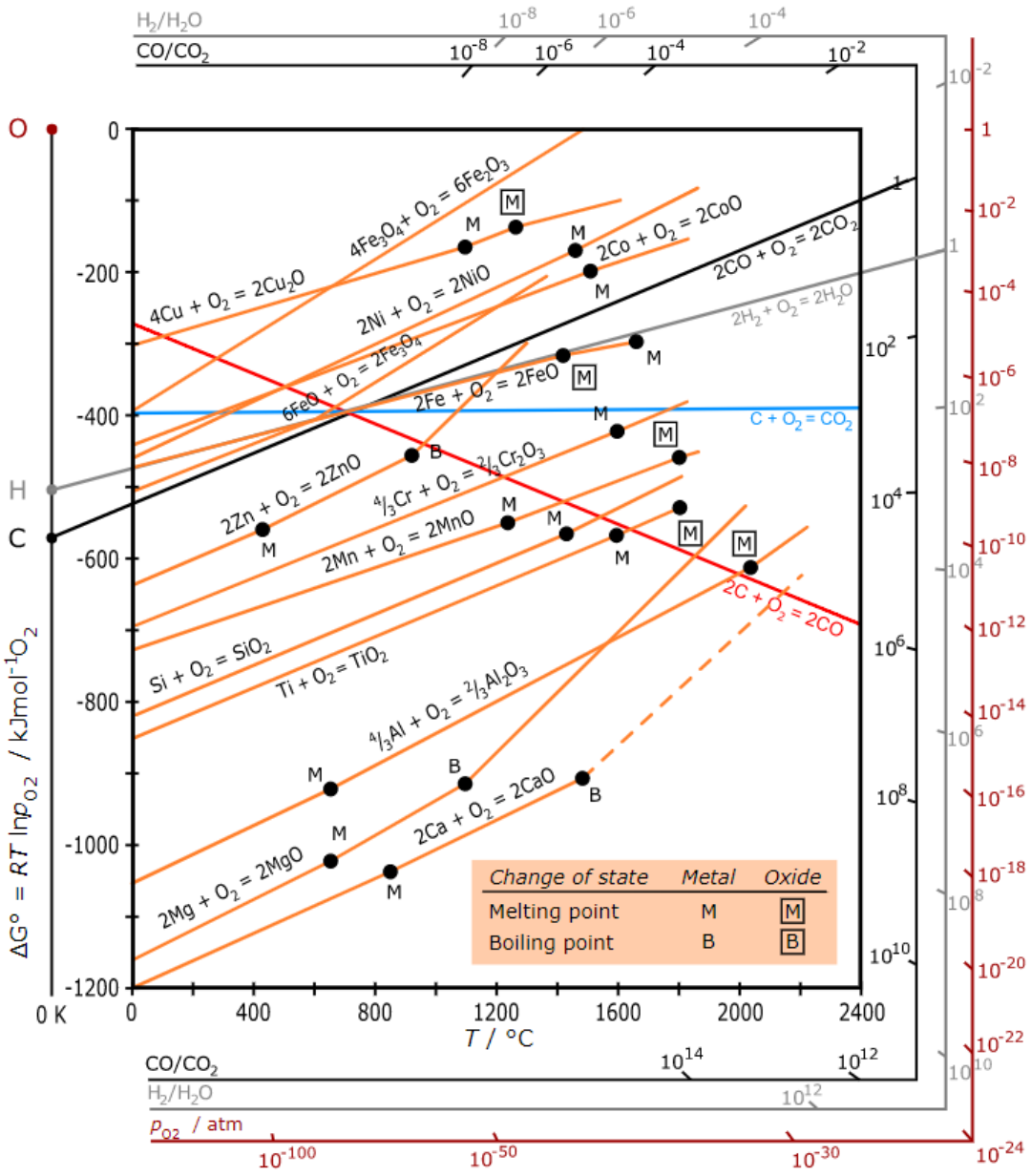

Figure 2.19: Ellingham-Richardson diagram showing the thermodynamic stability of several oxides at a range of temperatures [206].

Table 2.4: Equilibrium data for Mn/MnO in O_2-containing gas mixture [205].

	Temperature [°C]				
	600	800	1000	1100	1200
P_{O2} [Pa]	10^{-38}	10^{-30}	10^{-24}	10^{-22}	10^{-20}
H_2/H_2O	1 x 10^8	3 x 10^6	2 x 10^5	9 x 10^4	4 x 10^4
Dew point [°C]	-102	-80	-60	-57	-40

where ΔH is the change in enthalpy in J, T is the absolute temperature in K, and ΔS is the change in entropy in $\mathrm{J\,K^{-1}}$. In general, reactions situated towards the top of the diagram are related to more "noble" metals whose oxides are less stable, whereas reactions towards the lower part of the diagram have more stable oxides. With the incorporation of the nomographs[1] on the side of the diagram by Richardson, the diagram could further be used to determine the equilibrium partial pressure P_{O_2}, for a reaction at a temperature of interest by extending a straight line from the graph origin (i.e. O at $\Delta G = 0$) through the reaction line at a specific temperature, towards the P_{O_2} nomograph. The same could be done with the $\frac{H_2}{H_2O}$ and $\frac{CO}{CO_2}$ nomographs. By extending a line from the H and C origins respectively, through the reaction line towards the corresponding nomograph, one could estimate the equilibrium gas ratios to prevent oxidation.

When it comes to the FeMn system, the Ellingham diagram clearly shows that Mn is the more problematic element of the two with a difference in equilibrium P_{O_2} of six orders of magnitude. Considering only Mn oxidation, the diagram essentially points towards a set of atmospheric conditions[2] that are next to impossible to achieve in practice for the disassociation of Mn oxides, as presented in Table 2.4 [205, 207]. Published works on the subject have therefore focused more on reducing the extent of oxidation and finding ways to reduce the oxides formed.

[1] Graphical elements on the sides of the Ellingham diagram aimed for approximate calculations of atmospheric ratios.

[2] Dew point refers to the temperature at which the air becomes saturated with water vapour and starts to condense [205].

2.2.2.1.2 Influence of sintering atmosphere on oxidation and reduction of metal oxides

In view of sintering oxygen-sensitive elements like Mn, Šalak [205] explained the twofold importance of the chosen sintering atmosphere. The flow of a protective reducing gas

- reduces natural surface metal oxides allowing faster diffusion and neck growth at the clean metal surface, unimpeded by barrier oxides and
- facilitates transportation of oxidative species and potential contaminating delubrication products, away from the surfaces being sintered.

This leads to the question of what constitutes a protective atmosphere for an FeMn alloy. As will be summarised in upcoming sections of this review, H_2 and mixtures of N_2-H_2 are quite common when sintering FeMn based structures because of the well known capacity of H_2 to reduce a number of metal (Me) oxides, including Fe-oxides according to reaction 2.25 [208].

$$MeO + H_2(g) = Me + H_2O(g) \tag{2.25}$$

However, looking at the Ellingham diagram in Figure 2.19, one could also see that reduction via reaction 2.25 is only thermodynamically favourable at low temperatures. H_2 reduction would not be as effective as direct or indirect carbothermal reduction through solid carbon in the form of graphite or carbides according to reactions 2.26 and 2.27. Both reactions are positioned lower on the plot relative to the oxide formation reactions of interest [208].

$$MeO + C(s) = Me + CO(g) \tag{2.26}$$

$$MeO + CO(g) = Me + CO_2(g) \tag{2.27}$$

In his work, Šalak claims that reduction of MnO is only possible through formation of specific carbides as shown in reactions 2.28 and 2.29. Moreover, these reactions could only take place at temperatures higher than 1280°C.

$$5MnO + 7C = Mn_5C_2 + 5CO \tag{2.28}$$

$$2MnO + Mn_5C_2 = 7Mn + 2CO \tag{2.29}$$

De Oro Calderon *et al.* [209] used thermal analysis techniques to corroborate Šalak's claims. In their publications, the addition of 0.5 wt.% graphite results in a step-wise reduction of MnO_2 into Mn_2O_3 first, then into MnO and finally into Mn when heated in an inert argon atmosphere. The DTA/TG-MS (Differential Thermal Analysis/Thermogravimetry coupled with Mass Spectroscopy) plot presented in Figure 2.20, indicates that the first reduction stages at 611°C and 897°C are accompanied by CO_2 formation (m44 peaks) whereas the final reduction stage of the highly stable MnO takes place at 1373°C leading to the generation of CO (m28 peak). At this point, the temperature is well above what is known as the Boudouard equilibrium at approximately 720°C [207], at which point any CO_2 generated will preferentially react with C to form CO according to reaction 2.30 [208].

$$CO_2(g) + 2C(g) = 2CO(g) \tag{2.30}$$

While it is clear that carbothermal reduction of highly stable Mn oxides can take place in Ar, use of H_2 and N_2-xH_2 (x = 5 - 10%) mixtures remains quite common to encourage early reduction of Fe oxides and facilitate the formation of

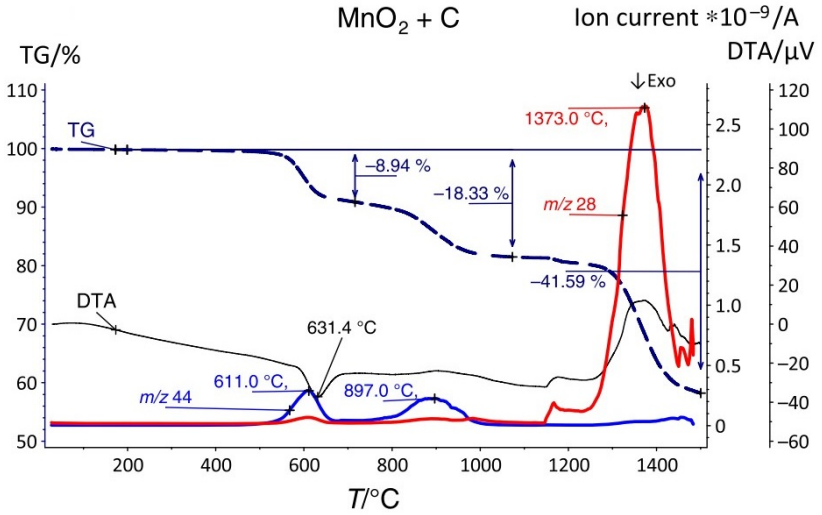

Figure 2.20: DTA/TG-MS analysis showing the reduction stages of MnO_2 intermixed with 0.5 wt.% C in Ar [209].

interparticle necks at higher temperatures [207, 211]. Figure 2.21(a) shows a similar scenario to that in Figure 2.20, where CO is detected at around 1195.4°C due to the reduction of a stable Mn-rich oxide by C in an Ar atmosphere. When the same material is sintered in H_2 one could observe an earlier peak associated with H_2O (m18 peak) detected at 412.2°C resulting from the reduction of less stable surface Fe-oxides, at a temperature at which reduction via H_2 is most favourable. That initial reduction of Fe oxides is associated with a slight weight loss that is

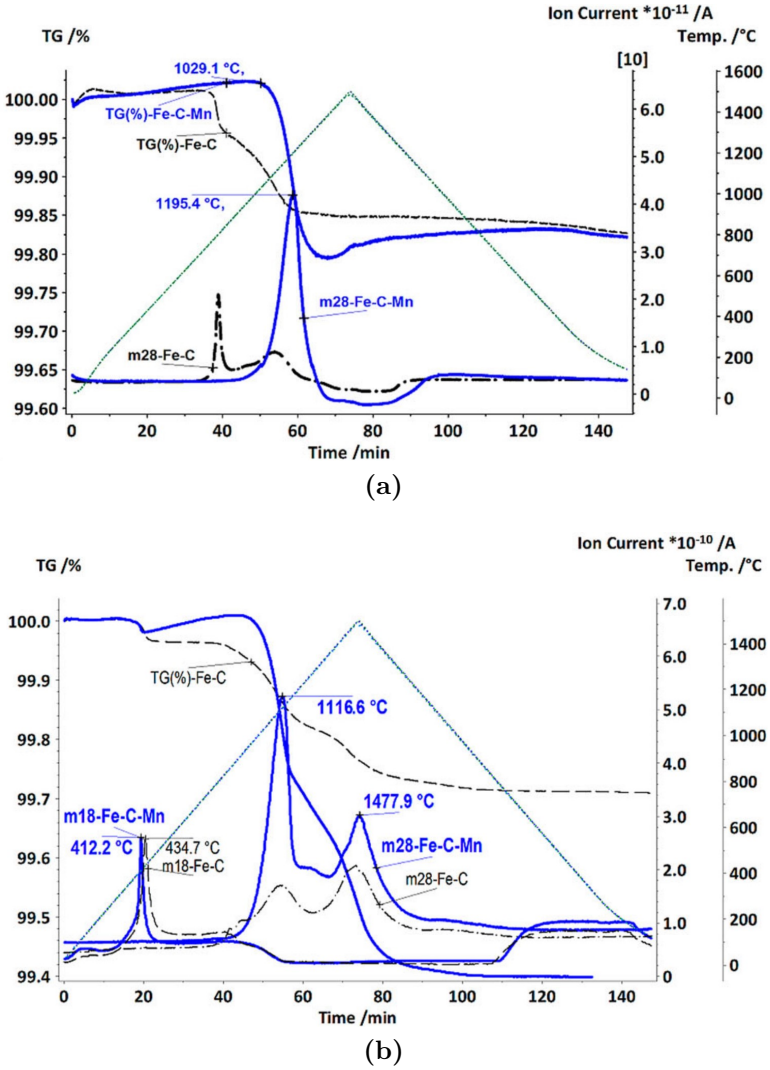

Figure 2.21: TG curves coupled with MS graphs of CO_2 (m44) and CO (m28) for reduction of Fe4Mn0.5C compacts sintered in (a) Ar and (b) H_2 [210].

immediately gained back. This is proof of what Šalak terms the "internal getter" effect, experienced in steels mixed with elements that has a high affinity to O. Even at this rather low temperature, Mn is highly reactive and readily oxidises in the presence of H_2O. It is also interesting to note, that most lubricants or organic additives used during processing of metal powders, experience gaseous decomposition around these temperatures as well, adding potential oxidative and contaminating species in the atmosphere around the reactive Mn [205, 212]. The next reduction peaks in Figure 2.20 only appear at 1116.6°C and 1477.9°C resulting in CO generation [210]. The initial CO peak would therefore be associated with the reduction of surface Mn-rich oxides whereas higher temperatures are required to reduce oxides deeper within the compacts/particles, or "internal oxides" [210, 213]. Since reduction of internal oxides is heavily dependant on diffusion of oxygen through the present FeMn phase at such high temperatures, the temperature at which the final reduction stage takes place is also highly dependant on the density of the compacts or size of the particles [214]. It is also interesting to note that processing in Ar, as in Figure 2.21 does not always show evidence of reduction of surface Fe-oxides. It seems, that at temperatures were carbothermal reduction is favourable even to reduce Fe-oxides, the reactivity of Mn is at a point where the products are instantly consumed to form more complex, often spinel-type, FeMn-oxides [209]. Since oxygen is essentially *transferred* from one metal to another, the TG does not show a loss *or* gain in weight.

Having recognised the importance of the atmosphere constitutents and positive impact of carbothermal reduction, Cias *et al.* suggested the use of an alternate approach to sintering Mn-containing steels in a number of studies [215–217]. They suggested placing samples in a stainless steel box, covered by a smaller overturned box and creating a glass-based seal that is activated at around 810°C in between, as shown in Figure 2.22. In this way, one could effectively create a semi-sealed microatmosphere that is less favourable for oxidation and more likely to reduce existing oxides and prevent decarburisation, irrespective of whichever "wet" gas is present in the rest of the furnace. Cias *et al.* showed that when using any carbon source, be it graphite within the compact or an organic product like naphthalene ($C_{10}H_8$), the $\frac{CO}{CO_2}$ ratio using this approach would be shifted to promote long-lasting reducing conditions in the semi-closed container. In fact,

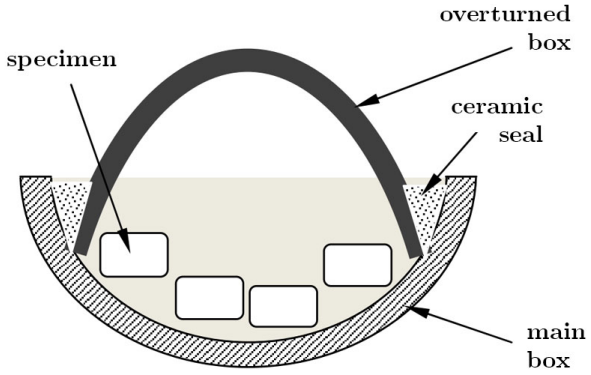

Figure 2.22: Schematic for the semi-closed container sintering approach proposed by Cias *et al.* [216].

bar the use of pure H_2 which gave the best results in terms of final oxygen content in the compact, any mixture of N_2-xH_2 (x = 5, 25, 75%) led to similar levels of reduced oxygen content when sintering Fe3Mn0.8C at 1120°C or 1250°C [215]. Note that even when adding only 3 wt.% Mn, Cias *et al.* were not successful in completely eliminating the formed Mn-rich oxides.

2.2.2.1.3 Influence of powder preparation method

When it comes to metal with high oxygen affinity, one approach that could reduce the reactivity of the metal by orders of magnitude, is the method of powder preparation [205]. Researchers refer to the following preparation techniques:

- blended metals, where the pure metals are simply mixed together often in a rotating mixer (Figure 2.23(a));
- intimately mixed or diffusion bonded, where the metals are mechanically milled for a short period of time or where the alloying element particles are slightly sintered to the main metal. In both cases the constituents are present as separate metals (Figure 2.23(b));
- use of a master-alloy, where the base metal is mixed with a master-alloy powder with a high concentration of the alloying element (Figure 2.23(c)); and

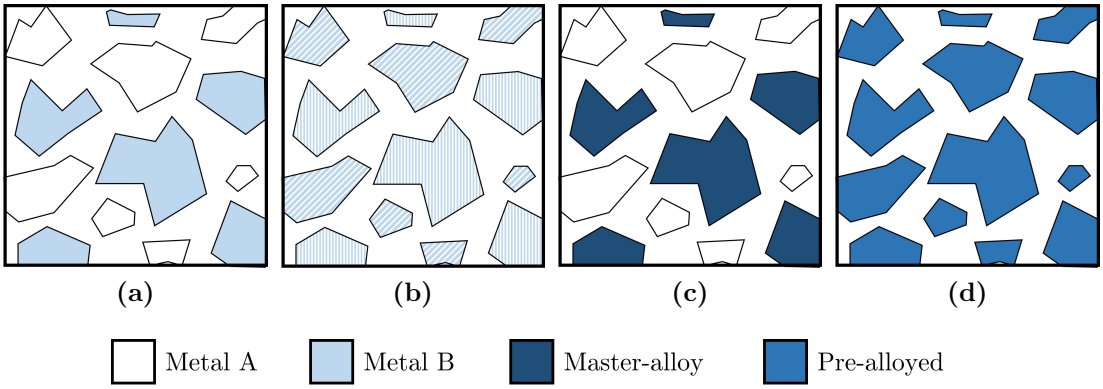

Figure 2.23: Variations of mixed and alloyed preparations of metal powders for processing including (a) blended (b) intimately-mixed (c) master-alloy mixed with base metal and (d) pre-alloyed powders. Adapted from [213].

- pre-alloyed, where the metals are pre-alloyed often using high energy mechanical alloying such that the starting powder during the sintering process already contains the metals in a homogenous concentration (Figure 2.23(d)) [213].

By incorporating Mn into the base metal in the ways listed above, one would effectively be changing the reactivity of the metal. Due to the fact that blended mixtures contain elemental Mn, the reactivity of blended powders tends to be the highest [205]. When the Mn is diffusion-bonded or mechanically milled at a low intensity in a ball miller with the base Fe, diffusion distances that could be in the order of tens of micrometers in the case of the blended mixtures, drop down to a few micrometers or even nanometers [213]. This facilitates the formation of complete solid solutions, as in pre-alloyed powders, wherein the reactivity is significantly lower. Since these preparation methods were mainly developed for compacted parts, the use of pre-alloyed powders generally led to issues with compressibility due to the increased strength attained by the powders following solid solution strengthening [211]. This in turn led to the use of master-alloys with the base metal. In such cases the pre-alloyed powders make up only a fraction of the powder being compacted, with the base metal providing the ductility to create relatively dense compacts [208, 210, 218].

Hryha *et al.* [211] studied the influence of powders used on the oxygen and carbon content in Fe0.8Mn0.5C sintered under strict atmospheric control in N_2-$10H_2$ at 1120°C or 1200°C for 30 min. The study compared the results when using admixed (or blended) powders with elemental Mn compared to pre-alloyed base powders combined with graphite. Lower oxygen contents were measured for pre-alloyed mixtures at all stages of analysis and for all sintering conditions. Moreover, more carbon was retained in pre-alloyed powders due to the lower necessity for its use in carbothermal reduction. Apart from this, microstructures for pre-alloyed compacts contained smaller, more rounded pores; a result of improved densification from cleaner particle surfaces. Moreover, the same microstructures exhibited a much more homogeneous distribution of the pearlite phase which suggested a faster and more even diffusion of carbon through pre-alloyed powders. This might be related to the higher defect density of most pre-alloyed powders that could lower activation energies for diffusion [219].

Few have discussed in detail the exact science behind the improved microstructures obtained with pre-alloyed powders however likely answers were given by de Oro Calderon *et al.* [209]. Figure 2.24 shows the final reduction peaks for Fe, Mn and C mixtures with the same stoichiometry but using different starting powders. The same figure compares these results to the reduction peak related to the MnO → Mn reaction when starting with a mixture of MnO_2+C. Whereas one would

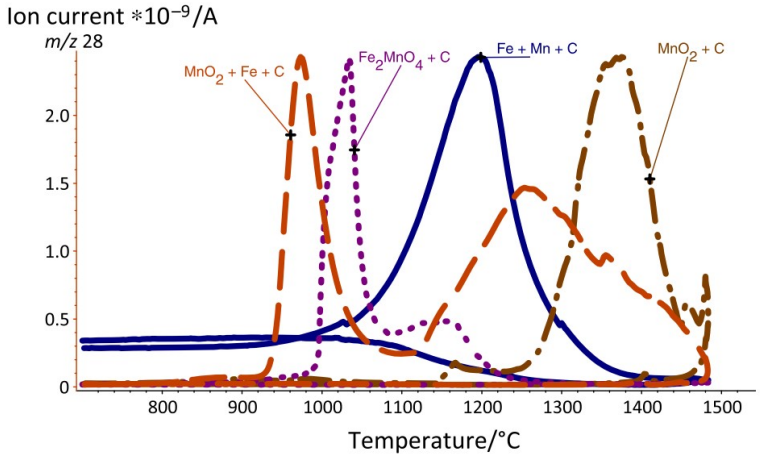

Figure 2.24: Degassing curves for CO (m28 peaks) when heating MnO_2+C and Fe_2MnO_4+C with the same stoichiometry, Fe+4Mn+0.5C and MnO_2+0.5C [209].

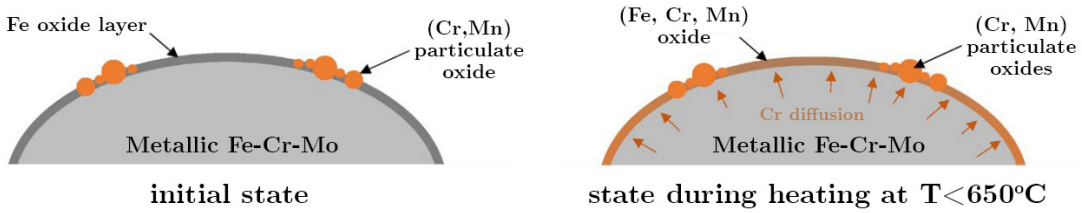

Figure 2.25: Schematic of "getter" effect exhibited by oxygen-sensitive Cr when using pre-alloyed FeCrMo powders in the formation of less stable mixed metal oxides [213].

assume that starting from a spinel Fe_2MnO_4 oxide, the formation of MnO would form following an intermediate reduction step, it seems that the final oxide that forms is a mixed metal oxide that is significantly less stable than MnO. The same could be said when mixing pure Fe with MnO_2+C. In the same way, the presence of Fe results in the formation of less stable mixed FeMn-oxides that are reduced at similar temperatures. The fact that blended elemental mixtures of Fe+Mn+C are at an intermediate point between the reduction of spinel FeMn-oxides and MnO_2 could indicate that Mn-oxides could either react with Fe at intermediate temperatures to form less stable mixed oxides, or that the dissolution of Mn in the surrounding Fe reduces its activity. The various modes of preparation could therefore offset both the reactivity of the Mn as well as the type of oxides formed on the metallic surfaces [209]. This was similarly explained for FeCrMo alloys wherein oxygen-sensitive metals could diffuse from the core of particles in which they are dissolved to form less stable mixed oxides instead of more stable particulate oxides, as represented in Figure 2.25.

2.2.2.1.4 Other factors affecting Mn oxidation and oxide reduction

A myriad of other parameters and powder characteristics can have overlapping influences on the sintering efficiency, oxidation and reduction of Mn-containing systems. Having taken a rather detailed look at thermodynamic implications on heating of oxygen-sensitive metals, Hryha *et al.* [207], also investigated the influence of kinetics on reduction of pre-alloyed FeCrMo powder mixed with 0.4 wt.% C, by varying the heating rate between 1 and 50 $K\,min^{-1}$ in Ar-10%H_2.

As with Mn-containing Fe, the presence of Cr in the metal results in a stepwise reduction of surface and internal oxides, each step needing an increasing amount of activation energy to take place, apart from favourable thermodynamic conditions. Hryha *et al.* showed how low heating rates resulted in more complete carbothermal reduction of stable oxides whereas for higher heating rates, the activation energies were reached within the following isothermal holding stage, risking incomplete reduction and trapping of deleterious oxides within the sintered structure. To the author's knowledge, similar studies have not be done with Mn-alloyed powder metallurgy steels. However, de Oro Calderon *et al.* mentioned that using a high heating rate between 600°C and 1000°C might help prevent formation of stable Mn-rich oxides due to the range being strongly reducing for Fe oxides but highly oxidising for Mn [220]. Despite this claim, using the rather high heating rate of 20 $\mathrm{K\,min^{-1}}$ when testing Fe4Mn0.5C in H_2 in Figure 2.21(b), did not prevent the Mn from instantly "gettering" the H_2O following the Fe oxide reduction stage at 412.2°C.

As already briefly mentioned, the particle size can also have a significant impact on both oxidation and reduction. Whereas small particles provide a higher reactive area resulting in a higher volume of generated surface oxides, smaller particles also carry a higher surface energy which in turn results in faster densification [196]. As Danninger *et al.* [221] explain, this could results in trapping of unwanted oxides within sintered structures that have adverse effects on the material performance in use. Moreover, carbothermal reduction is partly driven by the diffusion of the reactants to the surface. Therefore the larger the particles, the longer it takes for complete reduction to take place [213, 214, 222].

2.2.2.2 Sublimation

Another main characteristics of Mn, is its very high vapour pressure. Each element has a characteristic sublimation temperature at which the pressure of the solid reaches 1 atm. When this temperature is below the melting point, the element does not melt, but goes directly into vapour phase. For Mn, the vapour pressure is three orders of magnitude higher than that of Cu which is the next

Table 2.5: Vapour pressures of commonly used alloying elements in powder metallurgy at typical sintering temperatures [205].

Element	Temperature [°C]				
	900	1000	1100	1200	1300
	Vapour Pressure [Pa]				
Mo	2.03×10^{-17}	4.07×10^{-15}	3.73×10^{-13}	1.85×10^{-11}	5.66×10^{-10}
Si	2.25×10^{-17}	5.40×10^{-6}	8.13×10^{-5}	8.44×10^{-4}	6.49×10^{-3}
Ni	3.95×10^{-6}	1.17×10^{-15}	2.11×10^{-4}	2.68×10^{-3}	2.25×10^{-2}
Fe	2.99×10^{-6}	6.47×10^{-15}	8.85×10^{-4}	8.40×10^{-3}	5.93×10^{-2}
Cr	1.08×10^{-5}	2.36×10^{-4}	3.26×10^{-3}	3.13×10^{-2}	2.24×10^{-1}
Cu	4.23×10^{-4}	6.10×10^{-3}	5.94×10^{-2}	4.23×10^{-1}	2.33×10^{0}
Mn	0.38	3.23	20.0	95.0	367.0

most volatile element listed in the examples presented in Table 2.5. This particular characteristic makes samples containing Mn powder, susceptible to significant Mn losses during the sintering cycle.

Whereas some Mn vapour formed during the heat treatment will inevitably be lost, a significant portion will travel through the porous network, filling pores within the compact. Šalak describes how condensation of Mn vapour all over the particle surfaces, often in a needle-like morphology as shown in Figure 2.26a, generally results in more homogeneous distribution of Mn and aids the compositional homogenisation process [205]. Microstructures of Mn-steel cross-sections therefore, often reveal a Mn-rich shell resulting from inward diffusion of Mn following condensation. An instance of this is shown in Figure 2.26b for an Fe4Mn0.3C steel. However this has also been observed by groups in the biodegradable metals field with Mn contents between 25 and 35 wt.% [109, 110] wherein particles have ferritic cores surrounded by austenitic shells. The transport of Mn through the gas phase also results in a phenomenon termed as "Mn swelling" which Danninger *et al.* [218] confirmed using dilatometric measurements. Condensation over the

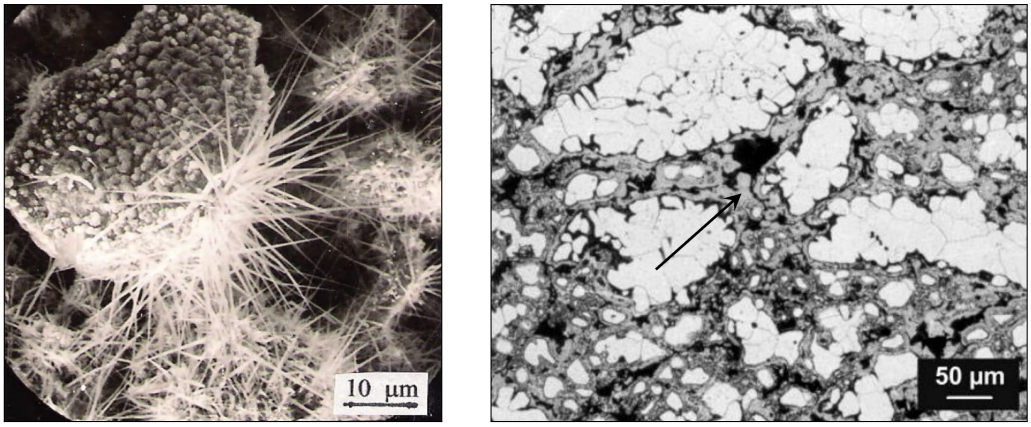

(a) **(b)**

Figure 2.26: (a) SEM image of needle-like condensation of Mn onto Fe-based particles following sublimation [205] and (b) cross-sectional microstructure of Fe4Mn0.3C sintered at 1120°C for 10 min, arrow pointing towards the Mn-rich shell following sublimation and condensation on surface [218].

particle surfaces results in an overall increase in dimensions that tends to become more prominent with increase in Mn content.

While sublimation aids homogenisation, the relocation of Mn towards the surface of the particles where it is more susceptible to reactions with oxygen-carriers in the sintering atmosphere, naturally also has adverse effects. As discussed in Section 2.2.2.1, should non ideal sintering parameters be used, incomplete carbothermal reduction could result in trapping of a significant volume of interconnected stable surface oxides. Moreover, since oxides deter efficient diffusion processes, stable Mn-rich oxides at particle surfaces could also result in more porous structures.

The rate of Mn sublimation could be affected by several system characteristics. Šalak notes how Mn sublimates preferentially from areas containing higher defects, sharp points and edges among other regions with high surface energy [205]. Moreover, smaller particles, which imply higher surface-to-volume ratios, also result in faster sublimation rates. In fact, data provided in Table 2.6, shows how decreasing particle size and increasing temperatures lead to phenomenally fast sublimation of 1 g of Mn powder.

As with oxidation, the method of powder preparation can also affect the

Table 2.6: Sublimation time for 1 g of Mn powder with sizes of 10, 20 and 50 µm at different temperatures [205].

	Sample size	**Temperature [°C]**			
		400	600	800	1000
Sublimation time [s]	10 µm	2.4×10^{10}	3.8×10^{5}	4.2×10^{2}	4.1
	20 µm	4.8×10^{10}	7.6×10^{5}	8.2×10^{2}	8.2
	50 µm	1.2×10^{11}	1.9×10^{5}	2.1×10^{3}	20.4
	Sample size	**Temperature [°C]**			
		1100	1150	1200	1250
Sublimation time [s]	10 µm	0.9	0.6	0.15	0.1
	20 µm	1.8	1.5	0.3	0.2
	50 µm	4.5	3.5	0.8	0.5

sublimation rate. In fact, reducing the reactivity of Mn by pre-alloying also allows for slower sublimation [205]. When it comes to biodegradable metals research, Feng *et al.* [179] mechanically alloyed their Fe30Mn6Si-1Pd alloys in Ar for 15 h at 300 rpm to avoid Mn sublimation however did not provide a reference material without pre-alloying to confirm whether this approach was successful in suppressing sublimation in this case. On the other hand, Xu *et al.* [124] have discussed the subject of sublimation in significant depth also with alloys aimed for biodegradable implant applications [122, 123, 125]. In an attempt to limit oxidation of Mn and Si, the authors repeatedly studied Fe28Mn4Si processed in vacuum. This naturally enhances the sublimation rate which causes the formation of a manganese depleted region, with the lowest manganese content being at the surface of the pressed compact, increasing towards the centre. However, Xu *et al.* demonstrated that using mechanically milled powders reduces this effect compared to blended elemental mixtures. In fact sintering at 1200°C for 3 h resulted in an 18.6% weight loss for blended elemental samples and approximately 9.5% weight loss for mechanically milled samples.

2.3 Scaffold processing methods

With an increase in interest in the study of biodegradable materials and their performance, also came rapid development of powder metallurgical methods to prepare biodegradable implants. This section outlines the main techniques discussed in literature for the fabrication of Fe-based porous structures. For the purposes of this review, only techniques suitable for the fabrication of orthopaedic scaffolds using metal powders as starting materials will be mentioned. Tailored, structurally organised implants are becoming an increasingly hot-topic in biodegradable implant research as the hopes of personalised scaffolds for improved healing has attracted the interest of practitioners and patients alike. Therefore, the following methods are categorised based on whether or not they result in structures that are customisable in any way. Where applicable, observations related to issues related to Mn processing discussed in Section 2.2.2, will also be brought to attention.

2.3.1 Fabrication techniques for non-ordered open-porous structures

2.3.1.1 Replication method

The replication method is a processing technique that has been used by multiple groups in the field to prepare randomly-ordered reticulated foam structures using Fe and Fe-based alloys. The technique involves the preparation of a slurry containing the metal powders of interest and some form of binder, like the commonly used polyvinyl alcohol (PVA). The slurry is then applied to the surface of a polymeric foam, typically reticulated polyurethane sponge, which serves as a template. Once the excess slurry is removed from the porous network of the template, it is then subjected to a heat treatment during which the template is burnt out and the remaining metal skeleton is sintered. The sintered foams characteristically consist of hollow triangular-sectioned struts framing pentagonal cell windows. In general, open porosities typically amount to around 80-90% [81, 189, 199].

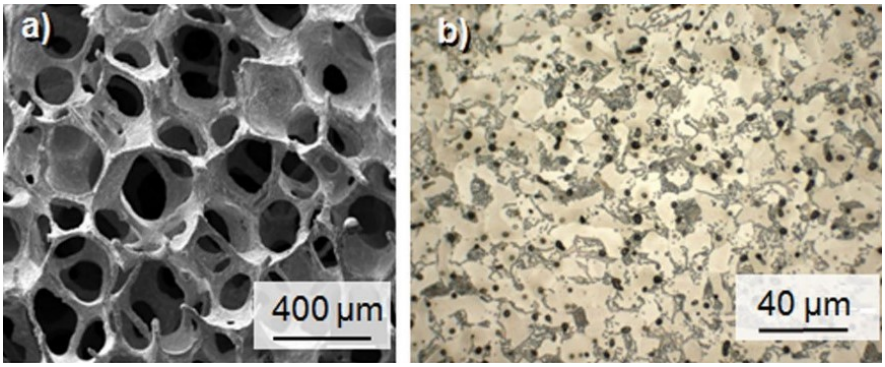

Figure 2.27: (a) SEM image of Fe0.6P foam prepared using the PU replication method and (b) optical image of a polished cross-section showing ferrite and pearlite phases [189].

Quadbeck *et al.* [199–201] first suggested using this technique to prepare bone scaffolds in 2007. Since then Fe, FeP, FeMg and FeCNTs were also prepared using this route [81, 183, 203]. Wegener *et al.* [189, 223] prepared Fe0.6P foams which they later implanted in the tibiae of merino sheep for up to 12 months. An SEM image and optical micrograph of the cross-section of a strut can be seen in Figure 2.27. *In vivo* results indicated positive response of the sheep to the implant but very little degradation was observed by the end of the test. To the author's knowledge, this technique has never been used to prepare Mn-containing foams.

2.3.1.2 Space-holder method

The space-holder method is a technique wherein the metal powders are mixed with a porogen and pressed into homogeneous compacts. The porogen takes up space within the compact which could then be reclaimed by dissolving or burning-out the same space-holder. In this way, increasing the vol.% of porogen used increases the potential for interconnected porosity and reduces the limitations that come with pressureless sintering when using techniques like the replication method.

Ammonium bicarbonate was used by Čapek *et al.* [224] and Zhang *et al.* [153] to prepare porous Fe and Fe35Mn respectively. By using up to 20 vol.% NH_4HCO_3, total pore volumes of up to 51% were achieved. When preparing porous Fe35Mn, the authors noted the presence of both austenite and ε-

martensite potentially indicating some form of Mn segregation during mixing or sintering. Feng *et al.* [179] also used this technique with sodium chloride crystals as porogen to prepare porous Fe30Mn6SiPd structures. The process resulted in fully austenitic structures with 62.3% porosity when adding 40 wt.% NaCl. The use of NaCl could lead to a situation where incomplete removal of porogen results in premature corrosion of the structure, however, Feng *et al.* used sublimation during the sintering as the removal method for NaCl which should decrease the likelihood of this being an issue.

When it comes to issues related to processing with Mn, Zhang *et al.* [153] used XRD to show the presence of a considerable peak of mixed (Fe,Mn)O relative to the main peak for austenite when processing Fe35Mn foams. No exact Mn concentrations were provided, however, the detection of ε-martensite indicates that at least regions of the foam experienced either incomplete homogenisation of Mn distribution or significant sublimation, as ε is generally not formed in Fe alloys containing more than around 27 wt.% Mn [101]. Feng *et al.* [179] did not comment on either oxidation or sublimation of Mn when processing their Fe30Mn6SiPd alloys using the space-holder method. However, it is likely that peaks for MnO or (Fe,Mn)O at approximately 35° and 40.5° were mislabelled to be Fe_2O_3, considering the much higher stability of the former.

2.3.2 Fabrication techniques for ordered open-porous structures

2.3.2.1 3D inkjet printing

One of the first methods used to prepare customised porous structures was developed by Chou *et al.* [112]. Fe30Mn porous structures with pore sizes down to 500 µm and porosities between 36 and 40%, were directly printed by extruding a paste composed of the metal powder and a water-based binder. The green parts were then debinded and sintered in ultra high purity N_2 at 1200°C. Figure 2.28a shows a part produced using this method, following tumble finishing. Similarly, Hong *et al.* [127] printed Fe34Mn1Ca using the same technique but sintering in Ar. In both cases debinding was done at a lower temperature to remove the

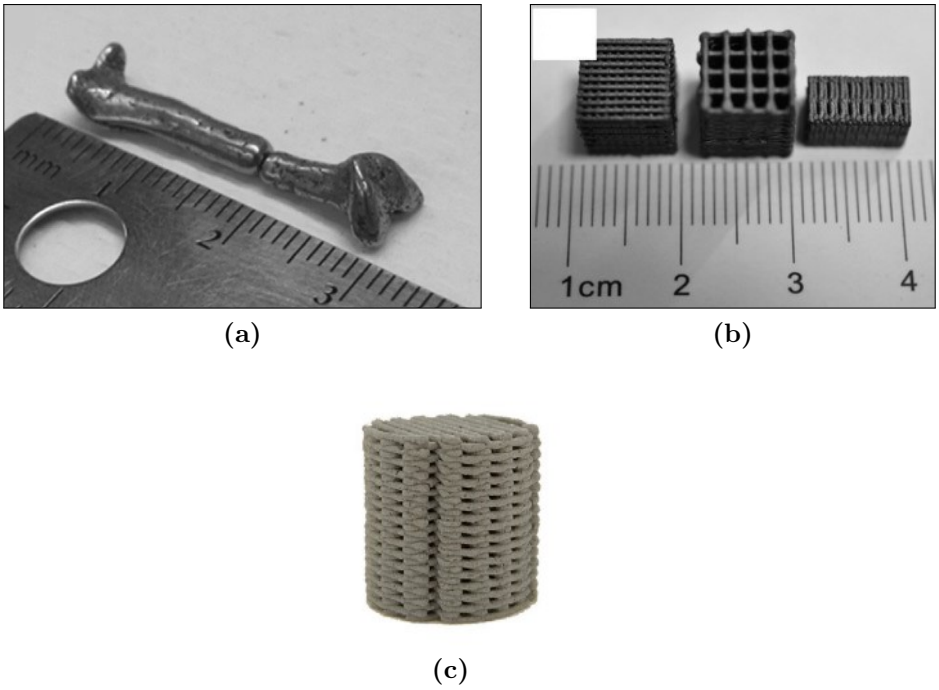

(a) (b)

(c)

Figure 2.28: 3D inkjet printed (a) Fe30Mn [112] and (b-c) Fe structures [225, 226].

binder. Since the extruded runs were not subjected to pressure in any way, either mechanical milling [112] or alloying [127] was employed in both studies to intimately bind or alloy the powders prior to the printing process, encouraging austenite formation during subsequent sintering as well as reduced oxidation and sublimation. Despite this, ε-martensite was still detected as a major phase in the printed samples. Chou *et al.* also noted that sintering in N_2 atmosphere led to considerable oxidation of their parts and mentioned the use of oxygen getters in future studies to alleviate this effect. On the other hand, the amount of C detected in the sintered structures was just 0.18 wt.% indicating sufficient binder burnout in the proposed process.

Two other groups, Yang *et al.* [225] and Putra *et al.* [226–228] used a similar approach to 3D print Fe and Fe35Mn scaffolds. The authors similarly mixed the metal powder with an aqueous binder and directly printed their structures. The green samples were then debinded and sintered in Ar at 1120°C [225] and at 1200°C [226]. The two groups achieved porous structures with porosities of around 67%. Structures prepared by both are shown in Figure 2.28b and (c).

All these processes achieved highly microporous solids, apart from the designed macroporosity. With regards to oxidation, Putra *et al.* [227] reported that just 2 wt.% of Mn-oxide was detected in the final printed parts sintered in pure Ar. SEM images of the structure surfaces also showed very clean surfaces.

2.3.2.2 TOPIS

In 2018, Sharma *et al.* [204] published the first work on the preparation of Topologically Ordered Porous Iron Scaffolds (TOPIS) or Foams (TOPIF) making use of polymer 3D printing coupled with pressureless microwave sintering. The process outline is represented in Figure 2.29. To prepare the structure, first a 3D template with the desired geometry is printed with a suitable polymer 3D printer. A phosphate-based investment mould is then prepared using the 3D printed part as the form. The mould containing the 3D print is then heated to 900°C to burn-out the polymer template. The mould cavity is filled with carbonyl iron powder[1] under ultrasonication and placed in a furnace where sintering takes place

[1]Variety of high purity Fe powder prepared through the decomposition of purified iron pentacarbonyl [205].

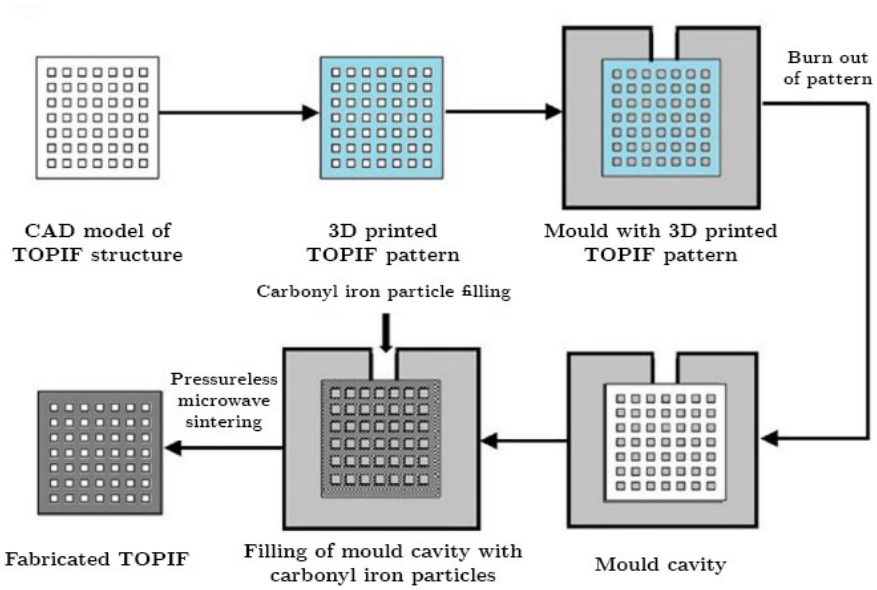

Figure 2.29: Schematic of process for optaining TOPIS structures [229].

at 948°C. Following sintering, the mould is removed and the sintered structure is shot blasted to acquire a better finish.

Further publications by the group proved that the technique could be rather flexible in terms of the geometries that can be fabricated. Due to the relatively low sintering temperature used, the structure contained a significant amount of microporosity which led to lowered electrochemical potentials and a shift towards pitting corrosion when tested electrochemically in SBF [229–232]. So far, the technique has not been tested for the preparation of Mn-containing foams.

2.3.2.3 Laser Bed Powder Fusion

Laser Bed Powder Fusion (LBPF), also referred to by the propriety name Selective Laser Melting (SLM), is a technique that has attracted a lot of attention in the biodegradable metals field. Although it does not involve solid-state sintering, LBPF uses metal powders that are selectively fused layer-by-layer, allowing for 3D printed complex structures to be fabricated.

Li *et al.* [233] first prepared Fe scaffolds using LBPF and went on to demonstrate the excellent corrosion fatigue resistance the structures possessed [234] while also testing the feasibility of printing functionally graded porous Fe structures to permit tailoured degradation rates among other characteristics [235].

More recently, Shuai *et al.* [108] attempted LBPF of an FeMn alloy. The resultant structure was dimensionally close to the designed specifications with 600-800 µm struts and 67% porosity. However, the detected Mn was rather segregated along grain boundaries and the content detected using EDS was between 19.2 and 20.3 wt.% compared to the 25 wt.% added. This indicated that despite the use of 2 hr-milled Fe25Mn powder, significant sublimation of Mn or formation of Mn oxides, took place during the process. Moreover, the equiaxed microstructure was also composed primarily of austenite but also contained α'-martensite which is generally undesirable.

The same was reported by Carluccio *et al.* [182] where despite the higher Mn content, at 35 wt.%, the authors observed ε-martensite in the microstructure, resulting from the high cooling rates following laser melting. The group reported successful printing of scaffolds with 400 µm pores and 600 µm struts and a total of

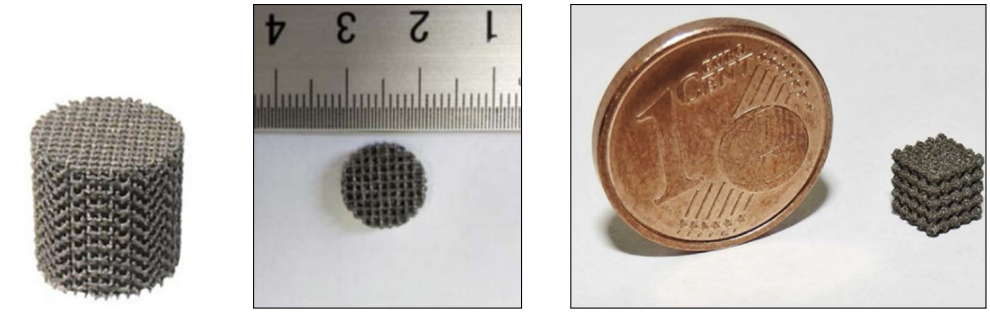

(a) (b) (c)

Figure 2.30: Scaffold structures prepared via LBPF made of (a) Fe [233] and (b-c) FeMn [108, 182].

42% porosity. With optimised laser energy, they also reduced the microporosity to $< 0.6\%$, enhancing the strength of the printed scaffolds [236]. In this case, none of the publications mentioned loss of Mn due to evaporation. Although it might have been something that the authors overlooked, lowered evaporation rates could be a result of using less reactive gas atomised Fe35Mn powders as starting material [237]. Scaffolds prepared in the studies mentioned in this section are shown in Figure 2.30.

Ongoing research by groups in the biodegradable metals field are conducting further investigations on the effects of processing parameters on the evporation of Mn and other microstructural features that could be used to tailor the implants' properties [149, 238, 239].

2.3.3 Summary of sintering parameters for Fe-based foams

Excluding Laser Bed Powder Fusion manufacture of metal foams, the techniques discussed in Section 2.3 all have sintering as one of the final steps. As has been discussed in detail in this review, sintering temperature and atmospheres in particular, play a very important role in the formation of the final microstructure of the sintered part. Table 2.7 summaries these two parameters as used in the principal studies discussed in this section.

Table 2.7: Summary of parameters used for sintering Fe and FeMn foams with different processing methods.

Composition	Processing method	Sintering temperature	Sintering atmosphere	Ref.
Fe	PU replication	1120°C	H_2	[201]
Fe/Fe-P	PU replication	1120°C	N_2-10H_2	[81]
Fe-P	PU replication	1080°C	H_2	[189]
Fe/Fe-CNTs/Fe-Mg	PU replication	1120°C	N_2-10H_2	[203]
Fe/Fe-CNTs/Fe-Mg	PU replication	1120°C	N_2-10H_2	[183]
Fe	Space-holder	1000°C	Vacuum	[224]
Fe35Mn	Space-holder	1200°C	Vacuum	[153]
Fe30Mn6SiPd	Space-holder	900°C	Vacuum	[179]
Fe	TOPIS	948°C	-	[204]
Fe30Mn	3D printing	1200°C	N_2	[112]
Fe34Mn1Ca	3D printing	1200°C	Ar	[127]
Fe	3D printing	1200°C	Ar	[226]

2.4 Conclusions

At a time when the field of biodegradable metals is celebrating a significant amount of success with Mg and Mg alloys, the community does not seem to be making a similar headway with research on Fe-based biodegradable alloys and devices. Whereas a lot of individual research groups are publishing encouraging results concerned with processing innovation, corrosion and biological research, few studies are coming together in a way that promises a noteworthy breakthrough related to Fe and its alloys for biodegradable implants, studies often terminating at, or prior to, *in vivo* testing.

When it comes to corrosion testing, one major limitation highlighted in this review has been the lack of testing protocols available for researchers in the field to streamline the research being done by different groups. The significant influ-

ence of aspects like sample processing methods, electrolyte formulations, testing setups and methodologies on the materials' performance, has made it increasingly difficult to identify the stumbling blocks being met with achieving higher, consistent and more suitable corrosion rates with Fe-based alloys.

Even more challenging is the effort to bridge the gap between *in vitro* and *in vivo* testing environments. With the latter being so complex, it has proved to be particularly challenging to translate successful results *in vitro*, to similar positive results with an animal model. Therefore, the efforts to enhance *in vitro* testing procedures to reflect better the mechanisms that govern *in vivo* degradation, have also been a focus point for active groups in the field irrespective of the materials of interest.

Having said this, alloying Fe with Mn to achieve a non-magnetic material and further alloying with a noble metal addition to encourage microgalvanic corrosion, remains an attractive approach based on the results discussed in this chapter. However, the various conflicting results as well as difficulties encountered by various groups when working with Pd and Ag in particular, clearly need further investigation.

On another note, the second part of this review underlined the major technologies being developed to prepare Fe-based scaffold structures. With powder metallurgy being such an attractive route for material and geometrical customisation, it is no surprise that the vast majority of innovative processes fall under this processing category.

Although various new technologies including capital-intensive additive manufacturing methods have been adapted to prepare ordered Fe-based scaffolds, so far, the only scaffold structures that have been subjected to *in vivo* testing were Fe0.6P foams prepared via the polyurethane replication method. Despite the fact that this method has been used by various different groups, it has not yet been applied to prepare FeMn structures, notwithstanding the alloy's prominence in the field. The reasons behind this could very likely be the processing issues brought about by the inclusion of Mn powders, including the formation of incredibly stable oxides, and Mn loss through sublimation.

2.5 Research questions and objectives

In view of the literature reviewed in this chapter, the following primary research questions will be addressed.

i. ***How does the addition of 35 wt.% Mn and 5 wt.% Ag to Fe via powder processing, influence the metals' degradation behaviour upon immersion and in subsequent hours?***

   With conflicting views presented in literature regarding the degradation mechanisms of FeMn and FeMnAg alloys alike, this work aims to study the evolution of degradation over an extended testing period by continuously monitoring these metals' behaviour *in situ*. It is likely that dominant corrosion mechanisms upon immersion, or after OCP monitoring, will be very different from the behaviour exhibited after 24 h, for instance.

ii. ***To what extent does the testing electrolyte composition, in particular the presence of Ca^{2+} ions and albumin, affect the degradation behaviour of Fe-based alloys?***

   While establishing the role of alloying elements, the change in corrosion behaviour brought about by changes in testing electrolyte formulation, will be investigated. Whereas the presence of Ca^{2+} ions has been implied to result in a decrease in corrosion rate, the role of said ions on the degradation of Fe and its alloys has not been studied in detail. The influence of protein on the degradation of the same metals is even more disputed.

iii. ***What are the distinctions between outcomes of in vivo testing of FeMn alloys with respect to their in vitro behaviour?***

   As described in detail in this chapter, the number of complete *in vitro-in vivo* studies on Fe-based alloys, is very low. Although it is expected that *in vivo* degradation progresses more slowly compared to degradation in any *in vitro* test, highlighting the differences in corrosion mechanisms, degradation products formed and any other observations could help inform the establishment of relevant standards which thus far have been lacking.

iv. ***Can powder pre-processing using ball-milling provide a feasible solution for the preparation of Fe35Mn scaffolds through the pressureless sintering route?***

High energy ball milling has been mentioned in a few publications related to the processing of FeMn for biodegradable alloys, however its use to prepare powders that can be used for scaffold fabrication using pressureless sintering processes, for e.g. the replication method, has thus far not been explored. The final part of this work is dedicated to address this question.

The principal objectives of this dissertation are listed hereunder.

Corrosion testing

i. To prepare and characterise powder-processed testing coupons with the following compositions: Fe, Fe35Mn, (Fe35Mn)5Ag. The aim is to first compare the outcomes of adding Mn to the findings published in literature and then determine the extent, if present, of micro-galvanic corrosion brought about by the addition of Ag. All or select alloys can then be analysed further following initial testing stages depending on early results;

ii. To analyse the degradation behaviour of the Fe-based alloys using a variety of techniques including:

- potentiodynamic testing;
- electrochemical impedance spectroscopy (EIS);
- *in situ* measurements of pH and dissolved oxygen (DO)

to provide a clearer picture of the degradation process over the first hours from immersion. Wherever logistically possible, tests are to be done over a period of at least 24 h in order to observe evolving trends following immersion;

iii. To identify the impact of powder processing on the degradation process;

iv. To determine the impact of the electrolyte composition on the degradation trajectory of the different alloys - to be done with particular focus on HBSS solutions most commonly used in the field, with and without Ca^{2+} ions;

v. To explore the role of protein added to the testing electrolyte on the degradation of Fe-based alloys using, in part, electrochemical impedance spectroscopy (EIS) to study changes in the corroding system over a period of at least 24 h following immersion;

vi. To analyse powder-processed Fe-based pins prepared by the candidate and used in a 6-month *in vivo* test, with respect to *in vitro* findings.

Powder processing of FeMn for scaffold applications

i. To prepare Fe35Mn powder using different pre-processing methods in order to induce different levels of chemical activity. The powders to be analysed should include a blended elemental mixture of Fe and Mn powders, ball-milled Fe and Mn in the same ratio, and fully alloyed Fe35Mn;

ii. To characterise the as-purchased and as-processed powders using SEM-EDS analysis and to make use of thermal analysis techniques that can provide information on melting points and mass changes affected while heating;

iii. To discuss the relationship between powder-processing method and the formation of stable oxides and/or reduction of the same oxides with powder coupons sintered at typical sintering temperatures for FeMn alloys;

iv. To explore the feasibility of processing Fe35Mn scaffold structures using a modified version of the traditional polyurethane replication method in which the polyurethane sponge used as the template in the latter, is replaced with a custom designed 3D-printed acrylate template;

v. To characterise samples prepared using the modified replication method using methods like XRD, SEM-EDS as well as the aforementioned thermal analyses techniques. Test results can be used to discuss the influence of material and process parameters on the elemental and phase composition of the resultant samples, in view of investigations carried out on powders and pressed coupons prepared using the same materials beforehand.

3

Methodology

This chapter describes in detail the materials and methods employed in order to achieve the objectives set out in Section 2.5. As with the research questions and objectives presented, the methods are shared in two distinct sections - one related to work carried out on *Corrosion testing* of FeMn alloys and another related to work on *Powder-processing of FeMn for scaffold applications*. These two sections are preceded by details related to the metallic powders and material characterisation techniques used throughout the whole work.

Work related to both the main testing sections has been split in distinct phases. Each testing phase contains analyses that informs decisions made in the subsequent testing phase when it comes to material/electrolyte selection for further analysis and choice of specific testing variables or parameters. Whereas the tests and corresponding results presented were generally carried out in the order that they are presented, the final presented phases were structured in a way that helps with the understanding and readability of the text. At the end of this chapter, one can find a diagram summarising the principal methods and order of presentation for all the testing phases described in detail in the following text. This should aid the reader in following the work progress throughout Chapter 4 which presents both the results and discussion sections related to the following methods.

3.1 Raw materials

3.1.1 Material specification

Manufacturer details related to the powder metallic materials used in this study, are provided in Table 3.1.

3.1.2 Material characterisation

Microstructural and compositional analysis was carried out using a Carl Zeiss FE-SEM Merlin Gemini II column (Germany) fitted with an Ametek EDAX energy dispersive X-ray detector (USA) and using a Secondary Electron detector[1]. For morphological observations, a sample for each powder material was stuck directly to conductive carbon-tape.

Cross-sections of the powder samples were also analysed using SEM by first mixing a sample of raw powder with pellets of hot-mounting material (Conducto-Mount 2, Metprep, UK) and consequently hot-mounted using a Remet IPA 30 (Remet, UK). Prior to analysis, all samples were ground to P2500 SiC paper (Metprep, UK), polished using 3 µm diamond suspension (Struers, Denmark) and finally by 0.25 µm colloidal silica (OP-S) (Struers, Denmark). Following the polishing procedure, all samples were ultrasonicated in acetone and ethanol for 5

[1]Unless otherwise indicated, SEM analysis throughout this work was conducted using this machine with a Secondary Electron (SE) detector for optimal topological resolution.

Table 3.1: Details of powder raw material used in this study.

Powder	Size	Preparation Method	Supplier
Fe, 99.0% purity	$<$ 45 µm	Steam atomisation	US Research Nanomaterials
Mn, 99.6% purity	$<$ 10 µm	Electrolytic	Alfa Aesar
Ag, 99,9% purity	4 – 7 µm	Chemical precipitation	Alfa Aesar
Master Alloy (MA) *[Fe-35Mn-4C]*	Not provided	Atomised	Atomising Systems Limited

min each, followed by vacuum drying. Samples were stored under vacuum up till the time of analysis[1].

Phase analysis of the as-received powders was carried out using X-Ray diffraction (XRD). A Bruker D8 Advance (USA) equipped with a copper source (Cu-Kα, $\lambda = 0.141$ nm) and a graphite monochromator, was used to run scans at 2θ angles between 30° and 70° using a step size of 0.02°. The diffractometer was set to move at $1^\circ\,\mathrm{min}^{-1}$ whereas the surface being analysed was set to spin at 15 rpm.

3.2 Corrosion testing

3.2.1 Specification of testing solutions

The sterile testing solutions used throughout this work were primarily supplied by Thermofisher Scientific (USA). Over the course of the study, two formulations of Hanks' Balanced Salt Solutions (14175, HBSS and 14025, HBSS+Ca) were used. In specified instances, testing was carried out in HBSS+Ca supplemented with 20.6 $\mathrm{g\,L}^{-1}$ Bovine Serum Albumin (Sigma-Aldrich A2153, BSA) as well as 1 vol.% penicillin-streptomycin (Gibco 15140122, PS) to prevent microbial growth in the presence of protein. The protein-containing solution will be referred to as HBSS+BSA. The full formulations of the testing solutions are provided in Table 3.2. Apart from the listed solutions, the study also mentions the use of physiological saline which comprises a 0.9 wt.% NaCl solution. The NaCl used was also supplied by Thermofisher Scientific.

3.2.2 Phase One - Corrosion testing of porous alloys

The first stage of corrosion testing was concerned with comprehensive testing of microporous Fe, FeMn and FeMnAg alloys, using both bulk material testing techniques like potentiodynamic testing (PDP) and Electrochemical Impedance Spectroscopy (EIS) testing. Specialised techniques that allow the researcher to observe changes happening at the surface on the micrometric scale, were also utilised. In this section, testing was carried out in two commonly used variations

[1] Unless otherwise specified, polished samples throughout this work were prepared using this procedure.

Table 3.2: Formulation for testing solutions used in the study.

	Concentration (mg/L)		
Constituent	**HBSS**	**HBSS+Ca**	**HBSS+BSA**
Inorganic Salts			
KCl	400.0	400.0	400.0
KH_2PO_4	60.0	60.0	60.0
$NaHCO_3$	350.0	350.0	350.0
NaCl	8000.0	8000.0	8000.0
Na_2HPO_4 (anhydr.)	48.0	48.0	48.0
$CaCl_2$ (anhydr.)	-	140.0	140.0
$MgSO_4 \cdot 7H_2O$	-	100.0	100.0
$MgCl_2 \cdot 6H_2O$	-	100.0	100.0
Other Components			
D-Glucose (Dextrose)	1000.0	1000.0	1000.0
Bovine Serum Albumin	-	-	20600.0
Penicillin-Streptomycin	-	-	10 [mL/L]

of Hanks' Balanced Salt Solutions to simultaneously investigate the impact of electrolyte composition over test outcomes. All techniques used and consequent characterisation, were aimed at gaining an insight into the degradation mechanisms operating at the metal surfaces and how these progress over the first hours upon immersion.

3.2.2.1 Material preparation

The powders specified in Section 3.1 were used to prepare powder mixtures of Fe35Mn and (Fe35Mn)5Ag. Elemental powders were placed in the desired weight ratios in 50 mL centrifuge tubes along with five hardened stainless steel balls with a diameter of 10 mm, to aid in achieving a homogeneous powder mixture. The tubes were tumbled for 5 h in a Bio-Components Inversina tumbler (Switzerland).

For electrochemical testing, 10 g of Fe and the Fe35Mn and (Fe35Mn)5Ag mixtures (subsequently referred to as Fe, FeMn and FeMnAg respectively) were uniaxially pressed at 520 MPa in a stainless steel die with a 22 mm diameter

bore using an Instron 8802 hydraulic press, to prepare green compacts. For local pH and dissolved oxygen (DO) measurements, 6 g powder was loaded in a custom die with an 8 mm diameter and pressed at 1.8 GPa to prepare cylinders approximately 18 mm long.

Both types of compacted coupons were sintered in a Nabertherm tube furnace (Germany) under 100 $\mathrm{L\,h^{-1}}$ flow of N_2-5H_2 gas. A heating rate of $180^{\circ}\mathrm{C\,h^{-1}}$ was used followed by a 3 h dwell at 1120°C. The samples were furnace cooled.

For electrochemical testing, the coupons were cut into 1 $\mathrm{cm^2}$ coupons with a thickness of approximately 4 mm. The 18 mm cylinders were turned using a machine lathe to prepare 15 mm long pins with a 3 mm diameter. In both processes, the thick manganese oxide layer formed at the surface during the heat treatment was fully removed.

3.2.2.2 Pre-testing characterisation

Microstructural and compositional analysis of the polished samples was carried out as specified in Section 3.1.2.

For purposes of a general comparison, each materials' surface porosity was estimated by measuring the percentage pore area. Thirty SEM images from three different coupons prepared from the same material, were binarised using ImageJ software. The percentage area representing the porosity was noted and the mean and standard deviation calculated. A better representation of the area would have been estimated with the use of non-contact profilometry combined with surface recreation using the "*surf*" function in Matlab. However, the availability of the machine as well as limited computational power available, limited the amount of data that could be processed such that it could not be considered representational. This aspect of characterisation was improved in the subsequent testing phases.

Phase analysis was carried out using X-Ray diffraction (XRD) on ground coupon surfaces. A Bruker D8 Advance XRD (USA) equipped with a copper source (Cu-Kα, $\lambda = 0.141$ nm) and a graphite monochromator was used to run scans at 2θ angles between 30° and 100° using a step size of 0.02°. The diffractometer was set to move at $1^{\circ}\,\mathrm{min^{-1}}$ whereas the surface being analysed was set to spin at 15 rpm.

3.2.2.3 Potentiodynamic testing

PDP tests were performed on Fe, FeMn and FeMnAg in HBSS as well as HBSS+Ca in order to obtain an indication of the relative corrosion rates of the materials in both testing environments. The cut coupons were mounted in cold-mounting epoxy resin (Epo-Set, MetPrep, UK) after attaching a piece of insulated copper wire, to leave an exposed apparent surface area of 1 cm^2. A clamping force was applied to the electrical connection between the wire and the coupon while the epoxy cured, to ensure a sound electrical connection. Once the epoxy cured, the samples were ground using SiC paper up till grade P2500, and ultrasonicated for 5 min in ethanol.

Tests were carried out using 300 mL of testing solution in a double-jacketed beaker with constant circulation of water at a temperature of 37 ± 2°C. The test sample was set as the working electrode and connected to a Saturated Calomel Electrode (SCE) as a reference and a platinum-coated rod as a counter-electrode

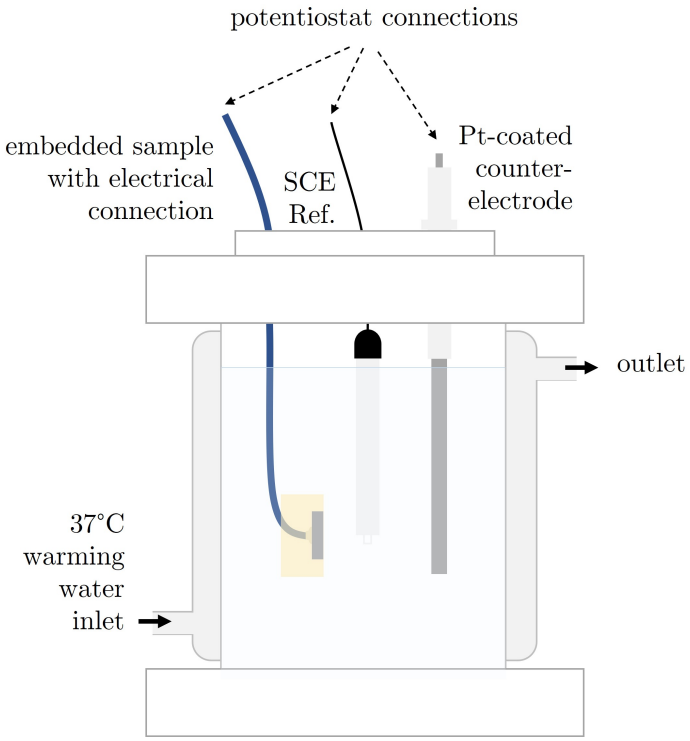

Figure 3.1: Schematic of three-electrode setup using for electrochemical testing.

in a standard three-electrode setup, as shown in Figure 3.1. A Gamry Interface 1000 potentiostat (USA), was set to scan potentials between -250 mV and +250 mV vs. OCP at a scan rate of 0.5 $mV\,s^{-1}$ after the system was allowed to stabilise for 1 h. The scan rate was set to be slightly faster than the 0.167 $mV\,s^{-1}$ scan rate recommended by ASTM G59-97 (Standard Test Method for Conducting Potentiodynamic Polarisation Resistance Measurements - 2020) [240], in order to prevent the OCP of the active material from shifting away considerably from the OCP measurement used as a datum for the test. Each test was carried out four times and for each condition, the corrosion current density, i_{corr}, was calculated using the Tafel extrapolation method described in Section 2.1.2.1.

3.2.2.4 Electrochemical Impedance Spectroscopy

EIS tests were carried out in 400 mL of HBSS and HBSS+Ca using the three-electrode setup illustrated in Figure 3.1. Samples were prepared in exactly the same way as for PDP tests, with an exposed apparent area of 1 cm^2. Frequencies were tested in the range between 100 kHz and 0.1 Hz at an interval of 10 pts/decade. The AC voltage amplitude was set to 10 mV rms from OCP. Frequencies lower than 0.1 Hz were not included due to the lengthiness of the data collection leading to detrimental surface polarisation. EIS scans were carried out over a period of 24 h with constant scans being run over the first 3 h followed by one test every 2 h interval over the subsequent 21 h. Each EIS scan was preceded by a 10 min OCP monitoring period to adjust the reference OCP value. Each test was repeated 3 times to ensure recurring trends. Following the tests, samples were rinsed well in deionised water and vacuum dried for further analysis.

A representative sample per condition, was subjected to SEM-EDS analysis to observe corrosion products adherent to the surface. Moreover, the impedance spectra were fitted using equivalent circuit models using EChem Analyst, a dedicated software provided by Gamry (USA). In this way, trends could be observed based on observed changes happening to individual components of the corroding system over the immersion period.

3.2.2.5 Local pH and DO monitoring

The measurement of pH and dissolved oxygen (DO) concentration upon and during exposure of Fe, FeMn and FeMnAg to HBSS and HBSS+Ca, was conducted using specialised equipment at the previously MagiC institute within the Helmholtz Zentrum Hereon in Geesthacht, Germany under the supervision of Dr Sviatlana Lamaka and with the help of then PhD student Dr Cheng Wang. Coupled with information from other tests, local measurements could give further insight into the corrosion mechanisms operating at the surface.

3.2.2.5.1 Setup

Prepared coupons machined into pins of 3 mm diameter, were mounted in cold-mounting epoxy and polished using 0.25 µm colloidal silica (OP-S, Struers, Denmark). The samples were then press-fitted into a custom-made, 3D printed water jacket that allowed for thermostat-controlled 37 ± 1°C water to control the temperature of the testing solution throughout the test. 4 mL of pre-warmed testing solution could then be pipetted onto the sample surface exactly prior to test initiation once all the probes were accurately setup as shown in the schematic representations in Figure 3.2. Constant refreshment of the testing electrolyte was ensured through the use of a hydrodynamic system that allowed for a flow rate of 1 $\mathrm{mL\,min^{-1}}$ of fresh testing solution.

3.2.2.5.2 Probes specifications and manipulation

DO measurements were carried out using a needle-type retractable fibre-optic oxygen micro-optode with a diameter of 50 µm couple with a Fire-StingO2 oxygen logging meter (Pyroscience, Germany). Prior to test initiation, the DO concentration in the electrolytes saturated with air, was measured at 5.8 ± 0.2 $\mathrm{mg\,L^{-1}}$. The pH was measured by a glass-type pH microelectrode with the tip length of 50 µm and tip diameter of 10 µm (Unisense, Denmark). Both pH and DO sensing probes were set at 50 µm above the sample surface, while they were spatially distanced from each other in the horizontal plane at a distance of 50 µm. This was possible through the use of a 3D motorized positioning system that forms

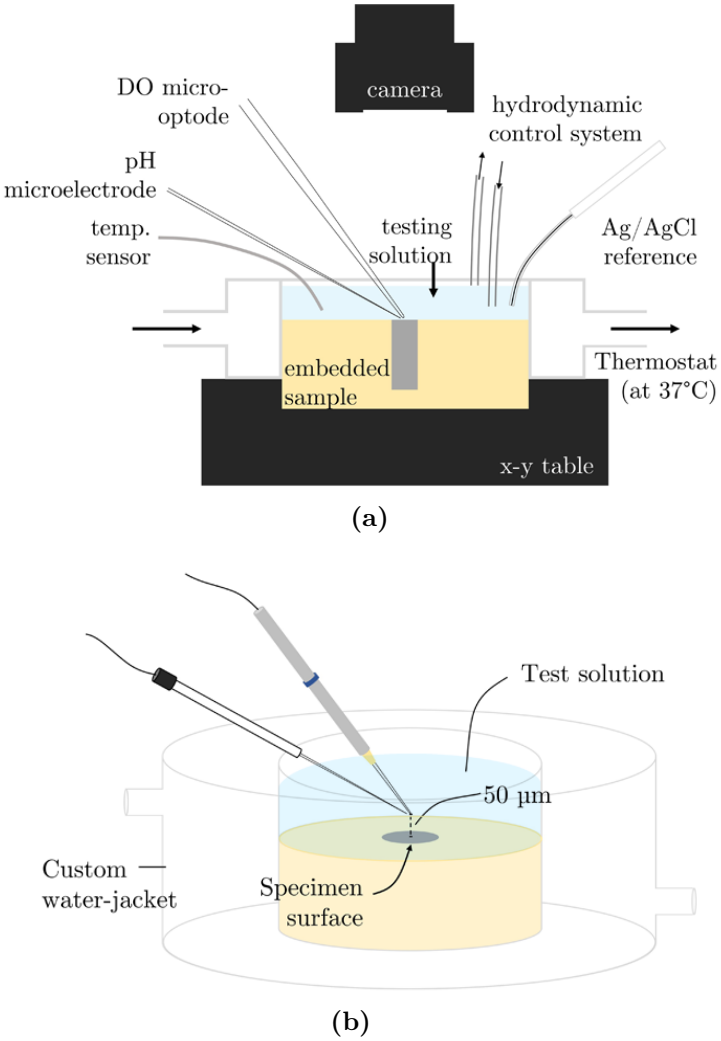

Figure 3.2: (a) General schematic of testing setup used for local pH and DO measurements and (b) close-up schematic of pH and DO probe placement 50 µm above the sample surface.

part of the Scanning Vibrating Electrode Technique (SVET) (Applicable Electronics and Sciencewares, USA) as well as dual-head stage micro-manipulators. A Ag/AgCl electrode was adapted as an external reference electrode. Both pH and DO probes were connected to a commercial SVET-SIET system (Applicable Electronics, USA) that allowed for accurate micromovement of the probes. Data logging was carried out using LV4 software (Sciencewares, USA) in parallel with PyroOxygenLogger (Pyroscience, Germany).

3.2.2.5.3 Data acquisition

The two probes were initially positioned at the centre of the specimen. Data logging was initiated prior to exposure of the sample surface to the test electrolyte. The pH and DO concentration was monitored for 15 min from immersion at a single point in the middle of the specimen to acquire the immediate response of the surface to the electrolyte. After 15 min, the general distribution of pH and DO over the whole sample surface was acquired by scanning an area of 4000 x 4000 µm at a rate of 200 µm/step. In this way, a general overview of the distribution could be observed as a whole with the edges of the map representing the bulk condition over the mounting epoxy surface. A representative area of 2000 x 4000 µm was then selected in order to monitor the progression in local environment conditions over the 24 h period, with a finer resolution of 80 µm per step. The sampling interval was 3 s and the total time for one map (25 × 50 grid) was approximately 1.5 h including the time needed to move the micro-sensors. Optical images were recorded at the end of each grid scan to record the progressive appearance of the sample surface. For reasons explained in detail in the following chapters, local measurements over FeMnAg in HBSS were not carried out as specified herein. Instead, line scans were carried out with a step length of 50 µm and a sampling interval of 5 s. The total time taken to carry out each 200-pt line, was around 15 min.

3.2.2.6 MEDUSA simulations

Initial observations of the corroded sample surfaces were correlated with theoretical simulations conducted with the aid of Hydra-Medusa freeware (KTH Royal Institute of Technology, Sweden) [241]. The Medusa software uses a Hydra database with thermodynamic stability constants for various ions, compounds and complexes at 25°C to generate custom diagrams based on specific system concentrations. The details input in the system to generate specific diagrams will be disclosed in the results section along with the diagrams themselves in order to assist with the analysis.

3.2.3 Phase Two - Further corrosion analysis using EIS

The second phase was aimed at investigating further the materials used in Phase One, especially with regards to certain hypotheses pointed out in the first discussion in Section 4.2.1.5. During an initial testing phase, the influence of Mn-rich oxide inclusions on corrosion was first targeted using porous samples, as used in Phase One. The results from the initial testing phase led to the modification of sample preparation methods to get a better approximation of the influence of porosity on modelled values of EIS equivalent circuit elements, thus achieving more representative fitting results. A similar approach was then taken when looking into the role of oxide inclusions on the degradation performance of Fe-Mn alloys.

3.2.3.1 Initial testing with porous MnO-free samples

3.2.3.1.1 Elimination of Mn-rich oxide

In order to eliminate the presence of Mn-rich oxides, the samples were subjected to an etching procedure in a 1 M HCl solution supplemented with 3.5 $\mathrm{g\,L^{-1}}$ hexamethylenetetramine (HMTA) which acts a corrosion inhibitor. This cleaning step was carried out in an ultrasonicator for 5 min. Samples were then rinsed with deionised water to dilute any remaining acid and subsequently ultrasonicated in ethanol for 5 min prior to drying. In this way, the acid could remove the metal oxide without the surrounding metal undergoing extensive attack.

3.2.3.1.2 Electrochemical Impedance Spectroscopy

EIS tests were initially carried out using porous MnO-free FeMn, following the same procedure described in Section 3.2.2.4. The testing electrolyte used was HBSS+Ca, based on the conclusions reached in the prior testing phase. The initial results presented in Section 4.2.2.1 led to a need for further EIS testing using porous powder-processed Fe as prepared in Phase One (Section 3.2.2.1), wrought pure Fe (Armco, USA) as well as porous FeMn etched in alternative concentrations of HCl and HMTA from the formulation described in Section 3.2.3.1.1

above. Specific details as to the preparation procedures for each test will be presented along with the results for better comprehension. In each case, the apparent testing area for the samples, measured 1 cm^2.

3.2.3.2 Modified sample preparation: Resin-impregnation of surface porosity

Following the initial results, sample preparation was modified to follow the schematic illustrated in Figure 3.3, in order to prevent the sample area pertaining to porosity from making contact with the testing electrolyte. First, the samples were cut to have a square cross-section of 1 cm^2. The samples were then placed face-up in a cold-mounting mould and impregnated with epoxy (Epo-Set, MetPrep, UK). The samples were placed under vacuum to reduce the amount of trapped air in the curing resin. Once cured, the epoxy was once again ground to expose the metal surface, with epoxy-filled pores. Care was taken not to over-grind the samples to reveal fresh open pores. Once the surface was ground to a finish of P4000 and dried, at least 20 optical microscopy images were taken using an objective lens of 10x and processed using ImageJ as described in Section

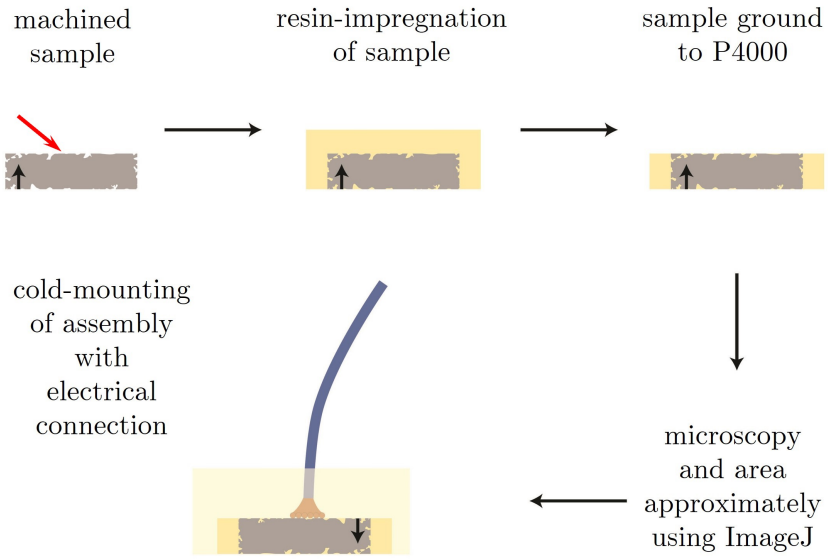

Figure 3.3: Schematic illustrating the mounting procedure for resin-impregnated porous samples. Red arrow points towards surface being prepared for testing.

3.2.3.4. Once finished, the sample was then placed face-down in a new mould and mounted together with an electrical connection, as described in Section 3.2.2.3.

3.2.3.3 EIS testing of resin-impregnated samples

As with the initial testing, EIS parameters were kept constant from Phase One. Testing was carried out in HBSS+Ca. EIS spectra and corresponding analysis including equivalent circuit modelling using EChem Analyst and SEM-EDS analysis, will be presented related to the following investigations:

1. Pore-free FeMn and FeMnAg - to investigate the role of porosity on the results acquired in Phase One;

2. MnO-free, pore-free FeMn and FeMnAg - to determine the extent of MnO inclusion influence on the long term corrosion behaviour.

When carrying out the investigation on the effect of MnO inclusions on corrosion, several tests were also run in physiological saline i.e. 0.9% NaCl, to assist with the analysis, as will be described in Section 4.2.2.

3.2.3.4 Active area measurement

For the measurement of active area i.e. the area of the prepared material subjected to the testing conditions, the samples were imaged using a Zeiss Axioscope 5 microscope (Germany) for at least 20 times. Each micrograph was then processed using ImageJ. The processing flow is presented in Figure 3.4a, where the original image was first changed into an 8-bit image (or grayscale) and then binarised (black and white). The last step was done using the threshold function in which the red area represented in Figure 3.4c was adjusted until only the black area was covered. Lighter gray areas represented either shallow pores which were not covered with the epoxy, or MnO inclusions. The binarised image could then be "measured" for the percentage pore area. The standard deviation was measured and the standard error was calculated (with a confidence interval of 95%).

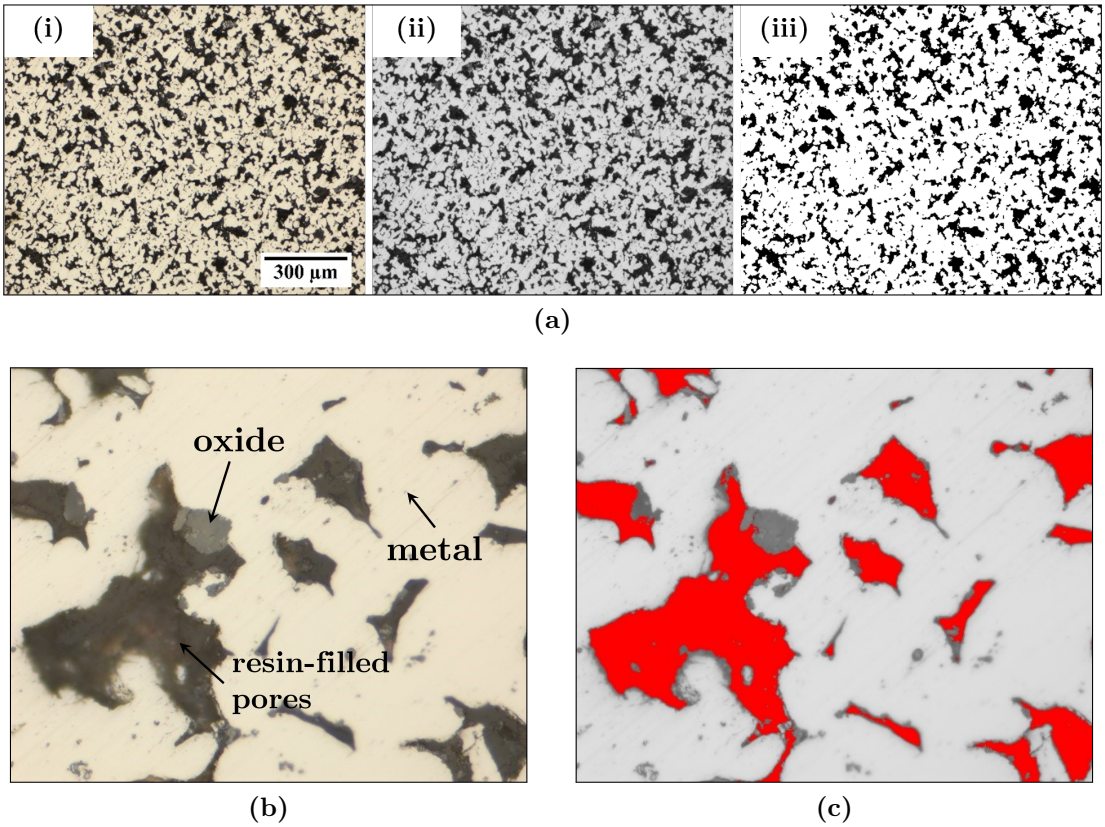

Figure 3.4: (a) Three-step process carried out using ImageJ including (i) imaging, (ii) changing the micrograph to greyscale and (iii) binarising (b) a high-magnification optical image of a ground resin impregnated coupon and (c) corresponding thresholding exercise for micrograph in (b) eliminating porosity but including MnO-rich inclusions.

3.2.4 Phase Three - Investigating the influence of BSA additions using EIS

Following the results achieved in the first two phases related to the use of HBSS and HBSS+Ca in *in vitro* testing, tests were carried out in HBSS+Ca with additions of 20.6 $g\,L^{-1}$ BSA, similar to the concentration of protein in interstitial fluid [242] - an attempt at taking the next step towards a more representative *in vitro* environment.

3.2.4.1 Choosing an antimicrobial

As discussed in Chapter 2, the prolonged exposure of protein-containing media to surroundings results in a high risk of microbial contamination. EIS tests were initially carried out using commonly utilised antimicrobial sodium azide (NaN_3) and penicillin-streptomycin (Pen-Strep) to evaluate whether their addition in recommended dosages affects the response of the system. The final formulation of the electrolyte HBSS+BSA based on the results of these experiments are presented in Table 3.2 in Section 3.2.1.

3.2.4.2 Electrochemical Impedance Spectroscopy

Electrochemical impedance spectroscopy tests and post-test characterisation were carried out following the same procedure described in Section 3.2.2.4. The material preparation for these tests was carried out according to the procedure outlined in Phase Two including the oxide-removal procedure, elimination of porosity and active area measurement.

3.2.4.3 Raman spectroscopy

In order to detect protein adsorption on the samples tested in HBSS+BSA, dried samples were subjected to Raman Spectroscopy. The analysis was carried out using a Horiba Scientific Raman spectrometer (Japan) fitted with a CCD multichannel detector. Spectra were collected at room temperature using a 532 nm laser (green light), a 1800 grating and an acquisition time of 25 s. The range of Raman shift analysed was between 800 and 1800 cm^{-1}. The resultant peaks were indexed using KnowItAll software (Wiley, USA).

3.2.5 Phase Four - Static immersion testing

As done in Phase Three based on the results of Phase Two, FeMn samples were once again chosen to conduct further tests aimed at evaluating the influence of the electrolyte and testing conditions over longer periods of time. For this purpose, static immersion tests were carried out in HBSS, HBSS+Ca and HBSS+BSA over a period of up to 28 days.

3.2.5.1 Sample preparation

The samples used for static immersion testing were prepared using the same procedure and sintering parameters used in previous phases according to the description in Section 3.2.2.1. In this case, the samples were machined to measure 15 x 10 x 4.5 mm and ground using SiC paper up till P2500. A 2 mm hole was drilled into the sample to facilitate suspension in the electrolyte during the test.

All samples were subjected to the MnO-removal procedure outlined in Section 3.2.3.1.1 wherein each sample was ultrasonicated for 5 min in 1 M HCl and 3.5 g L^{-1} HMTA followed by rinsing with deionised water and 5 min ultrasonication in ethanol[1]. All cleaned samples were dried and stored in a vacuum desiccator until use.

The list of samples prepared per interval is presented in Table 3.3 along with the post-characterisation testing carried out on each sample[2]. The same amount of samples and procedures were carried out for all three electrolytes used in this exercise i.e. HBSS, HBSS+Ca and HBSS+BSA.

[1]Removal of MnO inclusions was opted for to simplify the mass loss measurements described in Section 3.2.5.4

[2]Only two samples were used for the 7 day testing interval due to logistical limitations. Static immersion testing were carried out with available samples from previous sintering runs due to long-term unavailability of the tube furnace.

Table 3.3: Tests carried out on the samples used for static immersion testing. The same number of samples and tests apply for each set of FeMn samples tested in different electrolytes.

Interval	No. of samples	Test
7 days	1	Raman
	1	SEM-EDS
14 days	5	Weight measurements
	1	Raman
	1	SEM-EDS
28 days	5	Weight measurements
	1	Raman
	1	SEM-EDS

3.2.5.2 Static immersion setup

Considering the extent of the test duration, the samples were fully setup in a Fast V laminar flow hood (Dasit Group, Italy) to avoid the possibility of microbial growth during the test. The HBSS and HBSS+Ca specified in Section 3.2.1 were purchased in sterile-filtered condition and could therefore be used as-purchased. For the preparation of HBSS+BSA, 10.3 g of BSA (Sigma Aldrich A2153) was weighed and dissolved in 50 mL of HBSS+Ca. The concentrate was then sterile-filtered through 0.22 µm filters (Merck, USA) and added to 450 mL of sterile HBSS+Ca. Furthermore, 10 mL L^{-1} of Pen-Strep (Gibco 15140122) was added to the HBSS+BSA to further avoid microbial growth during the testing period. The pH of each solution was adjusted to 7.4 using a 0.1 M HCl solution.

Both testing cups and the prepared FeMn samples were sterilised with 70% ethanol and left to dry under laminar flow. Once dried, the samples were suspended using similarly sterilised nylon string. The cups were filled with 150 mL[1] of the testing electrolyte, labelled and firmly closed. The schematic of the indi-

[1]This volume exceeds the suggested volume-to-area ratio suggested by *ASTM G31 (2021)* ensuring sufficient electrolyte volume.

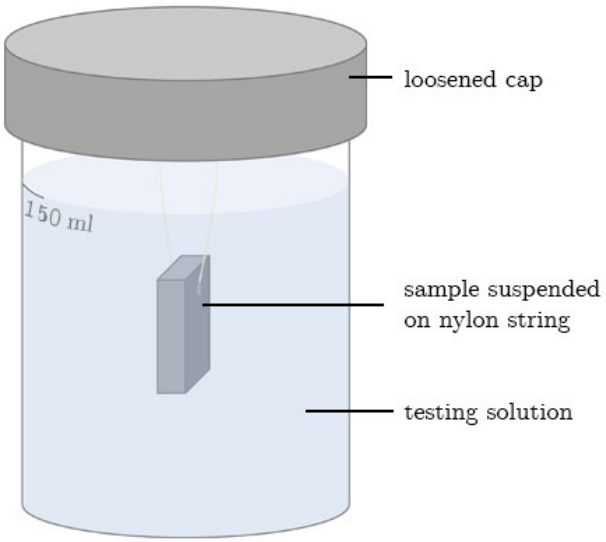

Figure 3.5: Schematic representation of immersion testing setup for individual samples.

vidual sample setup, is represented in Figure 3.5. For each condition, a sample cup containing just the electrolyte i.e. no metal sample, was exposed to the same testing conditions, to provide control measurements. This sample for each condition will be referred to as the blank.

The tests were conducted in an incubator (LEEC, UK) at 37°C. Since the HBSS formulation is designed to equilibrate with the CO_2 concentration in air [243], the tests were conducted in air with loosened caps.

3.2.5.3 pH measurement

The pH of the electrolytes following testing was measured for each test after the solution was allowed to return to room temperature, thus matching the conditions at which the pH of the electrolytes was originally set to 7.4. The pH of the blank solutions at each interval was also measured. Measurements were carried out using a calibrated Jenway 3510 pH meter (USA).

3.2.5.4 Mass loss measurement

Prior to the initiation of the static immersion testing period, FeMn samples were used to determine the influence of commonly used cleaning solutions suggested in ASTM G1 (Standard Practice for Preparing, Cleaning, and Evaluating Corrosion Test Specimens - 2017) [68] on the blank i.e. non-corroded metal, as suggested by the same standard. Any impact of the removal procedure on the metal could naturally influence the analysis of mass loss due to corrosion during the testing period.

The most commonly used formulation in literature is a mixture of 6 M HCl and 3.5 $g\,L^{-1}$ HMTA topped up with deionised water, as indicated in Table 2.2. A variation of this solution with 1 M of HCl instead of 6 M, is used in this study to eliminate MnO from the surface of FeMn samples. The same formulation was used in the successful removal of surface rust from a piece of rusted mild steel bar. The process was aided with ultrasonication for 15 min. The same procedure was therefore applied to 5 FeMn samples whose dimensions were measured accurately using Vernier calipers. Following the procedure, the samples were rinsed with deionised water, ultrasonicated for 5 min in ethanol and dried for several hours

in vacuum. The mass of the dry samples before and after the procedure were recorded with a Precisa precision balance (Switzerland) with a resolution of 0.0001 g. The mass lost by the blank FeMn was **2.28 ± 0.42** mg cm^{-2} (Std. error, n = 5).

Mass loss measurements were carried out with 5 samples from each condition as described in Table 3.3. The dimensions and mass of each cleaned sample were recorded prior to the test and following the cleaning procedure described herein. The area used throughout this analysis is the apparent area due to the lack of improved means to measure the additional area within the pores.

3.2.5.5 SEM-EDS analysis

SEM-EDS analysis was carried out on both representative sample surfaces as well as their cross-sections for better corrosion product characterisation. Each sample was mounted on an aluminium stub and gold-coated for 30 s using an Auto sputter coater (Agar, USA) to ensure corrosion products were sufficiently conductive for proper analyses.

Following SEM-EDS analysis of the surfaces, the samples were carefully removed and mounted on a tapered steel section (Struers, Denmark) and mounted in cold-mounting resin (MetPrep, UK) as shown in Figure 3.6. By grinding off an unspecified thickness of the mounted specimen to expose the sample, one could observe a magnified cross section of the exposed piece of sample, as schematically illustrated. The magnification factor is determined by the ratio of the thickness of exposed steel midsection relative to the thickness of the supporting edge, according to equation 3.1.

$$Magnification factor = \frac{b}{a} \tag{3.1}$$

Each cross-section was ground and polished down to a 0.25 µm colloidal silica (OP-S, Struers, Denmark) finish, ultrasonicated in ethanol for 5 min and dried in vacuum. Cross-sections were similarly sputter-coated with gold for 30 s for ease of analysis.

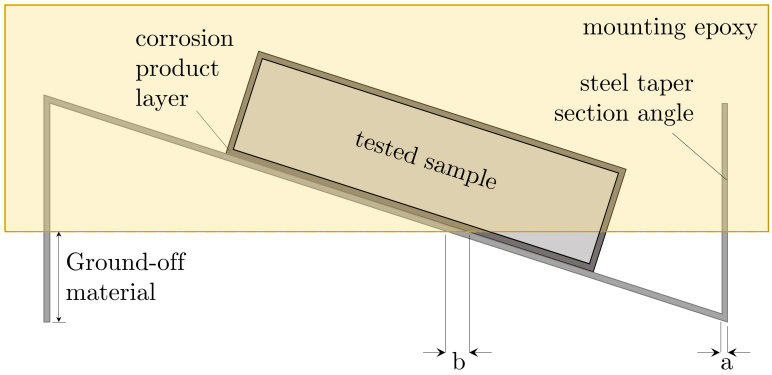

Figure 3.6: Schematic representation of sample mounting method for SEM-EDS analysis of static immersion testing sample cross-sections. The geometrical measurements necessary for calculating the magnification factor as a result of the use of the steel taper section, a and b, are also marked on the schematic.

3.2.5.6 Raman spectroscopy

Dried static immersion tested samples were analysed using Raman spectroscopy. The same equipment and settings described in Section 3.2.4.3 were used for this analysis. The range analysed was between 500 and 1800 cm^{-1}. The resultant peaks were indexed using KnowItAll software (Wiley, USA).

Note: XRD analysis of representative tested surfaces and ICP-OES (Inductively Coupled Plasma - Optical Emission Spectroscopy) analysis of the testing extracts were both planned to be carried out following test completion. Unfortunately both the ICP-OES instrument as well as the available diffractometer suffered breakdowns during the immersion tests and the analyses could not be performed. Whereas the ICP-OES instrument was unavailable indefinitely, select XRD patterns collected from the tested samples following the equipment maintenance, indicated a strong presence of $FeCl_2.4H_2O$, which signaled that corrosion progressed following test completion despite storage in sealed boxes with desiccant [244]. The results obtained would therefore not reflect the products formed during the testing period.

3.2.6 Phase Five - *In vivo* testing

In vivo testing was carried out as part of a Masters' thesis carried out by Mr. Luke Saliba M.D. who tested the same materials studied in this doctoral thesis. The procedure that follows was carried out by Mr. Saliba whereas all instances of sample preparation and analyses of the removed implants, was carried out by the undersigned. Due to this being partly dependant on Mr. Saliba's chosen methodology, the samples tested in *in vivo* also include (Fe35Mn)1Ag apart from the FeMn and FeMn5Ag tested thus far in this work.

3.2.6.1 Implant preparation

Coupons were initially prepared by pressing 10 g of mixed Fe35Mn (FeMn), (Fe35Mn)1Ag (FeMn1Ag) and (Fe35Mn)5Ag (FeMn5Ag) into a 22 mm die at a pressure of 442 MPa. The green coupons were sintered in a tube furnace (Nabertherm, Germany) at 1120°C for 3 h after a ramp rate of 180°C h^{-1}. Following furnace cooling, cylindrical pins with a diameter of 2.05 mm and a length of 5 mm were machined out of the sintered samples using a lathe. Samples were machined transversally from the sintered sample as shown in Figure 3.7. The machined samples were then etched in the oxide cleaning solution composed of 1 M HCl supplemented with 3.5 g L^{-1} hexamethylenetetramine (HMTA) for 5 min in an ultrasonicator. Following the etch, samples were immersed for 5 min in DI water and 5 min in ethanol and vacuum dried.

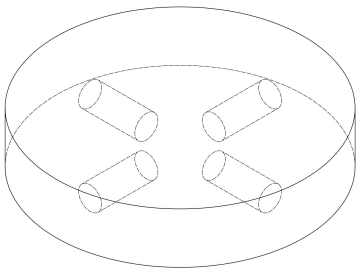

Figure 3.7: Schematic representation of position of machined pins for *in vivo* test as machined from sintered flat coupons.

3.2.6.2 Implantation procedure

In vivo testing was carried out using GAERS rats at the Department of Anatomy under the supervision of Prof. Pierre Schembri Wismayer M.D[1]. Each rat was anaesthetised using isoflurane and then operated on a constant temperature heating mat (Kent Scientific, USA) by Mr Luke Saliba M.D. Pins were implanted in the cancellous bone in the vertebrae at the base of the rat's tail. For each material, 8 pins were sterilised and implanted in separate rats. An OmniDrill35 micro-drill (World Precision Instruments, USA) was used to create a defect in the chosen vertebra such that the pin could be inserted perpendicularly with respect to the direction of the tail. Wounds were closed with Prolene sutures. Following 6 months of observation, the rats were euthanised using CO_2 and the tails removed.

3.2.6.3 Post-test characterisation

3.2.6.3.1 XRD analysis

For each implant, a sample was completely dislodged from the vertebrae, ultrasonicated in ethanol for 5 min and dried in vacuum. XRD analysis was carried out on the cylinrical face at 2θ angles between 30° and 70° with a step of 0.02° and a scan rate of $1^\circ\,\mathrm{min}^{-1}$. Diffraction was carried out using a Rigaku Ultima IV (Rigaku, Japan) set in Bragg-Brentano geometry and equipped with a Cu-Kα source ($\lambda = 0.141$ nm).

3.2.6.3.2 SEM-EDS analysis

The surface of the removed and dried implant was further analysed using SEM. Each sample was fixed from the cylindrical surface onto an aluminium stub using carbon tape and gold-coated for 30 s using an Auto sputter coater (Agar, USA) to ensure that the corrosion products at the surface were conductive enough for consequent analyses.

[1]Ethical approval was obtained from the Joint Faculty Research Ethics Committee (FREC) Animal Research Sectoral Sub-committee at the University of Malta.

Furthermore, for cross-sectional analysis, a separate tail was used from which an entire implant-containing vertebrae was dried and mounted in cold-mounting epoxy (Metprep, UK). The mounted bone was then ground until the implant was exposed and finished using P2500 SiC paper. The ground samples were then ultrasonicated in ethanol for 5 min and vacuum dried. Prior to SEM-EDS analysis, the surface was also gold-sputtered for 30 s.

3.3 Powder-processing of FeMn for scaffold applications

3.3.1 Powder preparation and analysis

The possibility of preparing FeMn foams for biodegradable implant applications through the powder metallurgy route, is reliant in part on the ability to prepare powders that have more adequate characteristics than using the highly reactive elemental Mn in the mix. In view of this, this first part of the investigation explores the characteristics of ball-milled and alloyed Fe35Mn in relation to elemental mixtures of Fe and Mn.

Table 3.4: List of powders used with designation and preparation method.

Name	Designation	Preparation Method
Blended Fe35Mn	B35	Ball-assisted tumbling of Fe and Mn in set wt. ratio for 5 hours
Alloyed Fe35Mn	A35	Ball milling for 12 hours
Milled Fe35Mn	M35	Ball milling for 2 hours
Master Alloy and Alloyed Fe35Mn mix (Fe35.35Mn1C)	MAM	Ball-assisted tumbling of MA and A35 in 1:3 wt. ratio for 5 hours

3.3.1.1 Preparation

The powders that will be used in this part of the work are listed in Table 3.4. Alloyed (A35) and milled (M35) powders were prepared using a Pulverisette 6 ball miller (Fritsch, Germany). In each case, a precision balance with a resolution of 0.1 mg was used to measure a total of 30 g of the Fe and Mn powder specified in Table 3.1 in the necessary ratios. A 500 mL hardened stainless steel bowl was then filled with 900 g of hardened stainless steel balls with a diameter of 10 mm. The powder was poured on top of the grinding media, setting a ball-to-powder ratio of 30:1. 1 mL of toluene was then added as a process control agent, as deemed suitable in previous work [245]. The grinding bowl was equipped with a gassing lid and an additional clamping system provided by Fritsch for maximum safety, and secured in the planetary miller holder. Ar gas was then used to purge the air out of the grinding bowl for 15 s. The miller was set to operate for 10 min and rest for 20 min at 350 rpm. When milling i.e. to prepare M35, the total milling time was set to 2 h which translates to 12 mill-rest cycles. When alloying i.e. to prepare A35, the total milling time was set to 12 h which translates to 72 cycles. Once the process was complete, the system was allowed to cool overnight to make sure that the powders inside do not spontaneously ignite. The clamped bowl was then transferred to a glove box which was purged of air using Ar and assisted by vacuum. The grinding media were separated from the processed powder using a vibratory sieve shaker (Fritsch, Germany), and stored in a desiccator.

For blended Fe35Mn (B35) and mixed MA and A35 (MAM), the mixtures were similarly weighed with a precision balance, placed into centrifuge tubes loaded with 5 stainless steel balls with a diameter of 10 mm, and tumbled in an Inversina tumbler (Bio-Components, Switzerland) for 6 h.

3.3.1.2 Characterisation

3.3.1.2.1 Carbon quantification

For measurement of C content in the powders of interest, a LECO-CS230 carbon analyser[1] (LECO Corporation, USA) machine was used with a flow of pure O_2.

[1]In this technique, the sample is heated via induction, assisted by a catalyst. The carbon in the sample is oxidised to CO_2 which is then detected using non-dispersive IR cells. The

The system was first calibrated using LECO standard no. 501-024 containing 3.29 ± 0.04% C. For each powder, four replicates were weighed using a precision balance with a resolution of 0.1 mg, aiming at a sample weight of approximately 500 mg. Tungsten flakes were added to the each sample to accelerate the reaction. LECO analysis was carried out at the Institute of Chemical Technologies and Analytics within the Technical University of Vienna under the supervision of Prof. Raquel de Oro Calderon.

3.3.1.2.2 SEM-EDS analysis

For general characterisation of the powders, particles from each sample were distributed liberally over a piece of carbon tape stuck to an aluminium stub. The size, morphology and general composition could then be qualitatively analysed using SEM-EDS. For a more accurate assessment of elemental distribution within individual particles, the powders were mixed with bakelite (Conducto-Mount, MetPrep, UK) and mounted using a Remet IPA 30 (UK). The mounted samples were then ground to SiC paper P2500, polished with 3 µm diamond suspension (Struers, Denmark) and finalised using 0.25 µm colloidal silica (OP-S) (Struers, Denmark). The polished samples were ultrasonicated for 5 min in ethanol and vacuum dried prior to SEM-EDS analysis.

3.3.1.2.3 XRD analysis

XRD was performed using a Bruker D8 Advance (USA) equipped with a copper source (Cu-Kα, $\lambda = 0.141$ nm) and a graphite monochromator. Scans were run at 2θ angles between 30° and 70° using a step size of 0.02° and a scan rate of $0.3° \, \text{min}^{-1}$. The sample was set to rotate at 15 rpm.

3.3.2 Analysis of pressed-and-sintered samples

The same materials that were initially studied in powder form were then analysed in pressed-and-sintered form. This analysis was aimed at providing information

measurement is based on the principle that CO_2 absorbs energy at specific wavelengths in the IR spectrum.

on how the materials differ in terms of densification during sintering, and their capacity for reduction following controlled sample preparation.

3.3.2.1 Sample preparation

For each material i.e. B35, M35, A35 and MAM, 10 g of sample was weighed using a precision balance with a resolution of 0.1 mg. The powder was then placed in a die with a cross-section of 55.4 x 6.0 mm and pressed at 200 MPa. The green samples were then placed in an alumina boat and sintered in a tube furnace (Nabertherm, Germany) equipped with an alumina tube. Following the results of powder thermal analysis in the first part of this investigation, two sets of samples were prepared. The first set was subjected to a heating ramp of 300°Ch^{-1} followed by 3 h of sintering at 1120°C. The second set of samples were subjected to the same heating ramp but sintered for 3 h at 1250°C. All samples were furnace cooled. The whole process was carried out under the flow of N_2-10H_2[1].

3.3.2.2 Characterisation

3.3.2.2.1 XRD analysis

A sample was sectioned from each sintered sample, ground to a finish of P1200 using SiC papers, ultrasonicated in ethanol and dried. XRD analysis was carried out between 30° and 70°C using a Philips X'pert MPDII (USA) equipped with a Cu source (Cu-Kα, $\lambda = 0.141$ nm). The samples was rotated during the duration of the test.

3.3.2.2.2 Microscopy

Samples used for XRD analysis were consequently mounted in bakelite and polished according to the standard procedure used in this work, as outlined in Section 3.1.2. After polishing, the samples were etched using a 2% Nital etchant for 10 s, dried and stored in vacuum until analysis.

[1]These tests were carried out at the Technical University of Vienna wherein use of premixed N_2-5H_2 gas as used in the rest of the dissertation, was not possible. The N_2-10H_2 was mixed in-line using N_2 and H_2. 10% H_2 was the lowest fraction of H_2 achievable by manual control of the equipped regulator flow gauges.

Optical microscopy was carried out using a Zeiss Axioscope 5 (Germany) whereas SEM analysis was performed using a Carl Zeiss FE-SEM Merlin Gemini II column (Germany) as described in Section 3.1.2. EDS analysis was also performed on regions-of-interest.

3.3.3 Scaffold preparation and analysis

Previous work carried out by postgraduate students [246, 247] within the same research group has demonstrated the possibility of fabricating customised scaffold structures by modifying the traditional replication method to include a tailored 3D printed template instead of reticulated off-the-shelf polyurethane foams. In this section, the methods employed to explore the potential of extending this process to prepare Fe35Mn foams using M35 and A35 powders, will be described.

3.3.3.1 The modified replication method

The principal steps included in the preparation of porous scaffold structures using the proposed modified replication method, are schematically represented in Figure 3.8a.

In the first step, a customised template is prepared using CAD software. For simplified testing purposes, this work only includes the use of simple cubic templates with orthogonally arranged pores and side lengths of 10.8 mm. Templates were printed in batches using a Formlabs Form 2 stereolithography (SLA) printer (Netherlands) and Standard Gray resin supplied by the same company, with layer thickness of 100 µm[1]. All models were orientated as illustrated in Figure 3.8b in order to encourage better dimensional accuracy. Following printing, the samples were subjected to a UV curing step for 2 h using UV light with a wavelength of 405 nm. In this way, samples were only partially cured leaving behind a layer of uncured resin that provided surface "tackiness". This characteristic proved useful in the next step of the process in which the templates were placed in a 50

[1]While the technology allows for layer thickness of as low as 25 µm, previous work using the same materials has indicated that reducing the thickness below 100 µm did not contribute to better replication using the metal powders used in this work [246]

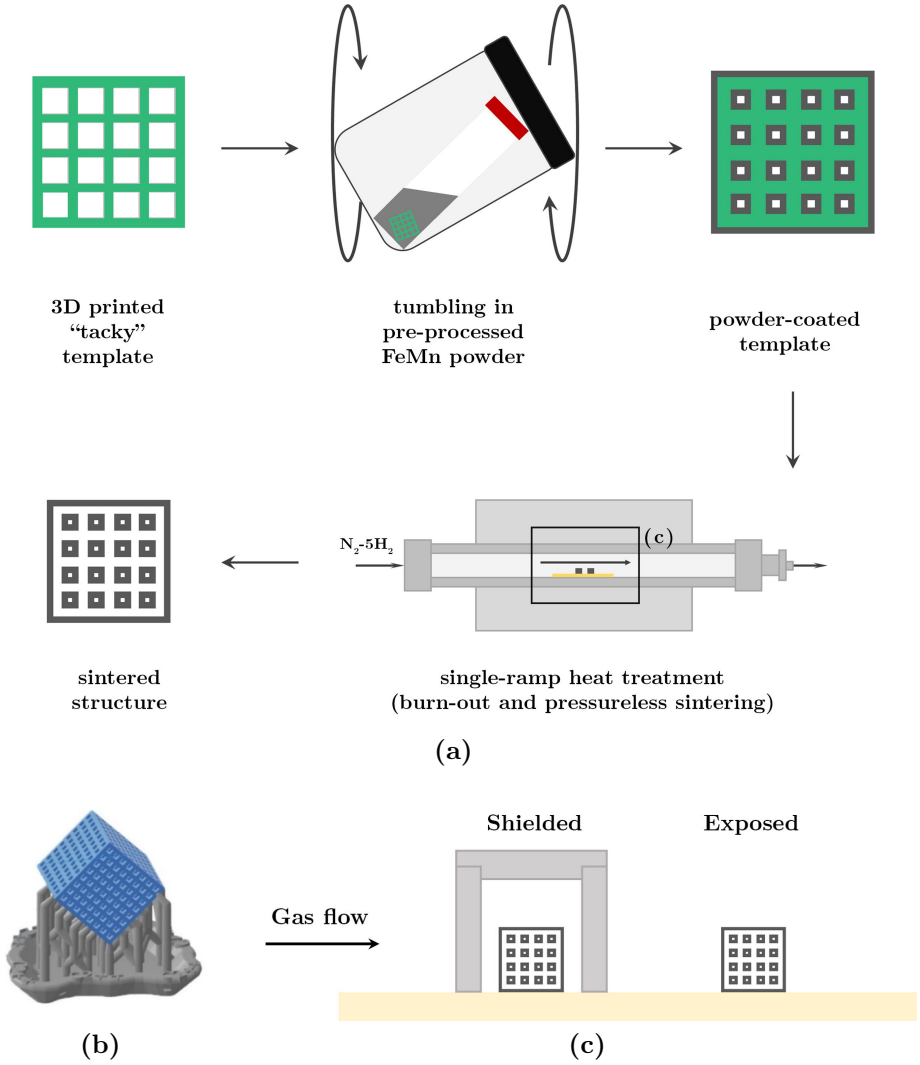

Figure 3.8: (a) Schematic outlining the principal steps for the preparation of customisable porous scaffolds using the modified replication method, (b) schematic showing the printing orientation used to avoid geometrical distortion during the printing process and (c) schematic of the two sintering configurations used in this work.

mL centrifuge tube along with approximately 15 g of the prepared metal powders, and tumbled in an Inversina tumbler (Bio-Components, Switzerland) for 30 min. Following this step, excess powder was removed using compressed air while wearing suitable safety equipment. Dry-coated samples were then placed on an alumina plate and sintered in a tube furnace for 3 h at 1120°C following a ramp

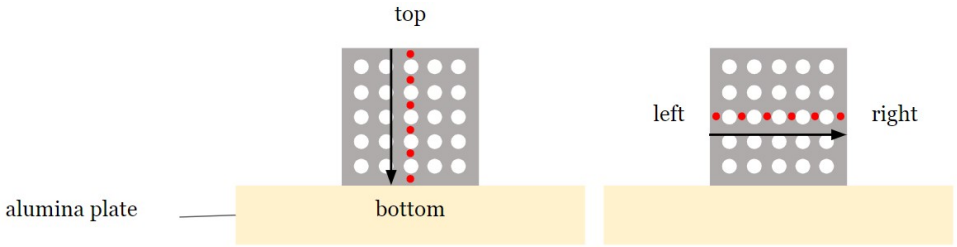

Figure 3.9: Schematic representation of sample cross-sections showing the systematic approach in which EDS analysis was done to identify any compositional trends, in particular with respect to wt.% Mn in the austenite matrix. The arrows and red points represent where analysis was carried out.

of 300°Ch^{-1}. Sintering was carried out under 120 L h^{-1} of N_2-5H_2 flow.

Related to this part of the study, results will be presented for samples sintered using two "configurations" within the tube furnace; *shielded* and *exposed* - the two are schematically represented in Figure 3.8c. Exposed samples were simply placed on the aforementioned alumina plate. Following the positive observations reported when using semi-closed containers to create micro-atmospheres for the sintering of Mn-containing steel coupons, this approach was also tested using a simple shielding setup in this work. Stainless steel (SAE 304) pipes with a diameter of 20 mm and wall thickness of 2 mm were used to provide shielding from the sides whereas round bars of the same material were machined to create "caps" as illustrated in the schematic.

In this work, foams were prepared using M35 and A35 powders in both *exposed* and *shielded* configurations. In each sintering treatment, two samples from each condition were sintered to make sure that any observations made were indeed repeatable[1].

3.3.3.2 Characterisation

3.3.3.2.1 XRD analysis

For XRD analysis, sintered foams were sectioned in half using a diamond wire cutter (WireTec, Italy), ground to a finish of P1200 using SiC grinding paper,

[1]The amount of repeats per treatment was limited by the constant heat volume of the tube furnace used.

ultrasonicated in ethanol for 5 min and dried. The ground surface was scanned using a Bruker D8 Advance (USA) equipped with a copper source and a graphite monochromator. Tests were run between 30° and 70° at a scan rate of 0.3°min^{-1}. The scans were run thrice in succession with the EVA software (Bruker, USA) integrating the signals to reduce the signal-to-noise ratio for the low-intensity data achieved.

3.3.3.2.2 SEM-EDS analysis

SEM-EDS analysis was carried out on both foam surfaces as well as cross-sections of the same samples. The as-sintered surfaces were first analysed using the same SEM equipment described in Section 3.1.2. To analyse cross-sections, representative samples were once again sectioned in half using a diamond wire cutter (WireTec, Italy) and cold-mounted using Epo-Set epoxy resin (MetPrep, UK). While curing, the cold-mounted samples were placed in vacuum to assist in removing trapped air from the sample porosity. When the epoxy was fully cured, the samples were polished down up to 0.25 µm colloidal silica (OP-S, Struers, Denmark). Samples were etched using 2% Nital etchant for 10 s before analysis. In order to enhance imaging, taking into consideration the non-conductive epoxy mount used, the samples were gold-coated for 30 s using an Agar sputter coater (Agar, USA).

In order to characterise any trends in the compositional make-up of the microstructure from one area of the foams structures to another, EDS was carried on the cross-sections systematically, taking at least three measurements per strut, moving across the cross-section from left to right and from top to bottom, as illustrated in Figure 3.9.

3.3.4 Thermal analysis

Thermal analyses of as-received and as-processed powders as well as delubricated samples, was carried out at the Institute of Chemical Technologies and Analytics within the Technical University of Vienna under the supervision of Prof. Raquel de Oro Calderon.

The analysis includes simultaneous Differential Thermal Analysis (DTA), thermogravimetry (TG) and mass-spectroscopy (MS) of approximately 100 mg of sample prepared in alumina crucibles. For each sample, weighing was carried out using a precision balance with a resolution of 0.1 mg before loading the crucible in a modular Simultaneous Thermal Analyzer Netzsch STA 449 C (Germany) coupled with an Aeolos quadrupole mass spectrometer (Netzsch) by a quartz capillary. Tests were run under Ar flow. In each case, the temperature was ramped to 1500°C at 20°C min^{-1}. Cooling was carried out at the same rate. For MS, the masses registered in these experiments were 12 (C), 14 (N), 15 (CH_3), 16 (CH_4, O), 17 (OH), 18 (H_2O), 28 (CO, N_2), 32 (O_2) and 44 (CO_2). In order to keep presented plots relatively simple, only the gases needed for complete interpretation of the results will be presented.

Raw and processed powders

Thermal analysis was firstly carried out on raw and processed powders i.e. as-supplied Fe, Mn and MA, as-processed M35 and A35 and as-tumbled B35 and MAM. Please refer to Table 3.4 for more details on powder preparation.

Delubricated foams

The same analysis was also carried out on *delubricated* samples. The sintering treatment could not be more accurately replicated during the thermal analysis cycles due to the spatial restrictions of alumina crucibles as well as to prevent polymeric degradation products from contaminating the sensitive equipment. To this end, the first stage of the replication method described in Section 3.3.3.1 was carried out in a Nabertherm tube furnace. Polymeric templates were likewise dry-coated with the specified powder and placed in either *exposed* or *shielded* configurations. The temperature was then ramped at 300°Ch^{-1} up till 700°C and held for 30 min. The process was carried out under the flow of N_2-10H_2. This process enabled the polymeric templates to be removed in the same manner as in the regular procedure. The resultant templates were very brittle pre-sintered foams that could easily be crushed into small chunks, more suitable for thermal analysis.

Carbon quantification was performed on delubricated samples subjected to the same procedure. The methodology for carbon measurement is identical to that described in Section 3.3.1.2.1, however in this case, the sample weight was approximately 50 mg. Tests were repeated thrice for statistical analysis.

For all tests, the data was analysed using Proteus, a dedicated software by Netzsch (Germany) that allows for facilitated examination and signal processing of multiple curves. DTA, TG and MS curves obtained when running blank experiments i.e. with an empty alumina crucible in the same conditions, were subtracted from all experimental data related to tested samples.

3.3.5 Summarised methodology

The following diagrams, Figures 3.10 and 3.11 summarise the principal tests carried out in each testing phase and the order in which they are presented in Chapter 4, for both the *Corrosion Testing* and the *Powder Processing* sections.

Corrosion testing

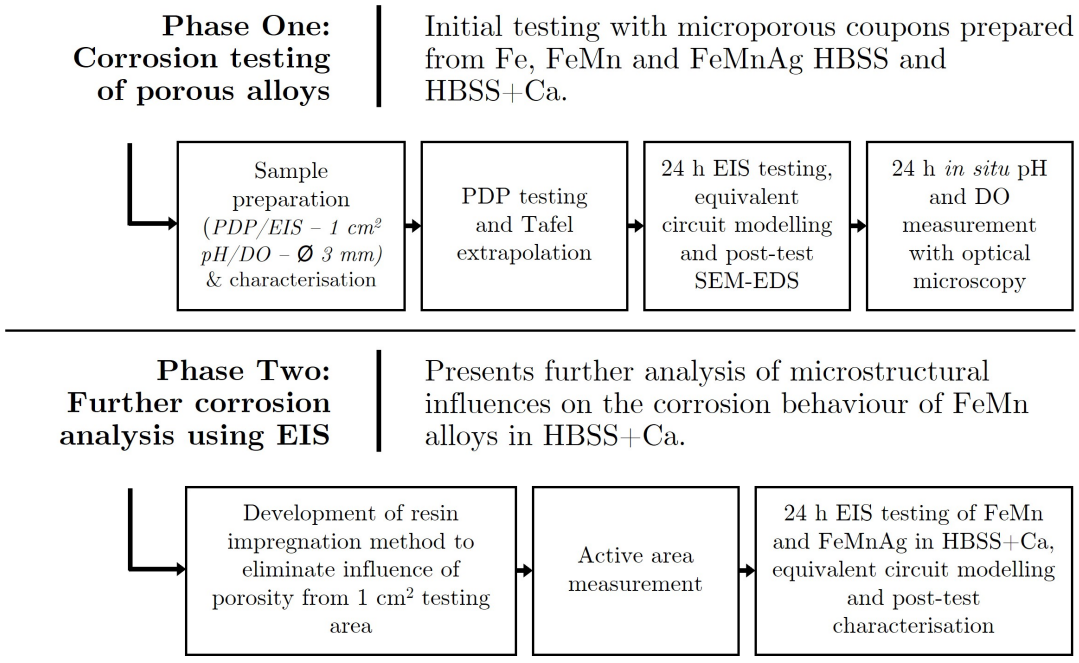

Figure 3.10: Diagram showing the summarised order of tests carried out in testing phases related to *Corrosion Testing*.

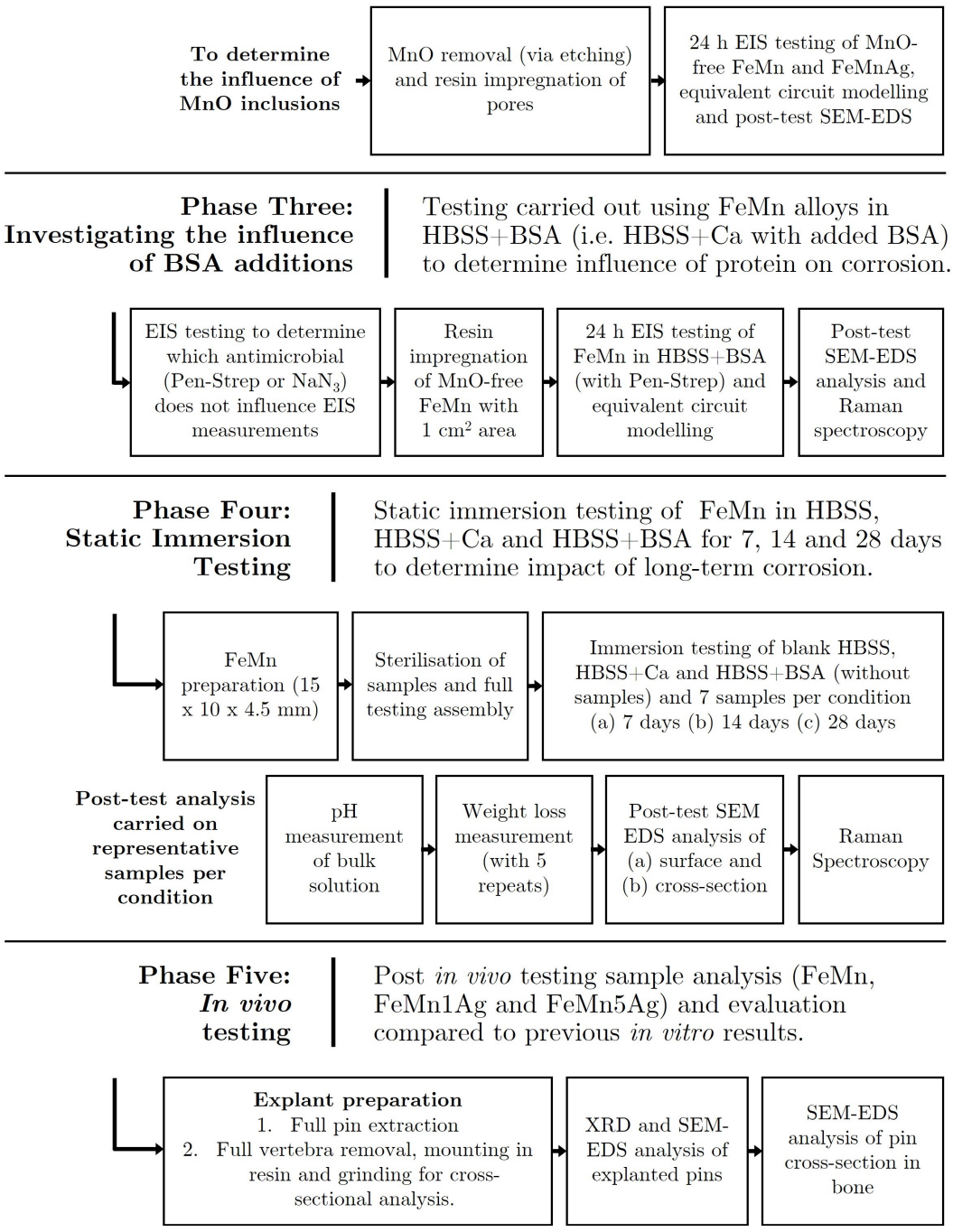

Figure 3.10 (continued): Diagram showing the summarised order of tests carried out in testing phases related to *Corrosion Testing*.

Powder processing of FeMn for scaffold applications

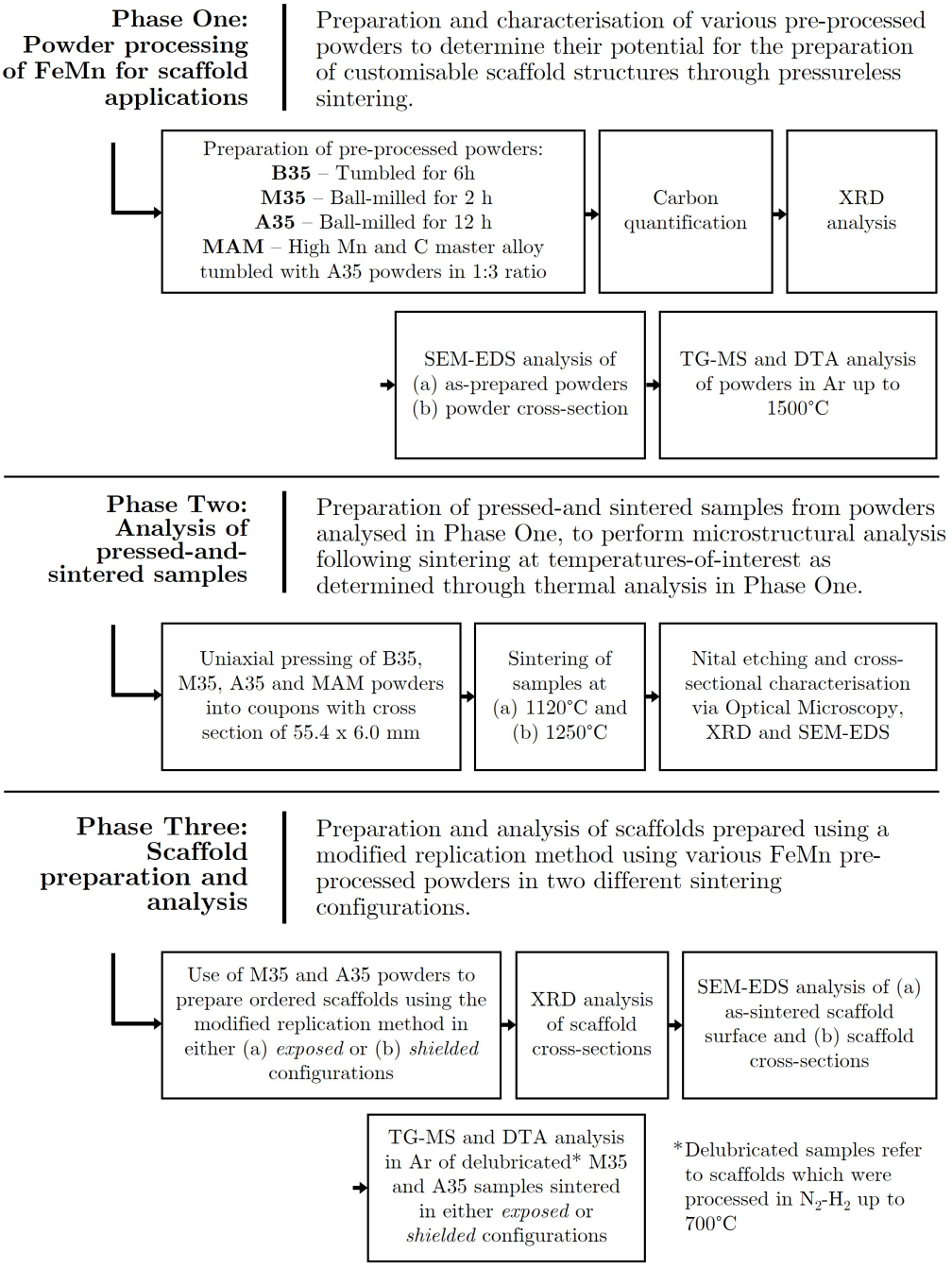

Figure 3.11: Diagram showing the summarised order of tests carried out in testing phases related to *Powder processing of FeMn powders for scaffold applications.*

4

Results and Discussion

Results achieved through execution of the methods described in Chapter 3, are presented and discussed in detail in this chapter. Following results of powder characterisation in Section 4.1, Sections 4.2 and 4.3 present the results related to *Corrosion testing* and *Powder processing of FeMn for scaffold applications*, respectively. Both these sections are split up according to the testing phases outlined in Chapter 3. Following presentation of results pertaining to each testing phase, the same testing outcomes are discussed in detail at the end of each phase, followed by a list of principal conclusions.

4.1 Powder characterisation

4.1.1 Microscopical analysis

Micrographs showing the size and morphology of the as-received Fe, Mn and Ag powder can be seen in Figure 4.1 (a), (c) and (e) respectively. The images reveal the rather rounded, albeit irregular shape of the Fe and Ag particles as opposed to the angular morphology of the more brittle Mn powder. One should note that the small size of the Ag powders led to agglomeration in storage and thus the clusters shown in Figure 4.1e are actually composed of multiple Ag particles.

Cross-sectional analysis of the powders was mainly carried out in order to identify any irregular inclusions incorporated within the elemental powders. In this way, one could eliminate any doubts as to the source of contamination related

Table 4.1: EDS analysis corresponding to regions-of-interest marked in Figure 4.1 in wt.%.

Pt.	Fe	Mn	O	C	Al	Ti	Si	Mg	Ca	V	Cr
1	35.62	1.13	34.43	5.21	8.55	6.74	-	0.92	-	2.95	4.45
2	31.71	2.09	39.84	6.70	0.54	0.43	12.43	4.09	2.17	-	-
3	36.40	5.47	35.11	8.24	3.61	9.02	0.25	1.80	0.10	-	-
4	36.48	6.21	34.62	8.85	0.13	0.27	6.76	5.72	0.95	-	-

to the as-received materials in subsequent testing. Figure 4.1 (b), (d) and (f) show cross-sections of Fe, Mn and Ag powder respectively, whereas corresponding EDS analysis of the marked regions-of-interest, is found in Table 4.1. The Fe powder cross-section revealed multiple labelled inclusions. In each case, a high wt.% O content was detected, often with lower amounts of highly oxidation-sensitive metals like Al, Ti, Si, Mg, Ca, V and Cr, most likely incorporated during the atomisation process used for powder production. Mn and Ag powders contained no observable foreign inclusions.

A similar SEM analysis for the Fe35Mn4C master alloy used during thermal analysis in Section 4.3.1, is presented in Figure 4.2. This powder contained no distinct inclusions. Arrows on Figure 4.2b, point towards points which contained slightly higher wt.% of O compared to the FeMnC matrix. Although EDS analysis of O concentration is not accurate, point analysis on these regions measured approximately 8-14 wt.% O. The rest of the FeMnC powder exhibited a matrix with an average wt.% Fe:Mn ratio of 63.9:36.1. C content on average measured unexpectedly high at 12.43 wt.% however with a measurement error % of 11.03%. For C quantification, more accurate results are presented in Section 4.3.1.3 with measurements carried out using a specialised carbon analyser.

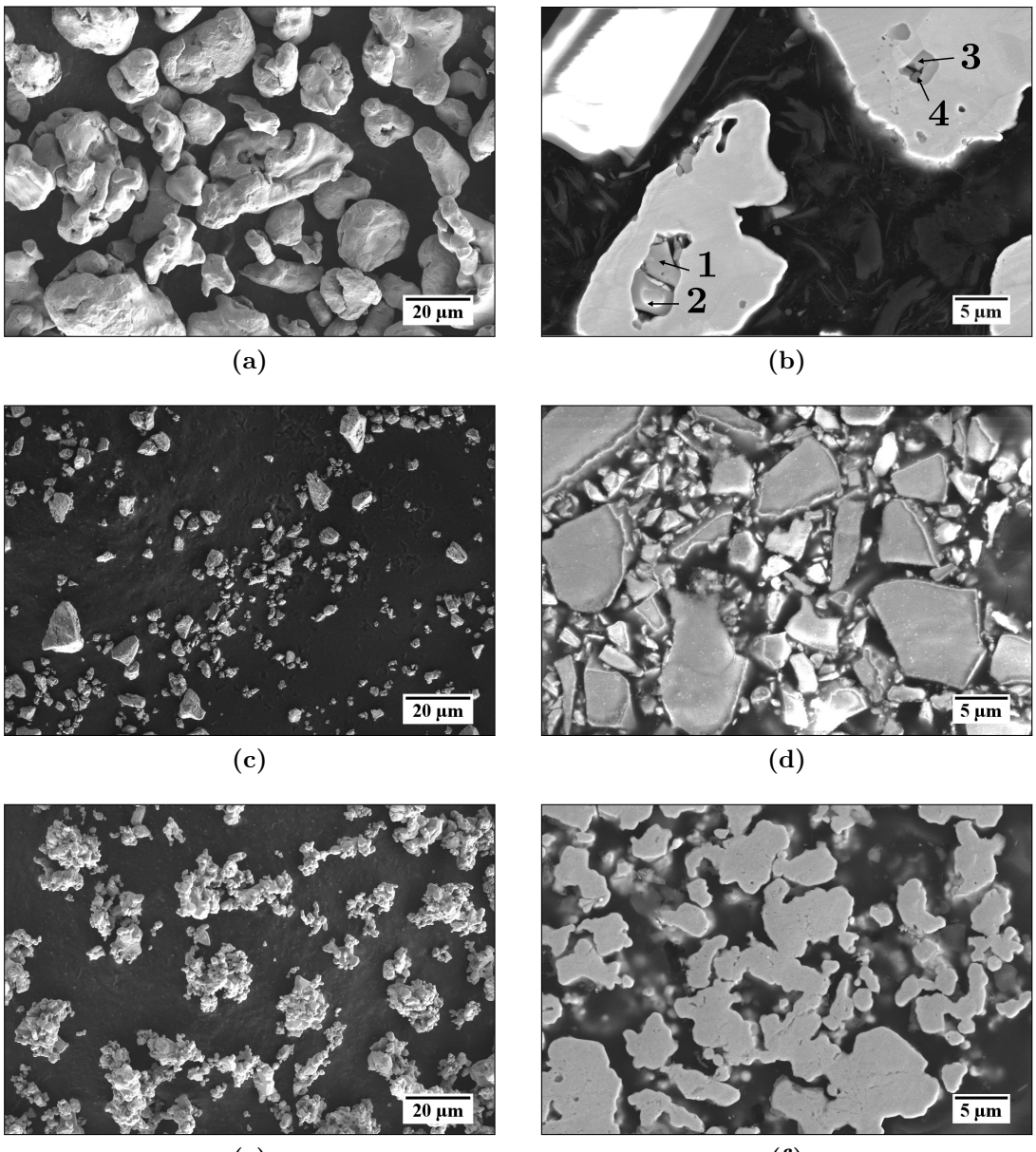

(a) (b) (c) (d) (e) (f)

Figure 4.1: SEM micrographs of elemental (a) Fe (c) Mn and (e) Ag and corresponding polished cross-sections in (b), (d) and (f) respectively. Markings indicating regions-of-interest for EDS analysis correspond to data in Table 4.1.

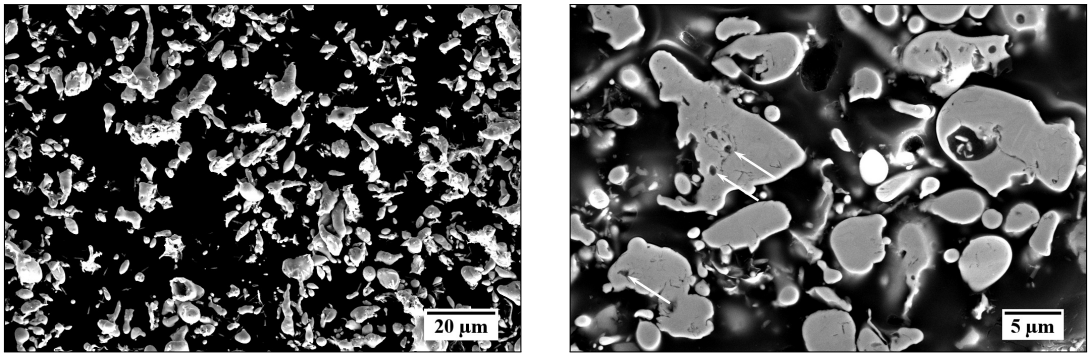

(a) (b)

Figure 4.2: SEM micrographs of (a) Fe35Mn4C master-alloy designated as MA and (b) its cross-section. Arrows in (b) point towards regions containing a slightly higher O wt.%.

4.1.2 Phase analysis

The results of X-ray diffraction analysis carried out on the elemental powders, is presented in Figure 4.3. All powders exhibited well-defined peaks that corresponded well with cards within the ICDD database. Card numbers 01-080-3816, 00-032-0637 and 00-04-0783 matched the Fe (BCC), Mn (BCC) and Ag (FCC) patterns respectively. Powders kept in storage for long periods of time, were re-analysed prior to use to make sure that the powders did not undergo any significant changes beyond natural oxidation in air.

4.2 Corrosion testing

As outlined in Chapter 3, the corrosion testing carried out in this work can be split in five main phases. In this chapter, the results for each phase will be presented followed by a discussion pertaining to that specific work.

4.2.1 Phase One - Corrosion testing of porous alloys

Phase One incorporates the initial tests carried out on uniaxially-pressed and sintered Fe, FeMn and FeMnAg coupons. The aim of this initial work, was to gain insight into the evolving degradation behaviour of Fe, FeMn and FeMnAg

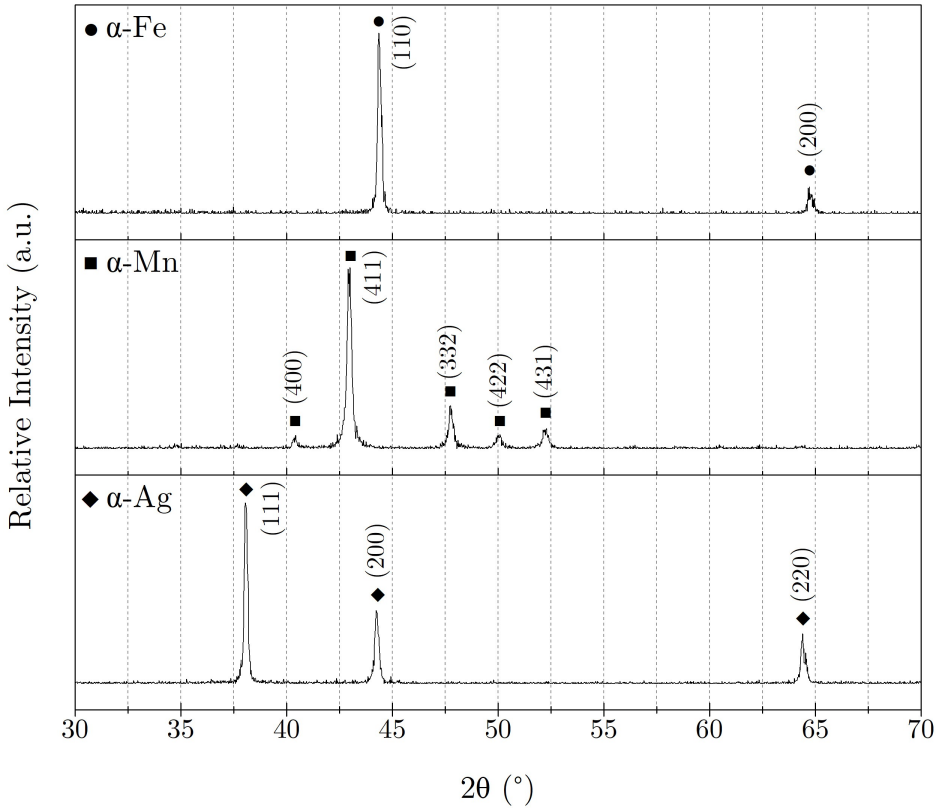

Figure 4.3: XRD patterns for elemental Fe, Mn and Ag powders.

over a 24 h period, using a variety of electrochemical techniques. In this way, any misleading advantages or disadvantages of alloying with Mn and noble Ag additions implied by extremely short-term *in vitro* tests, could be deconstructed based on the observed trends. Using the same techniques, this section also includes analyses on the influence of Ca^{2+} ions in the electrolyte on the degradation of Fe-based alloys, through testing in two commonly used solutions; HBSS and HBSS+Ca.

The vast majority of the work presented in this section has been published as a two-part collaborative publication in the peer-reviewed journal *Bioactive Materials* [76, 77].

4.2.1.1 Material characterisation

SEM images of the sintered Fe, FeMn and FeMnAg coupons are shown in Figure 4.4. The percentage porosity area based on binarisation of optical micrographs for each material, is presented in Table 4.2. The significantly lower percentage porosity in Fe coupons is due both to the higher compressibility of Fe relative to Mn-containing powder mixtures, as well as the facilitated self-diffusion of the pure metal mixture during sintering. The micrographs generally show a single phase composition for the Fe coupons whereas Figure 4.4 (d) and (f) reveal additional dark inclusions for FeMn and FeMnAg coupons. EDS mapping for these two materials presented in Figure 4.5, reveals that the darker inclusions as well as porous areas were both rich in Mn and O, suggesting the inclusion of Mn-rich oxides in the Mn-containing microstructures, as expected. The presence of oxides within the pores could have affected the rate of pore closure during sintering for FeMn and FeMnAg - another contributor to the higher porosity percentages presented in Table 4.2. The averaged wt.% of Mn in multiple areas on the FeMn and FeMnAg matrix are also presented in Table 4.2. Although 35 wt.% Mn was added to the mixture when preparing the green coupons, the final microstructures contained 33.75 ± 0.46 wt.% and 33.06 ± 0.74 wt.% Mn for FeMn and FeMnAg respectively. The slight loss in Mn is most likely either due to sublimation or losses for formation of Mn-rich oxides [205]. Furthermore, the microstructure of the FeMnAg coupon in Figure 4.4f shows a homogeneous distribution of a lightly coloured phase which corresponds to Ag. Since Ag melts at 962°C and is not

Table 4.2: Percentage area porosity and wt.% Mn in austenitic phase for Fe, FeMn and FeMnAg. Error represents standard error (n = 30).

Sample	Porosity area [%]	wt.% Mn in γ-FeMn
Fe	8.58 ± 0.52	-
FeMn	19.06 ± 1.27	33.75 ± 0.46
FeMnAg	18.45 ± 1.47	33.06 ± 0.74

soluble in either Fe or Mn, it flows to fill in a portion of the porosity above this temperature [132, 248].

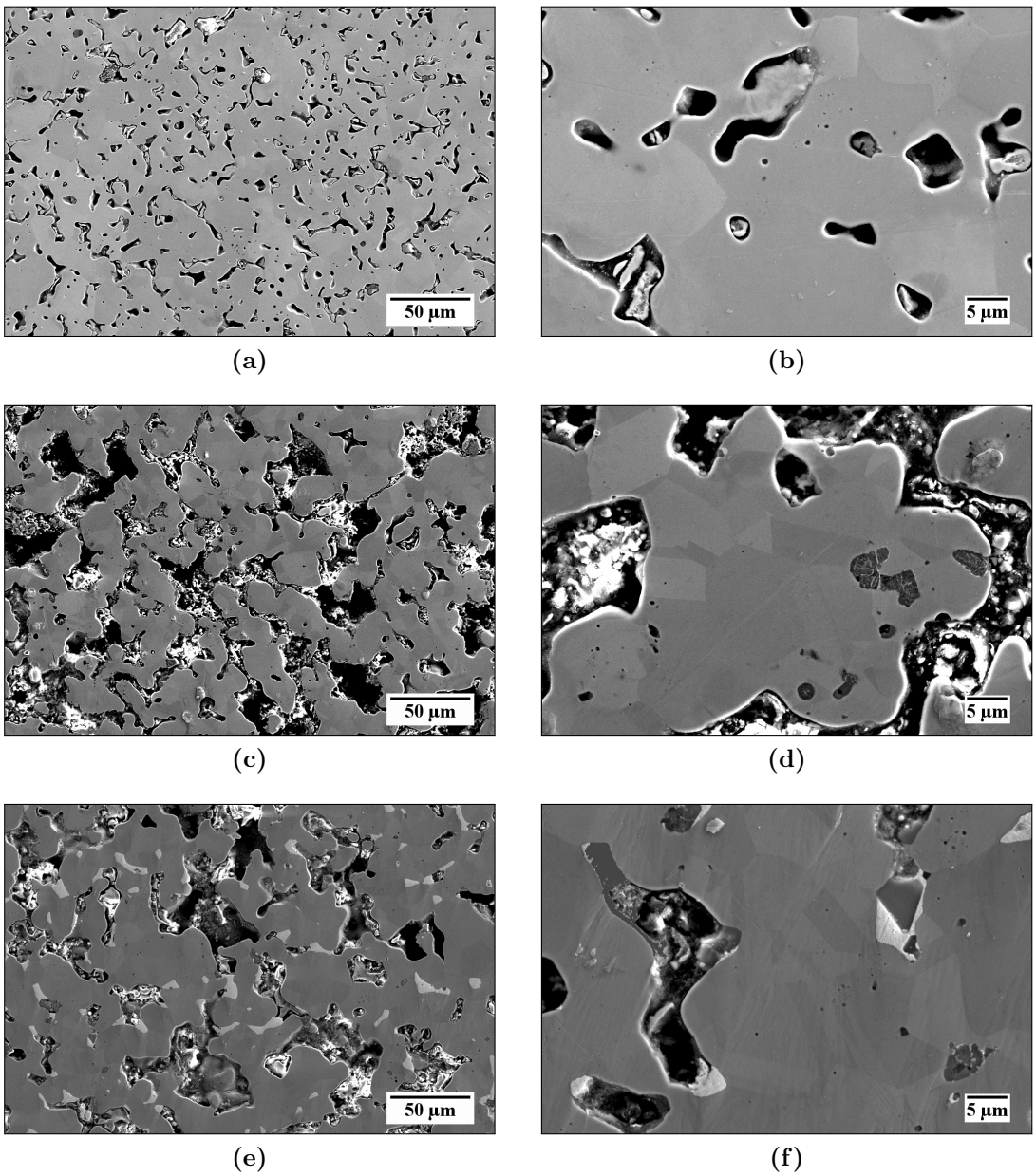

Figure 4.4: SEM micrographs of polished (a-b) Fe, (c-d) FeMn and (e-f) FeMnAg.

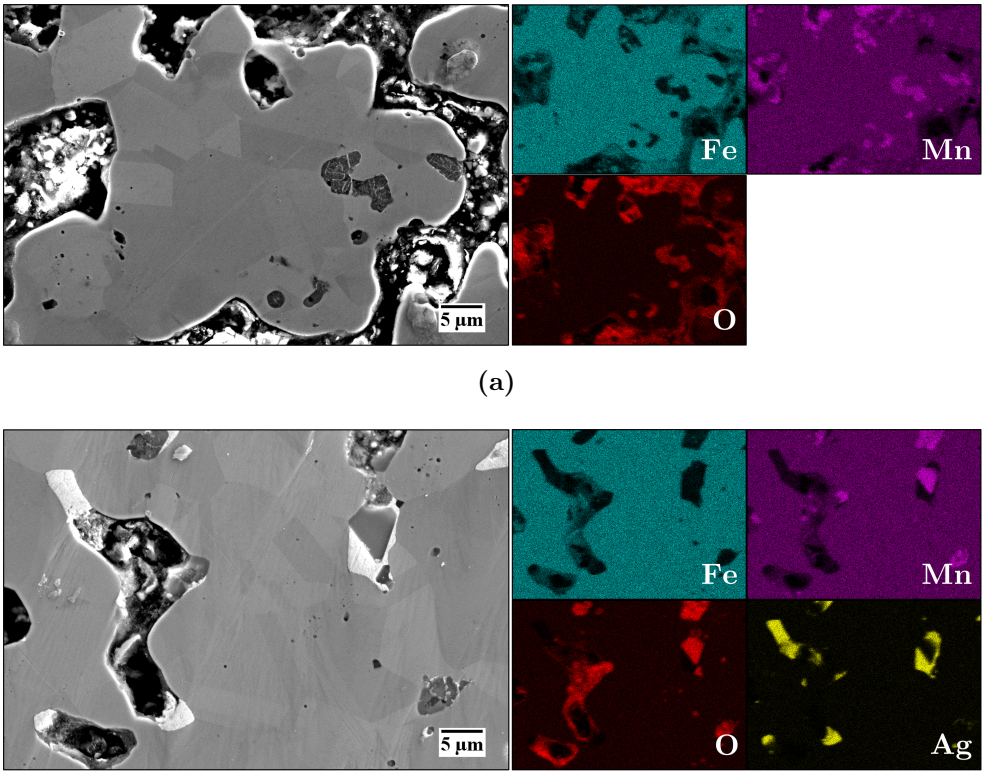

Figure 4.5: SEM micrograph of (a) FeMn and (b) FeMnAg with corresponding EDS distribution maps for Fe, Mn, O and Ag.

The XRD patterns for the sintered coupons, are exhibited in Figure 4.6. The results confirm the presence of a single ferritic phase for Fe (α-Fe, PDF Card No. 04-015-2437). It also confirms that the resultant Mn wt.% in the FeMn and FeMnAg matrices, is sufficient to stabilise the γ-austenite phase (γ-FeMn, PDF Card No. 04-006-6664), leaving no residual α-Fe and α-Mn. The oxide inclusions in the Mn-containing coupons were confirmed to be MnO (PDF Card No. 04-002-8159) although the similarity of the Fe and Mn atoms make it quite possible for certain oxide inclusions to contain substitutional Fe atoms to form (Fe,Mn)O, which shares a very similar XRD pattern. However, considering the relative reactivity of Mn, MnO is still the most likely oxide to form under the sintering conditions used. The XRD pattern for FeMnAg also shows peaks corresponding to a Ag-rich phase (PDF Card No. 01-080-4432).

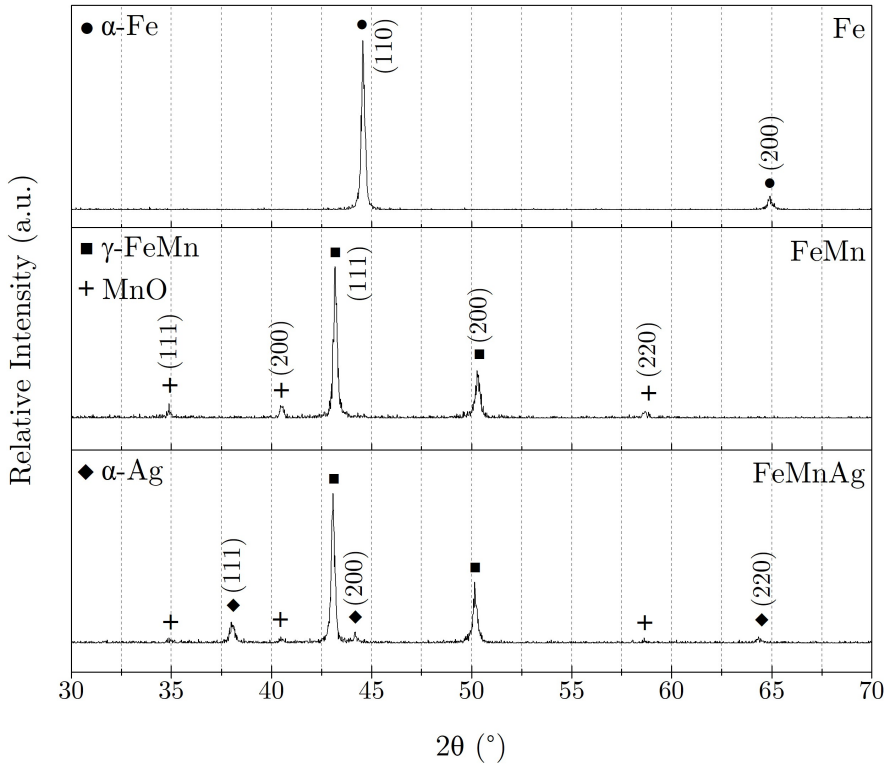

Figure 4.6: XRD patterns for ground Fe, FeMn and FeMnAg coupons.

4.2.1.2 Potentiodynamic testing

Representative Tafel plots for the PDP tests carried out on Fe, FeMn and FeMnAg in HBSS and HBSS+Ca, are presented in Figure 4.7a with corresponding calculated i_{corr} values in Figure 4.7b. The i_{corr} values clearly exhibited a large spread as represented by the significant calculated standard error. However, some clear differences are evident. In each case the current density measured at the surface of corroding Fe was considerably lower than for FeMn and FeMnAg. Moreover, both Fe and FeMn clearly generated higher current densities in HBSS compared to HBSS+Ca. In HBSS+Ca, FeMnAg corroded the most whereas in HBSS, FeMn generated the highest current densities.

It is important to note that despite the fact that the unit for current density is marked as µA, the data was normalised per unit *apparent* area, as measured using Vernier calipers. However, due to the difficulty in accounting for the *actual* area i.e. including exposed porosity area, there is a possibility that the values for

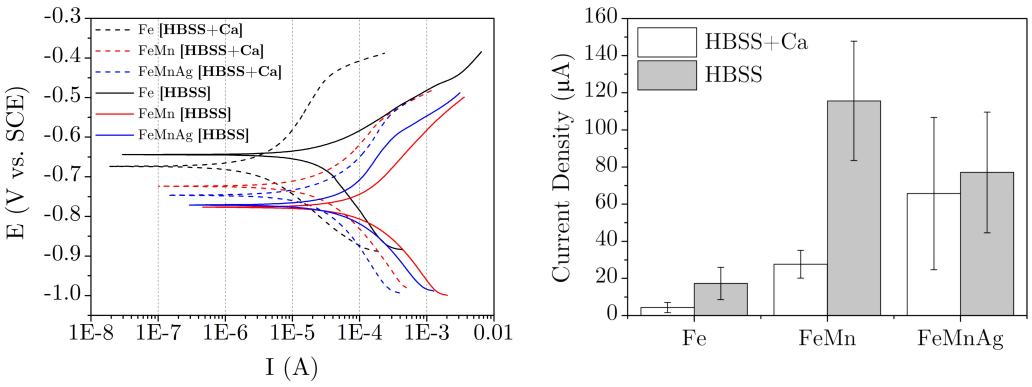

(a) **(b)**

Figure 4.7: Potentiodynamic test results (a) Tafel slopes for Fe, FeMn and FeMnAg tested in HBSS and HBSS+Ca and (b) corresponding average current densities. Error bars represent standard error [n = 4].

FeMn and FeMnAg in particular, are slightly overestimated relative to the values for Fe.

4.2.1.3 Electrochemical Impedance Spectroscopy

4.2.1.3.1 Test plots

Bode plots presented in Figure 4.8 show the change in absolute impedance and phase shift as a function of frequency for Fe, FeMn and FeMnAg tested in HBSS and HBSS+Ca over a 24 h period.

The most obvious distinction between the two sets of samples tested in the different electrolytes, is the additional time constant present at higher frequency for samples tested in HBSS+Ca. For the samples tested in HBSS, Figure 4.8 (a), (c) and (e), a single phase shift was observed around the same frequencies (1-100 Hz) that the charge transfer resistance and the electrical double layer of similar alloys generally respond [107, 134, 166]. On the other hand, samples tested in HBSS+Ca exhibited a second time constant between 1 and 10 kHz. After the initial 30 min of immersion, the mid-frequency time constant was not clearly discernible when testing pure Fe. However, there was still a clear deviation from the 0° phase shift displayed by the same metal at high frequencies when testing in HBSS, indicating the potential formation of corrosion products that behave as a

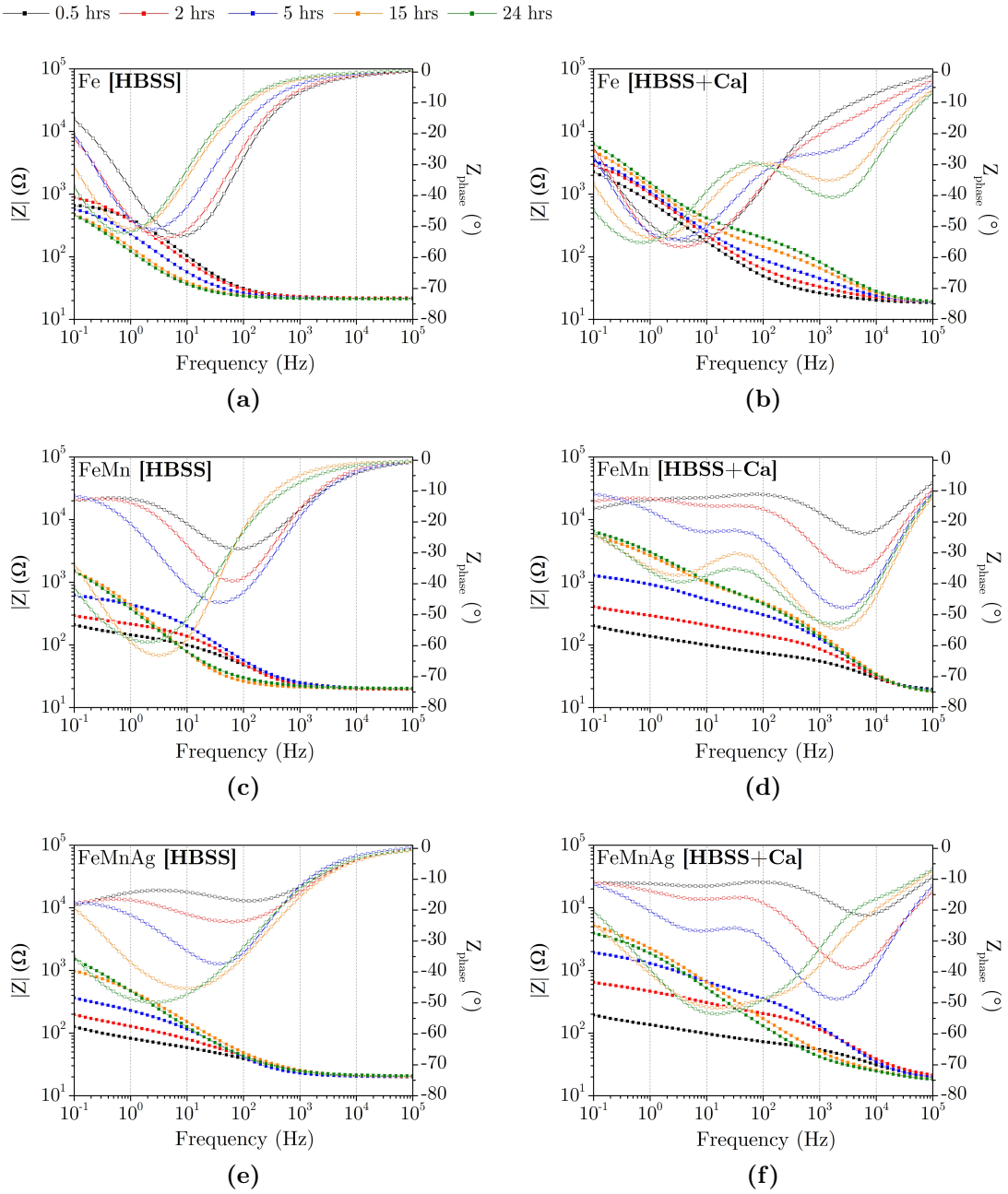

Figure 4.8: Bode plots for (a) Fe in HBSS (b) Fe in HBSS+Ca (c) FeMn in HBSS (d) FeMn in HBSS+Ca (e) FeMnAg in HBSS and (f) FeMnAg in HBSS+Ca.

partially protective barrier similar to what was observed by Mei *et al.* [159] with Mg alloys. In the case of FeMn and FeMnAg, the additional time constant was visible from the start of the test. In general, its evolution progressed similarly for all metals, with an increase in negative phase shift and a corresponding rise in mid-frequency impedance. For FeMnAg, the mid-frequency time constant showed a decreasing negative phase shift and decreased mid-frequency impedance after approximately 9 h.

4.2.1.3.2 Equivalent circuit modelling

The spectra for the alloys immersed in HBSS+Ca were modelled using the equivalent circuit model illustrated in Figure 4.9 to gain a better understanding of the corrosion layer evolution. The electrolyte resistance is represented by R_s, while the charge transfer resistance and double layer capacitance are represented by R_{ct} and CPE_{dl}, respectively. R_{layer} represents the additional protective layer's resistance, whereas CPE_{layer} stands for its capacitive behaviour. To account for the nonideal behaviour of features in realistic systems, constant phase elements (CPEs) were used instead of capacitors for reasons outlined in Section 2.1.2.2.4. The associated capacitance could then be calculated based on the CPE coefficient and exponent using equation 4.1, rewritten hereunder using the denoted symbols for the electrical components associated with the corrosion product layer.

$$C_{layer} = R_{layer}^{\frac{1-a_{layer}}{a_{layer}}} . CPE_{layer}^{\frac{1}{a_{layer}}} \tag{4.1}$$

Using this equation in this case was acceptable since the exponent, a_{layer}, was consistently in the vicinity of 0.7 or over, as the equation constrains. The full fitting results, including the goodness-of-fit indicator χ^2, can be found in Appendix A, Tables A.1, A.2 and A.3.

Graphical representations of the evolution of the fitting results of interest are presented in Figure 4.10. Figure 4.10 (b) and (c) depict the evolution of R_{layer} and C_{layer} over the 24 h period. In general, the resistance of the additional layer R_{layer} for Fe in HBSS+Ca increased gradually over the course of 24 h. In the case of FeMn, the R_{layer} value increased steeply upon immersion, followed by a gradual increase over the course of the test. Although the R_{layer} for FeMnAg

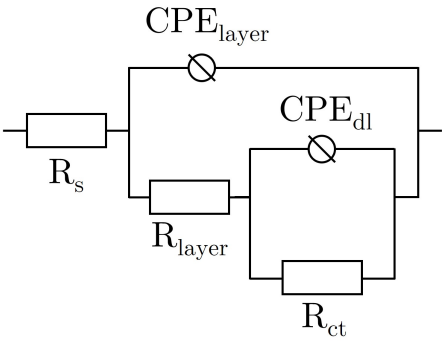

Figure 4.9: Nested equivalent circuit model used for modelling systems presented in Figure 4.8.

increased even more steeply upon immersion, the resistance began to drop after about 9 h, corresponding to the changes in mid-frequency phase shift observed in the Bode plot. A similar shift was observed in the C_{layer} evolution for FeMnAg, starting at around 11 h. The sudden increase in capacitance implied a drop in the impedance contribution from this component, due to the inverse proportional relationship between capacitance and impedance (equation 2.14). Following this increase, C_{layer} gradually dropped towards the initially measured values.

An additional relaxation process was observed at low frequencies particularly in the tests carried out on FeMn and FeMnAg. This could be easily observed in sample Nyquist plots shown in Figures 4.11 (a) and (b) with results obtained after 1 h from immersion. Not quite at 45° to the real impedance (Z') axis as in Warburg diffusion, the angled extension at low frequencies is more representative of a more complex diffusion process likely brought about by the highly porous nature of the FeMn and FeMnAg working electrodes. In fact, the tests performed with Fe did not display the same behaviour. Sharma *et al.* [230] similarly observed this low frequency relaxation when testing microporous Fe, the feature becoming more pronounced with increase in volume porosity and disappearing completely for dense Fe, as in Figure 4.8a (Fe in HBSS). Since neither Warburg elements nor CPE elements could accurately represent diffusion through the complex pore geometries [66, 67] and due to lower frequencies being most susceptible to distortion from active dissolution [166], the initial frequencies were excluded from the data fitting exercise.

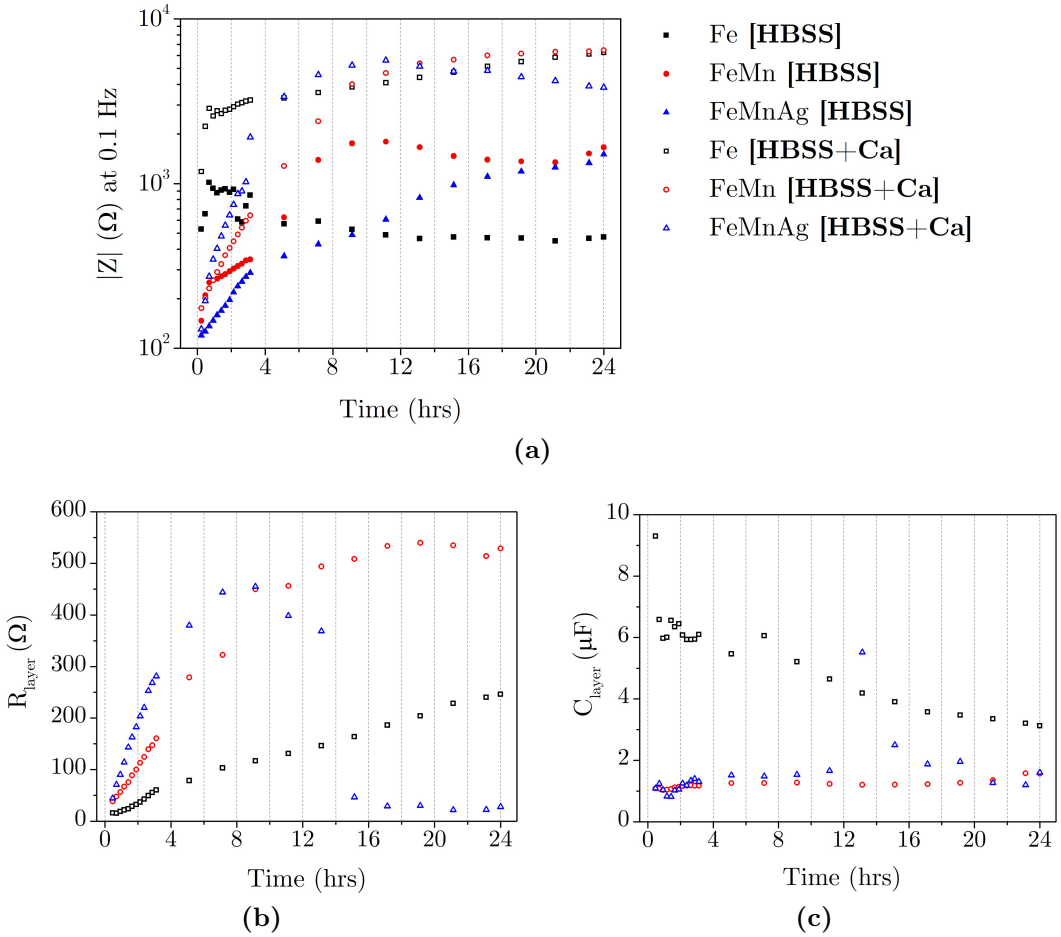

Figure 4.10: (a) Progression of total impedance at 0.1 Hz for Fe, FeMn and FeMnAg immersed in HBSS and HBSS+Ca for 24 h, (b) modelled values of R_{layer} and (c) C_{layer} for Fe-based alloys immersed in HBSS+Ca for 24 h. R_{layer} and C_{layer} correspond to the components in the model shown in Figure 4.9.

In tests conducted in HBSS, it was clear from the Bode plots in Figure 4.8 that FeMn and FeMnAg had much lower initial low frequency impedances than pure Fe. For FeMn and FeMnAg, this measure increased significantly during the test, while that of Fe decreased slightly. These trends were also observed in the tests conducted in HBSS+Ca. Figure 4.10a illustrates the progress of low-frequency impedance for the metals in both electrolytes. For this analysis, the low frequency impedance is most representative of the corrosion resistance of the metal in the absence of reliable modelled R_{ct} and C_{dl} values for samples tested in HBSS.

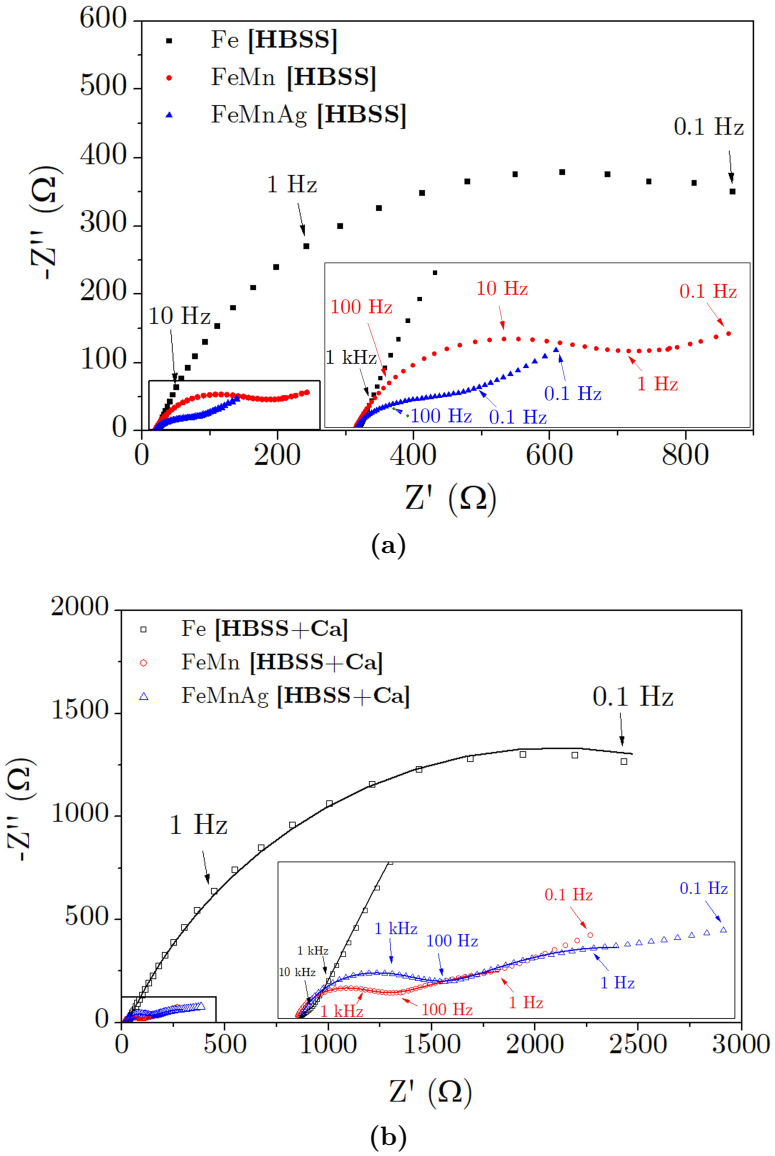

Figure 4.11: Nyquist plots for Fe, FeMn and FeMnAg immersed for 1 hr in (a) HBSS and (b) HBSS+Ca. Solid lines represent the fitted data presented in Figure 4.10.

4.2.1.3.3 Surface characterisation using SEM-EDS

Figures 4.12 and 4.13 show the surface morphologies of the Fe samples immersed in HBSS and HBSS+Ca following the 24 h EIS test, with corresponding elemental distribution maps. Numbered regions marked on the figures discussed in this

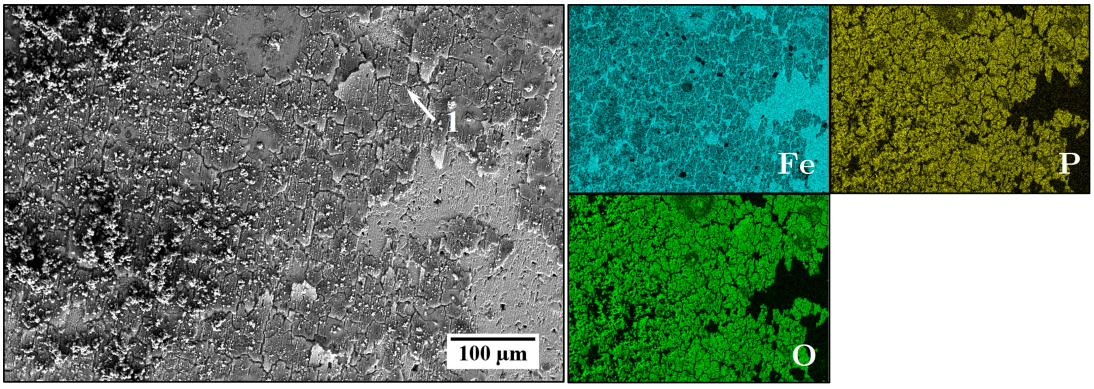

Figure 4.12: SEM images of surface morphology of Fe immersed in HBSS for 24 h and corresponding Fe, P and O distribution maps acquired by EDS. Numbered regions-of-interest correspond to EDS analysis presented in Table 4.3.

section correlate to the EDS analysis presented in Table 4.3. Both Fe surfaces were clearly partially covered by a flaky layer, the "flaky" characteristic generally being related to the post-test dehydration process, especially if drying is partially carried out in vacuum as used in this case[166]. Both surfaces show regions where the product flaked off, indicating loose attachment to the substrate. EDS results for regions (1) and (2) on the same corrosion product, indicate it to be an Fe/P-rich layer, formed both in HBSS and HBSS+Ca. Other than the Fe/P product, the result for area (2) also shows evidence of Ca on the surface. However, the map in Figure 4.13 was not particularly helpful at discerning which specific areas were rich in Ca, which implied that the Ca corresponded to the homogeneously distributed white products on top of the Fe/P layer.

When observing the surfaces of FeMn following the EIS tests, there was no evidence of a similar Fe/P layer on the surface. However, points (4) and (5) in Figures 4.14 (a) and (b) for FeMn immersed in HBSS, show localised Mn/P-rich products forming on the surface, when compared to the elemental composition of the rest of the metal surface sampled in area (3). In HBSS+Ca, the Mn/P-rich deposits were mostly replaced with Ca/P-rich clusters similar to that shown in Figure 4.14c at points (6) and (7).

The surfaces of FeMnAg following testing in HBSS and HBSS+Ca are shown in Figure 4.15 and 4.16 respectively, with complementary elemental maps. The corrosion products are very similar to what was observed on FeMn. Likewise,

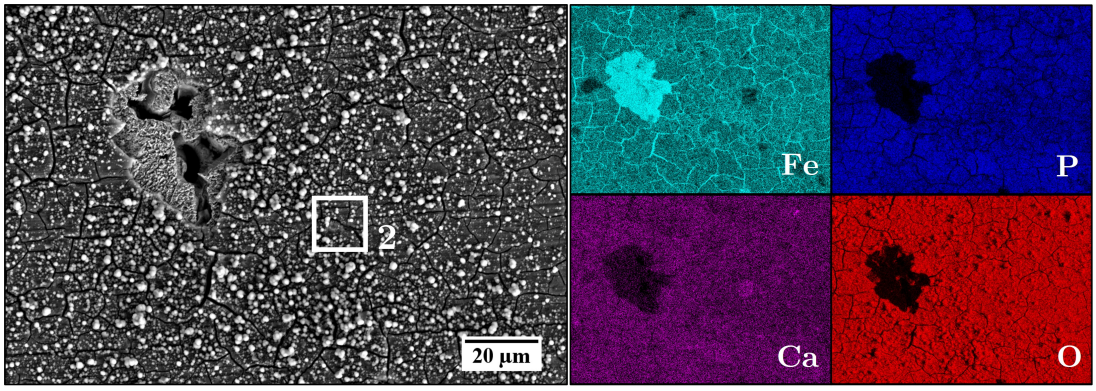

Figure 4.13: SEM images of surface morphology of Fe immersed in HBSS+Ca for 24 h and corresponding Fe, P, Ca and O distribution maps acquired by EDS. Numbered regions-of-interest correspond to EDS analysis presented in Table 4.3.

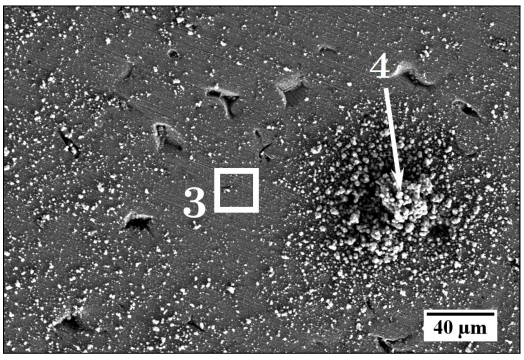

(a)

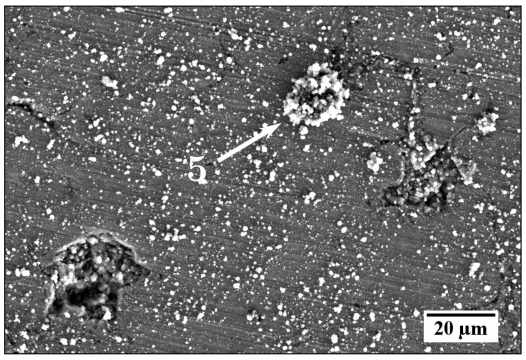

(b)

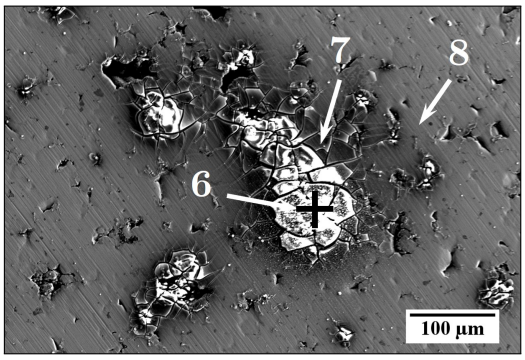

(c)

Figure 4.14: SEM images of surface morphology of FeMn immersed in (a-b) HBSS and (c) HBSS+Ca for 24 h. Numbered regions-of-interest correspond to EDS analysis presented in Table 4.3.

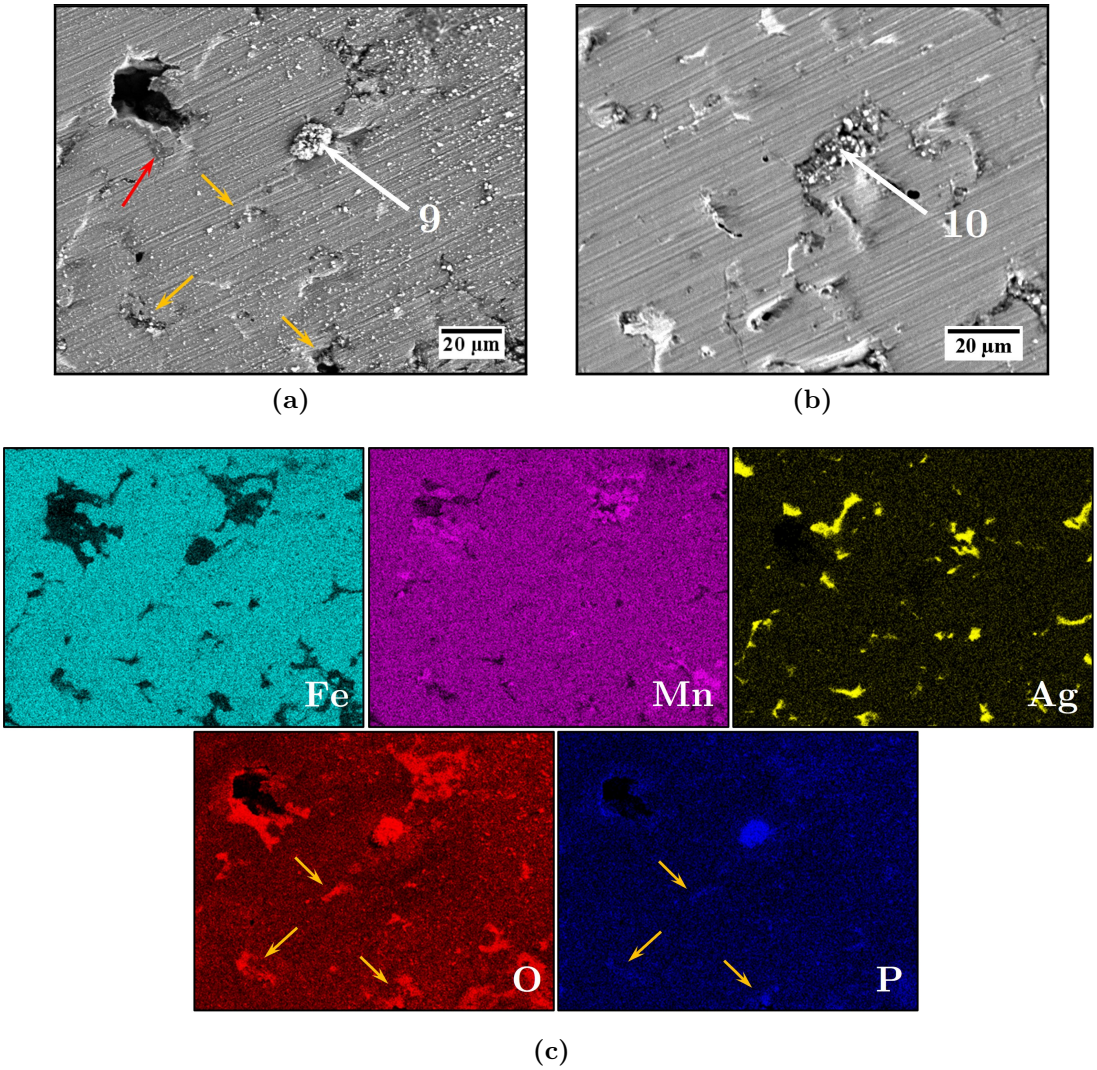

Figure 4.15: (a-b) SEM images of surface morphology of FeMnAg immersed in HBSS for 24 h and (c) corresponding Fe, Mn, Ag, O and P distribution maps acquired using EDS for SEM image in (a). Red arrow in (a) indicates presence of crack propagating through thin corrosion layer. Orange arrows point towards O and P-rich compounds present in selected pores. Numbered regions-of-interest correspond to EDS analysis presented in Table 4.3.

there was no dehydrated P-rich layer as observed on the Fe surfaces, but rather P-rich clusters. In HBSS, flower-like Mn/P-rich deposits like the ones in Figure 4.15a (point 9) were observed all over the sample surface whereas the pores were filled with products consisting primarily of mixed Fe/Mn and P (Figure 4.15a

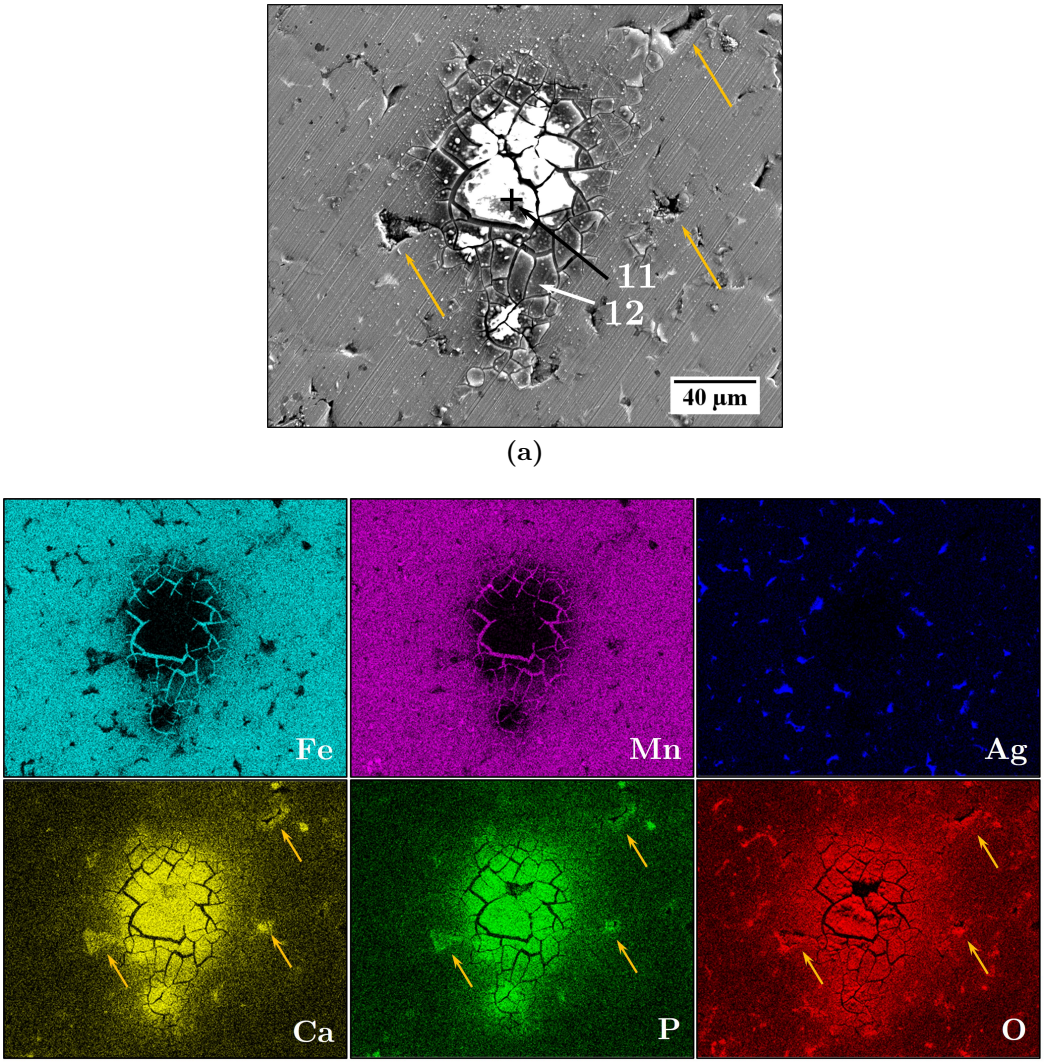

(a)

(b)

Figure 4.16: (a) SEM image of surface morphology of FeMnAg immersed in HBSS+Ca for 24 h and (b) corresponding Fe, Mn, Ag, Ca, P and O distribution maps acquired using EDS. Orange arrows point towards O, Ca and P-rich compounds present in selected pores. Numbered regions-of-interest correspond to EDS analysis presented in Table 4.3.

orange arrows and (b) point 10). In HBSS+Ca, very similar Ca/P clusters to those found on FeMn were once again observed on FeMnAg with EDS confirming similar compositional patterns. The orange arrows in Figure 4.16 also indicate that pores were enriched with Ca, P and O compared to the rest of the sample

Table 4.3: EDS analysis corresponding to regions-of-interest marked in Figures 4.12 to 4.16, in wt.%.

Pt.	O	Fe	Mn	P	Ca	Na	Cl	Mg	Si	Al	Ag	N	K
1	62.40	25.20	-	08.05	-	03.56	-	00.21	00.32	00.26	-	-	-
2	58.33	25.74	-	07.63	02.03	04.35	01.32	00.36	00.24	-	-	-	-
3	23.54	46.00	25.74	01.85	-	02.87	-	-	-	-	-	-	-
4	30.20	33.04	18.81	17.24	-	00.71	-	-	-	-	-	-	-
5	46.12	21.72	18.54	09.17	01.54	02.31	-	-	-	-	-	-	00.60
6	61.04	01.16	01.48	12.58	17.15	03.02	01.71	01.86	-	-	-	-	-
7	59.08	05.93	03.06	12.62	16.30	00.32	-	02.69	-	-	-	-	-
8	08.28	58.12	31.11	00.88	01.03	00.20	-	00.38	-	-	-	-	-
9	66.18	03.98	18.40	09.33	00.46	01.19	00.46	-	-	-	-	-	-
10	69.73	12.42	09.26	05.86	-	01.93	00.13	-	-	-	00.67	-	-
11	68.89	00.53	00.62	10.96	16.12	00.34	-	02.49	00.05	-	-	-	-
12	52.28	16.94	09.26	08.69	09.76	00.13	-	02.76	00.18	-	-	-	-
γ-FeMn region before test	02.84	57.02	27.86	-	-	-	-	-	00.44	-	-	11.84	-

surface.

Although the metal around the clustered P-rich deposits in both electrolytes does not seem to be covered by any substantial layers of corrosion product, EDS analysis of both points (3) and (8) in Figure 4.14 reveal the consistent detection of higher levels of O compared to a typical γ-FeMn region on the ground surface before the test, the elemental composition of which is also included in Table 4.3. This is likely an indicator that a thin layer of oxides/hydroxides is present all over the sample surface despite it not being clearly visible. Thin cracks around pores like the one pointed out with a red arrow in Figure 4.15a and in various regions in Figure 4.16a, also support this hypothesis. Naturally, relative to the concentration of O in dense oxides and phosphates present elsewhere on the surface, the O distribution maps could not clearly highlight the presence of such oxide layers.

4.2.1.4 Local pH and dissolved O_2 monitoring

4.2.1.4.1 Initial monitoring

The change in pH and dissolved O_2 (DO) 50 µm above the midpoint of the Fe, FeMn and FeMnAg samples during the first 15 min from immersion, is shown in Figure 4.17 for both HBSS and HBSS+Ca tests. It is important to remember at this point, that whereas DO consumption is mainly an indicator of a progressing cathodic reaction, the pH shows the resultant shift from the sum effects of various reactions. Lowered pH is generally a result of anodic or hydrolysis reactions, whereas generation of OH^- ions from the cathodic reaction, result in a pH increase.

In HBSS, Fe behaved somewhat differently than Mn-containing alloys. Whereas the pH and DO over the Fe sample gradually changed eventually settling at 7.44 units and 3.51 mg L^{-1} respectively, initial corrosion of FeMn and FeMnAg resulted in a notable spike in pH reaching values of 9 and 10.5 respectively, corresponding with a marked consumption of DO. The measurements were quick to stabilise over both alloys. While the pH levels remained close to the bulk 7.4, the DO levels stabilised at 3.71 mg L^{-1} and 0.53 mg L^{-1} for FeMn and FeMnAg. The latter is a clear indication of a strong oxygen reduction reaction taking place at the FeMnAg surface, as almost all the DO in the vicinity was immediately consumed within the first 15 min.

Considering the measurements taken in HBSS+Ca, the pH values over all alloys stabilised within similar ranges as in HBSS, between 7.09 to 7.44. However the situation with DO varied significantly. Although the DO levels over FeMnAg were initially quite low relative to the DO in the bulk (5.8 ± 0.2 mg L^{-1}), the plot exhibits a gradual increase towards a final value of 5.00 mg L^{-1}. Similarly, the DO over FeMn remained quite high at 4.57 mg L^{-1} although it dropped briefly at the start of the test at the same point that the pH probe detected a slight spike. Completely opposite to the situation in HBSS, the highest consumption of DO was recorded over the corroding Fe sample with a concentration of 2.84 mg L^{-1} being reached at the end of the test following a few minutes of increased consumption and concurrent low pH (at around 6.7) upon immersion.

It is important to remember that the pH and DO probes, although both placed at a height of 50 µm from the sample surface, were also situated 50 µm apart in

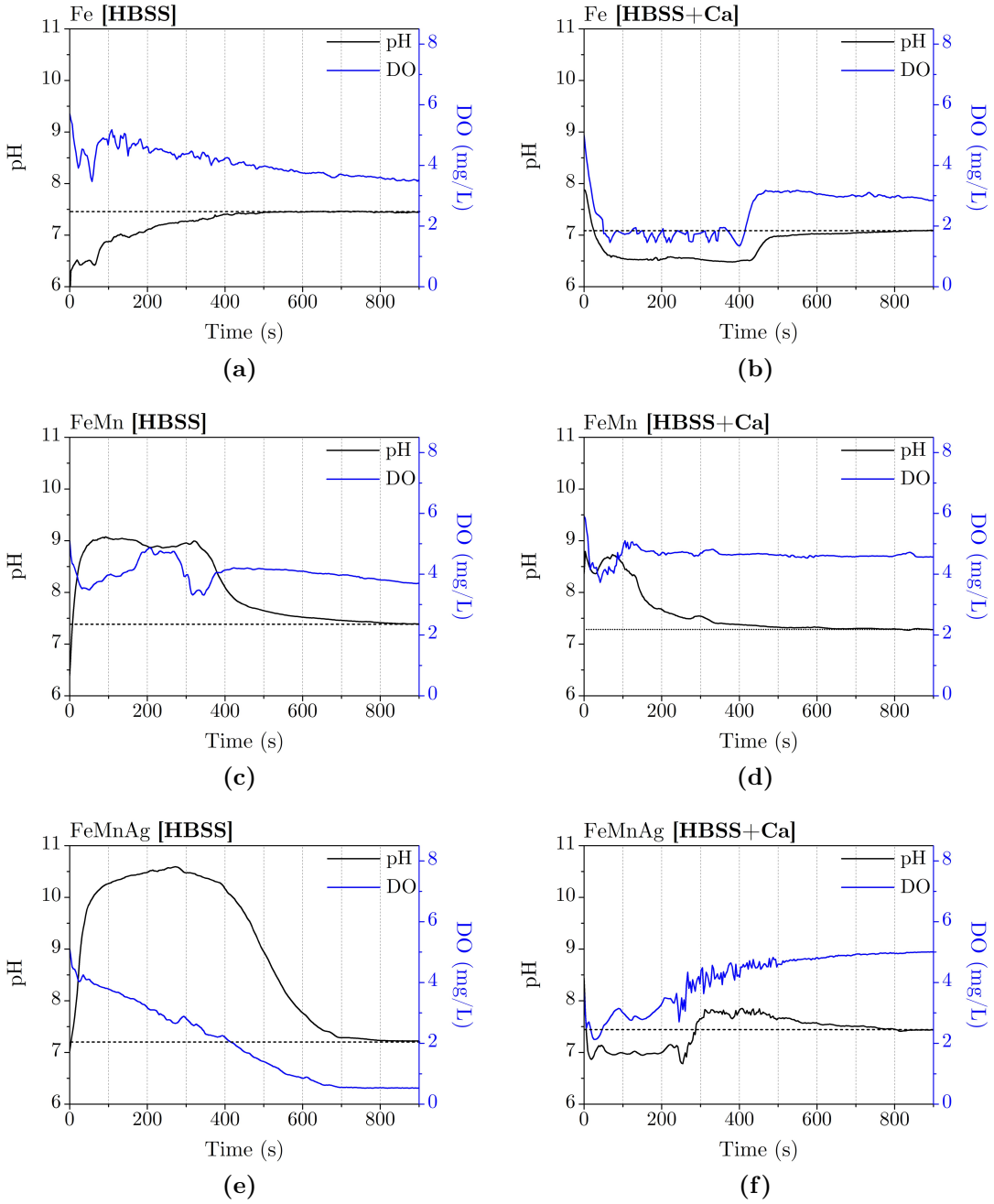

Figure 4.17: Monitoring of local pH and DO levels in the first 15 minutes upon immersion of (a) Fe in HBSS (b) Fe in HBSS+Ca (c) FeMn in HBSS (d) FeMn in HBSS+Ca (e) FeMnAg in HBSS and (f) FeMnAg in HBSS+Ca. The dashed line indicates the value at which the pH settles in each test.

the horizontal plane. Therefore, the measured values could be related to activity taking place in slightly dissimilar local environments.

4.2.1.4.2 Long-term mapping

Following the initial measurements over the midpoint of the sample upon immersion, full maps were measured over the course of 24 h to visualise the evolution of pH and DO over time and correlate to the progressing visual degradation as seen using optical microscopy.

Measurements in HBSS

Optical microscopy and corresponding pH and DO maps for Fe immersed in HBSS are shown in Figure 4.18. The first maps following 20 min from first contact with the electrolyte, clearly show a localised variation in the environment atop the corroding metal. The left side of the sample experienced a localised lowered pH (at approx. 6.8) that corresponded both with an increased DO consumption, as well as with the precipitation of brightly coloured corrosion products in the adjacent micrograph. The local environment was quick to stabilise and the maps reveal a rather homogenised environment over the mapped region. The optical micrographs showed sample surfaces that had been covered by the brightly coloured product after 12 h and that corrosion on the left part of the sample had started to darken the surface.

With FeMn, the results in Figure 4.19 show that corrosion of the metal in this case did not result in considerably different localised conditions as observed with Fe. Both the micrographs and the maps showed a rather homogeneous stabilisation of the environment. The pH did not change much from the original 7.4, measuring at 7.3 over the sample by the end of the test. On the other hand, similar to Fe, the DO levels continued to drop over the course of the test, indicating that there was a steady consumption of DO over the 24 h duration.

Compared to both Fe and FeMn, the initial map of FeMnAg after 20 min displayed a much more aggressive initiation of the corrosion process. This was somewhat expected based on the initial 15 min measurement of pH and DO at the midpoint of the sample, however the full map in Figure 4.20 shows the

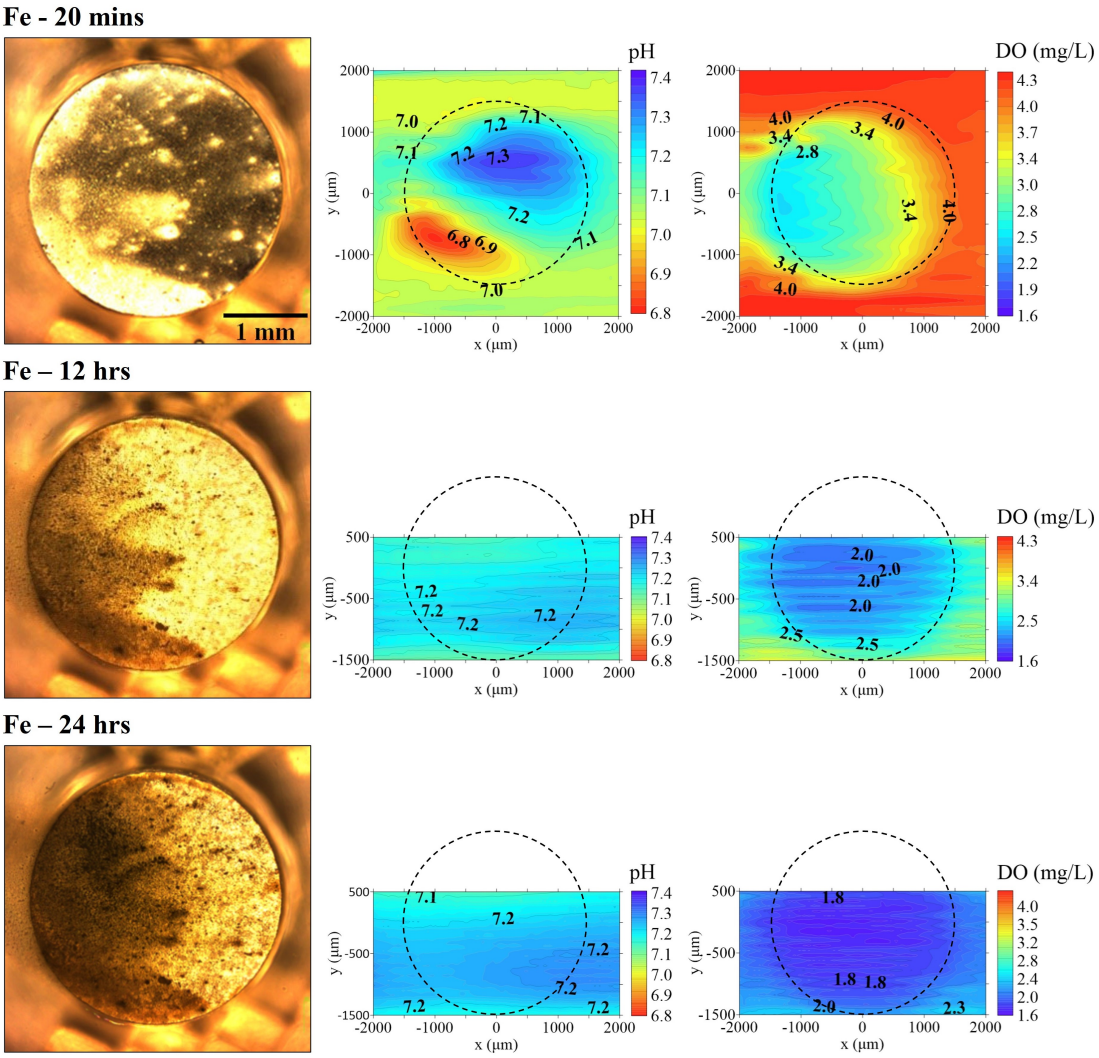

Figure 4.18: Optical micrographs of Fe surfaces immersed in HBSS after mapping carried out at 20 min, 12 h and 24 h, with corresponding pH and DO maps. Dashed circles in this and subsequent figures, indicate the placement of the sample relative to the measurements.

extent of the pH gap measured over the whole exposed area, with the lowest pH registered at 6.4 at anodic sites and 8.1 at cathodic regions. Moreover one could clearly see that the oxygen consumption was not extensive only at the midpoint but over the whole testing area. Based on the initial maps, the mapping procedure was believed to be too slow to efficiently monitor the evolution of the rapidly progressing corrosion. Line scans presented in Figure 4.22 were carried

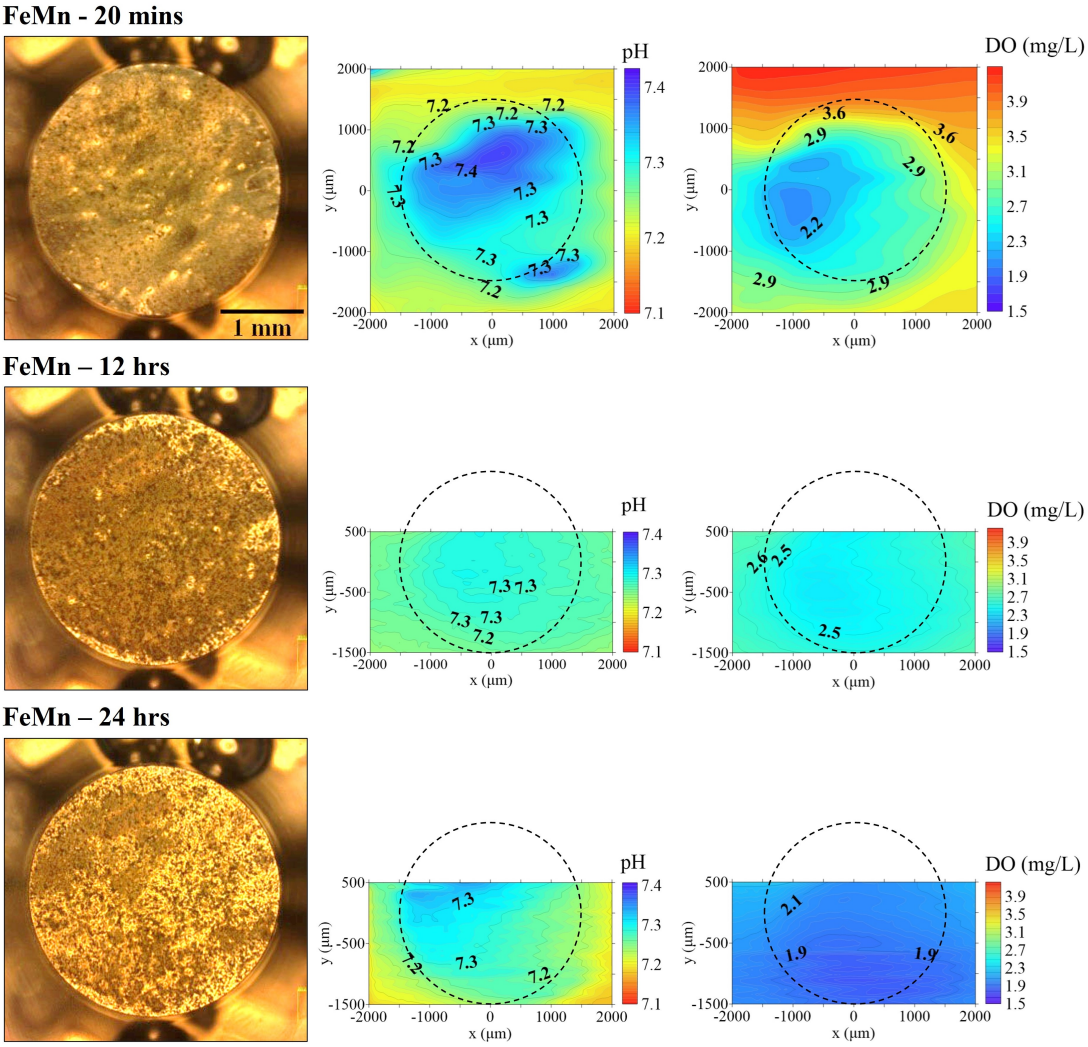

Figure 4.19: Optical micrographs of FeMn surfaces immersed in HBSS after mapping carried out at 20 min, 12 h and 24 h, with corresponding pH and DO maps.

at 1 h intervals with optical micrographs of the sample being tested presented in Figure 4.21. After just 30 min, the micrographs showed the formation of two distinct regions on the sample with the left side corroding preferentially. This half continued to darken with time while the right side accumulated corrosion products but did not seem to be completely covered by the end of the test. The first line scan collected 3 h after test initiation, showed that the electrolyte over the left side of the sample experienced significant acidification (approx. pH =

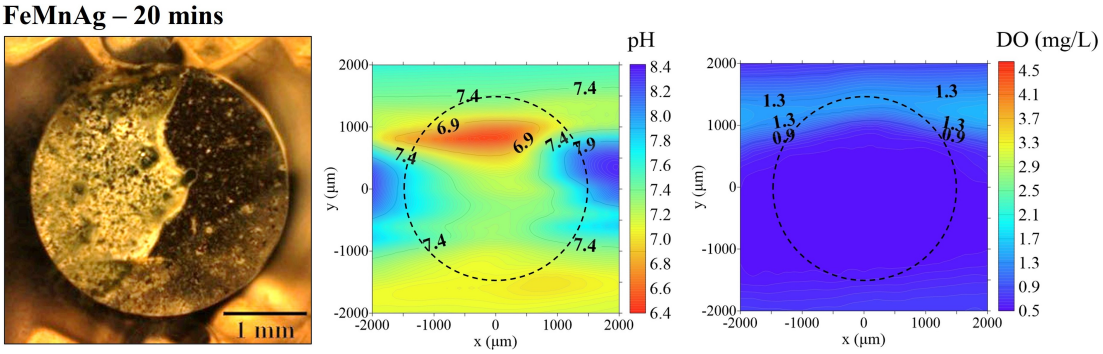

Figure 4.20: Optical micrographs of FeMnAg surface immersed in HBSS after mapping carried out at 20 min, with corresponding pH and DO maps.

6.6) whereas the pH over the right side approached a value of 8.4. At this time point, the DO was uniform at 0.5 mg L^{-1}. With time, the pH stabilised such that it measured between 7.4 and 7.6 over the sample width. Meanwhile, the DO levels gradually increased with time, the levels over the right side of the sample being slightly higher compared to the DO levels measured over the preferentially corroding half. Having said this, the final measurements were still lower than the DO levels measured over both Fe and FeMn after 24 h. The accumulation of corrosion products on the corroding FeMnAg in HBSS was such that after 15 h from immersion, the probes registered an interfering amount of adherent precipitates that could have caused irreversible damage to the sensors. This test was therefore terminated at the 15-h mark.

Measurements in HBSS+Ca

The pH and DO maps and corresponding optical micrographs for tests carried out on Fe, FeMn and FeMnAg in HBSS+Ca, are presented in Figure 4.23, 4.24 and 4.25-4.26, respectively.

Starting with the results for Fe in Figure 4.23, the micrographs showed the formation of bright products covering the majority of the surface after just 20 min. The same products continued to accumulate over the next 24 h with dark regions forming near the centre of the sample at around 12 h. Similar to the result in HBSS, the first pH maps showed distinct acidified/alkalised regions. However, the range of pH measured was narrower at 7.05-7.30 as opposed to 6.76-7.36 in

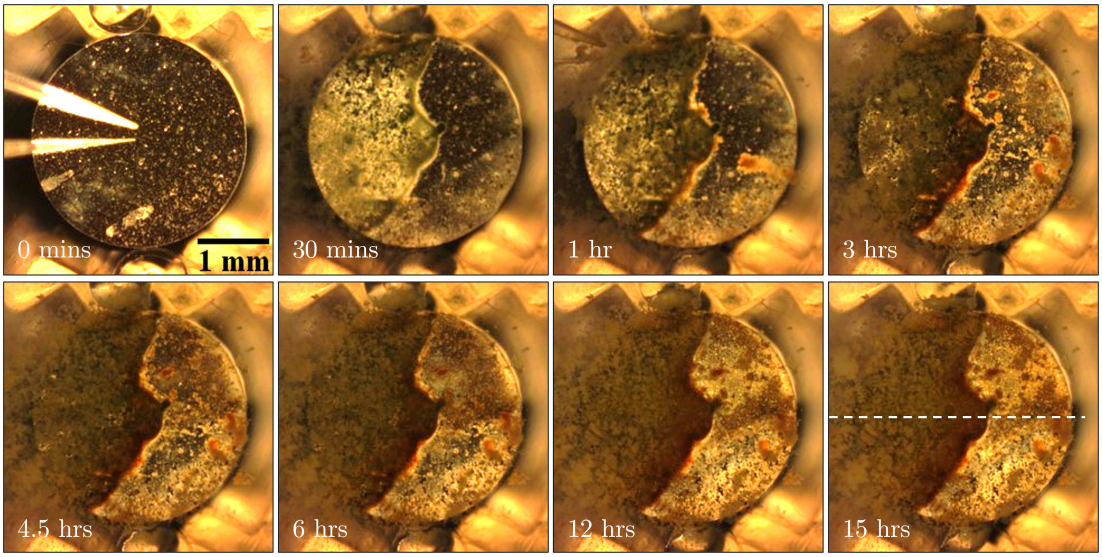

Figure 4.21: Optical micrographs showing the surface of FeMnAg immersed in HBSS at different time intervals. The white dashed line indicates the path taken by the probes for the line scans shown in Figure 4.22.

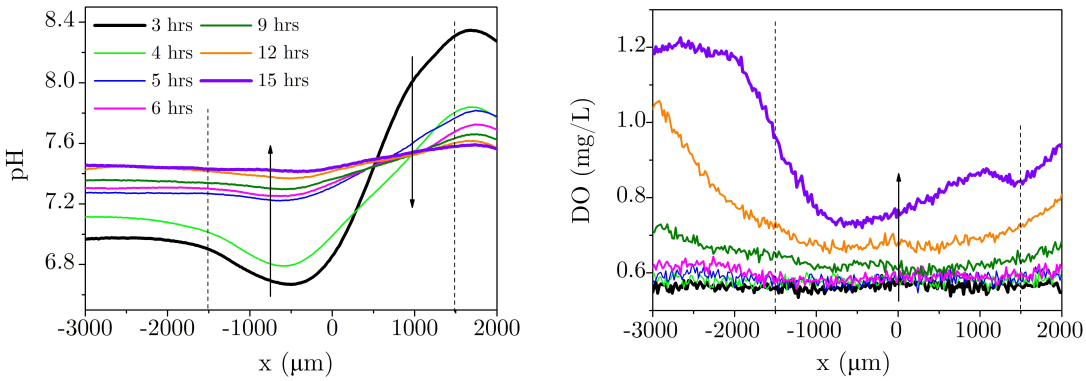

Figure 4.22: Line scans showing (a) pH and (b) DO evolution with time over the surface of FeMnAg immersed in HBSS. The lines correspond to the path indicated in Figure 4.21. Dashed lines indicate sample placement.

HBSS. The consequent maps showed that the pH had stabilised at around 7.3 by the 12-h mark. Completely opposite to the outcomes of the test in HBSS, the DO concentration continued to diminish following a strong initial drop, eventually reaching the lowest concentration of 0.45 mg L^{-1} in the 24 h scan.

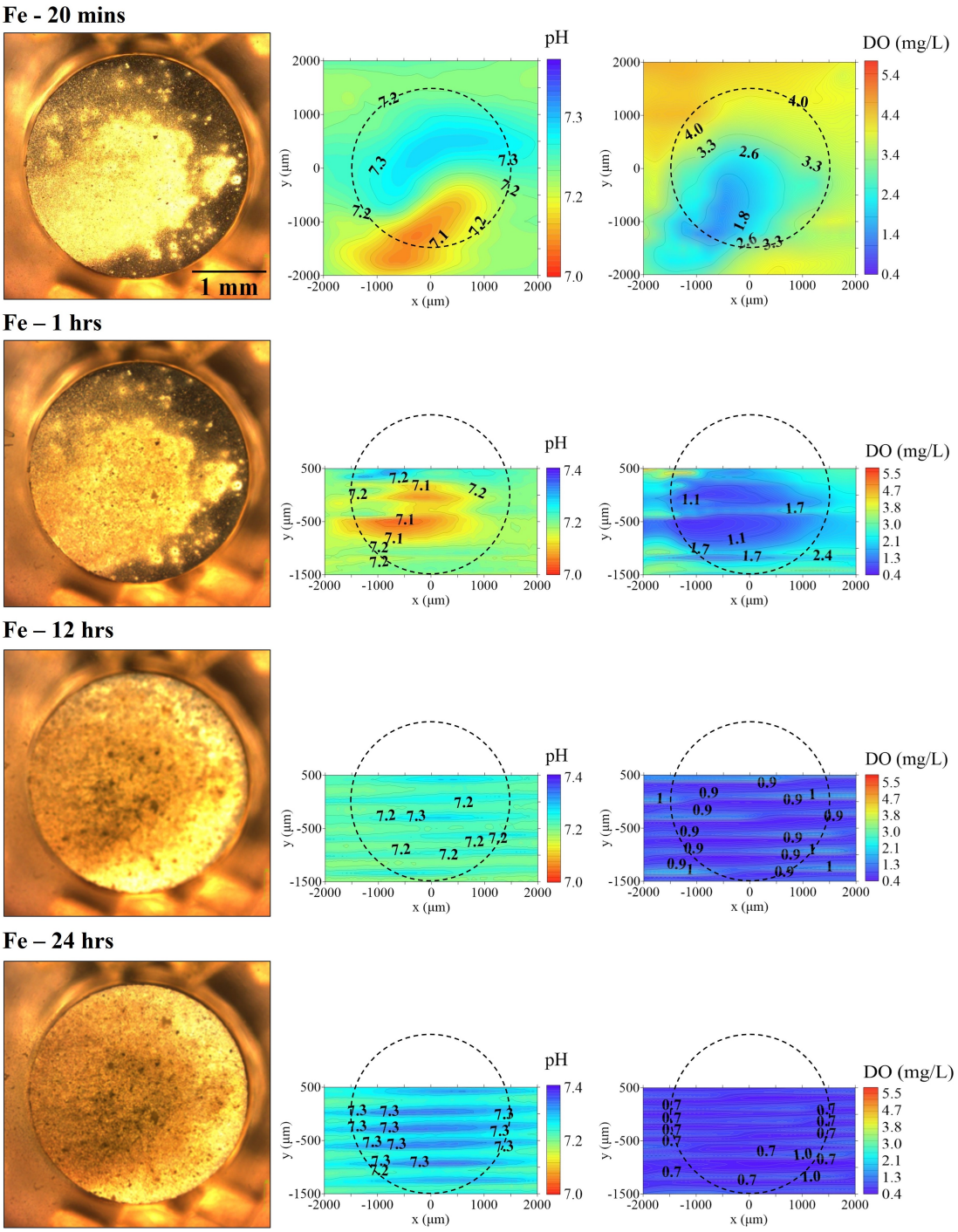

Figure 4.23: Optical micrographs of Fe surfaces immersed in HBSS+Ca after mapping carried out at 20 min, 1 h, 12 h and 24 h, with corresponding pH and DO maps.

Once again, the results for corrosion of FeMn in HBSS+Ca in Figure 4.24 show a rather uniform evolution both in the pH and DO measurements as well as in the changing events recorded in the micrographs. As was observed in HBSS, the pH was quite stable between 7.16 and 7.30 throughout the 24 h test. However, as seen with Fe in HBSS+Ca, the DO consumption was not similarly affected and the O_2 concentration dropped to a minimum of 1.90 mg L^{-1} by the 24 h mark. It is interesting to note that the initial values of DO were twice as high in HBSS+Ca at 4.15 mg L^{-1} compared to those recorded in HBSS at around 2.04 mg L^{-1}.

Results for FeMnAg in Figures 4.25 and 4.26 indicated that although the initial reaction generated significant localised acidification as in HBSS, the wide pH range measured by the initially strong microgalvanic reaction in HBSS was somewhat diminished in the presence of Ca^{2+} ions, dropping from 6.49-8.10 to 7.10-7.80 in HBSS+Ca, as measured after 20 min. The initial DO measurements also implied that the cathodic reaction was possibly inhibited as the range measured in the first map was 4.90-5.65 mg L^{-1}, contrasting with the 0.50-1.40 mg L^{-1} range measured in HBSS. Interestingly, with FeMnAg in HBSS+Ca, the evolution of localised pH variation in the generated maps, matched perfectly the changes observed in the optical micrographs. Over the first 6 h, barely any changes took place in the DO maps, however, shifting anodic sites corresponded to growing or emerging dark regions on the micrographs. By the 12-h mark, darkened corrosion products situated towards the lower left side of the sample on the 6 h micrograph, had grown considerably, as did the DO consumption in the corresponding location on the DO map. In the 6-h gap between the two maps, the DO consumption had in fact doubled, dropping from approximately 5.00 mg L^{-1} to 2.50 mg L^{-1}. Following this shift, the DO consumption continued to decrease consistently towards 0.40 mg L^{-1} while corrosion products further accumulated in the area. Notably, despite the consistent DO consumption at this stage, the pH levels stabilised and did not exceed 7.3, implying that any OH^- ions being generated in the oxygen reduction reaction were being immediately consumed in the formation of precipitates/corrosion products.

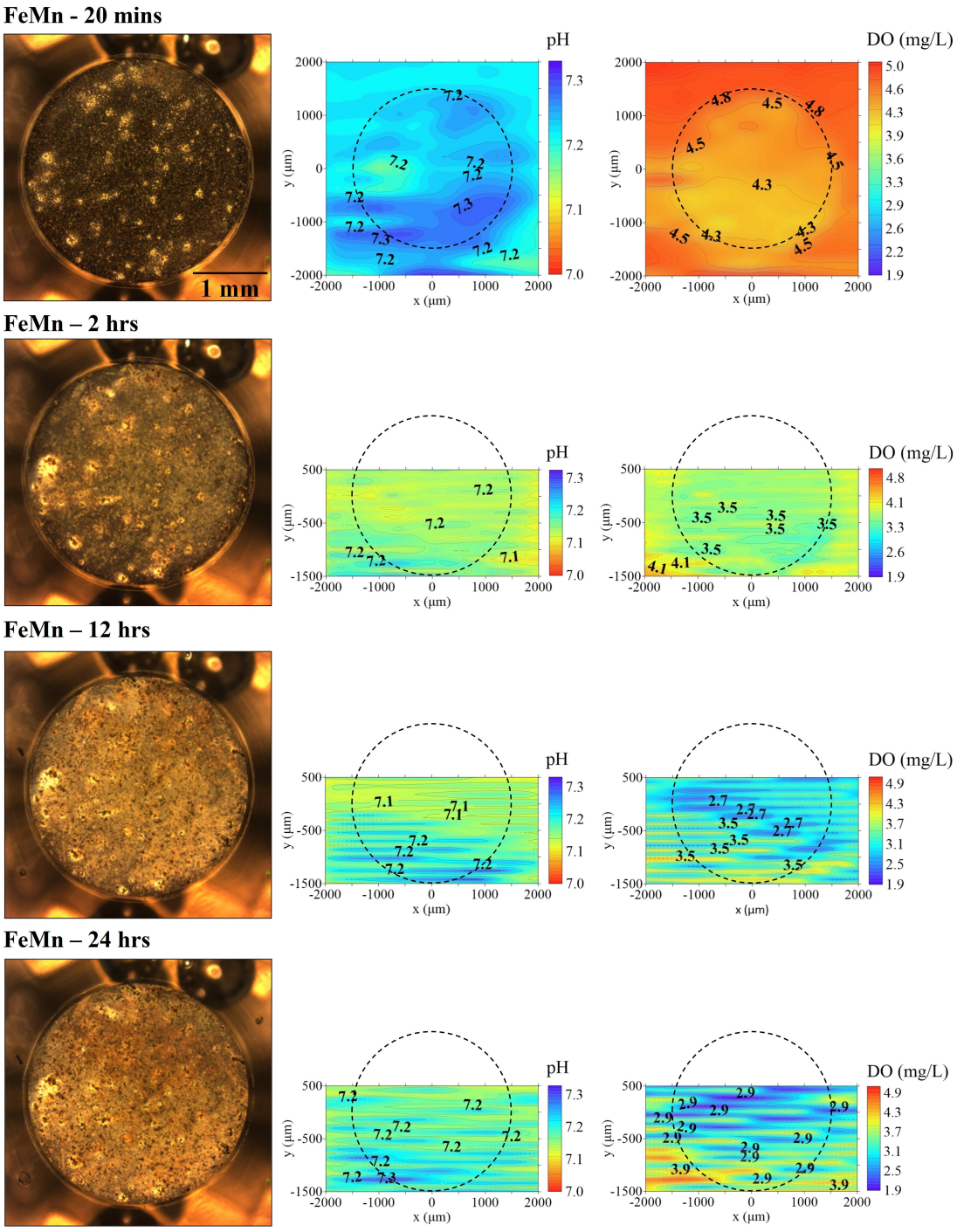

Figure 4.24: Optical micrographs of FeMn surfaces immersed in HBSS+Ca after mapping carried out at 20 min, 2 h, 12 h and 24 h, with corresponding pH and DO maps.

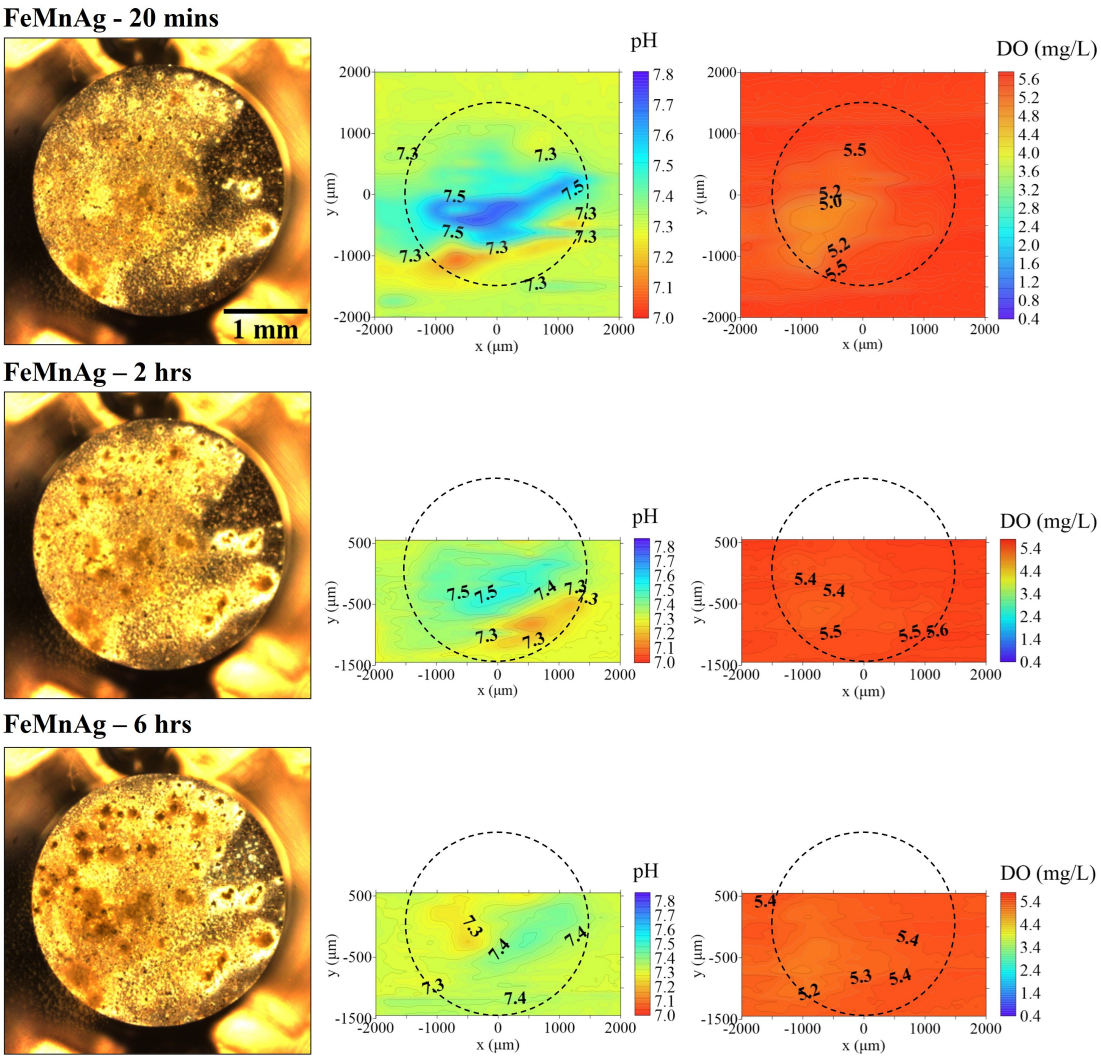

Figure 4.25: Optical micrographs of FeMnAg surfaces immersed in HBSS+Ca after mapping carried out at 20 min, 2 h and 6 h, with corresponding pH and DO maps. Test results continued in Figure 4.26.

Plots summarising the range of pH and DO measured over Fe, FeMn and FeMnAg in HBSS and HBSS+Ca over the course of the localised tests, are shown in Figure 4.27 (a) and (b), respectively.

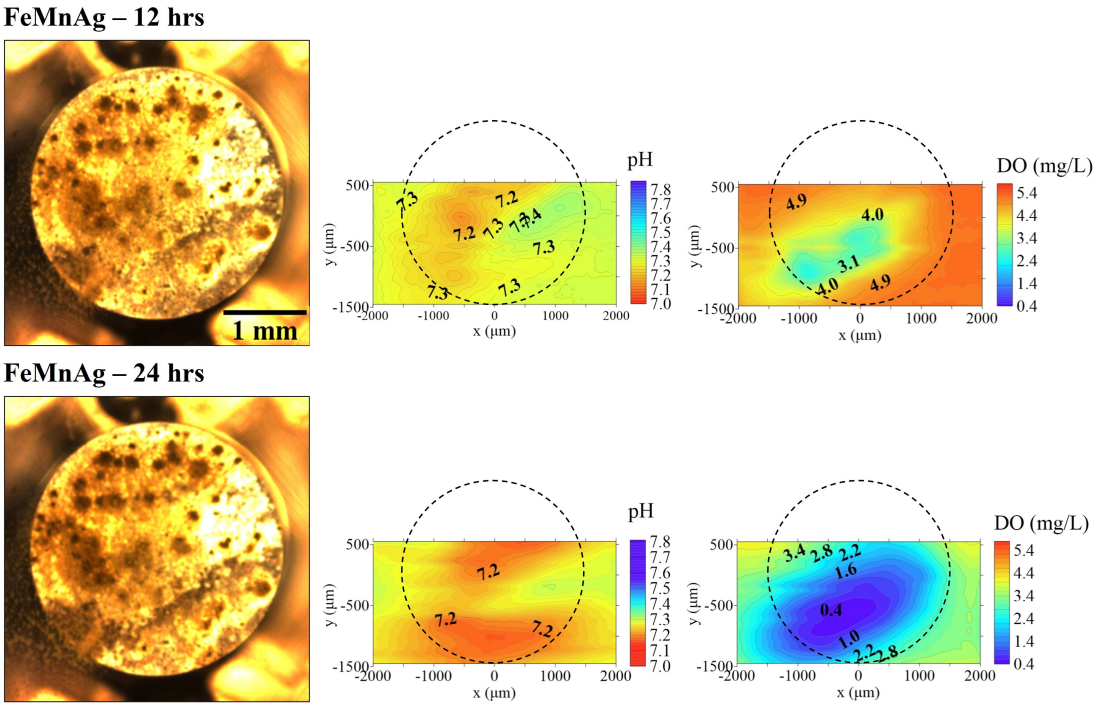

Figure 4.26: Optical micrographs of FeMnAg surfaces immersed in HBSS+Ca after mapping carried out at 12 h and 24 h, with corresponding pH and DO maps.

4.2.1.5 Discussion

The results presented in this testing phase explored the role of two important contributors to an established corroding system - the electrolyte, in particular, the role of Ca^{2+} ions, and the Fe alloy composition.

Prior to the 24 h tests, PDP tests were used to acquire an indicator as to the materials' performance in both HBSS and HBSS+Ca. The results must be analysed while keeping in mind that the outcomes cannot be simply projected onto either EIS or localised measurement results, both of which are carried out at the free corroding potential, unlike PDP. The results confirmed the general agreement in literature that Fe corrodes slower than FeMn alloys [107, 108, 111, 134, 137]. It also seemed to indicate that lower current densities were achieved in HBSS+Ca compared to HBSS.

As noted in Section 4.2.1.2, the i_{corr} values for Mn-containing alloys exhibited a large spread with significant overlap between FeMn and FeMnAg in HBSS. The variation itself could be due to several aspects that might cause micro-galvanic

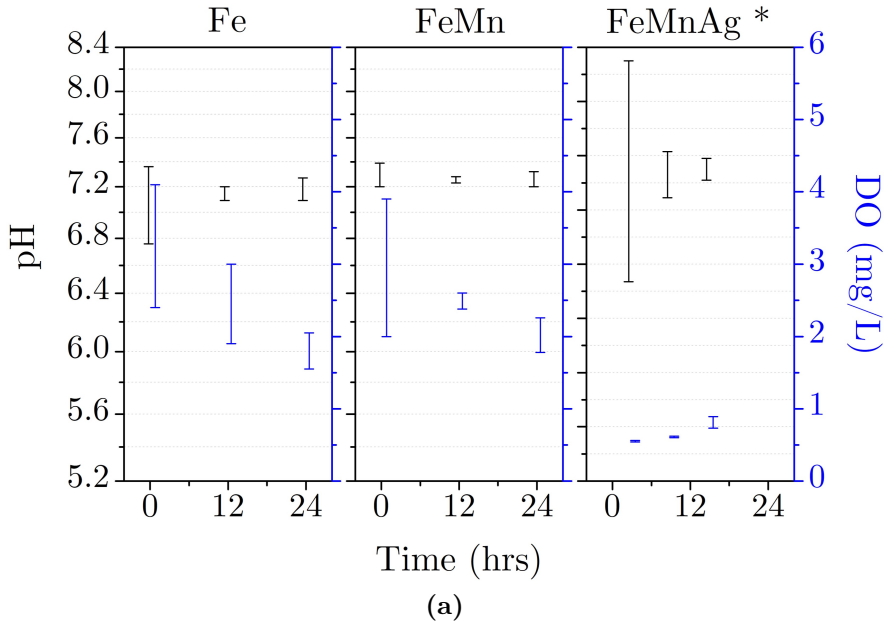

(a)

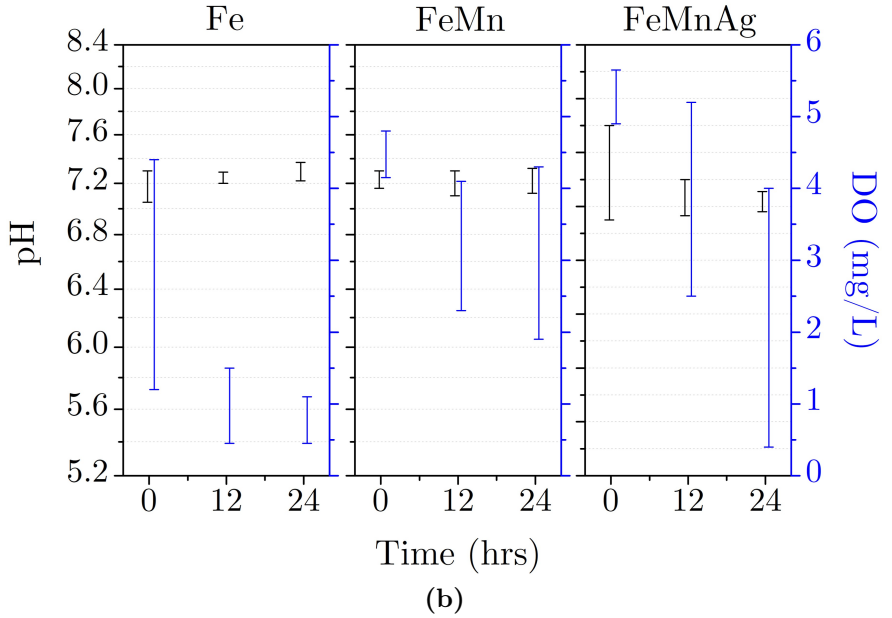

(b)

Figure 4.27: Summarised ranges of pH and DO measured over corroding Fe, FeMn and FeMnAg in (a) HBSS and (b) HBSS+Ca over 24 h. Both pH and DO measurements were taken simultaneously, however bars were offset to facilitate visual interpretation. *For FeMnAg immersed in HBSS+Ca, the range is expressed over 15 h as represented in the line scans in Figure 4.22.

acceleration. Although some compositional inhomogeneity was present in the austenitic matrix, as indicated in the wt.% values for Mn in Table 4.2, the more likely cause could be the MnO-phase [106, 110, 117], the varying amount and distribution of which is made difficult to measure by its presence in the samples' pores, as shown in Figure 4.5. Hermawan *et al.* [105] were the only group who commented on the potential cathodic role of MnO inclusions in powder processed Mn-steels, on the degradation of the austenitic matrix, however did not provide any experimental evidence to support their assumption. Should MnO really have a significant impact on corrosion progress, its impact would apply for both FeMn and FeMnAg. However, in Ag-containing alloys, the Ag-rich phase was included by design to serve as a microgalvanic accelerator, based on indicative results in literature [54, 111, 132, 134]. In HBSS+Ca, the added advantage of a homogeneous distribution of Ag, was evident in the increased i_{corr} values.

However, the inclusion of Ag was not similarly effective in HBSS wherein the highest i_{corr} values were achieved by FeMn. The reason most likely lies within the limitations of the PDP test itself. As noted in Chapter 2.1, Tafel extrapolation only applies for activation controlled reactions wherein both the metal ions and the necessary species for the cathodic reaction, in this case DO, are readily available at the metal surface. Localised measurements discussed in detail in the following section clearly show that the corrosion of FeMnAg in HBSS becomes concentration controlled during the 1 h it takes to establish the OCP prior to the actual PDP test, explaining the rather unexpected PDP result.

4.2.1.5.1 Corrosion of Fe alloys in HBSS (without Ca^{2+})

Looking at the results of the initial localised pH and DO measurements in Figure 4.17, the first reactions over corroding Fe in HBSS, did not cause any marked spikes in the measurements. The DO was slowly consumed as the pH gradually settled around the typical pH for the electrolyte at 7.44. The map showing the pH distribution after 20 min from immersion, in Figure 4.18, shows a slightly different scenario where locally distinct regions were evident despite uniform consumption of DO. Slightly localised acidified regions could be the result of the hydrolysis

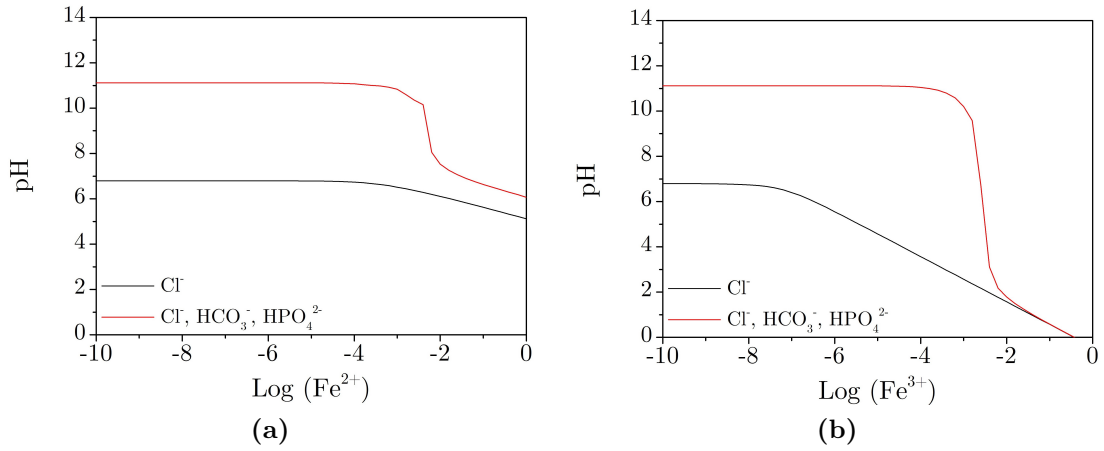

Figure 4.28: Change in pH caused by varying concentrations of (a) Fe^{2+} and (b) Fe^{3+} in either 143.26 mM Cl^- or 143.26 mM Cl^- supplemented with 0.78 mM HPO_4^{2-} and 4.17 mM HCO_3^-. Simulations carried out by Hydra-Medusa [241].

reactions 4.2 and 4.3 [47].

$$Fe^{2+} + 2H_2O \rightarrow Fe(OH)_2 + 2H^+ \tag{4.2}$$

$$Fe^{3+} + 3H_2O \rightarrow Fe(OH)_3 + 3H^+ \tag{4.3}$$

One should note, that this acidification was still somewhat limited in HBSS as a complex saline solution, compared to what would happen in a simple saline solution. Simulations presented in Figure 4.28 show how the presence of HPO_4^{2-} and HCO_3^- limit acidification with varying log concentration of ferrous and ferric ions, compared to what would happen in Cl^- only. Considering the consequent pH and DO maps for Fe in HBSS in Figure 4.18, the system was quick to stabilise with maps showing rather uniform pH and DO levels. While the pH remained stable, DO levels continued to drop, indicating that whichever corrosion products accumulated on the surface did not prevent O_2 from being consumed, either for the cathodic reaction or for the formation of further products.

With FeMn, the distinct increased DO consumption over the sample in the first few minutes coupled with the pH increase observed in Figure 4.17c, is indicative of an initially accelerated reaction. However the maps presented in Figure 4.19 show a very similar progression to Fe in the first 24 h. In fact, the pH and DO

summary plot in Figure 4.27a clearly illustrates the highly overlapping conditions over the two metals. Any compositional or structural differences in the corrosion products formed, as indicated in the SEM-EDS analysis in Section 4.2.1.3.3, do not seem to affect the progress of corrosion over the two metals in HBSS. One must remember, that despite the impressive resolution of the localised measurement equipment, it is still restricted to measure the conditions 50 µm above the surface and therefore any events taking place within the pores, possibly due to cathodic acceleration by MnO as hypothesised in this discussion, might not be registered in the scans.

Contrasting with the behaviour of both Fe and FeMn, FeMnAg continued to consume DO relentlessly in the first 12 min of the local measurements test, leaving only 0.53 $mg\,L^{-1}$ of DO. The DO was clearly contributing towards the reduction reaction which increased the pH to 10.5. Due to this, even in the absence of a physical corrosion product "barrier" for current exchange in the first few minutes, the accelerated microgalvanic reaction caused a concentration barrier limited by the diffusion rate of O_2 towards the surface. Figure 4.26 shows the result of the microgalvanic reaction. Reddish-brown corrosion products were observed rapidly accumulating on the left side of the FeMnAg surface which was clearly serving as the principal anodic region judging by the pH scans in Figure 4.22. The accumulated product served as an additional physical barrier, slowing down the reaction and leading to pH stabilisation and accumulation of DO on the surface, as evidenced in the line scans. The environment stabilisation could also have been a result of the Ag-rich phase on the exposed right side of the metal surface slowly being covered by forming corrosion products, limiting its cathodic influence. This was also the reason provided by Wiesener *et al.* [134] for dwindling corrosion rates when discussing the long-term ineffectiveness of the microgalvanic reaction on the degradation of wrought FeMnAg alloys.

EIS testing did not indicate that there was any secondary corrosion product barrier other than the typical metal-electrolyte interface, for any of the metals in HBSS. Therefore, any changes in the low-frequency impedance plotted in Figure 4.10a are due either to diffusion related phenomena taking place around the sample pores or due to the growth of a corrosion layer with properties similar to those of the natural oxide barrier formed over the Fe-based alloys. In fact, similar

EIS spectra were obtained by Hu *et al.* [249] when testing carbon steel in a 3% NaCl solution, with the increase in impedance attributed to the formation of α- and γ-FeOOH and Fe_3O_4.

In order to study how the sample and electrolyte constituents could affect the corrosion products formed, the Hydra thermodynamic stability constant database was used to plot equilibrium diagrams of specific ion concentrations against the pH, using the Medusa [241] software. The full ion concentrations used to prepare the Medusa diagrams in this discussion are provided in Table 4.4. The concentration of Fe^{2+} and Mn^{2+} were arbitrarily set at 0.65 mM and 0.35 mM respectively, assuming proportional release of both ions according to their concentration in the bulk material. Fe^{3+} concentration was also set at 0.65 mM to account for oxidation of Fe^{2+} ions. In general, the amount of metal ions detected in corrosion extracts in literature tend to be significantly lower [79, 123, 224, 232, 250], however, measurements using ICP-OES or atomic absorption spectroscopy (AAS) techniques measure the bulk concentration after a certain period of time, and not the higher concentrations present close to the surface participating in progressing corrosion reactions and product precipitation. In fact, the products listed among the potentials in the simulations carried out in this work, have been reported among detected products in multiple publications [109, 117, 162]. Having said this, the Medusa software has its limitations. It uses the stability constants of the various complexes and compounds at 25°C, not at 37°C, and it does not take into account the DO concentration in the electrolyte. These limitations were taken into consideration when interpreting and using the results as an aid during the analyses.

Based on the simulations for Fe and FeMn immersed in HBSS in Figure 4.29a, the corrosion products that could form at physiological pH include $Fe_3(PO_4)_2.8H_2O$, $MnHPO_4$, $FeCO_3$ and $Fe(OH)_{2.7}Cl_{0.3}$. Judging by the EDS results corresponding to the micrographs in Figure 4.12, the "flaky" layer could be an Fe-phosphate similar to the simulated $Fe_3(PO_4)_2.8H_2O$ product in the Medusa diagram. With the addition of Mn^{2+} ions to the simulation in Figure 4.29b, the stability of $Fe_3(PO_4)_2.8H_2O$ is reduced slightly and $MnHPO_4$ is introduced. Based on the absence of the "flaky" phosphate layer on the surface

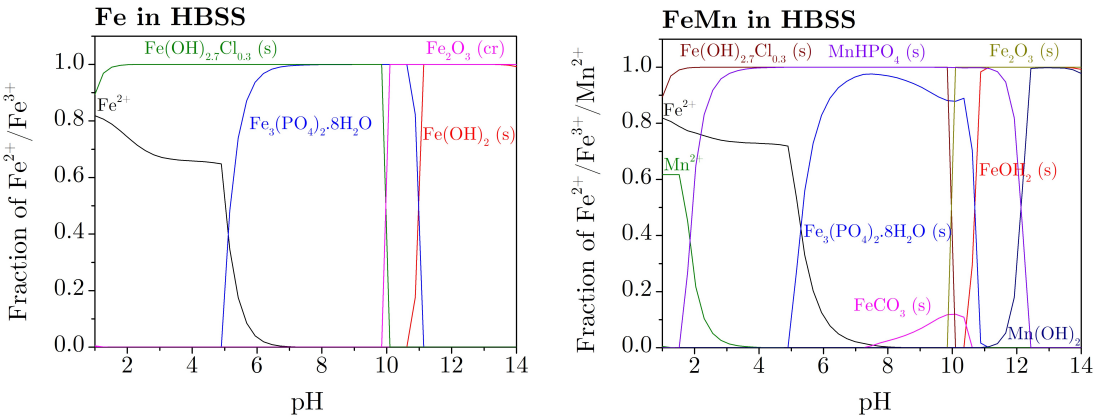

Figure 4.29: Fraction of Fe^{2+}, Fe^{3+} and Mn^{2+} with other species present in the electrolyte based on the constituents of HBSS. The simulations were carried out for products forming on corroding (a) Fe and (b) FeMn by Hydra-Medusa. The complete formulations used in the simulations are given in Table 4.4.

Table 4.4: Electrolyte formulations used for Medusa simulations presented in Figures 4.29 and 4.31.

Constituent (mM)	Fe in HBSS	FeMn in HBSS	Fe in HBSS+Ca	FeMn in HBSS+Ca
Fe^{2+}	0.65	0.65	0.65	0.65
Fe^{3+}	0.65	0.65	0.65	0.65
Mn^{2+}	-	0.35	-	0.35
Ca^{2+}	-	-	1.26	1.26
Mg^{2+}	-	-	0.90	0.90
K^{+}	5.77	5.77	5.77	5.77
Na^{+}	142.77	142.77	142.77	142.77
HPO_4^{2-}	0.78	0.78	0.78	0.78
HCO_3^{-}	4.17	4.17	4.17	4.17
Cl^{-}	143.26	143.26	146.77	146.77
SO_4^{2-}	-	-	0.41	0.41

of FeMn tested in HBSS in Figure 4.14 (a) and (b), Mn-phosphates like $MnHPO_4$ seem to take precedence over the formation of Fe-phosphates.

What software like Medusa allows one to do, is evaluate how localised scenarios could alter the chemistry of the formed products or allow for certain outcomes reported in literature to take place. By changing the Mn^{2+} ion concentrations in the simulation to 0.65 mM and 1.00 mM to simulate increased localised release of Mn over Fe ions, the plots in Figure 4.30 were generated. The plots show how with equal release of Fe^{2+} and Mn^{2+}, the stability of $Fe_3(PO_4)_2.8H_2O$ is further reduced, whereas further increase of Mn^{2+} ions also stabilise $MnCO_3$ formation despite the presence of relatively small concentrations of HCO_3^-. In this work Mn-phosphates formed in preference to carbonates based on the EDS results and the absence of the cubic-shaped products observed by Mouzou *et al.* [162] and Gambaro *et al.* [118] in Figure 4.14 (a) and (b). Moreover, considering the Bode plots in Figure 4.8 (a), (c) and (e), neither of the formed phosphates offer any additional "barrier" characteristics.

Going back to the low frequency impedance plot in Figure 4.10a, the starting impedance for Fe is significantly higher than that for FeMn and FeMnAg, once again pointing towards the superior corrosion resistance offered by the natural oxide formed on pure Fe. Whereas the low frequency impedance of Fe does not change drastically over the 24 h period, the impedance of FeMn and FeMnAg in-

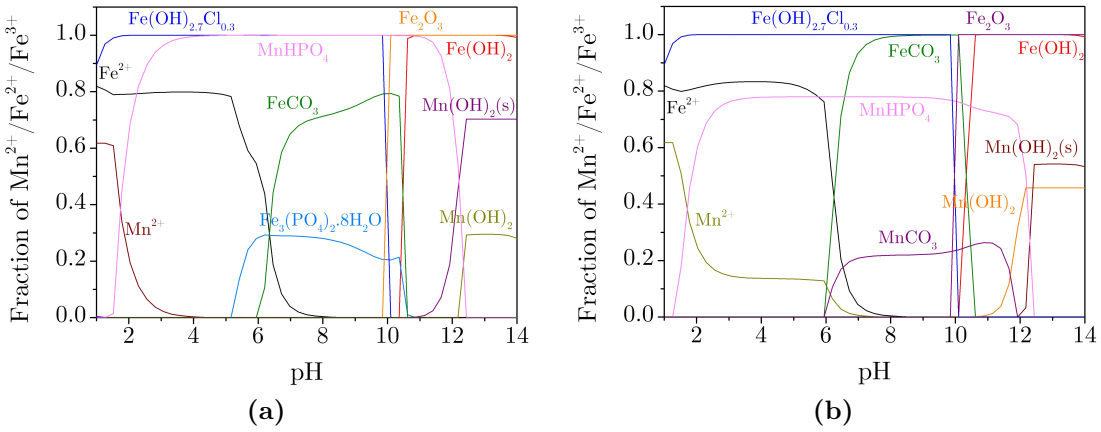

Figure 4.30: Medusa simulations for alternate scenarios of FeMn immersed in HBSS+Ca with (a) 0.65 mM Mn^{2+} and (b) 1.00 mM Mn^{2+}.

creases with time likely indicating the formation of thin uniform oxide/hydroxide layers as observed by Hu *et al.* [249]. The increased O concentrations presented in Table 4.3 as well as the small cracks observed on the seemingly non-corroded regions of the surfaces in Figures 4.14 (a) and (b) and 4.15, support this hypothesis. One must note that the lack of thermodynamic stability of either Fe or Mn-oxides indicated in any of the Medusa diagrams presented in this work, is due to the software's inability to take the DO levels into consideration when executing equilibrium calculations. In fact, the modified Pourbaix diagram in Figure 2.14a clearly shows the potential for $Fe(OH)_2$ and $Fe(OH)_3$ formation at a wide range of pH values, including around 7.4. The corrosion products formed were either not crystalline or present in minute amounts as none of the surfaces yielded any detectable peaks other than that of the substrate when analysed using XRD.

Whereas the various testing methods used in this phase provided a harmonious set of results and behaviours for the various metals, one rather prominent distinction is the variation in the corrosion products formed on FeMnAg in EIS and the local measurements. While a considerable amount of reddish-brown (possibly $Fe(OH)_3$) rust formed in the localised measurements, only thin layers of oxides and clustered phosphates were observed following the EIS test. It is likely that microgalvanic corrosion during localised measurements was exacerbated by the flow of electrolyte, as 25% of the 4 mL testing volume was consistently being refreshed causing a somewhat "dynamic" testing condition, enhancing dissolution as discussed in Section 2.1.4.3. During EIS, while the volume of electrolyte was sufficient to have refreshment around the corroding surface, the flow of fresh electrolyte was still limited to ionic diffusion.

4.2.1.5.2 Corrosion of Fe alloys in HBSS+Ca

When modifying the Medusa simulations to match the formulation of HBSS+Ca, the diagrams revealed the potential of $Ca_{10}(PO_4)_6(OH)_2$, $CaCO_3$ and $CaSO_4$ precipitation when testing Fe and FeMn alike, as shown in Figure 4.31. The results for FeMn in HBSS+Ca were split in two figures (b-c) to avoid overcrowding the plot. The formation of hydroxyapatite-like (HA-like) compounds like $Ca_{10}(PO_4)_6(OH)_2$, has often been mentioned in literature related to Fe-based

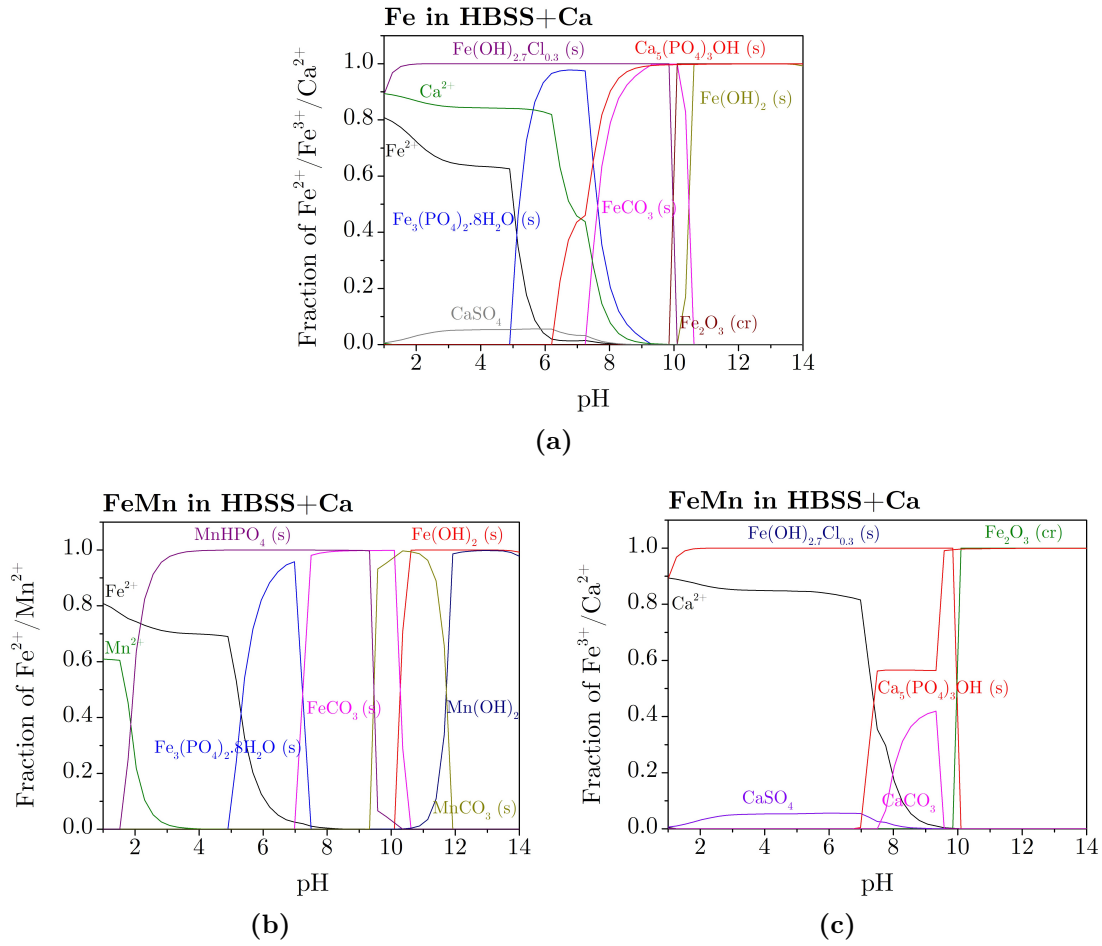

Figure 4.31: Fraction of Fe^{2+}, Fe^{3+}, Mn^{2+} and Ca^{2+} with other species present in the electrolyte based on the constituents of HBSS+Ca. The simulations were carried out for products forming on corroding (a) Fe and (b-c) FeMn by Hydra-Medusa. The complete formulations used in the simulations are given in Table 4.4.

biodegradable alloy research [46, 113, 115, 166]. In each case, the authors comment on the potential benefits the presence of such compounds could have on osseointegration, but few have discussed the correlation between precipitation of Ca-rich products and the electrolyte formulation. Since such products are generally observed in post-testing characteriation, it is often assumed that these precipitate later in the corrosion process as in the corrosion mechanism description published by Zheng *et al.* [10] and outlined in Section 2.1.1. In this work, this was proved to be somewhat of a misrepresentation.

Whereas the precipitation of phosphates like $Fe_3(PO_4)_2.8H_2O$ require only the availability of metal cations as in reaction 4.4, $Ca_{10}(PO_4)_6(OH)_2$ precipitation also requires hydroxyl ions generated in the cathodic oxygen reduction reaction, as in reaction 4.5.

$$3Fe^{2+} + 2{PO_4}^{3-} + 8H_2O \rightarrow Fe_3(PO_4)_2.8H_2O \tag{4.4}$$

$$6{PO_4}^{3-} + 10Ca^{2+} + 2OH^- \rightarrow Ca_{10}(PO_4)_6(OH)_2 \tag{4.5}$$

Therefore, with unhindered cathodic reactions, the HA-like product can precipitate anywhere in the medium and on the corroding surface. In turn, the consumption of generated OH^- restricts the extent of alkalinisation. In the initial pH and DO monitoring of FeMnAg in HBSS+Ca in Figure 4.17f for instance, the immediate consumption of DO points towards a similar microgalvanic reaction as observed in HBSS, however unlike in HBSS the pH was buffered around 7 and remained close to the physiological levels throughout the test. FeMn and FeMnAg consumed lower levels of DO compared to the HBSS tests, indicating that the partially protective Ca-rich layer precipitated in the first minutes was sufficient to limit the cathodic reaction rate. This also explains the lower i_{corr} measured for the metals in HBSS+Ca in the PDP tests.

The protectiveness of this HA-like layer was also represented by the additional mid-frequency time constant present in the EIS Bode plots. Although the earliest Bode plots in Figure 4.8 represent the system after 30 min from immersion, a previous EIS test conducted after 10 min and presented in Figure 4.32, also included the additional time constant for FeMn and FeMnAg. This particular Bode plot was not presented with the rest of the results due to poor Kramers-Kronig[1] fit at lower frequencies, indicating poor spectrum validity in this range.

The local pH and DO levels over the FeMn sample in HBSS+Ca followed a similar, albeit less pronounced, behavioural pattern to FeMnAg. Completely opposite, was the behaviour of Fe in the initial measurements presented in Figure 4.17b. The slow corrosion rate exhibited by the material in PDP results seems to have resulted in a slow cathodic reaction rate judging by the extended DO

[1]Fitting analyses carried out using EChem Analyst software that determines whether the EIS test is valid. Since the system is still approaching equilibrium within the first few minutes from test initiation, the K-K analyses tends to be poor at this point.

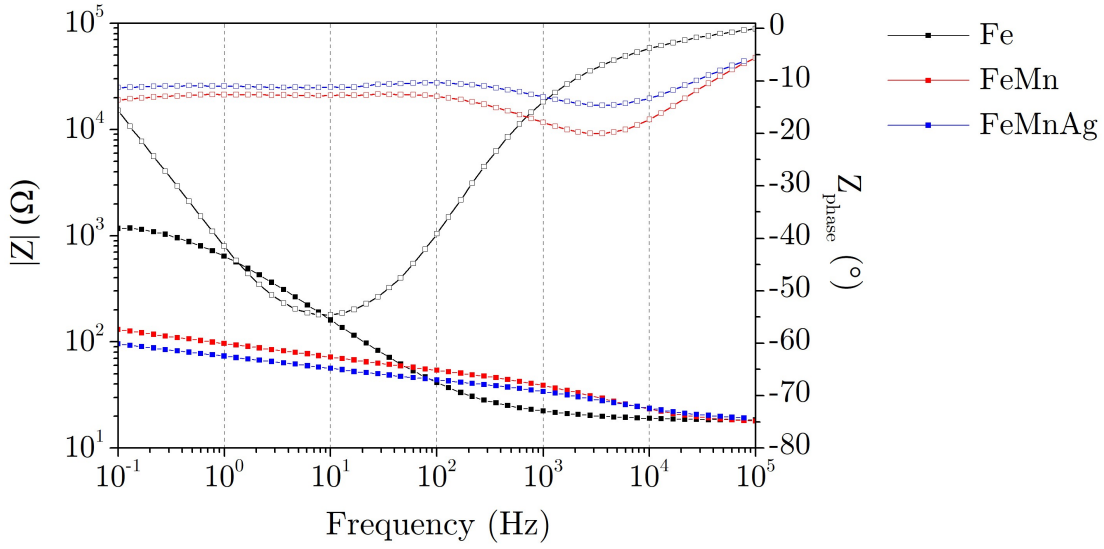

Figure 4.32: Bode plot for Fe, FeMn and FeMnAg after 10 min of OCP monitoring.

consumption period. This, in turn, prevented the rapid formation of the Ca-rich layer. This was also evident in the corresponding Bode plot in Figure 4.8b where the mid-frequency phase-shift for Fe remained in the vicinity of 0° in the first hours, as opposed to that for FeMn and FeMnAg.

While visual analysis of the Bode plots themselves is a good indicator of what is happening at the surface, equivalent circuit modelling provides a clearer picture as to the evolution of the protective nature of the corrosion product layer through the modelled R_{layer} and C_{layer} values. The corrosion product resistance R_{layer} for Fe, remains well below the corresponding measures for products growing on the Mn-containing alloys in Figure 4.10b. This leads to the rather consistent uniform consumption of DO measured over the next 24 h in Figure 4.23. Whereas the resistances for the products forming on all the alloys increased with time, the impedance for FeMnAg, exhibited the steepest increase in the first few hours, followed by FeMn and Fe. This corresponds perfectly with the local measurements as samples exhibiting the highest R_{layer} values consumed the least DO over the same period of time. The change in C_{layer} also complements the resistance modelling. Although the protective contribution of the degradation products is evident from the modelling results, the SEM images presented in Figure 4.14c

and 4.16 do not show a continuous Ca-rich layer on the tested surfaces. It is likely, based on the outcomes of the EDS analysis in the surface porosity, that some of the product was dislodged during the cleaning procedure leaving behind more adherent clusters.

Despite the protectiveness of the HA-like layer, 24 h mapping of the DO levels in Figures 4.23-4.26 as well as the summarised results in Figure 4.27b both show the continued increase in DO consumption with time. This is the reason why the HA-like layer, also observed on Mg and Mg-alloys by Mei *et al.* [159] has been labelled as *partially* protective, as it does not completely stifle the cathodic reaction and further corrosion product formation. This is most obvious in the summarised results in Figure 4.27. The DO levels in (b) are clearly higher for each metal at the start of the test when compared to (a) however, the measured values continuously drop over the 24 h.

An interesting development was observed in mid-frequency EIS results for FeMnAg in HBSS+Ca. Following the rapid formation of the HA-layer, both the impedance as well as the negative phase shift dropped rapidly after around 9 h from initial contact with the electrolyte. The fitting results in Figure 4.10 (b) and (c) also show the drastic decrease and increase in R_{layer} and C_{layer} respectively, both signifying a decrease in associated impedance. The DO maps for FeMnAg in Figure 4.25 and 4.26 seem to indicate that a similar event took place during the localised measurements as the DO levels dropped from 5.06-5.50 $mg\,L^{-1}$ at 6 h to 2.50-5.20 $mg\,L^{-1}$ at 12 h and further down to 0.40-4.00 $mg\,L^{-1}$ by the 24-h mark. All imply a change in the structure, uniformity or density of the HA-like layer, the reason for which is not clear, although some have remarked on the potential for corrosion product destabilisation when it reaches a certain thickness or when the surface is particularly porous [115, 153]. The sudden increase in DO consumption observed in Figure 4.26 also seemed to correspond to increased oxidation of existing corrosion products, likely from ferrous to ferric states. The shifting anodic locations and corresponding dark regions on the optical micrographs identified in previous scans presented in Figure 4.25, grew and spread considerably in the final 12 h of the test. These reactions could have contributed to the DO consumption

as indicated by reaction 4.6, and as suggested by Hermawan *et al.* [46].

$$4Fe(OH)_2 + O_2 + 2H_2O \rightarrow 4Fe(OH)_3 \text{ or } 2Fe_2O_3.6H_2O \tag{4.6}$$

The events described are generally indicative of pitting corrosion, often associated with microgalvanic corrosion mechanisms. In such a case, the pH would most likely be significantly lower within the affected pits/pores, however the measured pH in the localised setup would be somewhat buffered by the layers of corrosion products.

The behaviour exhibited by the FeMnAg in HBSS+Ca could suggest that while Ca^{2+} ions definitely have an influence on the corrosion rates and mechanisms of Fe-based alloys, particularly in the first few hours following initial contact, long-term "barriers" to corrosion as often reported *in vivo* [37, 114, 180, 190], are more likely a result of compact oxide/hydroxide formation. The gradual formation of protective oxides with similar electrical characteristics to the native Fe/O oxide present on Fe-based alloys, is evident in the gradual increase in the low-frequency impedance illustrated in Figure 4.10a. As observed in HBSS, the initial low frequency impedance for both FeMn and FeMnAg alloys was significantly lower than for Fe, however it quickly increased and attained similar impedance levels, shedding some doubt as to the long term advantages of alloying when targeting corrosion acceleration.

4.2.1.5.3 Conclusions

The principal conclusions from this phase are summarised hereunder:

i. The presence of Ca^{2+} ions in HBSS reduces the aggressiveness of the electrolyte. This was confirmed by PDP tests wherein the alloys generated lower current densities in HBSS+Ca when compared to HBSS, and in EIS tests wherein the R_{ct} values were consistently higher in HBSS+Ca;

ii. Powder-processed FeMn and FeMnAg exhibit a wide spread of corrosion current densities, possibly due to inaccurate measurements of testing area and/or the potentially cathodic influence of MnO inclusions;

iii. The addition of Ag has a strong microgalvanic effect in HBSS, particularly evident in localised measurements of pH and DO. In HBSS+Ca, the same effect was also evident and resulted in the maximum i_{corr} values measured using PDP. However, the immediate precipitation of HA-like products resulted in a rapid decline in the effectiveness of the cathodic Ag during the first 24 h;

iv. Metal-phosphates precipitated on all alloys in HBSS, did not offer any significant protective capacity;

v. The precipitation of HA-like products in HBSS+Ca, buffers the local pH over all corroding alloys to around the bulk electrolyte pH. Due to this, the range of pH measurements spanned a narrower range in Ca^{2+}-containing electrolytes;

vi. The protective capacity of the partially protective HA-like product over FeMnAg in HBSS+Ca was not consistent in the first 24 h from immersion, potentially due to instability of the growing product over a highly porous surface;

vii. DO levels continued to drop over the 24 h period despite the generally neutral pH levels for all alloys in both electrolytes. This implies that the protective hydroxides or phosphates formed are not completely impervious to O_2 diffusion and allow for corrosion to progress, albeit slowly. On the other hand, DO concentrations as low as 0.53 mg L^{-1} as measured in certain cases, might have serious implications on the physiological surroundings around implantation sites which need access to DO to function;

viii. The only alloy exhibiting any form of localised corrosion after 24 h in both electrolytes is FeMnAg, based on localised measurements. However, both the localised measurements as well as the measured low-frequency impedance for all tested alloys in HBSS+Ca, approach similar values within the initial 24 h testing period, leading one to question the benefits of alloying for accelerating the corrosion rate of Fe. Naturally, the function of adding Mn goes beyond that of corrosion acceleration and therefore FeMn in particular, remains an interesting material for further investigation.

4.2.2 Phase Two - Further corrosion analysis using EIS

The conclusions from the first testing phase included hypotheses on the potential influence of MnO inclusions commonly present in Mn-containing powder metallurgical alloys, including the samples used in this work, on corrosion behaviour. Phase Two was initialised with the intention of investigating these hypotheses using FeMn and FeMnAg.

4.2.2.1 Initial testing phase - Porous MnO-free FeMn

4.2.2.1.1 Eliminating Mn/O-inclusions

The original approach used to investigate the influence of MnO, was to compare EIS results of the original FeMn alloy (containing MnO) with the results obtained when testing a sample from which the MnO inclusions had been chemically removed using the method described in Section 3.2.3.1.1. This primarily included ultrasonication in 1 M HCl with 3.5 $\mathrm{g\,L^{-1}}$ of hexamethylenetetramine (HMTA) as corrosion inhibitor. The micrographs and corresponding EDS maps of a region-of-interest of a FeMnAg sample before and after being subjected to this procedure, are presented in Figure 4.33. The white arrows on the same figure point towards a specific inclusion which was shown to be successfully removed, as supported by the absence of Mn and O intensity in the corresponding location on the maps. XRD scans on the same sample before and after the procedure, presented in Figure 4.34, also indicate the complete absence of peaks corresponding to the oxide's presence.

4.2.2.1.2 EIS testing of porous samples

Bode plots for EIS tests carried out over 24 h using porous FeMn samples with and without MnO inclusions, are presented in Figure 4.35. The plots exhibit several very obvious distinct features. Whereas the Bode plot in Figure 4.35a is very similar to that presented in Figure 4.8d in Phase One, the Bode plot for the sample without MnO, featured impedances that were consistently an order of magnitude lower, and a very prominent relaxation feature at low frequencies at all time points. Moreover, the low frequency time constant associated with the

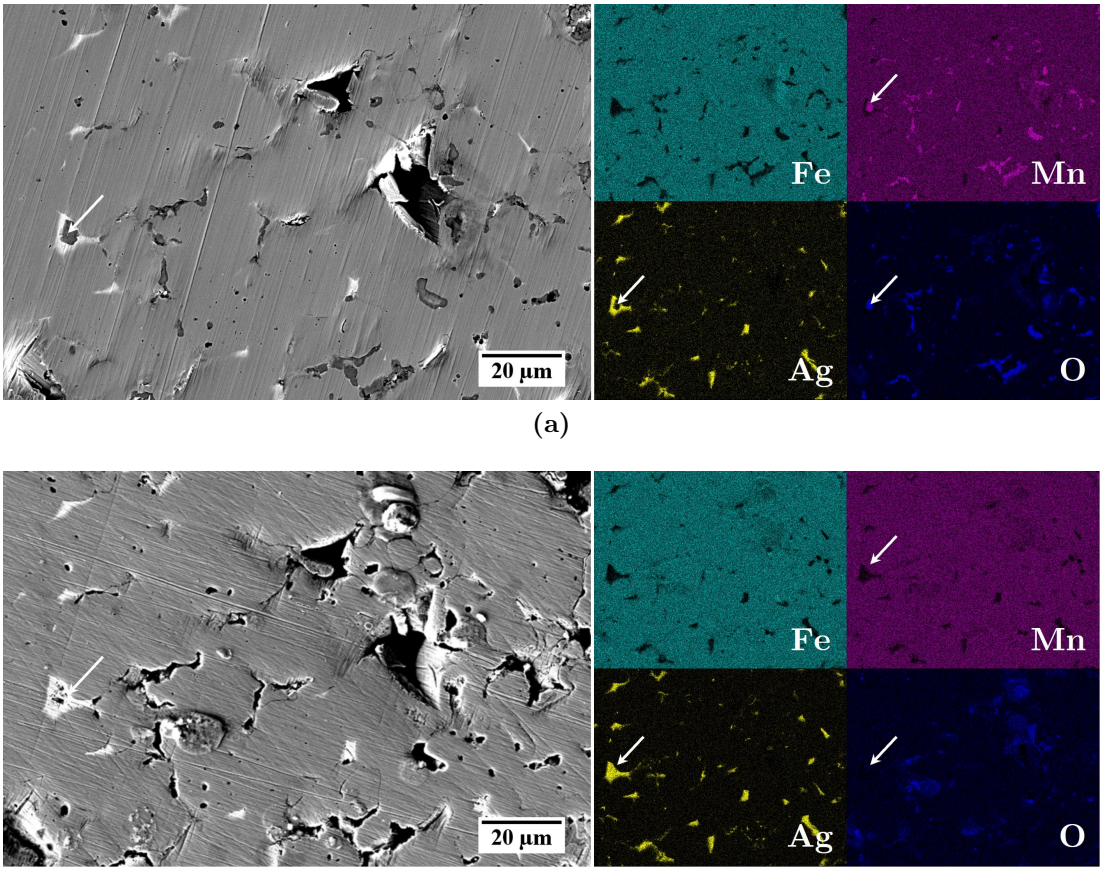

Figure 4.33: SEM images of FeMnAg (a) before and (b) after etching in a solution of 1 M HCl with 0.35 $g\,L^{-1}$ HMTA for 5 min. Corresponding EDS maps of Fe, Mn, Ag and O are presented next to the micrographs. White arrows point toward the location of a specific inclusion whose successful removal can be monitored in all the figures.

metal-electrolyte interface was almost indistinguishable when looking at Z_{phase} curves. It was very evident based on the listed observations, that the differences between the two Bode plots were clearly not exclusively due to the absence of MnO. In the previous discussion following the results from Phase One, the mentioned relaxation feature at low frequencies was said to be attributed to diffusional impedance through complex pore geometries. A question therefore arose related to the possibility of changes to the pore volume and/or surface roughness resulting from the etching procedure, being partly responsible for the notable

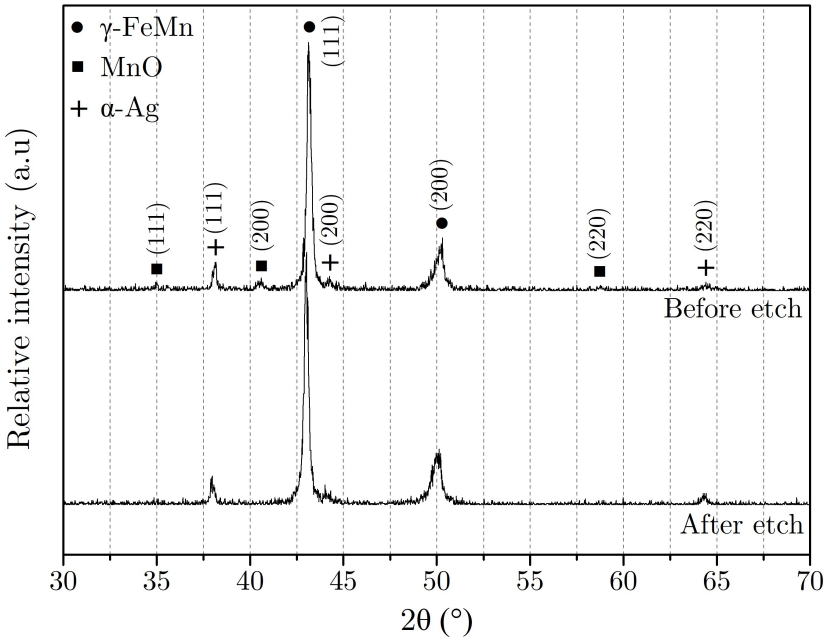

Figure 4.34: XRD analysis corresponding to the microstructures presented in Figure 4.33 for FeMnAg before and after etching in a 1 M HCl with 3.5 g L^{-1} HMTA solution.

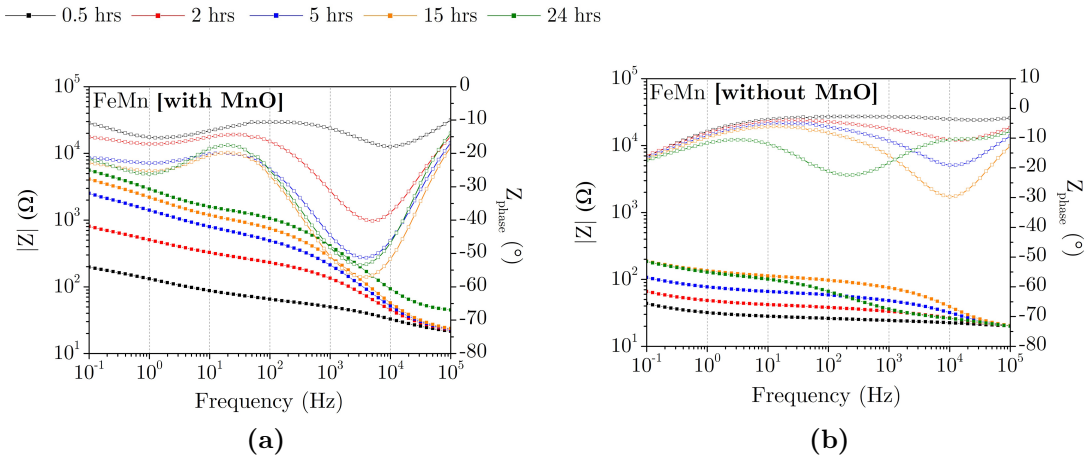

Figure 4.35: Bode plots for porous FeMn (a) with and (b) without MnO inclusions, tested in HBSS+Ca.

differences observed in electrochemical behaviour.

To simplify this investigation, the same tests were run on porous Fe i.e. the same samples used in Phase One, as well as wrought Fe samples supplied by

Armco (USA). In this way, the potential for MnO influence was eliminated by the absence of Mn as an alloying element, and the influence of the etchant on the metal could be more easily distinguished. The Bode plots corresponding to these tests, performed following 30 min of OCP monitoring, are presented as black curves in Figure 4.36. The surfaces used in this test were ground to a P2500 SiC paper finish, as with all previous EIS tests. Both porous and wrought Fe were shown to exhibit a single time constant at approximately 5 Hz and very similar low frequency impedances at 2284 Ω and 2305 Ω respectively. The slightly lower impedances measured for the porous samples at all frequencies could be a sign of underestimated surface area[1], however it could also be related to a higher corrosion resistance due to the more homogeneous nature of dense wrought microstructures relative to powder processed porous metals. In fact, the OCP for wrought Fe was -533.5 mV whereas the OCP for the porous Fe was -618.1 mV prior to the EIS test, suggesting a higher tendency for the porous Fe to corrode. It is also important to be reminded that the porous Fe samples were

[1]Note that to neutralise $|Z|$ in a Bode plot, the raw data needs to be *multiplied* by the surface area. Therefore, with samples whose exposed pore surface area is not taken into consideration, the values would be underestimated. Wherever the Bode plots are presented with y-axis units of Ω, this means that the raw data was multiplied only by the *apparent* surface area of the test samples.

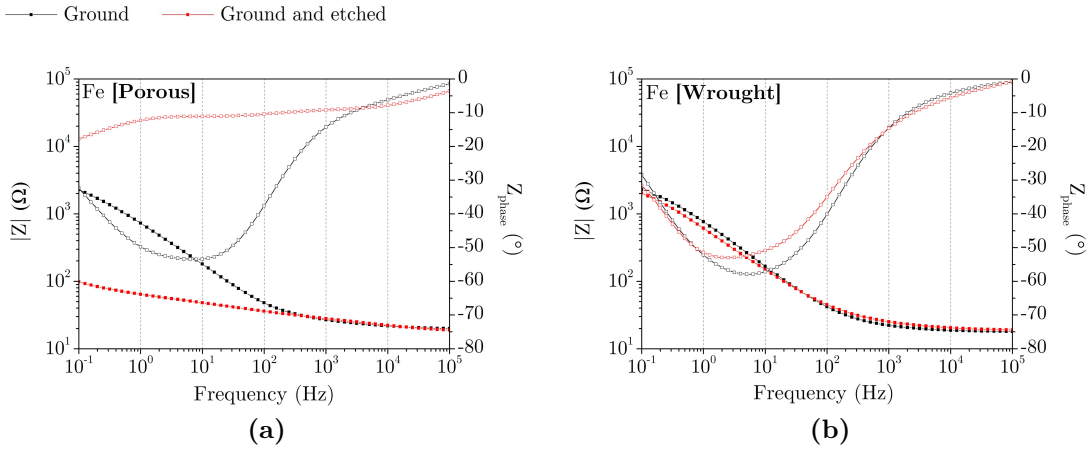

Figure 4.36: Bode plots for (a) porous and (b) wrought Fe samples after 30 min of OCP monitoring in HBSS+Ca. Each material was tested as-ground (black) and as-ground and etched (red).

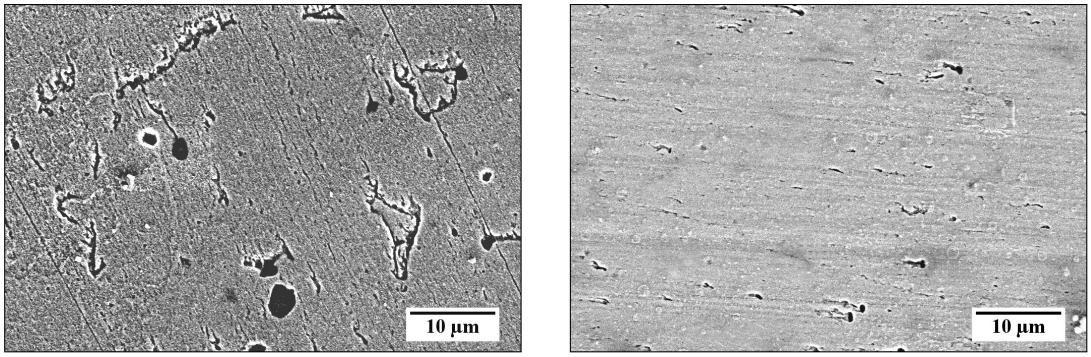

(a) (b)

Figure 4.37: SEM micrographs for ground and etched (a) porous and (b) wrought Fe prior to testing in HBSS+Ca.

significantly less porous than the FeMn and FeMnAg samples due to the higher compressibility of Fe powders. Therefore, any influence due to underestimated pore surface area, would be significantly more pronounced for the Mn-containing powder-processed samples.

The same metals were subjected to the etching procedure used to remove MnO inclusions. SEM images presented in Figure 4.37 show the etched surfaces for both metals. Evidently, etching of the porous Fe surface resulted in significant surface roughening compared to the wrought surface which consisted of several nanometric pits but remained comparably smooth. The EIS results corresponding to both surfaces are presented as red curves in Figure 4.36. The Bode plot for the etched wrought Fe was very similar to that of the ground wrought Fe, with the impedance being slightly lower at low frequencies and the phase shift also shifting a few degrees lower. On the other hand, the Bode curves for the etched porous Fe exhibited a very similar shift in their characteristics to those displayed by the etched porous FeMn in Figure 4.35b. The low frequency impedance likewise dropped drastically whereas the phase shift did not display any prominent time constant except for the relaxation feature attributed to diffusion phenomena at 0.1 Hz.

Based on these results, it seems that the behaviour of the metal could be affected by two main aspects. Firstly, significant roughening of the surface compared to the ground surface results in a relative underestimation of surface area

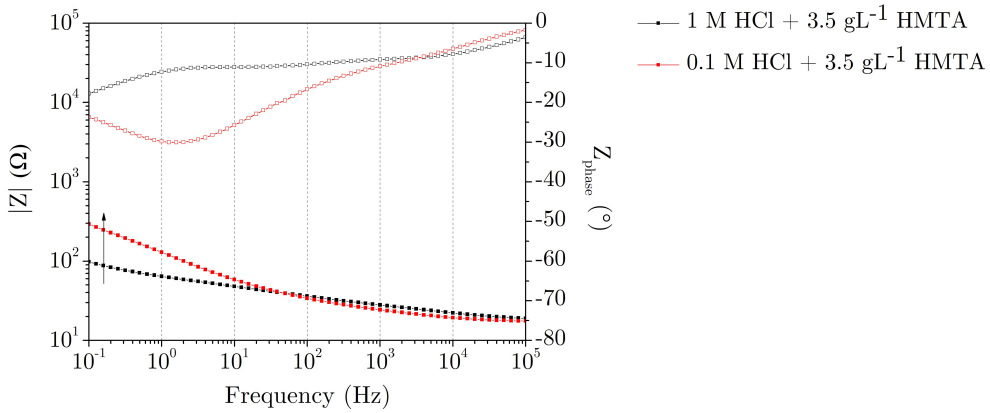

Figure 4.38: Bode plot for porous Fe etched in solutions with 0.1 M and 1 M HCl, both with 3.5 g L^{-1} HMTA. Tests conducted in HBSS+Ca.

for etched surfaces. Considering the wrought Fe, etching resulted in a less distinct difference in surface area compared to its ground counterpart, and therefore the underestimation observed in Figure 4.36b was considerably less significant. Moreover, etching of metal surfaces also affects the oxide layer that forms naturally on metal surfaces exposed to air [251]. This could also contribute in influencing the ability for the typical metal-electrolyte barrier characteristics to be observed in the phase shift curves. However, judging by the rather small differences observed in the Z_{phase} curves for ground and etched wrought Fe, it is more likely that the surface area and/or roughening, are the prime contributors to the observed changes in the EIS spectra.

These theories were further confirmed by running a test on porous Fe etched with an alternative etchant formulation. The Bode plot in Figure 4.38 shows that using 0.1 M of HCl as opposed to 1 M, lead to a higher low frequency impedances and a more defined time constant i.e. the curves approached the results for as-ground porous Fe when prepared using the less aggressive etchant. Diluting the HCl to 0.1 M resulted in less roughening of the surface, implying a less considerable underestimation of the surface area which in turn allowed for results closer to those obtained with the ground porous surface.

4.2.2.2 Eliminating the influence of porosity

Based on the conclusions of the initial tests, it was decided that the influence of porosity needed to be taken into account in tests carried out from this point forward. In order to do this, porous samples were subjected to a modified sample preparation procedure described schematically in Figure 3.3. Following successful implementation of this procedure, which will be referred to as the resin-impregnation method, the first step was to carry out tests on FeMn (with MnO) in HBSS+Ca to determine the extent by which the impedances measured when testing porous FeMn using EIS in Section 4.2.1.3 in Phase One, were underestimated.

4.2.2.2.1 Sample characterisation

The resin-impregnation method was successful at blocking the porosity, as shown in the SEM images before and after the procedure, in Figure 4.39. Further confirmation was achieved using non-contact profilometry. Figure 4.40a and (c) show the profile depth of a pore in the as-ground FeMn sample, with an approximate maximum depth of around 50 µm. Contrastingly a much larger pore in the resin-impregnated sample shown in (b), exhibited a flat profile in (d) with only a few defects in the resin resulting in minor deviations from the nominal surface level.

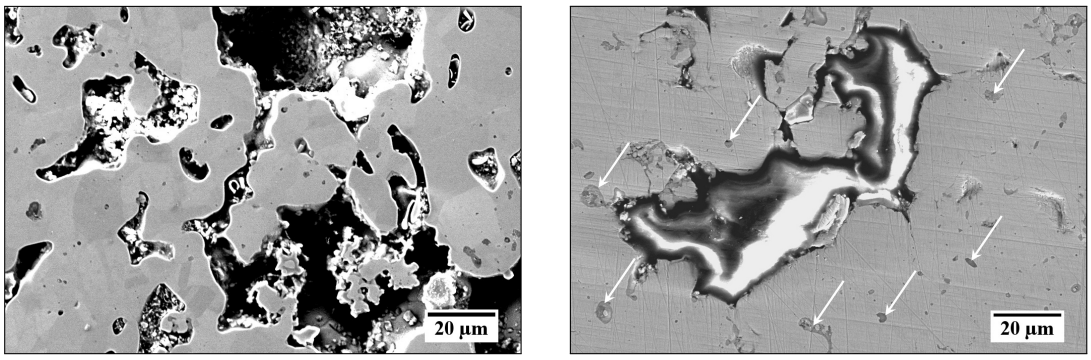

(a) **(b)**

Figure 4.39: SEM images of (a) as-ground FeMn surfaces and (b) resin-impregnated FeMn surfaces. White arrows point towards several of the remaining exposed MnO inclusions.

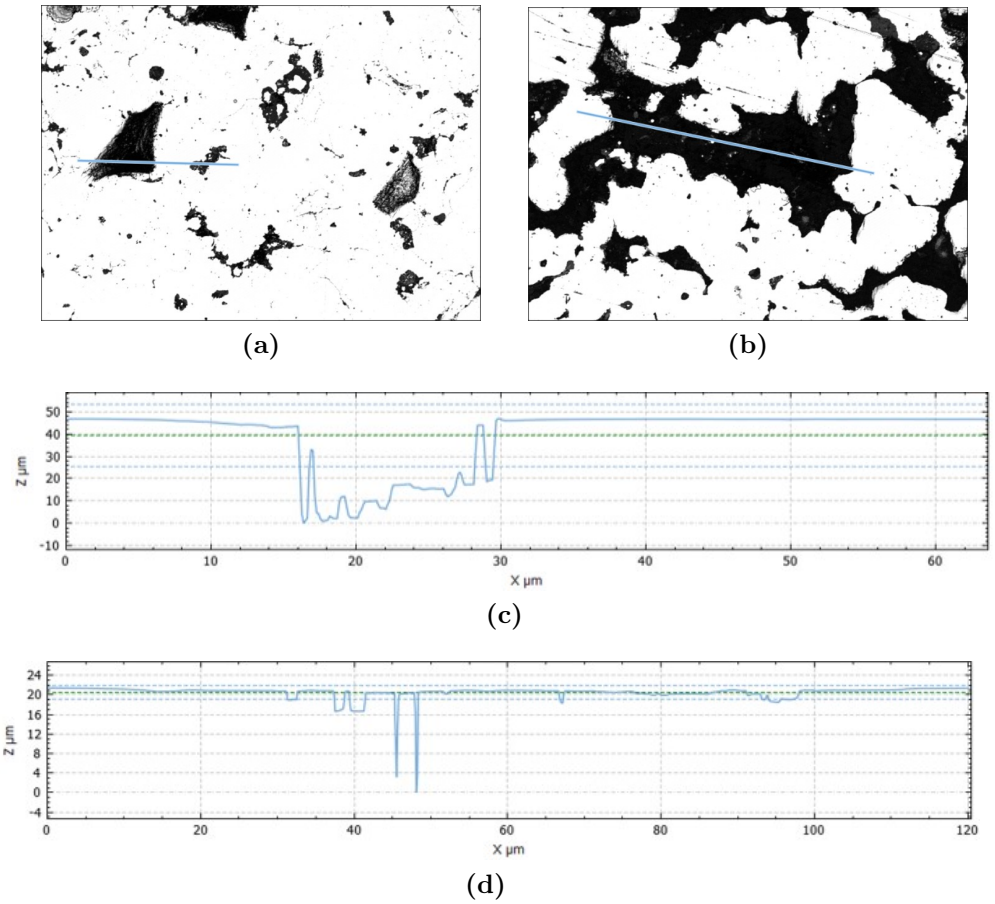

Figure 4.40: Binarised optical micrographs (a-b) and respective corresponding depth profiles (c-d) for (a, c) porous FeMn sample and (b, d) resin-impregnated FeMn sample.

4.2.2.2.2 EIS testing

Bode plots corresponding to several EIS tests carried out over 24 h in HBSS+Ca on porous and resin-impregnated FeMn, are presented in Figure 4.41. Despite the fact that the material used in both tests was identical, the impact of eliminating activity in the pores and neutralising the impedance measurements according to the exposed area, is clearly noticeable. To start, the total impedance for resin-impregnated samples at 0.1 Hz is considerably high at 1431.0 $\Omega \cdot cm^2$ compared to the underestimated 202.5 Ω measured for the porous FeMn. The lower surface area led to a more gradual increase in impedance over the 24 h test period as

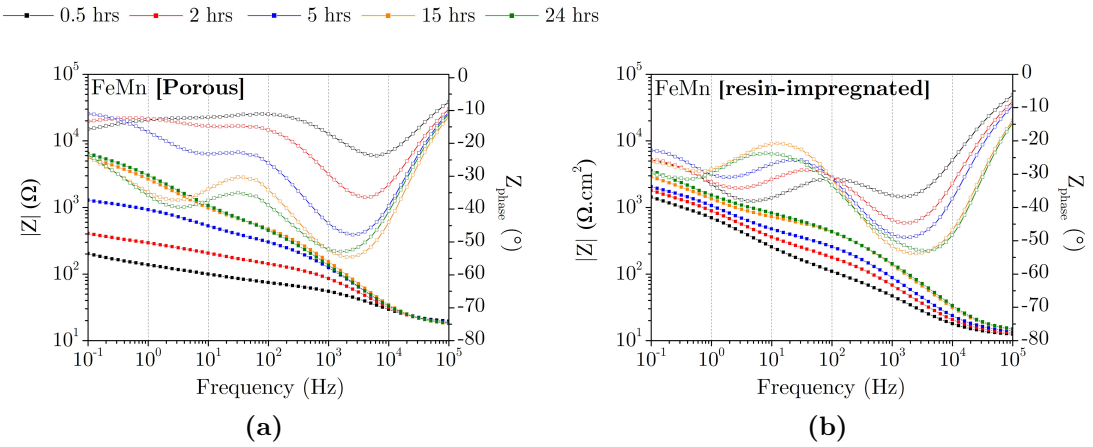

Figure 4.41: Bode plots for (a) porous and (b) resin-impregnated FeMn samples with MnO inclusions.

opposed to the rapid increase observed in Figure 4.41a. Looking at the phase shift curves, the relaxation feature at low frequencies related to diffusion, was largely suppressed with the elimination of the pores. Moreover, the low frequency phase shift associated with the characteristics of the metal-electrolyte interface was more defined at -38° as opposed to the approximately -12° shift observed with porous samples.

Contrary to Phase One, the implementation of the resin-impregnation procedure allows for modelling of the spectra over the full range of tested frequencies using the model represented in Figure 4.9. This was due to the ability to better approximate the testing area using the method described in Section 3.2.3.4, and due to the elimination of the diffusion influence on the low frequency measurements. The plots corresponding to the modelled values' evolution with time, are presented in Figure 4.42[1]. Each plot contains the results associated with three test repetitions to better visualise trends related to the material's behaviour. Each plot also includes the fitting results for porous Fe from Phase One[2]. None

[1]The lines connecting each point in this and similar plots in the following tests are only their for better visualisation. One can only hypothesise as to the changes taking place during the interval between one point and another.

[2]Testing with resin-impregnated Fe was also attempted following the same procedure used with FeMn. However, the small pores present in the porous Fe samples did not serve for sound adherence of the cured resin to the metal surface and the epoxy repeatedly peeled off during the grinding step, once again exposing the pores. Considering the similarity in the Bode plots

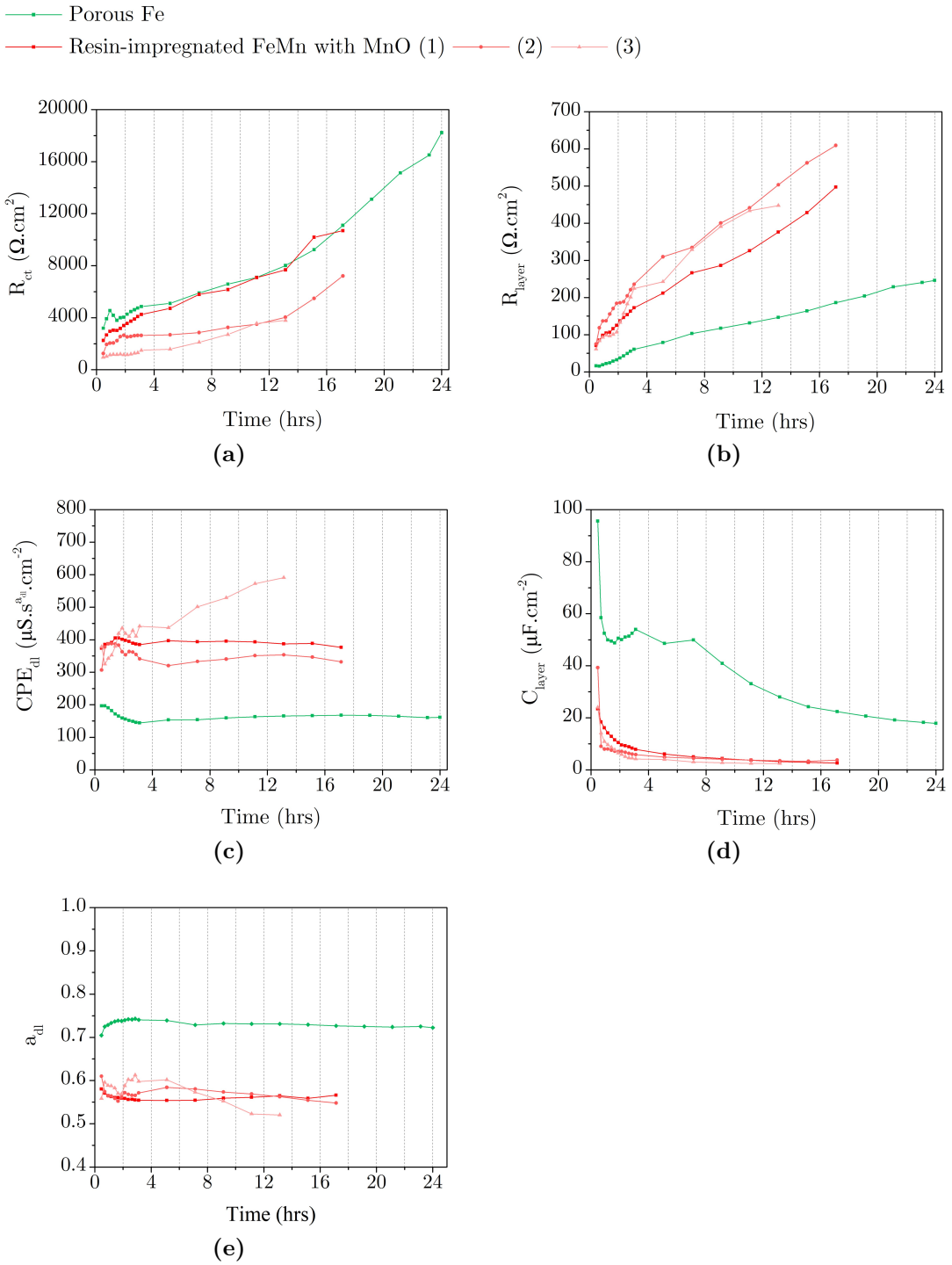

Figure 4.42: Evolution of fitting results for resin-impregnated FeMn immersed in HBSS+Ca. The fitting components correspond to the model in Figure 4.9.

of the fitting results include the modelled R_{el} values associated with the solution resistance since in highly conductive solutions like HBSS+Ca, R_{el} is mainly dependant on the physical distance between the reference electrode and the sample being tested, which was not strictly controlled in the used setup [62]. For each test carried out with resin-impregnated FeMn, the equivalent circuit modelled being used failed to give reliable results at a certain time point, most often due to insufficient data related to the low-frequency time constant which tended to shift to lower frequencies with time. Therefore, the fitting results are presented only up to that time point for each test. All included results had goodness-of-fit measures in the order of 1×10^4 or better.

Although not particularly repeatable, the modelled R_{ct} values for resin-impregnated FeMn were all below the R_{ct} for Fe upon test initiation. The evolution of the modelled values with time varied from one test to another. In one case, the R_{ct} curve overlapped that of Fe as observed in the evolution of the 0.1 Hz $|Z|$ in Figure 4.8a, measured in Phase One. However, the R_{ct} for the other two test repititions remained well below the curve for Fe, indicating lower corrosion resistance for the FeMn samples. Due to the relatively low a_{dl} values associated with the double layer CPE, the true double layer capacitance could not be calculated using Hsu and Mansfeld's conversion equation (equation 4.1 [65]) and the CPE_{dl} and a_{dl} are presented instead. Although relative CPE_{dl} values are generally interpreted in a similar way to actual capacitance, i.e. that a relatively high CPE_{dl} generally indicates lower impedance contribution due to the double layer of the material, one must make these assumptions with caution, since simultaneous shifts of the CPE exponent, a_{dl}, might influence that relationship. To this end, the double-layer CPE components are mostly included for completeness sake, rather than for their contribution to the analysis.

For values related to the higher frequency time constant, the resistance associated with the Ca/P-rich corrosion product precipitation (R_{layer}) for FeMn remained well above the R_{layer} contribution to the impedance of Fe, indicating

for ground porous and dense wrought Fe samples in Figure 4.36, the outcomes of the fitting exercise carried out with porous Fe in Phase One, were deemed suitable for comparison with these results.

a more rapid accumulation of corrosion products on the surface of FeMn. Compared to the evolution of the modelled C_{layer} values for the porous FeMn sample presented in Figure 4.8c, the curves for resin-impregnated FeMn follow a more similar trend to the C_{layer} values for Fe during the first few hours, although the capacitance remains significantly lower, likewise indicating a larger accumulation of protective corrosion products. Irrespective of the starting capacitance, the values for all the test repeats, converged to approximately 2.5 µF cm^{-2}.

4.2.2.2.3 Post-test characterisation

Figure 4.43 shows the surface of a resin-impregnated FeMn sample following EIS testing for 24 h in HBSS+Ca. The numbered regions-of-interest correspond to

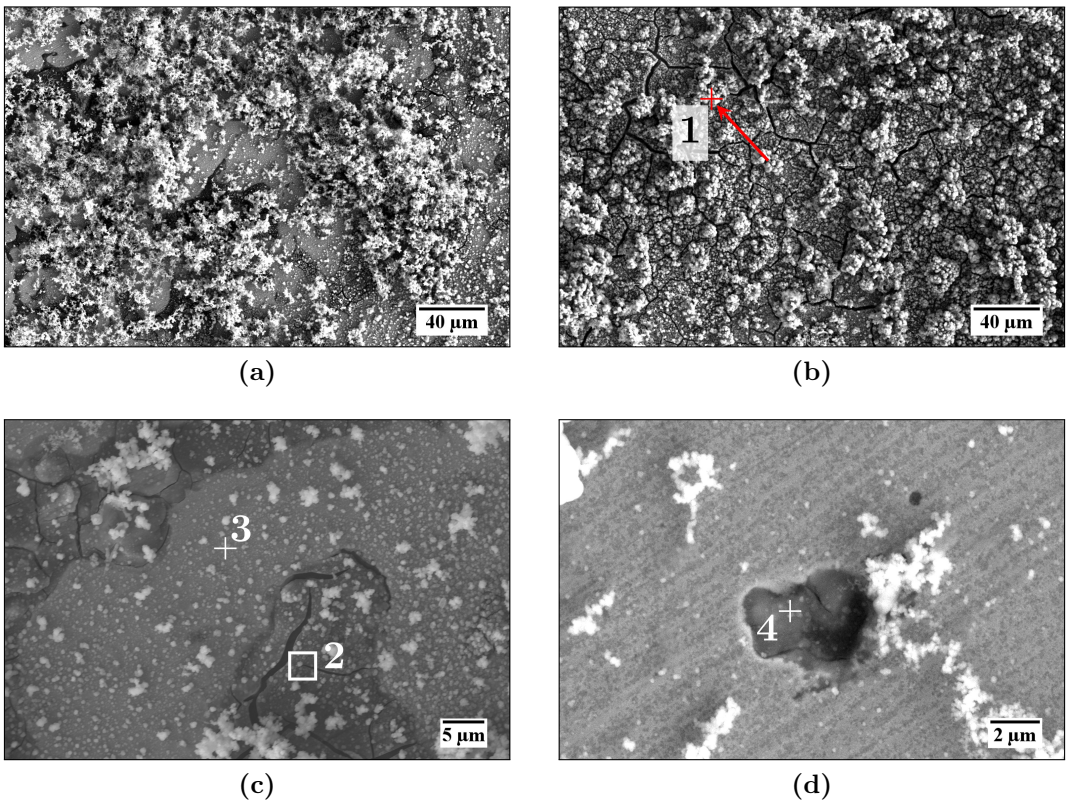

Figure 4.43: SEM micrographs of resin-impregnated FeMn sample (with MnO) following 24 h EIS testing in HBSS+Ca. Marked regions-of-interest correspond to EDS analysis presented in Table 4.5.

Table 4.5: EDS analysis in wt.% for resin-impregnated etched FeMn samples (with MnO) corresponding to marked regions-of-interest in Figure 4.43.

Pt.	O	C	Fe	Mn	P	Ca	Na	Cl	Mg	N
1	47.33	8.86	20.56	7.04	10.16	4.70	1.02	-	0.33	-
2	18.88	27.06	27.03	14.04	6.34	4.35	0.30	2.00	-	-
3	10.88	5.82	52.45	26.25	1.19	0.49	-	-	-	2.92
4	33.16	9.41	9.81	45.8	1.29	0.53	-	-	-	-

EDS data presented in Table 4.5. Although the surface distribution of the precipitated corrosion products varied slightly from region to region on the sample surface (Figure 4.43 (a) and (b) compared to more-sparsely populated corrosion products in (c) and (d)), the general coverage with Ca/P-rich products was significantly more abundant than the clusters observed on the porous surface in Phase One (Figure 4.14c). Relatively high Ca and P wt.% were detected both on dense dehydrated corrosion layers (point 1) as well as on less dense areas (points 2 and 3). Figure 4.43c in particular, shows the indiscriminate formation of a thin metal hydroxide layer on the surface of the metal (point 3), as well as on the resin blocking the porosity (point 2, high C content due to underlying epoxy)[1]. Moreover, the high magnification micrograph of the sample surface surrounding a MnO inclusion (Figure 4.43d, point 4) revealed uniform attack of the FeMn matrix surrounding the inclusion.

4.2.2.3 Eliminating MnO inclusions in resin-impregnated FeMn

4.2.2.3.1 Sample characterisation

The same EIS procedure and post-test characterisation were carried out with pre-etched resin-impregnated FeMn. SEM was initially used to confirm that the pre-etched surfaces had no (or minimal) remaining MnO inclusions at the surface.

[1] As mentioned earlier in this work, the accuracy of EDS measurements for light elements like O and C is low, however the relative measures could be used as an indicator combined with visual interpretation of the micrographs or other characterisation methods.

Figure 4.44b shows the absence of visible inclusions compared to the surface tested in Section 4.2.2.2, in which several inclusions are pointed out using white arrows.

4.2.2.3.2 EIS testing

A representative Bode plot for tests run using pre-etched resin-impregnated FeMn is presented in Figure 4.45b adjacent to the result with resin-impregnated FeMn (containing MnO) presented earlier in this testing phase. In this case, barely

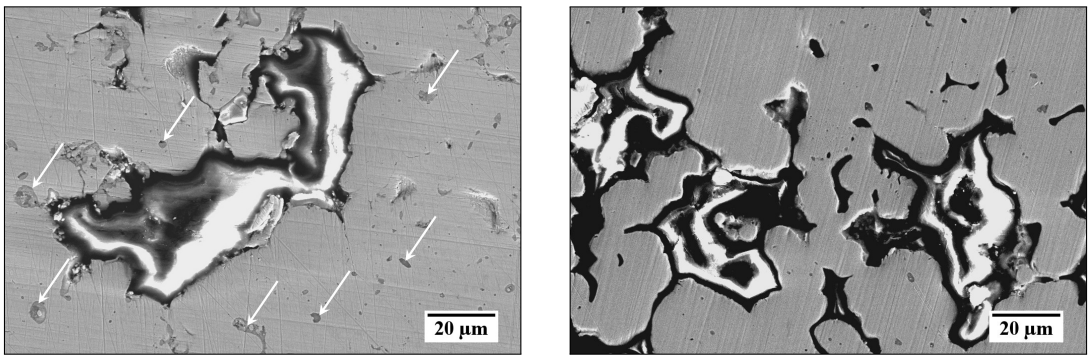

(a) (b)

Figure 4.44: SEM images of resin-impregnated (a) FeMn sample and (b) pre-etched FeMn sample. White arrows point towards several of the remaining exposed MnO inclusions.

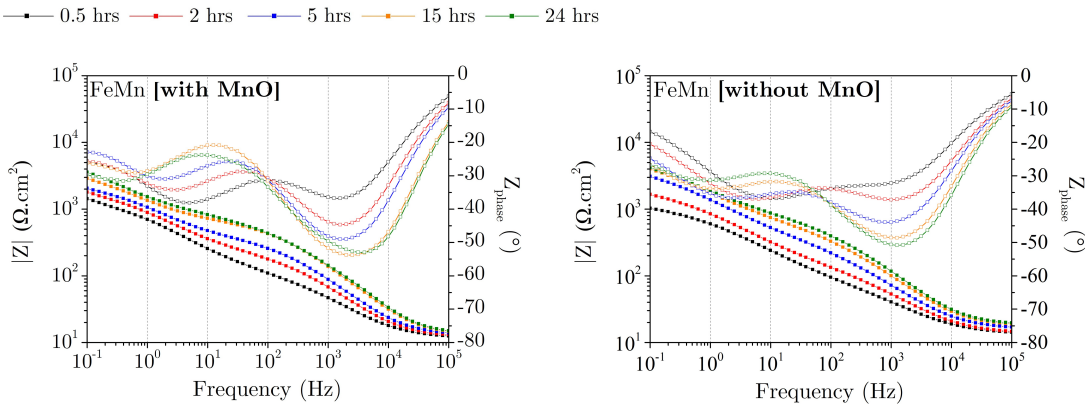

(a) (b)

Figure 4.45: Bode plots for resin-impregnated FeMn samples (a) with and (b) without MnO inclusions, tested in HBSS+Ca.

any differences were visible between the two plots. The impedances measured for both materials were generally in the same range and the evolution of both the low and high frequency phase shifts followed very similar trends.

This also translated to the evolution in the modelled parameters of the three repeated tests carried out with pre-etched FeMn using the same equivalent circuit model. The resultant plots presented in Figure 4.46, indicate significant overlap of fitting results. As observed with MnO-containing samples, the evolution of certain parameters for a single test from the three repeats carried out, did not stick to the trend exhibited by the other two, especially after the initial few hours when the substrate influence became less prominent due to the accumulation of corrosion products. However, looking closely at the inset showing a detail of the evolution of R_{ct} over the first 3 h, one could see that the resistances for samples without MnO followed a more repeatable trend. In fact the difference between the maximum and minimum modelled resistances spanned 792 $\Omega \cdot cm^2$ for MnO-containing samples and 385 $\Omega \cdot cm^2$ for pre-etched (MnO-free) samples.

4.2.2.3.3 Post-test characterisation

Micrographs of the pre-etched resin-impregnated FeMn samples after 24 h of EIS testing, are presented in Figure 4.47. Corresponding EDS analysis can be found in Table 4.6. As observed in MnO-containing samples, the amount of corrosion products varied from region to region on the sample surface. Once again, Ca/P-rich products were more homogeneously distributed over the surface (point 6) when compared to the clusters observed after 24 h testing of porous FeMn in Phase One. The metal underneath the Ca/P-rich products was once again high in wt.% O (points 7 and 10) and the metal hydroxide layer (point 9) formed all over the sample surface, including the resin-impregnated pores (point 8). In general, the surfaces in Figure 4.47 were visually and chemically indistinguishable from the samples containing MnO inclusions in Figure 4.43. The only notable difference could be seen in the high magnification image in Figure 4.47d compared to Figure 4.43d. As opposed to the latter, close observation of the surface did not reveal similar attack of the exposed FeMn matrix.

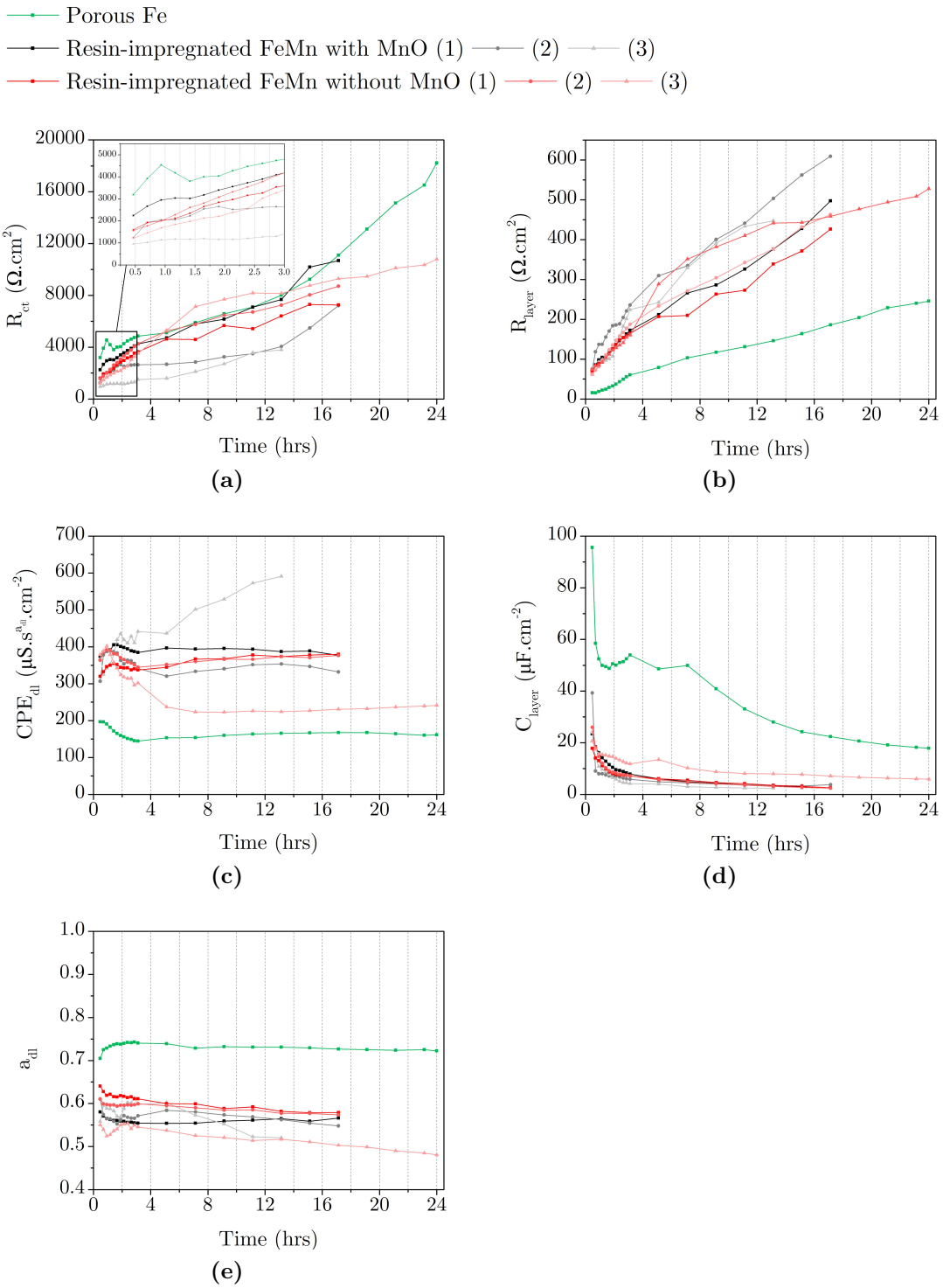

Figure 4.46: Fitting results for resin-impregnated FeMn with and without MnO, immersed in HBSS+Ca. The fitting components correspond to the model presented in Figure 4.9.

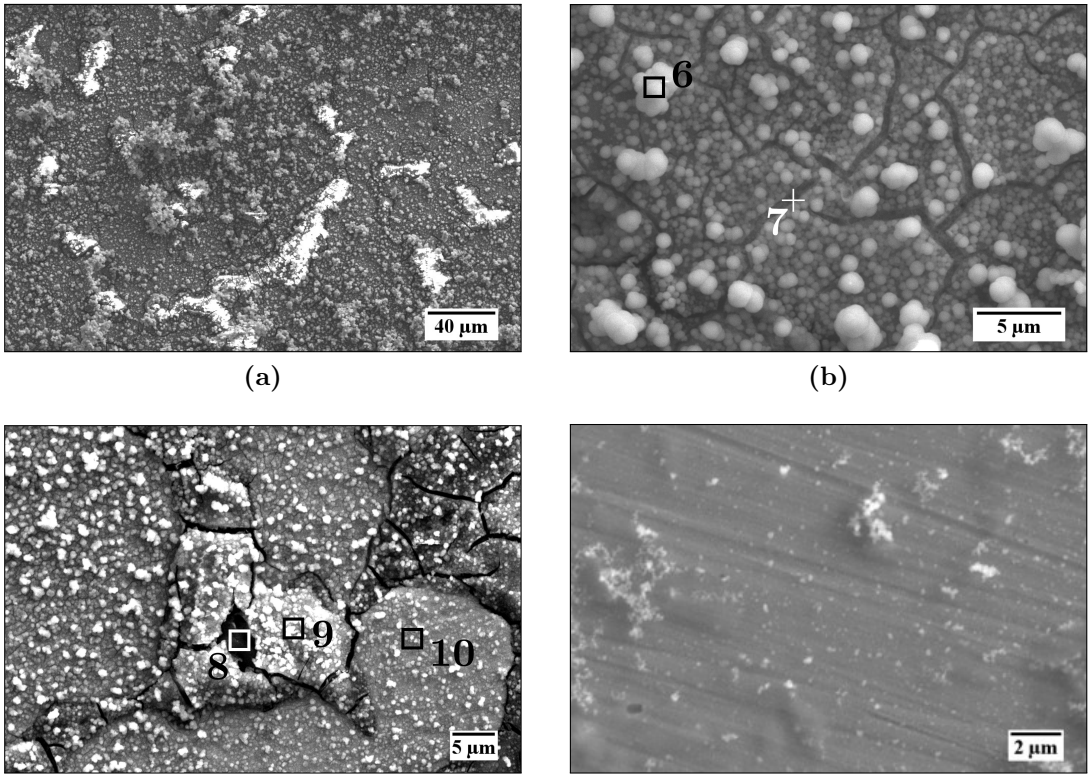

Figure 4.47: SEM micrographs of resin-impregnated etched FeMn sample (without MnO) following 24 h EIS testing in HBSS+Ca. Marked regions-of-interest correspond to EDS analysis presented in Table 4.6.

Table 4.6: EDS analysis in wt.% for resin-impregnated etched FeMn samples (without MnO) corresponding to marked regions-of-interest in Figure 4.47.

Pt.	O	C	Fe	Mn	P	Ca	Na	Cl	Mg	N
6	47.80	7.12	26.78	5.66	9.90	2.10	0.64	-	-	-
7	9.41	3.75	56.69	28.65	1.50	-	-	-	-	-
8	24.57	63.77	1.78	1.07	0.94	1.09	-	0.76	-	6.02
9	44.52	20.19	18.87	7.37	2.47	1.45	0.21	1.11	0.20	3.61
10	5.60	6.24	53.94	29.56	0.58	0.43	-	-	-	3.65

4.2.2.4 Testing with FeMnAg, with and without MnO

The resin-impregnation approach for eliminating the influence of porosity on the corrosion of the powder-processed Fe-based alloys, was also adopted to FeMnAg. Congruent to what was done with FeMn, tests were done on FeMnAg containing MnO inclusions to improve on the results achieved in Phase One. Consequently, EIS tests were also conducted on pre-etched FeMnAg, to determine whether MnO has any influence on the corrosion behaviour of the tertiary alloy with a proven separate effective cathode (Ag).

4.2.2.4.1 EIS testing

Representative Bode plots for FeMnAg samples with and without MnO, tested in HBSS+Ca for 24 h, are presented in Figure 4.48. At first glance, the plots seem almost identical. Close observation of the low-frequency impedance shows that samples without MnO inclusions consistently exhibited lower impedances (765.9 - 2686.2 $\Omega \cdot cm^2$ as opposed to 1426.4 - 4146.4 $\Omega \cdot cm^2$ for MnO-containing FeMnAg), indicating a generally lower corrosion resistance for MnO-free FeMnAg, contrary to primary expectations.

As done with previous EIS testing in this phase, the spectra of the three repeated tests for each condition were modelled using the model in Figure 4.9. The

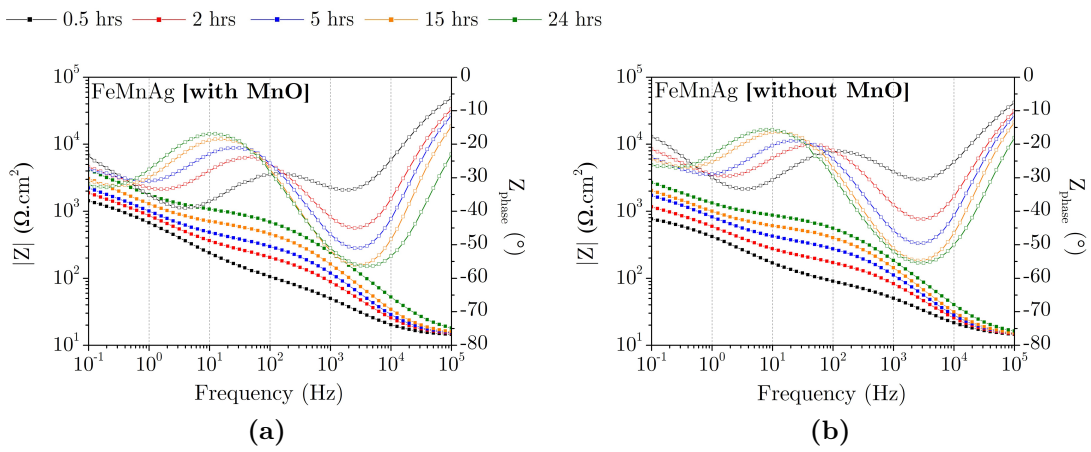

Figure 4.48: Bode plots for resin-impregnated FeMnAg samples (a) with and (b) without MnO inclusions, tested in HBSS+Ca.

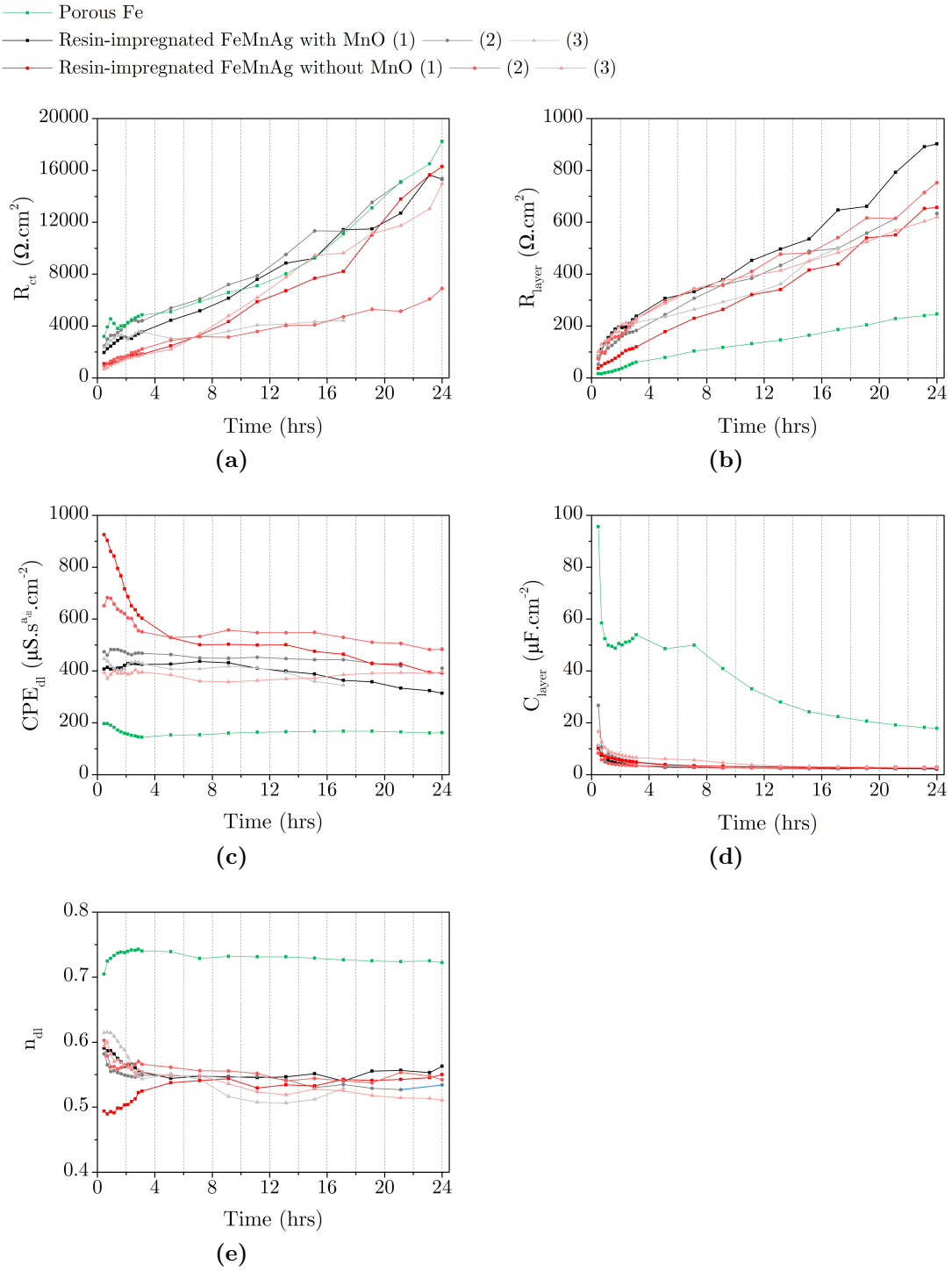

Figure 4.49: Evolution of fitting results for resin-impregnated FeMnAg with and without MnO, immersed in HBSS+Ca. The fitting components correspond to the model presented in Figure 4.9.

results are presented in plots in Figure 4.49. All plots displayed significant overlap between the two sets of fitting results. However, as the $|Z|$ Bode curve implied, the charge transfer resistance, R_{ct}, for pre-etched samples were consistently well below the R_{ct} for FeMnAg samples containing MnO during the first 3 h of the test. Following the first few hours, the resistances also started to overlap and the majority of the curves from both sets of tests approached the charge transfer resistance for the Fe sample, by the end of the test.

4.2.2.4.2 Post-test characterisation

SEM images of representative sample surfaces following the 24 h EIS test in HBSS+Ca, are presented in Figures 4.50 and 4.51 for samples with and without MnO respectively. Corresponding EDS analysis is presented in Table 4.7. Both samples were shown to be very similar irrespective of the presence of MnO. As observed with both FeMn samples, the FeMnAg surfaces were more homogeneously covered with corrosion product compared to their porous counterparts, presented in Phase One of this work. Cracks visible in all SEM images are indicative of the consistent growth of a product that EDS analysis indicates to be rich in Fe, Mn and O (points 1, 6, 11 and 12). EDS spots of the metal visible underneath the cracks (points 7 and 10) indicate the presence of the austenitic matrix with approximately 35 wt.% Mn. Ca and P were likewise present in all the analyses of the product but were more abundant in brightly-coloured clusters, similar to those observed in Figures 4.15 and 4.16 in Phase One (points 2, 5 and 9).

Interestingly, the Ag-rich regions on the metal surface were covered to various degrees with corrosion products on both surfaces. Considering the analysis of points 4, 8 and 13, each measurement picks up different concentrations of Ag from underneath varying thickness of corrosion products all of which consist of different intensities of Fe, Mn, O with minor concentrations of P and Ca. The EDS mapping presented in Figure 4.50c is a clear representation of the full coverage of the cathodic Ag by metal hydroxides and Ca/P-products. Contrastingly, in Figure 4.50b, the MnO inclusion seems to be clear of any corrosion products, as opposed to the adjacent Ag-rich region. Furthermore, the measurement performed on the inclusion itself (point 3), did not reveal the presence of Fe.

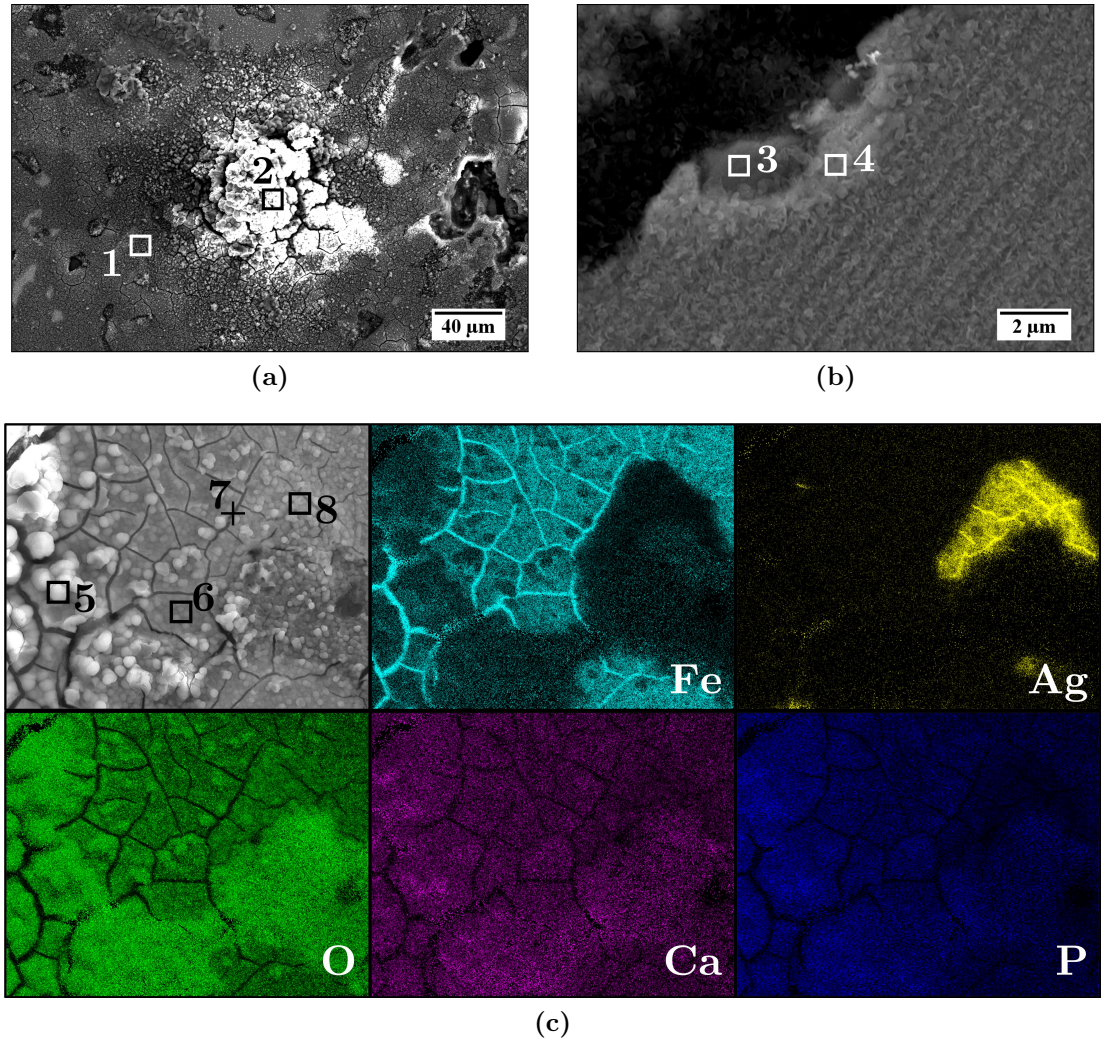

Figure 4.50: SEM micrographs of resin-impregnated FeMnAg sample (with MnO) following 24 h EIS testing in HBSS+Ca. Marked regions-of-interest correspond to EDS analysis presented in Table 4.7.

4.2.2.5 Discussion

The results presented in Phase One of this work, brought up two principal questions that were tackled in this phase. The first question related to the extent of the influence of porosity on the corrosion of the Fe-based alloys of interest, whereas the second regarded the role of MnO inclusions that frequently featured in literature, as well as in this work, but which very few have investigated.

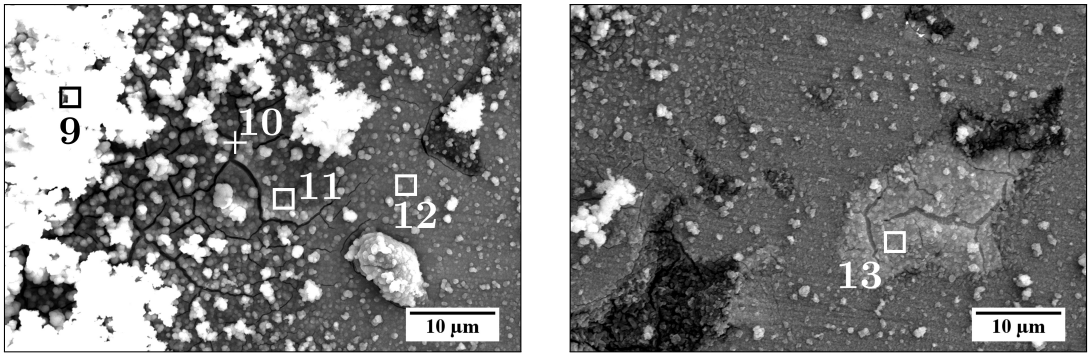

(a) (b)

Figure 4.51: SEM micrographs of resin-impregnated pre-etched FeMnAg sample (without MnO) following 24 h EIS testing in HBSS+Ca. Marked regions-of-interest correspond to EDS analysis presented in Table 4.7.

Table 4.7: EDS analysis in wt.% for resin-impregnated FeMnAg samples (with and without MnO) corresponding to marked regions-of-interest in Figure 4.50 and 4.51.

Pt.	O	C	Fe	Mn	Ag	P	Ca	Na	Cl	Mg
1	38.14	17.10	31.27	5.34	-	2.89	2.33	-	2.93	-
2	37.97	11.82	27.00	7.13	-	9.43	5.30	1.10	-	0.25
3	30.82	10.29	-	57.07	1.03	-	0.27	-	-	0.52
4	19.45	8.66	4.63	8.32	55.86	1.17	1.28	-	-	0.63
5	41.54	14.19	18.50	8.93	-	9.84	5.80	0.96	0.24	-
6	31.02	15.66	24.82	17.72	-	5.29	4.30	0.42	0.23	0.54
7	6.61	7.70	55.46	28.35	-	1.03	0.85	-	-	-
8	25.05	11.82	26.13	15.38	13.94	3.66	3.22	0.26	-	0.54
9	42.95	10.86	12.49	10.33	-	11.53	10.45	0.56	-	0.83
10	4.86	2.40	60.27	30.55	-	1.26	0.66	-	-	-
11	15.77	5.74	39.49	22.09	-	8.86	7.53	-	-	0.52
12	19.87	10.68	39.66	22.08	-	3.62	3.49	-	-	0.60
13	30.43	6.16	6.23	6.36	45.89	1.83	2.50	-	-	0.60

The impregnation of surface porosity with epoxy resin for better approximation of the testing area, was successful in correcting for the underestimation of

impedances noted in Phase One. The process that led to the development of the resin-impregnation sample preparation procedure, also revealed the considerable impact of surface roughness and porosity on the impedance and corresponding phase shift, especially at low frequencies, as shown in Figures 4.35 to 4.38. Although it was hypothesised that the change in impedance and phase shift could also be a result of damaged native oxide layer due to the etching procedure, the absence of a similar change when testing a wrought Fe sample in Figure 4.36 seemed to indicate otherwise. Moreover a study on the influence of similar etchant composition including HCl and HMTA on the corrosion rate of *wrought* carbon steel, yielded perfectly well defined time constants as opposed to the results presented for porous Fe alloys in Section 4.2.2.1, which continued to confirm the initial interpretation that the changes in the impedance spectra were due to porosity and surface roughness [252]. Other instances in literature seem to indicate similar patterns in their results. For instance, Sharma *et al.* [230] also noted a significant decrease in capacitive contribution to the phase shift associated with charge transfer across the metal-electrolyte interface when testing increasingly porous Fe (up to 39.6% porous) compared to dense Fe. Although this might be advantageous in terms of porous scaffold applications, the presence of porosity and lack of means to accurately measure the resultant surface area at this point, were interfering with carrying out a more accurately quantified investigation.

Micrographs of the tested FeMn and FeMnAg resin-impregnated samples after 24 h in Figure 4.43 and 4.50, showed significantly different corrosion product formation in the absence of open surface porosity. Corrosion products were more homogeneously spread over the sample surfaces compared to the surfaces in Figure 4.14 and 4.16 in Phase One. The resin blocking the pores did not influence the formation of metal hydroxide layers, indicating that oxide formation is not particularly influenced by the substrate, but rather takes place on any surface wherein the adjacent electrolyte contains the necessary species, as indicated by reactions such as reaction 2.3 and 2.4. Considering the same exact composition of the metals used in both Phase One and Two, it follows that the improvement in corrosion layer integrity is solely due to the elimination of porosity, confirming the claims of Zhang *et al.* [153] who suggested that porous surfaces result in poor

corrosion product adhesion. Further to this analysis, EIS testing of FeMnAg (with MnO) in this section did not result in any drastic changes to the R_{layer} and C_{layer} modelled values in Figure 4.49, as observed after around 9 h in Figure 4.8 (b) and (c) as well as in the local measurements of DO in Figure 4.26. In fact, on resin-impregnated surfaces, not only did metal oxides/hydroxides grow more evenly, but Ca/P-products were also detected all over the sample surface, with enriched clusters still forming on both surfaces.

4.2.2.5.1 The role of MnO inclusions on the corrosion of FeMn-based alloys

Modelling of repeated tests carried out with FeMn with and without MnO in Figure 4.46 did not indicate a notable shift in the modelled parameters. All plots show significant overlap between the two sets of data, although measurements for R_{ct} were visibly more repeatable, especially during the first few hours of the test, as shown in the inset in Figure 4.46a. SEM-EDS analysis of the surfaces without MnO in Figure 4.47, showed very similar surface morphologies and chemical compositions when compared to the surfaces containing MnO in Figure 4.43. However, whereas the FeMn matrix was visibly attacked surrounding the MnO inclusions (Figure 4.43d), similarly high magnification images of the pre-etched surfaces, did not reveal comparable features in regions wherein the underlying metal was exposed (Figure 4.47). The implications are, that in MnO-containing samples, the dissolution of the FeMn matrix surrounding the MnO inclusions is enhanced by cathodic activity of the same inclusions.

To investigate this further, MnO-containing resin-impregnated FeMn samples were immersed in physiological saline (0.9 wt.% NaCl) for 1 h, rinsed in ethanol and dried. 24 h tests were also carried out for the same purpose but the extent of surface degradation was too extensive to be able to spot any recurring trends occuring due to the original composition. As discussed in Section 2.1.4.2, using simple saline solutions tends to highlight the influence of the material more than when using more complex saline solutions likes HBSS. SEM micrographs of the surfaces are presented in Figure 4.52. In both micrographs, exposure to the saline solution clearly resulted in significant dissolution of the metallic matrix

but did not impact the Mn-rich inclusions similarly, rather allowing for corrosion products to start accumulating onto the unaffected surface, as indicated by the white arrow in Figure 4.52a. Figure 4.52b depicts further evidence of cathode-like behaviour with preferential attack of the FeMn at the inclusion-matrix interface. This kind of behaviour was also described by Wiesner *et al.* [134] when discussing microgalvanic corrosion resulting from cathodic Ag-rich phases in FeMnAg, with the microgalvanic influence being the strongest at distances closest to the cathode itself. Despite observing signs of a similar role of MnO inclusions when testing MnO-containing FeMn in HBSS+Ca, the more complex electrolyte formulation clearly diminishes this influence such that elimination of the same inclusions did not result in any notable changes to either electrochemical data or the surface itself.

Somewhat conflicting electrochemical results were acquired when testing resin-impregnated FeMnAg with and without MnO. Although the surface analysis of both representative samples in Figure 4.50 and 4.51 did not bring to attention any distinctive differences, the modelling results for R_{ct} in Figure 4.49a clearly indicated that FeMnAg samples without MnO had lower charge transfer resistance compared to samples containing MnO inclusions. Based on the previous assessment, that MnO behaves cathodically when present in FeMn alloys, the opposite would be expected, wherein its presence reduces R_{ct}. Although materials exist in

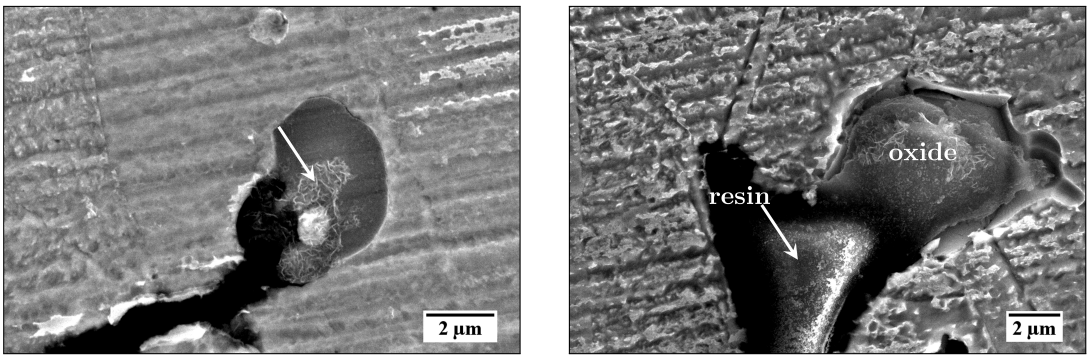

(a) **(b)**

Figure 4.52: SEM micrographs of resin-impregnated FeMn samples (with MnO) after 1 h immersion in physiological saline. White arrow in (a) points towards accumulation of corrosion product.

which corrosion is governed by the influence of multiple cathodes, the tendency is for this influence to be synergistic in accelerating the corrosion rate [253]. In this case, samples from which the second cathode was removed, generally exhibited lower corrosion resistance. This being said, as observed with FeMn, the values overlapped considerably as the test approached 24 h from initiation. In this case, Scanning Kelvin Probe Force Microscopy (SKPFM) could be used to determine the Volta potential between each couple i.e. austenite-MnO, austenite-Ag and MnO-Ag, to help with understanding why the presence of the two cathodes were less effective in reducing corrosion resistance compared to just Ag, during the initial hours of the test. For the purposes of this investigation, the overlap exhibited at the end of the test is indicative of the longer-term similarity in material performance when immersed in the body. There was no similarly stark differences between the two sets of data for all the other modelled parameters in Figure 4.49.

The discussion following the results presented for Phase One also questioned the influence of MnO inclusions on the performance repeatability. As discussed in this section, whereas the R_{ct} values seemed to be more repeatable in the absence of MnO when testing FeMn samples, the same could not be said when testing FeMnAg. However, looking at all the OCP values acquired at the start of the test i.e. after 30 min immersion of the samples in the indicated test electrolyte, the OCPs for samples without MnO consistently exhibited a smaller spread, as shown in Figure 4.53. Therefore, it is likely that the variability in the MnO quantities and distribution in MnO-containing FeMn-based alloys, *does* in fact influence the electrical properties of the material from a thermodynamic point-of-view but does not have a lasting influence on the degradation process.

4.2.2.5.2 On the long-term effectiveness of microgalvanic corrosion acceleration

The performance of FeMn and FeMnAg relative to Fe could be re-evaluated considering the improved EIS fitting results acquired using the resin-impregnation approach in this testing phase. Figure 4.54 compares the evolution of modelled results for pre-etched FeMn and FeMnAg, with porous Fe. Based on the inset in Figure 4.54a, the addition of Ag still gives a prominent advantage in terms of

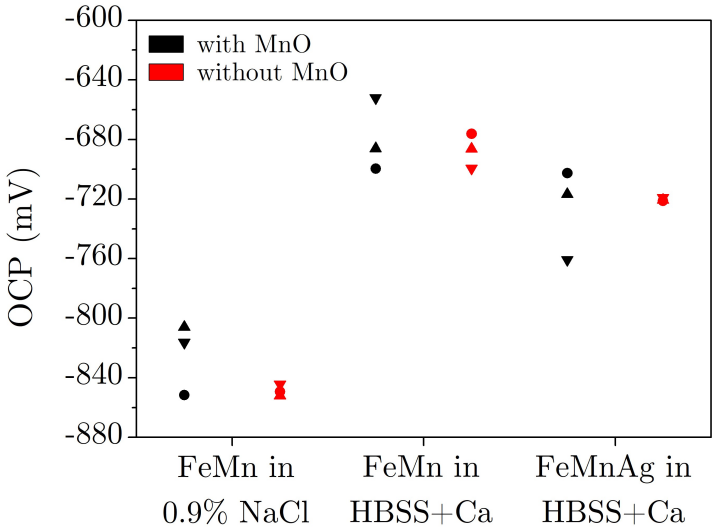

Figure 4.53: OCP values measured after 30 min for repeated tests carried out with resin-impregnated FeMn and FeMnAg, with and without MnO inclusions, in various media.

reducing charge-transfer resistance when compared to FeMn, whereas the latter is still less corrosion resistant than Fe. However, as mentioned multiple times throughout Phase Two, any advantage or distinction present in the early hours of the test, seems to become less prominent by the end of the 24 h period as the influence of the substrate becomes less and less impactful. In fact in this phase, due to more stable corrosion products structure, we could also observe the metal hydroxide layer as well as Ca/P products deposited on the Ag-rich phase in Figure 4.51b, both of which influence its effectiveness as a micro cathode.

In general, modelling results are congruent with the findings of Schinhammer *et al.* [166] who tested Fe21Mn0.7C (TWIP) and Fe21Mn0.7C1Pd (TWIP-Pd) steels in Ca^{2+}-containing SBF using EIS for around 20 h. Their modelling results when fitting the EIS spectra using the same model used in this study, are presented in Figure 4.55. In their work, R_p is analogous to R_{ct}, whereas R_{el} and C_{dp} are analogous to R_{layer} and C_{layer} respectively. The addition of Pd in this study prompted the precipitation of noble Pd-rich precipitates to induce microgalvanic corrosion. As observed in this work, the modelled R_{el} and C_{dp} values converged with time irrespective of material composition. When considering R_p, Schinhammer *et al.* observed a downward trend due to formation of pits which tend to

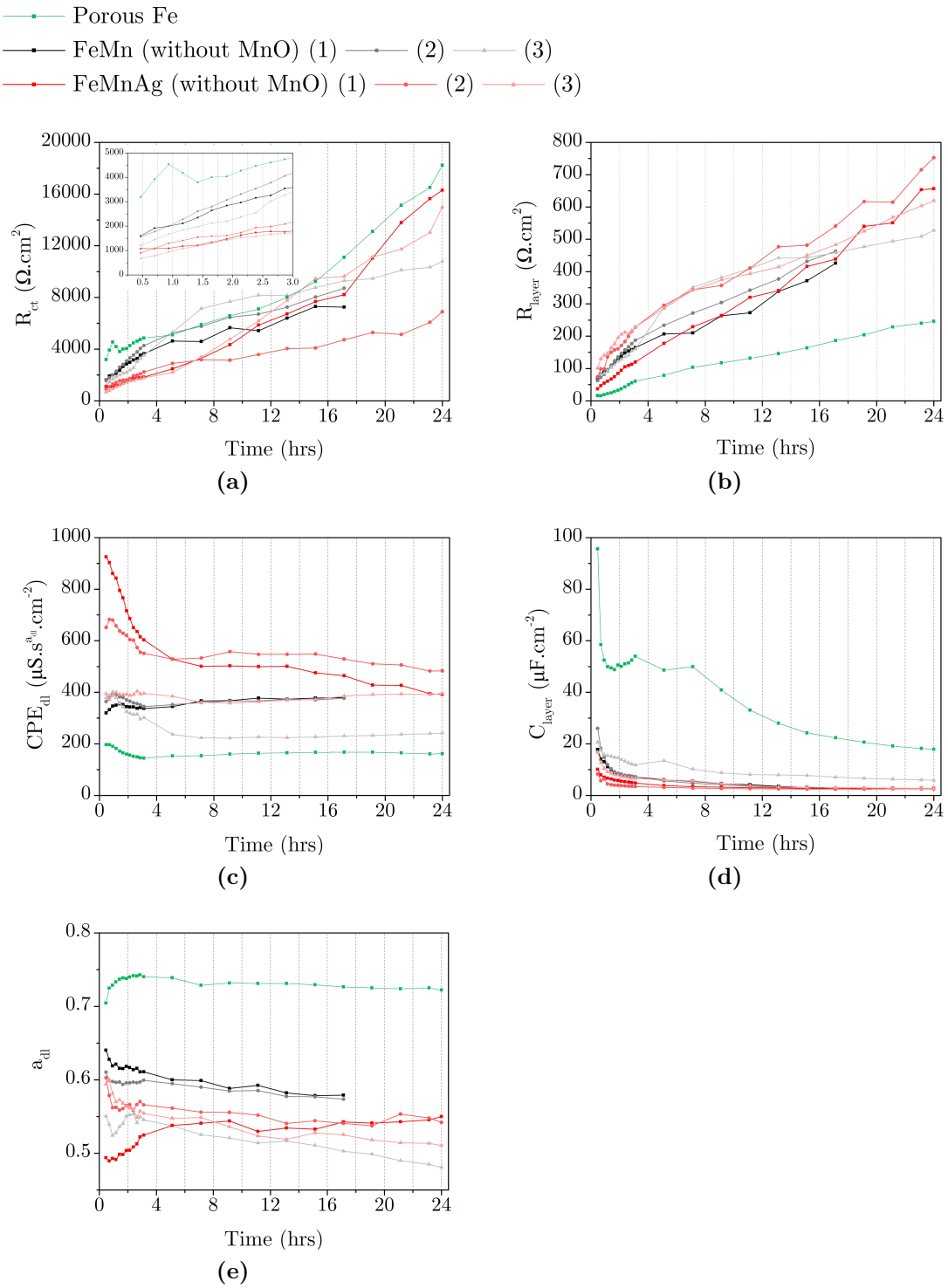

Figure 4.54: Comparison of modelling results for pre-etched (i.e. MnO-free) resin-impregnated FeMn and FeMnAg over 24 h in HBSS+Ca.

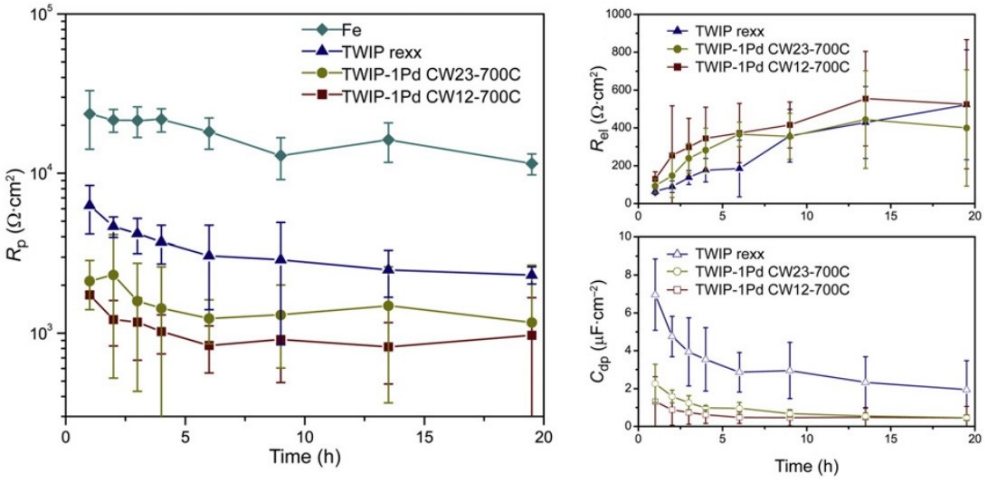

Figure 4.55: Polarisation resistance as well as resistance and capacitance of corrosion products for various TWIP (Fe21Mn0.7C) and TWIP-Pd (Fe21Mn0.7C1Pd) steels as a function of immersion time [166].

result in drops in corrosion resistance. Despite this, error bars corresponding to the final R_p approximation for Pd-containing and Pd-free TWIP, overlapped significantly. Also similar to what was observed in this study, Fe remained the most corrosion resistant throughout the test. Schinhammer *et al.* went on to test these materials *in vivo* [180] and noted that the Pd-containing alloy did not experience a significant amount of corrosion more than the pure Fe sample after 54 weeks. EIS results presented by Loffredo *et al.* [138] for long-term testing of TWIP (Fe-16Mn-0.7C) and TWIP-0.4Ag (Fe-16Mn-0.7C-0.4Ag) steels over 180 days resulted in low frequency impedances of approximately 30 $k\Omega \cdot cm^2$ irrespective of Ag content.

Based on the EIS results for all alloys tested in HBSS+Ca as well as the similarities observed between the Phase Two results and the published results by other groups [138, 166, 180], it is very likely that the addition of Ag for microgalvanic acceleration *in vivo*, does not offer long-term benefits.

4.2.2.5.3 Conclusions

The principal conclusions from this phase are summarised hereunder:

i. The volume of open surface porosity and surface roughness has a significant influence on the electrochemical behaviour of the material. Increase in porosity and roughness results in lower capacitive influence on the time constant associated with the metal-electrolyte interface and reduces the charge transfer resistance;

ii. Dense surfaces result in the formation of corrosion products with better structural integrity that present an increasingly "barrier"-like capacity for the degradation of the underlying metal as time progresses, based on evaluation over 24 h;

iii. Post-test surface analysis of FeMn in HBSS+Ca and physiological saline indicate that MnO inclusions could have a cathodic influence on the surrounding austenitic matrix in both solutions, in particular during the first few hours from initial contact with the testing electrolyte. Significant overlap of fitting results for FeMn with and without MnO, indicates that the long-term effects of MnO inclusions from a corrosion point-of-view, are not significant;

iv. The influence of MnO inclusions on initial corrosion of FeMnAg alloys needs further investigation as the likely presence of *two* cathodic phases relative to the austenitic FeMn matrix, does not have the expected synergistic effect on the charge transfer resistance. However, a similar overlap in the fitting results as well as surface analysis following 24 h of testing, seems to suggest that the long-term impact of MnO on corrosion, is similarly not significant;

v. The relatively rapid formation of corrosion products on FeMnAg when testing in HBSS+Ca, renders the cathodic Ag-rich phase rather ineffective. Due to this, the electrochemical performance of FeMn and FeMnAg seems to converge over 24 h of immersion. These results, backed up other published works, shed uncertainty on the *in vivo* applicability of including noble phases for effective long-term microgalvanic acceleration of FeMn degradation.

4.2.3 Phase Three - Investigating the influence of BSA additions to Ca-containing HBSS using EIS

The results in this section were presented at the 14th Biometal Conference in Alicante, in August 2022.

4.2.3.1 Choosing an antibacterial

The Bode plots for FeMn immersed in HBSS+Ca with 0.3 wt.% NaN_3 and HBSS+Ca with 1 vol.% Pen-Strep are shown in Figure 4.56. The same figure also includes the Bode plot for FeMn in HBSS+Ca from Phase Two for reference. The addition of NaN_3 clearly influenced the low-frequency impedance response

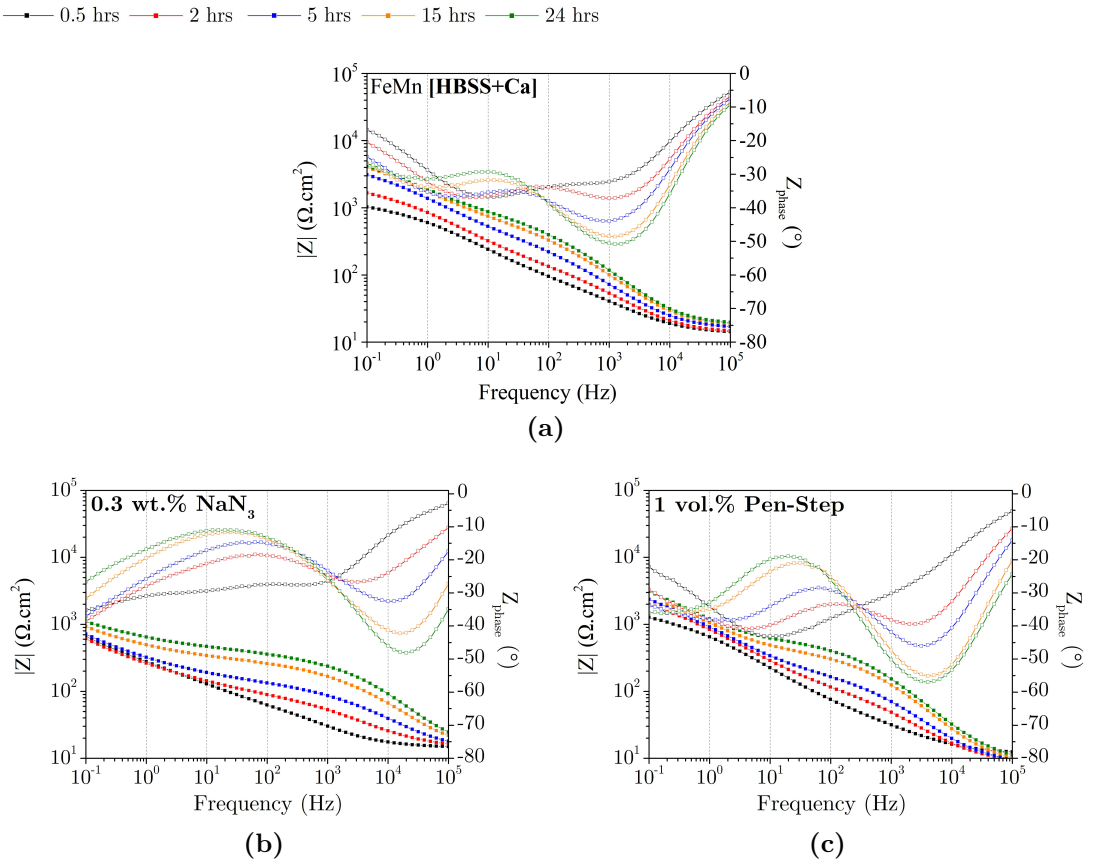

Figure 4.56: Bode plots for (a) FeMn in HBSS+Ca (from Phase Two) (b) FeMn in HBSS+Ca with 0.3 wt.% sodium azide (NaN_3) and (c) FeMn in HBSS+Ca with 1 vol.% Pen-Strep.

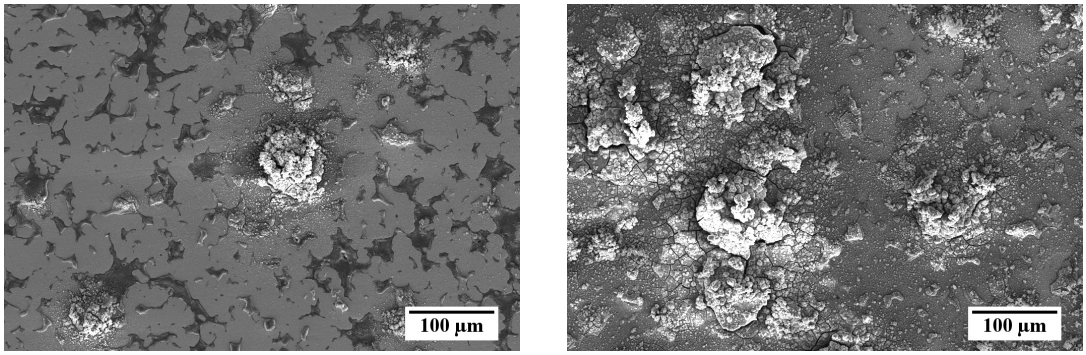

(a) (b)

Figure 4.57: SEM images of FeMn surface following a 24 h EIS test in HBSS+Ca with 1 vol.% Pen-Strep.

of the system and resulted in visible swelling of the mounting epoxy, including swelling of the epoxy within the porosity. In fact, similar to what was observed in Phase One with the highly porous FeMn samples (Figure 4.8 (b) and (e)), this sample also exhibited a relatively large negative phase shift at low frequencies indicating that the epoxy had been dislodged or otherwise rendered ineffective.

On the other hand, the addition of Pen-Strep to HBSS+Ca resulted in a very similar response at all frequencies. To confirm these observations, the results were modelled using the nested circuit in Figure 4.9. The fitting results are presented along with those for the tests carried out with BSA in Figure 4.59. The curve from this test corresponds very well to the repeated tests carried out with FeMn in HBSS+Ca from Phase Two. When observed using SEM, the surfaces tested in HBSS+Ca supplemented with Pen-Strep were shown to have similar corrosion product formations, as shown in Figure 4.57.

4.2.3.2 EIS testing with BSA

A representative Bode plot for FeMn immersed in HBSS+BSA is presented in Figure 4.58b adjacent to the result obtained for FeMn tested in HBSS+Ca in Phase Two for ease of reference. There were two main differences between the two plots. Impedance measurements for the sample tested in HBSS+BSA were generally lower by an order of magnitude over the 24 h testing period. Moreover, the phase shift in the EIS spectra from the first 2 h of the test barely exhibited

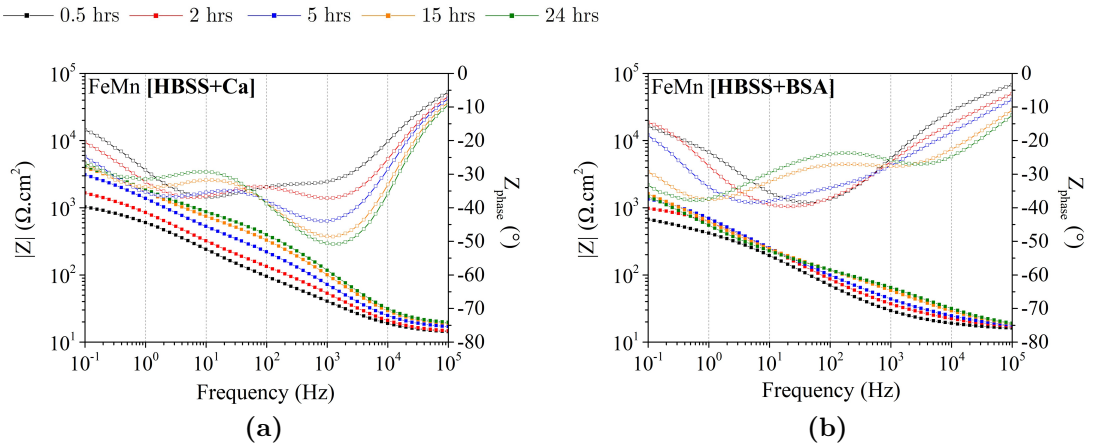

Figure 4.58: Bode plots for FeMn tested in (a) HBSS+Ca (from Phase Two) and (b) HBSS+BSA for 24 h.

any indication of the presence of a mid-frequency time constant associated with Ca/P-product precipitation.

In this section, a similar approach to the analysis presented in Phase Two is adopted wherein the fitting results for the repeated EIS spectra are presented in Figure 4.59 alongside the previous fitting results, for ease of comparison. This allows for easier evaluation of trends as opposed to error bars. Similarly, only data that was deemed reliable based on the goodness-of-fit and error measures calculated by EChem Analyst have been included in the plots, which is why some curves stop at an earlier time point than the 24 h test duration.

It is very apparent that the charge transfer resistance, R_{ct}, values for FeMn in HBSS+BSA were consistently lower than the R_{ct} values measured in HBSS+Ca. This confirms that the lower $|Z|$ values observed at low frequencies in the Bode plots were actually indicative of a generally lower corrosion resistance of FeMn in BSA-containing electrolyte. Furthermore, the delayed negative phase angle shift observed in Figure 4.58b, translated to relatively low R_{layer} values compared to those measured in HBSS+Ca. At around 3 h from immersion, R_{layer} increased quite drastically in all three repeats of the test, but started to decrease once again within approximately 2 h, converging at around 100 $\Omega \cdot cm^2$. As opposed to the fitting results presented in Phase One, the exponents of both CPE components representing the double layer capacitance (a_{dl}) and the capacitance of the cor-

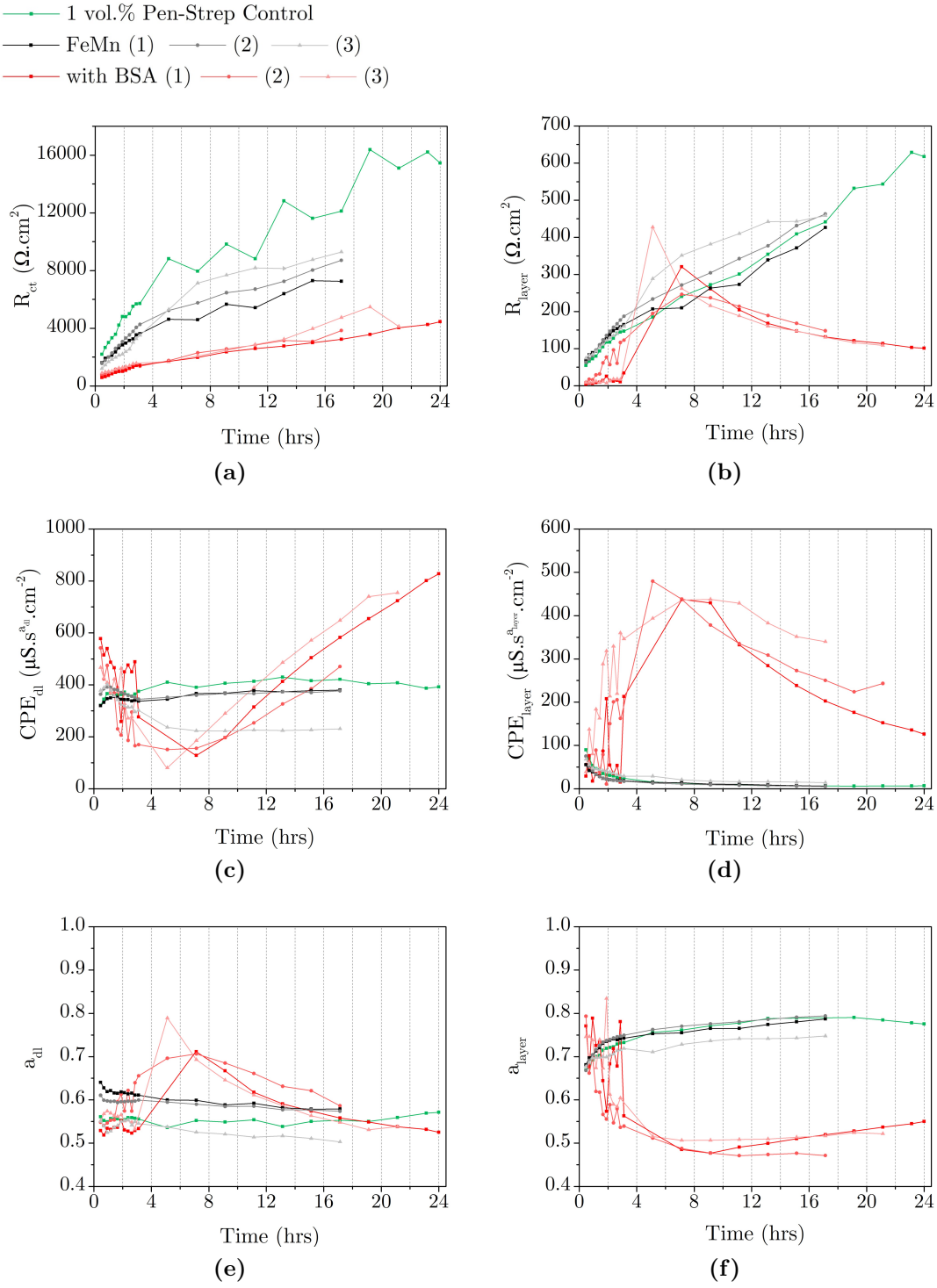

Figure 4.59: Fitting results for FeMn immersed in HBSS+BSA (with Pen-Strep) compared to HBSS+Ca (without Pen-Strep). The green curve shows the result of FeMn exposed to HBSS+Ca with 1 vol.% Pen-Strep. The fitted components correspond to the model presented in Figure 4.9.

rosion product layer (a_{layer}), both had values which were generally < 0.7. Due to the recommendations by Hsu and Mansfeld [65] not to use equation 4.1 to calculate the equivalent true capacitance in such cases, C_{layer} was not calculated for this data. Although CPE coefficients cannot be interpreted in the same way as true capacitances, observing the data in Figure 4.58 (c)-(f) can still provide some useful information. Firstly, the coefficient and exponent for both CPE components were considerably unstable compared to the stable behaviour exhibited' by their counterparts for FeMn tested in HBSS+Ca. For the CPE representing the double layer capacitance, the electrical characteristics in HBSS+BSA could be highly influenced by any adsorption of BSA molecules to the surface. Meanwhile whereas the evolution of CPE_{layer} seems to indicate that the impedance drops considerably for a few hours after around 3 h of immersion, the increase in $\mu S \cdot s^{a_{dl}} \cdot cm^2$ is accompanied by a simultaneous drop in the exponent value to signify less capacitive behaviour. Therefore, one cannot assume that the increase shown in Figure 4.59d is associated with a drop in impedance.

4.2.3.3 Post-testing SEM-EDS analysis

SEM micrographs of the samples tested in HBSS+BSA for 24 h are presented in Figure 4.60 with corresponding EDS analyses found in Table 4.8. The surface morphology of the sample tested in protein-containing electrolyte is clearly distinct from the surface tested in HBSS+Ca shown in Figure 4.47. Looking at the low magnification image in Figure 4.60a the surface is shown to be relatively uniform with isolated brightly-characterised clusters. EDS analysis in Figure 4.60b (point 1) shows that the clusters are rich in Ca, P, O and N. When observing higher magnification micrographs, the surface was shown to be covered by a uniform layer full of micro-cracks, likely due to dehydration. EDS analysis of the micro-cracked layer (point 2) shows enrichment in both C and O compared to corresponding regions on similar samples tested in HBSS+Ca (Table 4.6, point 10).

Several Ca/P-rich clusters all over the sample surface seemed to have collapsed, as shown in Figure 4.60 (c) and (d). It is not clear whether their structure was compromised during the testing period or during post-test material

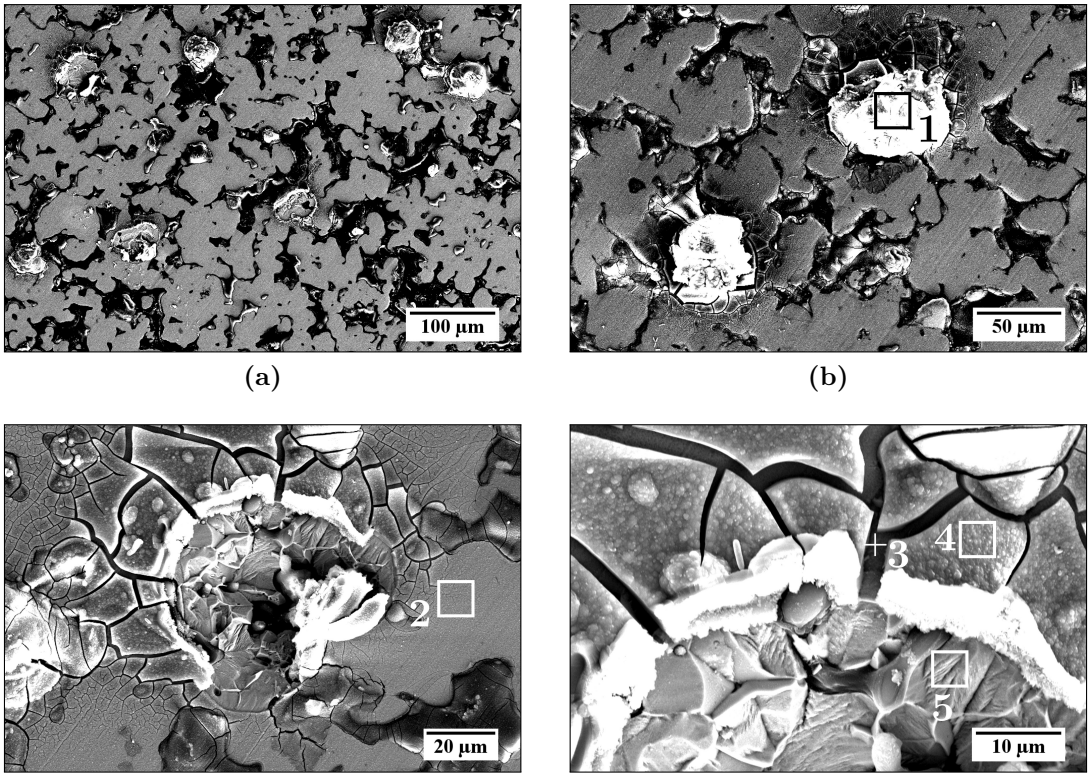

Figure 4.60: SEM-EDS analysis of FeMn surface following 24 h testing in HBSS+BSA. Numbered regions correspond to EDS analysis presented in Table 4.8.

Table 4.8: EDS analysis corresponding to regions-of-interest marked in Figure 4.60 in wt.%.

Pt.	O	C	Fe	Mn	P	Ca	Na	Cl	Mg	N
1	37.66	14.03	27.30	5.85	7.30	1.77	-	1.94	-	4.15
2	14.77	9.13	47.90	21.84	2.76	0.95	-	0.38	-	2.27
3	1.34	1.70	65.67	31.05	-	-	-	-	-	0.24
4	34.52	12.90	28.63	5.40	9.21	3.61	1.65	-	0.55	3.53
5	1.59	5.34	59.64	30.68	-	-	-	-	-	2.75

preparation for SEM analysis. However, pitted regions were commonly revealed underneath, exposing the original metal (points 3 and 5). The cracked layer

surrounding the pits (point 4), had a similar composition to that detected for isolated clusters (point 1) i.e. rich in Fe, O, Ca, P, C and N, relative to the rest of the surface.

4.2.3.4 Raman spectroscopy

Raman spectroscopy was carried out between 800-1800 cm^{-1} using a green laser (532 nm) on an untested FeMn surface and post-EIS surfaces tested in HBSS+Ca and HBSS+BSA. The spectra with labelled peaks are presented in Figure 4.61. The untested surface did not result in any discernible peaks other than the signal at around 1300 cm^{-1} which did not match any potential record from the database. The sample tested in HBSS+Ca exhibited a single peak that matched perfectly with *apatite* which exhibits a raman shift at 961.28 cm^{-1}. Records in the database for *calcium phosphate* and *hydroxyapatite* list their raman shifts at 965.07 cm^{-1} and 963.42 cm^{-1} respectively, both also very close to the detected peak. For the sample tested in HBSS+BSA, all the spectra followed the same trend exhibited by the representative spectrum presented in the graph. Major peaks corresponded to the carboxyl functional group (C=O) related to amino acids asymmetric (1600-1560 cm^{-1}) and symmetric (1420-1400 cm^{-1}) stretching, as well as C-N stretching (1500-1400 cm^{-1}). Although the other peaks are not particularly well defined,

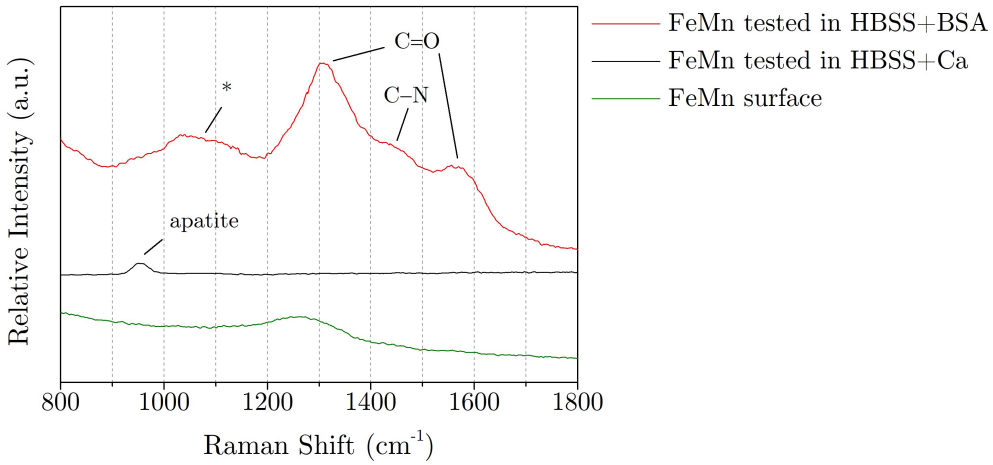

Figure 4.61: Raman spectra collected on untested FeMn, and 24 h EIS-tested FeMn in HBSS+Ca and in HBSS+BSA.

the spectrum for $CaCO_3$, exhibits its main peak at 1084.10 cm^{-1}, which falls within the non-indexed (*) region.

4.2.3.5 Discussion

Studies concerned with the behaviour of Fe-based alloys when exposed to protein-containing solutions have so far been limited to just a few, with the evolution of the corrosion mechanism over time remaining very much up for debate, as discussed in Section 2.1.4.2.3 [147, 150, 169–171]. From the available literature on the interaction of BSA with degrading metals, it is well known that there are two main affecting phenomena; chelation of divalent ions and adsorption of protein to the corroding metal surface.

The adsorption of protein onto the FeMn surfaces tested using EIS for 24 h was confirmed using Raman spectroscopy in Figure 4.61, where the carboxyl functional group C=O and the C-N bond were detected. Both groups are present in the dehydrated structure of BSA, as shown in Figure 4.62 and have previously been related to the presence of stretching vibrations of amide I in protein [175]. Although not the most reliable measure, the higher N content detected over corrosion products relative to that detected on the metal surface in EDS results presented in Table 4.8 (points 1 and 4), might also be indicative of residual protein on the tested surface. Therefore, while the isoelectric point (IEP) theory discussed in Section 2.1.4.2.3, indicates that it is less likely for BSA to adsorb to corroding Fe-based alloys when compared to degrading Mg-alloys for instance, adsorption of BSA to FeMn surfaces is still possible. Another sign of BSA interaction with

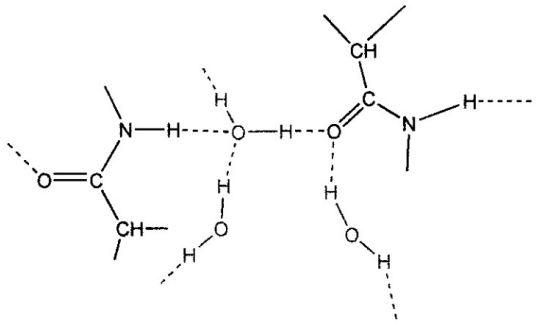

Figure 4.62: Variation of dehydrated structure of BSA [254].

the metal surface is evident in the evolution of the CPE_{dl} and a_{dl}. The formation of the double layer in HBSS+BSA was shown to be relatively complex based on the instability of both values relative to those modelled for FeMn tested in HBSS+Ca, as seen in Figure 4.58 (c) and (e). Whereas both the CPE coefficient and exponent had stabilised after 24 h in HBSS+Ca, in HBSS+BSA the values were still evolving, signifying an ever-changing scenario at the metal-electrolyte interface.

Despite the clear interaction of BSA with the FeMn surface, the charge-transfer resistance R_{ct} in Figure 4.58a, was considerably lower in HBSS+BSA compared to HBSS+Ca, both at the start of the test and in the consecutive 24 h. This was also observed by Huang *et al.* [171] who measured significantly lower $|Z|$ at 0.1 Hz for both Fe and Fe22Mn0.6C in SBF with 10 $g\,L^{-1}$ BSA, compared to SBF only. Similar to what was observed in this study, Huang *et al.* also reported an increase in the measured impedances with time, which they attributed to a growing "barrier" effect as the BSA starts to adsorb to the surface. However, as shown in Phase One and Two of this work, the R_{ct} values also increase for FeMn exposed to HBSS or HBSS+Ca and therefore the increase with time need not necessarily be due to the adsorption, but rather growing metal oxides or hydroxides. The corrosion product layer observed using SEM, particularly in Figure 4.60c, seemed particularly dense and rich in both metal as well as C and O. Although not necessarily a metal-carbonate, its formation provided conditions at the metal-corrosion product interface that encouraged pitting. Despite the fact that areas of localised corrosion were observed all over the sample surface, the extent of attack in these locations was not significant enough to result in major drops in the R_{ct} values, as is typical of pitting corrosion in stainless steels for instance [255]. However, it could have contributed to maintaining the resistance at relatively low $\Omega \cdot cm^2$. Facilitated release of metal ions could have also been facilitated by the chelating ability of BSA [147].

Fe^{2+} and Mn^{2+} ions are not the only ions chelated by BSA. Chelation of Ca^{2+} by the same protein has been reported in literature in various studies on biodegradable metals [75, 170]. Since Ca^{2+}-chelation is not dependant on the corrosion rate, it follows that it could take place upon addition of BSA to the electrolyte. This was evident in the results present in this testing phase by the

delayed increase in R_{layer} in Figure 4.58b, due to lack of availability of Ca^{2+} to react with phosphate and hydroxyl ions to precipitate HA-like products. Despite chelation, Ca/P-rich precipitates could still be observed on the sample surfaces in Figure 4.60. A combination of chelation [147] and corrosion product destabilisation by the formation of pits [153], could have led to the decrease in R_{layer} resistances after around 5 to 7 h from immersion and the associated instability in the CPE characteristics of the same layer. The modelling results indicate that the protective characteristic of this layer is not regained within the consecutive hours, at least when considering the R_{layer} component. Naturally, it is difficult to hypothesise how this result could be interpreted to predict how the HA-like layer would evolve *in vivo* in the presence of protein. In the *in vitro* situation, the test is exposed to a finite amount of BSA and Ca^{2+} ions and therefore product reprecipitation and/or constant binding of Ca^{2+} ions were not factored into this model.

An interesting observation was noted in the work published by Huang *et al.* [171] on the influence of 10 $g\,L^{-1}$ BSA added to SBF when testing wrought Fe22Mn0.6C. The authors also conducted 24 h tests using EIS however only modelled the final spectrum. The results of the fitting exercise, presented in Table 4.9, are considerably similar to the modelled values in this work for spectra collected between 3 and 5 h following immersion, in terms of the relative values with and without BSA in the two studies. However, Huang *et al.* did not observe any pitting in their work. This observation could indicate that increasing the BSA concentration from 10.0 $g\,L^{-1}$ to 20.6 $g\,L^{-1}$ could result in acceleration of the corrosion timeline. Having said this, the difference in processing method as well as the variation in the metal's composition surely have their own influence on the result.

Table 4.9: EIS fitting results for wrought Fe22Mn0.6C immersed in SBF and SBF with 10 $g\,L^{-1}$ BSA after 24 h. Results published by Huang *et al.* [171].

	$\mathbf{R_{ct}}$	$\mathbf{R_p}$	$\mathbf{CPE_{layer}}$	$\mathbf{a_{layer}}$	$\mathbf{CPE_{dl}}$	$\mathbf{a_{dl}}$
SBF	2470	16	71	0.68	811	0.81
SBF+BSA	941	3	504	0.86	327	0.74

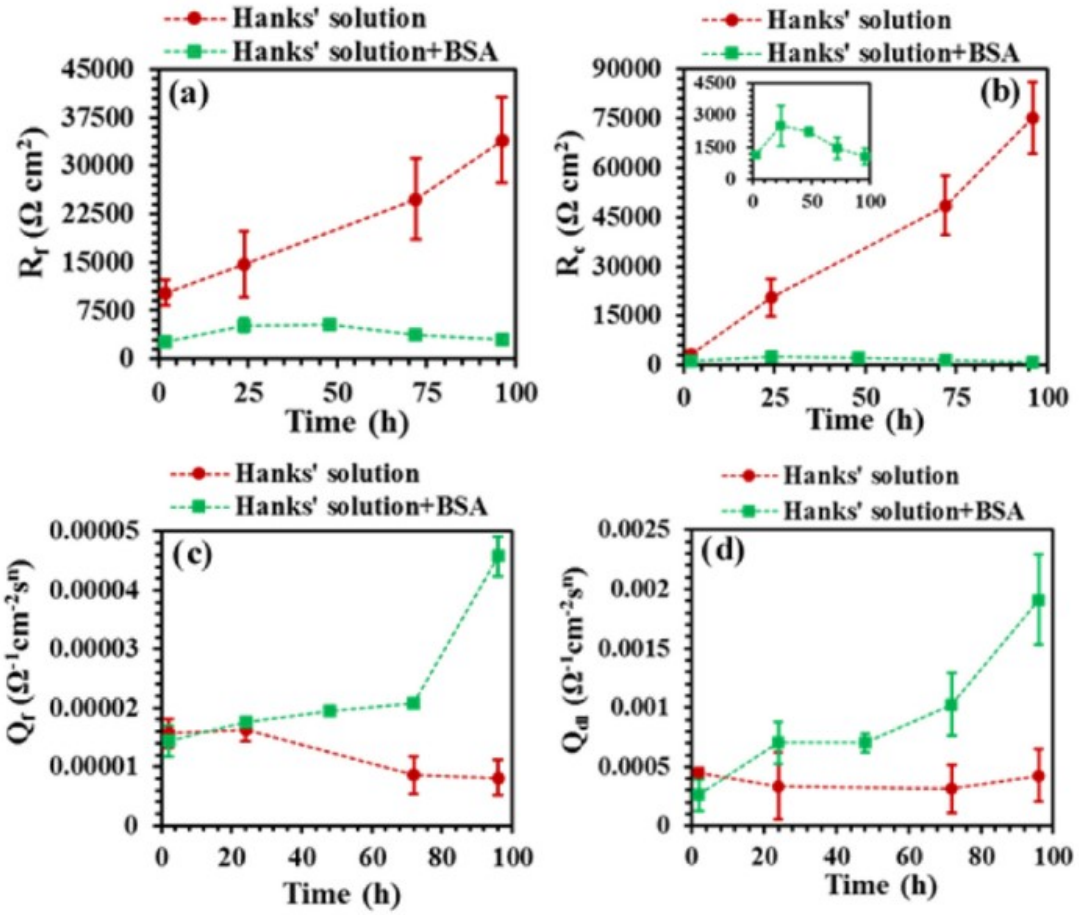

Figure 4.63: Evolution of modelled EIS values for AZ91D tested in HBSS and HBSS+BSA. Results obtained by Harandi *et al.* [172].

EIS evolution results for a Mg-alloy (AZ91D) in HBSS and HBSS+BSA by Harandi *et al.* [172] also seemed to indicate very similar trends in the evolution of the modelled R_{ct}, R_{layer}, CPE_{dl} and CPE_{layer} (R_c, R_f, Q_{dl} and Q_f respectively in the study) at the 24 h mark, according to plots presented in Figure 4.63. This raises a new question as to whether the alloy has significant influence on the corrosion behaviour when subjected to BSA-containing electrolyte in an *in vitro* environment. Should the trends published by Harandi *et al.* for the subsequent 75 h of EIS testing hold true also for FeMn, then the lack of protective product formation observed in the first 24 h could very likely persist in longer-term tests.

4.2.3.5.1 Conclusions

The conclusions from this section are summarised hereunder.

i. The addition of 20.6 $g\,L^{-1}$ BSA to HBSS+Ca results in the formation of corrosion product layers that are not particularly stable and whose barrier properties do not provide significant resistance to further corrosion;

ii. Chelation of Ca^{2+} ions results in delayed formation of the HA-like protective layer on the corroding surface and prevents its long-term stability in a finite testing volume;

iii. BSA additions to the testing electrolyte seem to encourage localised corrosion of Fe-based alloys when added in relatively large quantities (20.6 $g\,L^{-1}$), confirming existing observations in literature [147, 170];

iv. Increasing the complexity of the testing electrolyte seems to reduce the extent of the influence of the material composition on its corrosion behaviour.

4.2.4 Phase Four - Static Immersion Testing

This phase presents results and analysis following static immersion of porous FeMn samples tested over a period of 28 days. Following 24-h testing in previous testing phases, this phase was aimed at determining how the testing electrolytes considered throughout this study, could affect the degradation of FeMn over a longer period of time.

4.2.4.1 SEM-EDS analysis

4.2.4.1.1 Surfaces

SEM images of surfaces after 7, 14 and 28 days are shown in Figures 4.64-4.66 in each case showing FeMn tested in HBSS in (a), those tested in HBSS+Ca in (b) and samples tested in HBSS+BSA in (c). Multiple micrographs are presented to exhibit a clearer representation of varying surface morphologies on the same sample. Numbered regions on each micrograph correspond to EDS analysis collectively presented in Table 4.10.

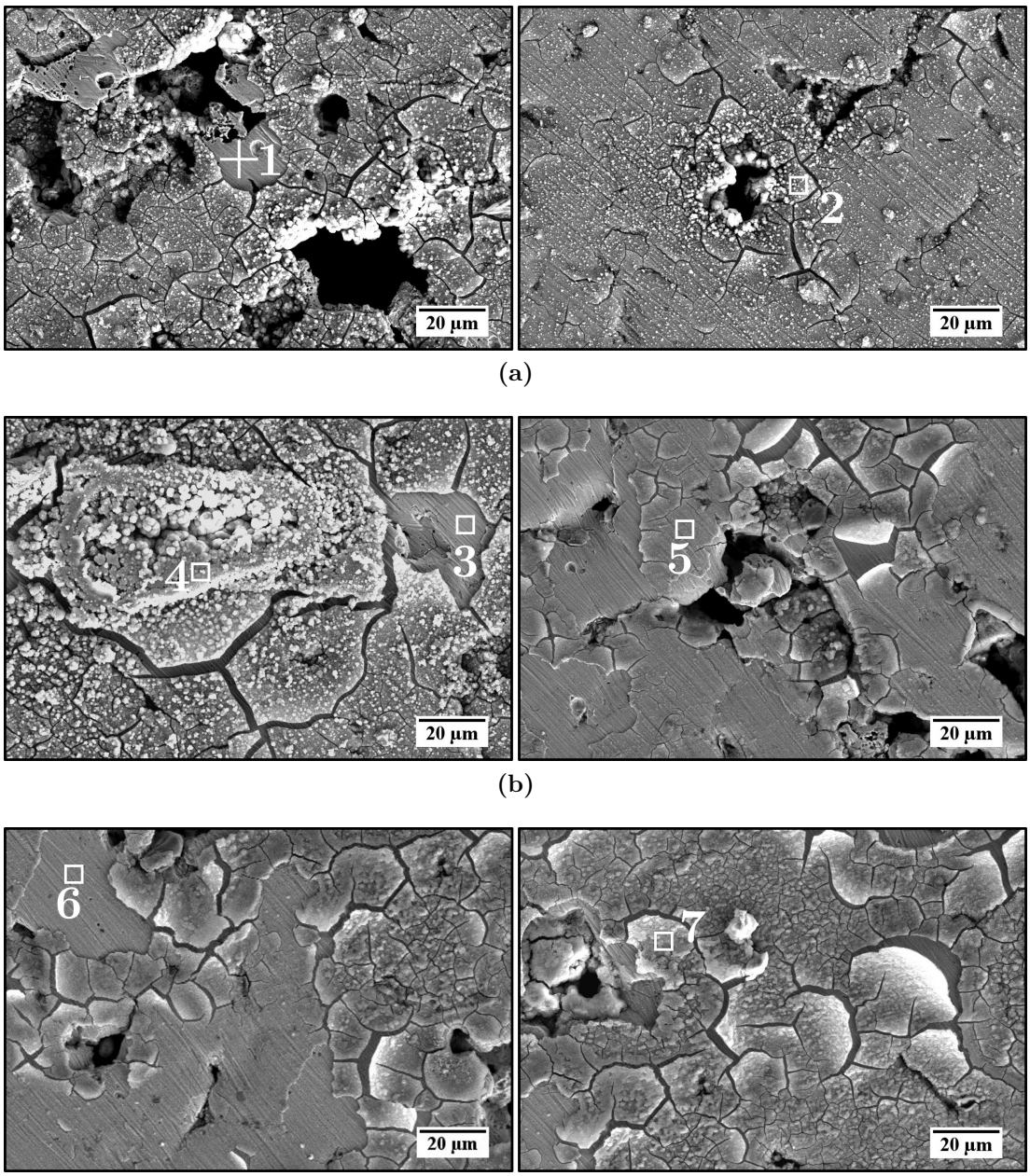

Figure 4.64: SEM images of the surface of representative FeMn samples following 7 days of immersion in (a) HBSS (b) HBSS+Ca and (c) HBSS+BSA at 37°C. Numbered regions-of-interest correspond to EDS analysis listed in Table 4.10.

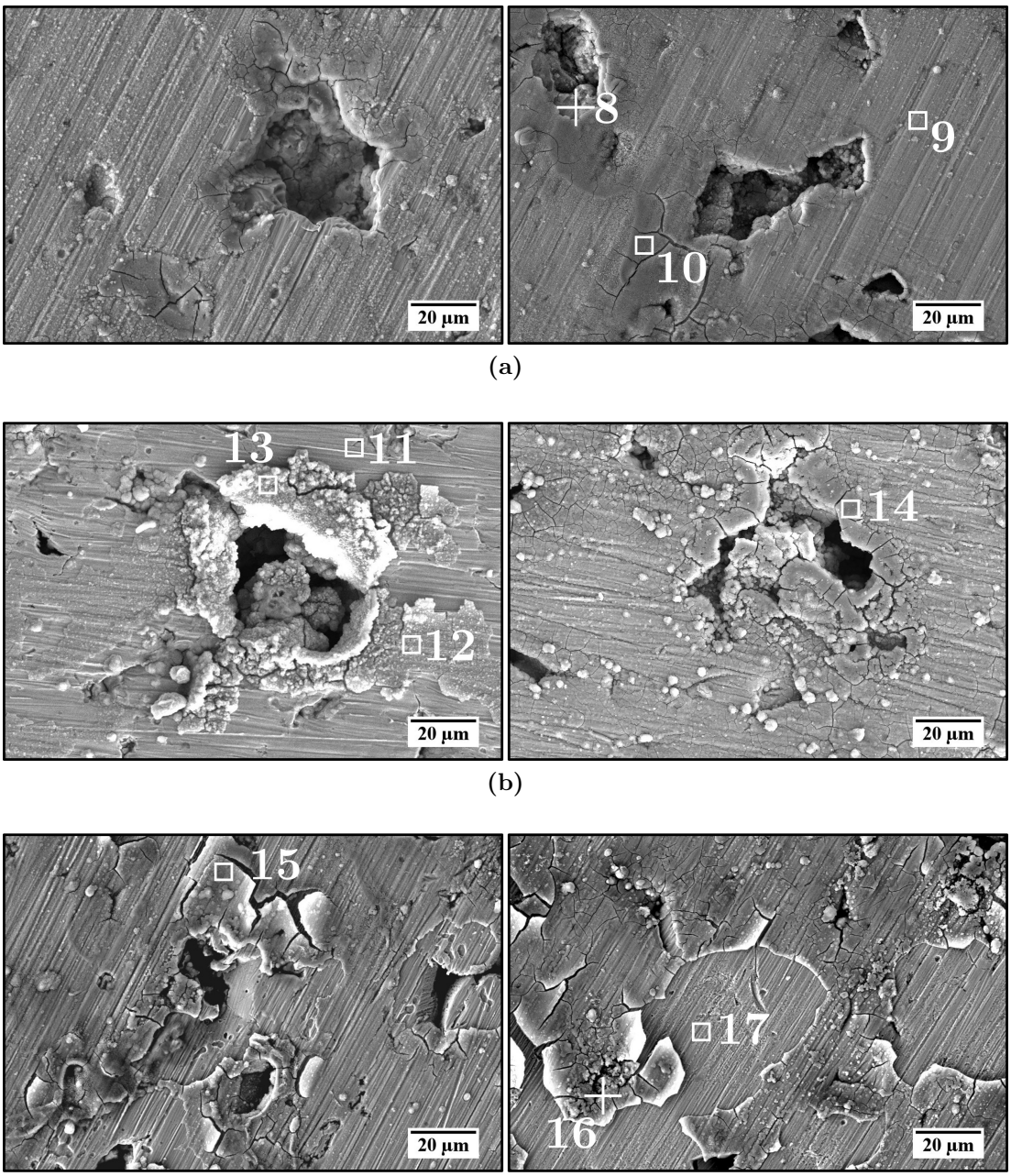

Figure 4.65: SEM images of the surface of representative FeMn samples following 14 days of immersion in (a) HBSS (b) HBSS+Ca and (c) HBSS+BSA at 37°C. Numbered regions-of-interest correspond to EDS analysis listed in Table 4.10.

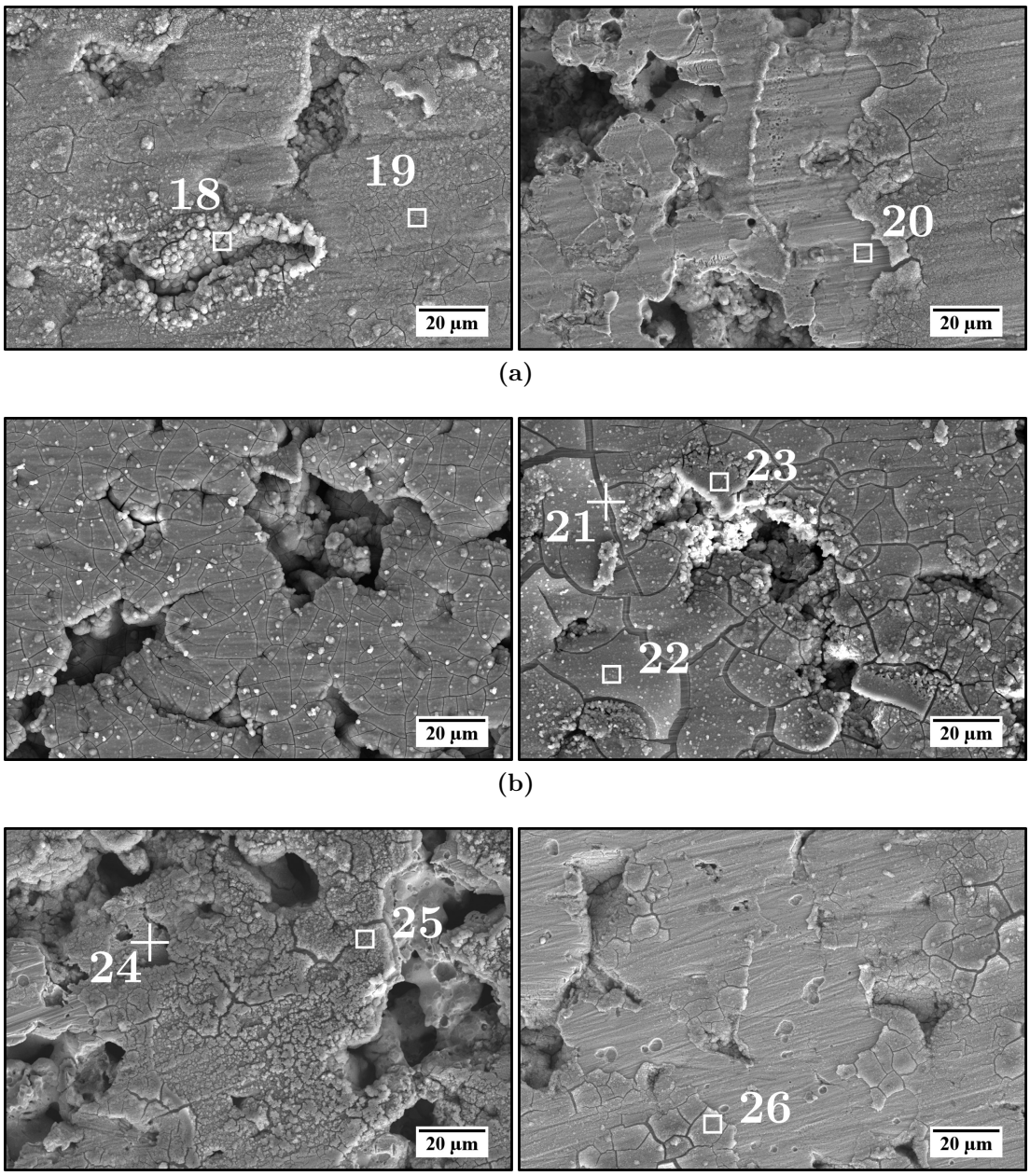

Figure 4.66: SEM images of the surface of representative FeMn samples following 28 days of immersion in (a) HBSS (b) HBSS+Ca and (c) HBSS+BSA at 37°C. Numbered regions-of-interest correspond to EDS analysis listed in Table 4.10.

Table 4.10: EDS analysis in wt.% corresponding to numbered regions-of-interest marked in Figures 4.64-4.66 for surfaces tested in HBSS, HBSS+Ca and HBSS+BSA for 7, 14 and 28 days.

					HBSS			HBSS+Ca			HBSS+BSA
	Pt.	**O**	**C**	**Fe**	**Mn**	**P**	**Ca**	**Na**	**Cl**	**Mg**	**N**
Day 7	**1**	01.43	03.83	30.72	63.23	00.25	-	00.44	00.10	-	-
	2	23.57	04.20	35.32	27.27	07.68	-	01.96	-	-	-
	3	01.90	03.68	62.48	31.19	00.48	-	00.27	-	-	-
	4	37.44	05.97	16.00	22.59	12.47	03.77	01.09	00.44	00.24	-
	5	22.62	05.28	33.65	25.97	07.85	03.38	00.87	-	00.38	-
	6	03.23	03.71	60.04	32.43	00.42	00.17	-	-	-	-
	7	22.87	06.62	36.12	25.87	05.69	01.90	00.41	00.27	00.25	-
Day 14	**8**	03.53	04.10	60.65	31.72	-	-	-	-	-	-
	9	12.75	04.49	49.07	28.19	02.84	-	00.59	-	00.19	01.88
	10	33.34	05.01	26.50	23.69	08.54	-	00.86	-	-	02.06
	11	02.16	04.69	59.31	31.73	-	-	-	-	-	02.11
	12	18.02	05.69	38.17	27.23	04.54	03.53	-	00.70	00.73	01.48
	13	27.83	07.59	29.13	28.81	01.67	-	-	03.29	-	01.68
	14	35.69	07.76	03.98	11.20	14.82	21.68	-	00.34	02.40	02.13
	15	12.80	05.96	46.50	25.50	03.90	02.40	00.45	00.39	00.41	01.72
	16	26.63	11.25	25.17	25.00	05.86	02.28	00.40	-	00.42	02.99
	17	01.16	04.16	60.72	31.78	-	-	-	-	-	02.18
Day 28	**18**	36.97	05.36	22.07	24.90	08.85	-	-	-	-	01.85
	19	14.05	05.27	50.17	26.57	02.12	-	-	-	-	01.82
	20	05.99	04.19	56.47	30.62	00.82	-	-	-	-	01.91
	21	02.54	04.32	58.18	31.50	00.41	00.45	-	-	-	02.60
	22	16.05	06.31	39.76	23.42	05.00	06.28	00.49	-	01.23	01.39
	23	38.98	07.56	00.99	10.31	16.08	21.44	00.59	-	02.18	01.87
	24	02.05	05.34	58.05	31.84	-	-	-	-	-	05.34
	25	18.99	08.07	37.96	22.22	05.57	03.36	00.59	00.66	00.68	01.91
	26	14.70	08.52	42.35	27.64	02.78	00.77	00.83	-	-	02.41

Samples immersed in HBSS (Figures 4.64-4.66 (a)) all showed signs of a corrosion product layer that was considerably uniform and grew more densely around and within porosity despite evident cracks in the same areas. Grinding marks were still clearly distinguishable after the first 14 days but became less so after 28 days. Similarly, samples tested in HBSS+Ca (Figures 4.64-4.66 (b)) showed evidence of a corrosion product layer present all over the sample surface. As evident in the images, the morphology varied significantly from one area to another, however as observed with samples tested in HBSS, corrosion products were particularly dense close to pores. In both electrolytes, the denser product was more rich in O, Mn, P and Ca (Pts 2, 4, 13, 14, 18, 23) compared to other regions of the corrosion product layers (Pts 5, 9, 12, 19, 22). Elemental analyses of samples tested in HBSS+BSA (Figures 4.64-4.66 (c)) generally followed similar patterns although the amount of Ca and P content detected on any part of the surface was considerably lower than any other point of analysis on surfaces tested in HBSS+Ca (Pts. 7, 15, 16, 25, 26). Micrographs for samples tested in HBSS+BSA in particular revealed shallow localised corrosion regions on the metal surface wherever the corrosion product flaked off to reveal the substrate underneath. There was no noticeable increase in N content on the tested surfaces which could be indicative of adsorbed BSA, however EDS is naturally not particularly reliable for detecting minute shifts in N wt.%.

4.2.4.1.2 Cross-sections

Cross-sections with corresponding EDS maps of C, Fe, Mn, O, P and Ca (where applicable) are presented in Figures 4.67-4.69. The scale bars on the SEM images take into consideration the varying magnification factors due to the use of tapered steel sections during cold mounting of the samples, as schematically represented in Figure 3.6[1].

Samples immersed in HBSS consistently showed the presence of a layer rich in both O and P with no clear differentiation indicating the formation of two separate layers of corrosion product. Since EDS analysis in Table 4.10 showed considerably higher wt.% of O detected in P or Ca/P-rich corrosion products

[1]Magnification is only achieved vertically, hence the vertical orientation of the scale bars.

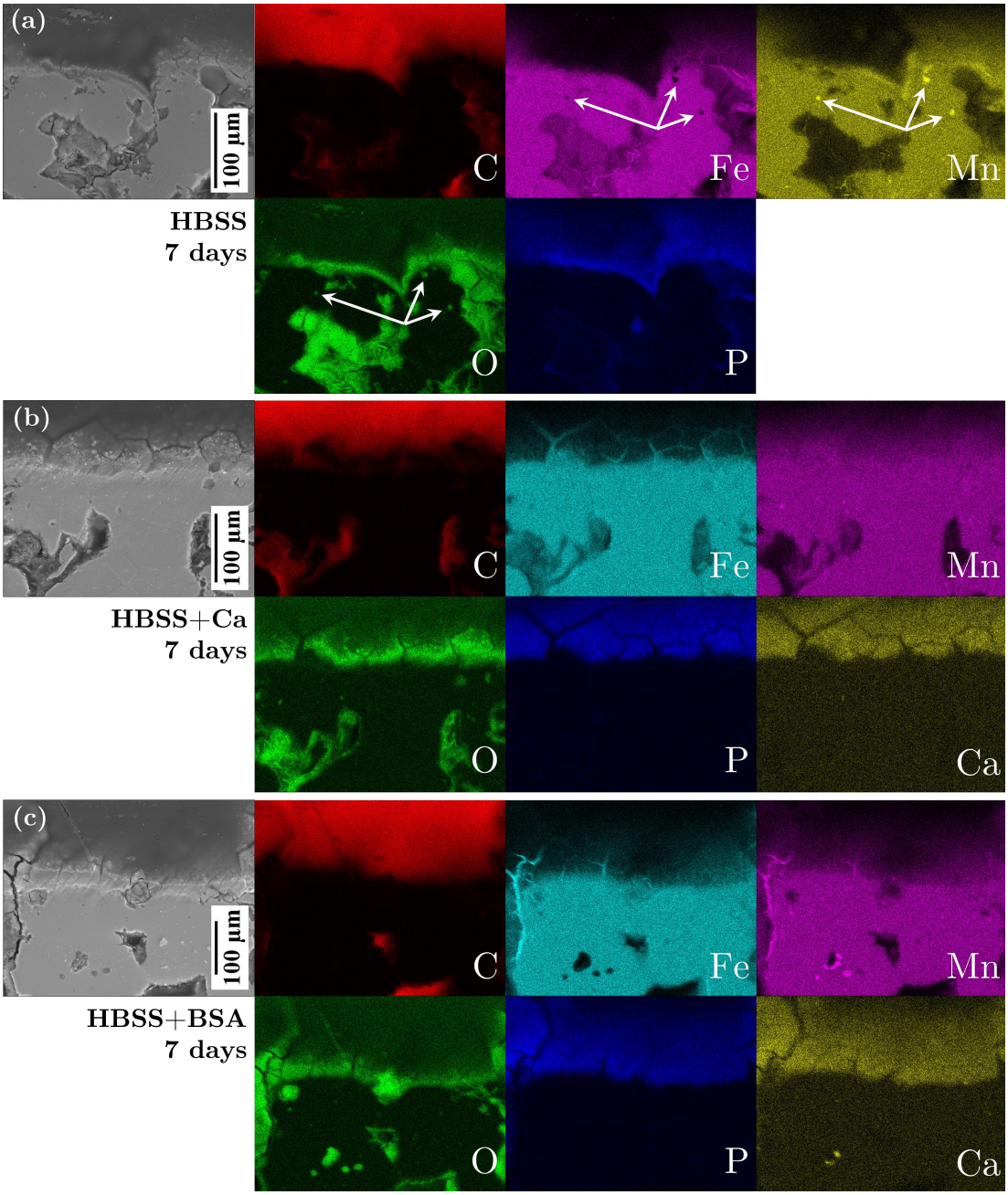

Figure 4.67: SEM image with corresponding EDS maps showing C, Fe, Mn, O, P and Ca distribution on representative cross-sections of FeMn samples immersed in (a) HBSS (b) HBSS+Ca and (c) HBSS+BSA for 7 days at 37°C. Arrows in (a) indicate the presence of MnO in the bulk.

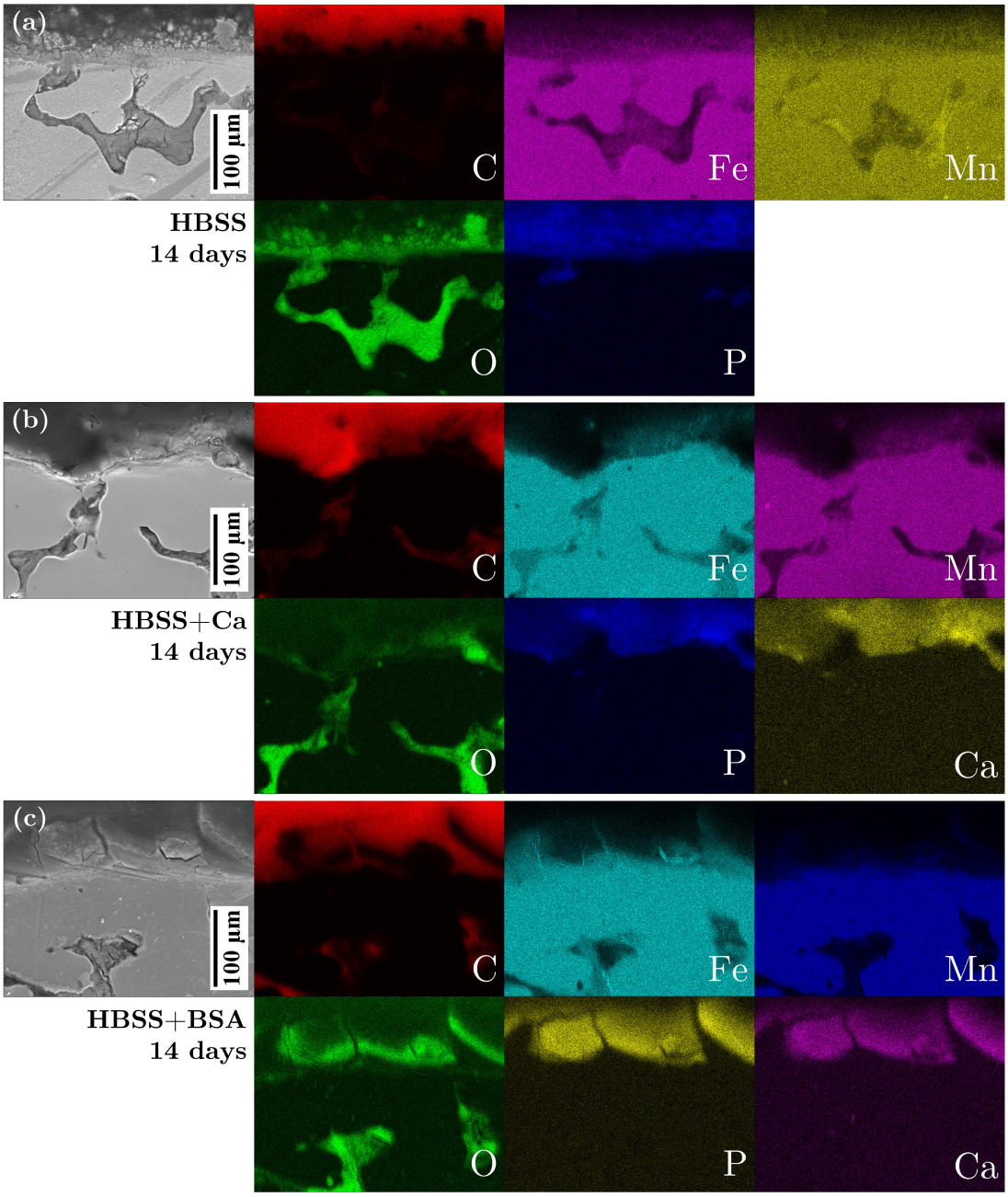

Figure 4.68: SEM image with corresponding EDS maps showing C, Fe, Mn, O, P and Ca distribution on representative cross-sections of FeMn samples immersed in (a) HBSS (b) HBSS+Ca and (c) HBSS+BSA for 14 days at 37°C.

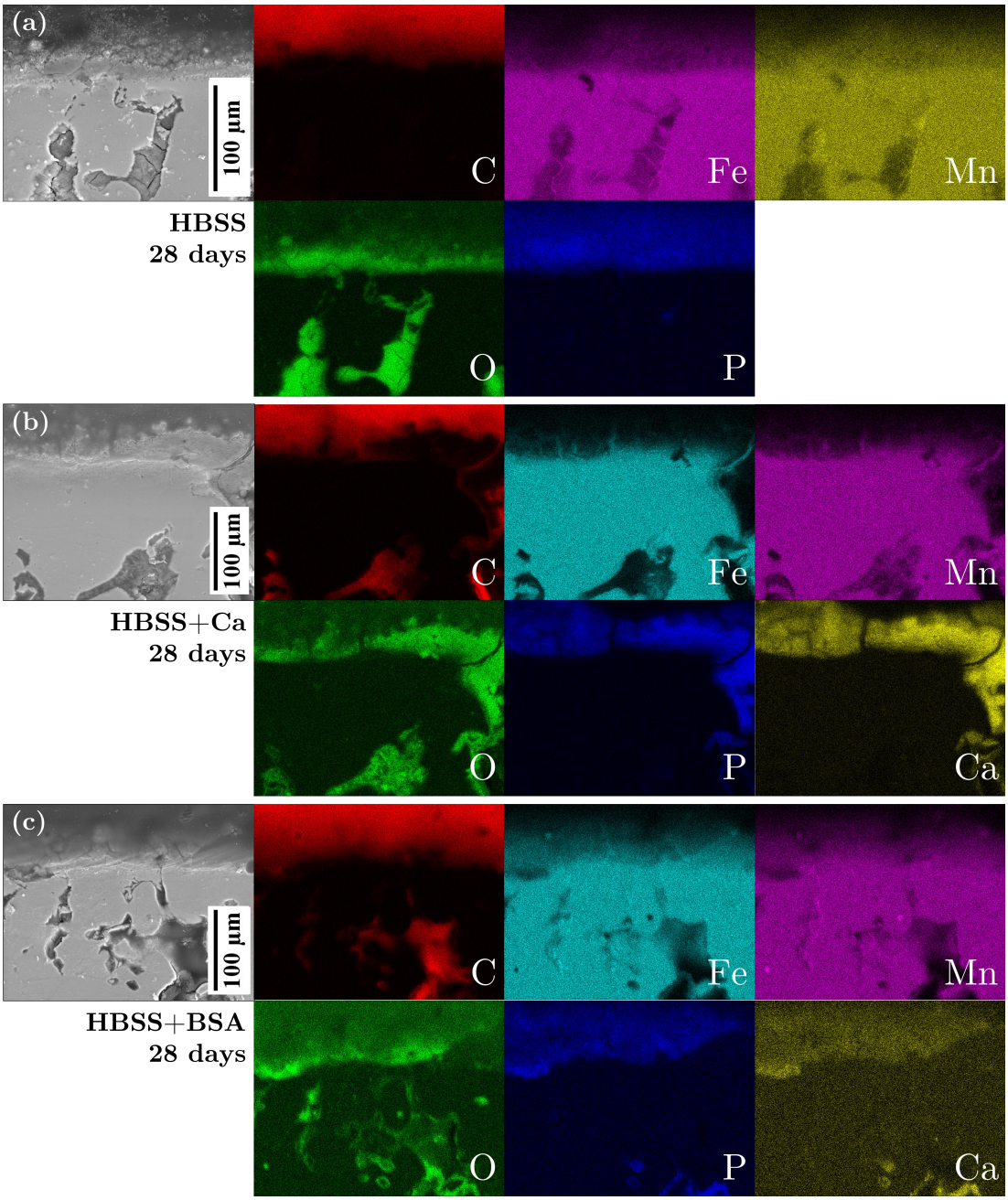

Figure 4.69: SEM image with corresponding EDS maps showing C, Fe, Mn, O, P and Ca distribution on representative cross-sections of FeMn samples immersed in (a) HBSS (b) HBSS+Ca and (c) HBSS+BSA for 28 days at 37°C.

compared with metal-rich oxide/hydroxide layers, the visibility of such a layer might be limited due to significantly less bright distribution of the O in elemental maps. Overlaying the maps onto the SEM image showed a slight enrichment of Mn around a pore-like depression in the substrate after 7 days of immersion in Figure 4.67a. After 14 and 28 days in HBSS, surfaces seem to be similarly composed of a layer of mixed metal phosphates. Samples immersed in HBSS+Ca exhibited a strong, if not uniform, presence of Ca and P products irrespective of the immersion time. Once again, there seemed to be an absence of a multi-layer structure to the products formed. Maps of P and Ca when analysing cross-sections for samples immersed in HBSS+BSA were generally less intense when compared to maps for samples immersed in HBSS+Ca, as expected. The O distribution indicated that even on these samples, a layer of corrosion product was rather uniformly present.

Elemental composition of corrosion products formed within the pores showed consistent enrichment in both Fe and O. Areas where an obvious high intensity of Mn correspond with a similarly intense region of O concentration (for instance areas pointed out by arrows in Figure 4.67a), indicate the location of MnO inclusions within the substrate and are naturally not a result of the corrosion test. The absence of a strong detection of elements like P and Ca in the corrosion products within the pores indicates that the electrolyte had limited penetration beyond the surface of the samples. Corrosion products formed within closed pores are likely the result of reactions with air and other potential contaminants trapped within during processing.

4.2.4.2 Weight loss measurements

The mass loss measurements following the corrosion product removal procedure after 14 and 28 days of testing, are presented in Figure 4.70. The average mass of samples after 14 days of immersion was higher than the original sample mass. Moreover there was not a statistically significant difference between the masses of the samples tested in different electrolytes. After 28 days, samples tested in HBSS exhibited the highest average mass loss at $25.41 \pm 2.81\ \mathrm{mg\,cm^{-2}}$. However, several samples tested in HBSS+Ca and HBSS+BSA for 28 days still exhibited

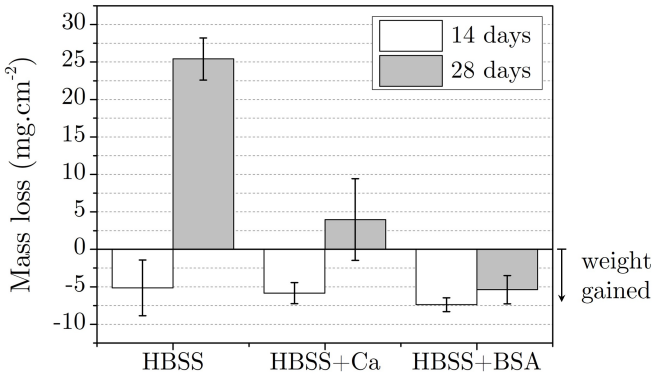

Figure 4.70: Mass loss measurements for FeMn in HBSS, HBSS+Ca and HBSS+BSA after an immersion period of 14 and 28 days. Error bars represent calculated standard error (n = 5).

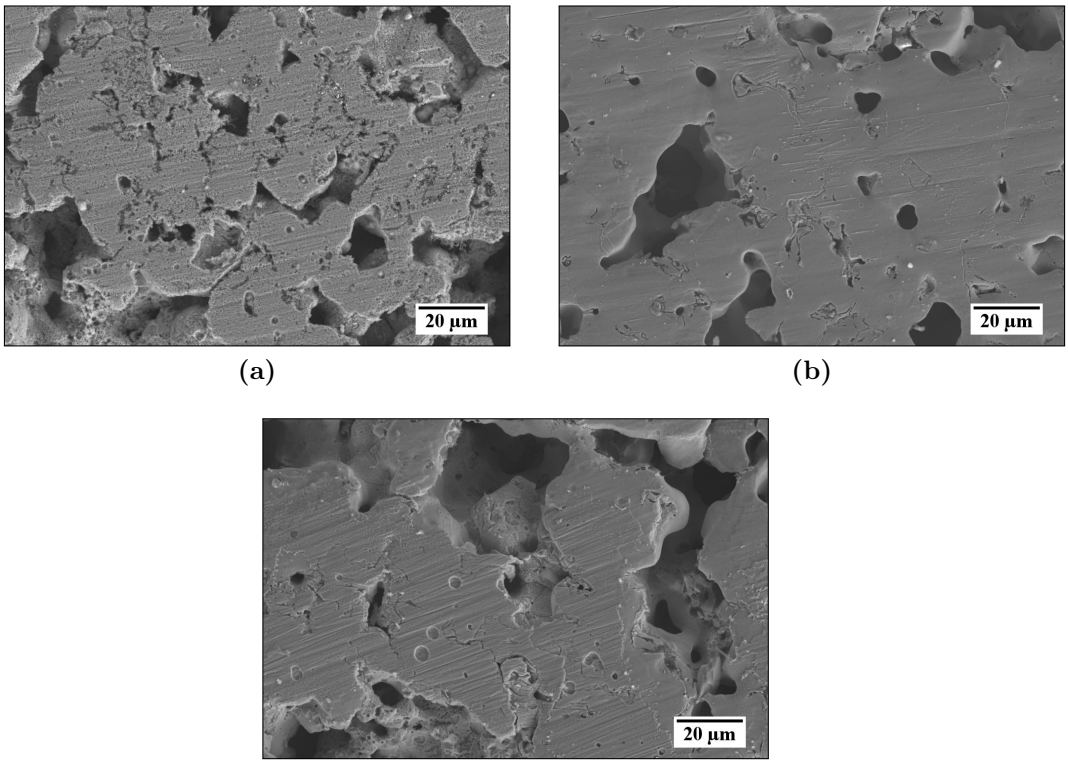

(a) **(b)**

(c)

Figure 4.71: SEM images of FeMn surfaces tested in (a) HBSS (b) HBSS+Ca and (c) HBSS+BSA for 28 days and cleaned from surface corrosion products using a 1 M HCl with 3.5 g L^{-1} HMTA solution for 5 min.

an increase in weight resulting in a negative average mass loss. This was recorded despite use of the cleaning procedure in 1 M HCL with 3.5 g L^{-1} HMTA, assisted by ultrasonication for 15 min.

Representative samples from the samples used for weight loss measurements after immersion for 28 days, were imaged using SEM after the etching procedure. The underlying metal surfaces are shown in Figure 4.71. The surface tested in HBSS was considerably attacked with the surface exhibiting what could be described as closely spaced shallow pits all over the surface. The same type of attack extended to within the pores as shown in the bottom left corner of the micrograph in Figure 4.71a. The sample tested in HBSS+Ca, shown in (b), was considerably free of the described morphology, however the grinding marks from the sample preparation stage were not visible in a significant portion of the analysed surface. In the case of the FeMn surface tested in HBSS+BSA, sections of the surface were similarly free of grinding marks however other areas which were not, also showed signed of localised attack as shown in (c).

4.2.4.3 pH measurement

The measurements of solution pH following each testing period are presented in Figure 4.72a. In (b) the pH of the testing solution blanks i.e. the same solutions exposed to the same testing conditions without containing any FeMn samples, were subtracted from the average pH of the testing solutions in which the samples were tested. The change represents the increase in pH units due to the influence of the corroding metal. The change in pH for HBSS testing solutions was consistently the highest, increasing by 1 unit after just 7 days and then remaining relatively stable. The pH of HBSS+BSA also increased by 0.25 units and remained stable in the next 3 weeks. On the other hand the pH of HBSS+Ca remained stable for the first two weeks and then increased to 0.3 units by the end of the 28 day testing period.

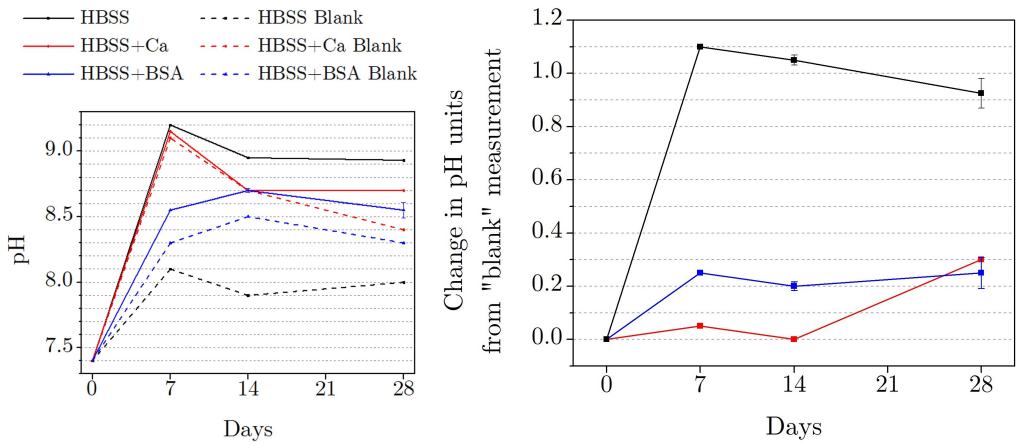

Figure 4.72: Plots of (a) average pH of solution after each testing period (standard error, n = 4) plotted along with pH measurement of corresponding blank solutions and (b) difference in pH units between the average measured pH (standard error, n = 4) and the pH of the blank. Note that no error was calculated for measurements carried out after 7 days since only 2 samples were tested for that interval.

4.2.4.4 Raman spectroscopy

Representative samples were analysed using Raman spectroscopy following each immersion period. The spectra are presented in Figure 4.73. Although the principal aim was to determine whether there were any signs of adsorbed BSA following the test as observed following 24 h EIS testing in Phase Three, testing all the samples was carried out to identify any other notable peaks that could assist in characterising the formed corrosion products.

The spectra for samples tested in HBSS all exhibited Raman shifts between 900-1200 cm^{-1} although the absence of any distinct peak within the range, limited the ability to identify the compound or functional groups that caused the shift. Rather intense peaks were also registered below 800 cm^{-1}. Once again the absence of a distinct peak presented similar difficulties however, based on Raman studies on Fe-based oxides by Testa *et al.* [256], a number of oxides including magnetite (Fe_3O_4), maghemite (γ-Fe_2O_3), hematite (α-Fe_2O_3) and wüstite (FeO), all exhibit major peaks between 500-800 cm^{-1} as seen in Figure 4.74a. The spectrum for maghemite is similar to the spectra obtained in this work how-

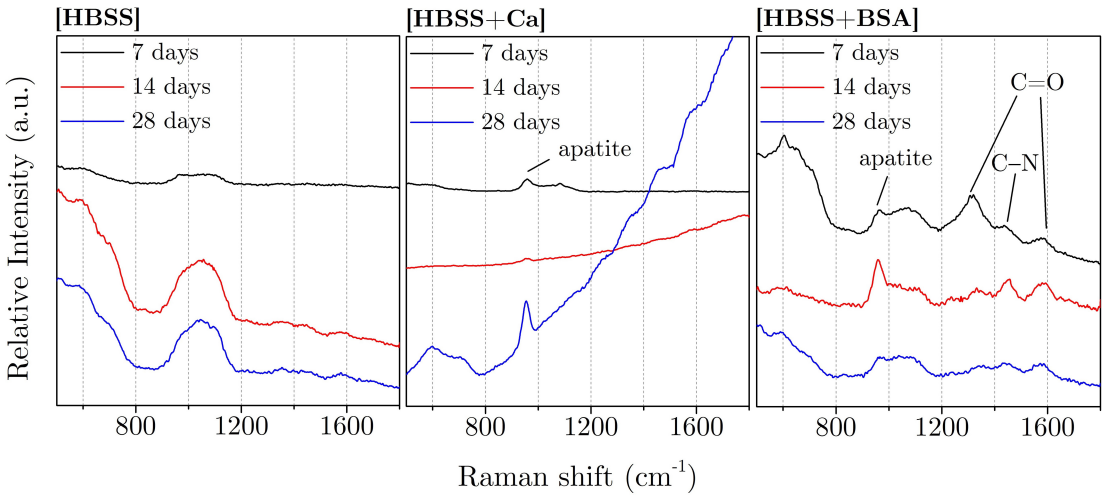

Figure 4.73: Raman spectrum collected on porous FeMn samples tested in HBSS, HBSS+Ca and HBSS+BSA after 7, 14 and 28 days.

ever Figure 4.74 (b) and (c) show how intermediate spectra in the transition from magnetite to hematite as well as stoichiometric variants of $(Fe,Mn)_3O_4$ all exhibit similar patterns. Huang *et al.* [171] also interpreted wide peaks within this region to be a sign of Fe_3O_4 presence on their FeMn alloy. One must note that in the present study, flecks of orange-brown products, typically associated with Fe_2O_3 [106] were observed on the samples tested in HBSS immediately after drying. To this end, the lower end of the spectra for FeMn tested in HBSS are indicative of a strong presence of mixed metal oxides that are more dominant after 14 days of immersion testing. Spectra for samples tested in HBSS+Ca showed similar peaks under 800 cm^{-1} after 28 days along with a peak corresponding to various apatite compounds at all intervals. The spectrum after 28 days exhibited what seemed like very intense background signals especially at higher cm^{-1}. The same phenomenon was picked up all over the sample surface. Unfortunately only one sample was reserved for this analysis so it is not clear whether this was a repeatable effect of long-term immersion in HBSS+Ca. Finally, samples tested in HBSS+BSA all exhibited varying intensities of the peaks associated with C=O and C-N bonding, as observed in Figure 4.61 in Phase Three. The peak corresponding to apatite as well as peaks related to metal oxides between 500-800 cm^{-1} were similarly detected after each testing interval.

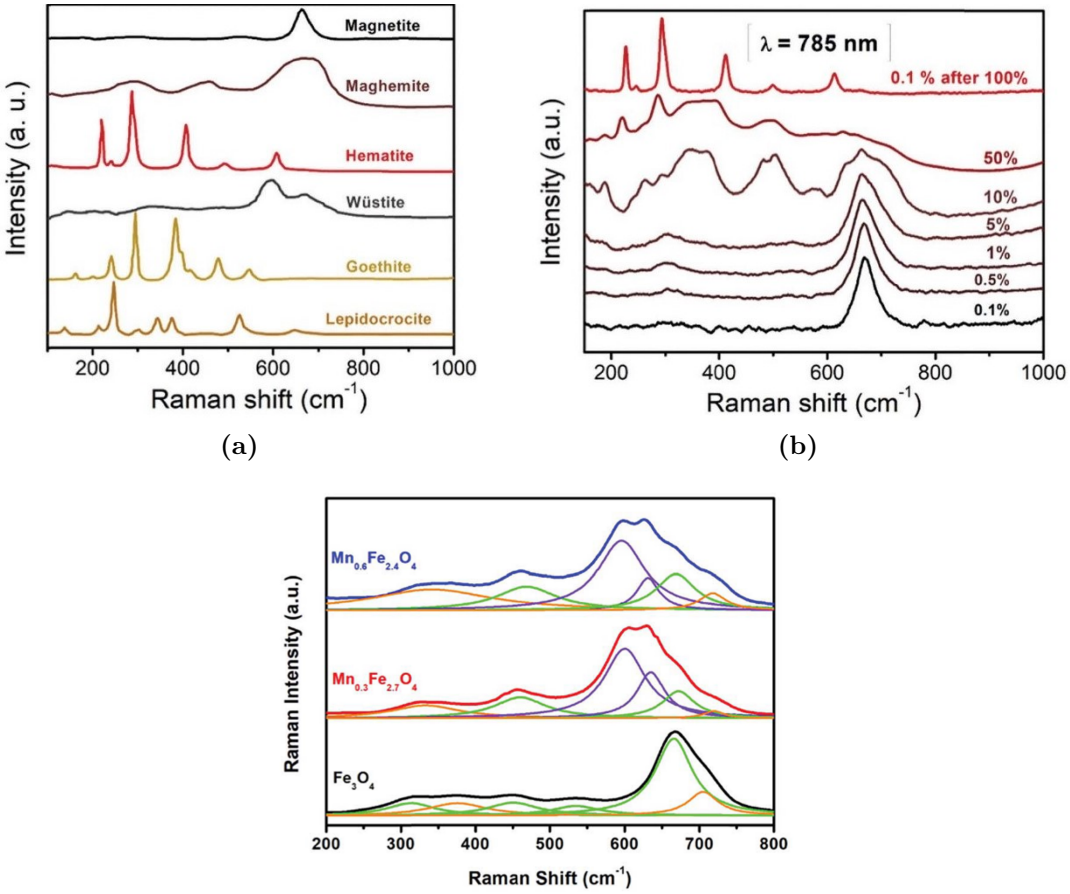

Figure 4.74: (a) Representative Raman spectra for typical Fe-based oxides and oxyhydroxides, (b) Raman spectra showing the heat-assisted transformation from magnetite to hematite through maghemite and (c) Raman spectra for several $(Fe,Mn)_3O_4$ with different stoichiometry [256]. In (b) the percentage indicates laser power with higher % resulting in more intense heat application.

It is important to emphasise that the y-axis of all the plots represent relative intensity that is specific to each plot i.e. the intensity scale of the plot for samples tested in HBSS was adjusted to best present the three spectra clearly but is not necessarily equivalent to the scale used for the plots of HBSS+Ca and HBSS+BSA. Therefore, the intensity between the spectra presented in the same plot may be compared but not the same could be done between different plots. Having said this, each spectrum was collected over a single spot over the sample

surface and although multiple spectra were collected to make sure that the presented spectrum is representative, the intensities do not necessarily represent the accurate proportion of a specific product on the whole sample surface.

4.2.4.5 Discussion

4.2.4.5.1 On the limitations of mass loss measurements for porous FeMn alloys

The results of the mass loss measurements presented in Figure 4.70 were not particularly helpful in determining the long-term influence of Ca^{2+} and BSA additions to HBSS on the corrosion of powder-processed FeMn. Although the SEM images of chemically cleaned FeMn surfaces following 28 days of immersion testing in Figure 4.71 seem free of corrosion products, the measured increase in dry weight clearly indicates otherwise. Degradation product-filled pores present deep within the core of the samples, as observed in cross-sections of the tested samples, were surely tedious to clean completely using the described procedure, especially considering the commonly reported use of brushes to assist with this step even when cleaning tested *wrought* samples [78, 107, 154, 180, 181]. From initial experiments on blank i.e. untested coupons, the chemical cleaning time affects the extent of substrate dissolution, therefore repeating the process until the dry mass became asymptotic as suggested in the relevant standard (ASTM G1 [68]), would not have yielded reliable results, particularly because the extent of corrosion product removal could not be visually assessed with porous samples. Alternatively suggested methods including repetitive ultrasonication in ethanol, is even less likely to prove successful for similar reasons [137, 162].

Rather than to estimate the corrosion rate in each electrolyte, these results were therefore included to stress the limitations of mass loss measurements with similar coupons and macro-porous scaffold structures. Several of these limitations have already been discussed in detail in Section 2.1.4.4 based on existing literature and have been confirmed in the present study, making any attempt to compare quantitative mass loss results across research groups rather futile.

Considering these outcomes along with those in literature, the candidate suggests that more definitive results could be acquired using µ-CT tomography to

derive measures of volume lost per unit area of exposed metal. While this approach could present its own difficulties [180], standardisation could be significantly simplified with such a non-invasive approach. Measures obtained using this technique, like all other existing methodologies, rely on the assumption that the principal corrosion mechanism is uniform degradation to derive a corrosion rate in mm/y, however full virtual visualisation of the implant gives a considerably more informative approach to assessing corrosion behaviour.

In this study, the other results presented in this phase will be relied on to deduce the corrosion behaviour of the metal in the various electrolytes of interest.

4.2.4.5.2 Long-term influence of Ca^{2+} on the degradation of powder-processed FeMn

When looking at the surfaces of FeMn tested in HBSS and HBSS+Ca in Figures 4.64-4.66 (a) and (b) respectively, there were no particularly prominent differences between the two sets of micrographs. Neither did the surfaces experience any significantly notable differences throughout the course of the tests. The same observations were made when looking at progressive micrographs of representative sample cross-sections in Figures 4.67-4.69 (a) and (b). None of the cross-sections revealed distinguishable hydroxide multilayers, as opposed to the dense Fe_3O_4 and Fe_2O_3 oxide formations on tested Fe35Mn samples by Hermawan *et al.* [106]. However, EDS maps corresponding to the cross-sections, revealed Fe/P-rich products on samples tested in HBSS and as expected, abundant Ca/P-rich products on samples tested in HBSS+Ca. The Ca/P-rich layer, which led to the presence of apatite peaks in all Raman spectra for samples tested in HBSS+Ca (Figure 4.73), did not seem to grow thicker with time, based on analysis of cross-sections. Results presented in Phase One of this work indicated how steady accumulation of apatite-like products on porous surfaces could lead to a sudden reduction in protective capacity of the same products that could be due to detachment of portions of the same product. Further testing in Phase Two then showed how non-porous surfaces retained a more uniform layer of corrosion products. The same was reported by Feng *et al.* [179] who observed discontinuous corrosion product layers

on porous Fe30Mn6Si1Pd, and the opposite on non-porous counterparts of the same metal.

Despite the absence of multilayers in cross-sections, EDS analysis presented in Table 4.10 showed that under respective phosphates, a layer that was mostly rich in Fe/Mn/O was present for each analysed sample irrespective of the electrolyte it was exposed to. Although specific oxides/hydroxides were not identified, Raman spectra corresponding to the same samples in Figure 4.73, showed the consistent presence of Fe-containing oxides on all samples tested in HBSS. Samples tested in HBSS+Ca exhibited a similar presence of Fe-containing oxides after 7 and 28 days[1].

The chemically cleaned surface micrographs of FeMn samples tested for 28 days, in Figure 4.71 (a) and (b), shed some light onto the principal corrosion mechanisms that the samples experienced in each electrolyte. Although one cannot be certain of what took place deep within the pores, surfaces tested in HBSS and HBSS+Ca both seem to have experienced uniform corrosion in various forms. In the absence of the formation of partially protective Ca/P-rich film, the surface tested in HBSS was covered in dimples of various sizes. On the hand, the sample tested in HBSS+Ca had a largely smoothed surface with signs of the grinding marks from the sample preparation stage only present in localised regions.

These observations tie in well with the influence that the degradation of the metals had on the pH of the solutions over the course of the testing period in Figure 4.72b. Although OH^- ions generated in the cathodic oxygen reduction reaction were definitely consumed for the formation of hydroxides detected in Raman spectra, as shown in potential reactions 4.7 and 4.8 [113], the rapid diffusion of OH^- relative to that of the metal ions' [257], allows for them to spread through the solution and influence the bulk pH.

$$Fe^{2+} + OH^- \rightarrow Fe(OH)_2 \tag{4.7}$$

$$2Fe(OH)_2 + 2OH^- \rightarrow Fe_2O_3.H_2O + 2H_2O + 2e^- \tag{4.8}$$

[1]A rather weak signal intensity collected from the FeMn samples tested in HBSS+Ca for 14 days might have interfered with resolving present peaks at similar Raman shifts.

This not mentioning that the product in reaction 4.8 could also be formed through reaction with dissolved oxygen according to reaction 4.9 [46].

$$4Fe(OH)_2 + O_2 + 2H_2O \rightarrow 2Fe_2O_3.6H_2O \tag{4.9}$$

Moreover, precipitation of the likely $Fe_3(PO_4)_2.8H_2O$ product (refer to Medusa simulation in Figure 4.29a), does not require OH^- to take place, as shown in reaction 4.10 [48].

$$3Fe^{2+} + 2{PO_4}^{3-} + 8H_2O \rightarrow Fe_3(PO_4)_2.8H_2O \tag{4.10}$$

The change in pH due to the degradation of FeMn in HBSS+Ca was minimal in the first 14 days, varying between 0 and 0.05 units, owing either to the rapid consumption of generated OH^- for Ca/P product precipitation or due to the limited cathodic reaction as affected by the same Ca/P product. Only after 28 days did the solution register a slight increase in pH by 0.25 units. These are likely attributed to changes to the Ca/P layer which drastically reduce its' charge transfer limiting capacity, as observed in Phase One results with porous FeMnAg after less than 10 h of testing.

Apart from the detection of hydroxides and typical Fe/P and Ca/P product precipitation, a notable trend in the surface EDS analysis that was also very noticeable in the cross-section of the sample immersed in HBSS for 7 days (Figure 4.67a), was the Mn enrichment in corrosion products formed around pores. High concentrations of Mn have previously been detected in the topmost layers of corrosion products [113, 166] when testing wrought FeMn alloys. Schinhammer *et al.* [166] speculated that Mn ions could be diffusing away from the corroding surface where they later react with dissolved oxygen to precipitate Mn-hydroxides as an outer corrosion product layer. In fact, groups who measure the ion concentrations in the testing extracts tend to find higher concentrations of Mn ions relative to Fe [117, 138]. The exceptions to this observation were studies in which a high concentration of carbonate ions were used prompting the precipitation of $MnCO_3$ [137, 162] which would otherwise unlikely take place [166]. Considering the absence of typical pit geometries as observed in stainless steels for instance, analysis of cross-sections did not indicate that pitting corrosion was particularly

prominent in the degradation of any of the samples. However, momentary occlusion within certain pores could have led to pitting-like behaviour with hydroxides forming preferentially around the pore entrance [153]. With Mn likely being available more readily in the solution, this could have been the cause for Mn enrichment in these areas.

4.2.4.5.3 Long-term influence of BSA additions on the degradation of powder-processed FeMn

The major differences between samples tested in HBSS+Ca and HBSS+BSA, based on surface and cross-section analyses, include a lower Ca/P ratio on samples tested in HBSS+BSA, as well as the formation of a thinner corrosion product layer in general. The former is quite expected based on previous evidence of Ca^{2+} chelation by BSA in Phase Three. The increase in pH due to FeMn degradation in HBSS+BSA compared to that measured in HBSS+Ca in Figure 4.72b, could also be an indication of a slower formation or lower concentrations of Ca/P-rich products precipitated on the surface. This being said, apatite was still detected in Raman investigation as shown in Figure 4.73. Similarly, signs of BSA adsorption were also detected by the same technique through the presence of C=O and C-N peaks which Dong *et al.* [175] attribute to stretching vibrations by amide I in protein. Thinner hydroxides could also be a sign of reduced availability of metallic ions due to similar chelation of divalent Fe and Mn ions by BSA; a phenomenon that some have hypothesised could result in faster metal dissolution [148].

SEM analysis of the chemically cleaned micrograph of FeMn tested in HBSS+BSA for 28 days in Figure 4.71c, showed regions which were smoothed in a similar way to the sample tested in HBSS+Ca with the addition of regular occurence of localised shallow pits. Although we cannot determine whether the addition of BSA resulted in accelerated corrosion, these features were exclusively present in samples tested in HBSS+BSA. Instances of localised "pit" formation was not unexpected considering the observation of localised attack following EIS testing for 24 h in Phase Three, as well as published results by Oriňaková *et al.* [147] who observed pits in Fe samples after testing for 1 h in HBSS with a similar concentration of BSA.

Based on these results, the corrosion mechanism of FeMn in HBSS+BSA seems to be very similar to the corrosion mechanism of Zn in BSA-containing electrolytes described by Dong *et al.* [175]. Adsorption of BSA to the metal surface takes place via electrostatic interactions as described in Section 2.1.4.2.3, potentially forming occluded sites between the metal's natural oxide and the protein. This could give rise to favourable conditions for localised corrosion to take place in such regions through Cl^- migration towards the site as well as metal hydrolysis according to reactions 4.11 and 4.12 [153, 175].

$$Fe^{2+} + H_2O \rightarrow FeOH^+ + H^+ \tag{4.11}$$

$$FeOH^+ + H_2O \rightarrow Fe(OH)_2 + H^+ \tag{4.12}$$

Since adsorbed BSA is only bound to the metal surface with weak secondary bonds [172], it could easy be displaced preventing the localised attack from progressing catastrophically. Incidentally, all studies in which no pitting or other indications of localised degradation was observed when testing Fe-based alloys in HBSS+BSA, were carried in Ca^{2+}-free electrolytes [150, 162]. Although the relation is not clear, it is possible that protein influences the mode of Ca/P precipitation in a way that allows for the formation of the observed features.

4.2.4.5.4 Improvements to testing methodology

Despite the fact that HBSS formulations are designed to equilibrate with air while buffering pH [243], Figure 4.72a indicates that the pH of blank solutions i.e. solutions without FeMn, increased considerably within the first testing week. The specified "buffering" capacity is therefore clearly limited to short test runs. In fact, a comparable increase in pH was observed in other studies using similar testing electrolyte formulations for long-term tests in the absence of pH buffers or a CO_2 environment [170, 258].

In order to compare the outcomes of the original tests in this phase to tests carried out in a more regulated environment, a 7 day immersion test was conducted with fresh samples immersed in HBSS, HBSS+Ca and HBSS+BSA, this time in an incubator at 37°C and 5% CO_2. Two samples were used per condition

due to limited sample availability. The pH of each testing and blank solution after the 7 day testing period, was **6.9**. This indicates that in the described testing setup, a lower concentration of CO_2 should be used to achieve the representative physiological pH of 7.4, irrespective of electrolyte formulation.

The samples used in this short test run were analysed in the same manner as samples tested in the original experiment. SEM micrographs of the surfaces are presented in Figure 4.75 with corresponding EDS analyses in Table 4.11 whereas cross-sectional SEM micrographs and associated EDS maps are presented in Figure 4.76. At first glance, the corrosion products accumulated on the surface were extremely similar to those formed on samples tested for 7 days in air, shown in Figure 4.64. However, close observation of the exposed substrate wherever the corrosion products flaked off during sample preparation, revealed shallow localised pits matching those observed on samples tested in HBSS+BSA in the first tests. In this case, rather than due to localised occluded regions between corrosion product or protein and the metal surface, they were possibly formed due to the slightly acidic bulk electrolyte that facilitate metal dissolution [47].

Fe/P products seem to have formed more profusely judging by EDS analysis of the corrosion products on the surface of the sample tested in HBSS as well as the consistently thicker layer observed along the sample cross-section in Figure 4.76a. The Medusa simulation for FeMn corroding in HBSS in Figure 4.29b, shows how the likely formed phosphate, $Fe_3(PO_4)_2.8H_2O$, becomes increasingly stable as the pH of the solution drops towards 6.9 from the pH of 9.2 detected after 7 days in the absence of a CO_2 atmosphere. The opposite is true for the stability of $Ca_5(PO_4)_3OH$ or similar apatite-like precipitates. The Medusa simulation in Figure 4.31c for FeMn corroding in HBSS+Ca shows a decreasing tendency for the product to form as the pH decreases towards 6.9. This accounts for the thinner corrosion product layers with lower intensities of Ca and P detected in the EDS maps presented in Figure 4.76 (b) and (c).

In a 30 day immersion test conducted by Dargusch *et al.* [107], powder-processed Fe35Mn samples were similarly tested in HBSS (with Ca^{2+}) at 37°C and in 5% CO_2. The authors noted that the corrosion product layer constituted a very thin layer of $(Fe,Mn)(OH)_2/(Fe,Mn)(OH)_3$ with considerable formation

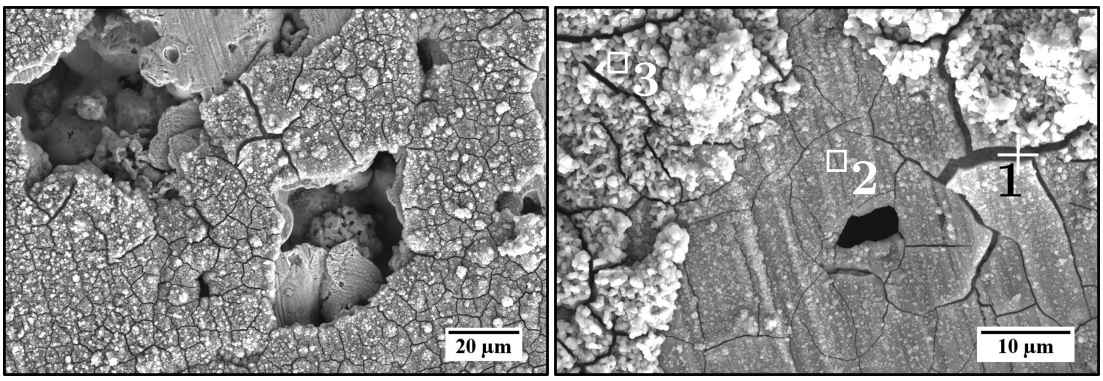

(a)

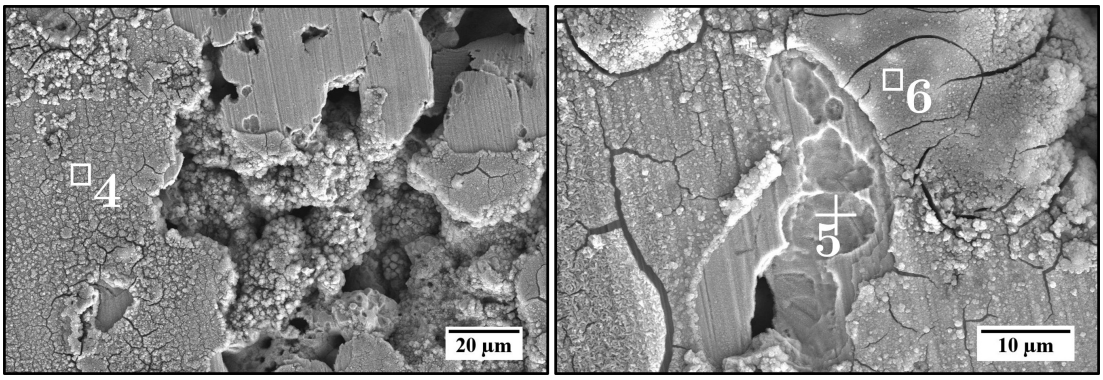

(b)

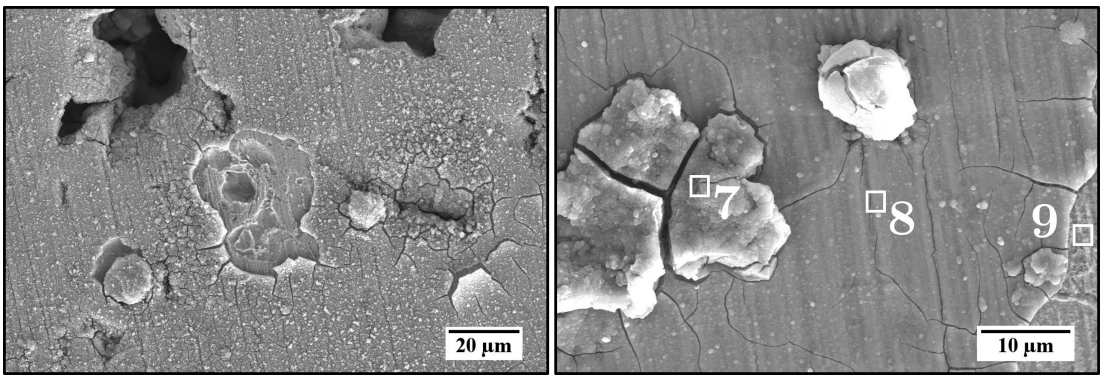

(c)

Figure 4.75: SEM images of the surface of representative FeMn samples following 7 days of immersion in (a) HBSS (b) HBSS+Ca and (c) HBSS+BSA at 37°C in 5% CO_2. Numbered regions-of-interest correspond to EDS analyses listed in Table 4.11.

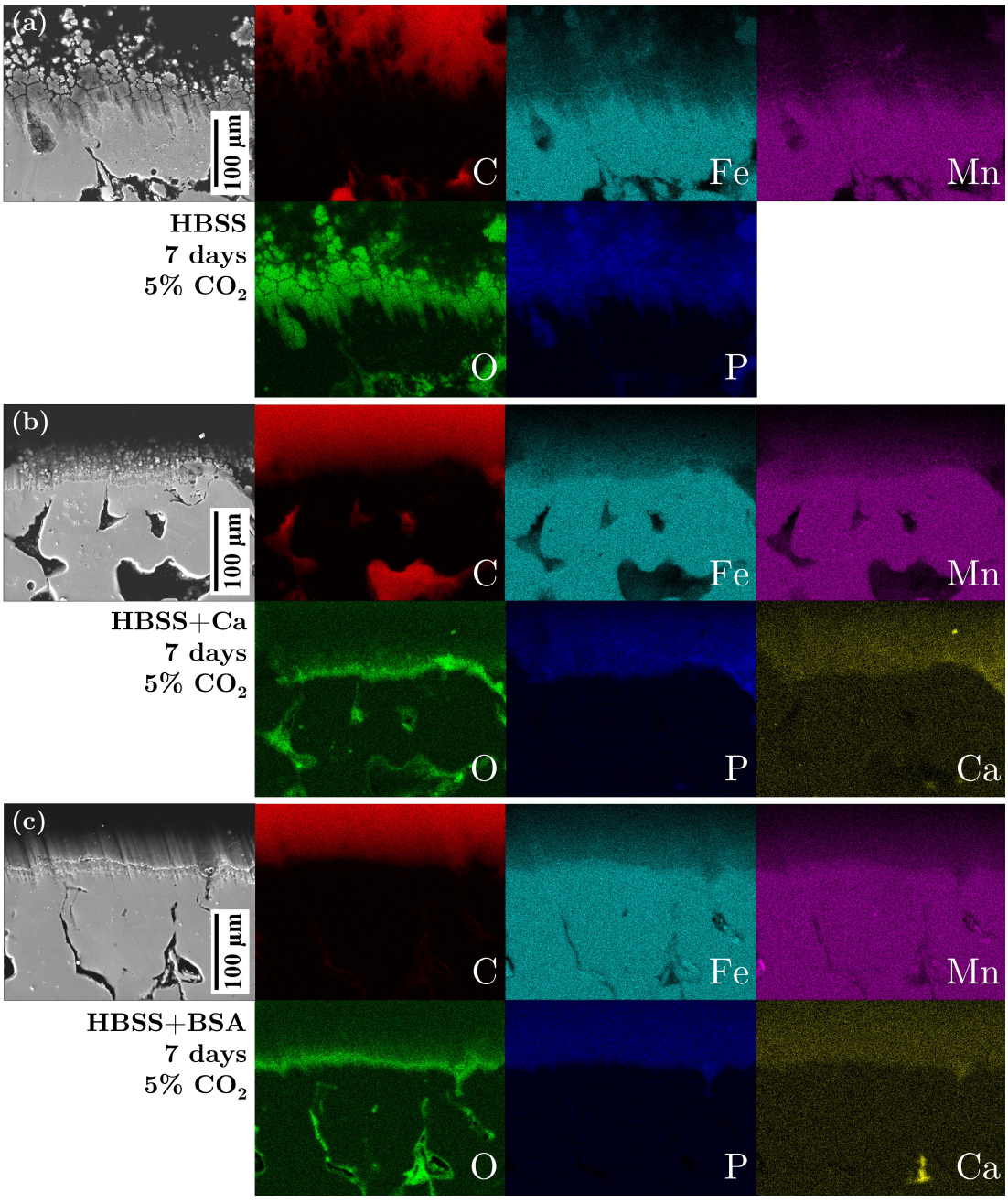

Figure 4.76: SEM image with corresponding EDS maps showing C, Fe, Mn, O, P and Ca distribution on representative cross-sections of FeMn samples immersed in (a) HBSS (b) HBSS+Ca and (c) HBSS+BSA for 7 days at 37°C and 5% CO_2.

Table 4.11: EDS analysis in wt.% corresponding to numbered regions-of-interest marked in Figure 4.75 for FeMn surfaces tested in HBSS, HBSS+Ca and HBSS+BSA for 7 days in 5% CO_2 environment at 37°C.

Pt.	O	C	Fe	Mn	P	Ca	Na	Cl	Mg	N
1	03.65	03.11	58.63	31.51	00.81	-	-	-	-	02.29
2	21.10	04.62	42.01	23.59	07.35	-	01.33	-	-	-
3	33.63	06.31	31.32	13.07	13.01	-	02.66	-	-	-
4	22.73	07.69	35.98	21.01	07.71	03.21	-	-	-	01.67
5	02.12	04.72	58.05	33.03	-	-	-	-	-	02.08
6	18.05	06.21	37.91	26.12	05.57	02.45	01.77	-	00.29	01.63
7	28.53	09.59	31.94	09.46	11.05	05.64	00.98	-	00.26	02.55
8	13.29	06.04	49.28	24.60	03.60	00.87	-	00.38	-	01.94
9	02.80	05.61	58.59	30.69	-	-	-	-	-	02.31

of Ca/P-products on top. This indicates that despite the fact that notable differences might be observed in the initial stages of corrosion when testing in the two different atmospheres, long-term testing will likely result in indistinguishable *in vitro*-tested samples. Naturally, biodegradable implants are required to serve their purpose for significantly longer than 30 days, making both testing outcomes relevant. Having said this, being able to accurately control the testing setup is always favourable for standardising purposes and therefore CO_2 testing atmospheres, especially if coupled by active regulation, should be advised [164].

4.2.4.5.5 Conclusions

The principal conclusions from this phase are summarised hereunder:

i. As observed in 24 h *in vitro* test runs in Phase One, metal-phosphates were the primary observed corrosion product in the absence of Ca^{2+} ions in the testing electrolyte, whereas Ca/P-rich products precipitated in both HBSS+Ca and HBSS+BSA. Raman spectra and EDS analyses both indicated the presence of a layer of metal hydroxides underneath the precipitated phosphates;

ii. Dense Mn-enriched products were consistently detected at the corroded surfaces around pores possibly due to "pitting"-like conditions forming within pores, despite the absence of signs of localised pitting corrosion. Mn ions have been previously proven to be more abundantly present than Fe ions in the bulk electrolyte following metal dissolution in HBSS;

iii. Testing in HBSS and HBSS+Ca resulted in various degrees of uniform degradation based on analysis of chemically cleaned tested surfaces and sample cross-sections;

iv. Testing in HBSS+BSA was confirmed to result in non-catastrophic localised corrosion of FeMn surfaces likely influenced by adsorption of BSA to the surface, as detected using Raman spectroscopy following all three testing intervals;

v. HBSS and other physiological media with similar concentrations of HCO_3^- and $H_2PO_4^-/HPO_4^{2-}$, should only be used in the absence of a controlled CO_2 atmosphere for short test runs. Since other synthetic pH buffers like HEPES and Tris-HCl have been known to directly interact with electrochemical species influencing *in vitro* degradation of biodegradable metals [159–161], buffering using CO_2 remains the preferred approach;

vi. Further effort is required to standardise methods of corrosion rates determined from long-term testing for porous powder-processed biodegradable Fe-based metals.

4.2.5 Phase Five - *In vivo* Testing

As discussed in Chapter 2, rigorous *in vitro* corrosion testing could never accurately represent the conditions the implant would be facing in the actual implantation site. It is therefore imperative that more groups complete their observations by carrying out *in vivo* testing following *in vitro* tests, to continue to build knowledge on the relation between the behaviour of specific metals in the two respective testing modes. Only in this way, could the effectiveness and reliability of *in vitro* testing improve over the next years.

In this study, *in vivo* testing with materials used in previous testing phases, was conducted using GAERS rats by Mr. Luke Saliba M.D. as part of his Masters' work. All rats recovered well from the operation, gaining weight during the subsequent 6 months up till euthanisation. Analysis of the explanted pins was performed by the candidate and is presented in this section. The pins removed from the rats after 6 months were all visually identical. The surface of each pin was covered in a visually black product with no sign of the metallic surface visible to the naked eye.

4.2.5.1 XRD analysis

The cylindrical surfaces of representative pins for each tested metal composition were analysed using XRD, yielding almost identical diffraction patterns. The original γ-FeMn and α-Ag peaks shown in the pre-corrosion testing scans in Figure 4.77a were not detected and were all replaced by the diffraction patterns displayed in Figure 4.77b, each corresponding to the pattern for $CaCO_3$ (PDF Card No. 01-075-6049). The same plot also includes labelling for MOOH and MCO_3 at 21.4°, 23.8° and 24.6° where *M* could signify either Fe and Mn, the respective

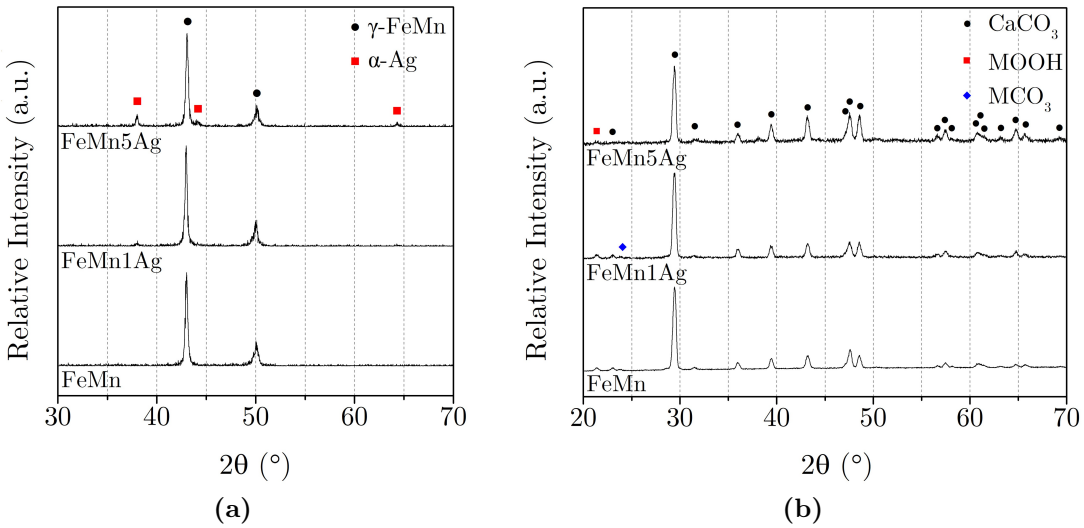

Figure 4.77: XRD analysis of FeMn, FeMn1Ag and FeMn5Ag pins (a) before and (b) after *in vivo* testing for 6 months.

compounds of which both exhibit only minimally offset peaks (α-FeOOH - PDF Card No. 01-073-9835, α-MnOOH - PDF Card No. 01-089-2354, $FeCO_3$ - PDF Card No. 01-087-2780 and $MnCO_3$ - PDF Card No. 01-073-4352). Any oxides, hydroxides or carbonates present, most likely underneath the more prominent presence of $CaCO_3$, could be rich in either or both metals. In reality, the accurate indexing of these peaks is somewhat difficult using this technique since each could correspond to any number of compounds composed of the metallic elements and any other surrounding elements derived from the implantation environment including C, O, P, Ca, K and Na.

4.2.5.2 SEM-EDS analyses

SEM images of representative pin surfaces for each tested metal composition can be seen in Figure 4.78, with corresponding EDS analyses of marked regions-of-interest presented in Table 4.12. Similar to other post-test SEM characterisation in previous testing phases, the corrosion product layers exhibit a "cracked-earth" effect that is most likely a result of the dehydration process that takes place in vacuum following ultrasonication in ethanol.

As observed with the XRD analysis, each alloy displayed very similar surface morphologies with a flaky-looking layer on top of a smoother substrate. EDS analysis of the top layer (points 2, 4 and 6) indicate a consistent enrichment in O, P, Ca and K whereas the underlying layer (points 1, 3 and 5) contained slightly higher Mn wt.% compared to the top layer. Despite the inaccuracy of EDS analysis for quantifying O content, the wt.% registered in Table 4.12 is indicative of the underlying layer likely being an oxide or hydroxide layer. The same could be said for the C content. Whilst not sufficiently accurate, the consistent presence of over 17 wt.% C is indicative of either carbonate presence in accordance with the XRD results, or C from the surrounding bone.

Further analysis of the tested pins could be seen in the SEM micrographs and corresponding EDS results of cold-mounted vertebrae cross-sections in Figure 4.79 and Table 4.13. None of the pins tested experienced extensive degradation as all analysed cross-sections retained a circular section of approximately 2-2.05 mm. The thickness of the corrosion product layer formed along the circumference of the

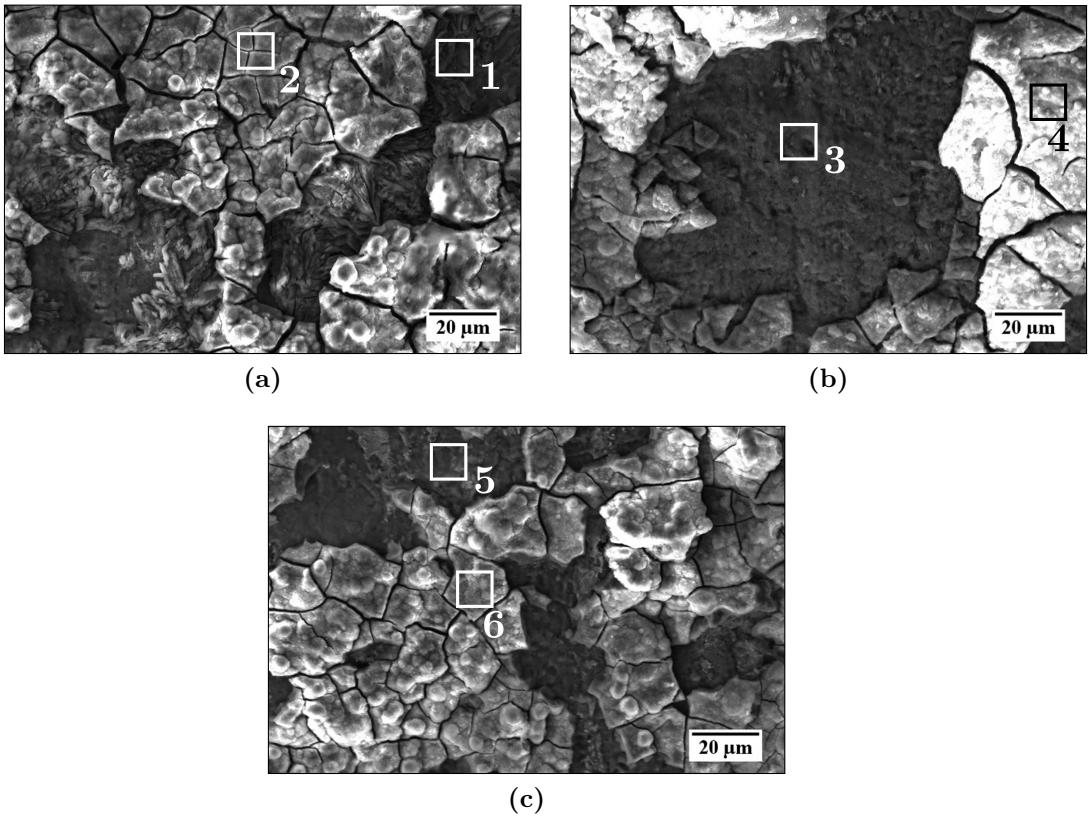

Figure 4.78: SEM images of representative explanted surfaces of (a) FeMn (b) FeMn1Ag and (c) FeMn5Ag pins following 6 months of *in vivo* testing. Numbered areas correspond to regions used for EDS analysis, the results for which are presented in Table 4.12.

different pins, although consistently present, varied considerably from one point to another. However, it was evident that increasing the Ag content resulted in higher accumulation of degradation products, with certain points along the corrosion layer over FeMn5Ag reaching a thickness of around 30 µm. EDS results for points 7 to 10 once again suggest that the alloy does not have a particularly strong influence on the formed corrosion product composition. Each point indicates considerable wt.% of O, C and Fe with varying traces of Mn, P, Ca, Na and K. Once again, the crack shown in Figure 4.79c for the FeMn5Ag pin, is likely either due to dehydration or due to stresses induced by the cold-mounting process.

The two-layer composition of the degradation products displayed in Figure 4.78 was not clearly evident in the cross-sections presented in Figure 4.79. EDS

Table 4.12: EDS analysis in wt.% of regions corresponding to numbered areas on explanted pin surfaces shown in Figure 4.78.

Pt.	O	C	Fe	Mn	P	Ca	Na	K	S	N
1	35.65	28.08	18.22	8.05	1.35	0.56	0.30	0.12	1.57	6.10
2	42.37	17.13	19.89	2.17	8.48	3.60	1.12	1.04	0.31	3.89
3	33.96	25.48	21.19	6.29	3.59	0.44	0.81	0.15	2.07	6.02
4	28.47	30.81	22.15	1.71	6.98	2.81	0.97	1.33	0.47	4.30
5	44.81	17.58	20.50	9.53	1.28	0.15	0.62	0.12	0.80	4.61
6	40.15	18.60	21.15	1.53	7.90	3.10	1.30	1.47	0.57	4.23

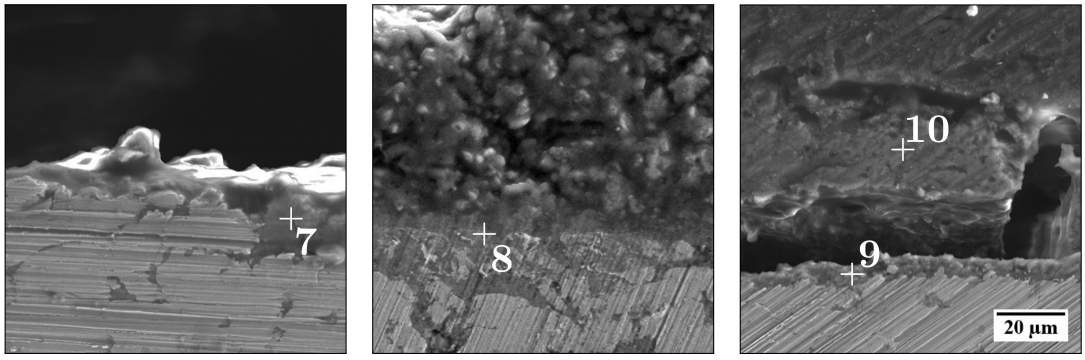

(a) **(b)** **(c)**

Figure 4.79: SEM images of cross-section of (a) FeMn (b) FeMn1Ag and (c) FeMn5Ag pins following 6 months of *in vivo* testing. Numbered spots correspond to regions used for EDS analysis, with results presented in Table 4.13.

Table 4.13: EDS analysis in wt.% corresponding to regions on the cross-sections of explanted pins, shown in Figure 4.79.

Pt.	O	C	Fe	Mn	P	Ca	Na	K
7	30.29	30.18	24.25	5.76	7.17	1.23	0.53	0.59
8	28.89	29.19	25.47	5.14	7.40	2.86	-	1.06
9	28.78	35.80	30.92	1.49	1.98	0.33	0.38	0.31
10	29.53	41.02	19.48	1.34	4.63	2.09	0.86	1.05

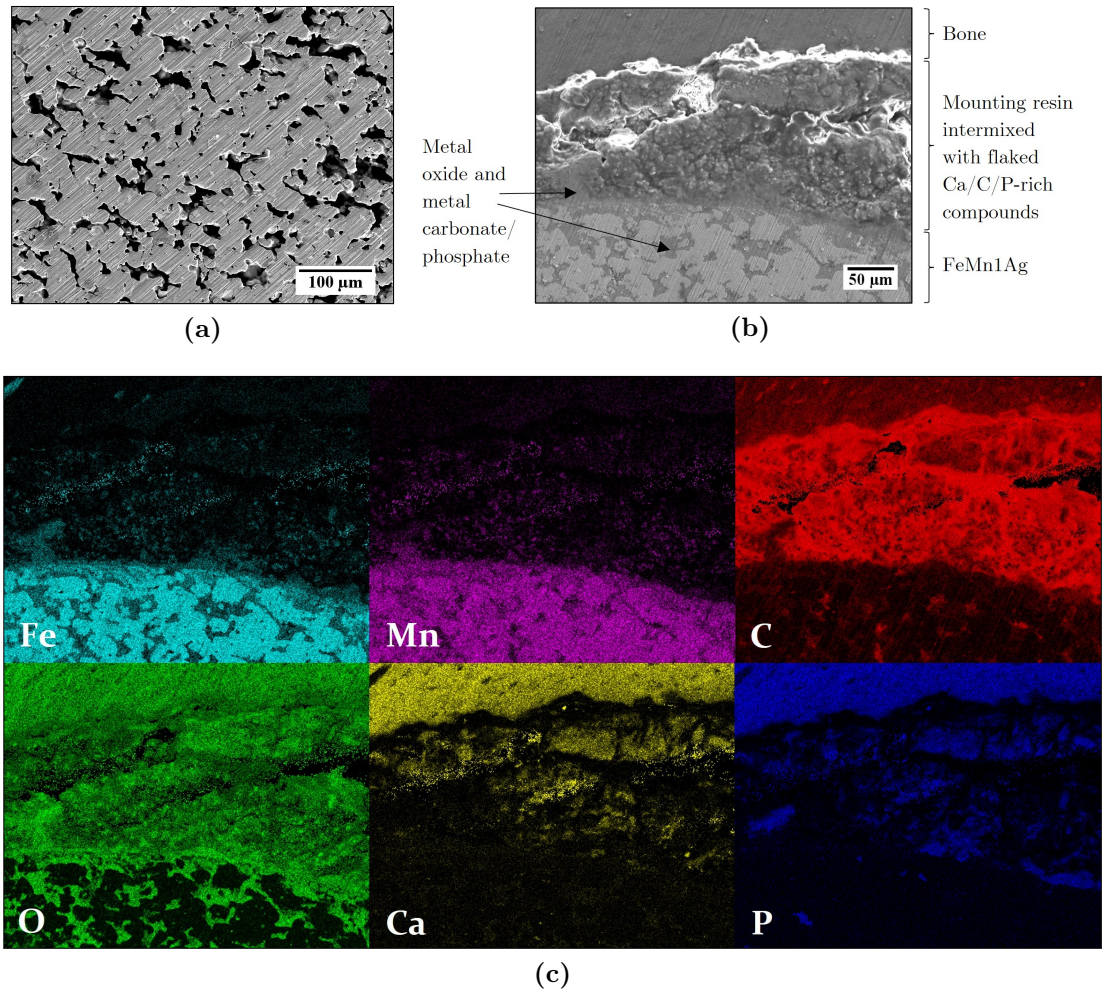

Figure 4.80: SEM micrographs of FeMn1Ag (a) before testing (b) after testing and (c) corresponding EDS distribution maps for Fe, Mn, C, O, Ca and P.

mapping of a region along the cross-section of the FeMn1Ag pin was aimed at clarifying the distribution and organisation of the two layers observed on the surfaces. The results are presented in Figure 4.80. The micrograph in (a) shows the microstructure of FeMn1Ag prior to the test with micro-voids resulting from the sintering process free from any corrosion products. The post-test micrograph in (b) and corresponding elemental distribution maps show that Ca and P-rich products were heavily intermixed with the mounting resin in between the pin and the surrounding host bone, whereas a layer rich in Fe, O and Mn formed a barrier-

like layer at the pin surface. Further metal oxides and potentially carbonates are also evidently present in the previously oxide-free pores.

4.2.5.3 Discussion

When analysing existent *in vivo* studies with Fe-based implants in Section 2.1.4.4, several groups mentioned the very slow corrosion rates caused by "barrier" layers which prevent further current flow across the metal interface [96, 114, 132, 180]. EDS analysis presented in this testing phase in Table 4.12 and 4.13 revealed the consistent high concentration of O wt.% in the corrosion product layer adjacent to the metal surface. Although the exact composition of this layer was not confirmed, it seems that irrespective of the underlying alloy composition, it was composed of mixed metal hydroxides like goethite (α-FeOOH) and groutite (α-MnOOH). Both, or a mixture of these hydroxides could have provided a similar "barrier" effect in this case, causing corrosion products to slowly accumulate on the surface and within pores but leaving the metal otherwise practically intact. Apart from this, SEM micrographs of the surface showed the presence of a second distinct layer which had a flakier morphology. This layer was consistently richer in elements originating from the surrounding environment, including Ca, P, C, Na and K. In *in vitro* testing, precipitated products composed of similar elements were also shown to increase the corrosion resistance of the materials in physiological testing fluids. Although the micrographs indicate that they were cracked and partially flaked off, the integrity of the layer *in vivo* could have been considerably higher, but was compromised during the sample preparation state. Moreover, XRD results indicated the presence of $CaCO_3$; a compound that is known to retard the degradation of Fe-based materials when present in hard water [180].

Having said this, the thickness of the accumulated corrosion product along the circumference of the pins, although not consistent, clearly varied depending on the alloy composition. Increasing the Ag wt.% resulted in thicker corrosion products, congruent with the results from the *in vivo* study by Dargusch *et al.* [132] wherein adding 1 wt.% of Ag to powder-processed FeMn led to approximately twice the corrosion rate. This increased accumulation is likely related to microgalvanic acceleration, however it is also possible that similar to *in vitro* observations, the

initial advantage granted by the presence of the more noble phase, diminishes relatively quickly. At its thickest along the observed cross-section, the product layer measured just 30 µm whereas the pin diameter remained very close to its original 2.05 mm[1]. Apart from the *in vitro* experimentation in this work, the work by Kraus *et al.* [180] also supports this hypothesis. The authors observed little change when analysing explanted pins after 4 and 52 weeks following femoral implantation of Fe, Fe10Mn1Pd and Fe21Mn0.7C1Pd pins in Sprague-Dawley rats, as shown in the optical micrographs in Figure 4.81 (a-f). Despite employing a similar microgalvanic acceleration approach to that used in this work, very

[1]Since one cannot say with certainty that the ground face of the mounted vertebrae is perfectly perpendicular to the vertical pin axis, one cannot be sure that the measurement reflects the actual diameter.

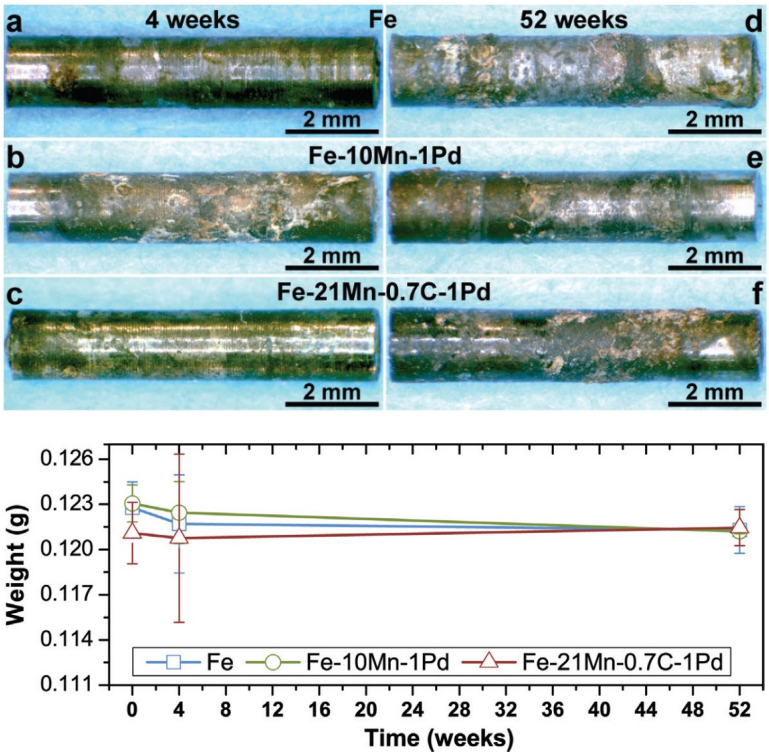

Figure 4.81: Optical images of Fe, Fe10Mn1Pd and Fe21Mn0.7C1Pd after (a-c) 4 weeks and (d-f) 52 weeks of *in vivo* testing in Sprague-Dawley femurs as well as (g) weight change of all the pins over the testing period as measured after chemical corrosion product removal [180].

limited corrosion was observed, this being attributed to the previously mentioned barrier effect caused by corrosion products measuring a similar thickness (10-30 µm). Although cross-sectional analysis by the same group showed a slight increase in the thickness of the corrosion products, EDS analysis revealed that the oxide layer remained approximately the same whereas Ca/P-products continued to accumulate on top. In fact, weight measurements displayed in Figure 4.81g show that the metal experienced no statistically significant changes to its weight over the course of the test.

Kraus *et al.* [180] also highlighted the influence of the implantation site. With the pins being implanted into bone, the metal was not in constant contact with the flow of blood and therefore the implantation site received a limited supply of dissolved O_2. Dargusch *et al.* [132] reported significantly different results when implanting Fe35Mn and Fe35Mn1Ag subcutaneously in Sprague-Dawley rats. Although they also observed a significant drop in the corrosion rate between the 4^{th} and 12^{th} week from implantation, increased O_2 availability especially at the start of the test, led to corrosion rates of 0.22 ± 0.017 mm/year in male rats. Although this is still considered to be a slow degradation rate for most applications [10], it is still an improvement on most reported results, including the observations in this work. However, one has to mention two other factors. Firstly, Dargusch *et al.* reported the evolution of H_2 at the implantation site, which is indicative of corrosion taking place at low pH based on the modified Pourbaix diagram presented by Qi *et al.* [145] (Figure 2.14). This might have been triggered by an inflammatory response which would in turn have delayed the formation of any barrier-like corrosion product layer and in itself accelerated metallic dissolution. Apart from this, the authors clearly point out the presence of a significant amount of MnO-inclusions in their powder-processed material, yet used 6 M HCl with 3.5 $g\,L^{-1}$ HMTA to clean the samples from corrosion products prior to mass loss measurements. Considering that a diluted formulation of the same etchant was used in this work precisely to eliminate MnO inclusions from the surface, it is highly probable that the quoted corrosion rates were overestimated and included mass lost from the removal of said MnO.

Once again considering the EDS analysis presented in this phase seems to indicate that the composition of the corrosion products is not particularly affected

by the alloy composition. Based on the cross-sectional analysis in Figure 4.79 and Table 4.13 in particular, it seems that hydroxide layers tend to be considerably more rich in Fe. As discussed in Phase Four, ICP-OES analysis of SBF solutions following static immersion testing of Fe30Mn1C by Gebert *et al.* [117] showed that Mn had a tendency to be present primarily in ionic state in physiological solutions whereas dissolved solid products were considerably richer in Fe. Histological specimens prepared from rat vertebrae in contact with FeMn pins and from control rats part of this experiment, are presented in Figure 4.82 (a) and (b) respectively. The analysis of samples[1] shows how the tissues surrounding the implantation site were considerably blackened compared to standard colouring of stained decalcified collagen in (b). This effect is known to take place in cases when Mn is present in bone as observed by Stathopoulou *et al.* [259] with Mn-containing fish bones.

Based on the results obtained in this phase, it does not seem that there was either extensive bone formation or significant attachment to the surrounding tissue, despite the fact that removal of pins from the vertebrae for XRD analysis was

[1]Kindly prepared by Prof. Pierre Schembri Wismayer M.D.

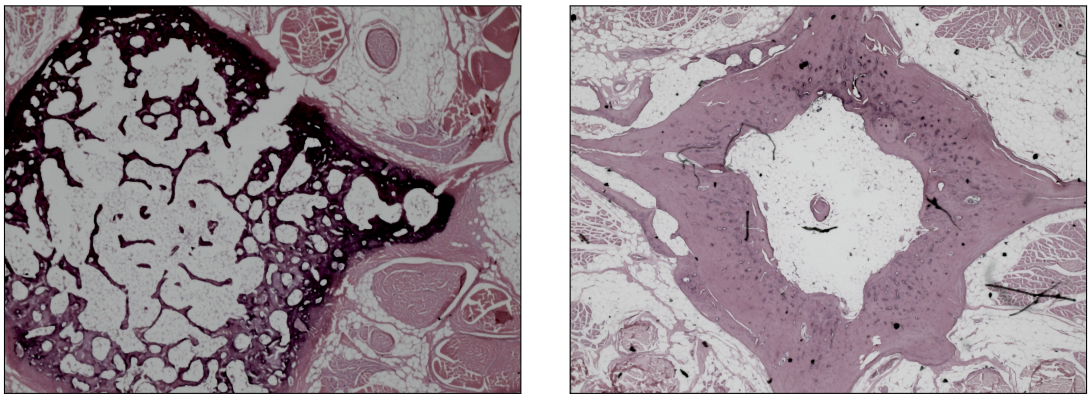

(a) **(b)**

Figure 4.82: Histological analysis showing stained histological specimens prepared from rat vertebrae. (a) shows blackened bone following contact with Mn-containing alloy and (b) standard colouring of stained decalcified collagen matrix from control rat which was not implanted with any metal. [Histological preparation of samples carried out by Prof. Pierre Schembri Wismayer M.D.]

a particularly tedious task. However, the consistent pick-up of Ca and P over the sample surface as well as the evidence of $CaCO_3$ presence by XRD, are both positive indicators of the samples' compatibility with the surrounding bone tissue. Proof of formation of $CaCO_3$ in *in vitro* experiments has never been presented, to the author's knowledge. However, its formation could be a sign that using electrolytes with a higher concentration of carbonates is more representative of the physiological fluid for these applications. The solutions used by Mouzou *et al.* [162] and Gambaro *et al.* [118] for instance, provide an example of using such electrolytes. Gambaro *et al.* [118] observed mostly $MnCO_3$ precipitation on their FeMnC alloys following static immersion, however also remarked on the possibility of Mn ions being substituted by other divalent cations like Ca^{2+} in the observed precipitate.

Considering the persistent limited degradation exhibited by Fe-based alloys *in vivo*, especially when implanted in bone, it seems that the way forward with such materials is to focus efforts on improving mechanical performance such that the surface-to-volume ratio of the implants could be increased significantly. In fact, the only appreciable degradation measured for Mn-containing Fe-based materials was by Nie *et al.* [191], wherein µ-CT volume changes following 48 weeks from implantation of high surface area scaffolds in rabbits' femurs, measured up to a 20.9% decrease[1]. The same study showed that the implants successfully resulted in considerable bone formation within the porous network. This notwithstanding, when testing a similar foam-like structure prepared from Fe-1.6P implanted in Merino sheep, the conclusions reached by Wegener *et al.* [223] still reflected the candidate's suggestion that reducing the starting amount of metal is crucial to achieving sufficient degradation when using Fe-based biodegradable implants.

[1]Needless to say, the possibility of implanting scaffold structures requires the availability and funding to carry out *in vivo* testing with larger animal models in which more complex structures could be implanted, which is likely why most studies including the present work have opted to implant pins and wires in mice and rats for the initial studies.

4.2.5.3.1 Conclusions

The conclusions from this section are summarised hereunder

i. FeMn, FeMn1Ag and FeMn5Ag experienced limited degradation over a period of 6 months implanted in the vertebrae of GAERS rats with pins retaining their original diameter and only accumulating up to 30 µm of corrosion product thickness at the surface;

ii. General corrosion product composition is not affected by the concentration of Mn and Ag, however slight variations in the thickness of the accumulated degradation products could be linked to initially microgalvanically-accelerated corrosion due to the inclusion of the more noble Ag;

iii. Detected corrosion products include $CaCO_3$, with Ca/P-rich products being present over Fe, and O-rich products, likely metal hydroxides;

iv. Mn release manifested primarily in absorption by the surrounding tissue as evidenced by histological analysis, whereas adherent corrosion products were richer in Fe;

v. There was no evidence of extensive bone formation, however the presence of Ca/P-rich products as well as $CaCO_3$ surrounding the implant is promising with regards to the metals' compatibility with orthopaedic implantation environments.

4.3 Powder-processing of FeMn for scaffold applications

In this second part of this work, results and corresponding analyses are presented related to some notable issues concerning the use of FeMn-based powder systems, especially considering the high Mn content that is generally deemed necessary for biodegradable metal applications. Issues related to oxidation and reduction of Mn-rich oxides and the influence of powder-preparation on the same phenomena as well as Mn sublimation, will be presented in the first parts of this section. This investigation was carried out by considering test outcomes when using blended Fe35Mn powder (B35), milled Fe35Mn powder (M35), alloyed Fe35Mn powder (A35) as well as a mixture containing an Fe35Mn4C master-alloy (MA), kindly provided by TU Wien.

The same powders were then used to investigate the potential of a modified replication method described in Section 3.3.3.1, proposed in previous work carried out within the same department [246].

4.3.1 Investigating FeMn powders

This part of the investigation was aimed at highlighting pre-processing influences on the characteristics of FeMn powders that might also have a notable effect on the applicability of the same powders for pressureless sintering in the modified replication method.

4.3.1.1 XRD analysis

XRD analysis of B35, M35 and A35 processed Fe35Mn powders are presented in Figure 4.83. As expected, blended powders exhibited two distinct phases, α-Fe and α-Mn. Following 2 h of milling, the α-Fe and α-Mn phases remained distinct in M35 powders. However, peaks experienced significant broadening associated with the reduced crystallite size and the residual strain within the powders as a result of the high energy milling process [260]. The same broadening was even more evident for the peaks displayed in the A35 diffraction pattern. Following 12 h of ball milling, the powders experienced even further crystalline refinement,

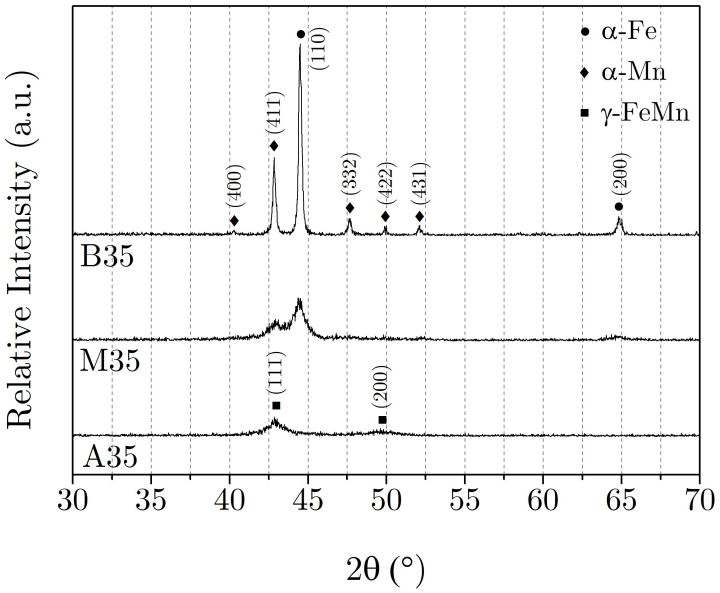

Figure 4.83: XRD patterns for processed B35, M35 and A35 powders.

more residual strain and a higher defect density. However, the aim of fully alloying the Fe and Mn powders was achieved for the A35 powders as the only phase detected was the austenitic γ-FeMn.

4.3.1.2 SEM-EDS analysis

The phases detected using XRD were clearly observed in EDS maps of powder cross-sections for B35, M35 and A35 powders, presented in Figure 4.84. The figure also includes a cross-section of the master alloy (MA) powder. The elemental distribution map for M35 clearly shows an intimate mixture of α-Fe and α-Mn within the same particle indicating that diffusion distances were indeed reduced to an order of µm in most cases, as with the diffusion-bonded powders described in Section 2.2.2.1.3. As for A35 and MA powders, Mn was fully dissolved in the α-Fe matrix resulting in full overlap of the two elemental maps.

4.3.1.3 Carbon quantification

The wt.% of C measured for as-supplied Fe, Mn and MA powders as well as as-processed M35 and A35 powders is shown in Figure 4.85. The same chart shows the calculated wt.% C for B35 and MAM powders (blended MA and A35

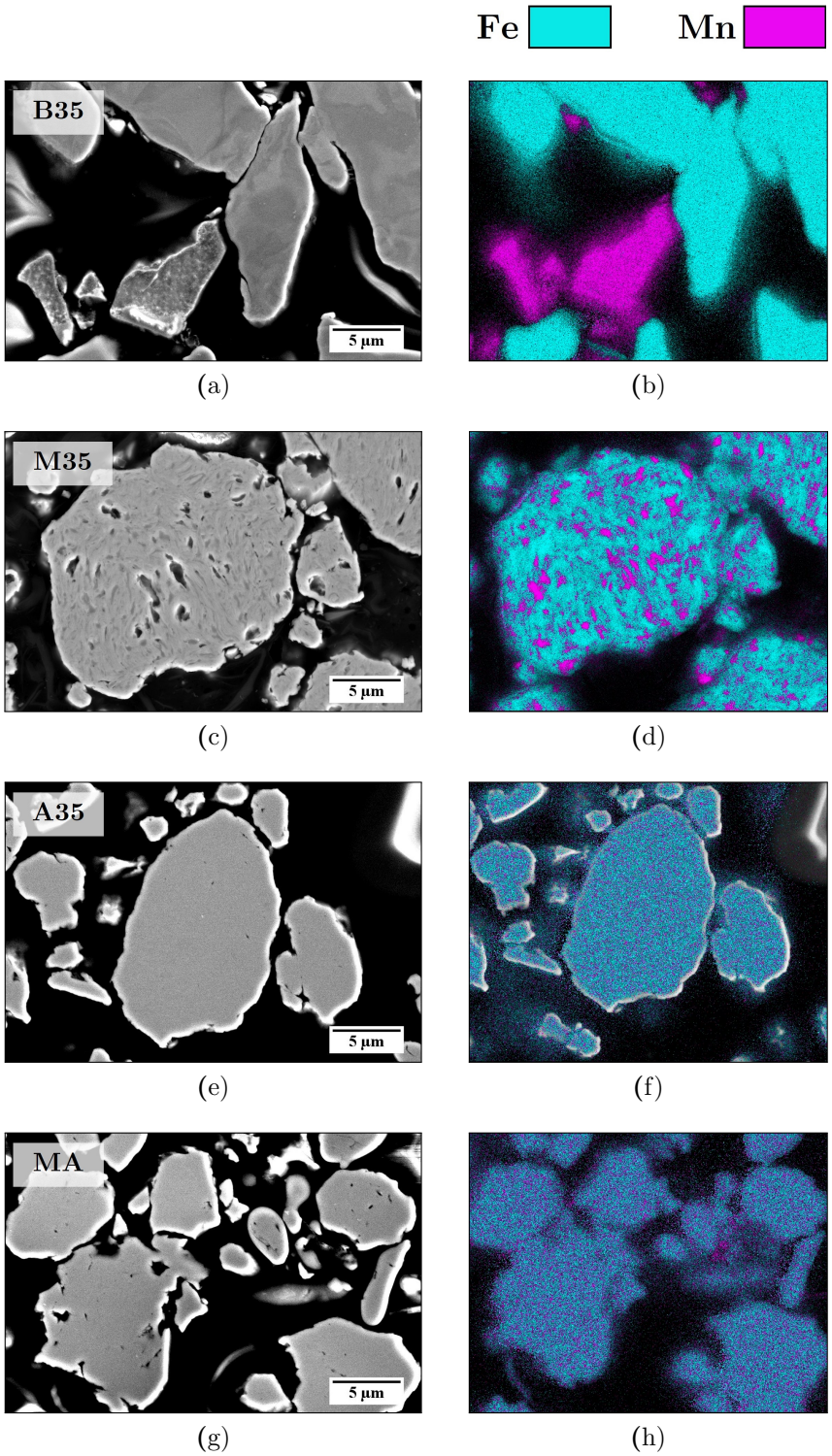

Figure 4.84: SEM images of powder cross-sections (a, c, e, g) and corresponding EDS distribution maps of Fe and Mn (b, d, f, h) for B35, M35, A35 and MA powders respectively.

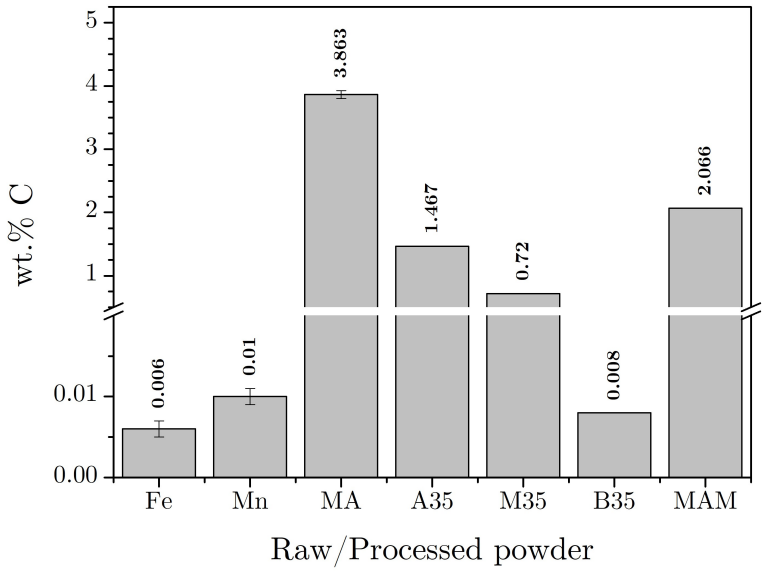

Figure 4.85: Carbon content in as-supplied Fe, Mn and MA powders, as-processed M35 and A35 powders and as-blended B35 and MAM powders. Error bar for measured quantities represents standard error (n = 4). *Refer to calculated values based on the measured carbon contents of constituents.

in 1:3 ratio) based on the C content of the mixtures' constituents, taking into consideration the used ratios.

The C content for as-supplied Fe and Mn was clearly very low at 0.006 ± 0.001 and 0.010 ± 0.001 wt.% for Fe and Mn respectively. It follows that the B35 powder mixture also has a minute amount of C at 0.008 wt.%. The MA on the other hand had 3.863 ± 0.012 wt.% C, a few points lower than the specified 4 wt.% by the supplier.

Ball-milled powders had significantly more C content than expected. The 1 mL of toluene added as a process control agent prior to the milling process clearly affected this measure for milled and alloyed powders with longer milling time resulting in higher C dissolution into the FeMn as A35 powders contained 1.467 ± 0.003 wt.% C whereas M35 powder contained 0.720 ± 0.003 wt.% C. Analysis carried out on milled powders with 15 wt.% and 25 wt.% C had very similar C content at 0.695 ± 0.006 and 0.712 ± 0.040 wt.% C respectively. This indicates that while the Mn content in the mixtures could have a minor influence on the uptake of C during ball milling, the influence is not as drastic as observed

with milling time. More work related to milled powders with varying Mn content was left out of this thesis to respect the page limit.

4.3.1.4 Thermal analysis

TG-DTA curves for tests carried out with B35, M35, A35 and MAM powders are presented in Figure 4.86a. TG curves clearly reveal that B35 powders exhibited a single drop in mass of 1.14% whereas M35, A35 and MAM powders each exhibited a two-step mass loss leading to total reduction of 2.54%, 2.51% and 2.30% for M35, A35 and MAM respectively.

The DTA curve in the same figure shows the endothermic peaks in the heating part of the graph corresponding to the melting points of the studied powders at 1405°C for B35, 1393°C for M35, 1354°C for A35 and finally 1314°C for the MAM powder mixture.

Figure 4.86b includes DTG curves as well as ion current intensities corresponding to CO (m18) detection. The DTG curves, as the first derivative of the TG curve in (a), highlight the inflection point of the mass loss region and therfore, coupled with the CO intensity peaks could give useful information about the nature of the reactions affecting measured mass loss. In general, DTG peaks up to the melting point for each powder, were clearly reflected in the CO peaks

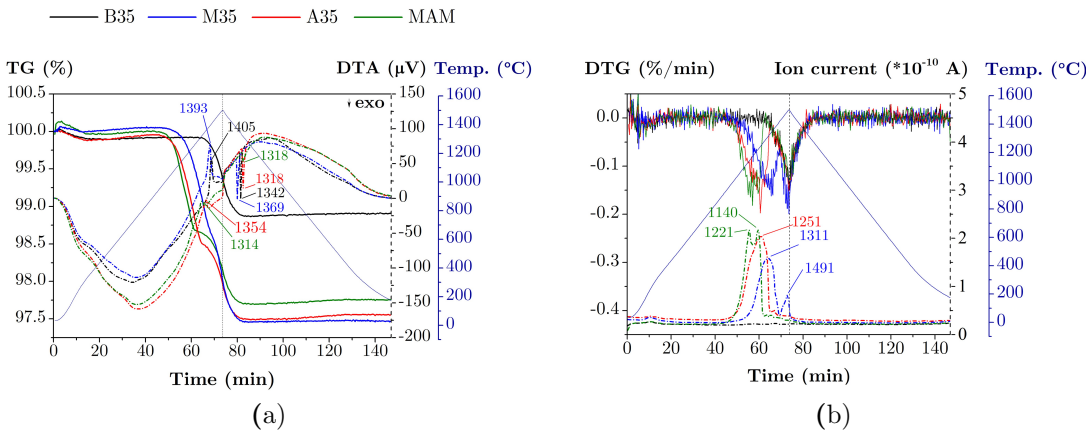

Figure 4.86: Thermal analysis plots for B35, M35, A35 and MAM powders. (a) shows TG (solid) and DTA (dashed) curves whereas (b) shows DTG (solid) and CO (m18) ion current signal from MS analysis. All tests were carried out in Ar. Each curve is presented as a function of temperature.

indicating that the mass lost was clearly due to carbothermal reduction, with the reaction taking place at increasingly higher temperatures for powders with less C content. B35 powders evidently did not exhibit any reduction at this stage. All powders exhibited another DTG peak at 1500°C which could be due to evaporation from the highly energised melt. However, in the case of M35 powders, this peak was also accompanied by a low intensity CO peak suggesting further reduction at this stage.

It is important to note that other gases were detected in very small amounts in all of the thermal analysis results presented in this thesis, however were omitted for clearer data representation. H_2O and H_2 were always detected in the initial minutes of the test as any adsorbed moisture at the surface evaporated, whereas low amounts of CO_2 generally accompanied CO peaks at temperatures below the Boudouard equilibrium.

4.3.1.5 Discussion

As discussed in detail when conducting a literature review relating to the use of Fe and Mn in powder metallurgy, the alloy variant, or the type of pre-processing carried out during preparation of the FeMn powder, has a strong influence on its behaviour during subsequent sintering. Whereas many studies have been conducted to investigate the relation between different types of Mn-containing powders and their high-temperature characteristics, these studies were limited to relatively low concentrations of Mn, as is of interest in other fields away from biodegradable metals applications [221]. Having said this, Sotoudehbagha *et al.* [111] and Xu *et al.* [124] both used ball-milling in order to reduce the reactivity of Mn elemental powder for these applications. Xu *et al.* [124] in fact proved that high-energy ball milling of Fe28Mn3Si powders significantly reduces the amount of sublimated material compared to a blended elemental mixture with the same constituents.

In this part of the investigation, SEM-EDS and XRD were used to correlate the microstructure and composition of powders pre-processed using varying routes, to their respective high-temperature behaviour. The elemental distribution maps in Figure 4.84 illustrate the varying presence of 35 wt.% Mn within the different

powders. This distribution could be used to draw assumptions on the respective chemical reactivity of the same powders, based on observations from literature discussed in Section 2.2.2.1.3. In B35, the presence of elemental Mn as distinct separate powder particles make the same particles more susceptible to oxidation whereas when fully dissolved to form austenite, as confirmed via XRD for A35 and MAM, the chemical reactivity was expected to be significantly lower. For M35, the behaviour was expected to place somewhere in between these two ends of the spectrum. Apart from differing reactivity, the plot in Figure 4.85 also showed that the same powders contained a wide range of wt.% C. For B35, which had negligible levels of C at 0.008 wt.%, the potential for carbothermal reduction was essentially insignificant. Conversely, the MAM powder had a much higher chance at self-cleaning at high temperatures, with 2.066 wt.% C.

In fact, thermal analysis presented in Figure 4.86 showed various levels of mass loss associated with oxide reduction for the different powder samples. Despite containing almost no C, B35 powders still exhibited 1.14% of mass loss after the temperature had exceeded the powder's melting point. Since this loss was not accompanied by detection of CO peaks in Figure 4.86, the mass lost is likely due to evaporation from the melt. When comparing the TG curves for the other three samples, despite having the highest C content at an average of 2.066 and 1.467 wt.% respectively, MAM and A35 powders exhibited the lowest mass loss. In this case, rather than an inferior capacity to reduce more oxide, the lower mass loss is more likely a reflection on the powders' lower reactivity which prevented extensive oxidation at lower temperatures. Apart from this, looking at the DTG curves and corresponding CO detection peaks, reduction was initiated at the same lower temperature for MAM and A35, indicating that reduction of similar oxides was taking place. On the other hand, reduction of surface oxides for M35 started at a later stage. As discussed in relation to Figure 2.24, this is a result of the varying distribution of Mn in the powders. The presence of elemental Mn distributed in M35 allowed for formation of more stable Mn-rich oxides during the heating ramp which consequently required higher temperatures to reduce. Apart from this, lower availability of C at the surface of M35 also presents kinetic limitations to reduction wherein the C first needed to diffuse to the surface along with any remaining internal oxides, for reduction to take place.

Another interesting observation related to the thermal analysis was that similar to what is generally observed for FeMnC powder mixtures in Ar (as exemplified in Figure 2.21a), there was no evidence of surface Fe-oxide reduction and corresponding mass loss at relatively low temperatures. This confirms that the oxides being reduced were likely (Fe,Mn)-oxides, considerably less stable than the notorious MnO, which is reduced at temperatures close to 1400°C [209].

The same kinetic limitations mentioned in relation to reduction for M35 powders, also resulted in the same powders giving rise to two CO peaks in Figure 4.86b. Since oxide reduction was not completed when the powders were in the solid state, reduction continued taking place from the melt. Contrarily MAM powders exhibited two separate peaks at lower temperatures with the peak at 1140°C resulting from the reduction of surface oxides and that at 1221°C resulting from the reduction of internal oxides, as described by de Oro Calderon *et al.* [213]. The peaks are therefore separated from each other by the amount of time and corresponding energy that it took for all the oxides within the powder particles to diffuse to the surface. A35 exhibited a wider peak at similar temperatures likely encompassing both the reduction of similar surface oxides to those present on MAM powders at the shoulder present at 1160°C, and reduction of internal oxides at the 1251°C peak. For these two powders, all these reactions took place below the melting points indicated in the DTA curves in Figure 4.86a.

In relation to this point, melting points also varied considerably for the studied powders, as expected due to the widely varying C content in the pre-processed particles. Since the metals' melting temperature relative to the chosen sintering temperature, could have considerable impact on the sintering behaviour of the same material, the influence of the powder composition on shifting melting temperatures is well worth discussing. To this end, Thermo-Calc (Thermo-Calc, Sweden) was used to generate a (65-x)Fe35MnxC phase diagram for varying C wt.% (x) to determine whether the predicted melting point based on the powders' initial composition, matches that indicated by the exothermic peaks presented in DTA curves in Figure 4.86a. The predicted melting points based on the phase diagram in Figure 4.87 for B35, M35, A35 and MAM, were 1382°C, 1349°C, 1307°C and 1271°C respectively. All temperatures were several tens of °C lower than the measured melting point.

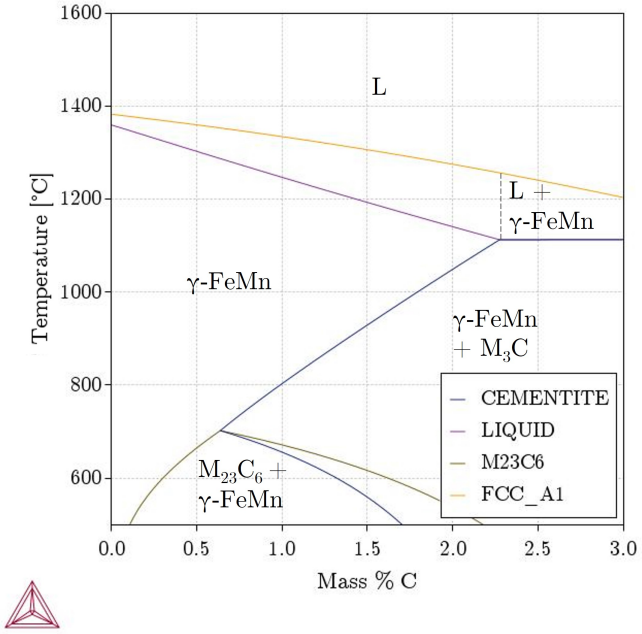

Figure 4.87: Thermo-Calc phase diagram for 35 wt.% Mn and (65-x) wt.% Fe where x is the mass % C. Unlabelled regions indicate regions for which there was insufficient information for Thermo-Calc to assign phases.

The C content was therefore re-evaluated by taking the assumption that the mass lost up till the melting point of the material during thermal testing, was due to reduction according to equation 2.26 for direct carbothermal reduction. This was done according to equation 4.13.

$$\frac{\text{Tested mass} - \text{Mass at m.p.}}{\text{Molar mass of CO}} \times \text{Molar mass of C} = \text{wt.\% C lost} \tag{4.13}$$

While B35 was naturally left out of this evaluation, this calculation indicated that at the melting point, the wt.% C for M35, A35 and MAM was actually closer to 0.19%, 0.77% and 1.46% respectively, bringing the melting point predicted by the same phase diagram, much closer to the measured melting temperature. This data is summarised in Figure 4.88.

The same diagram also includes the temperatures at which the principal reduction peaks were observed for all the powders. This summary of results highlights the issue that remains even when considering the better performing pow-

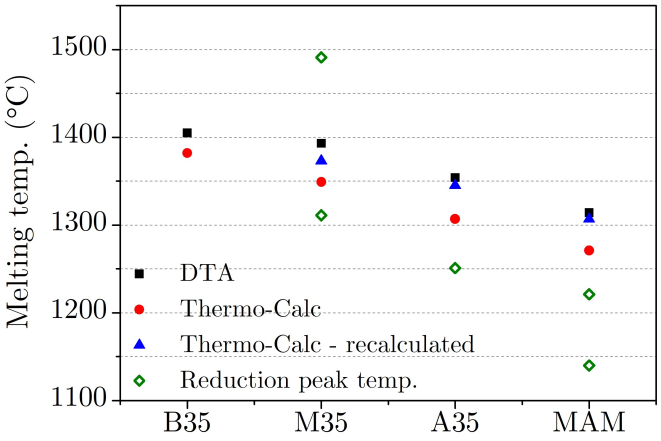

Figure 4.88: Melting points for B35, M35, A35 and MAM powders based on DTA results, Thermo-Calc phase diagram based on original wt.% C in processed powders and melting point derived from Thermo-Calc phase diagram according to recalculated wt.% C following mass loss during DTA.

ders like A35 and MAM, wherein the reduction temperature is still considerably higher then what is known to be the most common sintering temperature for Mn-containing steels, at around 1120°C.

4.3.2 Investigating pressed and sintered FeMn powders

The implications of the properties and characteristics of the powders established in Section 4.3.1, could be investigated through the study of microstructures for pressed and sintered coupons prepared using the same powder samples. In particular, the influence of the powders' respective oxide reduction capacity as well as the influence of the considerably high C content on the sintered microstructures, will be the focus on this part of the current study.

Although thermal analysis in Section 4.3.1 was limited to tests carried out in Ar atmosphere due to logistical limitations, the sintered coupons were processed in a N_2-10H_2 mixture, creating an environment closer to that used for sintering of Fe35Mn foams in the final part of this work (Section 4.3.3). Sintering was done at 1120°C, which is the most commonly used sintering temperature for Mn-containing steels [205], and at 1250°C. The latter was chosen based on the TG-MS analysis presented in Section 4.3.1 which showed that by the point that

this temperature is reached, all three C-containing powders had undergone some degree of carbothermal reduction.

Studying pressed-and-sintered microstructures processed under the described conditions could provide useful insight when analysing the results of the consequent and final investigation including sintering of the same materials in significantly more complex environments.

4.3.2.1 XRD analysis

Diffraction patterns corresponding to XRD scans carried out on ground surfaces of B35, M35, A35 and MAM samples pressed and sintered at (a) 1120°C and (b) 1250°C, are presented in Figure 4.89. The peaks corresponding to γ-FeMn at 43.1° and 50.1° were common in all the diffraction patterns and not central to this analysis. Therefore the intensity axis for each result was scaled up to enhance the peaks of secondary phases of interest.

Both patterns for the B35 samples exhibited well-defined peaks corresponding to MnO, or the more likely mixed-metal oxide (Fe,Mn)O. The same peaks were also evident in pattern corresponding to the M35 sample processed at 1120°C, but were not detected for the same material sintered at 1250°C. A similar trend could be observed for the A35 samples although the intensity of the (Fe,Mn)O peaks detected for the sample processed at the lower temperature were more broad and less intense compared to those present for the M35 sample. Diffraction patterns for both MAM samples did not show signs of the same oxide but contained well-defined peaks corresponding to the mixed metal carbide $(Fe,Mn)_3C$. The same carbide was also present in the diffraction pattern for the M35 sample processed at 1120°C in Figure 4.89a, albeit significantly less intense.

4.3.2.2 Optical Microscopy

Optical micrographs of polished and etched B35, M35, A35 and MAM samples sintered at 1120°C and 1250°C, are presented in Figure 4.90 (a, c, e, g) and (b, d, f, h) respectively.

Micrographs for pressed and sintered B35 samples in Figure 4.90 (a) and (b) both show microstructures containing a high percentage of porosity and oxide

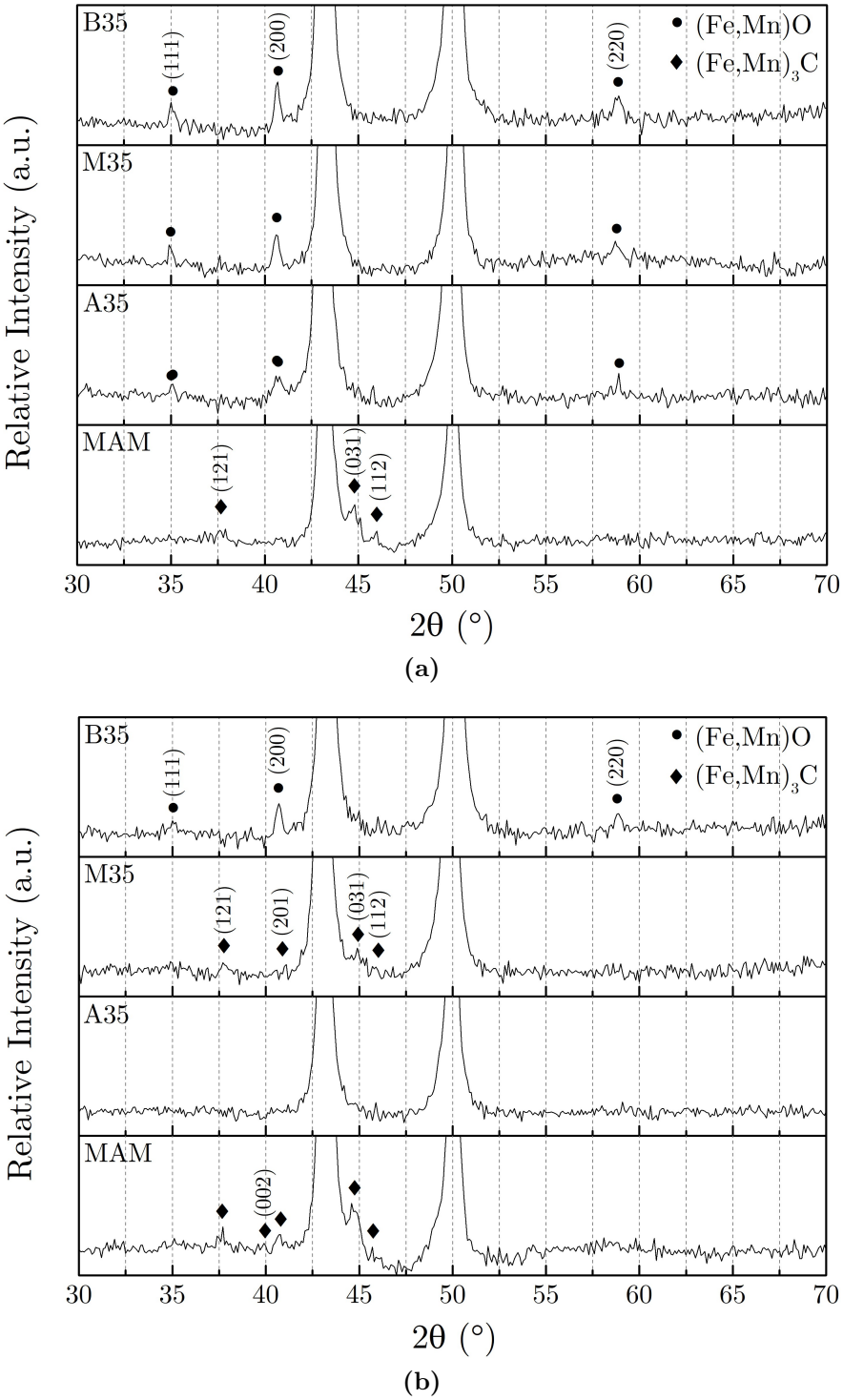

Figure 4.89: XRD analysis of ground cross-sections of B35, M35, A35 and MAM powders pressed and sintered at (a) 1120°C and (b) 1250°C in N_2-10H_2 atmosphere.

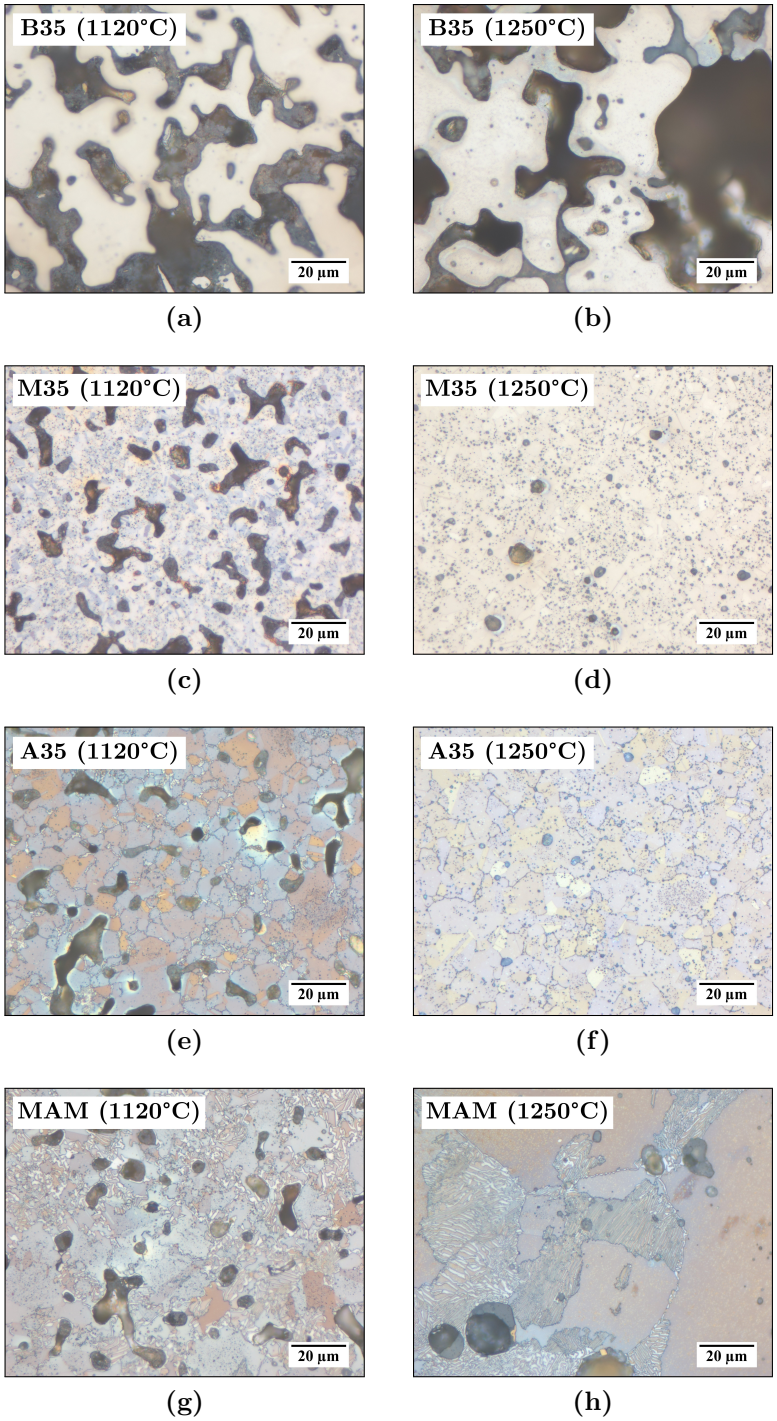

Figure 4.90: Optical microscopy images for B35, M35, A35 and MAM samples pressed and sintered at (a, c, e, g) 1120°C and (b, d, f, h) 1250°C in N_2-10H_2 atmosphere.

inclusions. The latter could be identified as the dark gray regions appearing in focus. In the presence of just 0.008% C, one could observe barely any difference between the two micrographs for samples processed at different temperatures.

The same could not be said for the M35 samples in Figure 4.90 (c) and (d). For the sample processed at 1120°C the microstructure consisted of a significant amount of porosity, smaller in size compared to the porosity observed in B35 microstructures. Apart from this, small dark spots littered the main metal matrix. Increasing the sintering temperature to 1250°C reduced the percentage porosity considerably, with remaining pores being much more rounded than in Figure 4.90c. Moreover, the dark grey inclusions, likely corresponding to the (Fe,Mn)O oxide detected using XRD, seemed to be less densely populating the matrix.

A similar trend could be observed for A35 microstructures in Figure 4.90 (e) and (f) when it comes to porosity, although once again, the amount of porosity in A35 samples was lower when compared to M35 samples. As opposed to B35 and M35 samples, both (e) and (f) displayed an additional phase that seemed to be situated at grain boundaries. The density of the same phase seemed to decrease with increase in sintering temperature. Following the XRD results corresponding to this work, this phase was suspected to be $(Fe,Mn)_3C$.

In the MAM microstructures presented in Figure 4.90 (g) and (h), the same M_3C phase was once again present. For the sample sintered at 1250°C, this phase was very evidently present in a lamellar form. Dark oxide inclusions seemed to be fewer and more sparsely distributed in the microstructure, especially for the MAM sample processed at 1250°C.

4.3.2.3 SEM-EDS analysis

A more detailed investigation of the same microstructures was carried out using SEM, assisted with EDS analysis. SEM micrographs of polished M35, A35 and MAM samples sintered at at 1120°C and 1250°C, are presented in Figure 4.91 (a, c, e) and (b, d, f) respectively. EDS analysis corresponding to numbered regions of interest in the same figures, is presented in Table 4.14. This particular analysis excluded B35 since optical micrographs as well as XRD analysis both clearly

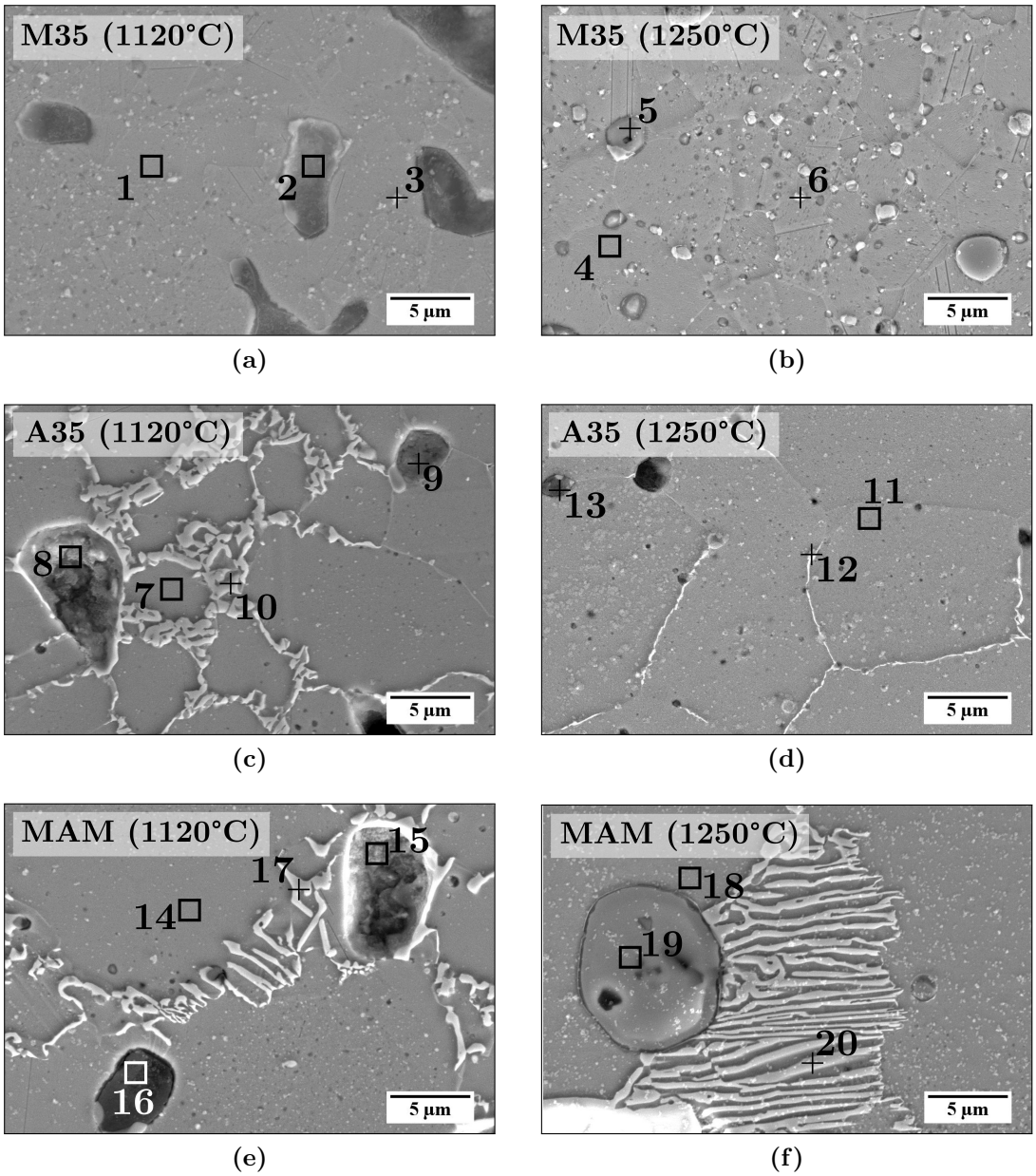

Figure 4.91: SEM micrographs for M35, A35 and MAM samples pressed and sintered at (a, c, e) 1120°C and (b, d, f) 1250°C in N_2-10H_2 atmosphere. Numbered regions correspond to EDS analyses presented in Table 4.14.

Table 4.14: EDS analysis in wt.% corresponding to numbered regions-of-interest marked in Figure 4.91.

	Pt.	O	C	Fe	Mn	Si	Ca	Mg	N	Ti
M35 1120°C	**1**	05.13	11.94	52.73	27.05	-	-	-	03.15	-
	2	19.13	08.54	41.83	22.66	07.84	-	-	-	-
	3	19.24	06.68	19.65	53.34	00.29	00.56	00.24	-	-
M35 1250°C	**4**	04.64	09.54	57.23	28.59	-	-	-	-	-
	5	29.44	04.72	02.02	63.42	-	-	00.40	-	-
	6	24.27	06.77	15.19	53.13	00.29	-	00.35	-	-
A35 1120°C	**7**	04.59	09.99	53.67	29.03	-	-	-	02.72	-
	8	22.10	09.04	42.17	26.21	00.48	-	-	-	
	9	20.58	14.81	41.31	20.13	02.59	00.58	-	-	-
	10	06.21	17.23	42.31	34.25	-	-	-	-	-
A35 1250°C	**11**	05.13	10.55	53.34	28.75	-	-	-	02.23	-
	12	19.03	05.32	08.11	48.44	00.30	-	00.42	11.11	07.27
	13	23.08	05.88	22.11	46.62	00.88	00.49	00.94	-	-
MAM 1120°C	**14**	05.26	11.23	52.53	28.70	-	-	-	02.28	-
	15	02.71	04.93	54.84	37.07	00.45	-	-	-	-
	16	40.82	08.87	24.33	11.48	14.50	-	-	-	-
	17	05.20	19.05	39.43	36.32	-	-	-	-	-
MAM 1250°C	**18**	05.18	11.82	52.31	28.50	-	-	-	02.19	-
	19	28.32	04.04	02.05	64.52	00.69	-	-	-	00.38
	20	05.14	15.26	47.21	32.25	00.14	-	-	-	-

pointed towards the presence of an austenitic FeMn matrix with (Fe,Mn)O inclusions whereas M35, A35 and MAM powders appeared to produce more complex microstructures and corresponding results.

Large-scale microstructures of M35 samples in Figure 4.91 (a) and (b) confirm the presence of a γ-FeMn matrix (pts. 1 and 4) with various mixed metal oxides (pts. 2, 3 and 6) and oxides highly-rich in Mn (pt. 5). While these were concen-

trated within pores, they were also scattered within the matrix with the preferred location for visibly bright oxides being at the faintly outlined grain boundaries.

Oxides were similarly present within pore surfaces (pts. 8 and 9) as well as at grain boundaries (pts. 12 and 13) in A35 microstructures in Figure 4.91 (c) and (d). However, the frequency of such inclusions was visibly reduced compared to M35 microstructures. Moreover, a brightly coloured C-rich phase (pt. 10) was also present at grain boundaries. For the sample processed at 1250°C, a similar phase formed as a very thin structure at grain boundaries, which proved difficult to examine by EDS.

Finally, in MAM microstructures, mixed metal (pt. 16) and Mn-rich oxide (pt. 19) inclusions were still present, however these were more sparsely distributed. Apart from this, metal oxides seemed to be absent from several pore surfaces, as in pt. 15, for which the EDS analysis seems to suggest the presence of γ-FeMn. As for A35, MAM microstructures also contained significant amounts of a C-rich phase (pts. 17 and 20). As already evident in optical microscopy, this phase seemed to precipitate in lamellar form, more evidently so at 1250°C.

4.3.2.4 Discussion

The results presented in this section show the considerable influence of wt.% C incorporated during powder pre-processing onto the sintered microstructures.

Both XRD results in Figure 4.89 and optical micrographs in Figure 4.90 (a) and (b) highlighted the similarity between the microstructures of the two B35 samples, irrespective of the sintering temperature. Based on research by de Oro Calderon *et al.* [210], natural Fe-oxides present at the surface of the elemental Fe powders were likely reduced by the 10% H_2 present in the processing atmosphere at around 435°C[1], however, due to the high chemical reactivity of elemental Mn, the oxygen would have been either transferred to Mn, or the Fe-oxide itself transformed into a more stable mixed metal oxide [209]. The formation of such a phase at particle surfaces in the early stages of the sintering process results in limited self-diffusion and densification. Naturally, the lack of C available to reduce these

[1]This temperature is based on reduction of typical Fe oxides in H_2 atmosphere in powder form, not in a green compact [210].

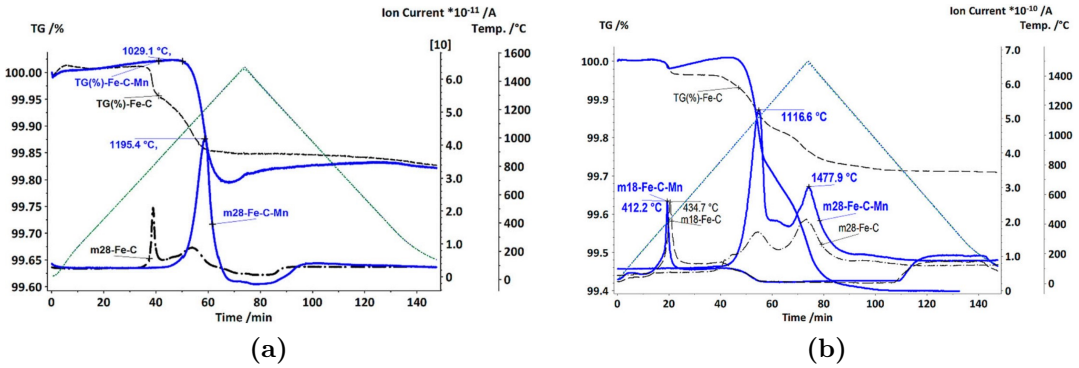

Figure 4.92: TG and degassing curves for Fe4Mn0.5C tested in (a) Ar and (b) H_2 [210].

oxides prevents any notable improvement between the microstructures in Figure 4.90 (a) and (b), with irregularly shaped porosity still present at 1250°C.

The increase in sintering temperature had a much more significant effect on the microstructures formed when using M35, A35 and MAM powders. In general both XRD as well as light and electron microscopy showed a visible decline in metal oxides present with increase in sintering temperature. Although it was not possible to carry out oxygen quantification when visiting TU Wien, the observed reduction of oxides is congruent to the results discussed in Section 4.3.1. As opposed to the testing carried out on the powders in that same section, i.e. without uniaxial pressing, the diffusion distances for oxides to be carbothermally reduced at the coupon-atmosphere interface, was generally two orders of magnitude higher and therefore it was expected to see a significant amount of trapped internal oxides when analysing sintered coupons. One must also keep in mind that the powder thermal analysis in Section 4.3.1 was carried out under Ar, as opposed to the sintering in this analysis. As shown in Figure 4.92 and in multiple examples in Chapter 2, when carried in different atmospheres, the reduction of surface oxides can take place at different temperatures and have varying effectiveness. Notwithstanding this, the positive influence of carbothermal reduction was evident for all three materials as, in contrast to what was observed with B35 samples, M35, A35 and MAM coupons all experienced a shift from a significant amount of irregular pores to a much reduced quantity of rounded porosity.

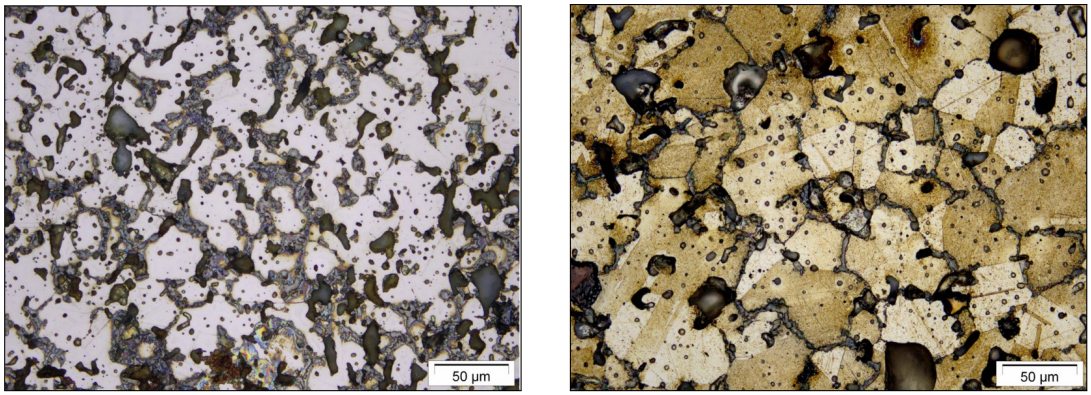

(a) **(b)**

Figure 4.93: Optical microscopy of Hadfield steel (Fe12Mn1C1Si) sintered at (a) 1150°C and (b) 1250°C [261].

Despite the fact that the XRD pattern for M35 sintered at 1250°C included two peaks which corresponded to the pattern for $(Fe,Mn)_3C$, no clear carbide phase was identified. Any precipitated carbides were therefore present as isolated precipitates. On the other hand in A35 as well as in the MAM samples sintered at 1120°C, where significant amount of C is likely to have been retained by the material even after carbothermal reduction, carbides were seen surrounding most grain boundaries. This is a common occurrence with Hadfield steels, as described by Schroeder *et al.* [261]. In fact, Figure 4.93 shows two micrographs for Hadfield steel (Fe12Mn1C1Si) sintered at (a) 1150°C and (b) 1250°C respectively. In both cases, carbides were shown to precipitate in a similar way in this work. Although carbothermal reduction was not addressed in this particular study by Schroeder *et al.* [261], one could see that the amount of carbides decreased with increase in sintering temperature as the oxides present in the metal became less stable and were carbothermally reduced. This was very evident for the A35 micrographs in Figure 4.91 (c) and (d) in this study. It is unclear why despite the fact that there was a significant fraction of $(Fe,Mn)_3C$ present for the sample sintered at 1120°C, no corresponding peaks were observed using XRD.

The occurrence of widespread pearlite presence in MAM microstructures was not particularly expected. Despite not being very evident for the sample sintered at 1120°C in Figure 4.91e, lower magnification SEM imaging showed similar

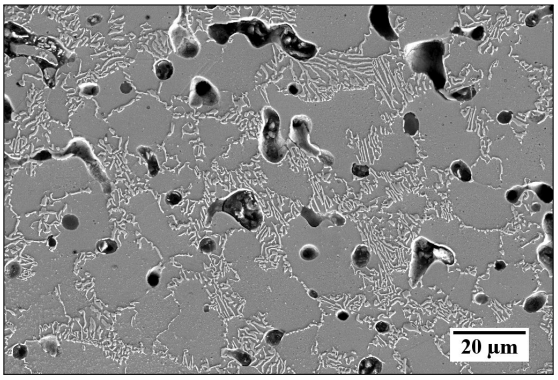

Figure 4.94: Lower magnification SEM micrograph of MAM sample sintered at 1120°C showing similar formation of lamellar M_3C as observed following sintering of the same material at 1250°C.

lamellar formation of M_3C, as shown in Figure 4.94. The absence of α-Fe peaks in XRD diffraction patterns generated for the MAM samples in Figure 4.89, is likely due to overlap of the main ferrite peak at around 44.5° with peaks for both γ-FeMn and M_3C.

Although the formation of pearlite in FeMnC systems is not unprecedented, studies mentioning pearlite formation were previously concerned with steels containing significantly less Mn and C wt.% [205]. To this end, Thermo-Calc software was once again utilised to generate a (65-x)Fe35MnxC phase diagram for varying wt.% C. The resulting phase diagram is shown in Figure 4.95. The phase diagram illustrates the possibility of having equilibrium formation of γ-FeMn and pearlite (α-Fe and M_3C) when the composition of the alloy is Fe35Mn(2.26 - 6.72)C. Although, the wt.% C content in MAM is lower, at around 2.066%, it is good to note, that for slightly lower concentrations of Mn, the stability of the γ-FeMn and pearlite regions shifts to lower wt.% C content.

The presence of networked M_3C as depicted in A35 and MAM microstructures, is not particularly desired in most load-bearing applications due to the resultant brittle nature of the material. As Schroeder *et al.* [261] displayed with their Hadfield steel, the use of such materials for most applications becomes more feasible when quenching the material to prevent carbide precipitation that takes place on equilibrium cooling. At the time of testing, there was not the possibility to quench the coupons from the sintering temperature and therefore the effect of

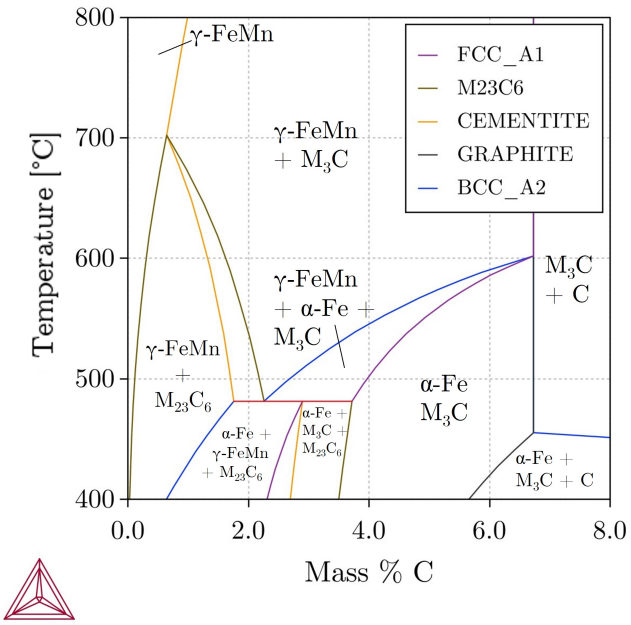

Figure 4.95: Thermo-Calc phase diagram for Fe35MnxC for varying wt.% C x showing a region of stabilised γ-FeMn and pearlite (α-Fe and M_3C).

this approach on the materials presented in this section, remains a question for future work.

4.3.3 Influence of powder preparation for FeMn on the modified replication method

The final part of the study on pre-processed Fe35Mn powder, in particular in the form of M35 and A35 powders, relates to these powders' applicability in what has been referred to in this work as the modified replication method. Using the well-known polyurethane replication method as inspiration, previous work within the department has demonstrated the ability to replace reticulated polyurethane foam with customisable 3D-printed templates and replicate the same template form with pure Fe powder [246].

In the following section, the applicability of M35 and A35 powders[1] in relation

[1]At the time of testing MA powder was not available to prepare MAM powder mixture and therefore this study was not extended to the applicability of the latter.

to this method, will be studied using XRD, SEM-EDS analysis, C quantification as well as thermal analysis.

4.3.3.1 Initial observations

Macro-scale images of the resultant structures of the modified replication method, are shown in Figure 4.96. Figures (a) and (c) show representative structures sintered using the *exposed* sintering configuration described in Section 3.3.3.1, with M35 and A35 powders respectively. Figures (b) and (d) show the corresponding

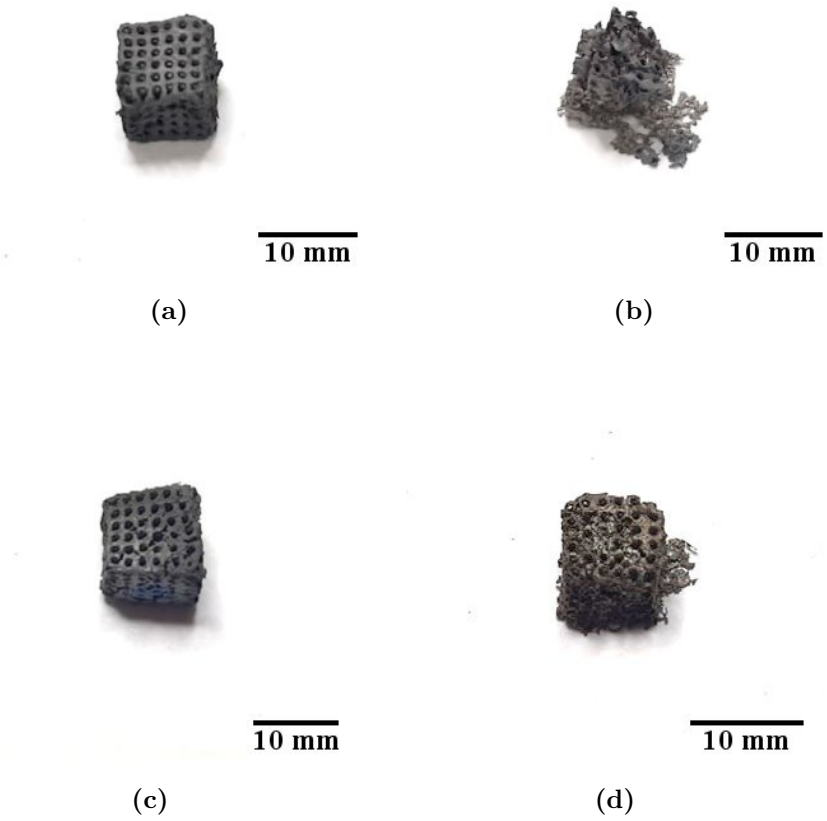

Figure 4.96: Macroscopic images of representative structures sintered at 1120°C under N_2-5H_2 flow using (a-b) M35 powder and (c-d) A35 powder. Samples (a) and (c) were *exposed* to the sintering atmosphere whereas (b) and (d) were *shielded*.

structures sintered in *shielded* configuration. The scale bars accompanying each image offers an approximate indication of the structure size following sintering.

Upon initial observations, *exposed* structures seemed to have repeatedly retained the template's form better when compared to *shielded* structures, some of which completely collapsed, as shown in Figure 4.96b. Closer inspection of the structures revealed instances of unequal shrinkage, with regions closer to the alumina base plate shrinking more than the rest of the structure, cracking, material loss and localised collapse in certain cases.

One must note that *exposed* structures displayed some mild attraction when approached with a regular magnet, whereas *shielded* structures displayed almost no attraction to the same magnet.

4.3.3.2 Carbon quantification

Figure 4.97 shows the C content of delubricated foams prepared using M35 and A35 powders. C content for both foams delubricated in *exposed* and *shielded* configurations are presented in the graphs and represent the amount of C taken

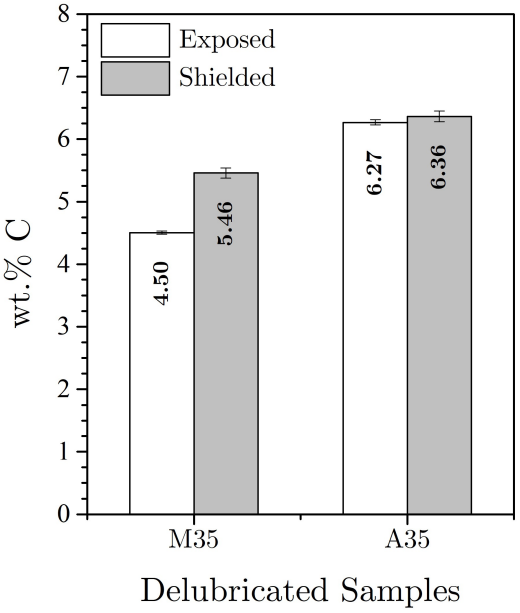

Figure 4.97: Carbon content in crushed foams processed using M35 and A35 powder and delubricated in *exposed* and *shielded* configurations. Error bar for measured quantities represents standard error (n = 3).

up by the structures during the first stage of the heating ramp ahead of sintering at higher temperatures.

Compared to the C content measured in as-processed M35 powders in Figure 4.85, foams gained 3.78 and 4.74 wt.% C during delubrication in *exposed* and *shielded* configurations respectively. Similarly A35 gained 4.80 and 4.89 wt.% C respectively. The bars seem to indicate that for structures prepared using A35 powder, the delubrication configuration had less of an impact on the measured C content. This might indicate that A35 powders might more readily and efficiently dissolve C from the surrounding atmosphere compared to M35 powders.

4.3.3.3 XRD

XRD patterns for as-ground foam cross-sections prepared using both M35 and A35 powders and sintered in either *exposed* or *shielded* configurations, are presented in Figure 4.98 (a) and (b) respectively.

All patterns indicate a mix of three principal phases: γ-FeMn, MnO (or mixed metal oxide) and $(Fe,Mn)_3C$. Oxide peaks were present in similar intensities relative to the principal γ-FeMn peak for each pattern and therefore further information related to the presence and distribution of this phase could be gained through microscopy. On the other hand, in both (a) and (b), $(Fe,Mn)_3C$ peaks in foams processed using A35 powders were more intense relative to the same peaks for foams processed using M35. Moreover, foams sintered using *shielded* configuration also seemed to contain more $(Fe, Mn)_3C$ compared to their *exposed* counterparts.

4.3.3.4 SEM-EDS analysis

4.3.3.4.1 Surface imaging

Representative SEM images of the sample surfaces following sintering are presented in Figure 4.99. Figures (a) and (b) show the surface of samples sintered in the *exposed* configuration with M35 and A35 powders respectively, whereas (c) and (d) show the same materials sintered in the *shielded* configuration. Insets in (a) and (b) show higher magnifications of the same surface with numbered regions corresponding to EDS analyses presented in Table 4.15.

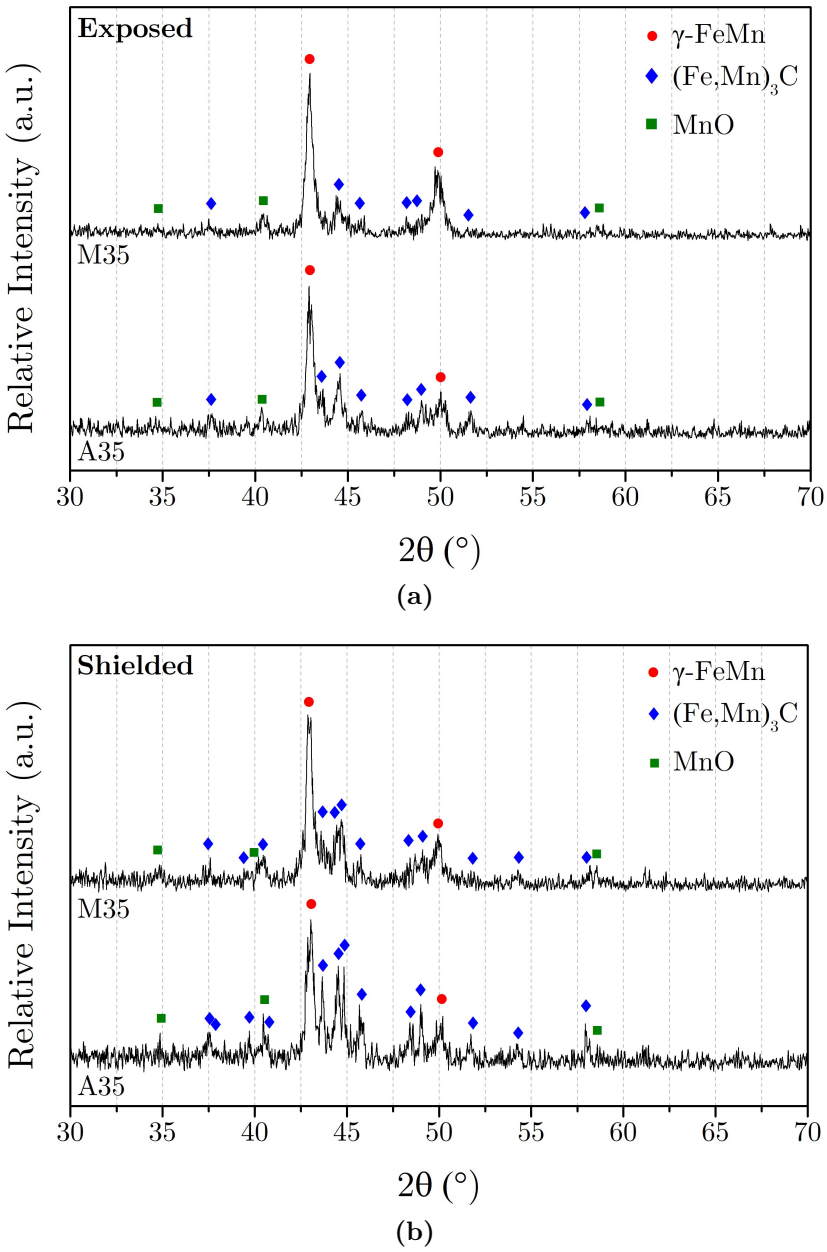

Figure 4.98: XRD patterns corresponding to ground cross-sections of foams prepared using M35 and A35 powders and sintered while (a) *exposed* to N_2-5H_2 flow or (b) *shielded* configuration.

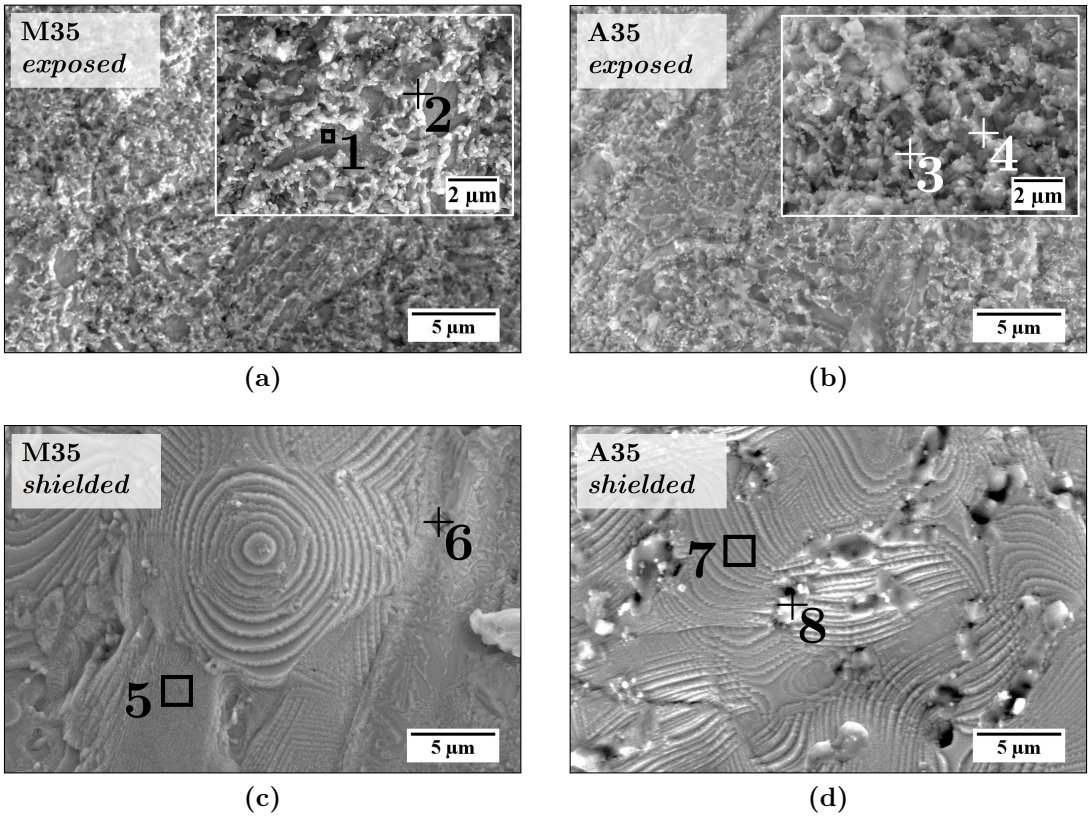

Figure 4.99: SEM micrographs of foam surfaces for foams processed (a) using M35 powder in *exposed* configuration (b) A35 powder in *exposed* configuration (c) M35 powder in *shielded* configuration and (d) A35 powder in *shielded* configuration. Numbered regions correspond to EDS analysis presented in Table 4.15.

Surfaces of structures exposed to gas flow during the sintering process, were covered with a bright interconnected phase irrespective of whether M35 or A35 powder was used in the replication process, as shown in Figure 4.99 (a) and (b). EDS analyses corresponding to the brighter phase i.e. pts. 2 and 4, showed that this phase was considerably enriched in O apart from variable amounts of Fe and Mn when compared to pts. 1 and 3 which mainly consisted of Fe and Mn in approximately the added ratios i.e. 65:35.

Samples which were shielded from direct contact with sintering atmosphere had a more distinct microstructure which was also not particularly affected by the powder used. Surfaces appeared more uniform with a layered structure and dispersed isolated inclusions. EDS analysis revealed that the principal phase i.e.

Table 4.15: EDS analysis in wt.% corresponding to Figure 4.99.

	Pt.	O	C	Fe	Mn	Si	Ca	Mg	N	Al	Ti
M35 Exposed	**1**	12.31	04.27	57.28	24.31	-	-	-	01.82	-	-
	2	20.44	07.29	35.76	33.32	-	-	-	03.20	-	-
A35 Exposed	**3**	14.41	04.69	50.44	30.46	-	-	-	-	-	-
	4	25.96	06.59	22.82	44.63	-	-	-	-	-	-
M35 Shielded	**5**	02.96	11.83	61.49	20.02	-	-	-	03.70	-	-
	6	24.74	10.47	27.99	19.29	03.96	07.05	00.24	-	5.78	00.48
A35 Shielded	**7**	01.84	06.12	68.66	20.58	-	-	-	02.80	-	-
	8	31.55	06.46	13.15	20.97	11.92	14.01	01.94	-	-	-

pts. 5 and 7, consisted primarily of Fe, Mn and C whereas inclusions were rich in O and a variety of other metals including Si, Ca, Mg, Al and Ti. All these metals were detected in cross-sections of the raw Fe powder (refer to Table 4.1), suggesting that the metal oxide inclusions originated from the raw material itself.

4.3.3.4.2 Cross-sectional imaging

Whereas the surface of sintered foams could be easily represented using a single micrograph, the composition of the sample bulk as represented via cross-sectional micrographs, could be better characterised by looking at multiple microstructures across the porous structure, as schematically illustrated in Figure 3.9. Figures 4.100 to 4.103 show said microstructures for foams processed using M35 and A35 powder in the *exposed* configuration and those processed using the same materials in the *shielded* configuration. Microstructures on the left of the figure are representative of the far left and right edges of the sintered structure whereas those on the far right represent the central regions of the foams.

In general, microstructures consisted of a dark phase often present in isolated rounded morphology, austenite with varying Fe:Mn ratios, and a C-rich phase that seemed distinctly "embossed" relative to the metallic phase following etching with 2% Nital. In structures sintered while exposed to the flow of gas, presented in

Figure 4.100 and 4.101, the morphology of the C-rich phase appeared to vary from the edge of the structure towards the centre, becoming more block-like towards the centre. On the other hand, the same phase in shielded foams' microstructures exhibited more homogeneity across the cross-section, as shown in Figures 4.102 and 4.103, with the phase being consistently block-like.

Oxide inclusions in foams processed using A35 foams appeared to be rounder compared to their M35 counterparts. Moreover the quantity of oxide formed in *exposed* foams appeared to increase closer to the edge of the structures[1].

Compositional homogeneity in structures sintered in *shielded* microstructures relative to those sintered in *exposed* configuration can also be observed when considering the EDS analysis presented in Figure 4.104. All plots compare the Mn wt.% measured repeatedly at points along the sample cross-section of samples prepared using M35 and A35 powders. Figures (a) and (b) show the results when taking measurements from the left edge to the right edge of the microstructure for samples sintered in *exposed* and *shielded* configurations respectively. Similarly (c) and (d) show the results for measurements taken from the top towards the bottom of the sample cross-sections, as schematically represented in Figure 3.9.

Results clearly showed that *shielded* foams developed more even austenitic matrix composition irrespective of whether M35 or A35 powders were used, with Mn wt.% varying between 24.7 and 28.2%. Measurements for foams prepared using A35 in the *shielded* configuration averaged lower than their M35 equivalents, possibly pointing towards higher Mn loss to carbide or oxide formation, or sublimation. For samples sintered using the *exposed* configuration, Mn wt.% clearly varied considerably more despite retaining relatively more Mn in the structures compared to *shielded* structures. Error bars for repeated measurements were noticeably larger and the composition at one edge of the structure could differ greatly from the composition at the opposite edge. For instance, for exposed A35 foams the average Mn wt.% varied between 28.1% to 31.3% in the same structure. The composition from the top to the bottom of the cross-section i.e. the face of the foam in contact with the base alumina plate illustrated in Figure 3.9, varied more erratically and followed different trends when using M35 and A35.

[1]The exact amount of oxygen in the samples could not be quantified using oxygen analysers since the equipment was down for maintenance during the available testing period.

Figure 4.100: Representative SEM micrographs of strut cross-sections of a porous structure prepared using M35 powder in *exposed* configuration. Micrographs on the far right of the image are closest to the centre of the structure whereas micrographs on the far left of the image correspond to struts at either edge of the cross-section.

Figure 4.101: Representative SEM micrographs of strut cross-sections of a porous structure prepared using A35 powder in *exposed* configuration. Micrographs on the far right of the image are closest to the centre of the structure whereas micrographs on the far left of the image correspond to struts at either edge of the cross-section.

Figure 4.102: Representative SEM micrographs of strut cross-sections of a porous structure prepared using M35 powder in *shielded* configuration. Micrographs on the far right of the image are closest to the centre of the structure whereas micrographs on the far left of the image correspond to struts at either edge of the cross-section.

Figure 4.103: Representative SEM micrographs of strut cross-sections of a porous structure prepared using A35 powder in *shielded* configuration. Micrographs on the far right of the image are closest to the centre of the structure whereas micrographs on the far left of the image correspond to struts at either edge of the cross-section.

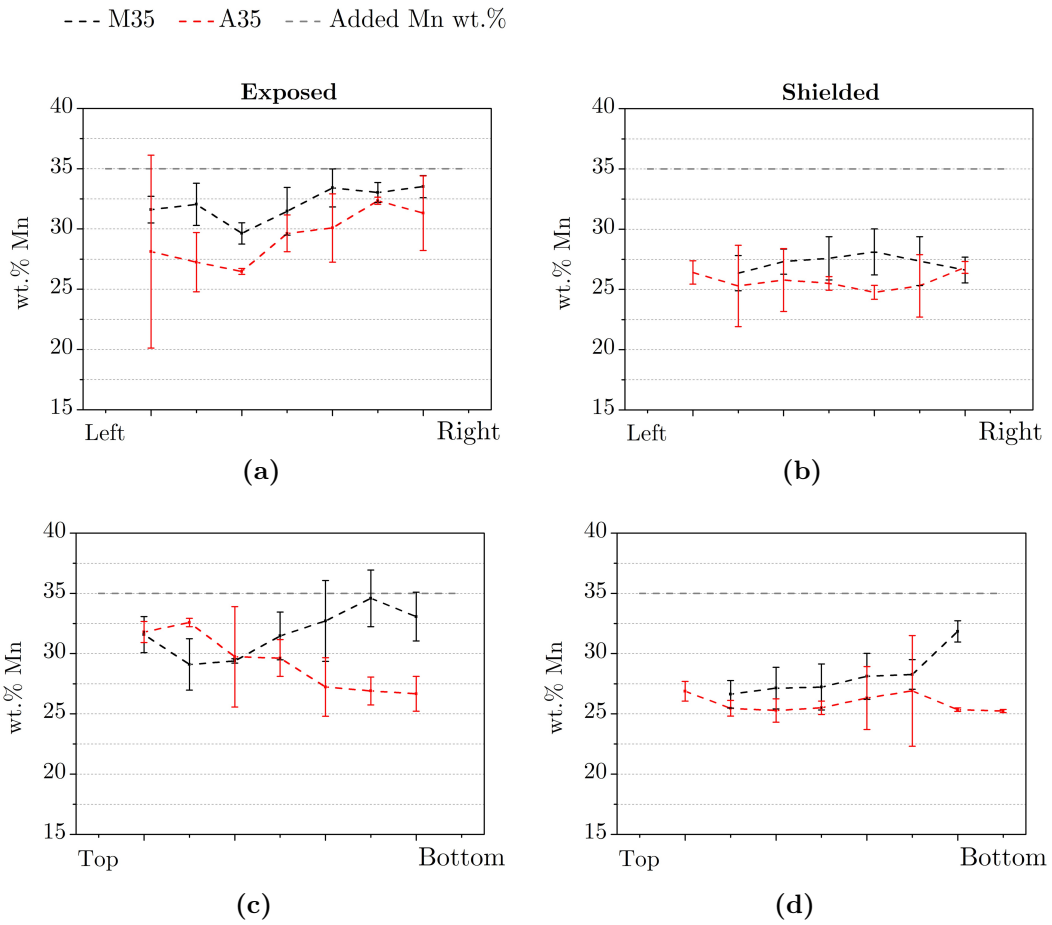

Figure 4.104: EDS analysis for foams processed using M35 and A35 powders in either *exposed* or *shielded* configurations. (a-b) show EDS analysis across the cross-section from the left to the right struts whereas (c-d) show EDS analysis across the cross-section from top to the bottom struts, as schematically illustrated in Figure 3.9. Dashed lines mark the wt.% Mn in the raw material at 35%. Error bars indicate the standard error for each set of measurements (n = 3).

4.3.3.5 Thermal Analysis

Results of thermal analysis carried out on delubricated foams prepared using M35 and A35 powders in either *exposed* or *shielded* configurations, are presented in Figure 4.105. Figures (a) and (b) show TG-DTA plots for *exposed* and *shielded* delubricated foams respectively whereas (c) and (d) show the corresponding DTG curves as well as CO ion current intensity peaks at temperature.

Despite the apparent different oxygen content as well as the measured dif-

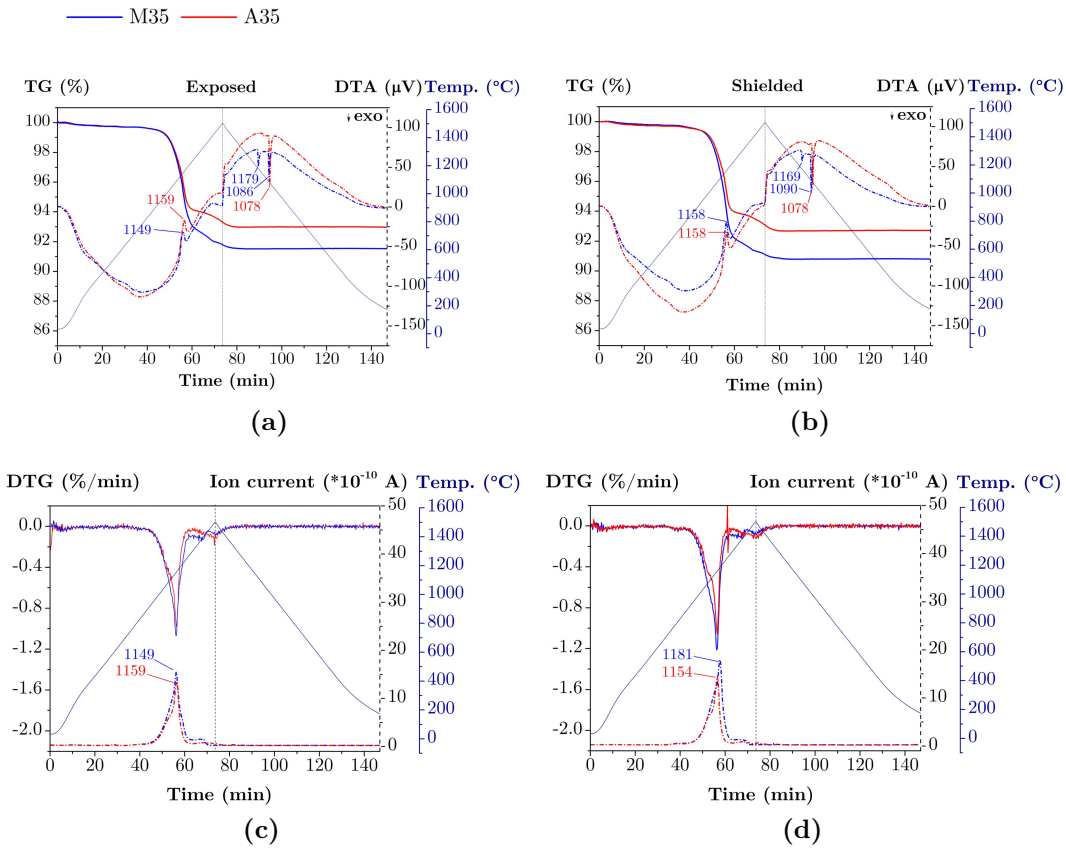

Figure 4.105: Thermal analysis plots for foams prepared using M35 and A35 powders. (a-b) show TG (solid) and DTA (dashed) curves whereas (c-d) show DTG (solid) and CO (m18) ion current signals from MS analysis (dashed). (a) and (c) show results for foams prepared in *exposed* configuration whereas (b) and (d) show results for foams prepared in *shielded* configuration.

ference in C content in each sample, the delubrication process seems to have somewhat homogenised the behaviour of the different specimen. In fact, the melting point for all materials was 1158/1159°C, with the exception of exposed delubricated M35 which still exhibited a relatively close melting point, at 1149°C.

Moreover, as opposed to the results for thermal analysis of the pre-processed powders in Figure 4.86, Figure 4.105 (c) and (d) showed perfectly overlapping DTG and CO ion current curves at the starting point of delubrication. Although a high intensity peak in both curves around the melting point suggested that in these experiments most of the oxides were reduced from the melt, the peaks appeared to be skewed, with a shoulder at an earlier time point suggesting some

reduction takes place around typical sintering temperatures. For both structures prepared using A35 powders, the shoulder was more pronounced in both DTG and ion current curves.

Looking at the TG curves in Figure 4.105, the weight lost by *exposed* and *shielded* delubricated A35 structures over the course of the test was very similar at 7.02% and 7.30% for *exposed* and *shielded* structures respectively. On the other hand, for delubricated foams prepared using M35 powders, the weight lost following delubrication in *shielded* configuration was considerably higher at 9.20% when compared to the 8.48% lost when delubricated while *exposed* to gas flow.

4.3.3.6 Discussion

Outcomes from previous dissertations within the group had presented a process flow to create well-replicated customisable scaffold structures using pure Fe powder applied to the modified replication method described in this work [246, 247]. The processing steps were reproduced by the doctoral candidate to prepare an L-shaped scaffold structure using solely Fe powder, as represented in Figure 4.106. Although not without defects, the general form and reticulated porous network of the template was maintained throughout the heat treatment as evident in Figure 4.106c. Naturally, the Fe structure was still magnetic, which is why in this final part of this dissertation, the aim was to repeat the process with antiferromagnetic Fe35Mn and study the resulting product.

Despite the predominant presence of the γ-FeMn phase in all structures, be they processed using M35 or A35 and in either *exposed* or *shielded* configurations, the structures all exhibited mild magnetic attraction. While stoichiometric MnO and Mn_3C are *not* magnetic [262, 263], the magnetic characteristics of mixed metal carbides and oxides can be significantly more complex. In fact, literature shows that FeMn-oxide foams with tailored magnetic properties have been prepared using the traditional replication method [264]. In the present study, *exposed* samples exhibited a stronger magnetic attraction relative to *shielded* structures. Surface SEM images in Figure 4.99 also showed that *exposed* samples were significantly more covered in oxides which implies that the magnetic character is correlated to the presence of the same oxides. XRD and cross-sectional EDS

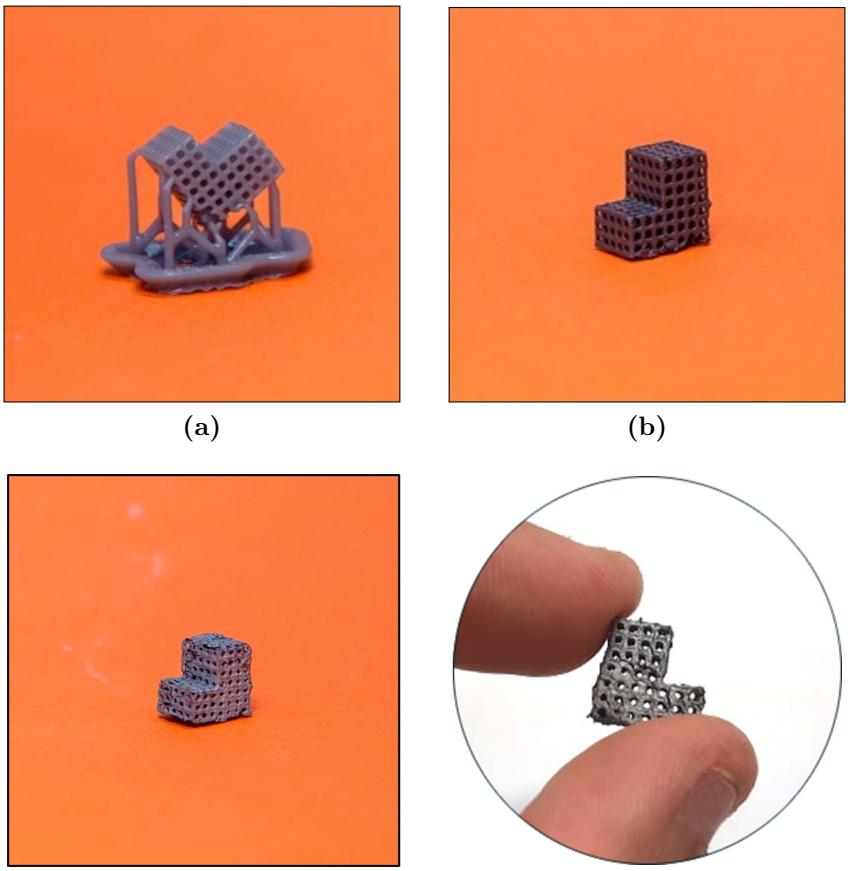

Figure 4.106: Successful replication of customised geometry using Fe powder. Processing steps showin 3D-printed template in (a), powder-coating template in (b) and sintered result in (c).

analysis of the samples did not seem to indicate a strong presence of α-ferrite due to Mn loss for oxide and/or carbide formation or loss due to sublimation. This reduces the likelihood that the magnetic characteristics are related to any localised ferrite formation.

4.3.3.6.1 Analysing the influence of powder pre-processing on the outcome of modified replication method

In the previous two parts of this investigation, A35 powders were shown to perform considerably better than M35 powders when it came to surface oxide re-

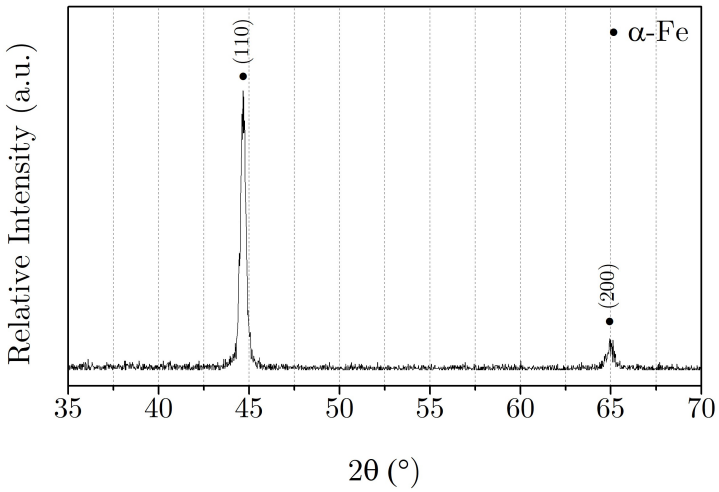

Figure 4.107: XRD pattern for cross-section of foam structure prepared using the modified replication method with pure Fe powders showing only α-ferrite presence [247].

duction and densification. The main negative aspect observed with sintered A35 samples in Section 4.3.2, was the higher amount of interconnected M_3C precipitates formed. In this part of the study, the benefits of using A35 powders were not as evident whereas carbide formation became even more problematic.

Delubricated A35 foam samples were shown to contain more C compared to M35 samples, providing available C both for carbothermal reduction but also for M_3C precipitation. In particular, XRD analysis confirmed the latter as the intensities of M_3C peaks relative to the γ-FeMn peaks were visibly higher for A35 samples, pointing towards a higher composition of the same phase in A35 samples. This was also evident in EDS analysis presented in Figure 4.104 (c) and (d) as precipitation of these Mn-rich carbides left the austenite with less wt.% Mn than the average wt.% Mn present in foams processed using M35 powders. Moreover, carbides consistently formed in a "block"-like morphology. The combination of these aspects likely led to the formation of more brittle structures which were more prone to collapse, as shown in Figure 4.96d. In fact, cross-sectional XRD analysis of better replicated scaffolds prepared using the same method with Fe powders in Figure 4.107, showed that there was no, or negligible, formation of metal oxides and carbides in well-replicated Fe scaffolds [247].

Despite the higher concentration of C in the A35 foam structures, less weight

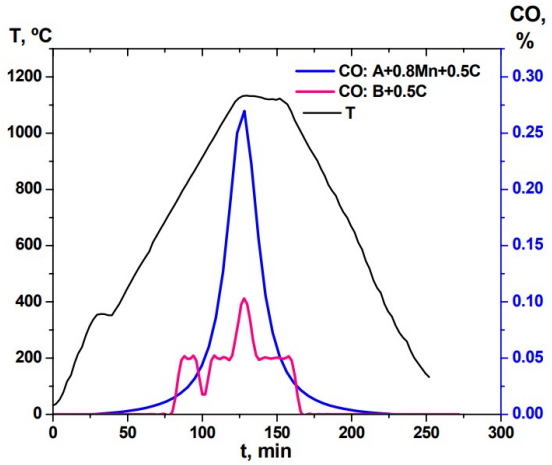

Figure 4.108: CO intensity profiles during sintering of prealloyed Fe0.3Mn powder (A) admixed with 0.5% elemental Mn and 0.5% C, and prealloyed Fe0.8Mn mixed with 0.5% C (B) [265].

was lost by delubricated A35 samples in the TG analysis when compared to M35, irrespective of the delubrication configuration. Although SEM micrographs of the sample surfaces in Figure 4.99 did not reveal any distinctive features between M35 and A35 foams processed using the same configuration, the observed lower mass loss is most likely an indication that the lower chemical activity of A35 powders resulted in less surface oxidation during the delubrication process and consequent thermal analysis. In fact, in a study by Hryha *et al.* [265], when using FeMn mixture which were fully prealloyed, less CO was generated from reduction when compared to using powder mixtures containing elemental Mn, as shown in Figure 4.108 [265]. As in the present study, lower CO generation is indicative of lower mass loss.

Aside from the reduced mass loss experienced by A35 samples, the differences in carbide and oxide quantities and morphologies observed in the microstructures in Section 4.3.3.4.2, did not cause any other distinctly different thermal behaviour. The onset of reduction of surface oxides from delubricated foams as well as the melting temperature for all samples fell within the same temperature range, between 1149°C and 1159°C, indicating that the delubrication process seemed to homogenise the thermal behaviour of the samples irrespective of configuration used. Having said this, the cooling portion of the DTA curves in Figures 4.105

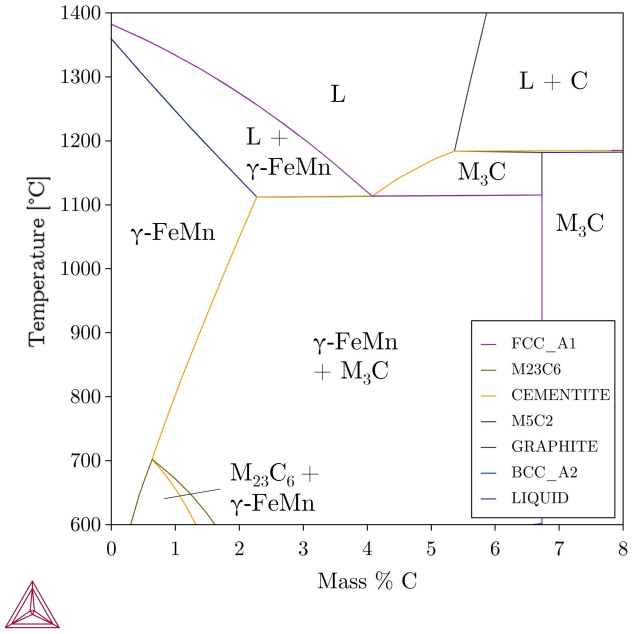

Figure 4.109: Phase diagram for Fe35MnxC with for x varying between 0 and 8 wt.%, generated using Thermo-Calc.

(a) and (b) indicate that experiencing more reduction, and therefore losing more C, placed the composition of delubricated M35 samples to the left of the eutectic point in Figure 4.109, with two distinct exothermic peaks. A35 delubricated samples on the other hand remained closer to the eutectic point, experiencing a single solidification point. The influence of these minor thermal differences between the materials is most probably not as influential on the final product as the fact that the melting point of the bulk of the materials is only 30 to 40°C away from the sintering temperature of 1120°C; a trait that is not particularly recommendable for structure stability during the process' high temperature plateau.

4.3.3.6.2 Analysing the influence of sintering configuration on the outcome of modified replication method

The most significant impact of the sintering configuration on the microstructures of M35 and A35 foams, was due to the different micro-atmospheres brought about by the different setups. Originally, the *shielded* configuration was tested in or-

der to determine how the constant contact of the N_2H_2 gas with the samples, influenced oxidation. However, the same configuration also had a pronounced influence on carbide precipitation.

Although the shielded setup does not create a sealed microatmosphere as in the procedure described by Cias *et al.* [216] in Figure 2.22, at the onset of template degradation, C-rich gases released from the degrading acrylate template are trapped within the steel shield to a certain degree, as illustrated in Figure 4.110 [266]. With *exposed* samples, most of the released C-rich products, especially those originating from the exposed outer struts of the structure, are quickly removed from the area by the flow of the N_2-$5H_2$.

Looking at the results from carbon analysis for delubricated samples in Figure 4.97, one could clearly see that the configuration had a pronounced influence on the C content for foams prepared using M35 powders, with *shielded* M35 structures containing 0.96% more C than *exposed* structures. This is naturally due to the extended period of exposure to the C-rich atmosphere in the *shielded* setup promoting further diffusion of C into the metal. The higher C content in foams delubricated using the *shielded* configuration in turn resulted in higher mass loss recorded in the TG curve in Figure 4.105b compared to the TG curve in (a).

On the other hand, foams prepared using different configurations with A35 powders did not exhibit the same trend, with just 0.09% C difference between *exposed* and *shielded* structures. In fact, TG curves in Figures 4.105a and (b) indicated that delubricated *shielded* material lost just 0.3% more mass than *ex-*

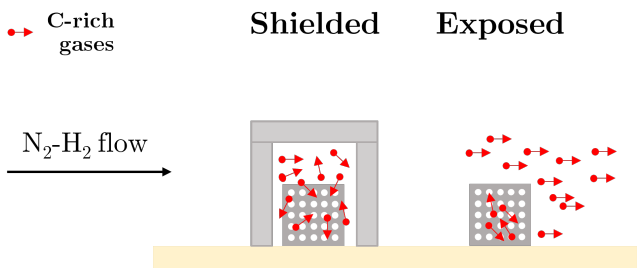

Figure 4.110: Schematic showing influence of sintering configuration on the distribution of C-rich degradation products around the foam samples during sintering in a tube furnace.

posed structures due to the slightly elevated C content. It has been previously shown in literature that higher defect densities reduce the activation energy for diffusion [219]. Having undergone high energy ball milling for six times the duration of M35 powders, foams prepared from A35 could dissolve more C in the microstructure from the surrounding C-rich atmosphere at a faster rate leading to similar C content in the two delubricated materials [267]. Apart from the C quantification results, cross-sectional SEM images in Figures 4.101 and 4.103 show similar quantities of blocky carbides in the microstructures of the two A35 samples.

The same cross-sectional SEM images in Section 4.3.3.4.2 illustrate how the configuration affects the variation in the microstructure from the edges towards the centre of the structure. Whereas with *shielded* structures in Figures 4.102 and 4.103 the distribution of carbides and oxide inclusions was considerably homogeneous, *exposed* structures contained higher carbide concentrations close to the centre with larger oxides littering the struts at the edge of the foam. The superior homogeneity displayed by *shielded* foams could be even better observed in the Mn concentration curves plotted in Figure 4.104. The variation in microstructures could also be attributed to the microatmospheres created by the different sintering configurations. The trapped degradation productions from template degradation as well as the restricted N_2-$5H_2$ flow, provide a rather even atmospheric makeup around the whole structure. Contrastingly, whereas the flow of N_2-$5H_2$ could immediately remove the C-rich gaseous products from around the outer struts of the *exposed* structures, the same flow seems to have been less effective in doing the same from the structures' central areas, leaving more C to diffuse into the central struts.

This also relates to the signs of carbothermal reduction influence observed in the sintered structures. Optical micrographs of representative struts from *shielded* structures prepared using M35 and A35 powders in Figure 4.111 (a) and (b), show a layer of around 5 µm from the surface of the strut which is free from dark oxide inclusions. The same effect was observed all over the sample cross-section owing to the high and rather homogeneous C content throughout the structure. Similar "clean" edges were observed around the centre of *exposed* structures irrespective of the powder material used, as shown in Figure 4.111 (c) and (d). The same could

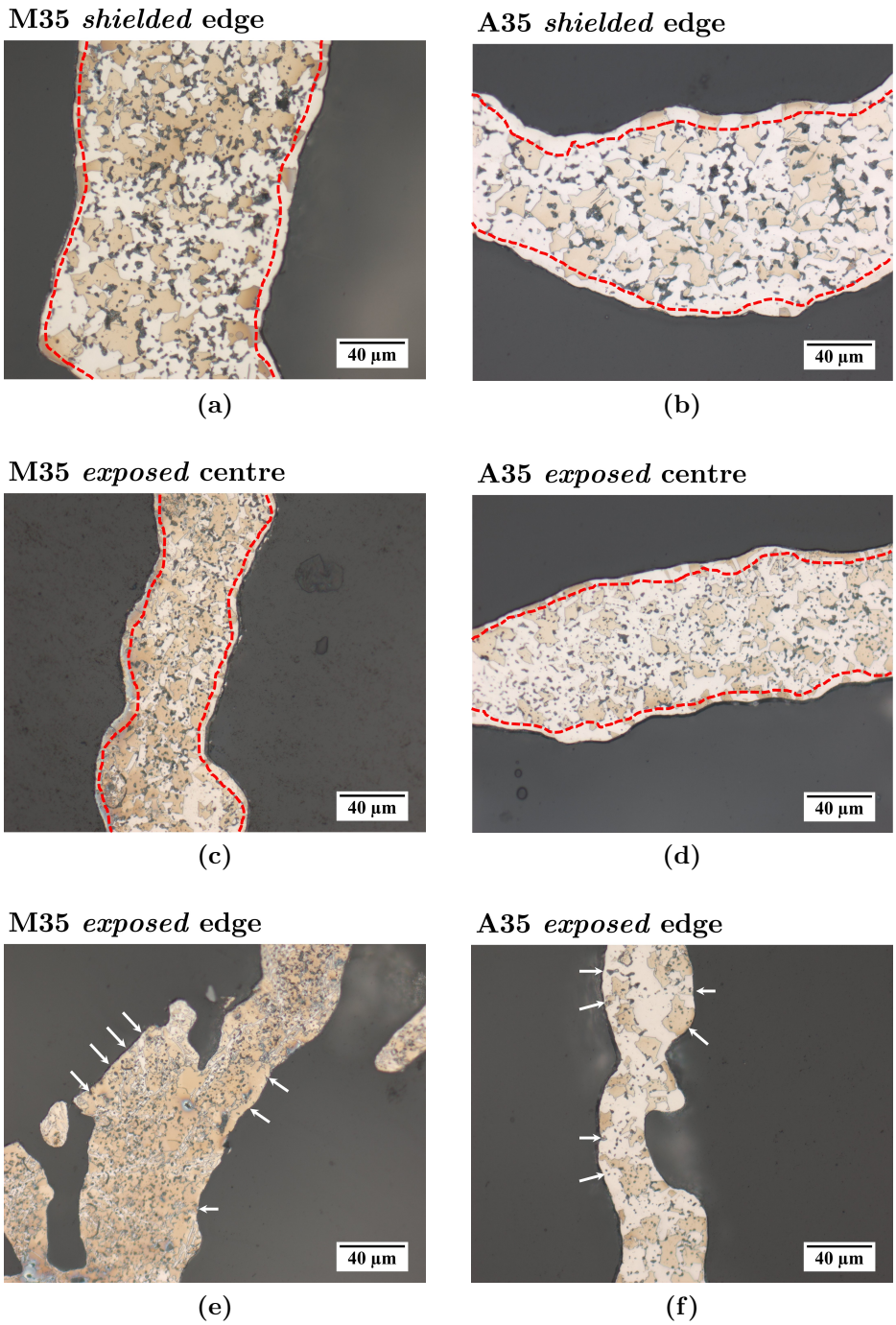

Figure 4.111: Optical microscopy images of strut cross-sections. Representative struts from *shielded* samples prepared using (a) M35 and (b) A35 powders as well as struts at the centre of *exposed* samples prepared using (c) M35 and (d) A35 powders show an oxide-free layer at the surface of each strut, marked in red. On the other hand, edge struts for *exposed* samples prepared using (e) M35 and (f) A35 powders show oxide inclusions extending to the surface. Instances of these oxides are pointed out with white arrows.

not be said for struts closer to the edge of *exposed* structures, shown in (e) and (f). The more efficient clearing of C-rich products from around the outer struts reduced the C diffusion and as a result, the potential of reduction from taking place around these areas. This is further evidenced in the SEM images of the structure surfaces in Figure 4.99. For both M35 and A35 materials, *exposed* edge structures in Figure 4.99 (a) and (b) were almost fully covered in oxides whereas for *shielded* edge struts in (c) and (d), the surface seemed to be generally free of continuous oxides with only dispersed inclusions likely related to contamination in the starting Fe powder.

It is not clear what caused the layered appearance of the *shielded* surfaces in Figures 4.99 (c) and (d). Analysis of etched cross-sections in Section 4.3.3.4.2 did not seem to reveal any microstructural features that could correspond to and provide further information on this outcome of the modified replication method. This therefore remains a question for future work.

4.3.3.6.3 Influence of template volume on the metal characteristics

As already mentioned, embrittlement of the sintered structures was at least partly due to the vast network of metal carbides formed in each and every sample. Since the formation of said carbides is a result of carburisation caused by the polymeric templates' degradation byproducts, tests were run with a customised template having half the strut size of the original template, the struts being 350 µm thick instead of 700 µm. This resulted in the test template having 55% the volume of the original template, thus reducing the source volume by approximately half.

Carbon analyser measurements presented in Figure 4.112 show the influence of this change on the C content in structures prepared using M35 powders in both configurations. The effect was prominent for structures sintered using both configurations with the wt.% C dropping significantly for both. For *exposed* delubricated samples the average C content dropped by 1.76%, to 2.74 wt.% C whereas for *shielded* structures the C content was reduced by 1.37%, down to to an average of 4.09 wt.% C. In general, the influence of longer exposure to C-rich microatmosphere, still resulted in a considerably higher concentration of C in *shielded* structures when compared to *exposed*.

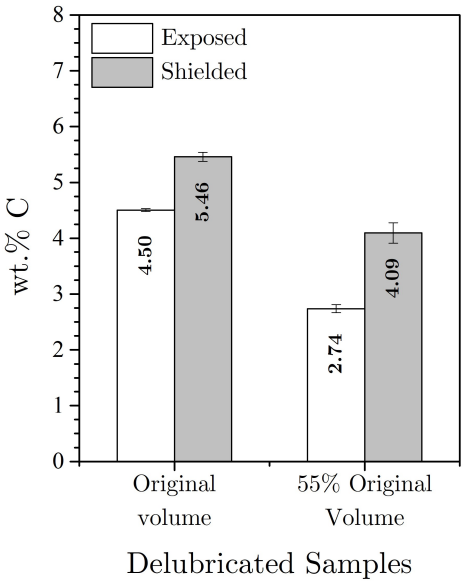

Figure 4.112: Carbon content in crushed foams processed using M35 powder and delubricated in *exposed* and *shielded* configurations with varying template volume. Error bar for measured quantities represents standard error (n = 3).

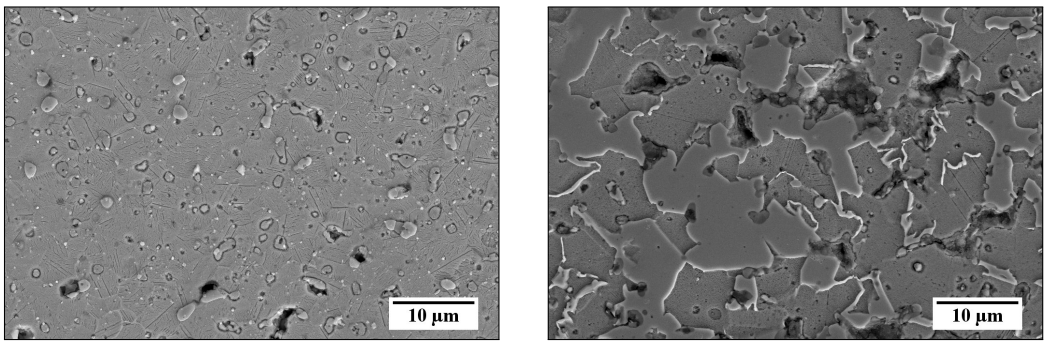

(a) **(b)**

Figure 4.113: Representative SEM micrographs of (a) *exposed* and (b) *shielded* structures prepared using M35 powder and templates with 55% of the original volume.

In fact, representative cross-sectional SEM micrographs for the reduced volume structures sintered using the *shielded* configuration in Figure 4.113b, showed that the "blocky" carbides where still abundantly present. The opposite was true for the *exposed* structures in which neither blocky nor interconnected grain boundary carbides were visible anywhere across the cross-section. The evenly

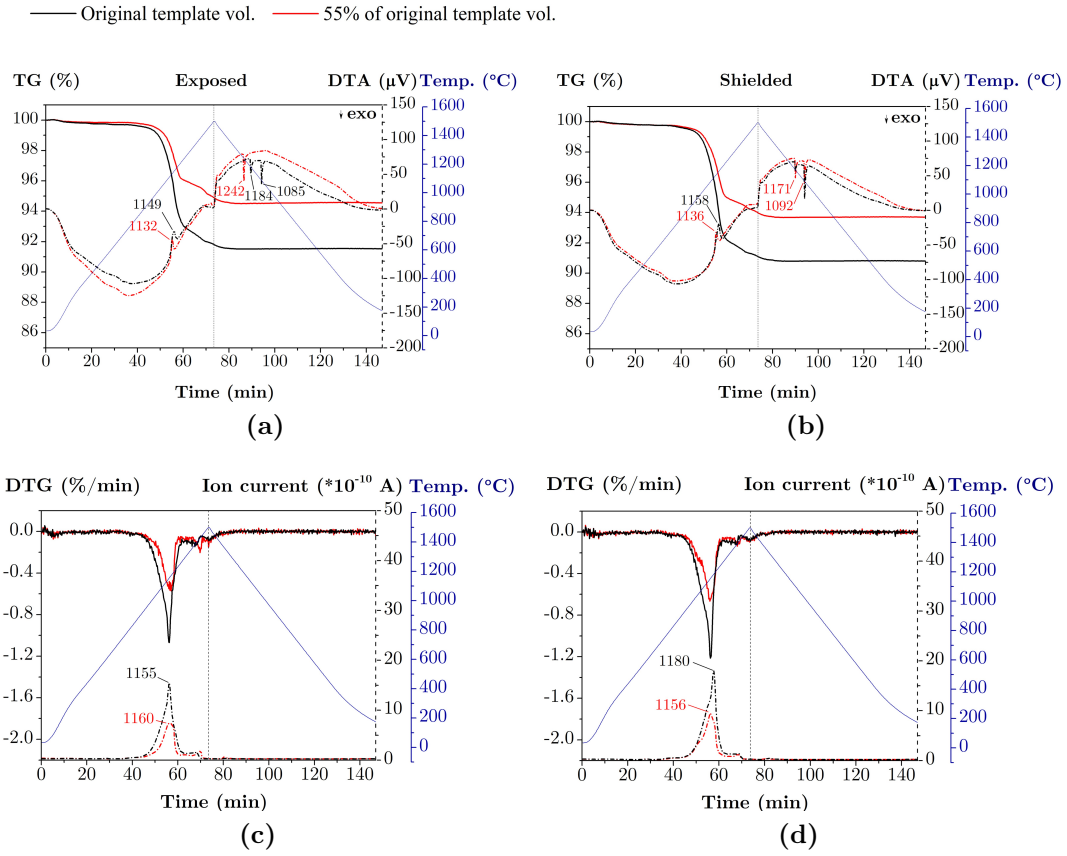

Figure 4.114: Thermal analysis plots for foams prepared using M35 powder with the original template volume and an alternative template consisting of 55% of the original volume. (a-b) show TG (solid) and DTA (dashed) curves whereas (c-d) show DTG (solid) and CO (m18) ion current signals from MS analysis (dashed). (a) and (c) show results for foams prepared in *exposed* configuration whereas (b) and (d) show results for foams prepared in *shielded* configuration.

distributed inclusions visible in Figure 4.113a, were all rich in oxygen. Therefore, whereas the formation of detrimental oxides was not drastically reduced, especially near the edges of the structure, the formation of brittle interconnected metal carbides was significantly reduced in the *exposed* structures with reduction in polymeric template volume.

Despite this, TG curves presented in Figure 4.114 (a) showed that the *exposed* structures prepared with thinner strutted templates, still retained the ability to reduce some of their oxides causing around 5.50% mass loss. Higher amounts of C in delubricated *shielded* struts resulted in slightly higher mass loss at 6.32%.

However when compared to structures prepared using the original templates, the mass loss was considerably reduced. Although the polymeric template degradation byproducts might have themselves caused some oxidation and therefore reducing the source of said byproducts might have resulted in some reduction of oxide formation [266], the reduced mass loss due to reduction was more likely limited by the reduced availability of C.

5

Conclusions and Future Work

Since the initial proposition by Peuster *et al.* to use pure Fe for biodegradable implant applications in 2001, hundreds of publications have discussed the feasibility of using various alloying elements, processing methods and coating treatments to improve the performance of these materials and push them further towards clinical application. FeMn alloys in particular have attracted a considerable fraction of that interest in the field due to its anti-ferromagnetism. Despite the widespread approach of powder metallurgical processing to prepare micro and macro-porous FeMn coupons and scaffold structures, literature reviewed in Chapter 2 still revealed conflicting results and views on the corrosion behaviour of these materials. Unanswered questions also remained regarding the viability of pressureless powder-processing of FeMn for scaffold fabrication.

Conclusions considering the work discussed in this thesis on both of the explored aspects related to FeMn alloys, are presented hereunder.

5.1 Corrosion testing of powder processed Fe-based alloys

When it comes to corrosion testing, the main aims of this work was to investigate the influence of Mn and Ag additions to Fe on the corrosion behaviour and how that behaviour changes with varying testing conditions, in particular the testing electrolyte.

Despite the absence of corrosion rate measurements, the tested alloys displayed clear behavioural differences particularly in simple HBSS i.e. without Ca^{2+} ions and short-term testing, as carried out in the vast majority of existent published articles. Irrespective of the testing technique used, Fe was always associated to a higher corrosion resistances compared to FeMn alloys. On the other end of the spectrum, additions of Ag consistently resulted in some form of microgalvanic acceleration as opposed to uniform degradation experienced by FeMn, most noticeable in the local pH and DO measurements conducted in Phase One. EIS testing in both Phase One and Two supported these observations.

However, trends observed when conducting 24 h EIS tests indicated that the performance of the corroding system as represented using electrical circuitry, either converged or overlapped irrespective of the metal being tested. For instance, quantifiably significant differences between charge transfer resistances measured upon immersion, generally became insignificant within the first 24 h. Analysis of results across testing phases indicated that this was most likely due to the build-up of metal hydroxides and a partially protective Ca/P-rich corrosion product layer whose formation rate is related to the corrosion rate of the material, but which in itself starts to limit the influence of the substrate it grows on within the first few hours from test initiation. Incidentally, this was also observed *in vivo* wherein Ag-containing pins clearly accumulated more corrosion products but did not experience any significant degradation, with the pins' diameters remaining close to the diameter machined during sample preparation.

Although testing in BSA-containing HBSS+Ca was only carried out on FeMn, the observed sample behaviour was very similar to that reported in literature by groups testing Mg and Zn in physiological media containing similar concentrations of BSA. The presence of protein chelated Ca^{2+} ions delaying the precipitation of protective apatite-like products and encouraged mild localised corrosion potentially due to occluded regions forming between the metal surface and adsorbed protein. Testing with protein in Phases Three and Four further confirmed that increasing the complexity of the testing electrolyte, diminishes the influence of the metal composition.

Although protein was added to the electrolyte in an attempt at making the *in vitro* testing electrolyte more representative of the *in vivo* environment, the

influence of protein on FeMn in *in vitro* testing did not seem to translate to the observed results following *in vivo* testing. It is possible that the chosen concentration of BSA content for *in vitro* tests in Phases Three and Four might have been overestimated compared to the concentration in vertebrae, despite the decision being based on published data. It is also possible that the influence of protein on the metal when in the body, manifests in a different way. Further to these observations between *in vitro* and *in vivo* results, implanted pins similarly accumulated Ca and P-rich products however none of the characterisation techniques used confirmed whether they precipitated in the preferred form of apatite-like products, as observed *in vitro*. On the other hand $CaCO_3$ was detected via XRD on explanted pins but was not similarly found on *in vitro* tested samples. Although techniques like XPS were not available to confirm this, studies in which carbonates precipitated in significant amounts were quite easily distinguished using EDS techniques. This discrepancy between the observed corrosion product compositions leads to the conclusion that the electrolytes used during *in vitro* testing might not be ideal for simulating environments related to orthopaedic applications and should contain a higher concentration of CO_3^{2-}.

As mentioned multiple times when discussing the resulted in Chapter 4, the biggest issue in collaborative advancement of most biodegradable metals and devices, and Fe-based alloys in particular, is the lack of clear standards available related to corrosion testing of these materials. However, ASTM representatives presenting at the conference attended by the undersigned in Alicante in August 2022, are well aware of this limitation and are setting up round robin corrosion studies that are aimed at identifying the key influencing factors that could introduce variability in results and address limitations specific to main materials of interest. In this work, issues were encountered related to incomplete corrosion product removal following long-term static immersion testing of porous metals as well as improper control of pH due to inadequate buffering mechanisms and atmosphere control. The considerable difference observed in the extent of microgalvanic corrosion incurred by FeMnAg tested in HBSS in Phase One in testing setups with (local measurements) and without (PDP and EIS) electrolyte flow, is also an indication of the dire need for strict testing guidelines.

To conclude, the results of this work when considered along with other published results in literature, indicate that the applicability of these materials can only be found if processed to have a highly porous geometry, as indicated in a recent study with Fe30Mn scaffolds by Nie *et al.* [191]. Otherwise, with wrought and micro-porous samples, the results indicate only limited degradation in orthopaedic implantation sites. Higher surface areas and implantation in sites with increased physiological fluid flow, could have considerably more positive outcomes.

Research questions

The following are responses to the principal research questions related to corrosion testing.

i. **How does the addition of 35 wt.% Mn and 5 wt.% Ag to Fe via powder processing, influence the metals' degradation behaviour upon immersion and in consequent hours?**

   The addition of 35 wt.% Mn leads to enhanced uniform corrosion upon immersion, however, results presented in this work showed that the addition of Mn alone, does not result in a long term increase in degradation, especially in Ca^{2+} environments as is the physiological environment for typical orthopaedic implantation sites. The addition of 5 wt.% Ag leads to noticeable microgalvanic corrosion acceleration *in vitro*, however, in the presence of Ca^{2+}, rapid precipitation of hydroxyapatite-like corrosion products significantly reduces the effectives of the Ag as a local cathode. These conclusions indicate that FeMnAg alloys could be promising alloys for use in cardiovascular applications wherein the physiological environment is less static and therefore the influence of the local cathode could be extended resulting in more favourable degradation rates.

ii. **To which extent does the testing electrolyte composition, in particular the presence of Ca^{2+} ions and albumin, affect the degradation behaviour of Fe-based alloys?**

The presence of both Ca^{2+} and albumin in the electrolyte have very evident influences on the evolution of the corrosion behaviour of FeMn alloys in HBSS. In particular, the addition of Ca^{2+} results in rapid formation of hydroxyapatite-like precipitates that consistently provides a barrier-like effect on corrosion progress. On the other hand, the addition of albumin results in retarded precipitation of the same precipitates *in vivo* that result in lowered corrosion resistance upon metal contact with the electrolyte when testing *in vitro*. Whereas *in vitro*, albumin consistently resulted in instances of localised corrosion attack, the same effect is not observed on FeMn and FeMnAg samples tested *in vivo*.

iii. **What are the distinctions between outcomes of *in vivo* testing of FeMn alloys with respect to their *in vitro* behaviour?**

Much like the patterns observed *in vitro*, Ag-containing pins *in vivo* also show signs of microgalvanically accelerated corrosion product precipitation. In both *in vitro* and *in vivo* tests, the rapid accumulation of Ca-rich products on the surface results in limited degradation soon after the initiation of the test, reducing the impact of the material composition on the observed results. One major distinction between the two test outcomes, was noted in the corrosion products observed in post-test analysis. Whereas *in vitro* the corrosion products are mainly composed of metal hydroxides along with metal and Ca-phosphates, on *in vivo* tested samples, $CaCO_3$ was also consistently detected using XRD. This result highlights the need to shift *in vitro* testing electrolytes to ones containing higher concentrations of carbonates.

5.1.1 Future Work

To build on the findings of this thesis, below are some suggestions for further investigations.

i. Further analysis needs to be carried out to determine a more representative electrolyte when testing materials aimed at orthopaedic applications. The absence of carbonate precipitation in *in vitro* tests in this work contrasted with the detection of $CaCO_3$ as the principal phase present on samples tested *in vivo*, indicating that the discrepancy lies not only in the testing environment present in the two testing modes, but also in the testing fluid composition;

ii. Whereas HBSS (without Ca^{2+}) has been confirmed to offer limited representation of the physiological environment, further tests could be run with HBSS+Ca and other complex electrolytes, for example Minimum Essential Medium (MEM). In particular, long term immersion tests in a controlled CO_2 environment, with and without electrolyte refreshment, and in both static and dynamic conditions, would help expand the community's knowledge of the influence of these parameters on the *in vitro* outcomes. It would also help inform the decisions being taken on creating standard testing procedures for these applications;

iii. Related to the previous point, further studies could be carried out to determine what concentration of BSA (or other proteins), best represents the target *in vivo* environment. Moreover, for target environments wherein the physiological fluid would be refreshed around the implantation site, the effect of having fresh Ca^{2+} ions at the surface could lead to more protective precipitates forming when compared to the situation observed in EIS testing in HBSS+BSA in this work. This might explain why no signs of localised corrosion were detected for samples tested *in vivo*, but further work must be carried out to confirm this hypothesis;

iv. So far, there has only been one publication which shares the promising outcomes of testing FeMn foams *in vivo* [191]. Considering the conclusions of this work which indicate that the most viable application of this material in orthopaedics is to have a very high surface-to-volume ratio, more studies need to be carried out to determine the best structural designs and processing methods to make load-bearing biodegradable FeMn scaffolds a potential option in future markets.

5.2 Powder-processing of FeMn for scaffold applications

Mn has long been known to be a problematic material to process through the powder route. However this has not stopped researchers in the field of precision steel manufacturing from researching it as an alternative to more expensive alloying elements like Cu, Ni and Si [205]. Neither has it prevented researchers in the biodegradable metals field from looking at developing solutions involving Mn.

The work across three main parts in Section 4.3, highlighted the challenges involved in achieving the right compositional balance to preserve the antiferromagnetism necessary, prevent extensive oxidation and at the same time allow for carbothermal reduction to take place when conditions are favourable.

Analysis of "clean" material samples i.e. powders and pressed-and-sintered samples prepared using the same powders, confirmed the limitations of blended elemental mixtures, in this work referred to as B35. The early onset of oxidation of pure Mn and lack of carbon available for reduction, resulted in early limits set on the extent of densification that could be achieved for pressed-and-sintered samples, due to MnO formation at the pore interface. Different pre-processing methods were adopted with the aim of reducing high-temperature reactivity of the Mn while including carbon to enhance the potential for self-cleaning through carbothermal reduction. Thermal analysis as well as analysis of pressed-and-sintered coupons revealed different degrees of improvement of both these aspects. Oxide inclusions in pressed microstructures were significantly reduced in size compared to those present in B35 microstructures. The same oxides became increasingly dispersed for samples prepared using M35, A35 and MAM respectively. In the same order, the powders also contained higher amounts of carbon which evidently contributed to significant carbothermal reduction with reduction temperatures also dropping towards typical sintering temperatures, as shown in the TG-MS analysis. DTA analysis showed the impact of the increased carbon content on the melting points of the raw material, with the melting point dropping as the carbon content in the powders increased. In fact, for MAM powders the melting point in Ar dropped as low as 1314°C; 91°C lower than the melting point of B35. This too could be a doubtful advantage when considering the preparation of highly porous

Fe35Mn scaffolds, where having the sintering and melting temperatures within a few tens of °C from each other, could adversely affect the structural stability of the structure. Naturally, the sintering temperature could be lowered accordingly, however this would once again reduce the possibility of effective carbothermal reduction.

Apart from this, carbon also led to the formation of interconnected grain boundary M_3C carbides, which posed a bigger concern for the potential brittleness of more intricate structures prepared using the same materials. In fact, when analysing the feasibility of preparing FeMn scaffold structures using the modified replication method, one of the major identified problems was the vast quantities of the same mixed metal carbides formed; an issue exacerbated by the use of a carbon-rich source as the 3D-printed template in addition to the carbon already present in the as-processed powders due to the process control agent used during ball-milling. This, along with the presence of oxides resulted in partial collapse of several of the test structures.

Thermogravimetric analysis of delubricated foams indicated that using pre-alloyed A35 powder to prepare the scaffold structures presented some minor advantages when it came to high temperature reactivity. However, when subjected to the modified replication method, the final microstructure seemed to be less impacted by the pre-processing method used and more dependent on the configuration used, be it *exposed* or *shielded*. This was confirmed both by thermal analysis as well as qualitative evaluation of cross-sectional microstructures. *Shielded* structures had superior compositional homogeneity compared to their *exposed* counterparts, despite losing more than 8 wt.% Mn on average from the austenitic matrix. With Mn already presenting the issue of sublimation, Mn loss to carbide and oxide formation led to the processing method allowing for rather poor control on the final composition of the structure.

Lastly, while carbothermal reduction was shown to assist with oxide reduction even when using the modified replication method, its benefits could only be appreciated at the very surface of the struts i.e. the first 5 to 10 µm from the surface. As with pressed and sintered samples, kinetic limitations prevented further oxide reduction despite the presence of plenty of carbon in the microstructure. Moreover, reduction also took place more uniformly for *shielded* structures wherein the

micro-atmosphere was more enriched with carbon as opposed to *exposed* structures wherein the C-rich atmosphere was constantly being flushed away by the flow of N_2-$5H_2$ gas.

To conclude, whereas the powders developed, in particular milled and alloyed powders, offer several advantages when considered as raw material to be used with alternative scaffold processing techniques in the same field, the modified replication method itself has presented a number of hurdles. The poor control on both the elemental and phase composition as well as the limited replicability of the customised template, reduces the attractiveness of the technique, despite the relatively low capital investment required to prepare the samples compared to techniques like Laser Bed Powder Fusion.

Research question

The following is a response to the principal research question related to the powder processing aspect of this work.

i. **Can powder pre-processing using ball-milling provide a feasible solution for the preparation of Fe35Mn scaffolds through the pressureless sintering route?**

   Both milled (M35) and alloyed (A35) powders showed interesting characteristics with regards to their ability to reduce the extent of high temperature oxidation during sintering. Both powders also exhibited a significant amount of self-cleaning through reduction of stable Mn-rich oxides. However, when used in the preparation of scaffolds through the modified replication method, these powders still fell short of producing scaffolds with favourable characteristics for orthopaedic implant applications. Having said this, small changes to ball-milling parameters as well as to variables within the modified replication method itself, could lead to significantly improved results. However, in general, successful use of ball-milled FeMn powders for this application is very difficult to achieve without improved process monitoring and process control facilities when it comes to the sintering procedure.

5.2.1 Future Work

While the benefits of using the modified replication method following the analysis presented are not plentiful, one must keep in mind that only a limited set of parameters were explored in this work. Investigating the technique further, as has been done with other methods like Laser Bed Powder Fusion [182] and 3D inkjet printing [227], could lead to more promising results. Some suggestions for future work are listed hereunder.

i. For further investigation of the modified replication method, the ball milling procedure could be modified such that less process control agent is used in the preparation of the pre-processed powders. In this way, the primary carbon source would be the thermal degradation products of the polymeric template and the as-processed powders would have lower concentrations of carbon to begin with;

ii. To explore other stereolithography technologies and 3D printing materials that could be used to prepare templates with thinner strut sizes and therefore further reduce the volume of the templates used. This, along with reduced carbon from the powder-processing step could lead to more suitable carbon concentrations in the final scaffold structures. Moreover, using thinner struts could also result in more complete oxide reduction across the strut cross-sections;

iii. In this work, the sintering parameters that could be controlled and measured during the process were the temperature and the flow rate of the N_2-H_2 gas. Sintering setups designed to study process control have been reported to have multiple sensors at different parts of the furnace (eg. gas inlet, region above the sample, gas outlet) to take measurements of dew point and CO/CO_2 ratio [265]. Such measurements could give a much clearer picture of how the atmosphere around the samples being sintered changes at different stages of the process to give the observed microstructures;

iv. Quenching could be employed to suppress the precipitation of carbides, as is often suggested for Hadfield steels.

References

[1] G. Tang, Z. Liu, Y. Liu, J. Yu, X. Wang, Z. Tan, and X. Ye, "Recent Trends in the Development of Bone Regenerative Biomaterials," *Frontiers in Cell and Developmental Biology*, vol. 9, no. May, pp. 1–18, 2021.

[2] G. Turnbull, J. Clarke, F. Picard, P. Riches, L. Jia, F. Han, B. Li, and W. Shu, "3D bioactive composite scaffolds for bone tissue engineering," *Bioactive Materials*, vol. 3, no. 3, pp. 278–314, 2018.

[3] C. B. Carter and M. G. Norton, "Ceramics in Biology and Medicine," in *Ceramic Materials*, pp. 660–676, New York, NY: Springer, 2013.

[4] N. E. Putra, M. J. Mirzaali, I. Apachitei, J. Zhou, and A. A. Zadpoor, "Multi-material additive manufacturing technologies for Ti-, Mg-, and Fe-based biomaterials for bone substitution," *Acta Biomaterialia*, vol. 109, pp. 1–20, 2020.

[5] S. Bose, M. Roy, and A. Bandyopadhyay, "Recent advances in bone tissue engineering scaffolds," *Trends in Biotechnology*, vol. 30, no. 10, pp. 546–554, 2012.

[6] M. A. Velasco, C. A. Narváez-Tovar, and D. A. Garzón-Alvarado, "Design, materials, and mechanobiology of biodegradable scaffolds for bone tissue engineering," *BioMed Research International*, vol. 2015, 2015.

[7] L. P. Corrales, M. L. Esteves, and J. a. E. Vick, "Scaffold design for bone regeneration. Journal of nanoscience and nanotechnology," *J Nanosci Nanotechnol*, vol. 14, no. 1, pp. 15–56, 2014.

[8] A. J. Teichtahl, A. E. Wluka, P. Wijethilake, Y. Wang, A. Ghasem-Zadeh, and F. M. Cicuttini, "Wolff's law in action: A mechanism for early knee osteoarthritis," *Arthritis Research and Therapy*, vol. 17, no. 1, pp. 1–9, 2015.

[9] F. Zivic, N. Grujovic, E. Pellicer, J. Sort, S. Mitrovic, D. Adamovic, and M. Vulovic, "Biodegradable metals as biomaterials for clinical practice: Iron-based materials," in *Biomaterials in Clinical Practice: Advances in Clinical Research and Medical Devices*, pp. 225–280, Springer International Publishing, 2017.

[10] Y. F. Zheng, X. N. Gu, and F. Witte, "Biodegradable metals," *Materials Science and Engineering R: Reports*, vol. 77, pp. 1–34, 2014.

[11] R. Zhao, R. Yang, P. R. Cooper, Z. Khurshid, A. Shavandi, and J. Ratnayake, "Bone grafts and substitutes in dentistry: A review of current trends and developments," *Molecules*, vol. 26, no. 10, pp. 1–27, 2021.

[12] M. G. Raucci, U. D'Amora, A. Ronca, and L. Ambrosio, "Injectable Functional Biomaterials for Minimally Invasive Surgery," *Advanced Healthcare Materials*, vol. 9, no. 13, pp. 1–20, 2020.

[13] J. Luo, H. Engqvist, and C. Persson, "A ready-to-use acidic, brushite-forming calcium phosphate cement," *Acta Biomaterialia*, vol. 81, pp. 304–314, 2018.

[14] L. L. Hench and J. R. Jones, "Bioactive glasses: Frontiers and Challenges," *Frontiers in Bioengineering and Biotechnology*, vol. 3, pp. 1–12, 2015.

[15] M. Rupp, L. Klute, S. Baertl, N. Walter, G. K. Mannala, L. Frank, C. Pfeifer, V. Alt, and M. Kerschbaum, "The clinical use of bone graft substitutes in orthopedic surgery in Germany—A 10-years survey from 2008 to 2018 of 1,090,167 surgical interventions," *Journal of Biomedical Materials Research - Part B Applied Biomaterials*, vol. 110, no. 2, pp. 350–357, 2022.

[16] European Medicines Agency, "Medical Device Regulation comes into application," 2021. https://www.ema.europa.eu/en/news/medical-device-regulation-comes-application.

[17] Spineart, "Tryptic(R)Ti Cervical Cage," 2022. https://www.spineart.com/us/products/tryptikti/.

[18] Zimmer Biomet, "Trabecular Metal (TM) Acetabular Revision System," 2022. https://www.zimmerbiomet.eu/en?_ga=2.255964171.1217211528.1674313721-699556324.1674313721.

[19] R. Oriňaková, R. Gorejová, Z. O. Králová, M. Petráková, and A. Oriňak, "Novel trends and recent progress on preparation methods of biodegradable metallic foams for biomedicine: a review," *Journal of Materials Science*, vol. 56, no. 25, pp. 13925–13963, 2021.

[20] American Academy of Orthopaedic Surgeons, "Bone-graft Substitues: Facts, Fictions and Applications," tech. rep., American Academy of Orthopaedic Surgeons, Las Vegas, 2009.

[21] X. Sun, C. Xu, G. Wu, Q. Ye, and C. Wang, "Review poly(lactic-co-glycolic acid): Applications and future prospects for periodontal tissue regeneration," *Polymers*, vol. 9, no. 6, pp. 1–19, 2017.

[22] P. Rola, S. Włodarczak, A. Doroszko, M. Lesiak, and A. Włodarczak, "The bioresorbable magnesium scaffold (Magmaris)—State of the art: From basic concept to clinical application," *Catheterization and Cardiovascular Interventions*, 2022.

[23] K. Kumar, R. S. Gill, and U. Batra, "Challenges and opportunities for biodegradable magnesium alloy implants," *Materials Technology*, vol. 33, no. 2, pp. 153–172, 2018.

[24] European Commision, "CE Marking," 2022. https://shorturl.at/hmwCL.

[25] National Library of Medicine (U.S.), "First in Man Trial - BIOSOLVE-I, Identifer: NCT01168830," 2011.

[26] National Library of Medicine (U.S.), "First in Man Study of the DREAMS 2nd Generation Drug Eluting Absorbable Metal Scaffold (BIOSOLVE-II), Identifer: NCT01960504," 2013.

[27] National Library of Medicine (U.S.), "Pre-market Study of the DREAMS 2G Drug Eluting Absorbable Metal Scaffold (BIOSOLVE-III), Identifer: NCT02716220," 2016.

[28] National Library of Medicine (U.S.), "BIOTRONIKS - Safety and Performance in de NOvo Lesion of NatiVE Coronary Arteries With Magmaris- Registry: BIOSOLVE-IV, Identifer: NCT02817802," 2016.

[29] National Library of Medicine (U.S.), "First in Men Study: BIOMAG-I, Identifier: NCT04157153," 2020.

[30] Y. Su, I. Cockerill, Y. Wang, Y. X. Qin, L. Chang, Y. Zheng, and D. Zhu, "Zinc-Based Biomaterials for Regeneration and Therapy," *Trends in Biotechnology*, vol. 37, no. 4, pp. 428–441, 2019.

[31] H. Yang, C. Wang, C. Liu, H. Chen, Y. Wu, J. Han, Z. Jia, W. Lin, D. Zhang, W. Li, W. Yuan, H. Guo, H. Li, G. Yang, D. Kong, D. Zhu, K. Takashima, L. Ruan, J. Nie, X. Li, and Y. Zheng, "Evolution of the degradation mechanism of pure zinc stent in the one-year study of rabbit abdominal aorta model," *Biomaterials*, vol. 145, pp. 92–105, 2017.

[32] P. K. Bowen, R. J. Guillory, E. R. Shearier, J. M. Seitz, J. Drelich, M. Bocks, F. Zhao, and J. Goldman, "Metallic zinc exhibits optimal biocompatibility for bioabsorbable endovascular stents," *Materials Science and Engineering C*, vol. 56, pp. 467–472, 2015.

[33] C. Redlich, P. Quadbeck, M. Thieme, and B. Kieback, "Molybdenum – A biodegradable implant material for structural applications?," *Acta Biomaterialia*, vol. 104, pp. 241–251, 2020.

[34] C. Redlich, A. Schauer, J. Scheibler, G. Poehle, P. Barthel, A. Maennel, V. Adams, T. Weissgaerber, A. Linke, and P. Quadbeck, "In vitro degradation behavior and biocompatibility of bioresorbable molybdenum," *Metals*, vol. 11, no. 5, pp. 1–16, 2021.

[35] E. Scarcello and D. Lison, "Are Fe-based stenting materials biocompatible? A critical review of in vitro and in vivo studies," *Journal of Functional Biomaterials*, vol. 11, no. 1, 2020.

[36] G. J. Kontoghiorghes and C. N. Kontoghiorghe, "Iron and Chelation in Biochemistry and Medicine: Treating Related Diseases," *Cells*, vol. 9, no. 1456, p. 43 pages, 2020.

[37] M. Peuster, P. Wohlsein, M. Brügmann, M. Ehlerding, K. Seidler, C. Fink, H. Brauer, A. Fischer, and G. Hausdorf, "A novel approach to temporary stenting: Degradable cardiovascular stents produced from corrodible metal - Results 6-18 months after implantation into New Zealand white rabbits," *Heart*, vol. 86, no. 5, pp. 563–569, 2001.

[38] J. Cheng, B. Liu, Y. H. Wu, and Y. F. Zheng, "Comparative invitro study on pure metals (Fe, Mn, Mg, Zn and W) as biodegradable metals," *Journal of Materials Science and Technology*, vol. 29, no. 7, pp. 619–627, 2013.

[39] M. Moravej, A. Purnama, M. Fiset, J. Couet, and D. Mantovani, "Electroformed pure iron as a new biomaterial for degradable stents: In vitro degradation and preliminary cell viability studies," *Acta Biomaterialia*, vol. 6, no. 5, pp. 1843–1851, 2010.

[40] B. Liu and Y. F. Zheng, "Effects of alloying elements (Mn, Co, Al, W, Sn, B, C and S) on biodegradability and in vitro biocompatibility of pure iron," *Acta Biomaterialia*, vol. 7, no. 3, pp. 1407–1420, 2011.

[41] G. Gąsior, J. Szczepański, and A. Radtke, "Biodegradable iron-based materials—what was done and what more can be done?," *Materials*, vol. 14, no. 12, 2021.

[42] D. Mei, S. V. Lamaka, X. Lu, and M. L. Zheludkevich, "Selecting medium for corrosion testing of bioabsorbable magnesium and other metals – A critical review," *Corrosion Science*, vol. 171, 2020.

[43] M. Barzegari, D. Mei, S. V. Lamaka, and L. Geris, "Computational modeling of degradation process of biodegradable magnesium biomaterials," *Corrosion Science*, vol. 190, p. 109674, 2021.

[44] P. Sekar, N. S, and V. Desai, "Recent progress in in vivo studies and clinical applications of magnesium based biodegradable implants – A review," *Journal of Magnesium and Alloys*, vol. 9, no. 4, pp. 1147–1163, 2021.

[45] J. Venezuela and M. S. Dargusch, "Addressing the slow corrosion rate of biodegradable Fe-Mn: Current approaches and future trends," *Current Opinion in Solid State and Materials Science*, vol. 24, no. 3, p. 100822, 2020.

[46] H. Hermawan, A. Purnama, D. Dube, J. Couet, and D. Mantovani, "Fe-Mn alloys for metallic biodegradable stents: Degradation and cell viability studies," *Acta Biomaterialia*, vol. 6, no. 5, pp. 1852–1860, 2010.

[47] S. Lamaka, R. Souto, and M. G. S. Ferreira, "In-situ visualization of local corrosion by Scanning Ion-selective Electrode (SIET)," in *Microscopy: Science, technology, Applications and Education*, pp. 2162–2173, Formatex, 2010.

[48] R. Gorejová, L. Haverová, R. Oriňaková, A. Oriňak, and M. Oriňak, "Recent advancements in Fe-based biodegradable materials for bone repair," *Journal of Materials Science*, vol. 54, pp. 1913–1947, 2019.

[49] T. Huang and Y. Zheng, "Uniform and accelerated degradation of pure iron patterned by Pt disc arrays," *Scientific Reports*, vol. 6, pp. 1–11, 2016.

[50] J. Cheng, T. Huang, and Y. F. Zheng, "Relatively uniform and accelerated degradation of pure iron coated with micro-patterned Au disc arrays," *Materials Science and Engineering C*, vol. 48, pp. 679–687, 2015.

[51] E. Zhang, H. Chen, and F. Shen, "Biocorrosion properties and blood and cell compatibility of pure iron as a biodegradable biomaterial," *Journal of Materials Science: Materials in Medicine*, vol. 21, no. 7, pp. 2151–2163, 2010.

[52] S. Zhu, N. Huang, L. Xu, Y. Zhang, H. Liu, H. Sun, and Y. Leng, "Biocompatibility of pure iron: In vitro assessment of degradation kinetics and cytotoxicity on endothelial cells," *Materials Science and Engineering C*, vol. 29, no. 5, pp. 1589–1592, 2009.

[53] T. Huang, Y. Zheng, and Y. Han, "Accelerating degradation rate of pure iron by zinc ion implantation," *Regenerative Biomaterials*, vol. 3, no. 4, pp. 205–215, 2016.

[54] R. Y. Liu, R. G. He, L. Q. Xu, and S. F. Guo, "Design of Fe–Mn–Ag Alloys as Potential Candidates for Biodegradable Metals," *Acta Metallurgica Sinica (English Letters)*, vol. 31, no. 6, pp. 584–590, 2018.

[55] C. S. Obayi, R. Tolouei, A. Mostavan, C. Paternoster, S. Turgeon, B. A. Okorie, D. O. Obikwelu, and D. Mantovani, "Effect of grain sizes on mechanical properties and biodegradation behavior of pure iron for cardiovascular stent application," *Biomatter*, vol. 6, 2016.

[56] K. D. Ralston, N. Birbilis, and C. H. J. Davies, "Revealing the relationship between grain size and corrosion rate of metals," *Scripta Materialia*, vol. 63, no. 12, pp. 1201–1204, 2010.

[57] D. Carluccio, M. Bermingham, D. Kent, A. G. Demir, B. Previtali, and M. S. Dargusch, "Comparative Study of Pure Iron Manufactured by Selective Laser Melting, Laser Metal Deposition, and Casting Processes," *Advanced Engineering Materials*, vol. 21, no. 7, 2019.

[58] E. McCafferty, *Introduction to Corrosion Science*. Springer Science+Business Media, 2010.

[59] D. Landolt, *Corrosion and surface chemistry of metals*. CRC Press, 2007.

[60] V. F. Lvovich, *Impedance spectroscopy: Applications to electrochemical and dielectric phenomena*. Wiley, 2015.

[61] L. Zhang and X. S. Zhao, "Carbon-based materials as supercapacitor electrodes," *Chemical Society Reviews*, vol. 38, no. 9, pp. 2520–2531, 2009.

[62] M. E. Orazem and B. Tribollet, *Electrochemical Impedance Spectroscopy*. Wiley, 2008.

[63] P. Córdoba-Torres, T. J. Mesquita, and R. P. Nogueira, "Relationship between the origin of constant-phase element behavior in electrochemical impedance spectroscopy and electrode surface structure," *Journal of Physical Chemistry C*, vol. 119, no. 8, pp. 4136–4147, 2015.

[64] J. B. Jorcin, M. E. Orazem, N. Pébère, and B. Tribollet, "CPE analysis by local electrochemical impedance spectroscopy," *Electrochimica Acta*, vol. 51, no. 8-9, pp. 1473–1479, 2006.

[65] C. H. Hsu and F. Mansfeld, "Concernng the conversion of the constant phase element parameter Y0 into a capacitance," *Corrosion*, vol. 57, no. 9, pp. 747–748, 2001.

[66] J. Huang, "Diffusion impedance of electroactive materials, electrolytic solutions and porous electrodes: Warburg impedance and beyond," *Electrochimica Acta*, vol. 281, pp. 170–188, 2018.

[67] S. J. Cooper, A. Bertei, D. P. Finegan, and N. P. Brandon, "Simulated impedance of diffusion in porous media," *Electrochimica Acta*, vol. 251, pp. 681–689, 2017.

[68] "ASTM G1 - 90: Standard Practice for Preparing, Cleaning, and Evaluating Corrosion Test Specimens.," 1999.

[69] E. L. Silva, S. V. Lamaka, D. Mei, and M. L. Zheludkevich, "The Reduction of Dissolved Oxygen During Magnesium Corrosion," *ChemistryOpen*, vol. 7, no. 8, pp. 664–668, 2018.

[70] A. S. Gnedenkov, S. L. Sinebryukhov, D. V. Mashtalyar, and S. V. Gnedenkov, "Localized corrosion of the Mg alloys with inhibitor-containing coatings: SVET and SIET studies," *Corrosion Science*, vol. 102, pp. 269–278, 2016.

[71] A. S. Gnedenkov, S. V. Lamaka, S. L. Sinebryukhov, D. V. Mashtalyar, V. S. Egorkin, I. M. Imshinetskiy, M. L. Zheludkevich, and S. V. Gnedenkov, "Control of the Mg alloy biodegradation via PEO and polymer-containing coatings," *Corrosion Science*, vol. 182, no. January, 2021.

[72] Q. Dong, X. Zhou, Y. Feng, K. Qian, H. Liu, M. Lu, C. Chu, F. Xue, and J. Bai, "Insights into self-healing behavior and mechanism of dicalcium phosphate dihydrate coating on biomedical Mg," *Bioactive Materials*, vol. 6, no. 1, pp. 158–168, 2021.

[73] S. V. Lamaka, J. Gonzalez, D. Mei, F. Feyerabend, R. Willumeit-Römer, and M. L. Zheludkevich, "Local pH and Its Evolution Near Mg Alloy Surfaces Exposed to Simulated Body Fluids," *Advanced Materials Interfaces*, vol. 5, no. 18, 2018.

[74] J. Gonzalez, S. V. Lamaka, D. Mei, N. Scharnagl, F. Feyerabend, M. L. Zheludkevich, and R. Willumeit-Römer, "Mg Biodegradation Mechanism Deduced from the Local Surface Environment under Simulated Physiological Conditions," *Advanced Healthcare Materials*, vol. 10, no. 13, 2021.

[75] D. Mei, C. Wang, S. V. Lamaka, and M. L. Zheludkevich, "Clarifying the influence of albumin on the initial stages of magnesium corrosion in Hank's balanced salt solution," *Journal of Magnesium and Alloys*, vol. 9, no. 3, pp. 805–817, 2021.

[76] C. Tonna, C. Wang, D. Mei, S. V. Lamaka, M. L. Zheludkevich, and J. Buhagiar, "Biodegradation behaviour of Fe-based alloys in Hanks' Balanced Salt Solutions: Part I. Material characterisation and corrosion testing," *Bioactive Materials*, vol. 7, pp. 426–440, 2022.

[77] C. Wang, C. Tonna, D. Mei, J. Buhagiar, M. L. Zheludkevich, and S. V. Lamaka, "Biodegradation behaviour of Fe-based alloys in Hanks' Balanced Salt Solutions: Part II. The evolution of local pH and dissolved oxygen concentration at metal interface," *Bioactive Materials*, vol. 7, pp. 412–425, 2022.

[78] M. Schinhammer, A. C. Hänzi, J. F. Löffler, and P. J. Uggowitzer, "Design strategy for biodegradable Fe-based alloys for medical applications," *Acta Biomaterialia*, vol. 6, no. 5, pp. 1705–1713, 2010.

[79] R. Oriňaková, A. Oriňak, M. Giretová, L. Medvecký, M. Kupková, M. Hrubovčïáková, I. Maskal'Ová, J. MacKo, and F. Kal'Avský, "A study of cytocompatibility and degradation of iron-based biodegradable materials," *Journal of Biomaterials Applications*, vol. 30, no. 7, pp. 1060–1070, 2016.

[80] B. Wegener, B. Sievers, S. Utzschneider, P. Müller, V. Jansson, S. Rößler, B. Nies, G. Stephani, B. Kieback, and P. Quadbeck, "Microstructure, cytotoxicity and corrosion of powder-metallurgical iron alloys for biodegradable bone replacement materials," *Materials Science and Engineering B: Solid-State Materials for Advanced Technology*, vol. 176, no. 20, pp. 1789–1796, 2011.

[81] M. Hrubovčáková, M. Kupková, and M. Džupon, "Fe and Fe-P Foam for Biodegradable Bone Replacement Material: Morphology, Corrosion Behaviour, and Mechanical Properties," *Advances in Materials Science and Engineering*, vol. 2016, 2016.

[82] J. Čapek, Š. Msallamová, E. Jablonská, J. Lipov, and D. Vojtěch, "A novel high-strength and highly corrosive biodegradable Fe-Pd alloy: Structural, mechanical and in vitro corrosion and cytotoxicity study," *Materials Science and Engineering C*, vol. 79, pp. 550–562, 2017.

[83] T. Huang, J. Cheng, and Y. F. Zheng, "In vitro degradation and biocompatibility of Fe-Pd and Fe-Pt composites fabricated by spark plasma sintering," *Materials Science and Engineering C*, vol. 35, no. 1, pp. 43–53, 2014.

[84] T. Huang, J. Cheng, D. Bian, and Y. Zheng, "Fe-Au and Fe-Ag composites as candidates for biodegradable stent materials," *Journal of Biomedical Materials Research - Part B Applied Biomaterials*, vol. 104, no. 2, pp. 225–240, 2016.

[85] J. Čapek, K. Stehlíková, A. Michalcová, Š. Msallamová, and D. Vojtěch, "Microstructure, mechanical and corrosion properties of biodegradable powder metallurgical Fe-2 wt.% X (X = Pd, Ag and C) alloys," *Materials Chemistry and Physics*, vol. 181, pp. 501–511, 2016.

[86] J. Frattolin, R. Barua, H. Aydin, S. Rajagopalan, L. Gottellini, R. Leask, S. Yue, D. Frost, O. F. Bertrand, and R. Mongrain, "Development of a Novel Biodegradable Metallic Stent Based on Microgalvanic Effect," *Annals of Biomedical Engineering*, vol. 44, no. 2, pp. 404–418, 2016.

[87] J. Frattolin, R. Roy, S. Rajagopalan, M. Walsh, S. Yue, O. F. Bertrand, and R. Mongrain, "A manufacturing and annealing protocol to develop a cold-sprayed Fe-316L stainless steel biodegradable stenting material," *Acta Biomaterialia*, vol. 99, pp. 479–494, 2019.

[88] J. Frattolin, E. Cattarinuzzi, S. Rajagopalan, D. Gastaldi, P. Vena, S. Yue, O. F. Bertrand, and R. Mongrain, "Development of a micro-scale method to assess the effect of corrosion on the mechanical properties of a biodegradable Fe-316L stent material," *Journal of the Mechanical Behavior of Biomedical Materials*, vol. 114, 2021.

[89] J. He, J. Fang, P. Wei, Y. Li, H. Guo, Q. Mei, and F. Ren, "Cancellous bone-like porous Fe@Zn scaffolds with core-shell-structured skeletons for biodegradable bone implants," *Acta Biomaterialia*, vol. 121, pp. 665–681, 2021.

[90] W. Q. Wang, J. Wang, and M. Qi, "Microstructure and in vitro biodegradable properties of fe-zn alloys prepared by electroforming," *Advanced Materials Research*, vol. 1033-1034, pp. 1200–1206, 2014.

[91] J. Cheng and Y. F. Zheng, "In vitro study on newly designed biodegradable Fe-X composites (X = W, CNT) prepared by spark plasma sintering," *Journal of Biomedical Materials Research - Part B Applied Biomaterials*, vol. 101, no. 4, pp. 485–497, 2013.

[92] J. He, F. L. He, D. W. Li, Y. L. Liu, and D. C. Yin, "A novel porous Fe/Fe-W alloy scaffold with a double-layer structured skeleton: Preparation, in vitro degradability and biocompatibility," *Colloids and Surfaces B: Biointerfaces*, vol. 142, pp. 325–333, 2016.

[93] M. K. Lee, H. Lee, C. Park, I. G. Kang, J. Kim, H. E. Kim, H. D. Jung, and T. S. Jang, "Accelerated biodegradation of iron-based implants via tantalum-implanted surface nanostructures," *Bioactive Materials*, vol. 9, no. April 2021, pp. 239–250, 2022.

[94] J. Cheng, T. Huang, and Y. F. Zheng, "Microstructure, mechanical property, biodegradation behavior, and biocompatibility of biodegradable Fe-Fe2O3 composites," *Journal of Biomedical Materials Research - Part A*, vol. 102, no. 7, pp. 2277–2287, 2014.

[95] M. Dehestani, E. Adolfsson, and L. A. Stanciu, "Mechanical properties and corrosion behavior of powder metallurgy iron-hydroxyapatite composites for biodegradable implant applications," *Materials and Design*, vol. 109, pp. 556–569, 2016.

[96] M. F. Ulum, A. Arafat, D. Noviana, A. H. Yusop, A. K. Nasution, M. R. Abdul Kadir, and H. Hermawan, "In vitro and in vivo degradation evaluation of novel iron-bioceramic composites for bone implant applications," *Materials Science and Engineering C*, vol. 36, no. 1, pp. 336–344, 2014.

[97] M. F. Ulum, A. K. Nasution, A. H. Yusop, A. Arafat, M. R. A. Kadir, V. Juniantito, D. Noviana, and H. Hermawan, "Evidences of in vivo bioactivity of Fe-bioceramic composites for temporary bone implants," *Journal of Biomedical Materials Research - Part B Applied Biomaterials*, vol. 103, no. 7, pp. 1354–1365, 2015.

[98] E. B. Montufar, M. Casas-Luna, M. Horynová, S. Tkachenko, Z. Fohlerová, S. Diaz-de-la Torre, K. Dvořák, L. Čelko, and J. Kaiser, "High strength, biodegradable and cytocompatible alpha tricalcium phosphate-iron composites for temporal reduction of bone fractures," *Acta Biomaterialia*, vol. 70, pp. 293–303, 2018.

[99] S. Wang, Y. Xu, J. Zhou, H. Li, J. Chang, and Z. Huan, "In vitro degradation and surface bioactivity of iron-matrix composites containing silicate-based bioceramic," *Bioactive Materials*, vol. 2, no. 1, pp. 10–18, 2017.

[100] H. Hermawan, D. Dubé, and D. Mantovani, "Development of degradable Fe-35Mn alloy for biomedical application," *Advanced Materials Research*, vol. 15-17, pp. 107–112, 2007.

[101] J. Martínez, S. M. Cotes, A. F. Cabrera, J. Desimoni, and A. Fernández Guillermet, "On the relative fraction of ϵ martensite in γ-Fe-Mn alloys," *Materials Science and Engineering A*, vol. 408, no. 1-2, pp. 26–32, 2005.

[102] L. Y. Pustov, S. D. Kaloshkin, E. I. Estrin, G. Principi, V. V. Tcherdyntsev, and E. V. Shelekhov, "Nanostructures: Synthesis, Functional Properties and Applications," *Nanostructures: Synthesis, Functional Properties and Applications*, pp. 329–337, 2003.

[103] R. Siquieri, J. Rezende, J. Kundin, and H. Emmerich, "Phase-field simulation of a Fe-Mn alloy under forced flow conditions," *European Physical Journal: Special Topics*, vol. 177, no. 1, pp. 193–205, 2009.

[104] P. Marinelli, A. Baruj, J. Pons, M. Sade, A. F. Guillermet, and E. Cesari, "The enthalpy change of the hcp $\rightarrow$ fcc martensitic transformation in Fe-Mn alloys: Composition dependence and effects of thermal cycling," *Materials Science and Engineering A*, vol. 335, no. 1-2, pp. 137–146, 2002.

[105] H. Hermawan, H. Alamdari, D. Mantovani, and D. Dubé, "Iron-manganese: New class of metallic degradable biomaterials prepared by powder metallurgy," *Powder Metallurgy*, vol. 51, no. 1, pp. 38–45, 2008.

[106] H. Hermawan, D. Dubé, and D. Mantovani, "Degradable metallic biomaterials: Design and development of Fe-Mn alloys for stents," *Journal of Biomedical Materials Research - Part A*, vol. 93, no. 1, pp. 1–11, 2010.

[107] M. S. Dargusch, A. Dehghan-Manshadi, M. Shahbazi, J. Venezuela, X. Tran, J. Song, N. Liu, C. Xu, Q. Ye, and C. Wen, "Exploring the Role of Manganese on the Microstructure, Mechanical Properties, Biodegradability, and Biocompatibility of Porous Iron-Based Scaffolds," *ACS Biomaterials Science and Engineering*, vol. 5, no. 4, pp. 1686–1702, 2019.

[108] C. Shuai, W. Yang, Y. Yang, H. Pan, C. He, F. Qi, D. Xie, and H. Liang, "Selective laser melted Fe-Mn bone scaffold: Microstructure, corrosion behavior and cell response," *Materials Research Express*, vol. 7, no. 1, 2019.

[109] M. Kupková, M. Hrubovcáková, M. Kupka, R. Orináková, and A. M. Turonová, "Sintering behaviour, graded microstructure and corrosion performance of sintered Fe-Mn biomaterials," *International Journal of Electrochemical Science*, vol. 10, no. 11, pp. 9256–9268, 2015.

[110] M. Dehestani, K. Trumble, H. Wang, H. Wang, and L. A. Stanciu, "Effects of microstructure and heat treatment on mechanical properties and corrosion behavior of powder metallurgy derived Fe–30Mn alloy," *Materials Science and Engineering A*, vol. 703, pp. 214–226, 2017.

[111] P. Sotoudeh Bagha, M. Khakbiz, S. Sheibani, and H. Hermawan, "Design and characterization of nano and bimodal structured biodegradable Fe-Mn-Ag alloy with accelerated corrosion rate," *Journal of Alloys and Compounds*, vol. 767, pp. 955–965, 2018.

[112] D. T. Chou, D. Wells, D. Hong, B. Lee, H. Kuhn, and P. N. Kumta, "Novel processing of iron-manganese alloy-based biomaterials by inkjet 3-D printing," *Acta Biomaterialia*, vol. 9, no. 10, pp. 8593–8603, 2013.

[113] J. Čapek, J. Kubásek, D. Vojtěch, E. Jablonská, J. Lipov, and T. Ruml, "Microstructural, mechanical, corrosion and cytotoxicity characterization of the hot forged FeMn30(wt.%) alloy," *Materials Science and Engineering C*, vol. 58, pp. 900–908, 2016.

[114] A. Drynda, T. Hassel, F. W. Bach, and M. Peuster, "In vitro and in vivo corrosion properties of new iron-manganese alloys designed for cardiovascular applications," *Journal of Biomedical Materials Research - Part B Applied Biomaterials*, vol. 103, no. 3, pp. 649–660, 2015.

[115] M. Heiden, E. Walker, E. Nauman, and L. Stanciu, "Evolution of novel bioresorbable iron-manganese implant surfaces and their degradation behaviors in vitro," *Journal of Biomedical Materials Research - Part A*, vol. 103, no. 1, pp. 185–193, 2015.

[116] J. Hufenbach, H. Wendrock, F. Kochta, U. Kühn, and A. Gebert, "Novel biodegradable Fe-Mn-C-S alloy with superior mechanical and corrosion properties," *Materials Letters*, vol. 186, pp. 330–333, 2017.

[117] A. Gebert, F. Kochta, A. Voß, S. Oswald, M. Fernandez-Barcia, U. Kühn, and J. Hufenbach, "Corrosion studies on Fe-30Mn-1C alloy in chloride-containing solutions with view to biomedical application," *Materials and Corrosion*, vol. 69, no. 2, pp. 167–177, 2018.

[118] S. Gambaro, C. Paternoster, B. Occhionero, J. Fiocchi, C. A. Biffi, A. Tuissi, and D. Mantovani, "Mechanical and degradation behavior of three Fe-Mn-C alloys for potential biomedical applications," *Materials Today Communications*, vol. 27, 2021.

[119] M. Schinhammer, I. Gerber, A. C. Hänzi, and P. J. Uggowitzer, "On the cytocompatibility of biodegradable Fe-based alloys," *Materials Science and Engineering C*, vol. 33, no. 2, pp. 782–789, 2013.

[120] B. Liu, Y. F. Zheng, and L. Ruan, "In vitro investigation of Fe30Mn6Si shape memory alloy as potential biodegradable metallic material," *Materials Letters*, vol. 65, no. 3, pp. 540–543, 2011.

[121] R. Drevet, Y. Zhukova, P. Malikova, S. Dubinskiy, A. Korotitskiy, Y. Pustov, and S. Prokoshkin, "Martensitic Transformations and Mechanical and Corrosion Properties of Fe-Mn-Si Alloys for Biodegradable Medical Implants," *Metallurgical and Materials Transactions A: Physical Metallurgy and Materials Science*, vol. 49, no. 3, pp. 1006–1013, 2018.

[122] Z. Xu, M. A. Hodgson, and P. Cao, "A comparative study of powder metallurgical (PM) and wrought Fe-Mn-Si alloys," *Materials Science and Engineering A*, vol. 630, pp. 116–124, 2015.

[123] Z. Xu, M. A. Hodgson, and P. Cao, "Effect of immersion in simulated body fluid on the mechanical properties and biocompatibility of sintered Fe-Mn-based alloys," *Metals*, vol. 6, no. 12, pp. 1–13, 2016.

[124] Z. Xu, M. A. Hodgson, and P. Cao, "Weight loss behavior of a vacuum sintered powder metallurgical Fe-Mn-Si alloy," *Journal of Materials Research*, vol. 32, no. 3, pp. 644–655, 2017.

[125] Z. Xu, M. A. Hodgson, K. Chang, G. Chen, X. Yuan, and P. Cao, "Effect of sintering time on the densification, microstructure, weight loss and tensile properties of a powder metallurgical Fe-Mn-Si alloy," *Metals*, vol. 7, no. 3, 2017.

[126] M. Heiden, E. Nauman, and L. Stanciu, "Bioresorbable Fe–Mn and Fe–Mn–HA Materials for Orthopedic Implantation: Enhancing Degradation through Porosity Control," *Advanced Healthcare Materials*, vol. 6, no. 13, 2017.

[127] D. Hong, D. T. Chou, O. I. Velikokhatnyi, A. Roy, B. Lee, I. Swink, I. Issaev, H. A. Kuhn, and P. N. Kumta, "Binder-jetting 3D printing and alloy development of new biodegradable Fe-Mn-Ca/Mg alloys," *Acta Biomaterialia*, vol. 45, pp. 375–386, 2016.

[128] Z. Ma, M. Gao, D. Na, Y. Li, L. Tan, and K. Yang, "Study on a biodegradable antibacterial Fe-Mn-C-Cu alloy as urinary implant material," *Materials Science and Engineering C*, vol. 103, 2019.

[129] S. Mandal, R. Ummadi, M. Bose, V. K. Balla, and M. Roy, "Fe–Mn–Cu alloy as biodegradable material with enhanced antimicrobial properties," *Materials Letters*, vol. 237, pp. 323–327, 2019.

[130] T. Niendorf, F. Brenne, P. Hoyer, D. Schwarze, M. Schaper, R. Grothe, M. Wiesener, G. Grundmeier, and H. J. Maier, "Processing of New Materials by Additive Manufacturing: Iron-Based Alloys Containing Silver for Biomedical Applications," *Metallurgical and Materials Transactions A: Physical Metallurgy and Materials Science*, vol. 46, no. 7, pp. 2829–2833, 2015.

[131] P. Sotoudehbagha, S. Sheibani, M. Khakbiz, S. Ebrahimi-Barough, and H. Hermawan, "Novel antibacterial biodegradable Fe-Mn-Ag alloys produced by mechanical alloying," *Materials Science and Engineering C*, vol. 88, no. December 2017, pp. 88–94, 2018.

[132] M. S. Dargusch, J. Venezuela, A. Dehghan-Manshadi, S. Johnston, N. Yang, K. Mardon, C. Lau, and R. Allavena, "In Vivo Evaluation of Bioabsorbable Fe-35Mn-1Ag: First Reports on In Vivo Hydrogen Gas Evolution in Fe-Based Implants," *Advanced Healthcare Materials*, vol. 10, no. 2, pp. 1–15, 2021.

[133] M. Caligari Conti, B. Mallia, E. Sinagra, P. Schembri Wismayer, J. Buhagiar, and D. Vella, "The effect of alloying elements on the properties of pressed and non-pressed biodegradable Fe–Mn–Ag powder metallurgy alloys," *Heliyon*, vol. 5, no. 9, 2019.

[134] M. Wiesener, K. Peters, A. Taube, A. Keller, K. P. Hoyer, T. Niendorf, and G. Grundmeier, "Corrosion properties of bioresorbable FeMn-Ag alloys prepared by selective laser melting," *Materials and Corrosion*, vol. 68, no. 10, pp. 1028–1036, 2017.

[135] N. Babacan, F. Kochta, V. Hoffmann, T. Gemming, U. Kühn, L. Giebeler, A. Gebert, and J. Hufenbach, "Effect of silver additions on the microstructure, mechanical properties and corrosion behavior of biodegradable Fe-30Mn-6Si," *Materials Today Communications*, vol. 28, 2021.

[136] R. Y. Liu, R. G. He, Y. X. Chen, and S. F. Guo, "Effect of Ag on the Microstructure, Mechanical and Bio-corrosion Properties of Fe–30Mn Alloy," *Acta Metallurgica Sinica (English Letters)*, vol. 32, no. 11, pp. 1337–1345, 2019.

[137] S. Loffredo, C. Paternoster, N. Giguère, M. Vedani, and D. Mantovani, "Effect of Silver on Corrosion Behavior of Plastically Deformed Twinning-Induced Plasticity Steel for Biodegradable Stents," *Jom*, vol. 72, no. 5, pp. 1892–1901, 2020.

[138] S. Loffredo, S. Gambaro, L. Marin De Andrade, C. Paternoster, R. Casati, N. Giguère, M. Vedani, and D. Mantovani, "Six-Month Long in Vitro Degradation Tests of Biodegradable Twinning-Induced Plasticity Steels Alloyed with Ag for Stent Applications," *ACS Biomaterials Science and Engineering*, vol. 7, no. 8, pp. 3669–3682, 2021.

[139] T. Huang, Y. Cheng, and Y. Zheng, "In vitro studies on silver implanted pure iron by metal vapor vacuum arc technique," *Colloids and Surfaces B: Biointerfaces*, vol. 142, pp. 20–29, 2016.

[140] A. M. Roman, V. Geanta, R. Compoesu, C. Munteanu, N. M. Lohan, G. Zegan, E. R. Cernei, I. Ionita, N. Compoesu, and N. Ionaid, "In-Vitro Analysis of FeMn-Si Smart Biodegradable Alloy," *Materials*, vol. 15, no. 568, 2022.

[141] R. Drevet, Y. Zhukova, P. Kadirov, and S. Dubinskiy, "Tunable Corrosion Behavior of Calcium Phosphate Coated Fe-Mn-Si Alloys for Bone Implant Applications," *Metallurgical and Materials Transactions A*, vol. 49, no. 12, pp. 6553–6560, 2018.

[142] M. Rabeeh VP and T. Hanas, "Enhancing biointerfacial properties of porous pure iron by gold sputtering for degradable implant applications," *Materials Today Communications*, vol. 31, 2022.

[143] A. H. M. Yusop, N. M. Daud, H. Nur, M. R. A. Kadir, and H. Hermawan, "Controlling the degradation kinetics of porous iron by poly(lactic-co-glycolic acid) infiltration for use as temporary medical implants," *Scientific Reports*, vol. 5, no. February, pp. 1–17, 2015.

[144] Y. Qi, H. Qi, Y. He, W. Lin, P.-z. Li, L. Qin, Y. Hu, L. Chen, Q. Liu, H. Sun, Q. Liu, G. Zhang, S. Cui, J. Hu, L. Yu, D. Zhang, and J. Ding, "Strategy of Metal-Polymer Composite Stent to Accelerate Biodegradation of Iron-Based Biomaterials," *ACS Applied Materials and Interfaces*, vol. 10, no. 1, pp. 182–192, 2018.

[145] Y. Qi, X. Li, Y. He, D. Zhang, and J. Ding, "Mechanism of Acceleration of Iron Corrosion by a Polylactide Coating," *ACS Applied Materials and Interfaces*, vol. 11, no. 1, pp. 202–218, 2019.

[146] R. Gorejová, R. Orinaková, Z. K. Orságová, M. Baláž, M. Kupková, M. Hrubovcáková, L. Haverová, M. Džupon, A. Orinak, F. Kal'avský, and K. Koval, "In Vitro Corrosion Behavior of Biodegradable Iron Foams with Polymeric Coating," *Materials*, vol. 13, no. 184, pp. 1–17, 2019.

[147] R. Orináková, R. Gorejová, Z. Orságová Králová, A. Orinak, I. Shepa, J. Hovancová, A. Kovalciková, Z. Lukácová Bujnáková, N. Király, M. Kanuchová, M. Baláz, M. Streckova, M. Kupková, M. Hrubovčïáková, F. Kalavsky, and M. Orinak, "Influence of albumin interaction on corrosion resistance of sintered iron biomaterials with polyethyleneimine coating," *Applied Surface Science*, vol. 509, 2020.

[148] R. Oriňaková, R. Gorejová, Z. O. Králová, and A. Oriňak, "Surface modifications of biodegradable metallic foams for medical applications," *Coatings*, vol. 10, no. 9, 2020.

[149] P. Liu, H. Wu, L. Liang, D. Song, J. Liu, X. Ma, and K. Li, "Microstructure, mechanical properties and corrosion behaviour of additively-manufactured Fe-Mn alloys," *Materials Science & Engineering A*, vol. 852, 2022.

[150] M. Caligari Conti, D. Aquilina, C. Paternoster, D. Vella, E. Sinagra, D. Mantovani, G. Cassar, P. Schembri Wismayer, and J. Buhagiar, "Influence of cold rolling on in vitro cytotoxicity and electrochemical behaviour of an Fe-Mn-C biodegradable alloy in physiological solutions," *Heliyon*, vol. 4, no. 11, 2018.

[151] M. Heiden, A. Kustas, K. Chaput, E. Nauman, D. Johnson, and L. Stanciu, "Effect of microstructure and strain on the degradation behavior of novel bioresorbable iron-manganese alloy implants," *Journal of Biomedical Materials Research - Part A*, vol. 103, no. 2, pp. 738–745, 2015.

[152] S. M. Huang, E. A. Nauman, and L. A. Stanciu, "Investigation of porosity on mechanical properties, degradation and in-vitro cytotoxicity limit of Fe30Mn using space holder technique," *Materials Science and Engineering C*, vol. 99, no. February, pp. 1048–1057, 2019.

[153] Q. Zhang and P. Cao, "Degradable porous Fe-35wt.%Mn produced via powder sintering from NH4HCO3 porogen," *Materials Chemistry and Physics*, vol. 163, pp. 394–401, 2015.

[154] Q. Zhang, X. G. Wang, P. Cao, and W. Gao, "Degradation behaviour of a biodegradable Fe-Mn alloy produced by powder sintering," *International Journal of Modern Physics: Conference Series*, vol. 06, pp. 774–779, 2012.

[155] Č. Donik, A. Kocijan, I. Paulin, M. Hočevar, P. Gregorčič, and M. Godec, "Improved biodegradability of Fe–Mn alloy after modification of surface chemistry and topography by a laser ablation," *Applied Surface Science*, vol. 453, pp. 383–393, 2018.

[156] M. Hočevar, Č. Donik, I. Paulin, A. Kocijan, F. Tehovnik, J. Burja, P. Gregorčič, and M. Godec, "Corrosion on polished and laser-textured surfaces of An Fe-Mn biodegradable alloy," *Materiali in Tehnologije*, vol. 51, no. 6, pp. 1037–1041, 2017.

[157] J. Gonzalez, R. Q. Hou, E. P. S. Nidadavolu, R. Willumeit-Römer, and F. Feyerabend, "Magnesium degradation under physiological conditions – Best practice," *Bioactive Materials*, vol. 3, no. 2, pp. 174–185, 2018.

[158] D. Mei, S. V. Lamaka, C. Feiler, and M. L. Zheludkevich, "The effect of small-molecule bio-relevant organic components at low concentration on the corrosion of commercially pure Mg and Mg-0.8Ca alloy: An overall perspective," *Corrosion Science*, vol. 153, pp. 258–271, 2019.

[159] D. Mei, S. V. Lamaka, J. Gonzalez, F. Feyerabend, R. Willumeit-Römer, and M. L. Zheludkevich, "The role of individual components of simulated body fluid on the corrosion behavior of commercially pure Mg," *Corrosion Science*, vol. 147, pp. 81–93, 2019.

[160] C. Wang, X. Liu, D. Mei, M. Deng, Y. Zheng, M. L. Zheludkevich, and S. V. Lamaka, "Local pH and oxygen concentration at the interface of Zn alloys in Tris-HCl or HEPES buffered Hanks' balanced salt solution," *Corrosion Science*, vol. 197, 2022.

[161] X. Liu, H. Yang, P. Xiong, W. Li, H. H. Huang, and Y. Zheng, "Comparative studies of Tris-HCl, HEPES and NaHCO3/CO2 buffer systems on the biodegradation behaviour of pure Zn in NaCl and SBF solutions," *Corrosion Science*, vol. 157, pp. 205–219, 2019.

[162] E. Mouzou, C. Paternoster, R. Tolouei, A. Purnama, P. Chevallier, D. Dubé, F. Prima, and D. Mantovani, "In vitro degradation behavior of Fe-20Mn-1.2C alloy in three different pseudo-physiological solutions," *Materials Science and Engineering C*, vol. 61, pp. 564–573, 2016.

[163] H. Dong, F. Lin, A. R. Boccaccini, and S. Virtanen, "Corrosion behavior of biodegradable metals in two different simulated physiological solutions: Comparison of Mg, Zn and Fe," *Corrosion Science*, vol. 182, 2021.

[164] M. Schinhammer, J. Hofstetter, C. Wegmann, F. Moszner, J. F. Löffler, and P. J. Uggowitzer, "On the immersion testing of degradable implant materials in simulated body fluid: Active pH regulation using CO2," *Advanced Engineering Materials*, vol. 15, no. 6, pp. 434–441, 2013.

[165] M. Moravej and D. Mantovani, "Biodegradable metals for cardiovascular stent application: Interests and new opportunities," *International Journal of Molecular Sciences*, vol. 12, no. 7, pp. 4250–4270, 2011.

[166] M. Schinhammer, P. Steiger, F. Moszner, J. F. Löffler, and P. J. Uggowitzer, "Degradation performance of biodegradable FeMnC(Pd) alloys," *Materials Science and Engineering C*, vol. 33, no. 4, pp. 1882–1893, 2013.

[167] M. G. Taryba, M. F. Montemor, and S. V. Lamaka, "Quasi-simultaneous Mapping of Local Current Density, pH and Dissolved O2," *Electroanalysis*, vol. 27, no. 12, pp. 2725–2730, 2015.

[168] S. Höhn, S. Virtanen, and A. R. Boccaccini, "Protein adsorption on magnesium and its alloys: A review," *Applied Surface Science*, vol. 464, no. August 2018, pp. 212–219, 2019.

[169] V. Wagener, A. S. Faltz, M. S. Killian, P. Schmuki, and S. Virtanen, "Protein interactions with corroding metal surfaces: Comparison of Mg and Fe," *Faraday Discussions*, vol. 180, pp. 347–360, 2015.

[170] Z. Mardina, J. Venezuela, M. S. Dargusch, Z. Shi, and A. Atrens, "The influence of the protein bovine serum albumin (BSA) on the corrosion of Mg, Zn, and Fe in Zahrina's simulated interstitial fluid," *Corrosion Science*, vol. 199, 2022.

[171] J. Huang, A. Gonzalez Orive, J. T. Krüger, K. P. Hoyer, A. Keller, and G. Grundmeier, "Influence of proteins on the corrosion of a conventional and selective laser beam melted FeMn alloy in physiological electrolytes," *Corrosion Science*, vol. 200, 2022.

[172] S. E. Harandi, P. C. Banerjee, C. D. Easton, and R. K. Singh Raman, "Influence of bovine serum albumin in Hanks' solution on the corrosion and stress corrosion cracking of a magnesium alloy," *Materials Science and Engineering C*, vol. 80, pp. 335–345, 2017.

[173] W. Yan, Y. J. Lian, Z. Y. Zhang, M. Q. Zeng, Z. Q. Zhang, Z. Z. Yin, L. Y. Cui, and R. C. Zeng, "In vitro degradation of pure magnesium—the synergetic influences of glucose and albumin," *Bioactive Materials*, vol. 5, no. 2, pp. 318–333, 2020.

[174] J. F. Foster, "Some aspects of the structure and conformational properties of serum albumin," in *Albumin: Structure, Function and Uses*, pp. 53–84, Pergamon, jan 1977.

[175] H. Dong and S. Virtanen, "Influence of bovine serum albumin on biodegradation behavior of pure Zn," *Journal of Biomedical Materials Research - Part B Applied Biomaterials*, vol. 110, no. 1, pp. 185–194, 2022.

[176] L. Liu, L. Lu, H. J. Zhang, and L. N. Wang, "Influence of bovine serum albumin on corrosion behaviour of pure Zn in phosphate buffered saline," *Journal of Materials Science: Materials in Medicine*, vol. 32, no. 9, 2021.

[177] I. B. Beech, J. A. Sunner, C. R. Arciola, and P. Cristiani, "Microbially-influenced corrosion: Damage to prostheses, delight for bacteria I.B.," *The International Journal of Artifical Organs*, vol. 29, no. 4, pp. 443–452, 2006.

[178] "ASTM G31 - 72: Standard Practice for Laboratory Immersion Corrosion Testing of Metals," 2004.

[179] Y. P. Feng, N. Gaztelumendi, J. Fornell, H. Y. Zhang, P. Solsona, M. D. Baró, S. Suriñach, E. Ibáñez, L. Barrios, E. Pellicer, C. Nogués, and J. Sort, "Mechanical properties, corrosion performance and cell viability studies on newly developed porous Fe-Mn-Si-Pd alloys," *Journal of Alloys and Compounds*, vol. 724, pp. 1046–1056, 2017.

[180] T. Kraus, F. Moszner, S. Fischerauer, M. Fiedler, E. Martinelli, J. Eichler, F. Witte, E. Willbold, M. Schinhammer, M. Meischel, P. J. Uggowitzer, J. F. Löffler, and A. Weinberg, "Biodegradable Fe-based alloys for use in osteosynthesis: Outcome of an in vivo study after 52 weeks," *Acta Biomaterialia*, vol. 10, no. 7, pp. 3346–3353, 2014.

[181] N. Mohd Daud, N. B. Sing, A. H. Yusop, F. A. Abdul Majid, and H. Hermawan, "Degradation and invitro cell-material interaction studies on hydroxyapatite-coated biodegradable porous iron for hard tissue scaffolds," *Journal of Orthopaedic Translation*, vol. 2, no. 4, pp. 177–184, 2014.

[182] D. Carluccio, C. Xu, J. Venezuela, Y. Cao, D. Kent, M. Bermingham, A. G. Demir, B. Previtali, Q. Ye, and M. Dargusch, "Additively manufactured iron-manganese for biodegradable porous load-bearing bone scaffold applications," *Acta Biomaterialia*, vol. 103, pp. 346–360, 2020.

[183] A. Oriňák, R. Oriňáková, Z. O. Králová, A. M. Turoňová, M. Kupková, M. Hrubovčáková, J. Radoňák, and R. Džunda, "Sintered metallic foams for biodegradable bone replacement materials," *Journal of Porous Materials*, vol. 21, no. 2, pp. 131–140, 2014.

[184] J. F. Zheng, H. Qiu, Y. Tian, X. Y. Hu, T. Luo, C. Wu, Y. Tian, Y. Tang, L. F. Song, L. Li, L. Xu, B. Xu, and R. L. Gao, "Preclinical Evaluation of a Novel Sirolimus-Eluting Iron Bioresorbable Coronary Scaffold in Porcine Coronary Artery at 6 Months," *JACC: Cardiovascular Interventions*, vol. 12, no. 3, pp. 245–255, 2019.

[185] Lifetech Scientific, "IBS Titan™ Iron Alloy Bioabsorbable Peripheral Stent System Approved by NMPA as National Innovative Medical Device," 2022. http://www.lifetechmed.com/en/news/n1/20210227/2661.aspx.

[186] National Library of Medicine (U.S.), "A First-in-Man Study of IBS (IBS-FIM), Identifer: NCT03509142," 2018. https://clinicaltrials.gov/ct2/show/NCT03509142.

[187] R. Waksman, R. Pakala, R. Baffour, R. Seabron, D. Hellinga, and F. O. Tio, "Short-term effects of biocorrodible iron stents in porcine coronary arteries," *Journal of Interventional Cardiology*, vol. 21, no. 1, pp. 15–20, 2008.

[188] T. C. Paim, D. P. Wermuth, I. Bertaco, C. Zanatelli, L. I. S. Naasani, M. Slaviero, D. Driemeier, L. Schaeffer, and M. R. Wink, "Evaluation of in vitro and in vivo biocompatibility of iron produced by powder metallurgy," *Materials Science and Engineering C*, vol. 115, 2020.

[189] B. Wegener, A. Sichler, S. Milz, C. Sprecher, K. Pieper, W. Hermanns, V. Jansson, B. Nies, B. Kieback, P. E. Müller, V. Wegener, and P. Quadbeck, "Development of a novel biodegradable porous iron-based implant for bone replacement," *Scientific Reports*, vol. 10, no. 1, pp. 1–10, 2020.

[190] M. Traverson, M. Heiden, L. A. Stanciu, E. A. Nauman, Y. Jones-Hall, and G. J. Breur, "In Vivo Evaluation of Biodegradability and Biocompatibility of Fe30Mn Alloy," *Veterinary and Comparative Orthopaedics and Traumatology*, vol. 31, no. 1, pp. 10–16, 2018.

[191] Y. Nie, G. Chen, H. Peng, S. Tang, Z. Zhou, F. Pei, and B. Shen, "In vitro and 48 weeks in vivo performances of 3D printed porous Fe-30Mn biodegradable scaffolds," *Acta Biomaterialia*, vol. 121, pp. 724–740, 2021.

[192] M. Fantanariu, L. C. Trinca, C. Solcan, A. Trofin, S. Strungaru, E. V. Sindilar, G. Plavan, and S. Stanciu, "A new Fe-Mn-Si alloplastic biomaterial as bone grafting material: In vivo study," *Applied Surface Science*, vol. 352, pp. 129–139, 2015.

[193] A. H. M. Sanchez, B. J. Luthringer, F. Feyerabend, and R. Willumeit, "Mg and Mg alloys: How comparable are in vitro and in vivo corrosion rates? A review," *Acta Biomaterialia*, vol. 13, pp. 16–31, 2015.

[194] M. Schinhammer, C. M. Pecnik, F. Rechberger, A. C. Hänzi, J. F. Löffler, and P. J. Uggowitzer, "Recrystallization behavior, microstructure evolution and mechanical properties of biodegradable Fe-Mn-C(-Pd) TWIP alloys," *Acta Materialia*, vol. 60, no. 6-7, pp. 2746–2756, 2012.

[195] H. Danninger, R. de Oro Calderon, and C. Gierl-Mayer, "Powder Metallurgy and Sintered Materials," *Ullmann's Encyclopedia of Industrial Chemistry*, pp. 1–57, 2017.

[196] H. E. Exner and E. Arzt, "Sintering Processes," in *Sintering Key Papers*, pp. 1885–1912, Elsevier Science Publisher BV, 1990.

[197] Scientific Group Thermodata Europe, "Ag-Fe phase diagram," 2017. https://shorturl.at/owMNV.

[198] Scientific Group Thermodata Europe, "Ag-Mn phase diagram," 2011. https://shorturl.at/hGW57.

[199] P. Quadbeck, G. Stephani, K. Kümmel, J. Adler, and G. Standke, "Synthesis and Properties of Open-Celled Metal Foams," *Materials Science Forum*, vol. 534-536, pp. 1005–1008, 2007.

[200] P. Quadbeck, R. Hauser, K. Kümmel, G. Standke, G. Stephani, B. Nies, S. Rößler, and B. Wegener, "Iron based cellular metals for degradable synthetic bone replace-ment," in *Proceedings of the World Powder Metallurgy Congress and Exhibition, World PM 2010*, vol. 4, 2010.

[201] P. Quadbeck, K. Kümmel, R. Hauser, G. Standke, J. Adler, G. Stephani, and B. Kieback, "Structural and material design of open-cell powder metallurgical foams," *Advanced Engineering Materials*, vol. 13, no. 11, pp. 1024–1030, 2011.

[202] R. Alavi, A. Trenggono, S. Champagne, and H. Hermawan, "Investigation on mechanical behavior of biodegradable iron foams under different compression test conditions," *Metals*, vol. 7, no. 6, 2017.

[203] R. Oriňáková, A. Oriňák, L. M. Bučková, M. Giretová, L. Medveckỳ, E. Labbanczová, M. Kupková, M. Hrubovčáková, and K. Koval, "Iron based degradable foam structures for potential orthopedic applications," *International Journal of Electrochemical Science*, vol. 8, no. 12, pp. 12451–12465, 2013.

[204] P. Sharma and P. M. Pandey, "A novel manufacturing route for the fabrication of topologically-ordered open-cell porous iron scaffold," *Materials Letters*, vol. 222, pp. 160–163, 2018.

[205] A. Šalak and M. Selecká, *Manganese in powder metallurgy steels*. Springer, 2012.

[206] University of Cambridge, "The Ellingham Diagram," 2008. https://shorturl.at/iPZ48.

[207] E. Hryha and J. Wendel, "Effect of heating rate and process atmosphere on the thermodynamics and kinetics of the sintering of pre-alloyed water-atomized powder metallurgy steels," *Journal of the American Ceramic Society*, vol. 102, no. 2, pp. 748–756, 2019.

[208] C. Gierl-Mayer, R. De Oro Calderon, and H. Danninger, "Sintering of ferrous metallic compacts: Chemical reactions that involve interstitial elements," *Journal of the American Ceramic Society*, vol. 102, no. 2, pp. 695–705, 2018.

[209] R. de Oro Calderon, C. Gierl-Mayer, and H. Danninger, "Application of thermal analysis techniques to study the oxidation/reduction phenomena during sintering of steels containing oxygen-sensitive alloying elements," *Journal of Thermal Analysis and Calorimetry*, vol. 127, no. 1, pp. 91–105, 2017.

[210] R. de Oro Calderon, C. Gierl-Mayer, and H. Danninger, "Master alloys in powder metallurgy: the challenge of exploring new alloying compositions," *Powder Metallurgy*, vol. 60, no. 2, pp. 86–96, 2017.

[211] E. Hryha, E. Dudrova, and L. Nyborg, "Critical aspects of alloying of sintered steels with manganese," *Metallurgical and Materials Transactions A: Physical Metallurgy and Materials Science*, vol. 41, no. 11, pp. 2880–2897, 2010.

[212] P. Quadbeck, B. Schreyer, A. Strauß, T. Weißgärber, and B. Kieback, "In-situ monitoring of gas atmospheres during debinding and sintering of PM steel components," *Proceedings of the World Powder Metallurgy Congress and Exhibition, World PM 2010*, vol. 2, 2010.

[213] R. de Oro Calderon, C. Gierl-mayer, and H. Danninger, "Interstitial chemistry in sintering of metallic materials – often overlooked but decisive," *European Journal of Materials*, vol. 2, no. 1, pp. 381–406, 2022.

[214] H. Danninger, C. Gierl, S. Kremel, G. Leitner, and Y. Yu, "Degassing And Deoxidation Processes During Sintering Of Unalloyed And Alloyed Pm Steels," *Powder Metallurgy Progress*, vol. 2, no. 3, pp. 125–140, 2002.

[215] A. Cias, S. C. Mitchell, K. Pilch, H. Cias, M. Sulowski, and A. S. Wronski, "Tensile properties of Fe-3Mn-0.6/0.7C steels sintered in semiclosed containers in dry hydrogen, nitrogen and mixtures thereof," *Powder Metallurgy*, vol. 46, no. 2, pp. 165–170, 2003.

[216] A. Cias, "A novel method of sintering hybrid steels in an improved semiclosed container system," *Science of Sintering*, vol. 45, no. 3, pp. 379–383, 2013.

[217] A. Cias, "Microatmosphere Sintering of Cr–Mn Steel In Furnace Atmospheres of Flowing Hydrogen and Technical Nitrogen," *Powder Metallurgy and Metal Ceramics*, vol. 54, no. 11-12, pp. 641–651, 2016.

[218] H. Danninger, R. Pöttschacher, S. Bradac, A. Šalak, and J. Seyrkammer, "Comparison of Mn, Cr and Mo alloyed sintered steels prepared from elemental powders," *Powder Metallurgy*, vol. 48, no. 1, pp. 23–32, 2005.

[219] K. Lu, C.-f. Huo, Y. He, J. Yin, J. Liu, and Q. Peng, "Grain Boundary Plays a Key Role in Carbon Diffusion in Carbon Irons Revealed by a ReaxFF Study," *The Journal of Physical Chemistry C*, vol. 122, pp. 23191–23199, 2018.

[220] R. Oro, E. Hryha, M. Campos, and J. M. Torralba, "Effect of processing conditions on microstructural features in Mn-Si sintered steels," *Materials Characterization*, vol. 95, pp. 105–117, 2014.

[221] H. Danninger, C. Gierl-Mayer, M. Prokofyev, M. C. Huemer, R. de Oro Calderon, R. Hellein, A. Müller, and G. Stetina, "Manganese–a promising element also in high alloy sintered steels," *Powder Metallurgy*, vol. 64, no. 2, pp. 115–125, 2021.

[222] E. Hryha and L. Nyborg, "Oxide transformation in Cr-Mn-prealloyed sintered steels: Thermodynamic and kinetic aspects," *Metallurgical and Materials Transactions A: Physical Metallurgy and Materials Science*, vol. 45, no. 4, pp. 1736–1747, 2014.

[223] B. Wegener, M. Behnke, S. Milz, V. Jansson, C. Redlich, W. Hermanns, C. Birkenmaier, K. Pieper, T. Weißgärber, and P. Quadbeck, "Local and systemic inflammation after implantation of a novel iron based porous degradable bone replacement material in sheep model," *Scientific Reports*, vol. 11, no. 1, pp. 1–12, 2021.

[224] J. Čapek, D. Vojtěch, and A. Oborná, "Microstructural and mechanical properties of biodegradable iron foam prepared by powder metallurgy," *Materials and Design*, vol. 83, pp. 468–482, 2015.

[225] C. Yang, Z. Huan, X. Wang, C. Wu, and J. Chang, "3D Printed Fe Scaffolds with HA Nanocoating for Bone Regeneration," *ACS Biomaterials Science and Engineering*, vol. 4, no. 2, pp. 608–616, 2018.

[226] N. E. Putra, M. A. Leeflang, M. Minneboo, P. Taheri, L. E. Fratila-Apachitei, J. M. Mol, J. Zhou, and A. A. Zadpoor, "Extrusion-based 3D printed biodegradable porous iron," *Acta Biomaterialia*, vol. 121, pp. 741–756, 2021.

[227] N. E. Putra, M. A. Leeflang, P. Taheri, L. E. Fratila-Apachitei, J. M. Mol, J. Zhou, and A. A. Zadpoor, "Extrusion-based 3D printing of ex situ-alloyed highly biodegradable MRI-friendly porous iron-manganese scaffolds," *Acta Biomaterialia*, vol. 134, pp. 774–790, 2021.

[228] N. Putra, A. Tigrine, S. Aksakal, V. de la Rosa, P. Taheri, L. Fratila-Apachitei, J. Mol, J. Zhou, and A. Zadpoor, "Poly(2-ethyl-2-oxazoline) coating of additively manufactured biodegradable porous iron," *Materials Science and Engineering: C*, 2021.

[229] P. Sharma and P. M. Pandey, "Morphological and mechanical characterization of topologically ordered open cell porous iron foam fabricated using 3D printing and pressureless microwave sintering," *Materials and Design*, vol. 160, pp. 442–454, 2018.

[230] P. Sharma and P. M. Pandey, "Corrosion behaviour of the porous iron scaffold in simulated body fluid for biodegradable implant application," *Materials Science and Engineering C*, vol. 99, 2019.

[231] P. Sharma and P. M. Pandey, "Rapid manufacturing of biodegradable pure iron scaffold using amalgamation of three-dimensional printing and pressureless microwave sintering," *Proceedings of the Institution of Mechanical Engineers, Part C: Journal of Mechanical Engineering Science*, vol. 233, no. 6, pp. 1876–1895, 2019.

[232] P. Sharma, K. G. Jain, P. M. Pandey, and S. Mohanty, "In vitro degradation behaviour, cytocompatibility and hemocompatibility of topologically ordered porous iron scaffold prepared using 3D printing and pressureless microwave sintering," *Materials Science and Engineering C*, vol. 106, 2020.

[233] Y. Li, H. Jahr, K. Lietaert, P. Pavanram, A. Yilmaz, L. I. Fockaert, M. A. Leeflang, B. Pouran, Y. Gonzalez-Garcia, H. Weinans, J. M. Mol, J. Zhou, and A. A. Zadpoor, "Additively manufactured biodegradable porous iron," *Acta Biomaterialia*, vol. 77, pp. 380–393, 2018.

[234] Y. Li, K. Lietaert, W. Li, X. Y. Zhang, M. A. Leeflang, J. Zhou, and A. A. Zadpoor, "Corrosion fatigue behavior of additively manufactured biodegradable porous iron," *Corrosion Science*, vol. 156, pp. 106–116, 2019.

[235] Y. Li, J. Yan, W. Zhou, P. Xiong, P. Wang, W. Yuan, Y. Zheng, and Y. Cheng, "In vitro degradation and biocompatibility evaluation of typical biodegradable metals (Mg/Zn/Fe) for the application of tracheobronchial stenosis," *Bioactive Materials*, vol. 4, pp. 114–119, 2019.

[236] D. Carluccio, A. G. Demir, L. Caprio, B. Previtali, M. J. Bermingham, and M. S. Dargusch, "The influence of laser processing parameters on the densification and surface morphology of pure Fe and Fe-35Mn scaffolds produced by selective laser melting," *Journal of Manufacturing Processes*, vol. 40, no. November 2018, pp. 113–121, 2019.

[237] D. Carluccio, M. Bermingham, M. S. Dargusch, A. G. Demir, L. Caprio, and B. Previtali, "Selective laser melting Fe and Fe-35Mn for biodegradable implants," *International Journal of Modern Physics B*, vol. 34, no. 1-3, pp. 1–7, 2020.

[238] M. Otto, S. Pilz, A. Gebert, U. Kühn, and J. Hufenbach, "Effect of build orientation on the microstructure, mechanical and corrosion properties of a biodegradable high manganese steel processed by laser powder bed fusion," *Metals*, vol. 11, no. 6, 2021.

[239] Č. Donik, J. Kraner, A. Kocijan, I. Paulin, and M. Godec, "Evolution of the ϵ and γ phases in biodegradable Fe–Mn alloys produced using laser powder-bed fusion," *Scientific Reports*, vol. 11, dec 2021.

[240] "ASTM G59 - 97: Conducting Potentiodynamic Polarization Resistance Measurements," 2003.

[241] I. Puigdomenech, "Hydra-Medusa Software," 2016. https://www.kth.se/che/medusa/.

[242] N. Fogh-Andersen, B. M. Altura, B. T. Altura, and O. Siggaard-Andersen, "Composition of interstitial fluid," *Clinical Chemistry*, vol. 41, no. 10, pp. 1522–1525, 1995.

[243] Thermofisher Scientific, "Balanced Salt Solutions," 2022. https://shorturl.at/fnswL.

[244] D. Watkinson and M. T. Lewis, "Desiccated storage of chloride-contaminated archaeological iron objects," *Studies in Conservation*, vol. 50, no. 4, pp. 241–252, 2005.

[245] M. J. Sultana, *Optimisation of powder processing for non-magnetic Fe-Mn and Fe-Mn-Ag biodegradable scaffolds*. M.sc., University of Malta, 2021.

[246] A. Curmi, *Biodegradable Iron-based Scaffolds: Developing a Replication Method using Additive Manufacturing*. B.eng., University of Malta, 2020.

[247] E. Galea, *Additive Manufacturing of Polymeric Templates to Manufacture Biodegradable Bone Scaffolds*. M.sc., University of Malta, 2022.

[248] P. S. Bagha, M. Khakbiz, S. Sheibani, S. Ebrahimi-Barough, and H. Hermawan, "In Vitro Degradation, Hemocompatibility, and Cytocompatibility of Nanostructured Absorbable Fe-Mn-Ag Alloys for Biomedical Application," *ACS Biomaterials Science and Engineering*, vol. 6, no. 4, pp. 2094–2106, 2020.

[249] J. Hu, S. A. Cao, and J. Xie, "EIS study on the corrosion behavior of rusted carbon steel in 3% NaCl solution," *Anti-Corrosion Methods and Materials*, vol. 60, no. 2, pp. 100–105, 2013.

[250] F. L. Nie, Y. F. Zheng, S. C. Wei, C. Hu, and G. Yang, "In vitro corrosion, cytotoxicity and hemocompatibility of bulk nanocrystalline pure iron," *Biomedical Materials*, vol. 5, no. 6, 2010.

[251] L. M. de Andrade, C. Paternoster, P. Chevallier, S. Gambaro, P. Mengucci, and D. Mantovani, "Surface processing for iron-based degradable alloys: A preliminary study on the importance of acid pickling," *Bioactive Materials*, vol. 11, no. October 2020, pp. 166–180, 2022.

[252] E. Bayol, K. Kayakirilmaz, and M. Erbil, "The inhibitive effect of hexamethylenetetramine on the acid corrosion of steel," *Materials Chemistry and Physics*, vol. 104, no. 1, pp. 74–82, 2007.

[253] Z. Yu, Q. Huang, W. Zhang, C. Luo, H. Guan, Y. Chen, H. Song, Z. Hu, and C. Luc, "Effect of Sn content on the mechanical properties and corrosion behavior of Mg-3Al-xSn alloys," *Materials Research Express*, vol. 7, no. 7, pp. 0–14, 2020.

[254] J. Grdadolnik and Y. Maréchal, "Bovine serum albumin observed by infrared spectrometry. II. Hydration mechanisms and interaction configurations of Embedded h2o molecules," *Biopolymers - Biospectroscopy Section*, vol. 62, no. 1, pp. 54–67, 2001.

[255] M. Hoseinpoor, M. Momeni, M. H. Moayed, and A. Davoodi, "EIS assessment of critical pitting temperature of 2205 duplex stainless steel in acidified ferric chloride solution," *Corrosion Science*, vol. 80, pp. 197–204, 2014.

[256] M. Testa-Anta, M. A. Ramos-Docampo, M. Comesaña-Hermo, B. Rivas-Murias, and V. Salgueiriño, "Raman spectroscopy to unravel the magnetic properties of iron oxide nanocrystals for bio-related applications," *Nanoscale Advances*, vol. 1, no. 6, pp. 2086–2103, 2019.

[257] Aqion, "Table of Diffusion Coefficients," 2015. https://www.aqion.de/site/194#fn:1.

[258] P. A. Marques, A. P. Serro, B. J. Saramago, A. C. Fernandes, M. C. Magalhães, and R. N. Correia, "Mineralisation of two phosphate ceramics in HBSS: Role of albumin," *Biomaterials*, vol. 24, no. 3, pp. 451–460, 2003.

[259] E. Stathopoulou, T. Theodoropoulou, and N. Phoca Cosmetatou, "Black fish bones in waterlogged deposits: The case of the Neolithic lake settlement of Dispilio, Greece," *Archaeofauna*, vol. 22, pp. 51–74, 2013.

[260] N. Safaie, M. Khakbiz, S. Sheibani, and P. S. Bagha, "Synthesizing of Nanostructured Fe-Mn Alloys by Mechanical Alloying Process," *Procedia Materials Science*, vol. 11, pp. 381–385, 2015.

[261] R. Schroeder, A. I. R. Filho, C. Binder, and A. N. Klein, "Adjusting the sintering cycle of a hadfield sintered steel produced by metal injection molding," *Materials Research*, vol. 18, pp. 83–90, 2015.

[262] X. Sun, E. Feng, Y. Su, K. Nemkovski, O. Petracic, and T. Brückel, "Magnetic properties and spin structure of MnO single crystal and powder," *Journal of Physics: Conference Series*, vol. 862, no. 1, 2017.

[263] H. Dierkes and R. Dronskowski, "High-resolution powder neutron diffraction on Mn3C," *Zeitschrift fur Anorganische und Allgemeine Chemie*, vol. 640, no. 15, pp. 3148–3152, 2014.

[264] Y. Feng, J. Fornell, H. Zhang, P. Solsona, M. D. Baró, S. Suriñach, E. Pellicer, and J. Sort, "Synthesis of α-Fe2O3 and Fe-Mn oxide foams with highly tunable magnetic properties by the replication method from polyurethane templates," *Materials*, vol. 11, no. 2, 2018.

[265] E. Hryha and E. Dudrova, "The sintering behaviour of Fe-Mn-C powder system, correlation between thermodynamics and sintering process, Mn distribution, and microstructure," *Materials Science Forum*, vol. 534-536, pp. 761–764, 2007.

[266] P. K. Johnston, E. Doyle, and R. A. Orzel, "Acrylics: A Literature Review of Thermal Decomposition Products and Toxicity," *International Journal of Toxicology*, vol. 7, no. 2, pp. 139–200, 1988.

[267] C. Suryanarayana, "Mechanical alloying and milling," *Progress in Materials Science*, vol. 46, no. 1-2, pp. 1–184, 2001.

Appendix A

EIS fitted data

A.1 Phase One

Table A.1: Complete fitting results for Fe in HBSS+Ca.

Fe in HBSS+Ca									
Time	$\mathbf{R_s}$ **[Ω.cm²]**	$\mathbf{R_{ct}}$ **[Ω.cm²]**	$\mathbf{CPE_{dl}}$ **[μS.s^{adl}/cm²]**	$\mathbf{a_{dl}}$	$\mathbf{R_{layer}}$ **[Ω.cm²]**	$\mathbf{CPE_{layer}}$ **[μS.s^{alayer}/cm²]**	$\mathbf{a_{layer}}$	χ^2	$\mathbf{C_{layer}}$ **[μF/cm²]**
0.47	18.1	3189	197	0.705	15.8	137	0.696	1.2E-04	9.39
0.70	18.4	3916	196	0.725	15.2	89	0.718	8.2E-05	6.65
0.93	18.2	4536	191	0.729	18.7	79	0.717	1.4E-04	6.03
1.17	18.0	4180	182	0.733	21.8	78	0.714	2.1E-04	6.06
1.42	18.0	3799	171	0.737	24.1	80	0.715	2.8E-04	6.62
1.65	18.1	4002	165	0.739	28.7	79	0.708	3.2E-04	6.41
1.90	18.6	4034	159	0.738	32.5	81	0.702	3.4E-04	6.51
2.13	18.5	4270	156	0.740	37.0	80	0.694	3.5E-04	6.14
2.38	18.4	4470	151	0.742	42.9	81	0.685	3.0E-04	5.99
2.63	18.3	4607	149	0.741	49.4	82	0.678	2.8E-04	5.99
2.87	18.3	4741	146	0.743	55.4	83	0.672	2.6E-04	6.00
3.12	18.3	4856	144	0.740	60.5	84	0.669	2.6E-04	6.16
5.12	17.7	5103	153	0.739	78.5	78	0.658	1.7E-04	5.52
7.13	18.0	5898	154	0.729	103.3	76	0.658	1.6E-04	6.12
9.13	17.7	6579	160	0.732	117.2	64	0.662	1.5E-04	5.26
11.13	17.5	7090	163	0.731	131.4	53	0.672	1.4E-04	4.69
13.13	17.4	8009	165	0.731	146.2	45	0.680	1.6E-04	4.23
15.13	17.5	9235	167	0.729	163.9	39	0.688	1.7E-04	3.94
17.13	17.5	11100	168	0.727	186.1	34	0.693	2.0E-04	3.61
19.13	17.5	13110	167	0.725	204.0	31	0.699	2.3E-04	3.50
21.13	17.6	15130	164	0.724	228.6	28	0.705	2.7E-04	3.38
23.13	17.4	16514	160	0.725	240.2	26	0.709	2.7E-04	3.24
24.00	17.4	18231	161	0.722	246.0	25	0.711	2.9E-04	3.16

Table A.2: Complete fitting results for FeMn in HBSS+Ca.

FeMn in HBSS+Ca									
Time	$\mathbf{R_s}$ **[Ω.cm²]**	$\mathbf{R_{ct}}$ **[Ω.cm²]**	$\mathbf{CPE_{dl}}$ **[μS.s^{adl}/cm²]**	$\mathbf{a_{dl}}$	$\mathbf{R_{layer}}$ **[Ω.cm²]**	$\mathbf{CPE_{layer}}$ **[μS.s^{alayer}/cm²]**	$\mathbf{a_{layer}}$	$\mathbf{\chi^2}$	$\mathbf{C_{layer}}$ **[μF/cm²]**
0.47	18.2	210	4059	0.353	38.4	10.4	0.779	4.7E-06	1.13
0.70	17.7	269	3815	0.343	47.6	9.3	0.785	6.1E-06	1.12
0.93	17.6	267	3017	0.364	56.7	8.6	0.786	8.7E-06	1.08
1.17	17.2	275	2434	0.382	67.2	8.9	0.779	9.9E-06	1.08
1.42	16.9	277	1826	0.408	75.7	8.9	0.778	9.1E-06	1.11
1.65	16.9	306	1529	0.419	88.7	8.6	0.782	1.0E-05	1.16
1.90	17.0	333	1272	0.433	100.1	8.2	0.786	1.1E-05	1.18
2.13	17.0	352	1071	0.451	113.4	8.1	0.786	1.2E-05	1.21
2.38	17.0	387	919	0.461	124.5	7.8	0.789	1.6E-05	1.22
2.63	17.0	421	790	0.475	139.6	7.6	0.790	1.7E-05	1.23
2.87	17.0	491	731	0.468	147.2	7.2	0.794	3.7E-05	1.22
3.12	17.0	528	654	0.478	160.9	7.0	0.795	3.8E-05	1.22
5.12	17.0	1094	276	0.550	278.8	6.9	0.790	4.4E-05	1.31
7.13	16.6	2558	180	0.568	322.5	6.4	0.796	1.7E-04	1.31
9.13	16.8	5050	139	0.580	449.8	5.8	0.801	1.8E-04	1.32
11.13	16.6	6957	131	0.583	456.4	5.6	0.802	2.1E-04	1.28
13.13	16.4	7946	125	0.583	493.8	5.3	0.805	2.2E-04	1.26
15.13	16.3	8474	120	0.585	508.8	5.2	0.807	2.3E-04	1.26
17.13	16.2	9095	115	0.585	533.8	5.2	0.807	2.3E-04	1.27
19.13	16.4	9282	110	0.585	539.8	5.5	0.803	2.3E-04	1.32
21.13	16.4	9523	106	0.582	535.0	6.1	0.796	2.1E-04	1.41
23.13	16.3	9161	99	0.587	523.3	7.8	0.779	1.6E-04	1.64
24.00	16.5	9511	98	0.580	528.9	7.7	0.780	1.8E-04	1.63

Table A.3: Complete fitting results for FeMnAg in HBSS+Ca.

FeMnAg in HBSS+Ca									
Time	$\mathbf{R_s}$ **[Ω.cm²]**	$\mathbf{R_{ct}}$ **[Ω.cm²]**	$\mathbf{CPE_{dl}}$ **[μS.s^{adl}/cm²]**	$\mathbf{a_{dl}}$	$\mathbf{R_{layer}}$ **[Ω.cm²]**	$\mathbf{CPE_{layer}}$ **[μS.s^{alayer}/cm²]**	$\mathbf{a_{layer}}$	χ^2	$\mathbf{C_{layer}}$ **[μF/cm²]**
0.47	18.3	140	3059	0.437	44.3	22	0.700	1.1E-05	1.13
0.70	18.7	236	2435	0.426	70.9	22	0.695	2.7E-05	1.29
0.93	19.0	329	1963	0.418	90.1	14	0.722	3.6E-05	1.07
1.17	19.1	381	1741	0.426	114.2	10	0.734	3.9E-05	0.86
1.42	19.2	430	1372	0.445	143.0	9	0.738	4.2E-05	0.85
1.65	18.9	492	1080	0.460	162.9	11	0.730	7.0E-05	1.06
1.90	18.7	540	801	0.490	182.5	11	0.729	9.0E-05	1.09
2.13	18.4	619	649	0.503	203.4	12	0.730	1.0E-04	1.30
2.38	18.4	735	514	0.520	220.2	11	0.733	1.0E-04	1.23
2.63	18.4	729	499	0.519	253.1	11	0.740	1.1E-04	1.39
2.87	18.5	860	397	0.539	268.3	11	0.742	1.1E-04	1.45
3.12	18.4	1014	361	0.537	281.1	10	0.746	1.1E-04	1.35
5.12	17.6	1826	208	0.566	379.7	9	0.765	9.6E-05	1.57
7.13	17.6	4080	157	0.566	443.8	8	0.774	1.2E-04	1.54
9.13	17.5	7011	148	0.556	454.8	8	0.777	1.3E-04	1.60
11.13	17.4	9480	143	0.540	398.5	9	0.773	8.7E-05	1.72
13.13	16.2	10266	83	0.496	368.4	54	0.636	9.2E-05	5.74
15.13	16.1	7822	16	0.708	46.6	102	0.593	1.8E-04	2.60
17.13	16.4	6852	24	0.740	28.8	95	0.603	2.4E-04	1.95
19.13	16.6	6826	22	0.750	29.9	95	0.604	2.3E-04	2.03
21.13	16.2	5375	49	0.698	21.7	68	0.623	1.9E-04	1.32
23.13	16.2	4870	57	0.686	22.3	63	0.626	1.7E-05	1.25
24.00	16.2	4987	40	0.719	27.7	85	0.606	2.4E-04	1.66